Modelización en diseño de fármacos: Exploración conformacional de ligandos y diseño de inhibidores multipotentes

Jordi Juárez Jiménez

Aquesta tesi doctoral està subjecta a la llicència ***Reconeixement- NoComercial – CompartirIgual 3.0. Espanya de Creative Commons***.

Esta tesis doctoral está sujeta a la licencia ***Reconocimiento - NoComercial – CompartirIgual 3.0. España de Creative*** **Commons**.

This doctoral thesis is licensed under the ***Creative Commons Attribution-NonCommercial-ShareAlike 3.0. Spain License***.

Universitat de Barcelona

MODELIZACIÓN EN DISEÑO DE FÁRMACOS:

EXPLORACIÓN CONFORMACIONAL DE LIGANDOS Y DISEÑO DE INHIBIDORES MULTIPOTENTES

JORDI JUÁREZ JIMÉNEZ

2014

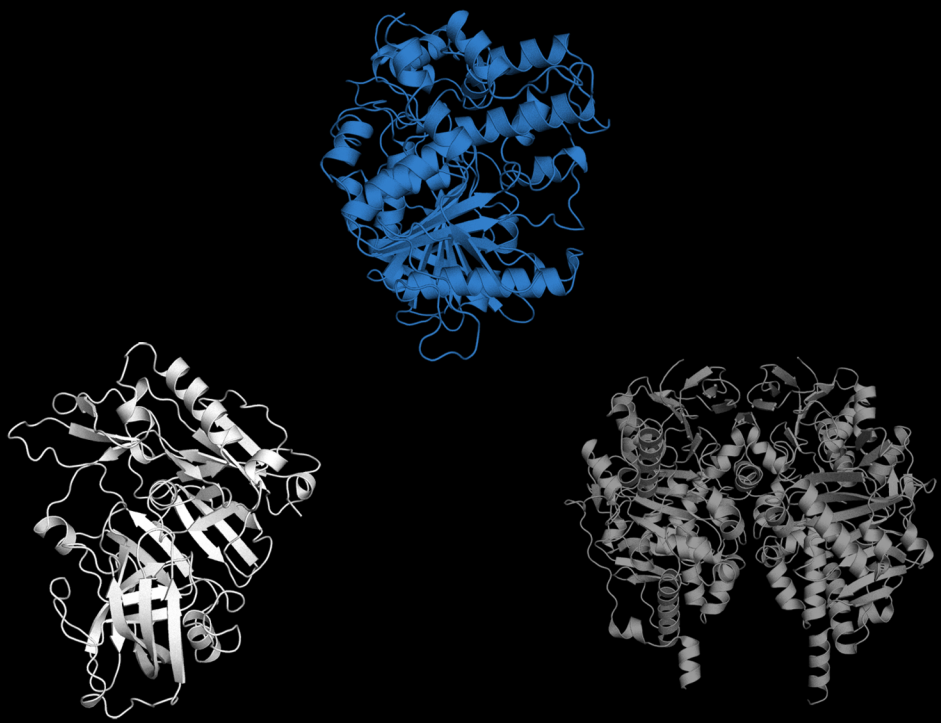

Universitat de Barcelona

Departament de Fisicoquímica
Facultat de Farmàcia
Universitat de Barcelona

MODELIZACIÓN EN DISEÑO DE FÁRMACOS: EXPLORACIÓN CONFORMACIONAL DE LIGANDOS Y DISEÑO DE INHIBIDORES MULTIPOTENTES

Jordi Juárez Jiménez
Barcelona, 2014

Departament de Fisicoquímica
Facultat de Farmàcia
Universitat de Barcelona

Programa de doctorado de Biomedicina
Bienio 2011 - 2012

MODELIZACIÓN EN DISEÑO DE FÁRMACOS: EXPLORACIÓN CONFORMACIONAL DE LIGANDOS Y DISEÑO DE INHIBIDORES MULTIPOTENTES

2014

Memoria presentada por Jordi Juárez Jiménez
para optar al título de Doctor por la Universitat de Barcelona

Dirigida por:

Dr. F. Javier Luque Garriga

Dr. Ramon Pouplana i Solé

Jordi Juárez Jiménez
Barcelona, 2014

A mi padre,
te echo de menos.

El placer más noble
es el júbilo de comprender.

Atribuida a Leonardo da Vinci
(1452-1519 arquitecto, músico, inventor,
ingeniero, pintor y escultor)

Han pasado cinco años desde que me senté por primera vez delante de una terminal Linux. Cinco años llenos de experiencias, anécdotas, penas y alegrías; decepciones y euforias, pero, por encima de todo, llenos de gente estupenda. A vosotros, a los que, sabiéndolo o no, me habéis ayudado a sacar adelante esta tesis, gracias de corazón. Lo que viene a continuación es una mención especial de aquellos a los que recuerdo en este momento y, si me dejo a alguien, por favor no os enfadéis, mi memoria ya sabéis…

En primer lugar quisiera agradecer a mis directores el Prof. F Javier Luque y el Prof. Ramon Pouplana que me brindaran la oportunidad de realizar con ellos mi tesis doctoral. Ramon, gracias por tu apoyo, enseñanzas, tu mirada crítica, tu sentido del humor e inverosímiles teorías. Javi, esta tesis no existiría sin tu orientación y enseñanzas: gracias por tu interés, por inculcarme la pasión por el trabajo bien hecho, por guiarme durante estos años de aprendizaje y, sobretodo gracias por ser un gran científico pero aún mejor persona. De corazón, siempre será un orgullo hayáis sido mis directores de tesis.

Mi paso por el laboratorio no hubiera sido el mismo sin la gente que he encontrado allí, porque todos me han enseñado algo, incluso aquellos que vinieron a aprender. Especialmente me gustaría dar las gracias en (no) estricto orden de aparición:

A la "vieja guardia": a Jordi Muñoz por convencerme de que el *Palomar Park* era un gran sitio para hacer la tesis. A Xavi por su cercanía y por actuar como director "en funciones" cuando la situación lo requería. A Carles (Curu), por toda tu ayuda (eres la Gaussianpedia) tu optimismo contagioso y por demostrarme que con trabajo duro, ganas y una sonrisa se puede llegar lejos. A Ignacio por iniciarme en la quántica y en "eso" llamado python. Por último, pero no menos importante, gracias Axel, por enseñarme, por ser el modelo a seguir y porque, entre tantos aspavientos, nunca hay un "no" a ayudar. A "los que llegaron antes": Óscar, Jesús, Peter y Moussumi, por facilitar mi llegada al laboratorio y responder las preguntas de este pipiolo y a "los que llegaron durante": Dani, Sergi, Ana, Yvonne, Montse, Aida, Laura, Elena, Kevin y casi, casi al final, William y Sonia, por el buen rollo y el gran ambiente de trabajo. Gracias también a los profesores del departamento de Fisicoquímica de la Facultad de Farmacia, en especial a Campa, Yolanda y Assumpta por los buenos ratos compartidos a la hora de comer.

Existen tres grupos de los que guardo un recuerdo especial: en primer lugar aquellos que han visitado el laboratorio, porque los buenos ratos pasados con ellos han contribuido a mi formación como científico y también como persona. Especial mención a los que más tiempo estuvieron aquí: Adrian, por su visión ácida de la ciencia y por enseñarme muchas cosas (como que los profesores también juegan a futbol) y Lula (y Leandro), porque juntos vivimos un

periodo de grandes cambios en mi vida y a vuestro lado fue muy fácil. No quiero olvidarme, sin embargo, de aquellos que pasaron menos tiempo y espero no dejarme a nadie: Lucas, Vicky, Pau, Marie, Peter, Pablo, Marcelo, Darío, Adrian T. y Antonio. En segundo lugar, guardo gran recuerdo de aquellos a los que he tenido el placer de enseñar durante estos cinco años: Sadiel, Esther, Daniel, Nelson (¡Agivaaa!), Javi y Toni. Gracias por vuestro interés y vuestro trabajo, de todos he aprendido y sigo aprendiendo. En tercer lugar, esta tesis hubiera sido imposible sin la colaboración de los grupos experimentales: a Santi, Diego, Irene(s), Eli, Matías, Marta(s), Eva, Mercedes, Rona y, en general, a todos aquellos con los que he tenido el placer de colaborar, os doy las gracias de corazón.

Desidero ringraziare il Prof. Andrea Cavalli e tutti coloro che lavorano nel suo gruppo presso l'Universita' Alma Mater Studiorum di Bologna, per averci accolto e trattato come due di loro. Grazie mille a Gianpaolo, Maria, Rosa, Federico, Mattia, Elisa e Dario. Un grazie speciale va a Matteo, non solo per la pazienza con cui ci ha guidati sul lavoro ma anche e, soprattutto, per essersi preso cura di noi durante dei momenti difficili.

Quiero dar las gracias también a esos compañeros que, a base de compartir horas de trabajo, se convierten en amigos: gracias a Carles, por ser un buen amigo, honesto y divertido con el que es fácil trabajar (excepto los días en los que no le apetece) y a Flavio, por su visión *optimística* de la vida y por las conversaciones *trans, meta y orto cendentes*. Gracias a Ornella por sus ganas de aprender, su simpatía y su risa contagiosa; a [l'energúmen de] Constantí, por las risas y las conversaciones gorileras y a "Los Ángeles de Charlie" (Andreana, Marina y Sylvana) por su espontaneidad, honestidad y por traer aire fresco al laboratorio. Gracias también a la persona que más me ha costado de situar, porque vino por un tiempo, vino a aprender y acabo quedándose y enseñándome que se debe ser feliz: Carol eres una de mis más queridas amigas.

También todo mi agradecimiento a las personas que, sin relación directa con esta tesis, tantísimo me han acompañado, corregido cuando era necesario, ayudado y sobretodo apoyado: mis padres, mis hermanos, mi *iaia* y toda mi familia, incluida la mejor suegra que se puede tener; el *Dream Farmateam* (Yoli, Edu, Silvia, Lorena, Eli, Sabin, Noelia, Xavi y Paula) y los amigos que llegaron poco a poco a mi vida, que siguen ahí a pesar de los años y que son indispensables (Bernat, Edu, Clara, Judith, Laura, Joan y Dani) .

Por último, gracias a la persona más especial. Salo eres lo mejor que me ha pasado, gracias por tu apoyo y cariño, nunca pensé que podría compartir mi vida con alguien como tú. Han sido tres años maravillosos y creo de verdad que lo mejor está por llegar.

El trabajo de modelización reflejado en esta memoria ha sido realizado en el Laboratorio de Biología Computacional y Diseño de Fármacos del Departamento de Fisicoquímica de la Facultad de Farmacia de la Universidad de Barcelona bajo la dirección de los doctores F. Javier Luque y Ramón Pouplana.

Quiero expresar mi gratitud al Instituto de Salud Carlos III (Ministerio de Economía y Competitividad) por la concesión de una ayuda *Predoctoral de Formación en Investigación en Salud* para la realización de esta Tesis Doctoral.

El presente trabajo ha sido financiado por el Ministerio de Ciencia e Innovación (SAF2008-05595), el Ministerio de Economía y Competitividad (SAF2011-27642) y la Generalitat de Catalunya (2009SGR249 y 2014SGR1189).

Los recursos computacionales han sido proporcionados por el *Barcelona Supercomputing Center* (BSC) y el *Consorci de Serveis Universitaris de Catalunya* (CSUC).

Prólogo

La presente Tesis Doctoral se presenta como compendio de publicaciones. De acuerdo a la normativa vigente se ha dividido en 5 capítulos que incluyen los apartados de Introducción, Objetivos, Discusión, Resumen global de resultados y Conclusiones. Los dos últimos se han redactado en inglés para optar al título de Doctor con Mención Internacional. Para mayor claridad, la discusión de los resultados correspondiente al trabajo metodológico se acomete de forma separada de la discusión correspondiente a los estudios de modelización aplicada.

El capítulo 1 contiene la introducción de la tesis, que a su vez se desglosa en tres partes. La primera versa sobre los aspectos generales del reconocimiento molecular y la modelización aplicada al diseño de fármacos. La segunda expone el fundamento teórico y los antecedentes en el desarrollo de la metodología Multinivel para la exploración conformacional de fármacos y pequeñas moléculas orgánicas. Finalmente, la tercera acomete una breve presentación sobre la enfermedad de Alzheimer y las estrategias terapéuticas actuales y en vías de desarrollo.

El capítulo 2 presenta los objetivos planteados en la presente Tesis Doctoral.

En el capítulo 3 se incluye la publicación "*Assessing the Suitability of the Multilevel Strategy for the Conformational Analysis of Small Ligands*" (*J. Phys. Chem. B*.) y se discuten los resultados obtenidos en la extensión de la estrategia Multinivel, (previamente desarrollada por el Dr. Forti en el seno del grupo de investigación) para hacer posible su combinación con campos de fuerza clásicos y evaluar la fiabilidad de la técnica al aplicarla al estudio de moléculas con carga neta.

En el capítulo 4 se incluyen los artículos "*Synthesis, Biological Evaluation and Molecular Modeling of Donepezil and N-[(5-(Benzyloxy)-1-methyl-1H-indol-2-yl)methyl]-N-methylprop-2-yn-1-amine Hybrids as New Multipotent Cholinesterase/Monoamine Oxidase Inhibitors for the Treatment of Alzheimer's Disease*" (*J. Med. Chem.*), "*Exploring the StructuralBbasis of the Selective Inhibition of Monoamine oxidase A by Dicarbonitrile Aminoheterocycles: Role of Asn181 and Ile335 Validated by Spectroscopic and Computational Studies"* (*BBA Proteins and*

Proteomics) y "*Synthesis and Multitarget Biological Profiling of a Novel Family of Rhein Derivatives As Disease-Modifying Anti-Alzheimer Agents.*" (*J. Med. Chem.*). Dichos trabajos son fruto de un esfuerzo multidisciplinar y de colaboración con diversos grupos de investigación para el diseño, síntesis y evaluación farmacológica de nuevos compuestos de potencial interés terapéutico en la enfermedad de Alzheimer. La discusión de este capítulo se analiza a la vista de los resultados obtenidos en la modelización y elucidación de modos de unión y relaciones estructura-actividad.

La presente memoria concluye con un resumen global de resultados en el capítulo 5 y el apartado de conclusiones en el capítulo 6.

Finalmente, en un apartado anexo se describen otras publicaciones afines a la temática y desarrolladas durante la elaboración de la presente Tesis Doctoral.

Abreviaturas y Acrónimos

ACh	Acetilcolina / *Acetylcholine*
AChE	Acetilcolinesterasa / *Acetylcholinesterase*
AD	Enfermedad de Alzheimer / *Alzheimer's Disease*
ADMET	Absorción-Distribución-Metabolismo-Excreción-Toxicidad / *Absorption-Distribution-Metabolism-Excretion-Toxicity*
AMPA	Ácido α-amino-3-hidroxi-5-metil-4-isoazolepropionico / *α-amino-3-hydroxi-5-methyl-4-isoazolepropionic acid*
APP	Proteina Precursora del Amiloide / *Amyloid Precursor Protein*
βA	Amiloide β / *β-amyloid*
BACE-1	β-secretasa / *β-secretase*
BuChE	Butirilcolinesterasa / *Butirylcholinesterase*
CAS	Sitio de unión catalítico / *Catalytic Anionic Site*
DFT	- / *Density Functional Theory*
FAD	Flavina-Adenina Dinucleotido / *Flavine-Adenine Dinucleotide*
FDA	- / *Food and Drug Administration*
gaff	- / *Generic Amber Force Field*
HF	Hartree-Fock
HL	Alto Nivel / *High Level*
K_d	Constante de disociación / *Dissociation Constant*
K_i	Constante de inhibición / *Inhibition Constant*
LL	Bajo Nivel / *Low Level*
MAO	Monoamino oxidasa / *Monoamine oxidase*
MC	Metropolis-Monte Carlo
MLS	Estrategia Multinível / *Multilevel Strategy*
MM/PBSA	- / *Molecular Mechanics/Poisson Boltzmann-Surface Area*
MTDL	Compuestos Multipotentes, *Multitarget Directed Ligands*
NMDA	N-Metil-D-aspartato / *N-Methyl-D-aspartate*
PAS	Sitio de unión periférico / *Periferal Anionic Site*
PDB	- / *Protein Data Bank*
PES	Superficie de Energía Potencial / *Potential Energy Surface*
RMN/NMR	Resonancia Magnética Nuclear / *Nuclear Magnetic Resonance*
ROS	Especies reactivas de oxígeno / *Reactive Oxygen Species*
SAR	Relaciones Estructura-Actividad / *Structure-Activity Relationships*
SIE	- / *Solvated Interaction Energy*
SNC / CNS	Sistema nervioso central / *Central Nervous System*
ZPE	Energía de Punto Cero / *Zero Point Energy*

Índice

1. Introducción **1**

1.1. Reconocimiento molecular 3

1.1.1. El modelo rígido de Fisher o de llave-cerradura 3

1.1.2. Modelos flexibles: Adaptación inducida y selección conformacional 4

1.1.3. Concepto de conformación bioactiva 5

1.2. Relaciones termodinámicas del reconocimiento molecular 6

1.3. Modelización molecular y diseño computacional de fármacos 7

1.4. Predicción conformacional en diseño de fármacos 10

1.5. La estrategia Multinivel 10

1.5.1. Fundamento teórico 10

1.5.2. Implementación original 13

1.6. La enfermedad de Alzheimer: Aproximaciones terapéuticas clásicas 16

1.6.1. Inhibidores de acetilcolinesterasa y restablecimiento de la actividad colinérgica en el sistema nervioso central 17

1.6.2. Disminución de la actividad glutamatérgica y control de la excitotoxicidad 19

1.7. Mecanismos patogénicos implicados en la EA: La búsqueda de nuevas estrategias terapéuticas 19

1.7.1. Formación de placas del péptido ß-amiloide 20

1.7.2. Agregación intracelular de la proteína Tau fosforilada 23

1.7.3. Desequilibrio de la neurotransmisión mediada por aminas biógenas y estrés oxidativo 23

1.8. Multipotencia: Fármacos inhibidores de múltiples dianas 26

1.8.1. Ejemplos de compuestos multipotentes de interés terapéutico en enfermedades neurodegenerativas 27

2. Objetivos **31**

2.1. Extensión de la estrategia Multinivel 33

2.2. Modelización de compuestos multipotentes de interés terapéutico en la enfermedad de Alzheimer 34

2.2.1. Inhibidores multipotentes ChE-MAO: Híbridos donepezilo-PFN9601 34
2.2.2. Explorando la inhibición selectiva en MAO: Dicarbonitrilo aminoheterociclos 34
2.2.3. Híbridos huprina-rheína: Hacia un fármaco con capacidad modificadora de la progresión de la enfermedad de Alzheimer 35

3. Metodología Multinivel **37**
3.1. Publicación: "*Assessing the Suitability of the Multilevel Strategy for the Conformational Analysis of Small Ligands*" 39
3.2. Extensión de la metodología Multinivel 51
3.2.1. Ajuste de la expresión Multinivel al uso de campos de fuerza clásicos 51
3.2.2. Aplicación a moléculas cargadas: Ariletilaminas 52
3.2.3. Aplicación a moléculas cargadas: Estreptomicina 56

4. Compuestos Multipotentes **61**
4.1. Publicación: "*Synthesis, Biological Evaluation and Molecular Modeling of Donepezil and N-[(5-(Benzyloxy)-1-methyl-1H-indol-2-yl)methyl]-N-methylprop-2-yn-1-amine Hybrids as New Multipotent Cholinesterase/Monoamine Oxidase Inhibitors for the Treatment of Alzheimer's Disease*" 63
4.2. Publicación: "*Exploring the Structural Basis of the Selective Inhibition of MonoamineOoxidase A by Dicarbonitrile Aminoheterocycles: Role of Asn181 and Ile335 Validated by Spectroscopic and Computational Studies*" 107
4.3. Publicación: "*Synthesis and Multitarget Biological Profiling of a Novel Family of Rhein Derivatives As Disease-Modifying Anti-Alzheimer Agents*" 133
4.4. Inhibidores Multipotentes ChE-MAO: Híbridos donepezilo-PFN9601 183
4.4.1. Inhibición de AChE 185
4.4.2. Inhibición de MAO 187
4.5. Exploración de la selectividad de inhibidores en MAO: Dicarbonitrilo aminoheterociclos 192

4.5.1. Modelización de la unión de **33a** a MAO A oxidada 195
4.5.2. Modelización de la unión de **33a** a MAO A reducida 197
4.6. Híbridos huprina-rheína: Hacia un fármaco con capacidad modificadora de la progresión de la enfermedad de Alzheimer 198
4.6.1. Inhibición de AChE 200
4.6.2. Inhibición de BACE-1 201

5. Summary **205**
5.1. Extension of the Multilevel strategy 208
5.2. Development of multitarget directed ligands against Alzheimer's Disease 211
5.2.1. Multipotent ChEi-MAOi: Donepezil-PFN9601 hybrids 211
5.2.2. Exploring the selective inhibition of MAO: Dicarbonitrile aminoheterocycles 213
5.2.3. Huprine-rhein hybrids: Toward a disease modifying agent for Alzheimer's Disease 214

6. Conclusions **217**
6.1. Extension of the Multilevel strategy 219
6.2. Development of multitarget directed ligands against Alzheimer's disease 219
6.2.1. Multipotent ChEi-MAOi: Donepezil-PFN9601 hybrids 219
6.2.2. Exploring the selective inhibition of MAO: Dicarbonitrile aminoheterocycles 220
6.2.3. Huprine-rhein hybrids: Toward a disease modifying agent for Alzheimer's Disease 220

7. Bibliografía **223**

8. Anexo I: Otras publicaciones **235**

Capítulo

1 Introducción

1.1 Reconocimiento molecular

Desde la replicación de un virus a la neurotransmisión en los organismos superiores, la interacción selectiva de dos entidades químicas es un fenómeno básico en casi todos los procesos biológicos[1]. Por ello, el reconocimiento molecular es objeto de numerosos estudios desde finales del siglo XIX. En el marco del diseño de fármacos es especialmente interesante conocer qué factores determinan que una pequeña molécula bioactiva (ligando, L) se una selectivamente a la macromolécula que constituye su diana terapéutica (receptor, R) para formar el complejo que origina una respuesta biológica. En los últimos 150 años, y paralelamente al desarrollo de disciplinas como la biología molecular, la física cuántica, la cristalografía, la termodinámica estadística o la informática, nuestro conocimiento sobre los mecanismos que subyacen en el reconocimiento molecular se ha incrementado notablemente, hasta el punto que, hoy en día, disponemos de las herramientas necesarias para describir a nivel atómico aquellos factores que influyen en la complementariedad entre ligando y receptor.

1.1.1 El modelo rígido de Fisher o de llave-cerradura

Para explicar la interacción enzima-sustrato, el químico y premio Nobel alemán Emil Fisher propuso en 1894 el primer mecanismo de reconocimiento molecular al concluir que "una enzima y un glucósido deben encajar como una llave en una cerradura para que tenga lugar una reacción química entre ellos"[2]. Este modelo introducía el concepto de complementariedad estructural entre las dos especies implicadas en el reconocimiento molecular, pero concebidas como estructuras rígidas, complementarias y no intercambiables. Semejantes restricciones hicieron que la validez del modelo de Fisher quedase restringida a situaciones muy concretas y hoy en día se

considera un modelo superado. A pesar de esto, el modelo de llave-cerradura constituyó una aportación de indudable importancia al estudio del reconocimiento molecular y sentó las bases para el desarrollo de posteriores estudios.

1.1.2 Modelos flexibles: Adaptación inducida y selección conformacional

Sesenta años después de la publicación del modelo de Fisher, Daniel E. Koshland presentó un estudio sobre síntesis proteica en un simposio de la Academia Nacional de Ciencias de EE.UU[3]. Dicho estudio evidenciaba las limitaciones del modelo rígido de reconocimiento molecular y sugería que la interacción con el sustrato originaba cambios en el enzima que maximizaban la complementariedad molecular en un proceso conocido como *adaptación inducida*. Construido sobre la base del modelo de Fisher, el modelo propuesto por Koshland introducía el concepto de flexibilidad en el reconocimiento molecular, aunque la supeditaba a la interacción con otra entidad química. Años más tarde, combinando las observaciones de Schellman sobre fluctuaciones conformacionales en proteínas y el concepto de adaptación inducida de Koshland, Bruno Straub propuso el modelo de *adaptación fluctuante*. El modelo de Straub proponía un enzima que alternaba diferentes conformaciones, de las cuales sólo una podía unirse al sustrato y ser estabilizada por la interacción con el mismo[4].

Desde el punto de vista de la dinámica macromolecular, ambos modelos descansan en conceptos diferentes. El modelo de Straub, también conocido como de *selección conformacional*, describe dos entidades químicas (enzima y sustrato) que fluctúan entre múltiples conformaciones. Algunas conformaciones favorecen la interacción entre ambas especies y, cuando ésta tiene lugar, dichas conformaciones son secuestradas por la formación del complejo, desplazándose el equilibrio hacia

poblaciones que favorecen la interacción[5]. El modelo de *adaptación inducida*, por el contrario, propone que las conformaciones que permiten formar el complejo son inducidas sólo cuando las dos especies están presentes y, por tanto, se añaden al número de conformaciones accesibles para cada una de ellas[6].

Figura 1.1 Comparación conceptual de los modelos flexibles de reconocimiento molecular. En el modelo de *adaptación inducida* el espacio conformacional del complejo sólo es accesible cuando ligando y receptor están presentes. En el modelo de *selección conformacional* los subconjuntos de conformaciones compatibles entre ligando y receptor determina el espacio conformacional del complejo .

Existe numerosa bibliografía que revisa y discute los méritos de ambos modelos [5,7–13] y aunque existen evidencias de que el modelo de *selección conformacional* es el que mejor describe el comportamiento de numerosos sistemas biológicos[12], en una revisión reciente se sugiere que un modelo híbrido entre los dos mecanismos sería el más adecuado para describir algunos sistemas[6].

1.1.3 Concepto de conformación bioactiva.

Independientemente del modelo, la concepción del reconocimiento molecular como la interacción entre entidades químicas flexibles apareja la noción de que algunas conformaciones de dichas entidades son más adecuadas para la interacción que otras. En el contexto del diseño de fármacos, el término *conformación bioactiva* se utiliza para designar la conformación adoptada por el ligando en su interacción con el receptor (o

viceversa). Indudablemente, esta concepción resulta reduccionista, pues para la mayoría de moléculas no existirá una única conformación bioactiva, sino un conjunto de conformaciones delimitado por las características del centro de unión. No obstante, dicho concepto, que está fuertemente influenciado por la visión estática asociada al uso de estructuras cristalográficas, resulta útil para describir la contribución que la reorganización conformacional tiene en la energía libre de unión asociada a la interacción ligando-receptor.

1.2 Relaciones termodinámicas del reconocimiento molecular

Las leyes de la física proporcionan las herramientas para el estudio cuantitativo del reconocimiento molecular. Para un proceso de formación del complejo ligando-receptor (ec. 1.1) la constante de disociación (K_d; ec. 1.2), permite caracterizar la afinidad entre un ligando y su receptor a partir de la energía libre de Gibbs de unión (ΔG°_{bin}; ec. 1.3)[14].

$$LR \underset{}{\overset{K_d}{\rightleftharpoons}} L + R \qquad \textbf{1.1}$$

$$K_d = \frac{[L][R]}{[LR]} \qquad \textbf{1.2}$$

$$\Delta G^{\circ}_{bin} = RT \ln K_d \qquad \textbf{1.3}$$

En base a las expresiones anteriores, es intuitivo que cuanto menor sea ΔG°_{bin}, más desplazado estará el equilibrio del proceso 1.1 hacia la formación del complejo y, por tanto, mayor será la afinidad del ligando por el receptor. Con objeto de analizar los diferentes factores que influyen sobre la afinidad ligando-receptor, conviene expresar ΔG°_{bin} a partir del ciclo descrito en la figura 1.1.

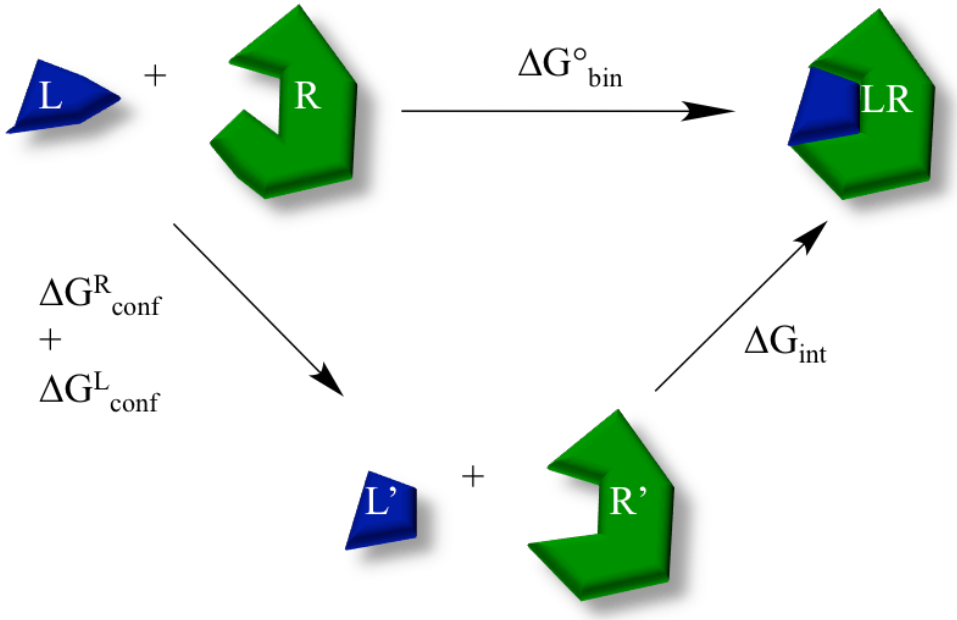

Figura 1.2 Ciclo termodinámico para el proceso de formación del complejo ligando receptor. La descomposición empleada permite considerar la energía libre de unión (ΔG°_{bin}) como la suma de contribuciones debida a la energía libre de interacción (ΔG_{int}) y el coste energético de adopción de la conformación bioactiva (ΔG_{conf}).

Según la figura 1.1, la energía libre de unión podría obtenerse a partir de las contribuciones debidas a la adopción de la conformación bioactiva por parte del receptor (ΔG^{R}_{conf}) y del ligando (ΔG^{L}_{conf}), así como a la interacción entre ellos (ΔG_{int}). Este último término es el componente que favorece la formación del complejo y es reflejo de la complementariedad estérica, electrostática e hidrofóbica entre el ligando y el receptor[15,16]. En contraposición, los términos ΔG^{R}_{conf} y ΔG^{L}_{conf} son desfavorables a la formación del complejo y reflejan el coste energético asociado a los cambios estructurales requeridos para adoptar la conformación bioactiva [17–19].

1.3 Modelización molecular y diseño computacional de fármacos

El físico británico Paul Dirac argumentó en 1929 que sólo la complejidad de las ecuaciones resultantes evitaba la descripción matemática de todos los procesos químicos y casi todos los procesos físicos, y preconizaba el desarrollo de modelos

simplificados que requiriesen menos poder de cálculo[20]. Lo que Dirac no podía intuir es que el desarrollo exponencial de la informática permitiría la solución de ecuaciones altamente complejas de forma rutinaria y el desarrollo de modelos cada vez más avanzados y de mayor exactitud. El campo de la Modelización Molecular es un ejemplo de este desarrollo y hoy en día es posible crear modelos computacionales de múltiples procesos químicos y biológicos[21]. En este contexto, el diseño computacional de fármacos plantea emplear herramientas informáticas para modelizar el reconocimiento de un pequeño ligando (el fármaco) con su receptor (la macromólecula que constituye su diana terapéutica), lo que a su vez dará origen a una determinada respuesta biológica.

Según lo descrito en el apartado 1.2, la obtención de un modelo predictivo de ΔG°_{bin} requerirá conocer los determinantes moleculares subyacentes a cada una de las contribuciones a la energía libre de unión. En primer lugar, ΔG_{int} refleja las contribuciones de diversos factores entálpicos y entrópicos[16]. Así, incluye las interacciones establecidas entre ligando y receptor[15], que a su vez dependerán del tamaño, la forma y las propiedades fisicoquímicas conferidas por los grupos químicos presentes en el ligando, de forma que una mayor complementariedad electrostática, estérica e hidrofóbica reflejará una mayor afinidad. Por otra parte, el establecimiento de interacciones intermoleculares requiere la desolvatación previa tanto del ligando como del sitio de unión del receptor, desplazando las moléculas de solvente (generalmente agua, en entorno fisiológico) que se encuentran en contacto con ligando y receptor. No obstante, el coste entálpico de romper las interacciones con el solvente se ve compensado por la ganancia entrópica que experimentan las moléculas de agua y, en última instancia, la contribución de la desolvatación a la ΔG_{int} depende del balance entre estos dos términos. A su vez, ΔG_{conf} refleja el coste energético para la adopción de la conformación bioactiva. También en este caso intervienen factores entálpicos,

debidos al coste energético de reorganización, y entrópicos, ya que adoptar dicha conformación bioactiva impone restricciones al espacio conformacional de las especies implicadas, lo que apareja una disminución entrópica.

Intuitivamente, es evidente que los fármacos más afines por su receptor serán aquéllos cuya unión para formar el complejo ligando-receptor conlleve cambios en ΔG_{int} sustancialmente estabilizantes, así como nulas penalizaciones por reorganización conformacional. Cabe hacer notar que, debido a la relación exponencial entre energía de unión y constantes de disociación, una diferencia de 1.4 kcal/mol se traduce en un orden de magnitud de diferencia en la afinidad. Así, pues, la afinidad entre ligando y receptor depende de diferencias sutiles en el balance entre ΔG_{int}, ΔG^{R}_{conf} y ΔG^{L}_{conf}.

En este contexto, la presente tesis doctoral ha abordado dos problemas altamente relevantes en el diseño de fármacos. Por un lado, se ha contribuido al desarrollo, extensión y evaluación de una metodología Multinivel para la exploración de las preferencias conformacionales de pequeñas moléculas bioactivas. Por otro lado, en el marco de esfuerzos multidisciplinares y de colaboración teórico-experimentales, se han aplicado técnicas computacionales contrastadas para contribuir el desarrollo de nuevas moléculas de potencial interés terapéutico en la enfermedad de Alzheimer.

1.4 Predicción conformacional en diseño de fármacos

En el proceso de *hit to lead* es una situación común que series de compuestos estructuralmente relacionados sean ensayados para encontrar el ligando más afín a un receptor común. Si se considera que modificaciones químicas dentro de la misma serie pueden alterar drásticamente el panorama conformacional de una molécula sin por ello afectar a las interacciones que esta establece con el receptor, resulta evidente el efecto positivo que herramientas de predicción del coste de reorganización conformacional de pequeñas moléculas podrían tener en el proceso de desarrollo fármacos. Conocer *a priori* el coste asociado a la selección de la conformación bioactiva permitiría valorar la capacidad de un compuesto para llegar a ser un buen candidato a fármaco y ahorrar tiempo y recursos al permitir descartar aquellas moléculas con mayor coste de reorganización conformacional.

1.5 La estrategia Multinivel

Como parte de la tesis del Dr. Flavio Forti, en el grupo de investigación se concibió la estrategia Multinivel (*MLS*)[22] como una herramienta para la exploración conformacional de pequeñas moléculas y la predicción del coste conformacional asociado a la adopción de conformaciones bioactivas.

1.5.1 Fundamento teórico

La aproximación de estados predominantes desarrollada por Gilson *et. al.* [23,24] establece que el espacio conformacional de una molécula se puede dividir en un conjunto de mínimos locales (M) y que la integral configuracional es igual a la suma sobre todos los pozos de las integrales configuracionales individuales. En este contexto,

la energía libre (A) de una molécula flexible puede aproximarse a partir de las contribuciones de un número finito de pozos conformacionales. (ec. 1.4).

$$A \approx -RT\ ln \sum_{j=1}^{M} e^{-A_j/RT} \quad \textbf{1.4}$$

$$A_j \approx -RT\ ln \left[\frac{v_j}{N_j} \sum_{\substack{k=i \\ k \in j}}^{N_j} e^{-E_k/RT} \right] \quad \textbf{1.5}$$

donde A_j corresponde a la energía libre asociada al pozo *j,* v_j es el volumen del espacio conformacional muestreado para ese pozo, N_j es el número de estados conformacionales y E_k es la energía de cada estado perteneciente al pozo.

Para caracterizar las preferencias conformacionales de un ligando, es especialmente interesante centrar la atención en las diferencias relativas entre mínimos conformacionales. La diferencia de energía libre entre dos pozos *i* y *j* (ΔA_i^j) vendría dada por la expresión 1.6.

$$\Delta A_i^j = A_j - A_i = -RT \ln \frac{\frac{v_j}{N_j} \sum_{k=1}^{N_j} e^{-E_k/RT}}{\frac{v_i}{N_i} \sum_{l=1}^{N_i} e^{-E_l/RT}} \quad \textbf{1.6}$$

en la que la energía libre de cada pozo conformacional puede indicarse relativa al confórmero de mínima energía (ec. 1.7).

$$A_i = -RT \ln \frac{v_i}{N_i} \left(e^{-E_{i\_min}/RT} \sum_{k=1}^{N_i} e^{-\Delta E_k/RT} \right) =$$

$$= E_{i\_min} - RT \ln \sum_{k=1}^{N_i} e^{-\Delta E_k/RT} - RT \ln \frac{v_i}{N_i} \quad \textbf{1.7}$$

donde E_{i_min} es la energía del mínimo conformacional y $\Delta E_k = E_k - E_{i\_min}$ es la diferencia de energía relativa entre dicho mínimo y el resto de conformaciones pertenecientes al mismo pozo, de tal forma que el término central de la expresión 4.6

describe la curvatura o distribución de conformaciones asociada a dicho pozo *i* (A_i^{local}; ec. 1.8).

$$A_i^{local} = -RT \ln \sum_{k=1}^{N_i} e^{-\Delta E_k / RT} \quad \textbf{1.8}$$

Con ello, es posible rescribir la ecuación 1.7 de una forma más compacta tal como se indica en la expresión 1.9, que permite conocer la diferencia de energía entre dos pozos i y j a partir de las diferencias de energía entre sus conformaciones más estables y la curvatura local de los pozos, teniendo en cuenta que el último término de la ec. 1.7 cancelará si se realiza un muestreo uniforme de los volúmenes asociados a cada pozo.

$$\Delta A_i^j = \Delta E_{i_{min}, j\_min} + \Delta A_{i,j}^{local} - RT \ln \frac{v_j N_i}{v_i N_j} \quad \textbf{1.9}$$

Basándose en las consideraciones anteriores, la estrategia multinivel propone emplear métodos de bajo nivel de teoría (*Low Level*, LL) para muestrear la superficie de energía potencial (PES), identificar mínimos de energía y caracterizar su energía libre local (A^{local}), para, posteriormente caracterizar con exactitud la contribución de la conformación (E_{min}) más estable empleando métodos de alto nivel de teoría (*High Level*, HL).

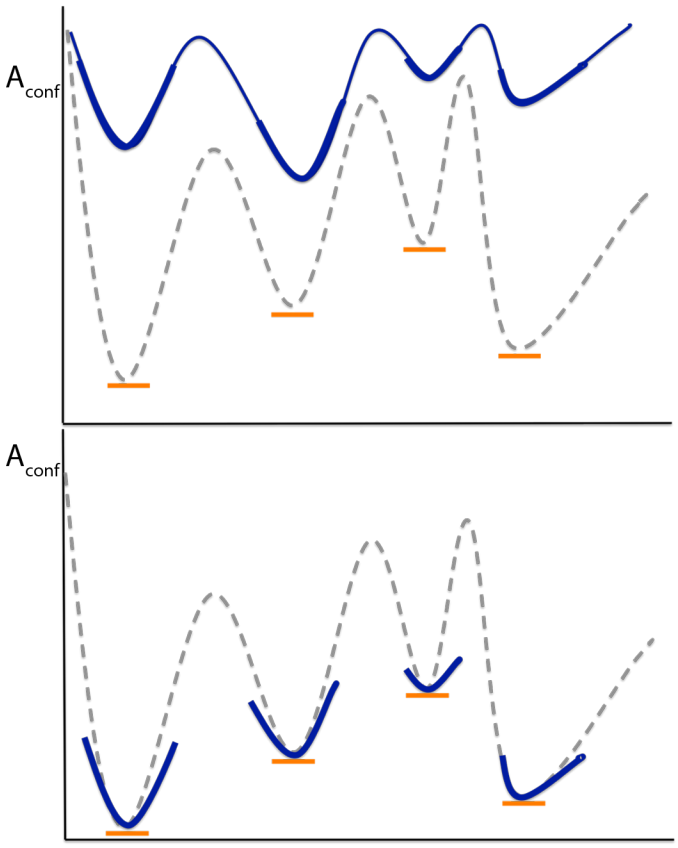

Bajo Nivel (LL)

Los métodos semiempíricos o los campos de fuerza clásicos permiten explorar la superficie de energía libre a un bajo coste computacional pero no predicen con exactitud su estabilidad relativa.

Alto Nivel (HL)

Los métodos *Ab initio* permiten gran exactitud en la predicción de energía pero solo pueden ser aplicados a un número reducido de estructuras.

Multinivel (ML)

La energia libre conformacional se puede aproximar localizando los mínimos con una técnica de bajo nivel (LL) y, a continuación, aplicando una técnica de alto nivel a una estructura representativa de cada pozo energético,

$$A(ML) \approx E_{i\_\min}(HL) + A_i^{local}(LL)$$

Figura 1.3 Representación esquemática de la Estrategia Multinivel. El empleo de un método de bajo nivel de teoría permite explorar un gran número de conformaciones y estimar la energía libre asociada a cada pozo de energía potencial, mientras que el re-escalado de estructuras puntuales con un método de alto nivel permite describir con exactitud la energía potencial del mínimo.

1.5.2 Implementación original

En la implementación original del método[22], el muestreo de la PES se llevaba a cabo empleando un algoritmo de Metropolis Monte Carlo (MC)[25,26] empleando el hamiltoniano semiempírico RM1[27] para describir la energía del sistema. En el caso de una exploración en fase gas, la energía de una determinada conformación era descrita por su energía interna obtenida con dicho hamiltoniano. En el caso de una simulación en solución, se utilizaba una energía efectiva obtenida al combinar la energía interna de la conformación con la energía libre de solvatación estimada mediante la versión RM1 del método IEF-MST[28].

Para la descripción HL, se realizaba un cálculo puntual a nivel MP2/aug-cc-pvDZ sobre las geometrías optimizadas a nivel B3LYP/6-31G(d), incluyendo la energía de punto cero (ZPE), considerando los efectos del solvente mediante la versión B3LYP del modelo contínuo polarizable IEF-MST[29]. La estimación final de la energía de un mínimo conformacional empleando la estrategia multinivel (A_i^{ML}) se obtenía de la aplicación de la expresión 1.10.

$$A_i^{ML} = E_{i\_min}^{MP2} + A_{solv,i\_min}^{B3LYP||IEF-MST} + ZPE_{i\_min}^{B3LYP||IEF-MST} + A_i^{local,RM1} \qquad \textbf{1.10}$$

donde el primer término corresponde a la energía de la conformación de mínima energía determinada a nivel MP2/aug-cc-pVDZ ($E_{i\_\min}^{MP2}$), el segundo y tercer términos a la energía de solvatación y a la ZPE respectivamente, ambos determinados a nivel IEF-MST/B3LYP/6-31G(d), y el último término a la energía conformacional del pozo, obtenida mediante la expresión 1.8, empleando el hamiltoniano RM1.

Mientras que el valor de los tres primeros términos de la ec. 1.10 se obtenía mediante cálculo cuántico, el valor de A_i^{local} requería el post-procesado del muestreo LL. Concretamente, para determinar el tamaño de cada pozo conformacional, los resultados de las simulaciones MC IEF-MST/RM1 se proyectaban sobre una cuadrícula *n*-dimensional (siendo *n* el número de torsiones activas) espaciada a intervalos regulares, de forma que cada conformación (entendida como una combinación de valores de sus torsiones activas) quedaba asignada a un punto (Figura 1.4). Si dos estructuras eran asignadas al mismo punto de la cuadrícula, sólo la estructura de mínima energía se retenía como representativa de ese punto. Posteriormente, la estructura de mínima energía en la cuadrícula se empleaba como punto de partida para una búsqueda sistemática sobre cada una de las *n* dimensiones a su alrededor. Cuando la búsqueda sobre una determinada dimensión encontraba una estructura de mayor energía que el

punto precedente, se asumía que correspondía al mismo pozo conformacional que la estructura de partida. Si, por el contrario, la búsqueda encontraba una estructura de menor energía, se consideraba perteneciente a otro pozo y se detenía la búsqueda en esa dirección. También cesaba la búsqueda si no se encontraba ninguna estructura en un punto determinado de la cuadrícula, ya que se consideraba que correspondía a estructuras de muy alta energía (y por tanto excluidas del pozo). Cuando la búsqueda finalizaba en las *n* dimensiones, el tamaño del pozo se estimaba en base a los valores de las torsiones más externos en el espacio *n*-dimensional y se repetía el proceso buscando la estructura de mínima energía una vez excluido el espacio conformacional ya asignado a un pozo. Una vez definidos sus límites, para cada pozo era posible obtener el valor de A_i^{local} (ec. 1.8).

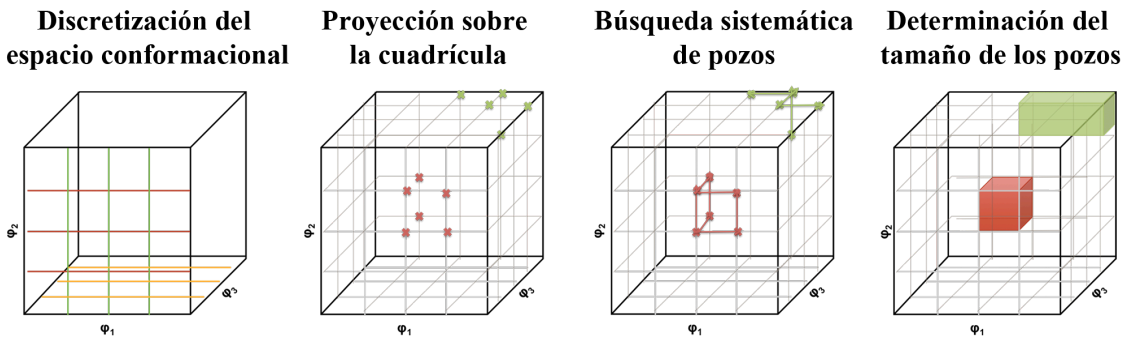

Figura 1.4 Representación esquemática de la generación de la cuadrícula y del proceso de búsqueda de pozos en el espacio conformacional. Se toma como ejemplo un espacio conformacional tridimensional. Tras la generación de la cuadrícula a intervalos regulares, se proyectan las estructuras sobre ella y se buscan sistemáticamente aquellas estructuras relacionadas (ver texto). El tamaño de los pozos se determina en base a los valores extremos de las torsiones activas.

1.6 La enfermedad de Alzheimer: Aproximaciones terapéuticas clásicas

Descrita por primera vez en 1906 por el psiquiatra del hospital de Frankfurt Alois Alzheimer, la enfermedad de Alzheimer (EA) es un trastorno neurodegenerativo que se caracteriza por una insidiosa pérdida de capacidades cognitivas y la paulatina aparición de desórdenes neuropsiquiátricos y del comportamiento que desembocan en demencia en el estadio final de la enfermedad[30]. En el año 2000 alrededor de 25 millones de personas padecían la EA en todo el mundo y se estima que, sin terapias neuroprotectoras efectivas, la cifra de casos alcanzará los 114 millones a mediados de siglo[31].

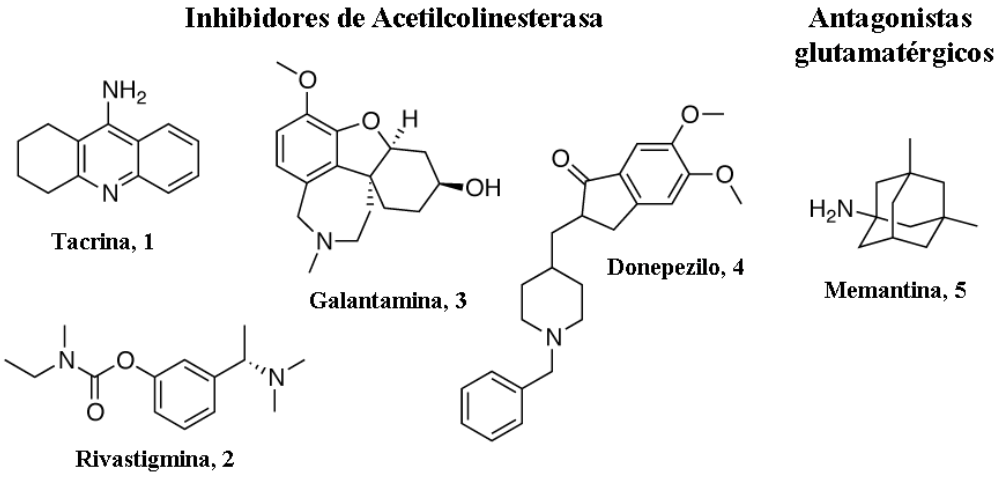

Figura 1.5. Estructura química de los fármacos tacrina, galantamina, rivastigmina, donepezilo y memantina. Los inhibidores de AChE incrementan la neurotransmisión colinérgica y alivian la sintomatología cognitiva. Memantina modula la actividad del receptor NMDA de glutamato y reduce la excitoxicidad.

El elevado coste social y económico de la EA ha hecho que la comunidad científica de todo el mundo haya dedicado gran atención al desarrollo de fármacos contra la enfermedad. A día de hoy, sin embargo, sólo cinco fármacos (Figura 1.5) han

sido aprobados por la *Food and Drug Administration* (FDA) estadounidense y por la *European Medicines Agency* (EMA) para el tratamiento de la EA.

Entender las estrategias y los principios terapéuticos detrás de estos fármacos resulta imprescindible como un primer paso al desarrollo ulterior de nuevas entidades químicas de potencial interés en el tratamiento de la enfermedad.

1.6.1 Inhibidores de acetilcolinesterasa y restablecimiento de la actividad colinérgica en el sistema nervioso central

La pérdida de memoria y de capacidades cognitivas durante la EA se asocia principalmente al descenso del número y actividad de neuronas colinérgicas en el núcleo basal. La llamada hipótesis colinérgica establece que empleando agentes colinomiméticos es posible compensar el déficit de acetilcolina (ACh) en el sistema nervioso central (SNC) y mejorar así la sintomatología de la EA[32]. Debido a los efectos secundarios asociados a la administración de agentes colinérgicos directos, la estrategia terapéutica consiste en aumentar los niveles de ACh mediante la inhibición de la principal enzima encargada de su metabolización, la acetilcolinesterasa (AChE, E.C. 3.1.1.7). Desde el punto de vista del desarrollo de fármacos, esta estrategia es la que ha cosechado mayor éxito, ya que cuatro de los cinco fármacos aprobados por la FDA son inhibidores reversibles de esta proteína.

La AChE humana es una proteína de 583 aminoácidos (más un péptido señal de 31 residuos) que cataliza la hidrólisis de ACh en la fosa sináptica interrumpiendo el estímulo colinérgico. La reacción tiene lugar en el sitio catalítico (*Catalytic Anionic Site*, CAS) de la enzima localizado en el extremo interno de un canal de 20 Å de largo denominado como garganta catalítica. En el CAS se localiza la tríada catalítica formada

por los residuos Ser203-His447-Glu334 (Ser200-His440-Glu327 en *Torpedo Californica, Tc*AChE) y los residuos accesorios Trp86 y Gln202 (Trp 84 y Glu199 en *Tc*AChE), que contribuyen a orientar y estabilizar el sustrato durante la hidrólisis. En el extremo externo del canal se localiza el centro de unión periférico (*Periferal Anionic Site*, PAS), que facilitaría el proceso de unión de ACh, aumentando de esta forma la eficiencia del enzima a bajas concentraciones de sustrato[33].

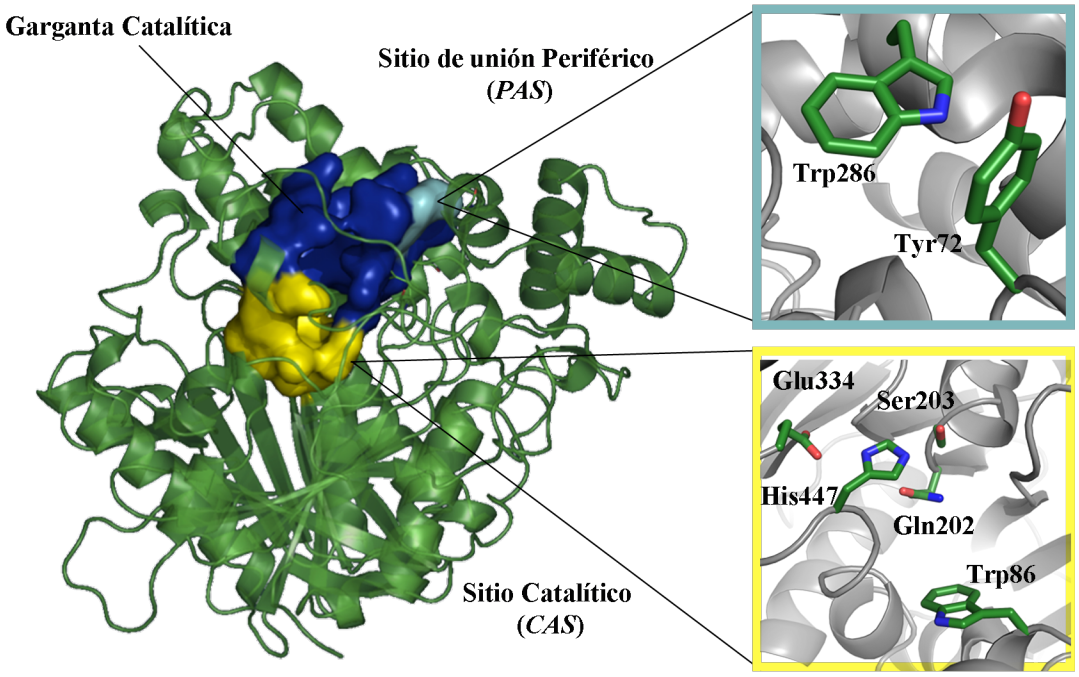

Figura 1.6. Estructura de AChE con detalle de los sitios de unión catalítico (CAS) y periférico (PAS). En el sitio catalítico se localiza la triada Ser203-His447-Glu334. El sitio periférico actúa como inductor de la agregación de βA.

Recientemente, Inestrosa *et al.* describieron la presencia de AChE en las placas seniles y la posibilidad de que el PAS permitiera que AChE actuara como chaperona promotora de la agregación del péptido ß-amiloide (ßA)[34]. Este descubrimiento posibilitó un nexo de unión entre las hipótesis colinérgica y amiloidogénica (ver sección 1.6.2), siendo la base del diseño y síntesis de los conocidos como inhibidores de sitio de unión dual de AChE, con los que mediante la inhibición simultáqnea del sitio catalítico

y del PAS se buscaba incrementar los niveles de ACh y reducir la agregación inducida por AChE del ßA.

1.6.2 Disminución de la actividad glutamatérgica y control de la excitotoxicidad

El glutamato es el principal neurotransmisor estimulador del sistema nervioso central en mamíferos y, mediante la activación de receptores NMDA, kainato y AMPA, la transmisión glutamatérgica tiene un papel decisivo en el desarrollo de procesos cognitivos y de aprendizaje[35,36]. En el enfermo de EA, se observa una liberación sostenida de pequeñas cantidades de glutamato, que si bien son inferiores a las producidas durante la neurotransmisión, provocan una sobrexcitación continuada del receptor NMDA, que se ha asociado con un incremento del estrés oxidativo, un procesado alterado de la proteína precursora de ßA (APP) y la muerte neuronal en un proceso conocido como excitoxicidad[37]. A día de hoy, memantina, un inhibidor no competitivo del canal NMDA, sigue siendo el único fármaco que no actúa sobre AChE aprobado para el tratamiento de la EA.

1.7 Mecanismos patogénicos implicados en la EA: La búsqueda de nuevas estrategias terapéuticas.

A pesar de los esfuerzos de la comunidad científica, la variedad y complejidad de los mecanismos implicados en el establecimiento y progresión de la EA hacen que el éxito de las aproximaciones terapéuticas clásicas sea muy limitado. La búsqueda de nuevos fármacos debería aprovechar la experiencia en el uso clínico de inhibidores de AChE y del canal NMDA para desarrollar fármacos con un mejor perfil farmacológico e, idealmente, ser capaces de modificar la progresión de la enfermedad. Si bien una

revisión pormenorizada de los diversos mecanismos propuestos para el establecimiento y progresión de la EA excede el ámbito de la presente tesis, es conveniente describir los mecanismos que en años recientes han sido validados como dianas terapéuticas de potencial interés.

1.7.1 Formación de placas del péptido ß-amiloide.

La hipótesis amiloidogénica de la EA sitúa la formación, agregación y deposición de ßA en el espacio extraneuronal como el factor desencadenante de una cascada de procesos neurotóxicos que conlleva la muerte neuronal masiva, causa última de la sintomatología[38,39]. Los agregados de ßA, conocidos como placas seniles, constituyen uno de los rasgos histopatológicos característicos de la EA. Se trata de mezclas complejas, insolubles, de gran tamaño (60 μM), que además de ßA contienen otros componentes como proteoglicanos o restos celulares[34] y cuya formación se asocia a un procesado anómalo de la APP. Así, en condiciones fisiológicas, la APP es sustrato, de forma secuencial y preferente, de las enzimas proteolíticas α- y γ-secretasa, originando fragmentos solubles[40,41]. En el enfermo de EA, en cambio, la APP es procesada en primer lugar por la enzima ß-secretasa (BACE-1; E.C. 3.4.23.46) y tras la acción de la γ-secretasa origina péptidos de 42 aminoácidos ($ßA_{42}$), insolubles y cuya elevada tendencia a autoagregarse origina las placas seniles. Las estrategias terapéuticas basadas en la hipótesis amiloidogénica tratan de reducir la formación de placas seniles principalmente por dos vías: 1) disminuir la formación de $ßA_{42}$, ya sea inhibiendo la actividad de BACE-1 y/o γ-secretasa o promoviendo la actividad de α-secretasa; y 2) inhibiendo la agregación del péptido $ßA_{42}$ ya formado y promoviendo su eliminación[42] (Figura 1.7).

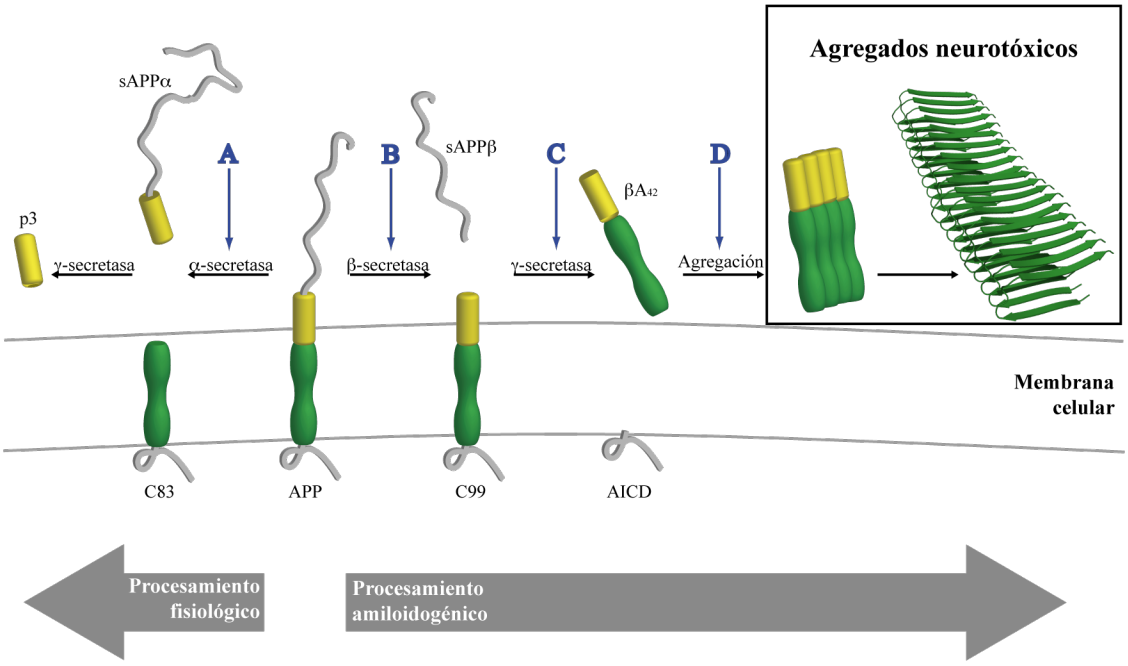

Figura 1.7 Esquema del procesamiento de la APP y estrategias terapéuticas enfocadas a reducir la formación de péptido ßA. **A:** Inducción de la actividad α-secretasa. **B:** Inhibición de β-secretasa; **C:** inhibición de γ-secretasa y **D:** Inhibición de la agregación de péptido βA ya formado.

La falta de eficacia mostrada en ensayos clínicos de fase III del inhibidor de γ-secretasa semagacestat (Lilly)[43] y del anticuerpo monoclonal anti-ßA bapineuzumab (Wyeth)[44,45] han posicionado la inhibición de β-secretasa como la estrategia más prometedora para desarrollar un fármaco capaz de retrasar la progresión de la EA.

BACE-1 es una aspartil proteasa expresada de forma heterogénea en todos los tejidos, pero especialmente presente en cerebro[46]. Su atractivo como diana terapéutica reside principalmente en el hecho de que estudios con ratones BACE-1-*knockout* muestran que estos animales no producen ß-amiloide, una indicación de que no existen mecanismos compensatorios en mamíferos[42,46]. A diferencia del modelo knockout para γ-secretasa[47], estos animales son viables y el principal defecto fenotípico detectado, una hipomielinización severa de los nervios centrales y periféricos asociado a

esquizofrenia[48,49], no se reproduce cuando se administran de forma crónica inhibidores de BACE-1 a ratones normales adultos[50].

Existe abundante información cristalográfica de BACE-1 (280 entradas en Agosto de 2014 en el *Protein Data Bank*) que ha permitido su caracterización estructural. Se trata de una proteína monomérica con dos dominios que adopta el plegamiento común a la familia de las proteasas. El sitio de unión es una hendidura hidrofílica de 20 Å de longitud y de más de 1000 $Å^3$ situada en la interfície entre los dos dominios[51]. Parte de la hendidura se encuentra parcialmente ocluida por la región tapa o *flap,* un *hairpin-loop* altamente flexible que regula el acceso del sustrato a la cavidad catalítica, dónde se localiza la díada Asp32 y Asp228.

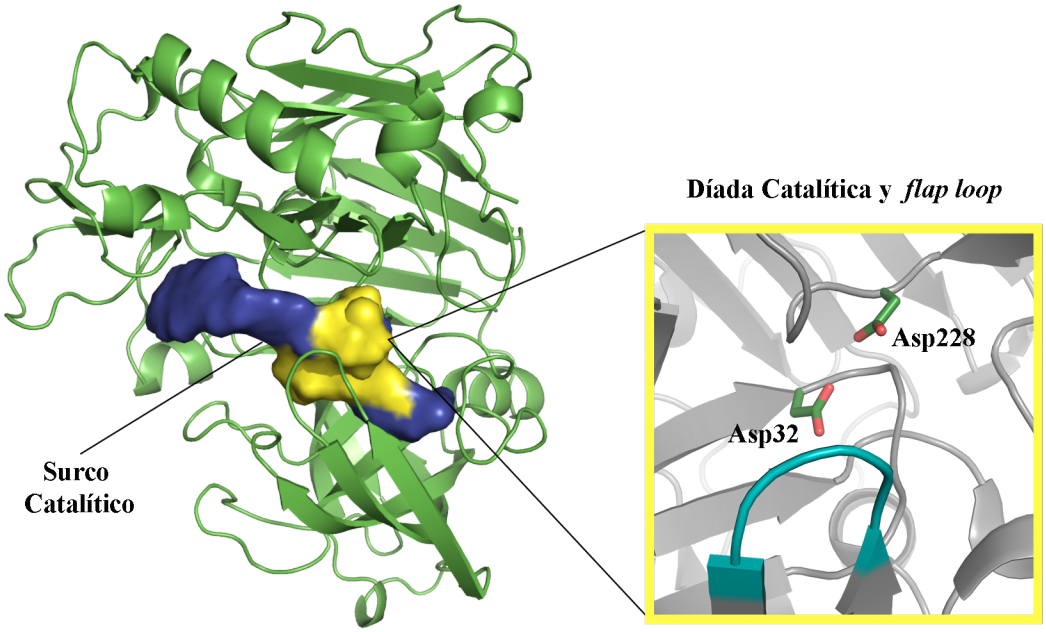

Figura 1.8 Estructura de la β-secretasa con detalle del sitio catalítico. La díada Asp32-Asp228 se localiza aproximadamente en el centro del surco y el acceso es regulado por la región de tapa (en azul).

1.7.2 Agregación intracelular de la proteína Tau fosforilada

Junto con las placas seniles, la presencia de ovillos intraneuronales de proteína Tau (τ) es el otro rasgo histopatológico característico de la EA. En el cerebro sano, tau es una proteína soluble que forma parte del citoesqueleto de las neuronas y que facilita la actividad de los microtúbulos en el transporte axonal. En el cerebro de los pacientes de EA, en cambio, se produce una fosforilación excesiva de esta proteína, su agregación en forma de ovillos y su precipitación. En el desarrollo de la EA estarían involucrados tanto el efecto tóxico directo de estos agregados como la disminución del transporte axonal asociada a los bajos niveles de τ en forma fisiológica[52].

Existen *a priori* dos aproximaciones farmacológicas posibles para reducir la formación de los ovillos intraneuronales: inhibir la agregación de τ fosforilada o, aceptando la premisa de que la hiperfosforilación es la causa de la agregación, emplear inhibidores de kinasas para prevenir dicho proceso.

1.7.3 Desequilibrio de la neurotransmisión mediada por aminas biógenas y estrés oxidativo

Aunque la depleción colinérgica se encuentra en la base de la pérdida de capacidades cognitivas del enfermo de EA, otras vías de neurotransmisión como la serotoninérgica y la noradrenérgica también se ven severamente afectadas y contribuyen a la sintomatología de la enfermedad[53,54]. De forma análoga a como los inhibidores de AChE incrementan la neurotransmisión colinérgica, la inhibición de Monoamino Oxidasa (MAO; E.C. 1.4.3.4), contribuye a restablecer los niveles de neurotransmisión monoaminérgica.

MAO es una flavoenzima mitocondrial que cataliza la desaminación oxidativa de aminas biógenas. El sitio de unión es un canal que conecta la superficie de la proteína con el anillo de isoxazolina del cofactor Flavín Adenín Dinucleótido (FAD) y en el que pueden diferenciarse dos cavidades (Figura 1.9). La región próxima a la superficie de la proteína, o región de entrada, es hidrofóbica, con un volumen de 290 $Å^3$ y cuya entrada queda parcialmente ocluida por el *loop* 99-112[55]. El sitio catalítico se encuentra más allá de la región de entrada y consiste en una cavidad más amplia (de aproximadamente 400 $Å^3$), altamente hidrofóbica y en la que el sustrato se encuentra con el cofactor. Entre la cavidad de entrada y la cavidad catalítica se sitúan los residuos del *bottleneck*, que juegan un papel clave en la selectividad de sustrato por las isoformas A y B.

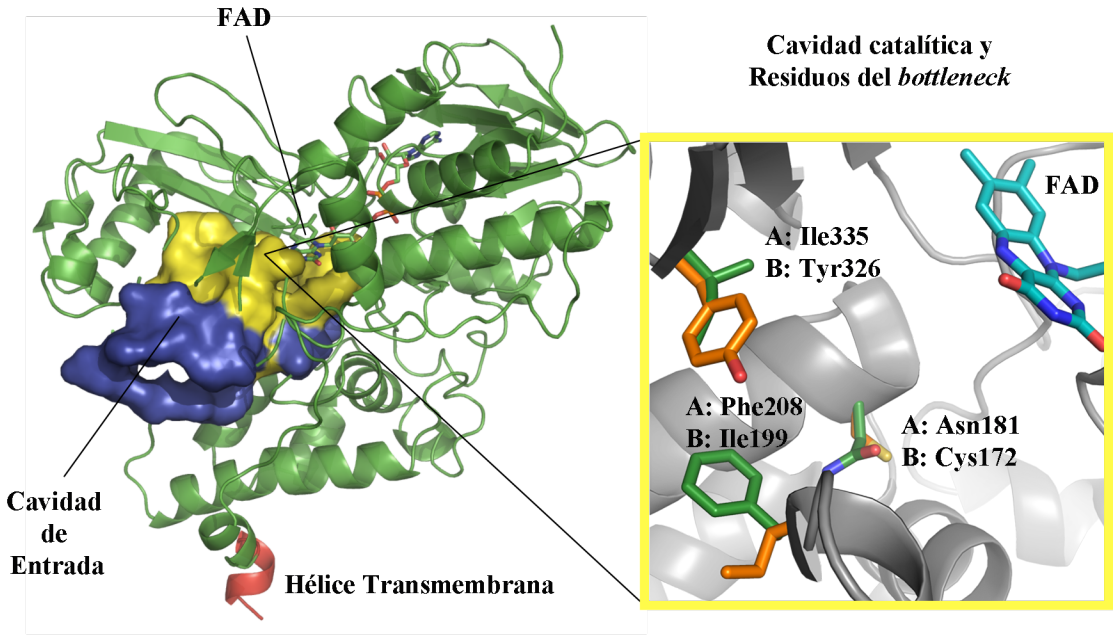

Figura 1.9. Estructura de MAO con detalle de las principales diferencias entre los sitios de unión de MAO A y MAO B. Las diferencias en la región de *bottleneck* juegan un papel clave en la selectividad de sustrato.

La existencia de isoformas con diferente selectividad de sustrato es un hecho extremadamente relevante en el desarrollo de inhibidores de MAO. Concretamente, MAO A preferentemente metaboliza serotonina, adrenalina y noradrenalina, en tanto que los sustratos preferentes de MAO B son benzilamina y ß-feniletilamina[56]. Los inhibidores irreversibles no selectivos de MAO (iMAO), como ipronazid, fueron empleados ampliamente como antidepresivos a partir de la segunda mitad del siglo XX. A pesar de su eficacia en la restauración de la neurotransmisión monoaminérgica, los iMAO fueron cayendo en desuso debido principalmente a un efecto adverso de alta incidencia conocido como "enfermedad del queso", que se daba en pacientes en tratamiento con iMAO que consumían queso y otros alimentos fermentados ricos en la amina simpaticomimética tiramina. En homeostasis, esta amina es metabolizada por la MAO intestinal (correspondiente a la isoforma A en un 80%) en especies inocuas, pero en el paciente tratado con un inhibidor irreversible y no selectivo de MAO, la tiramina accede al torrente sanguíneo causando un incremento de la liberación de noradrenalina que puede dar lugar a crisis hipertensivas muy severas[57].

A principios del siglo XXI, el interés por los inhibidores de MAO volvió a crecer por el papel que podrían jugar en controlar el establecimiento y progresión de enfermedades neurodegenerativas como la enfermedad de Parkinson o la EA. Así, además de mejorar la transmisión monoaminérgica, podrían ayudar a paliar el cuadro depresivo que muchas veces acompaña a estas enfermedades[58]. Por otra parte, el uso de iMAOs se asocia con una disminución de la formación de peróxido de hidrógeno y aldehídos, compuestos derivados de la actividad enzimática de MAO, que promueven la formación de especies reactivas de oxígeno (*Reactive Oxigen Species,* ROS). Estas especies, como el anión superóxido (O_2^-), tienen una reactividad extrema y son susceptibles de causar daños en la célula en situación de estrés oxidativo[59].

Existen tres características neuronales[60] que apoyan un papel determinante del estrés oxidativo en el establecimiento y progresión de la EA:

I) El bajo contenido neuronal de glutatión.

II) El alto contenido en ácidos grasos poliinsaturados de la membrana neuronal.

III) La alta demanda de oxígeno por parte del metabolismo cerebral.

A pesar de su potencial, la severidad de las reacciones adversas anteriormente descritas descartaba la inclusión de iMAOs clásicos en la terapia de enfermedades neurodegenerativas, dado que su uso requería desarrollar inhibidores selectivos MAO B o inhibidores MAO A reversibles que ejercieran su efecto exclusivamente en el sistema nervioso central (SNC)[57].

1.8 Multipotencia: Fármacos inhibidores de múltiples dianas

La complejidad de la EA pone en evidencia las limitaciones de la aproximación clásica del diseño de fármacos, consistente en optimizar la interacción de moléculas bioactivas para su interacción con una sola diana. Esta estrategia es cuestionable en el caso de enfermedades de etiología multifactorial como la EA, pero también en el caso del cáncer, las enfermedades cardiovasculares o la diabetes tipo II entre otras.

Una alternativa ha consistido en el empleo simultáneo de diversas especialidades, lo que es conocido como cóctel de fármacos. Con un claro impacto en la esperanza de vida de los pacientes (por ejemplo, enfermos de SIDA), esta aproximación presenta diversos inconvenientes, sobretodo en cuanto a posibles efectos adversos (dado que los diferentes perfiles de ADMET pueden superponerse y potenciar los efectos adversos) y del cumplimiento terapéutico. En este último caso, es posible desarrollar

especialidades farmacéuticas que contengan más de un principio activo, siempre y cuando sea viable según la tecnología farmacéutica.

Asimismo, varios autores[61–64] han propuesto que el tratamiento de enfermedades multifactoriales precisa un cambio de paradigma desde el clásico "una molécula, una diana terapéutica" hacia uno nuevo: "una molécula, múltiples dianas, una enfermedad". Potencialmente, el desarrollo de un compuesto multipotente o multidiana (MTDL, de sus siglas en inglés) presenta múltiples ventajas, pues permitiría obtener los beneficios de las terapias combinadas manteniendo perfiles ADMET más sencillos y sin los inconvenientes de las mezclas galénicas. También presenta ventajas económicas, dado que sólo requeriría la realización de un único conjunto de estudios de fase preclínica y clínica, mientras que para una combinación de fármacos es necesario estudios separados de cada molécula y, en ocasiones, de la mezcla. No obstante, el diseño de un compuesto multidiana presenta tres grandes desafíos. Así, es necesario conseguir un balance adecuado de afinidades hacia las dianas involucradas. Además, la estrategia de hibridación molecular empleada para desarrollar estos fármacos, que consiste en la combinación de farmacóforos contra las potenciales dianas en una molécula, puede llevar a compuestos fuera del espacio definido por las reglas de Lipinsky[65], lo que se asocia con perfiles de ADMET problemáticos. Por último, al tratarse de moléculas promiscuas, es posible su interacción con otras dianas terapéuticas más allá del espectro deseado, lo que podría originar efectos adversos.

1.8.1 Ejemplos de compuestos multipotentes de interés terapéutico en enfermedades neurodegenerativas

A pesar de que su desarrollo es previo al trabajo de Inestrosa, donepezilo puede considerarse un ejemplo de fármaco multipotente. De acuerdo con la información

cristalográfica, este inhibidor ocupa toda la garganta catalítica de AChE e interacciona simultáneamente con el residuo Trp86 en el CAS y el residuo Trp286 en el PAS, lo que se traduce en una sobresaliente actividad inhibitoria (IC_{50} = 6.7 nM)[66]. Simultáneamente, la interacción con el PAS le confiere un efecto antiagregante de ßA moderado.

Siguiendo la línea de donepezilo y los descubrimientos de Inestrosa, existen diversos ejemplos en la literatura de inhibidores de la AChE de sitio de unión dual que han sido descritos como inhibidores de la agregación de ßA. Así, cabe citar como ejemplos dímeros de tacrina[67], derivados de donepezilo y cumarina[68] y de tacrina e indol[69] o bien híbridos, como tacrina-huprina[70] y tacrina-propidio[71], entre otros.

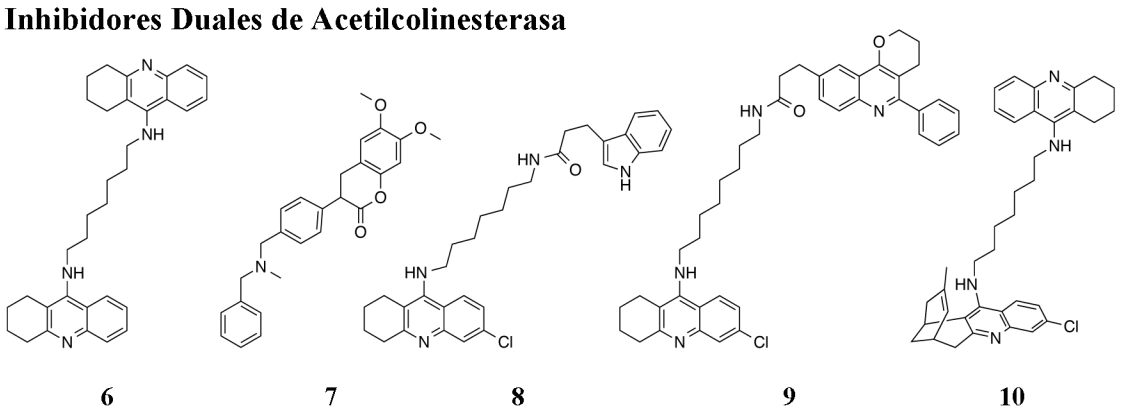

Figura 1.10 Inhibidores duales de la AChE con actividad sobre la agregación de péptido βA. bis(7)-tacrina (**6**)[67], AP2238 (**7**)[68] e híbridos clorotacrina-indol (**8**)[69] , clorotacrina-propidio (**9**)[71] y tacrina-huprina (**10**)[70].

Además de los inhibidores duales de AChE, compuestos multipotentes que combinan diversos mecanismos de acción han demostrado que pueden ser de potencial interés en el tratamiento de la EA y de otras enfermedades neurodegenerativas. Cabe destacar dos ejemplos especialmente relevantes. En primer lugar ladostigil[72], que fue desarrollado como un inhibidor mixto ChE-MAO. Si bien este compuesto no superó los

ensayos clínicos de fase II como tratamiento de la EA, en la actualidad se investiga como neuroprotector en ensayos de fase III por su capacidad de reducir el estrés oxidativo en las células de microglia[73]. En segundo lugar, cabe destacar memoquina, un compuesto surgido de una colaboración teórico-experimental en el ámbito académico[74], concebido como fármaco anti-EA. Su sobresaliente perfil farmacológico combina una excelente actividad inhibitoria de AChE (IC_{50} = 1.5 nM), una gran capacidad de inhibición de la agregación de βA tanto espontánea (IC_{50} = 6 μM) como inducida por AChE (28 μM), así como una elevada actividad inhibitoria de BACE-1 (IC_{50} = 108 nM) y un importante efecto antioxidante[64].

Inhibidor Multipotente AChE/BACE-1

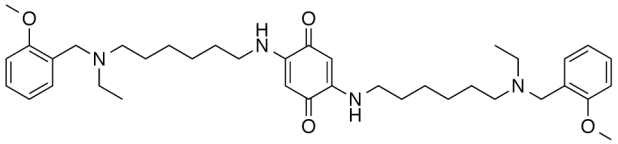

Memoquina, 11

Inhibidor Multipotente AChE/MAO B

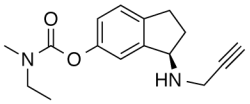

Ladostigil, 12

Figura 1.11 Inhibidores multipotentes diseñados como anti-EA. Memoquina (**11**) presenta un perfil farmacológico sobresaliente que combina actividad neuroprotectora y antioxidante con gran afinidad por AChE y BACE-1. Ladostigil (**12**) combina propiedades neuroprotectoras derivadas de la inhibición de MAO B con la mejora de la neurotransmisión colinérgica derivada de la inhibición de AChE.

Capítulo

2 Objetivos

El coste de reorganización conformacional asociado a la interacción de un ligando con su diana, así como la complementariedad de las propiedades fisicoquímicas del ligando y de los residuos presentes en el centro de reconocimiento de la diana, son factores clave en la afinidad entre ligando y receptor. La modelización de estos fenómenos plantea el reto científico de describir con exactitud y de forma cuantitativa los determinantes moleculares que subyacen en dichas propiedades.

Con el objetivo de contribuir al estudio de estas cuestiones, que son cruciales en diseño de fármacos, esta tesis plantea dos líneas de investigación. Por un lado, desde un punto de vista metodológico, la tesis persigue la expansión y validación del Método Multinivel propuesto por el grupo de investigación como una herramienta para la exploración conformacional de pequeñas moléculas y la determinación del coste asociado a la adquisición de la conformación bioactiva. Por otra parte, en el marco de colaboraciones teórico-experimentales en diseño racional de fármacos, la tesis plantea el uso de técnicas contrastadas de modelización molecular y diseño basado en estructura para el desarrollo de moléculas multipotentes, diseñadas siguiendo el paradigma de "*una molécula, múltiples dianas*", de potencial interés terapéutico en el tratamiento de la Enfermedad de Alzheimer.

2.1 Extensión de la estrategia Multinivel

En la vertiente metodológica, los objetivos específicos del presente trabajo son:

1) la adaptación del método Multinivel para que sea posible emplear campos de fuerza clásicos en la exploración de bajo nivel, y

2) la evaluación del método para la predicción conformacional de moléculas cargadas, teniendo presente el reto computacional que plantea la descripción entre interacciones intramoleculares y la contribución debida a la solvatación.

2.2 Modelización de compuestos multipotentes de interés terapéutico en la enfermedad de Alzheimer

En la línea de aplicación, se combinaron diversas técnicas de modelización molecular aplicadas al diseño de fármacos y se definieron las relaciones estructura-actividad para dos familias de fármacos multipotentes, de acuerdo con los objetivos siguientes:

2.2.1 Inhibidores multipotentes ChE-MAO: Híbridos donepezilo-PFN9601

La modelización de inhibidores multipotentes frente a acetilcolinesterasa, butirilcolinesterasa y monoamino oxidasas A y B, prestando especial énfasis en la elucidación de los determinantes moleculares que influyen en el perfil farmacológico de los compuestos.

2.2.2 Explorando la inhibición selectiva en MAO: Dicarbonitrilo aminoheterociclos

La identificación de residuos relacionados con la selectividad de sustrato entre isoformas de MAO, de cara a la exploración de motivos estructurales alternativos susceptibles de mejorar el perfil farmacológico de dichos inhibidores multipotentes.

2.2.3 Híbridos huprina-rheína: Hacia un fármaco con capacidad modificadora de la progresión de la enfermedad de Alzheimer.

La modelización de inhibidores híbridos huprina-rheína y la identificación del modo de unión en BACE-1, una actividad no prevista inicialmente en el diseño de dichos compuestos.

Capítulo

3 Metodología Multinivel

3.1 Publicación:

Assessing the Suitability of the Multilevel Strategy for the Conformational Analysis of Small Ligands

Journal of Physical Chemistry B

Jordi Juárez-Jiménez,[†] Xavier Barril,[‡,§] Modesto Orozco,[&,≠,£] Ramon Pouplana,[‡] and F. Javier Luque[†*]

[†] Departament de Fisicoquímica and Institut de Biomedicina (IBUB), Facultat de Farmàcia, Universitat de Barcelona, 08921 Santa Coloma de Gramenet, Spain

[‡] Departament de Fisicoquímica and Institut de Biomedicina (IBUB), Facultat de Farmàcia, Universitat de Barcelona, 08028 Barcelona, Spain

[§] Catalan Institution for Research and Advanced Studies (ICREA), Barcelona, Spain

Institute for Research in Biomedicine (IRB Barcelona), 08028 Barcelona, Spain

[≠] Joint BSC-GRG-IRB Program in Computational Biology, Barcelona, Spain

[£] Departament of Biochemistry and Molecular Biology, Biology Faculty, University of Barcelona, Barcelona, Spain

[*] Corresponding author. Phone: +34 93 402 45 57. E-mail: fjluque@ub.edu

THE JOURNAL OF PHYSICAL CHEMISTRY B

Article

pubs.acs.org/JPCB

Assessing the Suitability of the Multilevel Strategy for the Conformational Analysis of Small Ligands

Jordi Juárez-Jiménez,[†] Xavier Barril,[‡,§] Modesto Orozco,[∥,⊥,#] Ramon Pouplana,[‡] and F. Javier Luque*[,†]

[†]Departament de Fisicoquímica and Institut de Biomedicina (IBUB), Facultat de Farmàcia, Universitat de Barcelona, Avda. Prat de la Riba, 171, 08921 Santa Coloma de Gramenet, Spain

[‡]Departament de Fisicoquímica and Institut de Biomedicina (IBUB), Facultat de Farmàcia, Universitat de Barcelona, Avda. Diagonal 643, 08028 Barcelona, Spain

[§]Catalan Institution for Research and Advanced Studies (ICREA), Passeig Lluís Companys 23, 08010 Barcelona, Spain

[∥]Joint BSC-GRG-IRB Program in Computational Biology, C/ Baldiri Reixac 10-12, 08028 Barcelona, Spain

[⊥]Departament of Biochemistry and Molecular Biology, Biology Faculty, University of Barcelona, Diagonal, 643, 08028 Barcelona, Spain

[#]Institute for Research in Biomedicina (IRB Barcelona), C/ Baldiri Reixac 10-12, 08028 Barcelona, Spain

ABSTRACT: Predicting the conformational preferences of flexible compounds is a challenging problem in drug design, where the recognition between ligand and receptor is affected by the ability of the interacting partners to adopt a favorable conformation for the binding. To explore the conformational space of flexible ligands and to obtain the relative free energy of the conformation wells, we have recently reported a multilevel computational strategy that relies on the predominant-state approximation—where the conformational space is partitioned into distinct conformational wells—and combines a low-level method for sampling the conformational minima and high-level ab initio calculations for estimating their relative stability. In this study, we assess the performance of the multilevel strategy for predicting the conformational preferences of a series of structurally related phenylethylamines and streptomycin in aqueous solution. The charged nature of these compounds and the chemical complexity of streptomycin make them a challenging test for the multilevel approach. Furthermore, we explore the suitability of using a molecular mechanics approach as a source of approximate ensembles in the first stage of the multilevel strategy. The results support the reliability of the multilevel approach for obtaining an accurate conformational ensemble of small (bio)organic molecules in aqueous solution.

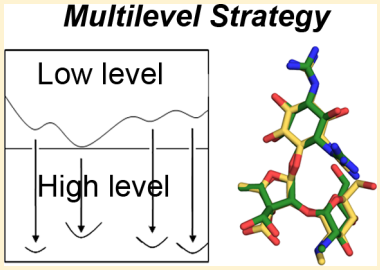

INTRODUCTION

The chemical complementarity between the functional groups present in the ligand and the residues that delineate the binding site is an essential requirement for enhancing the binding affinity in ligand−receptor complexes.[1−5] Achieving such complementarity often requires the occurrence of conformational changes in both ligand and receptor.[6−11] The structural changes in the receptor may involve a range of conformational alterations of different amplitude and extent, varying from rearrangements affecting either the side chains or the backbone of residues in the binding cavity to large-scale shifts in secondary structural elements or even domains. With regard to the ligand, those conformational changes are related to the selection of the "bioactive" conformation, that is, the conformation adopted in the bound state, from the set of conformational families populated in aqueous solution. The conformational changes triggered upon ligand binding contribute to the binding free energy, which can be expressed as the addition of the free-energy contribution due to the recognition between ligand and receptor in the bound state and the reversible work associated with the selection of the bioactive conformation (in both ligand and receptor) from the equilibrium ensemble in solution.

Finding the bioactive conformation of a flexible ligand is a challenging question in drug design, as the outcome of virtual screenings of compound libraries for hit identification depends on the ability to generate conformers that mimic the ligand in the bound state.[12−21] Because the bioactive conformation of the ligand may differ from the global minimum of the free ligand in the physiological environment, one has to evaluate the energetic cost required for adopting the bioactive conformation. Nevertheless, the uncertainties in the free-energy penalty associated with selecting the bioactive species may lead to a significant error in the predicted activity of the compound.[22−25]

To address these issues, we have recently reported a multilevel strategy conceived as an efficient methodology for the conformational search of drug-like compounds in solution and for estimating the relative stability of the most populated

Special Issue: William L. Jorgensen Festschrift

Received: July 8, 2014
Revised: October 9, 2014

 © XXXX American Chemical Society dx.doi.org/10.1021/jp506779y | J. Phys. Chem. B XXXX, XXX, XXX−XXX

conformations.[26] This approach relies on the predominant-states approximation adopted by Gilson and coworkers.[27,28] In this framework, one can assume that the conformational space can be partitioned into M local energy wells and that the sum of the configurational integral within each well equals the full configurational integral. Hence, the free energy (A) of a flexible molecule can be approximated from the free-energy contributions (A_m) of a finite number of M conformational wells (eq 1).

$$A \approx -RT \ln \sum_{m=1}^{M} e^{-A_m/RT} \tag{1}$$

and

$$A_m \approx -RT \ln \left[\frac{\nu_m}{N_m} \sum_{\substack{k=1 \\ k\in m}}^{N_m} e^{-E_k/RT} \right] \tag{2}$$

where v_m is the volume of configurational space for the energy well m and N_m denotes the number of conformational states for the conformational well m.

For a given well, the conformational free energy can be expressed as noted in eq 3, which separates the contribution of the minimum energy conformer from the rest of conformers that populate the conformational family.

$$\begin{aligned} A_m &= -RT \ln \frac{\nu_m}{N_m} (e^{-E_{m\_min}/RT} \sum_{k=1}^{N_m} e^{-\Delta E_k/RT}) \\ &= E_{m\_min} + A_m^{local} - RT \ln \frac{\nu_m}{N_m} \end{aligned} \tag{3}$$

where E_{m_min} is the energy of the minimum energy conformer in well m, ΔE_k is the relative energy of conformer k relative to the minimum energy conformer ($\Delta E_k = E_k - E_{m\_min}$), and A_m^{local} stands for the local curvature of the well (eq 4).

$$A_m^{local} = -RT \ln \sum_{k=1}^{N_m} e^{-\Delta E_k/RT} \tag{4}$$

By adopting the preceding expression, the relative free-energy difference between two conformational wells i and j ($\Delta A_{i,j}$) can then be rewritten as noted in eq 5, where the first term in the right-hand side denotes the relative energy between the minimum energy conformations in wells i and j (eq 6), and the second term stands for the free-energy contribution due to the distribution of conformational states in those wells (eq 7).

$$\Delta A_{i,j} = \Delta E_{i\_min,j\_min} + \Delta A_{i,j}^{local} - RT \ln \frac{\nu_j N_i}{\nu_i N_j} \tag{5}$$

$$\Delta E_{i\_min,j\_min} = E_{j,min} - E_{i,min} \tag{6}$$

$$\Delta A_{i,j}^{local} = -RT \ln \frac{\sum_{k=1}^{N_j} e^{-\Delta E_k/RT}}{\sum_{l=1}^{N_l} e^{-\Delta E_l/RT}} \tag{7}$$

If a uniform sampling of the conformational volume associated with wells i and j is performed, then the last term in eq 5 cancels. In this case, the accuracy in predicting the relative stability between two conformational families is mainly determined by the energy difference between the minimum energy structures of the conformational wells (eq 6) and the relative contribution due to the curvature around these minima (eq 7). To satisfy these requirements, the multilevel strategy combines a low-level (LL) method to explore the conformational landscape of a flexible compound and a high-level (HL) method to refine the relative stability of the structures corresponding to the minima of the conformational wells (eq 8). This approach is thus reminiscent of previous composite formalisms proposed for the study of complex chemical systems.[29,30]

$$\Delta A_{i,j} = \Delta E_{i\_min,j\_min}(HL) + \Delta A_{i,j}^{local}(LL) \tag{8}$$

In our previous work,[26] the Metropolis Monte Carlo (MC) technique was used in conjunction with the semiempirical RM1 Hamiltonian[31] as LL sampling method due to a two-fold reason. First, this choice avoids the need to carry out the explicit parametrization of any (bio)organic ligand, as the RM1 method was developed using data of 1736 compounds relevant in organic and biochemical areas, thus avoiding the substantial effort and intrinsic limitations assumed in the force-field parametrization of drug-like compounds. Second, solvent effects can be accounted for consistently due to the implementation of the MST continuum in the RM1 framework.[32] Following Riley et al.,[33] the HL refinement of the structures chosen as minimum energy conformers was performed by means of single-point calculations at the MP2/aug-cc-pVDZ level using the molecular geometries optimized at the B3LYP/6-31G(d) level[34] with inclusion of solvent effects with the B3LYP-parametrized version of the IEF-MST continuum model.[35,36]

We pursue the analysis of our multilevel approach by examining two open issues. First, while the original calibration of the multilevel strategy was focused on a variety of neutral molecules, the performance of the method to unravel the conformational landscape of charged, highly flexible ligands has to be examined. Second, because the main limitation of the preceding implementation was the computational cost associated with the LL semiempirical sampling, classical force fields might be a suitable alternative to carry out the LL sampling. To this end, we report here the results obtained for the conformational preferences of two classes of compounds, which encompass a series of structurally related 2-phenylethylamines, which is the scaffold found in catecholamines, and streptomycin, which is an aminoglycoside antibiotic chosen for its high chemical complexity. The conformational preferences are examined in light of the available experimental data (see below), which will allow us to test the accuracy of the multilevel strategy.

METHODS

Low-Level Conformational Sampling. To perform the LL conformational search, we ran a series of classical molecular dynamics (MD) simulations using the CUDA-accelerated version of the PMEMD module as implemented in AMBER12[37] software package. The necessary parametrization of molecules was made taking advantage of the AnteChamber tool. Briefly, the series of phenylethylamines were parametrized using the *gaff* force field,[38] while the parm99bsc-ILDN[39,40] force field was used to assign atom types to streptomycin. For all compounds the atomic point charges were determined using the RESP[41] procedure by fitting the HF/6-31G(d) electrostatic potential calculated with Gaussian 09.[42]

Each ligand was immersed in an octahedral box of TIP3P[43] water molecules, and the Xleap module was used to add the

dx.doi.org/10.1021/jp506779y | J. Phys. Chem. B XXXX, XXX, XXX−XXX

proper number of Cl^- counterions[44] to neutralize the overall charge of the simulated system. Prior to the production runs, the energy of each system was minimized, and then the system was equilibrated by rising the temperature from 50 to 298 K in 200 ps at constant volume. Finally, the density of the system was equilibrated in a subsequent 200 ps run using the NPT (298 K, 1 bar) ensemble. For production runs SHAKE[45] was used for bonds involving hydrogen atoms, concomitantly with an integration time step of 1 fs, periodic boundary conditions at constant volume and temperature, Particle Mesh Ewald[46] for the treatment of long-range electrostatic interactions, and a cutoff of 11 Å for nonbonded interactions.

For the sake of comparison, besides the classical force field, the LL sampling was also performed using the Metropolis MC technique in conjunction with an effective energy for the ligand in aqueous solution, which was determined by adding the energy of the ligand determined with the RM1 Hamiltonian and the hydration free energy estimated with the IEF-MST/RM1 method, following the strategy reported in our previous work.[26]

Mining Conformational Wells. To determine the extent of a conformational well, we projected the results from the MC IEF-MST/RM1 simulations onto a regularly discretized *n*-dimensional grid (*n* being the number of active torsions) so that each conformation (characterized by a set of active torsions) is assigned to a given element of the grid. When two or more structures are assigned to the same grid element, then only the structure with the lowest effective energy is retained as a representative conformation for the corresponding set of conformational variables. This procedure then yields a uniformly distributed sampling of the conformers in the *n*-dimensional grid, which results in the cancellation of the last term in eq 4. Then, the lowest energy structure in the grid is identified and used as a starting point to determine the extension of the conformational well. When a higher energy structure is found in the neighboring grid element, it is assigned to the same conformational well of the minimum energy conformer. When the search leads to a grid element where the energy of the representative structure is lower compared with the energy of the preceding grid element, then the search is stopped. Alternatively, the search is ceased when it leads to a grid element that contains no representative structure. This procedure allows us to define the outermost grid elements of the conformational well. The whole process is then repeated by searching for the lowest energy conformation upon exclusion of the conformational space already assigned to the previously found energy minima.

The application of this procedure to the conformational distribution obtained from the LL classical MD sampling would require, for each conformation of the ligand projected onto the *n*-dimensional grid, to combine the internal energy of the ligand and the solvation free energy arising from the surrounding solvent molecules, which would increase the complexity and computational time of the postprocessing analysis. To generate the uniformly distributed sampling, we projected the conformers collected along the MD trajectory onto the *n*-dimensional grid, and for each grid element the centroid of the projected structures was chosen as the representative conformation. Furthermore, the effective (free) energy of the representative conformer associated with each grid point of a given conformational well was obtained from the conformer population in the MD trajectory (eq 9).

$$\Delta A_k = -RT \ln \frac{p_k}{p_{\mathrm{ref}}} \tag{9}$$

where p_k denotes the population of sampled structures that correspond to the torsional grid element k and p_{ref} stands for the population of grid point containing the largest number of structures sampled along the MD trajectory.

High-Level Refinement. The HL protocol was taken from the implementation calibrated in the previous study.[26] In essence, the geometry of the representative structure chosen as the minimum energy conformer for each conformational well was first optimized using the IEF-MST//B3LYP/6-31G(d) continuum model, and the minimum energy nature of the stationary point was verified by analysis of the vibrational frequencies. Then, the energy of the optimized structure was refined by a single-point calculation at the MP2/aug-cc-pVDZ level. The final estimate of the relative free-energy conformational families *i* and *j* is then determined as

$$\Delta A_{i,j}^{\mathrm{MULTI}} = \Delta E_{i\_\mathrm{min},j\_\mathrm{min}}^{\mathrm{MP2}} + \Delta(ZPE)_{i\_\mathrm{min},j\_\mathrm{min}}^{\mathrm{IEF-MST/B3LYP}} + \Delta\Delta A_{\mathrm{hyd}}^{\mathrm{IEF-MST/B3LYP}} + \Delta A_{i,j}^{\mathrm{local}}(\mathrm{LL}) \tag{10}$$

where the terms on the right-hand side stand for the relative energy of the conformational minima determined at the MP2/aug-cc-pVDZ ($\Delta E_{\mathrm{i\_min,j\_min}}^{\mathrm{MP2}}$) level, the difference in the zero-point energy correction calculated at the IEF-MST/B3LYP/6-31G(d) level ($\Delta(ZPE)_{\mathrm{i\_min,j\_min}}^{\mathrm{IEF-MST/B3LYP}}$), the relative hydration free energy derived from IEF-MST computations ($\Delta\Delta A_{\mathrm{hyd}}^{\mathrm{IEF-MST/B3LYP}}$), and the difference in the local free energy contribution of wells *i* and *j* determined from the LL sampling ($\Delta A_{i,j}^{\mathrm{local}}$(LL); eq 7).

RESULTS

Phenylethylamines. Catecholamines are known to play an important role in neurotransmission and endocrinal signaling. The basic structural motif is an arylethylamine unit, which is also found in compounds of therapeutic interest (i.e., ephedrine) or drugs of abuse (i.e., amphetamine). The relatively simple structure of these molecules has been the focus of several conformational analyses due to their relevance to gain insight into the biological activity of this class of compounds and the interaction with their biological targets. Thus, a significant number of NMR-based studies have examined the conformational preferences of these compounds in aqueous solution, paying attention to the effect of substituents on the balance between trans and gauche conformations.[47−57]

With the aim to assess the performance of the multilevel approach for predicting the conformational preferences of catecholamines and the suitability of the LL classical sampling, we have examined a series of six compounds (Figure 1), which include phenylethylamine (PEA), amphetamine (AMP), adrenaline (AD), noradrenaline (NA), ephedrine (EPH), and norephedrine (NE).

The conformational landscape of these compounds is primarily dictated by the relative abundance of the gauche and trans rotamers around the $C_\alpha-C_\beta$ bond, which, in turn, depends on the balance between the intramolecular contacts that can be formed by the distinct functional groups and the intermolecular interactions formed with the hydrating water molecules in aqueous solution. In particular, such solvation terms are expected to be important because the amine group

dx.doi.org/10.1021/jp506779y | J. Phys. Chem. B XXXX, XXX, XXX−XXX

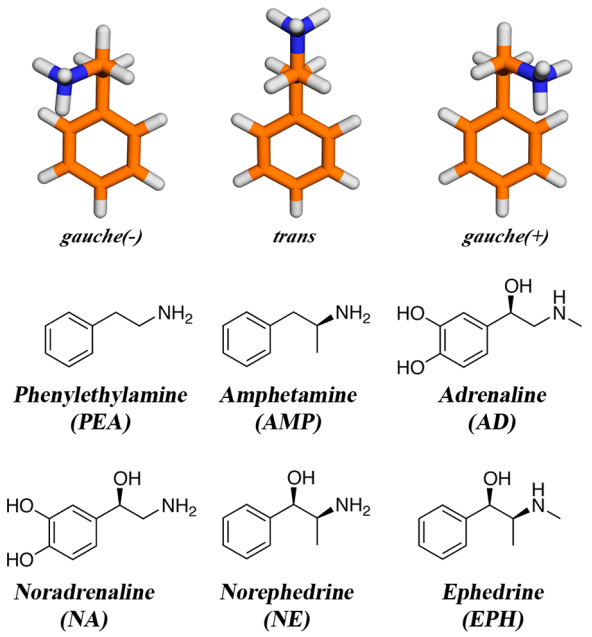

Figure 1. Representation of the major rotameric species arising from the conformational flexibility around the C_α–C_β bond in the series of cathecolamines: phenylethylamine (PEA), amphetamine (AMP), adrenaline (AD), noradrenaline (NA), norephedrine (NE), and ephedrine (EPH).

will be protonated at physiological pH, thus leading to enhanced interactions with water molecules. Hence, they represent an appropriate set for calibrating the suitability of the multilevel strategy in predicting the conformational distribution of these compounds.

Low-Level Sampling. The LL classical sampling was performed by running a 100 ns MD of the hydrated compound, with structures saved every picosecond. Additionally, an MC IEF-MST/RM1 sampling (4×10^5 configurations) was performed for each compound, allowing us to compare the results obtained with the two sampling approaches. It is worth noting that the length of the classical simulations was found to be adequate for achieving a converged distribution of the conformational families in water.

The coverage of the conformers obtained from LL samplings was generally larger than 97% for the MD(gaff) simulations and 94% for the MC(IEF-MST/RM1) calculations. Only for AMP and NE was the coverage of the MC(IEF-MST/RM1) sampling found to be slightly lower (~90%).

Although the LL MD and MC samplings led to similar conformers, there were notable differences regarding the relative abundance of the conformational families (Table 1). Thus, whereas the RM1 sampling showed a clear tendency to overestimate the population of the trans conformations, the classical sampling led to a more balanced distribution between gauche and trans conformers. In fact, the conformational distribution obtained for PEA, AMP, AD, and NA from the classical MD sampling is in close agreement with the experimental values, as the population of the trans conformer ranges from 39% for AMP to 69% for AD, which compare with the available experimental values (from 50 to 77%, respectively). In contrast, the LL RM1 sampling predicts a population of the trans conformer higher than 70% in all cases. Moreover, whereas the population of the gauche(−) conformer is in the range 13−17% for EPH and NE, thus reflecting the experimental data (10−21%), the RM1 sampling leads to a much higher population (53 and 81% for EPH and NE, respectively).

High-Level Refinement. As a first step, the geometry of the representative minimum energy conformer chosen for each conformational well was optimized at the IEF-MST//B3LYP/6-31G(d) level. The QM optimization did not lead to drastic changes in the torsional angles of the conformers, which resembled the starting structures taken from the LL sampling. (Typically the RMSD between starting and optimized geometries was <0.4 Å.)

Introduction of the HL correction in the framework of the multilevel strategy yields a distribution of conformational families almost independent of the LL sampling method, as noted in the values shown in Table 2. The largest difference between the conformational preferences obtained from the two LL samplings is found for AMP, where the population of the trans conformer is predicted to be 75 and 55% according to the HL calculations performed for the conformational structures taken from the LL MC(IEF-MST/RM1) and MD(gaff) samplings, respectively. This represents a significant decrease in divergence relative to the populations obtained at the LL sampling (87 and 39% at the MC(IEF-MST/RM1) and MD(gaff) levels, respectively; see Table 1). The population of the trans conformer of AMP obtained after HL refinement is closer to the experimental value (50%; see Table 2).

The multilevel results exhibit a close agreement with the experimental data, leading to a quantitative prediction of the distribution of conformers. This is shown in Figure 2, which displays the population of the trans conformer determined experimentally and from the multilevel calculations. (Note that for EPH and NE, the representation includes the population of both trans and gauche(+) conformers, as they could not be determined separately in the experimental studies.) The largest discrepancy between predicted and experimental populations of

Table 1. Relative Population (%) of Conformational Species Obtained from the LL Sampling (obtained from either MC and MD sampling simulations; see text) for the Series of Phenylethylamines

	MC (IEF-MST/RM1)			MD (gaff)			experimental[a]		
compound	g (−)	trans	g (+)	g (−)	trans	g (+)	g (−)	trans	g (+)
PEA	2	90	2	22	56	22	22	56	22
AMP	0	87	4	5	39	53	5	50	45
AD	5	80	12	15	69	13	6	77	17
NA	1	71	24	27	62	11	10	76	14
EPH	53	40	2	13	61	22	10	90	
NE	81	4	2	17	53	30	21	79	

[a]Data taken from refs 48 and 52.

dx.doi.org/10.1021/jp506779y | J. Phys. Chem. B XXXX, XXX, XXX−XXX

Table 2. Relative Population (%) of Conformational Species Obtained from the Multilevel (HL Refinement) Strategy for the Series of Phenylethylamines

	MC (IEF-MST/RM1)			MD (gaff)			experimental[a]		
compound	g (−)	trans	g (+)	g (−)	trans	g (+)	g (−)	trans	g (+)
PEA	20	54	26	33	33	34	22	56	22
AMP	2	75	23	6	55	38	5	50	45
AD	3	96	1	3	95	2	6	77	17
NA	3	91	6	12	80	7	10	76	14
EPH	1	92	7	1	92	7	10	90	
NE	2	64	34	2	76	22	21	79	

[a]Data taken from refs 48 and 52.

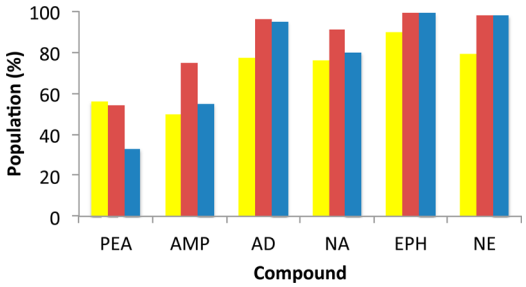

Figure 2. Representation of the population of the trans conformer determined experimentally (yellow) and from the multilevel strategy after HL refinement of the LL MC(IEF-MST/RM1) and MD (gaff) samplings (red and blue, respectively). For EPH and NE, the representation includes both trans and gauche(+) conformers.

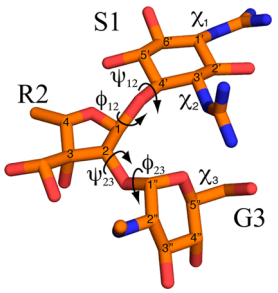

Figure 3. Representation of streptomycin and numbering of the dihedral angles used in this work (ϕ_{12}: O-1-O-4′; ψ_{12}: 1-O-4′-3′; ϕ_{23}: O-1″-O-2; ψ_{23}: 1″-O-2−1). The torsional angles of selected functional groups are also shown (χ_1: 6′-1′−N-C; χ_2: 2′-3′−N-C; χ_3: 4″-5″−C-O). The streptidine, streptose, and *N*-methyl-α-L-glucosamine subunits are denoted as S1, R2, and G3, respectively.

the trans conformer amounts to 25% for AMP (i.e., a discrepancy in free energy <0.3 kcal/mol) when the MC-(IEF_MST/RM1) sampling is considered and to 24% for PEA when the LL MD(gaff) sampling is used in the multilevel framework. This agreement is very encouraging, especially when one realizes the subtle differences between gauche and trans conformers associated with the different patterns of chemical substitutions present in the series of phenylethyl-amines Noteworthy, this trend is of particular relevance for EPH and NE, as the multilevel strategy is capable of reverting the preference for the gauche(−) conformer found at the LL semiempirical sampling.

Streptomycin. This aminoglycoside represents a more challenging test for the multilevel strategy due to its high structural complexity, as streptomycin comprises three rings and three positively charged groups at physiological pH. Streptomycin can be decomposed into three units: the streptidine moiety (S1 subunit), which is linked to a central α-L-streptose core (R2 subunit), which, in turn, is bound to an *N*-methyl-α-L-glucosamine (G3 subunit) residue (Figure 3). Protruding from this core, up to five flexible side chains may influence the conformational preferences at physiological pH: the streptidine moiety bears two guanidinium groups and the glucosamine moiety contains a charged *N*-methyl-amine group. In aqueous solution, the aldehyde group in R2 subunit is hydrated, forming a germinal diol.

The conformational flexibility of streptomycin is primarily dictated by two pairs of endocyclic dihedral angles, which describe the relative arrangement between streptidine and streptose subunits (ϕ_{12}/ψ_{12}) and between this latter unit and the glucosamine moiety (ϕ_{23}/ψ_{23}). To the best of our knowledge, two experimental works have examined the conformational preferences of streptomycin in aqueous solution.[58,59] Using a combination of NMR experiments and computational studies, Corzana et al.[58] reported that the three rings of streptomycin are primarily found in two conformational arrangements. The first family has a relative population of 50−60% and is characterized by dihedral angles ϕ_{12}/ψ_{12} = 270/190° and ϕ_{23}/ψ_{23} = 265/60°. The second family (40−45%) is defined by dihedral angles ϕ_{12}/ψ_{12} = 295/265° and ϕ_{23}/ψ_{23} = 290/165°. The authors highlighted that the two pairs of endocyclic bonds change in a concerted way. This conformational distribution has been challenged by the recent work reported by Blundell et al.,[59] as their NMR data led to two conformations that differ only in the pair of torsional angles ϕ_{23}/ψ_{23}. Thus, the major conformation (∼62%) is characterized by dihedral angles ϕ_{12}/ψ_{12} = 285/225° and ϕ_{23}/ψ_{23} = 257/103°, and the minor one (∼38%) is defined by torsional angles ϕ_{12}/ψ_{12} = 285/225° and ϕ_{23}/ψ_{23} = 279/173°. Taking into account the fact that the values of ϕ_{12} and ψ_{12} reported by Blundell et al.[59] lie within the range of torsional angles determined by Corzana et al.[58] and that the librational amplitudes are 16 and 22° for ϕ_{12} and ψ_{12}, respectively, it is clear that the conformational preferences of streptomycin primarily depend on the relative arrangement of the R2 and G3 subunits.

Low-Level Sampling. The LL sampling of streptomycin was performed by means of four independent 250 ns MD simulations. In the first simulation, the starting structure was generated from the data reported by Blundell et al.[59] for the major conformational species. Then, the snapshot sampled at 100 ns was used as the starting structure for the second 250 ns simulation (with reassignment of velocities), and this procedure was subsequently repeated for the third and forth runs.

The analysis of the classical sampling shows that the dihedral angle ϕ_{12} has a bimodal distribution, as it adopts values around 200 and 290°, whereas the angle ψ_{12} is primarily centered in the

dx.doi.org/10.1021/jp506779y | J. Phys. Chem. B XXXX, XXX, XXX−XXX

range 200−250°, although a minor population around 90° is also found (Figure 4). The dihedral angle ϕ_{23} is close to 295°, while a bimodal distribution is also found for ψ_{23} (with values around 90 and 160°), in agreement with the experimental data.

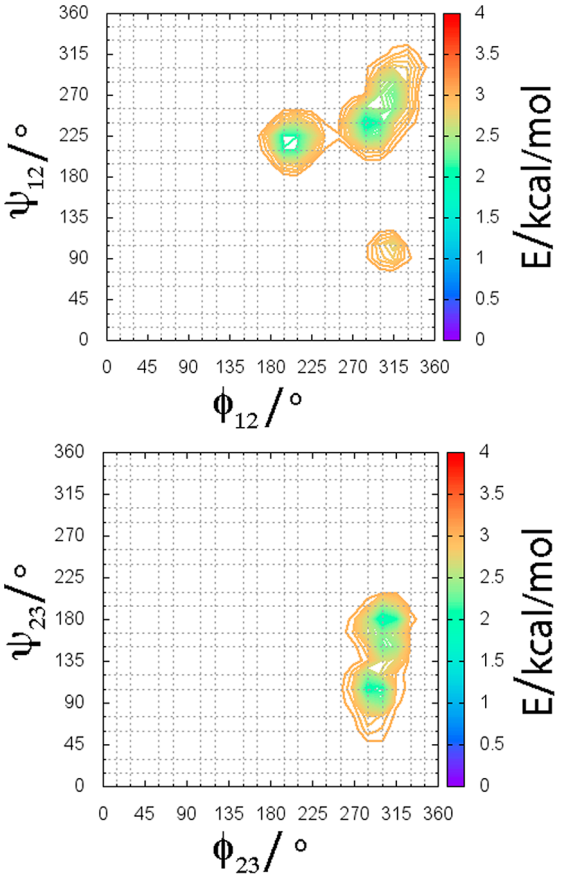

Figure 4. Heatmap representation of the torsional angles found for streptomycin in the LL MD simulations.

Up to five major conformational families (i.e., with a population equal or larger than 5%), which account for ~89% of the structures sampled in the MD simulations, are found in the LL sampling (Table 3). The population of the major conformational state (I in Table 3) is 41% and is characterized by representative dihedral angles ϕ_{12}/ψ_{12} = 190/200° and ϕ_{23}/ψ_{23} = 295/170°, thus differing from the relative orientation found experimentally for the streptidine and streptose subunits (see above). Compared with conformation I, a conformational state characterized by similar dihedral $\phi_{12}/\psi_{12}/\phi_{23}$ angles but differing in ψ_{23} is found with a minor population (5%; IV in Table 3). The conformational family more similar to the experimentally predominant state (II in Table 3) is found to account for ~20% of the sampled conformers. Finally, the experimentally minor conformational state is reflected in conformation III, which has a population of 18%. Overall, even though the two conformational states derived from NMR data are found in the LL sampling, they do not correspond to the predominant state, which would be conformation I, nor do they reflect the different population found experimentally between major and minor conformations.

Table 3. Representative Dihedral Angles for the Five Major Conformational Families Obtained from the LL MD Simulations of Streptomycin in Aqueous Solution[a]

conformer	ϕ_{12}	ψ_{12}	ϕ_{23}	ψ_{23}	%
I	190	200	295	170	41
II	280	220	275	85	20
	285	225	257	103	*~62*
III	290	250	290	150	18
	285	225	279	173	*~38*
IV	205	215	290	105	5
V	300	90	285	120	5

[a]Dihedral angles of the major and minor conformation found from NMR data by Blundell et al.,[59] and their population is indicated in italics.

High-Level Refinement. The use of the multilevel approach leads to a relatively simple conformational landscape, which is characterized by two conformations (Table 4). The major conformer is characterized by representative dihedral angles ϕ_{12}/ψ_{12} = 277/212° and ϕ_{23}/ψ_{23} = 272/95°, accounting for a population of 85%, in agreement with the experimental data.[58,59] This conformation contains two subfamilies, which differ in the orientation of the guanidinium group bound at position 1′ (see Figure 3), which is found in two orientations characterized by dihedral torsions (χ_1) of either 95 or 140°. This trend agrees with the experimental data, as this group has a bimodal distribution with mean angles of 78 and 162°.[59] The guanidinium group bound at position 3′ adopts a single conformation with a torsional angle (χ_2) of 98°, which reflects the unimodal behavior (χ_2 = 128°) found in NMR analysis.[59] Such behavior is dictated by the formation of hydrogen-bond interactions between the guanidinium unit and the oxygen atoms of the glucosamine ring and the hydroxyl group attached to position 5″. Nevertheless, whereas the orientation of this group is predicted to have an average angle (χ_3) of 175°, the experimental data reflects a mean angle close to 300°.

Table 4. Representative Dihedral Angles for the Two Main Conformational Families Obtained from the Multilevel Analysis for Streptomycin in Aqueous Solution

conformer	ϕ_{12}	ψ_{12}	ϕ_{23}	ψ_{23}	χ_1	χ_2	χ_3	%
I	277	212	272	95	95	98	175	47
					140	96	177	38
II	191	209	272	149	140	135	178	14

The multilevel approach also suggests the existence of a minor conformation (14%) characterized by dihedral angles ϕ_{12}/ψ_{12} = 191/209° and ϕ_{23}/ψ_{23} = 272/149° (Table 4 and Figure 5). Compared with the major conformation (I in Table 4), it reflects a distinct arrangement of streptidine and streptose units that breaks the intramolecular hydrogen bond of the guanidinium unit, which becomes more exposed to the aqueous solvent. This conformational family, however, is not reflected in the NMR-derived conformational preferences of the free streptomycin in solution. This discrepancy can be attributed to the difficulties in reproducing the delicate balance between the internal energy of conformers and the hydration contribution, highlighting the difficulty of continuum solvation models to provide an accurate description of the solvation contribution in highly charged molecules. In turn, this makes it necessary to search for further refinements in the description of solvent effects, such as the inclusion of a reduced set of discrete water molecules. This can be easily achieved by means of QM/MM techniques, as illustrated for instance in the study of the

dx.doi.org/10.1021/jp506779y | J. Phys. Chem. B XXXX, XXX, XXX−XXX

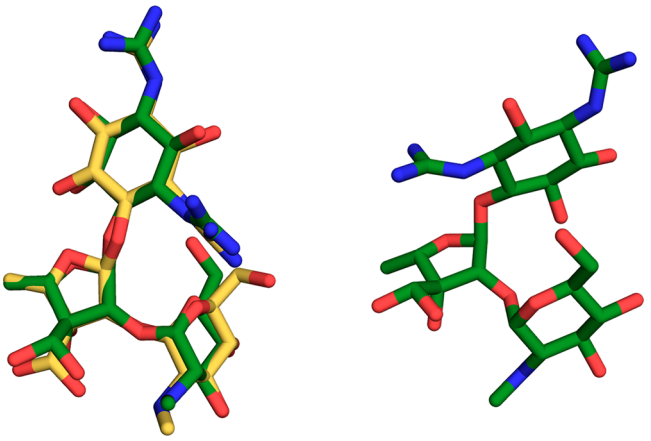

Figure 5. (Left) Representative conformations of the major conformation found for streptomycin in aqueous solution from the multilevel approach (green sticks) and NMR data (yellow sticks). (Right) Minor conformation found with the multilevel approach.

reactive properties of volatile organic compounds at the air/water interface.[60] Future studies will address these issues, which can be of particular relevance in the refinement of the molecular geometries during the transition from the LL sampled structures to the HL ones.

As a final remark, it is worth noting that present results support the suitability of MD simulations as LL sampling method in the framework of the multilevel strategy. In our previous study, the LL sampling was performed using a Monte Carlo search in conjunction with the effective energy derived from the IEF-MST version of the RM1 Hamiltonian.[26] This alleviates the need to carry out a careful parametrization of the ligand, which would demand an intense effort if the conformational analysis has to be performed for a series of chemically diverse small-molecule ligands. Nevertheless, because the multilevel results obtained from both MC(IEF-MST/RM1) and MD(gaff) samplings are very consistent, the availability of generalized force fields for (bio)organic compounds appears promising for exploring the LL sampling of drug-like compounds with classical simulations. Furthermore, this permits to take into account the structural effects played by the hydrating water molecules, an effect that is not properly accounted for in continuum solvation models. Finally, from a computational point of view, the MD simulations carried out for ephedrine and streptomycine (calculated using an M2090 NVIDIA GPU) are very similar despite the significant increase in ligand size. In contrast, the cost of the MC(IEF-MST/RM1) approach (run in a 64-bit Intel Xeon X7542 processor) for ephedrine is estimated to be around three times larger compared with the classical approach. Hence, it can be deduced that the expensiveness of the MC(IEF-MST/RM1) sampling would have been much larger for streptomycin, thus making this latter approach less efficient for larger (bio)organic compounds.

CONCLUSIONS

In this work, we have provided evidence that supports the reliability of the multilevel strategy as a tool for exploring the conformational landscape of molecules in solution, keeping a reasonable balance between chemical accuracy and computational expensiveness. In particular, the results obtained for the series of phenylethylamines point out that the conformational preferences of these compounds are independent of the LL conformational sampling methodology. Accordingly, the multilevel strategy can benefit from the use of both classical force fields and semiempirical methods to perform the LL sampling. We also have proven that this strategy is capable of finding the major conformation of streptomycin in aqueous solution, leading to a representative conformer that agrees well with the available NMR data.

Despite this encouraging finding, the results also point out that caution is needed for the application of the multilevel approach to molecules with multiple charged sites due to the need of maintaining a very accurate description of intramolecular interactions and solvation effects. In our view, further methodological improvements, including the explicit description of solvent molecules at the HL step, may contribute to enhance the predictive power of the technique. Furthermore, the extension of these studies to (bio)organic molecules with complex chemical scaffolds is also necessary to calibrate the suitability of computational methods for achieving an accurate description of the conformer distribution in small biomolecules and drug-like compounds.

AUTHOR INFORMATION

Corresponding Author

*Tel: +34 93 402 45 57. E-mail: fjluque@ub.edu.

Notes

The authors declare no competing financial interest.

ACKNOWLEDGMENTS

This work was supported by the Spanish MINECO (SAF2011-27642, SAF2012-33481, BIO2012-32868) and the Generalitat de Catalunya (2014SGR1189 and 2014SGR134). J.J.-J. is a fellow from the Fondo de Investigaciones Sanitarias, Ministerio de Economía y Competitividad. M.O. and F.J.L. are ICREA-Academia fellows. Computational facilities provided by the Centre de Supercomputació de Catalunya and Barcelona Supercomputing Center are acknowledged.

REFERENCES

(1) Gohlke, H.; Klebe, G. Approaches to the Description and Prediction of the Binding Affinity of Small-Molecule Ligands to Macromolecular Receptors. *Angew. Chem., Int. Ed.* **2002**, *41*, 2644−2676.

(2) *Protein−Ligand Interactions. From Molecular Recognition to Drug Design*; Böhm, H. J., Schneider, G., Eds.; Wiley-VCH: Weinheim, Germany, 2003.

(3) Hunter, C. A. Quantifying Intermolecular Interactions: Guidelines for the Molecular Recognition Toolbox. *Angew. Chem., Int. Ed.* **2004**, *43*, 5310−5324.

(4) Bissantz, C.; Kuhn, B.; Stahl, M. A Medicinal Chemist's Guide to Molecular Interactions. *J. Med. Chem.* **2010**, *53*, 5061−5084.

(5) *Physico-Chemical and Computational Approaches to Drug Discovery*; Luque, F. J., Barril, X., Eds.; Royal Society of Chemistry; Drug Discovery Series No. 23; Cambridge, U.K., 2012.

(6) Spyrakis, F.; Bidon-Chanal, A.; Barril, X.; Luque, F. J. Protein Flexibility and Ligand Recognition: Challenges for Molecular Modeling. *Curr. Top. Med. Chem.* **2011**, *11*, 192−210.

(7) Carlson, H. A.; McCammon, J. A. Accommodating Protein Flexibility in Computational Drug Design. *Mol. Pharmacol.* **2000**, *57*, 213−218.

(8) Lin, J.-H.; Perryman, A. L.; Schames, J. R.; McCammon, J. A. Computational Drug Design Accommodating Receptor Flexibility: The Relaxed Complex Scheme. *J. Am. Chem. Soc.* **2002**, *124*, 5632−5633.

(9) Cavasotto, C. N.; Singh, N. Docking and High-Throughput Docking: Successes and the Challenge of Protein Flexibility. *Curr. Comput.-Aided Drug Des.* **2008**, *4*, 221−234.
(10) Cozzini, P.; Kellogg, G.; Spyrakis, F.; Abraham, D.; Gabriele, C.; Emerson, A.; Fanelli, F.; Gohlke, H.; Kuhn, L.; Morris, G.; Orozco, M.; Perthinhez, T.; Rizzi, M.; Sotriffer, C. Target Flexibility: An Emerging Consideration in Drug Discovery and Design. *J. Med. Chem.* **2008**, *51*, 6237−6255.
(11) Finch, H. The Conformational Musing of a Medicinal Chemist. *Drug Discovery Today* **2014**, *19*, 320−325.
(12) Kirchmair, J.; Wolber, G.; Laggner, C.; Langer, T. Comparative Performance Assessment of the Conformational Model Generators Omega and Catalyst: A Large-Scale Survey of the Retrieval of Protein-Bound Ligand Conformations. *J. Chem. Inf. Model.* **2006**, *46*, 1848−1861.
(13) Li, J.; Ehlers, T.; Sutter, J.; Varma-O'Brien, S.; Kirchmair, J. CAESAR: A New Conformer Generation Algorithm Based on Recursive Buildup and Local Rotational Symmetry Consideration. *J. Chem. Inf. Model.* **2007**, *47*, 1923−1932.
(14) Loferer, M.; Kolossváry, I.; Aszódi, A. Analyzing the Performance of Conformational Search Programs on Compound Databases. *J. Mol. Graph. Model.* **2007**, *25*, 700−710.
(15) Agrafiotis, D. K.; Gibbs, A. C.; Zhu, F.; Izrailev, S.; Martin, E. Conformational Sampling of Bioactive Molecules: A Comparative Study. *J. Chem. Inf. Model.* **2007**, *47*, 1067−1086.
(16) Brameld, K. A.; Kuhn, B.; Reuter, D. C.; Stahl, M. Small Molecule Conformational Preferences Derived from Crystal Structure Data. A Medicinal Chemistry Focused Analysis. *J. Chem. Inf. Model.* **2008**, *48*, 1−24.
(17) Liu, X.; Bai, F.; Ouyang, S.; Wang, X.; Li, H.; Jiang, H. Cyndi: A Multi-Objective Evolution Algorithm Based Method for Bioactive Molecular Conformation Generation. *BMC Bioinformatics* **2009**, *10*, 101.
(18) Takagi, T.; Amano, M.; Tomimoto, M. Novel Method for the Evaluation of 3D Conformation Generators. *J. Chem. Inf. Model.* **2009**, *49*, 1377−1388.
(19) Chung, S.; Parker, J. B.; Bianchet, M.; Amzel, L. M.; Stivers, J. T. Impact of Linker Strain and Flexibility in the Design of a Fragment-Based Inhibitor. *Nat. Chem. Biol.* **2009**, *5*, 407−413.
(20) Watts, K. S.; Dalal, P.; Murphy, R. B.; Sherman, W.; Friesner, R. A.; Shelley, J. C. ConfGen: A Conformational Search Method for Efficient Generation of Bioactive Conformers. *J. Chem. Inf. Model.* **2010**, *50*, 534−546.
(21) Rupp, M.; Bauer, M. R.; Wilcken, R.; Lange, A.; Reutlinger, M.; Boeckler, F. M.; Schneider, G. Machine Learning Estimates of Natural Product Conformational Energies. *PLoS Comput. Biol.* **2014**, *10*, e1003400.
(22) Perola, E.; Charifson, P. S. Conformational Analysis of Drug-Like Molecules Bound to Proteins: An Extensive Study of Ligand Reorganization upon Binding. *J. Med. Chem.* **2004**, *47*, 2499−2510.
(23) Tirado-Rives, J.; Jorgensen, W. L. Contribution of Conformer Focusing to the Uncertainty in Predicting Free Energies for Protein-Ligand Binding. *J. Med. Chem.* **2006**, *49*, 5880−5584.
(24) Butler, K. T.; Luque, F. J.; Barril, X. Toward Accurate Relative Energy Predictions of the Bioactive Conformation of Drugs. *J. Comput. Chem.* **2009**, *30*, 601−610.
(25) Pisani, P.; Piro, P.; Decherchi, S.; Bottegoni, G.; Sona, D.; Murino, V.; Rocchia, W.; Cavalli, A. Describing the Conformational Landscape of Small Organic Molecules through Gaussian Mixtures in Dihedral Sapce. *J. Chem. Theory Comput.* **2014**, *10*, 2557−2568.
(26) Forti, F.; Cavasotto, C.; Orozco, M.; Barril, X.; Luque, F. J. A Multilevel Strategy for the Exploration of the Conformational Flexibility of Small Molecules. *J. Chem. Theory Comput.* **2012**, *8*, 1808−1819.
(27) Head, M. S.; Given, J. A.; Gilson, M. K. Mining Minima: Direct Computation of Conformational Free Energy. *J. Phys. Chem. A* **1997**, *101*, 1609−1618.
(28) Chen, W.; Chang, C.; Gilson, M. K. Calculation of Cyclodextrin Binding Affinities: Energy, Entropy, and Implications for Drug Design. *Biophys. J.* **2004**, *87*, 3035−3049.
(29) Retegan, M.; Matins-Costa, M.; Ruiz-López, M. F. Free Energy Calculations Using Dual-Level Born-Oppenheimer Molecular Dynamics. *J. Chem. Phys.* **2010**, *133*, 064103.
(30) Chung, L. W.; Hirao, H.; Morokuma, K. The ONIOM Method: Its Foundation and Applications to Metalloenzymes and Photobiology. *WIREs Comput. Mol. Sci.* **2012**, *2*, 327−350.
(31) Rocha, G. B.; Freire, R. O.; Simas, A. M.; Stewart, J. J. P. RM1: A Reparametrization of AM1 for H, C, N, O, P, S, F, Cl, Br, and I. *J. Comput. Chem.* **2006**, *27*, 1101−1111.
(32) Forti, F.; Barril, X.; Luque, F. J.; Orozco, M. Extension of the MST Continuum Solvation Model to the RM1 Semiempirical Hamiltonian. *J. Comput. Chem.* **2008**, *29*, 578−587.
(33) Riley, K. E.; Op't Holl, B. T.; Merz, K. M. Critical Assessment of the Performance of Density Functional Methods for Several Atomic and Molecular Properties. *J. Chem. Theory Comput.* **2007**, *3*, 407−433.
(34) Stephens, P. J.; Devlin, F. J.; Chabalowski, C. F.; Frisch, M. J. Ab Initio Calculation of Vibrational Absorption and Circular Dichroism Spectra Using Density Functional Force Fields. *J. Phys. Chem.* **1994**, *98*, 11623−11627.
(35) Soteras, I.; Curutchet, C.; Bidon-Chanal, A.; Orozco, M.; Luque, F. J. Extension of the MST Model to the IEF Formalism: HF and B3LYP Parametrizations. *J. Mol. Struct.: THEOCHEM* **2005**, *727*, 29−40.
(36) Curutchet, C.; Bidon-Chanal, A.; Soteras, I.; Orozco, M.; Luque, F. J. MST Continuum Study of the Hydration Free Energies of Monovalent Ionic Species. *J. Phys. Chem. B* **2005**, *109*, 3565−3574.
(37) Case, D. A.; Darden, T. A.; Cheatham, T. E., I. I. I.; Simmerling, C. L.; Wang, J.; Duke, R. E.; Luo, R.; Walker, R. C.; Zhang, W.; Merz, K. M.; et al. *AMBER 12*; University of California: San Francisco, CA, 2012.
(38) Wang, J.; Wolf, R. M.; Caldwell, J. W.; Kollman, P. A.; Case, D. A. Development and Testing of a General Amber Force Field. *J. Comput. Chem.* **2004**, *25*, 1157−1174.
(39) Hornak, V.; Abel, R.; Okur, A.; Strockbine, B.; Roitberg, A.; Simmerling, C. Comparison of Multiple Amber Force Fields and Development of Improved Protein Backbone Parameters. *Proteins* **2006**, *65*, 712−725.
(40) Lindorff-Larsen, K.; Piana, S.; Palmo, K.; Maragakis, P.; Klepeis, J. L.; Dror, R. O.; Shaw, D. E. Improved Side-Chain Torsion Potentials for the Amber ff99SB Protein Force Field. *Proteins* **2010**, *78*, 1950−1958.
(41) Bayly, C. I.; Cieplak, P.; Cornell, W.; Kollman, P. A. A Well-Behaved Electrostatic Potential Based Method Using Charge Restraints for Deriving Atomic Charges: The RESP Model. *J. Phys. Chem.* **1993**, *97*, 10269−10280.
(42) Frisch, M. J.; Trucks, G. W.; Schlegel, H. B.; Scuseria, G. E.; Robb, M. A.; Cheeseman, J. R.; Scalmani, G.; Barone, V.; Mennucci, B.; Petersson, G. A. et al. *Gaussian 09*, revision C.01; Gaussian, Inc.: Wallingford, CT, 2010.
(43) Jorgensen, W. L.; Chandrasekhar, J.; Madura, J. D.; Impey, R. W.; Klein, M. L. Comparison of Simple Potential Functions for Simulating Liquid Water. *J. Chem. Phys.* **1983**, *79*, 926−935.
(44) Joung, I. S.; Cheatham, T. E. Determination of Alkali and Halide Monovalent Ion Parameters for Use in Explicitly Solvated Biomolecular Simulations. *J. Phys. Chem. B* **2008**, *112*, 9020−9041.
(45) Ryckaert, J.-P.; Ciccotti, G.; Berendsen, H. J. *J. Comput. Phys.* **1977**, *23*, 327−341.
(46) Darden, T.; York, D.; Pedersen, L. Particle Mesh Ewald: An N-log(N) Method for Ewald Sums in Large Systems. *J. Chem. Phys.* **1993**, *98*, 10089−10092.
(47) Neville, G. A.; Deslauri, R.; Blackburn, B. J.; Smith, I. C. P. Conformational Studies of Amphetamine and Medicinally Important Derivatives by Nuclear Magnetic Resonance Spectroscopy. *J. Med. Chem.* **1971**, *14*, 717−721.

(48) Bright, S.; Platano, J.; Jacobus, J. Amphetamine. Specific Labeling and Solution Conformation. *J. Org. Chem.* **1973**, *38*, 2554−2555.
(49) Berg, R. W.; Shim, I.; White, P. C.; Abdali, S. Raman Optical Activity and Raman Spectra of Amphetamine Species−Quantum Chemical Model Calculations and Experiments. *Am. J. Anal. Chem.* **2012**, *3*, 410−421.
(50) Godfrey, P. D.; McGlone, S. J.; Brown, R. D. The Shape of Neurotransmitters by Millimetrewave Spectroscopy: Amphetamine. *J. Mol. Struct.* **2001**, *599*, 139−152.
(51) Godfrey, P. D.; Hatherley, L. D.; Brown, R. D. The Shapes of Neurotransmitters by Milimeter-Wave Spectroscopy: 2-Phenylethylamine. *J. Am. Chem. Soc.* **1995**, *117*, 8204−8210.
(52) Ison, R. R.; Partington, P.; Roberts, G. C. K. The Conformation of Catecholamines and Related Compounds in Solution. *Mol. Pharmacol.* **1973**, *9*, 756−765.
(53) Melandri, S.; Ragno, S.; Maris, A. Shape of Biomolecules by Free Jet Microwave Spectroscopy: 2-Amino-1-Phenylethanol and 2-Methylamino-1-Phenylethanol. *J. Phys. Chem. A* **2009**, *113*, 7769−7773.
(54) Graham, R. J.; Kroemer, R. T.; Mons, M.; Robertson, E. G.; Snoek, L. C.; Simons, J. P. Infrared Ion Dip Spectroscopy of a Noradrenaline Analogue: Hydrogen Bonding in 2-Amino-1-Phenylethanol and its Singly Hydrated Complex. *J. Phys. Chem. A* **1999**, *103*, 9706−9711.
(55) Snoek, L. C.; Van Mourik, T.; Simons, J. P. Neurotransmitters in the Gas Phase: A Computational and Spectroscopic Study of Noradrenaline. *Mol. Phys.* **2003**, *101*, 1239−1248.
(56) van Mourik, T. The Shape of Neurotransmitters in the Gas Phase: A Theoretical Study of Adrenaline, Pseudoadrenaline, and Hydrated Adrenaline. *Phys. Chem. Chem. Phys.* **2004**, *6*, 2827−2837.
(57) Çarçabal, P.; Snoek, L. C.; Van Mourik, T. A Computational and Spectrosocpic Study of the Gas-Phase Conformers of Adrenaline. *Mol. Phys.* **2005**, *103*, 1633−1639.
(58) Corzana, F.; Cuesta, I.; Bastida, A.; Hidalgo, A.; Latorre, M.; González, C.; García-Junceda, E.; Jiménez-Barbero, J.; Asensio, J. L. Molecular Recognition of Aminoglycoside Antibiotics by Bacterial Defence Proteins: NMR Study of the Structural Features of Streptomycin Inactivation by *Bacillus subtilis* Aminoglycoside-6-Adenyl Transferase. *Chem.—Eur. J.* **2005**, *11*, 5102−5113.
(59) Blundell, C. D.; Packer, M. J.; Almond, A. Quantification of Free Ligand Conformational Preferences by NMR and Their Relationship to the Bioactive Conformation. *Bioorg. Med. Chem.* **2013**, *21*, 4976−4987.
(60) Martins-Costa, M. T. C.; Anglada, J. M.; Francisco, J. S.; Ruiz-Lopez, M. F. Reactivity of Volatile Organic Compounds at the Surface of a Water Droplet. *J. Am. Chem. Soc.* **2012**, *134*, 11821−11827.

3.2 Extensión de la metodología Multinivel

La implementación original de la MLS se utilizó para la exploración conformacional del dicloroetano y de la histamina neutra, tanto en vacío como en medio acuoso, así como para estimar el coste energético ligado a la adopción de la conformación bioactiva de un conjunto de inhibidores de la retro-transcriptasa del VIH[22]. Si bien los resultados fueron alentadores, dejaban en el aire dos cuestiones clave. En primer lugar, las moléculas ensayadas eran neutras y era necesario evaluar la efectividad de la MLS en el caso de moléculas flexibles con carga. En segundo lugar, aunque el uso del hamiltoniano RM1[27] permitía eludir la parametrización de compuestos, conllevaba una gran carga computacional que incrementaba notablemente el coste global de la estrategia.

Para dar respuesta a esta cuestiones, en la presente tesis se llevó a cabo la extensión del método MLS en dos etapas. Primero, se compararon las preferencias conformacionales obtenidas para un grupo de catecolaminas cuando el muestro conformacional LL se realizaba empleando el hamiltoniano RM1 o el campo de fuerzas clásico *gaff*[75]. Segundo, se exploró el espacio conformacional del antibiótico aminoglucósido estreptomicina empleando el campo de fuerzas parm99-nmr-ildn[76,77] durante el muestro LL y se evaluó el comportamiento del método comparando los resultados con los datos de RMN disponibles en la literatura[78,79].

3.2.1 Ajuste de la expresión Multinivel al uso de campos de fuerza clásicos

En el caso de una simulación de dinámica molecular en solvente explícito, obtener la energía efectiva de una determinada conformación requeriría separar la

contribución de la energía interna del ligando de la contribución de la energía libre de solvatación. Si bien sería posible realizar un post-procesado de las trayectorias, ello resultaría complejo e incrementaría el coste computacional del método. Por ello, alternativamente se planteó el uso de una energía libre efectiva basada en la abundancia relativa de cada estructura representada en la cuadrícula *n*-dimensional obtenida directamente de la trayectoria de dinámica molecular (ec. 3.1)

$$\Delta A_k = -RT \ln \frac{P_k}{P_{i,min}} \qquad \textbf{3.1}$$

donde P_k corresponde a la población de estructuras en un punto k de la cuadrícula y $P_{i,min}$ a la población del punto más poblado del pozo conformacional.

3.2.2 Aplicación a moléculas cargadas: Ariletilaminas

El motivo estructural ariletilamina y derivados como la ariletanolamina o la arilpropanolamina son parte integral de muchos compuestos de interés terapéutico y/o biológico. Así, neurotransmisores como la dopamina o la noradrenalina son ejemplos de catecolaminas con un papel en la neurotransmisión, pero también encontramos fármacos como el antihistamínico efedrina o compuestos psicoactivos como la anfetamina que pueden adscribirse a estas familias estructurales. Debido a la diversidad de funciones asociadas a esta estructura, durante décadas ha habido gran interés en describir las preferencias conformacionales de cara a comprender su efecto en la actividad biológica[80–90].

Para calibrar la exactitud de la metodología en el caso de moléculas cargadas y la influencia del nivel de teoría escogido para el muestreo LL (el hamiltoniano RM1 o el campo de fuerza *gaff*), aplicamos la estrategia Multinivel a un conjunto de 6 compuestos tipo ariletilaminas (Figura 4.3) formado por feniletilamina, anfetamina,

adrenalina, noradrenalina, efedrina y norefedrina (PEA, AMP, AD, NA, EPH y NE). Con el fin de comparar los resultados con estudios de RMN disponibles en la literatura, el panorama conformacional se describió en función de la orientación del enlace central C_α-C_β agrupando las conformaciones en los tres rotámeros clásicos, *gauche*(-), *trans* y *gauche*(+). Cabe hacer notar que las poblaciones conformacionales dependerán no sólo de los contactos intramoleculares, sino que, debido al carácter básico del grupo amina, que se encontrará protonado a pH fisiológico, dependerá notablemente de las interacciones con el solvente. Si estos efectos se describiesen con exactitud, sería posible conocer el conjunto de conformaciones accesibles para una molécula a una determinada temperatura, ya que sólo estarán pobladas significativamente (> 3%) aquellas conformaciones cuya diferencia de energía libre respecto al mínimo global sea inferior o similar a $4K_BT$ (2.4 kcal/mol a 298K).

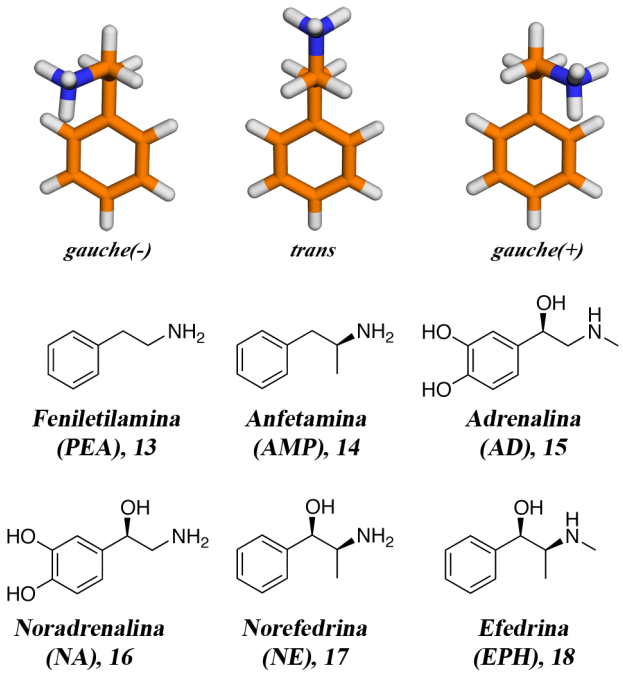

Figura 3.1 Rotámeros clásicos sobre un enlace sencillo y estructuras estudiadas empleando la metodología Multinivel. Las moléculas comparten la unidad estructural ariletilamina y su conformación en agua difiere en función de los sustituyentes sobre la cadena alifática.

Los resultados del muestreo a bajo nivel revelaron notables discrepancias según el método empleado (Tabla 3.1). Así, mientras la simulación de Monte Carlo con RM1 mostraba una tendencia a sobrestimar la población del confórmero *trans* en el caso de PEA, AMP, AD y NA, la exploración empleando el campo de fuerzas clásico daba lugar a una representación de confórmeros más equilibrada, concordante con los resultados experimentales. Como ejemplo, cabe mencionar que la conformación *trans* determinada experimentalmente para PEA, AMP, AD y NA oscila entre 50 y 77%, en tanto que los valores obtenidos por dinámica molecular con el campo de fuerza *gaff* varían entre 39 y 69%. Asimismo, el muestreo con el hamiltoniano semiempírico mostró una sobrestimación de la población del confórmero *gauche*(-) en el caso de NE y EPH, que contrastaba tanto con la predicción obtenida mediante el campo de fuerzas como con los resultados experimentales.

	MC (IEF-MST/RM1)			**MD (gaff)**			**Experimental**		
	g (-)	*trans*	*g* (+)	*g* (-)	*trans*	*g* (+)	*g* (-)	*trans*	*g* (+)
PEA	2	90	2	22	56	22	22	56	22
AMP	0	87	4	5	39	53	5	50	45
AD	5	80	12	15	69	13	6	77	17
NA	1	71	24	27	62	11	10	76	14
EPH	53	40	2	13	61	22	10	90	
NE	81	4	2	17	53	30	21	79	

Tabla 3.1 Población relativa (%) de las especies conformacionales obtenida del muestreo LL. La exploración empleando el campo de fuerzas clásico (MD) es coherente con los resultados experimentales[80,85] y contrasta con los resultados obtenidos empleando el método semiempírico.

Al aplicar las correcciones HL al muestreo anterior, sin embargo, se obtiene una predicción de las preferencias conformacionales muy similar, independientemente del método de muestreo empleado y en consonancia con los resultados experimentales

(Tabla 3.2). De hecho, puede considerarse que empleando la metodología multinivel es posible obtener una predicción cuantitativa de las preferencias conformacionales del conjunto estudiado de ariletilaminas, ya que las mayores discrepancias (de aproximadamente un 25%) corresponden a diferencias de energía libre inferiores a 0.3 kcal/mol.

	MC (IEF-MST/RM1)			MD (gaff)			Experimental		
	g (-)	*trans*	*g* (+)	*g* (-)	*trans*	*g* (+)	*g* (-)	*trans*	*g* (+)
PEA	20	54	26	33	33	34	22	56	22
AMP	2	75	23	6	55	38	5	50	45
AD	3	96	1	3	95	2	6	77	17
NA	3	91	6	12	80	7	10	76	14
EPH	1	92	7	1	92	7	10	90	
NE	2	64	34	2	76	22	21	79	

Tabla 3.2 Población relativa (%) de las especies conformacionales obtenida tras la aplicación de la Metodología Multinivel. El refinado HL permite obtener una predicción similar independiente del método de muestreo inicial y coherente con los resultados experimentales[80,85].

En conclusión, los resultados revelan que la metodología multinivel no varía al emplear un campo de fuerzas clásico para llevar a cabo el muestreo de bajo nivel. Por ello, la disponibilidad de campos de fuerza generales, como *gaff*, permitiría obviar el tedioso proceso de parametrización de ligandos y llevar a cabo la exploración LL mediante dinámica molecular, permitiendo así tener en cuenta el efecto de las interacciones directas con el solvente, como la formación de puentes de hidrógeno, sobre la flexibilidad conformacional.

3.2.3 Aplicación a moléculas cargadas: Estreptomicina

En base a los resultados precedentes, se usó la misma estrategia clásica en el caso de una molécula mucho más compleja: el antibiótico aminoglucósido estreptomicina, cuya estructura incluye tres anillos, cinco cadenas laterales flexibles y tres cargas positivas.

Desde el punto de vista estructural, la estreptomicina se puede descomponer en tres subunidades correspondientes a tres motivos estructurales cíclicos (Figure 3.2): el anillo de estreptidina (subunidad S1), el anillo central de α-L-estreptosa (subunidad R2) y el anillo de N-metil-α-L-glucosamina (subunidad G3). A este esqueleto central se encuentran unidos cinco grupos flexibles (dos grupos guanidil, un grupo N-metilamina, un grupo hidroximetil y un grupo diol geminal proveniente de la hidratación del aldehído en la subunidad R2). De ellos, sólo los grupos guanidil y el grupo hydroxi-metil parecen tener un papel determinante en la conformación de la molécula[79].

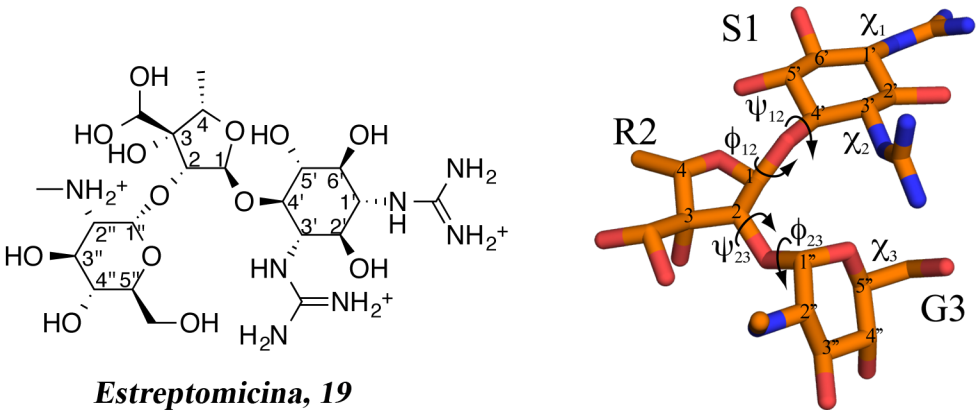

Figura 3.2 Estructuras 2D (izquierda) y 3D (derecha) de estreptomicina. Se destacan los ángulos diedro que dictan la conformación en agua.

La disposición relativa de los tres anillos determina la conformación que adopta la molécula en medio acuoso, que según los trabajos de Corzana *et. al.*[78] y de Blundell

et. al.[79], depende de las torsiones ϕ_{12}/ψ_{12} para describir la orientación relativa entre las subunidades S1 y R2, y ϕ_{23}/ψ_{23} para las subunidades R2 y G3. Los resultados de RMN indican que las subunidades S1 y R2 se orientan principalmente en una conformación con valores ϕ_{12}/ψ_{12} = 282º(±13º) / 227º(±38º), mientras que las subunidades R2 y G3 se hallan en dos conformaciones: la mayoritaria (con una abundancia de alrededor del 60%) quedaría definida por unos valores de diedro ϕ_{23}/ψ_{23} = 261º(±4º) / 81º(±22º), en tanto que en la minoritaria serían ϕ_{23}/ψ_{23} = 284º(±5º) / 169º(±4º).

El muestreo a bajo nivel se llevo a cabo mediante 4 simulaciones de 250 ns empleando coordenadas y velocidades iniciales diferentes, obteniéndose un total de 10^6 conformaciones. Al agrupar estas conformaciones por el valor de sus ángulos diedros endocíclicos, se obtuvieron 5 familias conformacionales de abundancia relativa superior al 5% (Tabla 3.3).

Familia Conformacional	ϕ_{12}	ψ_{12}	ϕ_{23}	ψ_{23}	%
I	190	200	295	170	41
II	280	220	275	85	20
III	290	250	290	150	18
IV	205	215	290	105	5
V	300	90	285	120	5

Tabla 3.3 Valores de ángulos diedro endocíclicos y población relativa (%) de las familias conformacionales obtenida del muestreo LL. Sólo se consideraron representativas aquellas familias con poblaciones superiores al 5%.

El análisis del muestreo a bajo nivel reveló que, aunque las familias conformacionales descritas experimentalmente eran capturadas a este nivel de teoría, su abundancia relativa quedaba lejos de los valores experimentales. Concretamente, las familias II y III (las más similares a las familias experimentales mayoritaria y minoritaria respectivamente) quedan lejos de las abundancias descritas por RMN, en

tanto que la familia I que sería mayoritaria según la simulación de dinámica molecular, no es descrita en ninguno de los trabajos experimentales previos.

En contraste con los resultados anteriores, la re-evaluación de las familias conformacionales en el marco de la estrategia Multinivel permitió obtener un panorama conformacional más simple y cercano a los resultados experimentales. De acuerdo con esta metodología, existiría un confórmero mayoritario (con una abundancia del 85%) caracterizado por los diedros ϕ_{12}/ψ_{12} = 277º / 212º y ϕ_{23}/ψ_{23} = 272º / 95º, valores cercanos a los descritos experimentalmente para la conformación más abundante. De hecho, al comparar esta estructura con la orientación de los diedros descrita por Blundell *et. al.* (Figura 3.3 A y B) puede comprobarse el alto grado de similitud entre ellas. De esta forma, se demostró que la reevaluación de los mínimos a alto nivel permitía corregir deficiencias en el muestreo a bajo nivel y proporcionaba una mejor descripción del panorama conformacional de la molécula.

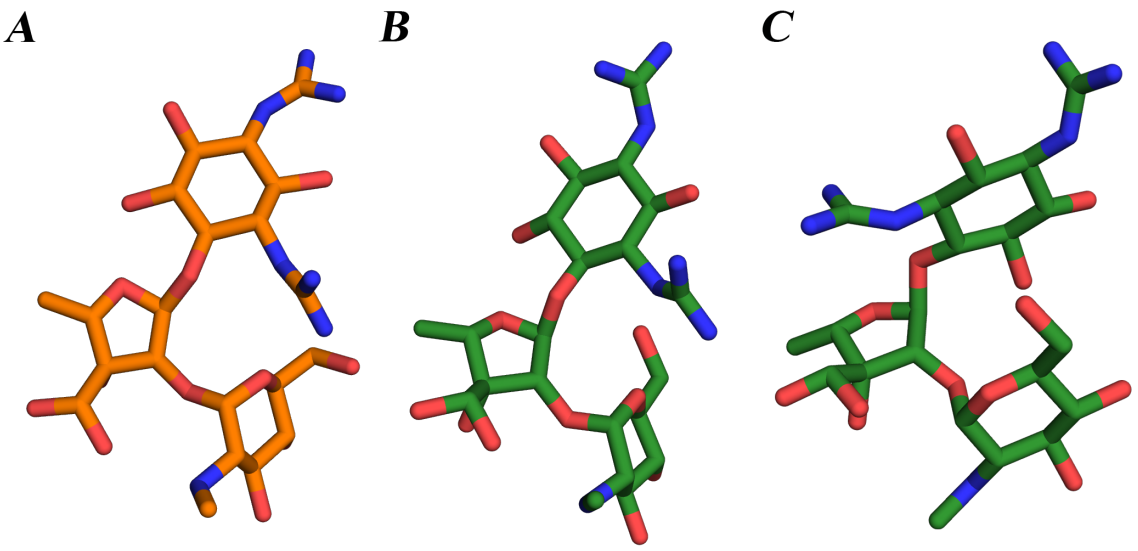

Figura 3.3 Conformaciones representativas de estreptomicina en solución acuosa. Las conformaciones mayoritarias halladas por resonancia magnética (**A**)[79] y mediante la metodología multinivel (**B**) son coincidentes. La estructura minoritaria (**C**) se caracteriza por una mayor exposición a solvente de los grupos polares.

Es importante destacar, sin embargo, que además de la familia mayoritaria, la metodología predijo una segunda familia (abundancia del 15%) caracterizada por una orientación diferente de las subunidades S1 y R2 (ϕ_{12}/ψ_{12} = 191º / 209º) que conllevaba una gran exposición a solvente de los grupos guanidil, especialmente del descrito por el ángulo diedro χ_3 y una disposición eclipsada de las subunidades S1 y G3, tal y como puede apreciarse en la figura 3.3 C. Esta familia no había sido reflejada por los estudios de RMN y su presencia en el análisis final debería atribuirse a la dificultad de describir de forma ponderada el balance entre la energía interna de los confórmeros y la contribución de hidratación, que es especialmente relevante en esta molécula debido a la presencia de tres cargas positivas.

Considerados globalmente, los resultados permitieron identificar el confórmero más estable en solución de un fármaco de estructura compleja pero, simultáneamente, resaltaron los puntos de la técnica que son susceptibles de ser mejorados en próximas implementaciones del método. En particular, en futuros estudios se considerará la posible inclusión de aguas discretas con objeto de obtener una mejor representación entre efectos intra e intermoleculares en el balance conformacional.

Capítulo

4 Compuestos Multipotentes

4.1 Publicación:

Synthesis, Biological Evaluation and Molecular Modeling of Donepezil and *N*-[(5-(Benzyloxy)-1-methyl-1H-indol-2-yl)methyl]-*N*-methylprop-2-yn-1-amine Hybrids as New Multipotent Cholinesterase/Monoamine Oxidase Inhibitors for the Treatment of Alzheimer's Disease

Journal of Medicinal Chemistry

(*J. Med. Chem.* **2011,** 54, 8251-8270**)**

Irene Bolea[†α], Jordi Juárez-Jiménez[‡α], Cristóbal de los Ríos[§], Mourad Chioua[&], Ramon Pouplana[‡], F. Javier Luque[‡], Mercedes Unzeta[*†], José Marco-Contelles[*&] and Abdelouahid Samadi[&].

[†] Departament de Bioquímica I Biología Molecular, Facultat de Medicina, Institut de Nerurociències, Universitat Autònoma de Barcelona, 08193 Bellaterra, Barcelona, Spain.

[‡]Departament de Fisicoquímica, Facultat de Farmàcia and institut de Biomedicina (IBUB), Universitat de Barcelona, Av. Diagonal 643, E-08028, Barcelona, Spain.

[§] Instituo Teófilo Hernando, Fundación de Investigación Biomédica, Hospital Universitario de la Princesa, C\ Diego de León, 62, E-28029, Madrid, Spain.

[&] Laboratorio de Radicales Libres y Química Computacional (IQOG, CSIC), C\ Juan de la Cierva 3, E-28006, Madrid, Spain.

α These authors have contributed equally to this work.

Journal of Medicinal Chemistry

Article

pubs.acs.org/jmc

Synthesis, Biological Evaluation, and Molecular Modeling of Donepezil and *N*-[(5-(Benzyloxy)-1-methyl-1*H*-indol-2-yl)methyl]-*N*-methylprop-2-yn-1-amine Hybrids as New Multipotent Cholinesterase/Monoamine Oxidase Inhibitors for the Treatment of Alzheimer's Disease

Irene Bolea,[†,⊥] Jordi Juárez-Jiménez,[‡,⊥] Cristóbal de los Ríos,[∥] Mourad Chioua,[§] Ramón Pouplana,[‡] F. Javier Luque,[‡] Mercedes Unzeta,*[,†] José Marco-Contelles,*[,§] and Abdelouahid Samadi[§]

[†]Departament de Bioquímica i Biología Molecular, Facultat de Medicina, Institut de Neurociències, Universitat Autònoma de Barcelona, 08193 Bellaterra, Barcelona, Spain

[‡]Departament de Fisicoquímica, Facultat de Farmàcia, and Institut de Biomedicina (IBUB), Universitat de Barcelona, Av. Diagonal 643, E-08028, Barcelona, Spain

[§]Laboratorio de Radicales Libres y Química Computacional (IQOG, CSIC), Juan de la Cierva 3, E-28006, Madrid, Spain

[∥]Instituto Teófilo Hernando, Fundación de Investigación Biomédica, Hospital Universitario de la Princesa, C/Diego de León, 62, E-28029, Madrid, Spain

Supporting Information

ABSTRACT: A new family of multitarget molecules able to interact with acetylcholinesterase (AChE) and butyrylcholinesterase (BuChE), as well as with monoamino oxidase (MAO) A and B, has been synthesized. Novel compounds (**3**–**9**) have been designed using a conjunctive approach that combines the benzylpiperidine moiety of the AChE inhibitor donepezil (**1**) and the indolyl propargylamino moiety of the MAO inhibitor *N*-[(5-benzyloxy-1-methyl-1*H*-indol-2-yl)methyl]-*N*-methylprop-2-yn-1-amine (**2**), connected through an oligomethylene linker. The most promising hybrid (**5**) is a potent inhibitor of both MAO-A (IC_{50} = 5.2 ± 1.1 nM) and MAO-B (IC_{50} = 43 ± 8.0 nM) and is a moderately potent inhibitor of AChE (IC_{50} = 0.35 ± 0.01 μM) and BuChE (IC_{50} = 0.46 ± 0.06 μM). Moreover, molecular modeling and kinetic studies support the dual binding site to AChE, which explains the inhibitory effect exerted on Aβ aggregation. Overall, the results suggest that the new compounds are promising multitarget drug candidates with potential impact for Alzheimer's disease therapy.

A multipotent MAO+ChE inhibitor for Alzheimer's Disease

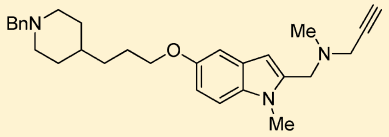

N-((5-(3-(1-benzylpiperidin-4-yl)propoxy)-1-methyl-1*H*-indol-2-yl)methyl)-*N*-methylprop-2-yn-1-amine

IC_{50} (nM) MAO-A	IC_{50} (nM) MAO-B	IC_{50} (μM) EeAChE	IC_{50} (μM) eqBuChE
5.2 ± 1.1	43 ± 8.0	0.35 ± 0.01	0.46 ± 0.06

INTRODUCTION

Alzheimer's disease (AD), the most common form of adult onset dementia, is an age-related neurodegenerative disorder characterized by a progressive memory loss, a decline in language skills, and other cognitive impairments.[1] Although the etiology of AD is not completely known, several factors such as amyloid-β (Aβ)[2] deposits, τ-protein aggregation,[3] oxidative stress,[4,5] and low levels of acetylcholine (ACh) are thought to play significant roles in the pathophysiology of the disease.[6] The selective loss of cholinergic neurons in AD results in a deficit of ACh in specific brain regions that mediate learning and memory functions.[7] However, alterations in other neurotransmitter systems, especially serotoninergic and dopaminergic,[8,9] are also thought to be responsible for the behavioral disturbances observed in patients with AD.[10] This evidence has led to the suggestion that inhibitors of monoamine oxidase (IMAOs) might be also valuable for the treatment of AD.[11,12] Thus, monoamine oxidase (MAO, EC 1.4.3.4), the enzyme that catalyzes the oxidative deamination of a variety of biogenic and xenobiotic amines,[13] is also an important target to be considered for the treatment of specific features of this multifactorial disease. MAO exists as two distinct enzymatic isoforms, MAO-A and MAO-B, based on their substrate and inhibitor specificities.[14] MAO-A preferentially deaminates serotonin, adrenaline, and noradrenaline and is selectively and irreversibly inhibited by clorgyline. In contrast, MAO-B preferentially deaminates β-phenylethylamine and benzylamine and is irreversibly inhibited by *R*-(−)-deprenyl.[15] Selective inhibitors for MAO-A have been shown to be effective antidepressants, whereas MAO-B inhibitors, although apparently devoid of antidepressant action, are useful in the

Received: February 25, 2011
Published: October 24, 2011

 © 2011 American Chemical Society

treatment of Parkinson's disease.[16] Besides the increased amine neurotransmission, the beneficial properties of IMAOs are also related to the reduction of the formation of the neurotoxic products, such as hydrogen peroxide and aldehydes, which promote the formation of reactive oxygen species (ROS) and may ultimately contribute to increased neuronal damage.[17,18] Moreover, AD patients commonly present depressive symptoms that have even been considered as a risk factor for the development of the disease.[19] Increased MAO-B levels due to enhanced astrogliosis in the brain of AD patients have also been reported.[11] Overall, these observations suggest that dual inhibition of MAO-A and MAO-B, rather than MAO-B alone, may be of value for AD therapy.

At present, there are three FDA-approved drugs (donepezil, galanthamine, and rivastigmine)[20−22] that improve AD symptoms by inhibiting acetylcholinesterase (AChE, EC 1.1.1.7), i.e., the enzyme responsible for the hydrolysis of ACh, and thereby raising ACh content in the synaptic cleft. Apart from the beneficial palliative properties of AChE inhibitors in AD,[23−25] cholinergic drugs have shown little efficacy to prevent the progression of the disease. In fact, the multifactorial nature of AD supports the most current innovative therapeutic approach based on the "one molecule, multiple targets" paradigm.[26,27] Thus, a single drug that acts on a specific target to produce the desired clinical effects might not be suitable for the complex nature of AD. Accordingly, the multitarget-directed ligand (MTDL) approach has been the subject of increasing attention by many research groups, which have developed a variety of compounds acting on very diverse targets.[28−33] A very successful approach came from the combination of the carbamate moiety of rivastigmine with the indolamine moiety present in rasagiline, a well-known MAO-B inhibitor, leading to the compound ladostigil.[34] Besides inhibiting MAO and AChE, it possesses neuroprotective and antiapoptotic activities,[35] which have been attributed to the propargylamine group present in the molecule, thus retaining the beneficial properties observed for rasagiline.[36] The potential therapeutic effect of this compound, which has reached clinical trials,[37] is also supported by recent findings showing the ability of propargylamine-containing compounds to modulate cleavage of β-amyloid protein precursor.[38] Hybrid compounds targeting cholinesterases and amyloid plaques,[39] as well as site-activated chelators targeting MAO and AChE, have also been recently attempted.[40−43]

In the development of IMAOs for the treatment of neurodegenerative diseases, our group initially extensively investigated the effect of the introduction of a benzyloxy group in a series of acetylenic and allenic derivatives of tryptamine, which were previously reported to be selective for MAO-A.[44] We observed that the introduction of this moiety changed the selectivity toward the B isoform of the enzyme and that it was significantly decreased when a hydrogen atom was attached to the nitrogen atom of the indole ring and/or the side chain was substituted by a CH_3 group.[45,46] On the basis of these previous works, we have designed a novel family of hybrid compounds of type I to act as potential inhibitors of both MAO and AChE (Figure 1). The novel hybrids have been conceived by a conjuctive approach that combines donepezil (**1**) and *N*-[(5-benzyloxy-1-methyl-1*H*-indol-2-yl)methyl]-*N*-methylprop-2-yn-1-amine (**2**), which is one of the most interesting IMAOs previously investigated in our laboratory.[46] The underlying strategy is to retain the 1-benzylpiperidine fragment present in donepezil (**1**), which binds to the catalytic and mid-gorge sites

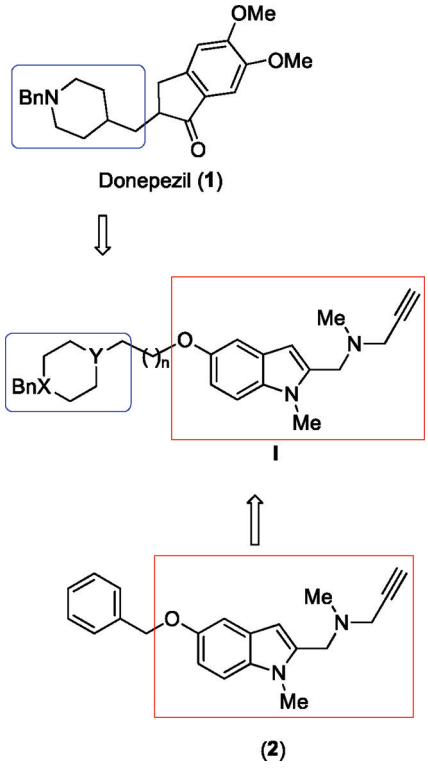

Figure 1. Schematic representation of the conjunctive approach designed to synthesize the novel IMAO/IAChE hybrids.

of AChE, with the 1-methyl-1*H*-indol-2-yl)methyl]-*N*-methylprop-2-yn-1-amine moiety shown in compound **2** (Figure 1), which should occupy the substrate binding site in MAO.

With this conjunctive approach, the novel hybrids are expected to behave as dual binding site AChE inhibitors, since the 1-methyl-1*H*-indol-2-yl)methyl]-*N*-methylprop-2-yn-1-amine moiety could presumably interact at the peripheral anionic site (PAS) of AChE. The possibility of targeting both catalytic active site (CAS) and PAS of AChE will largely depend on the length of the linker, a crucial structural feature to facilitate the binding of both 1-benzylpiperidine and [(1-methyl-1*H*-indol-2-yl)methyl]-*N*-methylprop-2-yn-1-amine moieties to CAS and PAS, respectively, in AChE. This particular mode of action should result in a significant AChE inhibitory potency, of interest for the management of the symptomathology of AD arising from the cholinergic deficit, but more interestingly, it could also recognize the peripheral site, which appears to mediate the Aβ proagreggating action of AChE.[47−50] On the other hand, the correct alignment of the 1-benzylpiperidine and 1-methyl-1*H*-indol-2-yl)methyl]-*N*-methylprop-2-yn-1-amine moieties in MAO will also depend on the tether, as the length and chemical nature of the linker should also affect the accommodation of the hybrid through the residues that define the bottleneck between the entrance and substrate cavities in MAO.

In this work we describe the synthesis, pharmacological evaluation, and molecular modeling of representative molecules of this new family of compounds (**I**, Figure 1). The pharmacological evaluation of these novel compounds includes AChE and butyrylcholinesterase (BuChE) inhibition, the inhibition of MAO-A and MAO-B, the kinetics of enzyme inhibition, and the AChE-dependent and self-induced Aβ aggregation. Finally, molecular modeling studies are performed

to gain insight into the binding mode and structure–activity relationships of the novel hybrid compounds.

RESULTS AND DISCUSSION

Chemistry. To explore the suitability of the conjunctive strategy outline above, compounds **3**–**9** (Figure 2) were

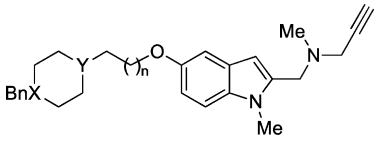

3 X= N, Y= CH, n= 0
4 X= N, Y= CH, n= 1
5 X= N, Y= CH, n= 2
6 X= N, Y= CH, n= 3
7 X= CH, Y= N, n= 1
8 X= CH, Y= N, n= 2
9 X, Y= N, n= 2

Figure 2. General structure for the target molecules **3**–**9**.

synthesized, differing in the length of the tether and the location and/or the number of nitrogens in the tethered-benzyl substituted cyclohexane ring linked to the indolyl moiety.

The 1-benzyl 4-substituted piperidine derivatives **3**–**6** were synthesized by sodium hydride/DMF promoted reaction of compounds **10**–**13** and 1-methyl-2-{[ethyl(prop-2-yn-1-yl)-amino]ethyl}-1*H*-indol-5-ol **14**[51] (Scheme 1).

Scheme 1[a]

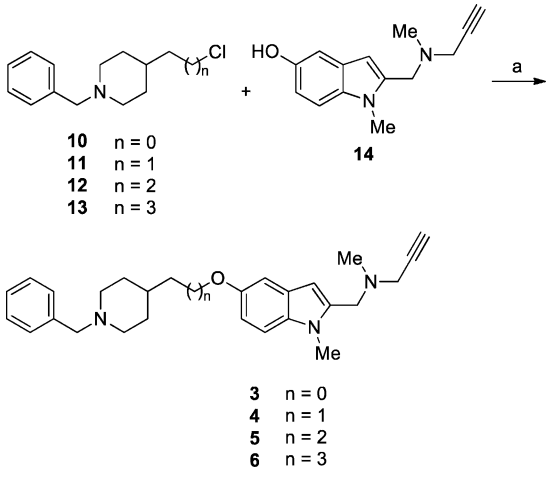

[a]Reagents and conditions: (a) NaH, DMF, room temp.

1-Benzyl-4-(chloromethyl)piperidine **10** and 1-benzyl-4-(chloroethyl)piperidine **11** were synthesized following the methods reported in the literature.[52] 1-Benzyl-4-(3-chloropropyl)piperidine **12** was prepared as shown in Scheme 2, starting from commercial 4-pyridinecarboxaldehyde **15**, via the known intermediate **16**,[53] whose hydrogenation,[54] under Pd/C and PtO_2, in the presence of hydrochloric acid and workup with methanol afforded methyl ester **17**.[55] Next, N-benzylation to give 1-benzylpiperidine **18**, reduction with lithium aluminum hydride (LAH) to provide alcohol **19**,[56] and treatment with thionyl chloride furnished the chloride derivative **12** in quantitative yield.

1-Benzyl-4-(4-chlorobutyl)piperidine **13** was prepared as shown in Scheme 3. Treatment of commercial 1-benzyl-4-

Scheme 2[a]

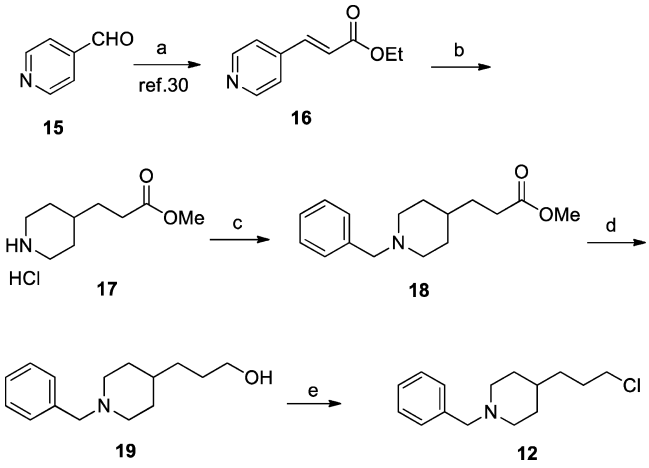

[a]Reagents and conditions: (a) $(EtO)_2P(O)CH_2CO_2Et$, THF, K_2CO_3, reflux (92%); (b) (i) H_2, Pd/C 10%, PtO_2, 4 N HCl in dioxane, EtOH, room temp; (ii) MeOH (90%); (c) BnBr, TEA, CH_2Cl_2 (75%); (d) $LiAlH_4$, THF, reflux (98%); (e) $SOCl_2$, CH_2Cl_2, reflux (99%).

Scheme 3[a]

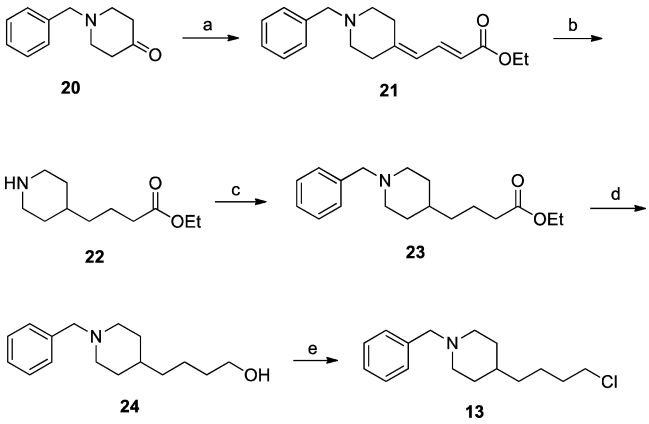

[a]Reagents and conditions: (a) $(EtO)_2P(O)CH_2CH{=}CHCO_2Et$, EtOH, NaH, reflux (78%); (b) H_2, Pd/C 10%, EtOH, room temp (99%); (c) BnBr, TEA, CH_2Cl_2 (70%); (d) $LiAlH_4$, THF, reflux (99%); (e) $SOCl_2$, CH_2Cl_2, reflux (99%).

piperidone **20** with triethyl 4-phosphonocrotonate in the presence of sodium hydride in dry ethanol afforded compound **21** in 78% yield, whose catalytic hydrogenation over Pd/C in ethanol at room temperature gave ester **22** in 99% yield.[57] Next, reaction of **22** with benzyl bromide to give ester **23** followed by reduction with LAH gave the desired alcohol **24**, which was then treated with thionyl chloride to give the chloro derivative **13** in almost quantitative yield.[57]

Compounds **7**–**9** (Figure 2) were synthesized as shown in Schemes 4 and 5. Reaction of indole **14** with 1,2-dibromoethane gave **25**, which after treatment with 4-benzylpiperidine afforded **7** (Scheme 4).[51] Similarly, the reaction of indole **14** with 1,3-dibromopropane gave intermediate **26**, whose reaction with 4-benzylpiperidine or 1-benzylpiperazine afforded **8** and **9**, respectively (Scheme 5).[51]

All new compounds showed analytical and spectroscopic data in good agreement with their structures (see Experimental Part).

dx.doi.org/10.1021/jm200853t | J. Med. Chem. 2011, 54, 8251–8270

Scheme 4[a]

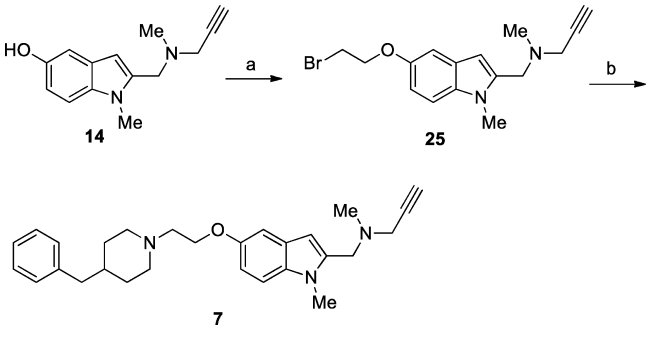

[a]Reagents and conditions: (a) $Br(CH_2)_2Br$, 2-butanone, K_2CO_3, 85 °C, 6 h (37%); (b) 4-benzylpiperidine, $K_2CO_{3)}$ THF, 80 °C (77%).

Scheme 5[a]

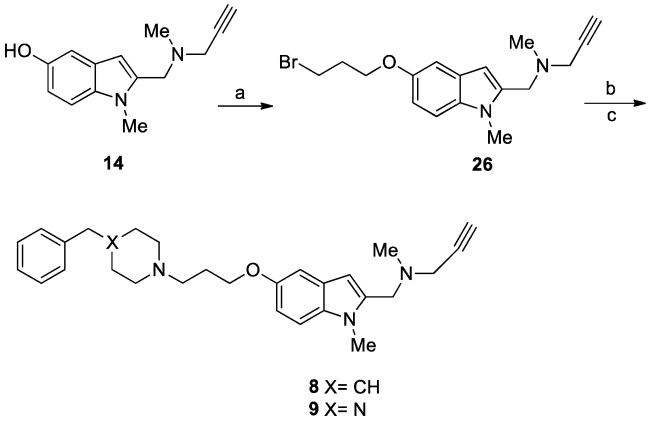

[a]Reagents and conditions: (a) $Br(CH_2)_3Br$, 2-butanone, K_2CO_3, 85 °C, 6 h (80%); (b) 4-benzylpiperidine, K_2CO_3, THF, 80 °C (64%); (c) 1-benzylpiperazine, K_2CO_3, THF, 80 °C (85%).

AChE and BuChE Inhibition. To study the multipotent profile of the hybrid compounds, they were first evaluated as inhibitors of AChE and BuChE. The AChE inhibitory activity was tested against the *Electrophorus electricus* enzyme (*Ee*AChE), and the inhibition of BuChE was carried out using the equine serum enzyme (eqBuChE). The inhibitory activities of the hybrids were compared with those determined for the parent compounds, donepezil (**1**) and *N*-[(5-benzyloxy-1-methyl-1*H*-indol-2-yl)methyl]-*N*-methylprop-2-yn-1-amine (**2**).[46]

Biological Evaluation. The 1-benzylpiperidin-4-yl derivatives **3**–**6** were found to be moderately potent regarding the inhibition of *Ee*AChE. IC_{50} values were similar in all cases (ranging from 0.26 to 0.42 μM, Table 1). Moreover, they exhibit similar potencies against eqBuChE, as IC_{50} values range from 0.46 to 2.1 μM, leading to a very slight selectivity for AChE (the ratio IC_{50}(eqBuChE)/IC_{50}(*Ee*AChE) varies from 1.3 to 5.0). Accordingly, the length of the linker does not seem to be a crucial factor for the inhibitory potency against AChE and BuChE. The most potent compounds are **5** and **6**, which are characterized by IC_{50} values of 0.35 and 0.26 μM against AChE and IC_{50} values of 0.46 and 0.99 μM against BuChE. Compared with donepezil (**1**), they are, respectively, 52- and 39-fold less potent for the inhibition of AChE but 16- and 7-fold more potent regarding the BuChE inhibition.

Compared to derivatives **3**–**6**, reversion of the piperidine ring in **7** and **8** has a dramatic effect on the inhibitory potency in *Ee*AChE. A drastic reduction in activity is also found upon replacement of the piperidine by a piperazine unit (leading to compound **9**). Thus, compounds **7** and **9** are completely inactive against *Ee*AChE, whereas the inhibitory activity of **8** is decreased 52-fold. Nevertheless, these chemical modifications have less effect on the eqBuChE potency, as compounds **7**–**9** are roughly equipotent (**7**) or slightly less potent (**8** and **9**) compared to **3**–**6**.

Table 1. AChE and BuChE Inhibitory Activities of Donepezil (1), the Reference Compound 2, and *N*-[(1-Methyl-1*H*-indol-2-yl)methyl]-*N*-methylprop-2-yn-1-amines 3–9

	IC_{50} (μM)[a]		
compd	*Ee*AChE	eqBuChE	selectivity eqBuChE/*Ee*AChE
1 (donepezil)	0.0067 ± 0.0004	7.4 ± 0.10	1100
2	>100	>100	>100
3 (*n* = 0)	0.31 ± 0.04	1.1 ± 0.20	3.5
4 (*n* = 1)	0.42 ± 0.04	2.1 ± 0.20	5.0
5 (*n* = 2)	0.35 ± 0.01	0.46 ± 0.06	1.3
6 (*n* = 3)	0.26 ± 0.07	0.99 ± 0.08	3.8
7 (*n* = 1)	>100	0.80 ± 0.10	>100
8 (*n* = 2)	18.1 ± 0.40	2.2 ± 0.40	0.12
9 (*n* = 2)	>100	7.6 ± 0.40	>100

[a]Values are expressed as the mean ± standard error of the mean of at least three different experiments in quadruplicate.

Overall, the results point out the relevant role played by the 1-benzylpiperidin-4-yl unit on the AChE inhibitory activity, suggesting that this moiety is the main factor in mediating the binding to AChE. On the other hand, it is worth noting that compounds **3**–**6** are active for the BuChE inhibition. This is particularly important in view of the renewed interest in dual AChE/BuChE cholinergic inhibitors as therapeutic agents for AD, as they have been described to improve cognition.[58] More specifically, compound **5** is presented as a dual ChE inhibitor by having both AChE and BuChE inhibition in the same submicromolar level. For this reason and because of its pharmacological properties, we evaluated its inhibitory activity against human recombinant AChE (hrAChE), the cerebral enzyme expressed in the HEK-293 cell line, and human serum BuChE (hBuChE). Thus, compound **5** inhibited hrAChE with an IC_{50} of 0.38 ± 0.05 μM (tacrine, used as a standard, inhibited hrAChE with an IC_{50} of 122 ± 2 nM) and hBuChE with an IC_{50} of 1.7 ± 0.2 μM (tacrine inhibited hBuChE with an IC_{50} of 36 ± 4 nM).

Kinetic Studies. To gain further insight into the mechanism of action of this family of compounds on AChE, a kinetic study was carried out with the most promising compound of the series, **5**, using *Ee*AChE. Graphical analysis of the reciprocal Lineweaver–Burk plots (Figure 3) showed both increased slopes (decreased V_{max}) and intercepts (higher K_m) at increasing concentration of the inhibitor. This pattern indicates a mixed-type inhibition and therefore supports the dual site binding of this compound. Replots of the slope versus concentration of compound **5** gave an estimate of the inhibition constant, K_i, of 149 nM.

MAO Inhibition. To complete the study of the multipotent biological profile of the hybrid compounds, the inhibitory activity against MAO-A and MAO-B (from rat liver mitochondria) was determined and compared with the inhibition exerted by the parent compounds donepezil (**1**)

dx.doi.org/10.1021/jm200853t | *J. Med. Chem.* 2011, 54, 8251–8270

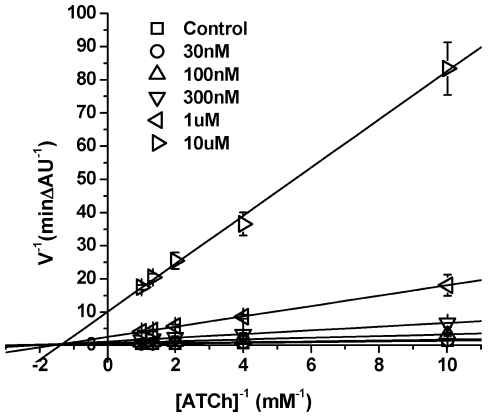

Figure 3. Kinetic study on the mechanism of *Ee*AChE inhibition by compound **5**. Overlaid Lineweaver–Burk reciprocal plots of AChE initial velocity at increasing substrate concentration (0.1–1 mM) in the absence of inhibitor and in the presence of **5** are shown. Lines were derived from a weighted least-squares analysis of the data points.

and *N*-[(5-benzyloxy-1-methyl-1*H*-indol-2-yl)methyl]-*N*-methylprop-2-yn-1-amine (**2**).

Biological Evaluation. The 1-benzylpiperidin-4-yl derivatives **3**–**6** showed a potent MAO-A inhibition (Table 2), acting

Table 2. MAO-A and MAO-B Inhibitory Activities of Donepezil (1), Reference Compound 2, and the *N*-[(1-Methyl-1*H*-indol-2-yl)methyl]-*N*-methylprop-2-yn-1-amine Derivatives (3–9)

	IC_{50} (nM)[a]		
compd	MAO-A	MAO-B	selectivity MAO-B/MAO-A
1 (donepezil)	850000 ± 13000	15000 ± 2200	0.020
2	100 ± 7.0	63 ± 2.0	0.63
3 (n = 0)	82 ± 3.0	750 ± 20	9.1
4 (n = 1)	6.7 ± 1.8	130 ± 41	19
5 (n = 2)	5.2 ± 1.1	43 ± 8.0	8.3
6 (n = 3)	10 ± 4.0	2700 ± 110	260
7 (n = 1)	140 ± 44	1400 ± 500	10
8 (n = 2)	65 ± 17	11000 ± 2400	170
9 (n = 2)	31 ± 14	1600 ± 710	54

[a]Values are expressed as the mean ± standard error of the mean of at least three different experiments in quadruplicate.

in the nanomolar range (IC_{50} ranging from 82 ± 3.0 to 5.2 ± 1.1 nM). In contrast, they were less potent against MAO-B, with the exception of **5**, which was found to be the most potent compound toward both isoforms (IC_{50} of 5.2 ± 1.1 and 43 ± 8.0 nM for MAO-A and MAO-B, respectively). The most selective inhibitor was compound **6** (n = 3) toward MAO-A, whereas **5** was much less selective. It is worth noting the large sensitivity of the inhibitory potency on the length of the tether. Thus, removal of a single methylene group in **6** to yield **5** increased the inhibitory potency against MAO-A and MAO-B by a factor of 2 and 63, respectively. Likewise, further reduction of the tether to just one methylene (from **5** to yield **4**) did not affect the MAO-A inhibitory potency but reduced the potency against MAO-B by 3-fold.

Compounds **7** and **8**, bearing a 4-benzylpiperidin-1-yl residue, also inhibited MAO-A quite potently but showed less potency toward MAO-B. Similarly, compound **9**, containing a 4-benzylpiperazin-1-yl residue, also showed a good MAO-A inhibitory potency but a lower activity toward MAO-B. Interestingly, we found that compound **7** was 21-fold and 11-fold less potent for MAO-A and MAO-B, respectively, than the analogous inhibitor **4**. Similarly, compounds **8** and **9** were significantly less potent for both isoforms than the analogous inhibitor **5** (12-fold and 6-fold for MAO-A and 256-fold and 38-fold for MAO-B, respectively). Altogether, these results show that compounds bearing the donepezil 1-benzylpiperidin-4-yl motif were the best MAO inhibitors and that, among them, **5** was the most potent inhibitor, even more than the reference compound **2**.

Kinetic Studies. To study the type of inhibition toward MAO, we analyzed the reversibility/irreversibility of the binding of compound **5**, the most potent inhibitor of the series. We observed that **5** irreversibly inhibited MAO-A, since the inhibition was not reverted after three consecutive centrifugations and washings with buffer (Figure 4A). This hypothesis is also in agreement with the time-dependent inhibition of MAO-A upon incubation with the inhibitor (Figure 4B) and thus reflects the inhibition mechanism found for the parent compound **2**.[46] Strikingly, whereas the inhibition of MAO-B was also found to depend on the incubation time (Figure 4D), a significant fraction (80.5 ± 3.3%) of the activity was recovered by washing the enzyme three times after incubation for 30 min (Figure 4C). These findings point out that the addition of the benzylpiperidine unit to the reference compound **2** in order to yield **5** does not affect the proper alignment of the indolylpropargylamino moiety in the binding cavity of MAO-A, thus leading to the complete inactivation of the enzyme by chemical modification of the cofactor. However, the present results suggest that docking of **5** into the binding cavity of MAO-B is more impeded than in MAO-A, which should prevent the proper alignment of the propargylamino moiety, thus making less efficient the inactivation of the enzyme.

To clarify the different behavior of **5** toward MAO-A and MAO-B, we further investigated the progress curves of substrate consumption for a longer period in the presence of the inhibitor. As expected, the final rate became zero in both cases, proving that the inhibition of **5** toward both MAO-A and MAO-B occurs in an irreversible process. Nevertheless, the time needed for the total inactivation of MAO-B was higher than that needed for MAO-A (Figure 5), thus showing that although irreversible, the inactivation of MAO-B by **5** is clearly slower. These findings explain the different behavior found in the reversibility studies, which were performed preincubating the enzymes with **5** for 30 min. Figure 5 shows that at this time the velocity of the reaction for MAO-A was clearly decreased and thus substrate consumption was rapidly approaching zero. In contrast, the velocity of the reaction for MAO-B shows a little reduction at 30 min preincubation time, thus supporting the suggestion that docking of **5** into the cavity of MAO-B is more impeded than in MAO-A, resulting in a slower substrate consumption and explaining the recovery of MAO-B activity in the reversibility study.

The kinetic behavior of **5** toward MAO-B determined from the initial rates showed that this compound behaves as a noncompetitive inhibitor, as shown in the Lineweaver–Burk plot (Figure 6A). Thus, the V_{max} decreased as the amount of **5** was increased, whereas the K_M value remained constant (Figure 6B). Determination of Michaelis constants gave a value of K_M = 6.7 ± 0.3 μM and V_{max} = 277.8 ± 6.1 pmol/min for MAO-B

dx.doi.org/10.1021/jm200853t | *J. Med. Chem.* 2011, 54, 8251–8270

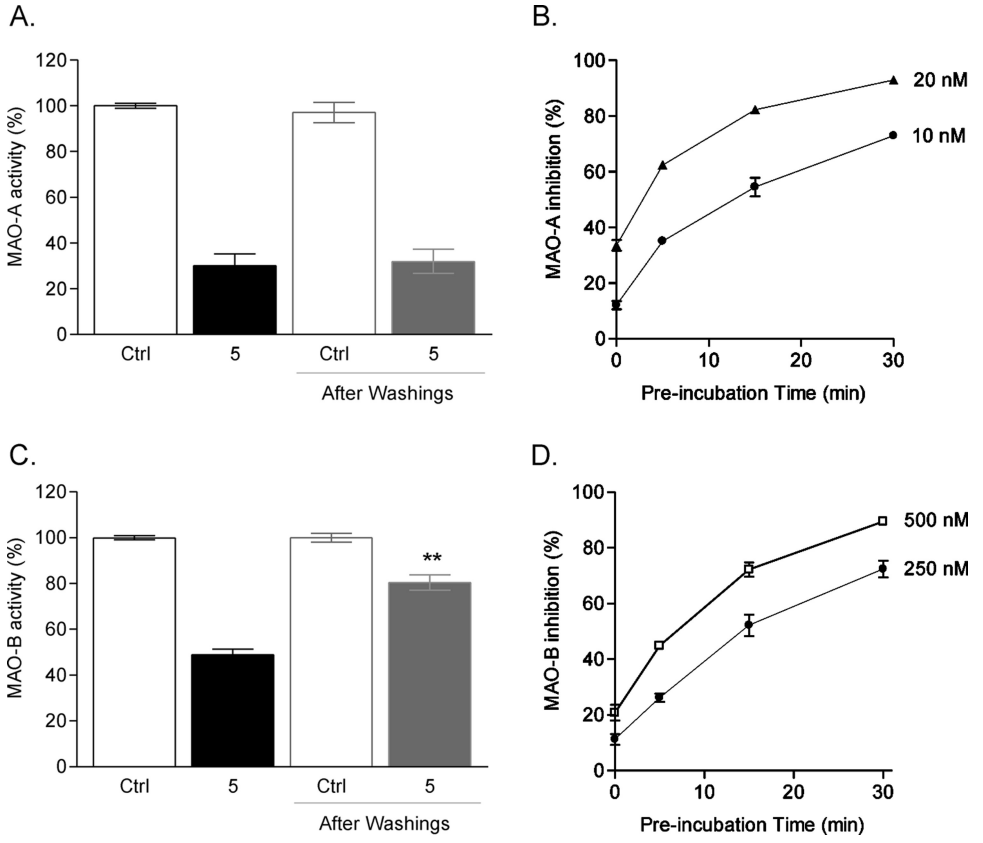

Figure 4. Reversibility studies of MAO-A and MAO-B inhibition by compound **5**. MAO-A (A) and MAO-B (C) were inhibited at 6 and 45 nM **5**, respectively, for 30 min. Then three consecutive washings were performed with buffer. MAO-B inhibition (C) was reverted (recovering 80.5 ± 3.3% of enzyme activity), whereas the inhibition of MAO-A remained unaltered after washings (A). Time-dependence inhibition was studied at several times of preincubation (0−30 min) of MAO with compound **5**. Both MAO-A (B) and MAO-B (D) inhibition were found to be time-dependent. Data are the mean ± SEM of four independent experiments in triplicate.

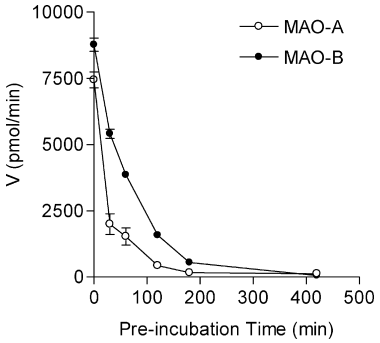

Figure 5. Progress curves of substrate consumption for MAO-A (5-HT, 100 μM) and MAO-B (PEA, 20 μM) in the presence of **5** (10 nM for MAO-A and 100 nM for MAO-B). MAO-A and MAO-B were preincubated with the inhibitor for a long period (0−420 min), and the catalytic activity was determined. The time needed for the total inactivation of the enzyme was greater for MAO-B than for MAO-A. Data are the mean ± SEM of three independent experiments in triplicate.

substrate, β-phenylethylamine (PEA), and an estimated K_i of 11.0 ± 0.39 nM.

Molecular Modeling. The preceding studies point out that **5** seems to be a promising multitarget inhibitor. However, they also show distinctive trends in the pharmacological profile. First, it is unclear why the inhibitory potency against AChE (and BuChE) is slightly affected by the length of the tether, whereas it has a large effect in the inhibition of both MAO-A and MAO-B. Moreover, reversion of the piperidine unit in compounds **5** and **8** notably affects the inhibition of both AChE and MAO. Finally, **5** leads to an irreversible inhibition of MAO-A, whereas inactivation of MAO-B is slower. To shed light onto these questions, a series of docking and molecular dynamics (MD) simulations were conducted to identify the binding mode of **5** to AChE, BuChE, MAO-A, and MAO-B.

AChE Inhibition. The binding mode of **5** to AChE was investigated by considering three structural models of the enzyme, which were built up taking advantage of the X-ray structure of donepezil bound to *Torpedo californica* AChE (*Tc*AChE, PDB entry 1EVE).[59] These models retain the structural details of the benzylpiperidine moiety bound to the AChE gorge but differ in the orientation of Trp279 (numbering in *Tc*AChE), as the inspection of the available X-ray structures for complexes of AChE with dual site binding inhibitors reveals that Trp279 adopts three main conformations at the PAS.[60,61] Thus, the side chain of Trp279 can be characterized by dihedral angles χ_1 (N−C_α−C_β−C_γ) and χ_2 (C_α−C_β−C_γ−$C_{\delta 2}$) close to (i) −60° and −80°, (ii) −120° and +50°, and (iii) −160° and −120°. Representative structures of these orientations are PDB entries 1EVE, 2CKM, and 1Q83, which correspond to the AChE complexes with donepezil, bis(7)-tacrine,[62] and *syn*-TZ2PA6,[63] respectively. In the following these models will be denoted AChE(1EVE), AChE(2CKM) and AChE(1Q83).

The binding of **5** to the three AChE models was first explored by docking calculations performed with rDock,[64,65] which yielded reliable predictions for the binding mode of

dx.doi.org/10.1021/jm200853t | *J. Med. Chem.* 2011, 54, 8251−8270

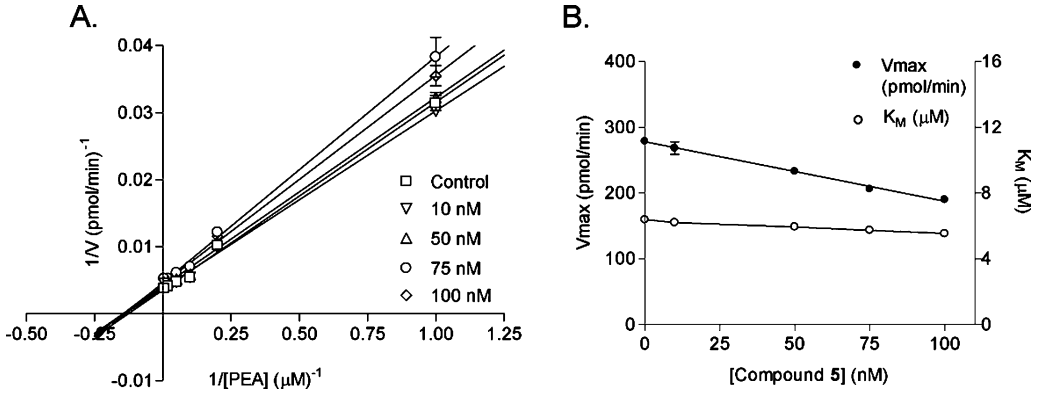

Figure 6. Kinetic study on the mechanism of MAO-B inhibition by **5**. (A) Overlaid Lineweaver–Burk reciprocal plots of MAO-B initial velocity at increasing substrate concentration (PEA, 1–200 μM) in the absence or presence of **5** (10–100 nM) are shown. Lines were derived from a weighted least-squares analysis of the data points. (B) V_{max} decreased as the amount of **5** increased, whereas the K_M value remained constant. Data are the mean ± SEM of four independent experiments in triplicate.

known dual site binding AChE inhibitors.[60] Suitable restraints were introduced to impose the benzylpiperidine moiety to mimic the known binding mode of the same fragment of donepezil in its complex with *Tc*AChE.[59] In turn, this permits enhancement of the conformational sampling of the indolylpropargylamino moiety at the PAS. Finally, the structural integrity and energetic stability of the binding mode proposed for each AChE–**5** complex were examined from the snapshots sampled in 20 ns MD simulations. For the sake of comparison, an additional 20 ns MD simulation was run for the complex between AChE and donepezil.

MD simulations yielded stable trajectories in the last 10 ns, as noted by the time evolution of the potential energy and the root-mean-square deviation (rmsd) of the protein backbone, which ranged from 1.4 to 1.6 Å (a rmsd value of 1.3 Å was obtained for the AChE–donepezil complex; see Figures S1 and S2 in Supporting Information). The rmsd values of the residues that delineate the binding site in catalytic, mid-gorge, and peripheral sites (defined as those residues with at least one atom placed at a distance less than 4 Å from the ligand) were stable for AChE–donepezil (1.4 Å) and AChE(1EVE)–**5** (1.6 Å) complexes, they being similar to the rmsd values determined for the backbone. Larger rmsd values were found for the binding site residues in AChE(2CKM) (2.0 Å) and AChE-(1Q83) (1.7 Å).

No large structural alterations were found in the catalytic site, and the benzylpiperidine moiety adopts a similar arrangement in all cases (Figure 7). Little structural fluctuations were also found in the mid-gorge and peripheral sites for complexes AChE–donepezil and AChE(1EVE)–**5**. In particular, the indanone unit of donepezil and the indolyl ring of **5** were stacked against Trp279, whose side chain was stable along the trajectory. Thus, the torsional angles χ_1 and χ_2 showed small fluctuations around average values of −70° and −110° (see Figure S3 in Supporting Information; the corresponding angles in 1EVE are −52° and −84°). In contrast, larger rearrangements were found at the PAS, mainly involving Trp279, for AChE(1Q83)–**5** and AChE(2CKM)–**5**. In the former case χ_1, which was initially assigned a value close to 180° (as found in 1Q83), remained stable during the first 11 ns but then suddenly changed to a value close to −60° (see Figure S3). Thus, the initial binding mode, which was chosen to mimic the orientation of *syn*-TZ2PA6 bound to *Tc*AChE, was lost and Trp279 adopted a new arrangement close to the conformation

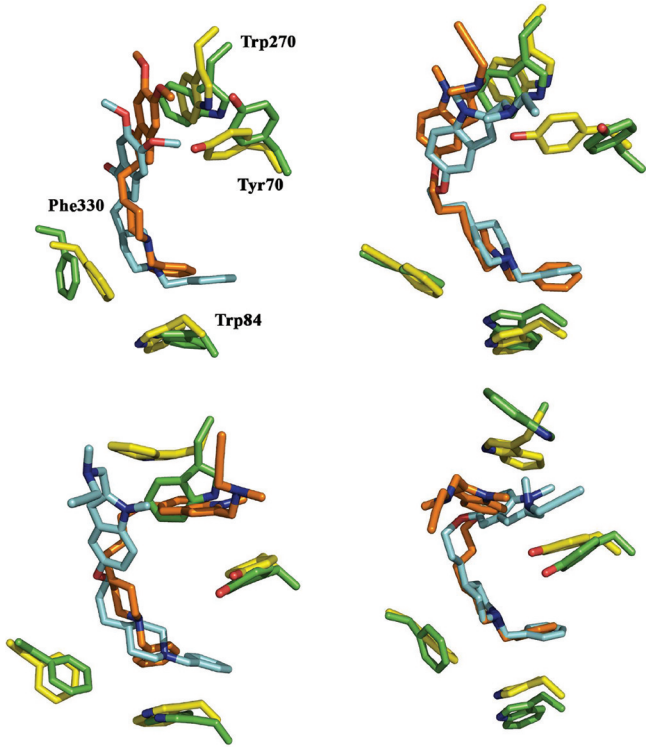

Figure 7. Representation of the binding mode of donepezil and **5** at the beginning and end of the MD simulations: (top left) AChE–donepezil (started from the X-ray structure in PDB entry 1EVE); (top right) AChE(1EVE)–**5**; (bottom left) AChE(1Q83)–**5**; (bottom-right) AChE(2CKM)–**5**. Relevant residues at the catalytic (Trp84, Phe330) and peripheral (Trp279, Tyr70) binding sites are also shown. The ligand/residues at the end of the simulations are shown in blue/green, respectively (the representation at the beginning of the simulation is made in orange/yellow).

found in the AChE–donepezil and AChE(1EVE)–**5** complexes (see above and Figure 7). With regard to AChE(2CKM)–**5**, Trp279 was initially oriented to reproduce the conformation found in the *Tc*AChE–bis(7)-tacrine complex (characterized by χ_1 and χ_2 close to −120° and +50°). After 3 ns, the angle χ_1 changed to 180° and remained stable for 3 ns but then changed to a new value of +60°, which was stable along the rest of the trajectory (see Figure S3 in Supporting Information). Such a change was accompanied by the readjustment of χ_2, which

dx.doi.org/10.1021/jm200853t | *J. Med. Chem.* 2011, 54, 8251–8270

adopted a value close to +90°. At the end of the simulation, a novel structure was obtained where the protonated propargylamino unit remains close to Tyr70 but has lost the interactions with Trp279 (see Figure 7).

The preceding analysis demonstrates the structural integrity of the AChE(1EVE)−**5** model, which mimics the structural features of the binding of donepezil to *Tc*AChE. The reliability of this binding mode is reinforced by the conformational change observed in the PAS of the AChE(1Q83)−**5** complex, which leads to a binding mode close to that found in AChE(1EVE)−**5**, and by the structural change found in AChE(2CKM)−**5**, which leads to a binding mode characterized by a conformation of Trp279 that, to the best of our knowledge, has no counterpart in the available X-ray structures of AChE complexes deposited in the PDB. As a further test, we have determined the relative binding affinity between models AChE(1EVE)−**5** and AChE(2CKM)−**5** by means of MM/PBSA calculations. They were performed for 100 snapshots taken evenly during the last 5 ns of the trajectories using both the standard radii implemented in the AMBER force field and an alternative set of atomic radii that have been explicitly optimized for their use in MM/PBSA calculations with AMBER.[66] The results (see Table S1 in Supporting Information) indicate that binding of **5** to AChE(1EVE) is favored by near 2.3 (standard radii) and 4.0 (optimized radii) kcal/mol relative to AChE(2CKM). Similar trends were observed when MM/PBSA computations were performed by retaining a single water molecule that was hydrogen-bonded to the protonated nitrogen of the piperidine unit of the ligand along the trajectories (data not shown).

The preceding structural and energetic analysis suggests that compound **5** mimics the binding mode of donepezil (see Figure S4). Thus, the benzylpiperidine moieties of donepezil and **5** exhibit a similar alignment in the CAS, though there is a weaker overlap between the benzene unit of **5** and the indole ring of Trp84. More importantly, there is a change in the orientation of residues Tyr334 and Asp72, which remain hydrogen-bonded but are displaced toward the PAS. In turn, this structural change facilitates the stacking of the indole ring of **5** between the aromatic rings of Tyr334 and Trp279. On the other hand, there is a water molecule that bridges the protonated nitrogen of the piperidine unit with the hydroxyl groups of Tyr121 and Ser122 (not shown in Figure 8 for the sake of clarity). Finally, the largest structural flexibility of the inhibitor is localized in the propargylamino unit, which forms transient van der Waals interactions with the benzene ring of Tyr70.

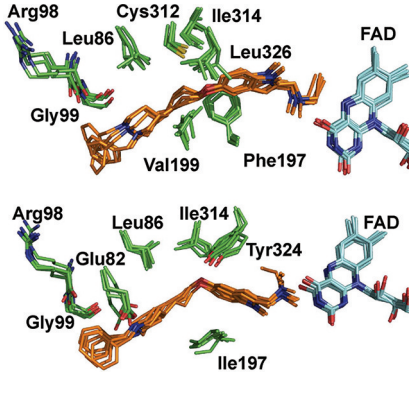

Figure 8. Representation of the binding mode of **5** in (top) MAO-A and (bottom) MAO-B. Five snapshots taken every ns along the last 5 ns of the trajectory are superposed. The ligand is shown as orange sticks, FAD as blue sticks, and selected residues in the entrance and substrate cavities as green sticks.

This binding mode allows us to rationalize the low sensitivity of the inhibitory activity on the length of the tether, as (i) it is reasonable to expect that the benzylpiperidine moiety will fill the same binding pocket but (ii) shortening or lengthening of the tether will be accompanied by displacements of the indole ring of **5** along the gorge that would retain the stacking against Tyr334 or Trp279 (see Figure S5 in Supporting Information). On the other, the lower inhibitory potency associated with reversion of the piperidine unit (compounds **5** and **8**) can be explained by two factors: (i) the lost of the water-assisted hydrogen bonds formed between the protonated nitrogen and Tyr121 and Ser122 (data not shown) and (ii) the weakening of the electrostatic stabilization due to cation−π interactions with the aromatic rings of Phe330 and Trp84 and with the negative charges of Asp72 and Glu198 (see Figure S6).

As a final test, we explored the suitability of an alternative binding mode where the orientation of **5** was reverted so that the propargylamino group fills the CAS and the benzylpiperidine moiety occupies the PAS. As in the preceding discussion, compound **5** was docked in the binding site of the enzyme for the three AChE structural models (1EVE, 1Q83, and 2CKM) but without imposing positional restraints. Inspection of the first ranked poses showed a preference for the placement of the benzylpiperidine moiety in the CAS. Thus, only 1, 7, and 2 poses out of the first 13, 15, and 7 ranked solutions (covering a range of 8 kcal/mol in the score in each case) corresponded to the reverted orientation of **5** upon docking to models AChE_1EVE, AChE_1Q83 and AChE_2CKM, respectively, which reinforces the reliability of the binding mode discussed above. To further explore the suitability of the inverted binding mode, a series of 20 ns MD simulations were run for the three AChE complexes with the reversed orientation of the inhibitor. Inspection of the binding mode sampled along the last 10 ns of the trajectory run for AChE_1EVE (Figure S7) shows that the propargylamino unit remains stacked onto the indole ring of Trp84, filling part of the region occupied by the benzyl moiety of donepezil. However, there are notable structural fluctuations of the methylated indole ring of **5**, which eventually leads to steric clashes with the benzene ring of Phe330. Similarly, the large fluctuations of the benzylpiperidine moiety also argue against a firm stacking with Trp279 at the PAS. The structural instability of the ligand was also found in the simulations run for AChE_1Q83 and AChE_2CKM (see Figure S7), particularly seen in the large mobility of the ligand at the PAS, which affects the stacking between Trp279 and Tyr70. In fact, comparison of the relative free energies determined from MM/PBSA calculations for the different AChE complexes also supports the energetic destabilization of the inverted binding mode (see Table S2). Finally, let us remark that the enhanced flexibility of the piperidine moiety in the PAS, which reflects the lack of strong interactions, does not provide a straightforward explanation to the significant reduction in the inhibitory potency found upon reversion of the ring (compare **5** and **8** in Table 1).

BuChE Inhibition. The binding mode of **5** to BuChE was explored by means of docking calculations (see Experimental Part). The results indicate a marked preference for the insertion of the benzylpiperidine moiety in the CAS, as noted by the fact that only 4 out of the first 20 ranked poses (comprising a range of 5 kcal/mol in the score) were found with the inverted

arrangement (in fact, the first inverted pose was ranked as the ninth solution). Hence, a new docking calculation was run imposing the benzene unit of **5** to stack against Trp79 (equivalent to Trp84 in the CAS of AChE), thus mimicking the interaction found in the AChE complex with donepezil (PDB entry 1EVE). Even in this case, the results indicate a substantial degree of flexibility to accommodate **5** in the binding site of BuChE, especially regarding the indolylpropargylamine moiety but also even the piperidine ring (see Figure S8). Nevertheless, this finding is not unexpected because of the wider volume of the binding site in BuChE compared to AChE, which can be ascribed to mutations between specific binding site residues in the two enzymes, such as the replacement of Phe330 in the CAS of AChE by Ala, the substitution of Tyr70 and Phe290 at the mid-gorge of AChE by Asn and Val, respectively, and the mutation of Trp279 in the PAS of AChE by Ala. Accordingly, it can be expected that the binding of **5** to BuChE will be mainly guided by the interactions due to the benzylpiperidine moiety, thus explaining the lack of large differences in the selectivity between the two enzymes.

MAO Inhibition. The binding mode of hybrid **5** in MAO-A and MAO-B was investigated in order to explain the different inhibitory behavior found for the two isoforms. To this end, we first explored the potential binding mode of **5** by means of docking calculations, which showed a clear preference to accommodate the indolylpropargylamino unit in the substrate cavity. In fact, this is not surprising, as the reference compound **2** was found to be an irreversible inhibitor of the two MAO isoforms, which indicates that the binding mode places the propargylamino unit properly oriented to react with the flavin adenine dinucleotide (FAD) present in the substrate cavity of both MAO-A and MAO-B.[43] Then a representative member of the most populated cluster of the docked poses was chosen as starting structure for MD simulations of the complexes of **5** with MAO-A and MAO-B. In the two cases MD simulations yielded stable trajectories, as noted by inspection of the time evolution of the potential energy and by the small fluctuations of the rmsd profile along the last 5 ns of the trajectories (see Figures S9 and S10). Thus, the rmsd determined for the protein backbone in the MD simulations run for MAO-A and MAO-B is close to 1.4 Å, whereas the rmsd determined for the residues that define the walls of the binding cavity amounts to 2.0 Å.

Inspection of Figure 8 clearly shows that binding of **5** to MAO-A has little effect on the residues that delineate the binding site, suggesting a suitable fit of the indolylpropargylamino unit in the substrate cavity. In fact, the indole fragment of **5** matches well the corresponding moiety in harmine, as noted upon superposition of the X-ray structure of the human MAO-A–harmine complex[67] and the last snapshot of the MD simulation (see Figure S11). The only exception to the structural integrity of the binding pocket concerns few residues located at the entrance of the gorge leading to the substrate cavity, which reflects the adjustment of the ligand, as expected from the larger flexibility of the solvent-exposed loops that shape the entrance cavity (see Figure S11). It is worth noting how the tether fills the hydrophobic region that defines the bottleneck of the binding pocket, which is mainly due to Phe208 and Ile325. The dependence of the inhibitory potency with the length of the tether can be explained by the steric contraints imposed by the side chains of vicinal apolar residues, such as Leu97, Leu337, Val210, and Cys323, as shortening of the tether would lead to steric clashes with the piperidine unit of the ligand. On the other hand, simulations also show that the positive charge of the piperidine unit in **5** is stabilized by water-mediated hydrogen bond interactions with the backbone carbonyl groups of Arg109 and Gly110.

The structural integrity of the binding mode of **5** in MAO-B is also supported by inspection of the snapshots collected at the end of the trajectory (Figure 8). The five-membered ring of the indole moiety of **5** superposes the benzene ring of deprenyl in its complex with human MAO-B (PDB entry 2BYB;[67] see Figure S12). As in MAO-A, the tether occupies the hydrophobic region delineated by residues Ile199, Ile316, Tyr326, and Leu88, which presumably would lead to steric clases with the piperidine ring upon shortening of the methylenic chain of the inhibitor. Finally, besides water-mediated contacts with the carbonyl groups of Arg100 and Gly101, the positive charge of the piperidine unit in **5** appears to be stabilized by the carboxylate group of Glu84.

As noted above, treatment of MAO-A with **5** leads to a significant inactivation of the enzyme, which remains unaltered after repeated washings. In contrast, a significant recovery of MAO-B activity is found after washings because of a slower inactivation of this isoform. This different behavior suggests that the propargylamino moiety of **5** in MAO-A is better oriented for chemical modification of FAD than in MAO-B. Nevertheless, since both ligand and FAD are treated classically in MD simulations, the electronic effects that promote the chemical inactivation of the enzyme by the propargyl moiety are not properly accounted for. Therefore, we have compared the relative orientation of **5** obtained from MD simulations with the orientation found for clorgyline, deprenyl, rasagiline, and its ((ethyl(methyl)amino)carbonyl)oxy derivative (PDB entries 2BXR, 2BYB, 1S2Q, and 2C65),[67−69] paying attention to the relative positioning of the carbon atom attached to the protonated amine of **5** relative to the nitrogen atom of FAD involved in chemical modification by the irreversible inhibitors. Inspection of Figure 9 shows that in MAO-A such carbon atom is slightly closer to the FAD nitrogen atom than in MAO-B. Thus, the distance between those atoms (averaged over the snapshots sampled in the last 5 ns) amounts to 6.8 ± 0.3 Å in MAO-A and to 7.7 ± 0.4 Å in MAO-B (see Figure S13). The larger separation found in MAO-B agrees with the lower degree of enzyme inactivation found upon incubation with **5**.

To further check this assumption, we have run additional simulations forcing the nitrogen atom of the propargylamino group to occupy the position and orientation relative to FAD found for the corresponding atom in complexes of MAO-A with clorgyline, and MAO-B with deprenyl, rasagiline, and its ((ethyl(methyl)amino)carbonyl)oxy derivative (structurally related to ladostigil). Noteworthy, superposition of the X-ray structures of those complexes reveals that the nitrogen atom of the inhibitor occupies the same spatial location in the binding site, as expected from the similar geometrical arrangement of the propargylamino unit after chemical reaction with FAD (see Figure 9). To this end, restrained simulations (1 ns) were run in triplicate for each enzyme in order to force compound **5** to occupy the position expected after chemical reaction with FAD. With the aim to avoid artifactual results arising from steric clashes of the propargylamino group with binding site residues while steering the nitrogen atom, a methyl unit was used to replace the propargyl moiety. Finally, we have determined the difference in the interaction energy (from MM/PBSA calculations) between the inhibitor and the enzyme.

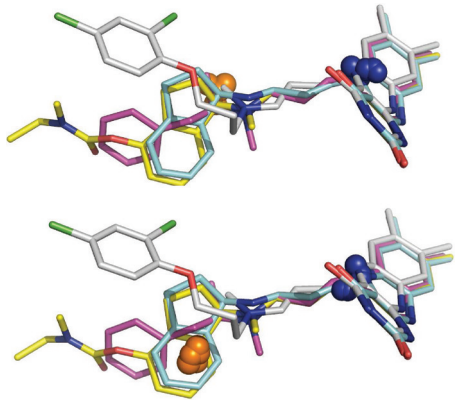

Figure 9. Superposition of the X-ray crystallographic structures of MAO-A complexed with clorgyline (white, PDB entry 2BXR) and MAO-B complexed with deprenyl (magenta, PDB entry 2BYB), rasagiline (blue, PDB entry 1S2Q), and its ((ethyl(methyl)amino)-carbonyl)oxy derivative (yellow, PDB entry 2C65). The spheres show the position of the carbon atom that bears the protonated amine of **5** (orange) and the chemically modified nitrogen atom of FAD (blue). Representation includes the positions of those atoms in snapshots taken every ns along the last 5 ns of the trajectory run for the complex (top) MAO-A−**5** and (bottom) MAO-B−**5**.

Figure 10 shows the time evolution of the distance between the ligand carbon atom (linked to the amino nitrogen) and the

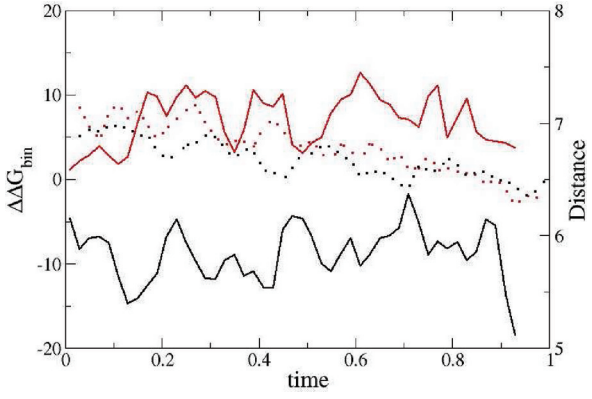

Figure 10. Time evolution of the distance between the ligand carbon atom (linked to the amino nitrogen) and the nitrogen atom of FAD along the restrained MD simulation (shown in dashed lines; MAO-A in black and MAO-B in red). The change in the interaction energy (estimated from MM/PBSA calculations) is shown by solid lines (MAO-A in black and MAO-B in red). For clarity of comparison, the interaction energy profiles are shown relative to the initial snapshot.

nitrogen atom of FAD along the restrained trajectories, and the corresponding change in the ligand−receptor interaction free energy estimated from MM/PBSA computations. The restrained simulations bring the nitrogen atom of **5** to the position expected for the covalent adduct with FAD (distance N(inhibitor)···N(FAD) at around 5.0 Å), the attached carbon atom being located at around 6.4 Å. Interestingly, the results indicate that the interaction energy in MAO-A becomes more negative (relative to the initial state) at around 7 kcal/mol, whereas it is destabilized at around 6 kcal/mol in MAO-B. Therefore, from a qualitative point of view, these results reinforce the notion that adoption of a reactive configuration of **5** in MAO-B is more impeded than in MAO-A, which agrees with the different rates of enzyme inactivation.

Finally, additional 20 ns MD simulations were run to simulate the adduct of **5** covalently bound to FAD. In the two cases MD simulations yielded stable trajectories, as noted by inspection of the time evolution of the potential energy (see Figure S14) and by the small fluctuations of the rmsd profile along the last 5 ns of the trajectories (see Figure 11). However,

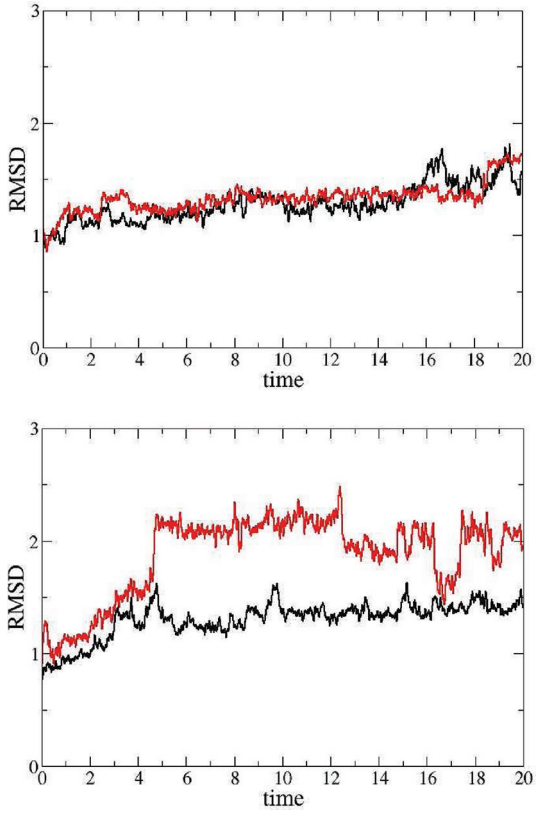

Figure 11. Time evolution of the rmsd determined for the backbone atoms (black) and the heavy atoms of the residues that define the binding site (red) along the trajectories run for the (top) MAO-A−**5** adduct and (bottom) MAO-A−**5** adduct.

it is also worth stressing the different profile of the rmsd along the whole trajectory. Thus, whereas there is a slight increase in the rmsd determined for both the backbone atoms and the heavy atoms of the residues that define the binding site in the simulation run for the MAO-A−**5** adduct (the rmsd increases from 1 to 1.5 Å; see Figure 11), there is a more abrupt increase in the rmsd determined for the binding site residues in the simulation run for the MAO-B−**5** adduct (the rmsd increases from 1 to 2.2 Å; see Figure 11). This trend agrees with the results derived from the restrained MD simulations discussed above and indicates that the proper accommodation of the inhibitor in a conformation suitable for covalent attachment to FAD requires a larger rearrangement in the binding site of MAO-B.

The different trends regarding the inhibitory activity of **5** in MAO-A and MAO-B can be mainly ascribed to the residues that define the bottleneck in the gorge that leads to the substrate binding site. In particular, the replacement of Ile199 in MAO-B by Phe208 in MAO-A pushes the inhibitor toward the FAD, whereas the replacement of Ile325 in MAO-A by Tyr326 in MAO-B triggers the opposite effect. Thus, even though there is a slight net stabilization in the interaction energy of the inhibitor covalently bound to FAD in both MAO-

dx.doi.org/10.1021/jm200853t | J. Med. Chem. 2011, 54, 8251−8270

A and MAO-B (relative to the noncovalent form; see Table S3), present results suggest that there is a larger barrier for the proper accommodation of **5** in MAO-B. In this context, though the methylenic (n = 2) tether designed for **5** seems well suited to fit the gorge in the two isoforms, the spatial constraints imposed on the orientation of the indole ring upon binding to MAO-B leads to a less effective chemical interaction with the FAD. In turn, these findings suggest that extension of the ((methyl)amino)propargylamino unit in **5** could be a useful strategy to enhance the inactivation of MAO-B while reducing the inhibition at MAO-A. This strategy could be beneficial to minimize side effects related to the potentiation of the cardiovascular effect of tyramine (the so-called "cheese effect"), a limited side effect of older generation of nonselective MAO inhibitors.

Inhibition of Aβ Self-Aggregation and AChE-Induced Aggregation. A number of dual binding site AChE inhibitors have been found to exhibit a significant inhibitory activity on Aβ self-aggregation.[60,70−75] Thus, compound **5** was also tested for its ability to inhibit the self-induced $A\beta_{1-42}$ aggregation and the AChE-induced $A\beta_{1-42}$ aggregation. In the former case a 47.8 ± 2.1% inhibition was found when compound **5** was tested at 10 μM (Table 3) (concentration ratio Aβ/inhibitor = 4/1).

Table 3. Inhibition of AChE-Induced $A\beta_{1-40}$ Aggregation and $A\beta_{1-42}$ Self-Induced Aggregation by Compound 5

	% inhibition of Aβ aggregation ± SEM	
compd	AChE-induced[a,c]	self-induced[b,c]
5	32.4 ± 7.0	47.8 ± 2.1

[a]Inhibition of AChE-induced $A\beta_{1-40}$ aggregation. The concentration of **5** and $A\beta_{1-40}$ was 100 and 40 μM, respectively. The ratio Aβ/AChE was equal to 100/1. [b]Inhibition of self-induced $A\beta_{1-42}$ aggregation (40 μM) produced by **5** at 10 μM. [c]Data are the mean ± SEM of at least three independent experiments.

We used propidium iodide (PI) as reference compound, and we obtained a reduction of Aβ self-induced aggregation of 33.3 ± 2.1%, this value being significantly lower than that found for **5**. When PI was tested at equimolar concentrations (Aβ/PI = 1/1), similar to that previously reported by other groups, we found a reduction of Aβ aggregation of 78.6 ± 3.8%. This effect is significantly higher than that reported for donepezil (<5%) under similar experimental conditions[72] and similar to that found for other IAChE.[60,71,72] Then **5** can be considered a moderate inhibitor of $A\beta_{1-42}$ self-induced aggregation. Regarding the inhibition of the human AChE-dependent $A\beta_{1-40}$ aggregation, the results indicate that **5** at 100 μM was able to prevent hAChE-induced $A\beta_{1-40}$ aggregation in a 32.4 ± 7.0% (Table 3). This value is similar to the inhibition elicited by donepezil (22%) and significantly higher than that found for tacrine (7%), two of the first FDA-approved drugs for the treatment of AD. However, it is significantly lower than that of propidium[76] and other IAChEs previously described,[70−72] which show potencies in the low micromolar range.

CONCLUSIONS

A new series of hybrid compounds containing the benzylpiperidine moiety of donepezil and the indolylpropargylamino moiety of *N*-[(5-benzyloxy-1-methyl-1*H*-indol-2-yl)methyl]-*N*-methylprop-2-yn-1-amine have been investigated as novel multitarget agents against AChE, BuChE, and MAO (A/B). These new compounds have been designed to simultaneously interact with the active, peripheral, and mid-gorge binding sites of AChE, as well as to occupy the substrate binding site in MAO.

The length of the tether that connects the two main structural fragments of the novel hybrids has a relevant effect on the binding to MAO, whereas it seems to have little impact on the inhibitory activity against AChE and BuChE. Among these hybrid compounds, **5** is the most potent IMAO, even more than the parent compounds. Surprisingly, although donepezil (**1**) is a slight inhibitor of BuChE and **2** is not even active, the ability of **5** to inhibit BuChE is found on the submicromolar range. This is particularly important in view of the renewed interest in dual cholinergic inhibitors as therapeutic agents for AD.[58] Normally, AChE predominates in the brain, while BuChE activity levels are low. However, in AD the relative enzymatic activity is altered such that BuChE increases while AChE decreases.[77,78] Then, if the therapeutic goal is to increase ACh levels in the brain, a compound able to inhibit both AChE and BuChE would be valuable to elicit a larger protective response. In addition, the inhibition of MAO-B by **5** might be beneficial for modulating the cholinergic neurotransmission and for restoring the serotoninergic neurotransmission. Moreover, the potent MAO-A inhibition enables the drug to exert an antidepressant activity like that of amitriptyline and moclobemide, two triciclic antidepressants primarily used to treat depression. Compound **5** also presents a significant inhibitory profile of Aβ-self-induced and human AChE-dependent aggregation, being more potent (human AChE-dependent) than or similar (self-induced) to the parent compound donepezil (**1**). Overall, the present data indicate that **5** not only is an interesting lead compound for the design of novel MTDL with a good IMAO/IAChE inhibitory potency and a significant activity against amyloid aggregation but also may have a potential disease-modifying role in the treatment of AD.

EXPERIMENTAL PART

General Methods. Melting points were determined in a Koffler apparatus and are uncorrected. ^{1}H NMR and ^{13}C NMR spectra were recorded at room temperature in $CDCl_3$ or DMSO-d_6 at 300, 400, or 500 MHz and at 75.4, 100.6, or 125.6 MHz, respectively, using solvent peaks [$CDCl_3$, 7.27 (D), 77.2 (C) ppm; DMSO-d_6, 2.50 (D) and 39.7 (C) ppm] as internal references. The assignment of chemical shifts is based on standard NMR experiments (^{1}H, ^{13}C, ^{1}H−^{1}H COSY, ^{1}H−^{13}C HSQC, HMBC, DEPT). Mass spectra were recorded on a GC/MS spectrometer with an API-ES ionization source. TLC was performed on silica F254. Detection was by UV light at 254 nm or by spraying with phosphomolybdic-H_2SO_4 dye reagent. Column chromatographies were performed on silica gel 60 (230 mesh). "Chromatotron" separations were performed on a Harrison Research model 7924. The circular disks were coated with Kieselgel 60 PF254 (E. Merck). The chlorydrate salts were prepared by solubilizing the compound in a minimum of ether, and a solution of ether saturated with HCl(g) was added dropwise. A white solid was formed immediately. The precipitated hydrochloride was separated by filtration, washed with ether, and dried. The purity (≥95%) of the samples was determined by elemental analysis, carried out at the IQOG (CSIC, Spain).

Methyl 4-(Piperidin-4-yl)butanoate (17).[55] A solution of (*E*)-ethyl 3-(pyridin-4-yl)acrylate **16**[52] (1.52 g, 8.58 mmol) in EtOH (20 mL) and 4 N HCl in 1,4-dioxane (2 mL) was hydrogenated under 10% Pd/C (0.152 g) and PtO_2 (152 mg) overnight at room temperature. Then the catalyst was filtered off, washed with MeOH, and the filtrate was concentrated. The residual solid was triturated with Et_2O, filtered, washed with Et_2O, and dried to give the known methyl

dx.doi.org/10.1021/jm200853t | J. Med. Chem. 2011, 54, 8251−8270

ester **17** (1.60 g, 90%) as a solid. ^{1}H NMR (300 MHz, DMSO-d_6) δ 9.29−9.10 (br, 2H), 3.55 (s, 3H, CO_2CH_3), 3.16−3.12 (m, 2H), 2.78−2.67 (m, 2H), 2.31−2.27 (m, 2H), 1.73−1.69 (m, 2H), 1.46−1.21 (m, 5H); MS (ES) m/z 172 $[M + H]^+$.

1-Benzyl-4-piperidinepropanol (19).[56] To a solution of methyl 4-(piperidin-4-yl)butanoate **17**[55] (1.60 g, 7.21 mmol) and benzyl bromide (1.85 g, 10.82 mmol) in 20 mL of CH_2Cl_2 was added triethylamine (3.3 mL, 21.65 mmol) while the internal temperature in the mixture was below 20 °C by cooling with an ice−water bath. The mixture was stirred at room temperature overnight. After complete reaction (TLC analysis), the mixture was concentrated and purified by column chromatography to give methyl 3-(1-benzylpiperidin-4-yl)propanoate (**18**) [(1.41 g, 75%): oil; ^{1}H NMR (300 MHz, $CDCl_3$) δ 7.35−7.23 (m, 5H), 3.66 (s, 3H, CO_2CH_3), 3.51 (s, 2H, CH_2-Ph), 2.89 (br d, J = 11.5 Hz, 2H), 2.32 (br t, J = 7.5 Hz, 2H, CH_2-CO_2CH_3), 1.94 (t, J = 10.9 Hz, 2H), 1.66−1.54 (m, 4H), 1.34−1.21 (m, 3H, CH + CH_2); MS (EI) m/z (%) 91 (100) $[PhCH_2]^+$, 188 (66) $[M - CH_2CH_2CO_2Me]^+$, 202 (13) $[M - CO_2Mt]^+$, 230 (19) $[M - OMe]^+$, 246 (9) $[M - CH_3]^+$, 260 (73) $[M - H]^+$, 261 (50) $[M]^+$], which was used in the next reaction without further analysis.

To a suspension of LAH (0.176 g, 4.66 mmol, 2 equiv) in dry THF (10 mL) was added methyl 3-(1-benzylpiperidin-4-yl)propanoate (**18**) (0.61 g, 2.33 mmol, 1 equiv) in dry THF (10 mL), at 0 °C. The mixture was refluxed for 2 h, and after cooling unreacted $LiAlH_4$ was quenched by careful addition of 10% NaOH solution (20 mL). The solution was filtered and washed with H_2O and EtOAc. The filtrate was extracted with EtOAc, and the combined organic layers, dried over Na_2SO_4, were concentrated to give known compound **19**[56] (0.535 g, 98%): oil; ^{1}H NMR (300 MHz, $CDCl_3$) δ 7.32−7.20 (m, 5H), 3.60 (t, J = 6.4 Hz, 2H, CH_2O), 3.48 (s, 2H, CH_2Ph), 2.87 (br d, J = 11.5 Hz, 2H), 1.92 (br d, J = 11.1 Hz, 2H), 1.68−1.60 (m, 2H), 1.61−1.49 (m, 2H), 1.30−1.15 (m, 5H); MS (EI) m/z (%): 91 (100) $[PhCH_2]^+$, 142 (26) $[M - CH_2Ph]^+$, 156 (17) $[M - Ph]^+$, 174 (8) $[M - (CH_2)_3OH]^+$, 188 (18) $[M - (CH_2)_2OH]^+$, 202 (14) $[M - CH_2OH]^+$, 232 (37) $[M - H]^+$, 233 (20) $[M]^+$.

1-Benzyl-4-(3-chloropropyl)piperidine (12). To a solution of 1-benzyl-4-piperidinepropanol (**19**)[56] (0.53 g, 2.27 mmol) in CH_2Cl_2 (5 mL), $SOCl_2$ (0.66 mL, 9.08 mmol, 4 equiv) was added dropwise with ice cooling. The mixture was refluxed for 3 h and then evaporated. The residue was rendered alkaline with 10% K_2CO_3 solution and extracted with CH_2Cl_2. The organic layer, dried over Na_2SO_4, was evaporated under reduced pressure to give compound **12** (0.582 g, 99%): oil; IR 3027, 2923, 2849, 2800, 2756, 1672, 1493, 1452, 1366, 1342, 1263, 738, 698 cm^{-1}; ^{1}H NMR (400 MHz, $CDCl_3$) δ 7.22−7.36 (m, 5H), 3.51 (t, J = 8.0 Hz, 2H, CH_2Cl), 3.51 (s, 2H, CH_2Ph), 2.89 (br d, J = 11.5 Hz, 2H), 1.95 (br t, J = 11.0 Hz, 2H), 1.78 (dt, J = 11.9 and 6.9 Hz, 2H, CH_2-CH_2Cl), 1.65 (br d, J = 11.4 Hz, 2H), 1.32−1.42 (m, 2H), 1.21−1.30 [m, 3H, CH + CH_2-$(CH_2)_2Cl$]; ^{13}C NMR (100 MHz, $CDCl_3$) δ 138.1 (C-Ph), 129.1 (2 × CH-Ph), 128.0 (CH-Ph), 126.8 (CH-Ph), 63.3 (CH_2-Ph), 53.6 ($2CH_2$-piperidine), 45.2 (CH_2Cl), 35.1 (CH), 33.6 [CH_2-$(CH_2)_2Cl$], 32.1 ($2CH_2$-pieridine), 29.9 (CH_2, CH_2-CH_2Cl); MS (EI) m/z (%) 91 (100) $[PhCH_2]^+$, 160 (23) $[M - Bn]^+$, 174 (27) $[M - (CH_2)_3Cl]^+$, 188 (17) $[M - (CH_2)_2Cl]^+$, 202 (9) $[M - CH_2Cl]^+$, 216 (88) $[M - Cl]^+$, 250 (35) $[M - 1]^+$. Anal. Calcd for $C_{15}H_{22}ClN$: C, 71.55; H, 8.81; N, 5.56. Found: C, 71.84; H, 9.02; N, 5.83.

1-Benzyl-4-(4-chlorobutyl)piperidine (13). To a solution of 1-benzyl-4-(4-hydroxybutyl)piperidine (**24**)[57] (0.508 g, 2.05 mmol) in CH_2Cl_2 (5 mL), $SOCl_2$ (0.6 mL, 8.214 mmol, 4 equiv) was added dropwise with ice cooling. The mixture was refluxed for 2 h and then evaporated. The residue was rendered alkaline with 10% K_2CO_3 solution and extracted with CH_2Cl_2. The organic layer, dried over Na_2SO_4, was evaporated under reduced pressure to give compound **13** (0.54 g, 99%) as a yellow oil. IR 3062, 3027, 2921, 2847, 2799, 2757, 1493, 1454, 1366, 1341, 1311, 1287, 1126, 1073, 1029, 979, 737, 698 cm^{-1}; ^{1}H NMR (300 MHz, $CDCl_3$) δ 7.34−7.21 (m, 5H), 3.53 (t, J = 6.7 Hz, 2H, CH_2Cl), 3.50 (s, 2H, CH_2Ph), 2.88 (br d, J = 11.4 Hz, 2H), 1.93 (br t, J = 11.9 Hz, 2H), 1.75 (tt, J = 8 Hz, 2H, CH_2-CH_2Cl), 1.70−1.59 (m, 2H), 1.49−1.37 (m, 2H), 130−1.20 (m, 5H); ^{13}C NMR (100 MHz, $CDCl_3$) δ 32.2 ($2CH_2$), 32.7 (CH_2, CH_2-CH_2Cl), 32.8 (CH_2), 36.2 (CH_2), 45.0 (CH_2Cl), 53.8 ($2CH_2$), 63.4 (CH_2-Ph), 126.8 (CH-Ph), 128.0 (2 × CH-Ph), 129.1 (2 × CH-Ph), 138.3 (C-Ph); MS (EI) m/z (%) 91 (100) $[PhCH_2]^+$, 174 (42) $[M - (CH_2)_4Cl]^+$, 188 (43) $[M - (CH_2)_3Cl]^+$, 202 (16) $[M - (CH_2)_2Cl]^+$, 216 (8) $[M - CH_2Cl]^+$, 230 (28) $[M - Cl]^+$, 264 (45) $[M]^+$. HRMS (ES+), exact mass calcd for $C_{16}H_{25}ClN$ $(M + H)^+$: 266,1676. Found: m/z 266.1687.

***N*-((5-((1-Benzylpiperidin-4-yl)methoxy)-1-methyl-1*H*-indol-2-yl)methyl)-*N*-methylprop-2-yn-1-amine (3).** To a solution of 1-methyl-2-{[ethyl(prop-2-yn-1-yl)amino]ethyl}-1*H*-indol-5-ol **4**[52] (0.21 g, 0.94 mmol) and 1-benzyl-4-(chloromethyl)piperidine **10**[27] (0.33 g, 1.51 mmol, 1.5 equiv) in acetonitrile (5 mL), NaH (120 mg, 3 mmol, 3 equiv, 60% mineral oil) was added. The reaction mixture was stirred at 50 °C for 10 h. After complete reaction (TLC analysis), the mixture was concentrated, diluted with water, and extracted with CH_2Cl_2. The organic phase was washed with brine, dried ($MgSO_4$), and evaporated. The crude product was purified by flash chromatography (CH_2Cl_2/MeOH, 100:1) to give compound **3** (126.3 mg, 32%) as white solid: R_f = 0.24 (CH_2Cl_2/MeOH, 10:1); mp 123−5 °C; IR (KBr) ν 3252, 2938, 2913, 1620, 1489, 1466, 1195, 1163, 1029, 1008 cm^{-1}; ^{1}H NMR (400 MHz, $CDCl_3$) δ 7.35−7.24 (m, 5H), 7.18 (d, J = 8.8 Hz, 1H, CH7-indole), 7.04 (d, J = 2.3 Hz, 1H, CH4-indole), 6.86 (dd, J = 8.8 and 2.3 Hz, 1H, CH6-indole), 6.34 (s, 1H, CH3-indole), 3.85 (d, J = 6.0 Hz, 2H, -CH_2O-), 3.73 (s, 3H, N-CH_3), 3.68 (s, 2H, indole-CH_2-N), 3.53 (s, 2H, CH_2-Ph), 3.31 (d, 2H, J = 2.2 Hz, CH_2-C≡CH), 2.95 (d, J = 11.4 Hz, 2H), 2.35 (s, 3H, N-CH_3), 2.30 (t, J = 2.2 Hz, C≡CH), 2.02 (t, J = 16, 2H), 1.91−1.81 (m, 3H), 1.49−1.39 (m, 2H); ^{13}C NMR (100 MHz, $CDCl_3$) δ 153.3 (C5-indole), 138.3 (C1′-Ph), 137.8 (C2-indole), 133.3 (C7a-indole), 129.1 (2 × CH-Ph), 128.1 (2 × CH-Ph), 127.5 (C3a-indole), 126.8 (CH4′-Ph), 111.9 (CH6-indole), 109.5 (CH7-indole), 103.3 (CH4-indole), 102.0 (CH3-indole), 78.4 (-C≡), 73.6 (CH_2-O), 73.4 (≡CH), 63.4 (CH_2-Ph), 54.0 (2 × CH_2), 63.4 (Ph-CH_2), 53.4 (2 × CH_2), 51.7 (Ind-CH_2-N), 44.6 (CH_2-C≡), 41.5 (N-CH_3), 35.9 (CH-piperidine), 29.8 (N-CH_3), 29.1 (2 × CH_2); MS (EI) m/z (%) 416 (100) $[M + H]^+$, 438 (2) $[M + Na]^+$. **3**·2HCl: white powder; mp 230−3 °C; IR (KBr) ν 3423, 3200, 2933, 2511, 1620, 1486, 1466, 1208 cm^{-1}; ^{1}H NMR (300 MHz, D_2O) δ 7.34−7.25 (m, 6H, CH7-indole + 5H-Ph), 7.05 (d, J = 2.2 Hz, 1H, CH4-indole), 6.85 (dd, J = 9.0, 2.2 Hz, 1H, CH6-indole), 6.59 (s, 1H, CH3-indole), 4.47 (s, 2H, CH_2), 4.11 (s, 2H, CH_2), 3.86 (d, J = 2.4 Hz, 2H, CH_2-C≡CH), 3.79 (t, J = 6.0 Hz, 2H, O-CH_2-), 3.59 (s, 3H, indole-CH_3), 3.38 (d, J = 12.8 Hz, 2H, CH_2), 2.97 (t, J = 2.3 Hz, 1H, C≡CH), 2.85 (t, J = 12.7 Hz, 2H, CH_2), 2.76 (s, 3H, N-CH_3), 1.98 (d, J = 12.8 Hz, 2H, CH_2), 1.89−1.83 (m, 1H, CH), 1.48−1.34 (m, 2H, CH_2). Anal. Calcd for $C_{27}H_{35}Cl_2N_3O$: C, 66.39; H, 7.22; Cl, 14.52; N, 8.60. Found: C, 66.21; H, 7.43; Cl, 14.42; N, 8.63.

***N*-{[5-(2-(1-Benzylpiperidin-4-yl)ethoxy)-1-methyl-1*H*-indol-2-yl]methyl}-*N*-methylprop-2-yn-1-amine (4).** To a solution of 1-methyl-2-{[ethyl(prop-2-yn-1-yl)amino]ethyl}-1*H*-indol-5-ol **14**[52] (160 mg, 0.7 mmol) and 1-benzyl-4-(2-chloroethyl)piperidine **11**[53] (0.25 g, 1.05 mmol, 1.5 equiv) in DMF (5 mL), NaH (84 mg, 2.1 mmol, 3 equiv, 60% mineral oil) was added. The reaction mixture was stirred at room temperature for 3 h. After complete reaction, the solvent was removed and the crude was diluted with water and extracted with CH_2Cl_2. The organic phase was washed with brine, dried ($MgSO_4$), and evaporated at reduced pressure. The crude product was purified by flash chromatography (CH_2Cl_2/MeOH, 100:1) to give compound **4** (0.216 g, 72%) as a white solid: R_f = 0.27 (CH_2Cl_2/MeOH, 10:1); mp 86−7 °C; IR (KBr) ν 3275, 2941, 2921, 2876, 2807, 2782, 2768, 1619, 1488, 1473, 1289, 1250, 1207, 1161, 1030 cm^{-1}; ^{1}H NMR (400 MHz, $CDCl_3$) δ 7.34−7.23 (m, 5H), 7.18 (d, J = 8.8 Hz, 1H, CH7-indole), 7.03 (d, J = 2.4 Hz, 1H, CH4-indole), 6.85 (dd, J = 8.8 and 2.4 Hz, 1H, CH6-indole), 6.33 (s, 1H, CH3-indole), 4.03 (t, J = 6.5 Hz, 2H, O-CH_2-), 3.74 (s, 3H, N-CH_3), 3.67 (s, 2H, N-CH_2), 3.52 (s, 2H, CH_2-Ph), 3.31 (d, 2H, J = 2.3 Hz, CH_2-C≡CH), 2.91 (d, J = 11.6 Hz, 2H), 2.34 (s, 3H, N-CH_3), 2.29 (t, J = 2.3 Hz, C≡CH), 2.0 (t, J = 10.8, 2H), 1.77−1.72 (m, 4H), 1.41−1.31 (m, 2H), 1.62−1.52 (m, CH); ^{13}C NMR (100 MHz, $CDCl_3$) δ 153.5 (C5-indole), 138.4 (C-Ph), 133.6 (C-indole), 137.2 (C-indole), 129.5

(2 × CH-Ph), 128.3 (2 × CH-Ph), 127.7 (C-indole), 127.2 (CH-Ph), 112.2 (CH6-indole), 109.5 (CH7-indole), 103.5 (CH4-indole), 102.0 (CH3-indole), 78.6 (-C≡), 73.6 (≡CH), 66.7 (CH_2-O), 63.6 (CH_2-Ph), 53.9 (2 × CH_2), 52.0 (CH_2-indole), 44.9 (CH_2-C≡CH), 41.8 (N-CH_3), 36.2 (CH_2), 32.8 (CH_2), 32.4 (CH_2), 30.1 (N-CH_3); MS (EI) *m/z* (%) 91 (48) $[PhCH_2]^+$, 202 (100), 361 (3) $[M - NCH_3CH_2C{\equiv}CH)]^+$, 429 (4) $[M]^+$. Anal. Calcd for $C_{28}H_{35}N_3O$: C, 78.28; H, 8.21; N, 9.78. Found: C, 77.99; H, 8.45; N, 9.79. **4**·2HCl: white powder; mp 221−3 °C; IR (KBr) ν 3424, 3195, 2928, 2561, 2506, 1619, 1486, 1471, 1210 cm^{-1}; ^1H NMR (300 MHz, D_2O) δ 7.33−7.25 (m, 6H, CH7-indole + 5H-Ph), 7.06 (d, J = 2.4 Hz, 1H, CH4-indole), 6.84 (dd, J = 9.0, 2.4 Hz, 1H, CH6-indole), 6.58 (s, 1H, CH3-indole), 4.45 (s, 2H, CH_2), 4.08 (s, 2H, CH_2), 3.96 (t, J = 6.2 Hz, 2H, O-CH_2-), 3.84 (d, J = 2.4 Hz, 2H, CH_2-C≡CH), 3.59 (s, 3H, indole-CH_3), 3.32 (d, J = 12.6 Hz, 2H, CH_2), 2.96 (t, J = 2.4 Hz, 1H, C≡CH), 2.85−2.75 (m 5H, CH_2 + N-CH_3), 1.84 (d, J = 13.6 Hz, 2H, CH_2), 1.75−1.63 [m, 1H, CH], 1.61−1.53 (m, 2H, CH_2-CH_2O-), 1.32−1.18 (m, 2H, CH_2). Anal. Calcd for $C_{28}H_{35}N_3O{\cdot}2HCl{\cdot}^1/_3(H_2O)$: C, 66.13; H, 7.47; Cl, 13.94; N, 8.26. Found: C, 66.04; H, 7.89; Cl, 13.84; N, 8.59.

***N*-{[5-(3-(1-Benzylpiperidin-4-yl)propoxy)-1-methyl-1*H*-indol-2-yl]methyl}-*N*-methylprop-2-yn-1-amine (5).** To a solution of 1-methyl-2-{[ethyl(prop-2-yn-1-yl)amino]ethyl}-1*H*-indol-5-ol **4**[52] (0.22 g, 0.963 mmol) and 1-nenzyl-4-(3-chloropropyl)piperidine **12** (0.36 g, 1.44 mmol, 1.5 equiv) in DMF (5 mL), NaH (69.4 mg, 1.73 mmol, 1.8 equiv, 60% /mineral) was added. The reaction mixture was stirred at room temperature overnight and then heated at 100 °C for 1 h. After complete reaction (TLC analysis), the mixture was concentrated, diluted with water, and extracted with CH_2Cl_2. The organic phase was washed with brine, dried ($MgSO_4$), and evaporated at reduced pressure. The crude product was purified by flash chromatography (CH_2Cl_2/AcOEt, 10:1 to 5:1, v/v) to give compound **5** (0.268 g, 63%) as a white solid: R_f = 0.28 (CH_2Cl_2/MeOH, 20:1); mp 90−91 °C; IR (KBr) ν 3265, 2935, 2908, 2799, 2760, 1619, 1489, 1471, 1395, 1269, 1204, 1190, 1160, 1029 cm^{-1}; ^1H NMR (400 MHz, $CDCl_3$) δ 7.35−7.25 (m, 5H, Ph), 7.19 (d, J = 8.8 Hz, 1H, CH7-indole), 7.05 (d, J = 2.14 Hz, 1H, CH4-indole), 6.85 (dd, J = 8.8 and 2.3 Hz, 1H, CH6-indole), 6.35 (s, 1H, CH3-indole), 3.98 (t, J = 6.6 Hz, 2H, O-CH_2-), 3.75 (s, 3H, indole-CH_3), 3.69 (s, 2H, indole-CH_2), 3.52 (s, 2H, CH_2-Ph), 2.33 (d, J = 2.2 Hz, 2H, CH_2-C≡CH), 2.91 (d, J = 10.8 Hz, CH_2), 2.36 (s, 3H, N-CH_3), 2.31 (t, J = 2.0 Hz, C≡CH), 1.97 (t, J = 12 Hz, 2H, CH_2), 1.83 [m, 2H, CH_2-(CH_2O)], 1.72 (d, J = 9.1 Hz, 2H, CH_2), 1.46−1.41 [m, 2H, CH_2-(CH_2)$_2$O], 1.29−1.31 (m, 3H, CH+CH_2); ^{13}C NMR (100 MHz, $CDCl_3$) δ 153.2 (C5-indole), 138.3 (C-Ph), 136.9 (C2-indole), 133.3 (C-indole), 129.2 (2 × CH-Ph), 128.0 (2 × CH-Ph), 127.4 (C-indole), 126.8 (CH-Ph), 112.0 (CH6-indole), 109.5 (CH7-indole), 103.3 (CH4-indole), 102.0 (CH3-indole), 78.3 (-C≡), 73.4 (≡CH), 69.0 (CH_2-O), 63.4 (CH_2-Ph), 53.8 (2 × CH_2), 51.7 (indole-CH_2), 44.6 (CH_2-C≡), 41.5 (N-CH_3), 35.5 (CH-piperidine), 32.8 [CH_2-(CH_2)$_2$O], 32.2 (2CH_2), 29.8 (indole-N-CH_3), 26.7 [CH_2-CH_2O]; MS (EI) *m/z* (%) 91 (77) $[PhCH_2]^+$, 352 (22) $[M - CH_2Ph]^+$, 374 (100) $[M - NCH_3CH_2C{\equiv}CH)]^+$, 404 (7) $[M - CH_2C{\equiv}CH)]^+$, 428 (5) $[M - CH_3]^+$, 443 (40)$[M]^+$. Anal. Calcd for $C_{29}H_{37}N_3O$: C, 78.51; H, 8.41; N, 9.47. Found: C, 78.36; H, 8.31; N, 9.23. **5**·2HCl: white powder; mp 203−5 °C; IR (KBr) ν 3193, 2937, 2512, 1619, 1486, 1469, 1209 cm^{-1}; ^1H NMR (300 MHz, D_2O) δ 7.32−7.22 (m, 6H, CH7-indole + 5H-Ph), 7.05 (d, J = 2.2 Hz, 1H, CH4-indole), 6.83 (dd, J = 9.0, 2.3 Hz, 1H, CH6-indole), 6.58 (s, 1H, CH3-indole), 4.45 (s, 2H, CH_2), 4.07 (s, 2H, CH_2), 3.90 (t, J = 6.1 Hz, 2H, O-CH_2-), 3.83 (d, J = 2.2 Hz, 2H, CH_2-C≡CH), 3.59 (s, 3H, indole-CH_3), 3.30 (d, J = 12.0 Hz, 2H, CH_2), 2.97−2.94 (m, 1H, C≡CH), 2.81−2.72 (m 5H, CH_2 + N-CH_3), 1.84−1.75 (m, 2H, CH_2), 1.65−1.55 (m, 2H, CH_2), 1.49−1.36 (m, 1H, CH), 1.41−1.46 [m, 2H, CH_2-(CH_2)$_2$O], 1.29−1.09 (m, 4H). Anal. Calcd for $C_{29}H_{37}N_3O{\cdot}2HCl$: C, 67.43; H, 7.61; Cl, 13.73; N, 8.13. Found: C, 67.38; H, 7.81; Cl, 13.13; N, 8.02.

***N*-{[5-(4-(1-Benzylpiperidin-4-yl)butoxy)-1-methyl-1*H*-indol-2-yl]methyl}-*N*-methylprop-2-yn-1-amine (6).** To a solution of 1-methyl-2-{[ethyl(prop-2-yn-1-yl)amino]ethyl}-1*H*-indol-5-ol **4**[52] (0.35 g, 1.56 mmol) and 1-benzyl-4-(4-chlorobutyl)piperidine **13** (0.5 g, 1.88 mmol, 1.2 equiv) in 8 mL of DMF, NaH (0.1 g, 2.5 mol, 1.6 equiv, 60% mineral oil) was added. The reaction mixture was stirred at room temperature overnight and then heated at 70 °C for 8 h. Then the mixture was concentrated, diluted with water, and extracted with CH_2Cl_2. The organic phase was washed with brine, dried ($MgSO_4$), and evaporated. The crude product was purified by flash chromatography (CH_2Cl_2/MeOH, 50:1 to 30:1, v/v) to give compound **6** (0.547 g, 76%) as a white solid: R_f = 0.28 (CH_2Cl_2/MeOH, 20:1); mp 93−94 °C; IR (KBr) ν 3260, 2937, 2918, 1619, 1489, 1472, 1203, 1193, 1160, 1008 cm^{-1}; ^1H NMR (500 MHz, $CDCl_3$) δ 7.32−7.23 (m, 5H), 7.17 (d, J = 8.8 Hz, 1H, CH7-indole), 7.03 (d, J = 2.3 Hz, 1H, CH4-indole), 6.85 (dd, J = 8.8 and 2.4 Hz, 1H, CH6-indole), 6.32 (s, 1H, CH3-indole), 3.98 (t, J = 6.6 Hz, 2H, -CH_2O-), 3.67 (s, 2H, CH_2-N), 3.73 (s, 3H, N-CH_3), 3.49 (s, 2H, CH_2-Ph), 3.31 (d, J = 2.4 Hz, CH_2-C≡CH, 2H), 2.88 (d, J = 10.5 Hz, 2H, CH_2pip), 2.34 (s, 3H, N-CH_3), 2.28 (t, J = 2.4 Hz, 1H, C≡CH), 2.00−1.85 (m, 2H, CH_2pip), 1.83−1.73 (m, 2H, CH_2-CH_2O), 1.66 (br d, J = 9.4 Hz, CH_2pip), 1.51−1.45 (m, 2H, CH_2-(CH_2)$_2$O), 1.34−1.22 (M, 4H, CH_2pip + CH_2-(CH_2)$_3$O); ^{13}C NMR (125 MHz, $CDCl_3$) δ 153.5 (C5-indole) 138.5 (C-Ph), 137.0 (C2-indole), 133.3 (C7a-indole), 129.2 (2 × CH_2Ph), 128.1 (2 × CHPh), 127.5 (C3a-indole), 126.8 (CH-Ph), 112.0 (CH6-indole), 109.5 (CH7-indole), 103.4 (CH4-indole), 102.0 (CH_3-indole), 78.4 (-C≡), 73.4 (≡CH), 68.8 (CH_2-O), 63.5 (CH_2-Ph), 53.9 (2 × CH_2-piperidine), 51.8 (N-CH_2-indole), 44.7 (CH_2-C≡CH), 41.7 (N-CH_3), 36.3 (CH_2-(CH_2)$_3$O), 35.6 (CH-piperidine), 32.3 (2 × CH_2-piperidine), 29.8 (N-CH_3), 29.7 (CH_2-CH_2O), 23.3 [CH_2-(CH_2)$_2$O]; MS (EI) *m/z* (%) 91 (55) $[PhCH_2]^+$, 172 (71), 228 (45), 366 (41) $[M - Bn]^+$, 388 $[M - NCH_3CH_2C{\equiv}CH)]^+$, 418 (8) $[M - CH_2C{\equiv}CH)]^+$, 457 (26) $[M]^+$. Anal. Calcd for $C_{30}H_{39}N_3O$: C, 78.73; H, 8.59; N, 9.18. Found: C, 78.65; H, 8.71; N, 9.07. **6**·2HCl: white powder; mp 197−9 °C; IR (KBr) ν 3421, 3195, 2928, 2851, 2561, 2509, 1619, 1485, 1472, 1458, 1408, 1209 cm^{-1}; ^1H NMR (300 MHz, D_2O) δ 7.33−7.24 (m, 6H, CH7-ind + 5H-Ph), 7.05 (d, J = 2.2 Hz, 1H, CH4-ind), 6.84 (dd, J = 9.0, 2.4 Hz, 1H, CH6-ind), 6.59 (s, 1H, CH3-ind), 4.48 (s, 2H, CH_2), 4.05 (s, 2H, CH_2), 3.90 (t, J = 6.5 Hz, 2H, O-CH_2-), 3.86 (d, J = 2.2 Hz, 2H, CH_2-C≡CH), 3.58 (s, 3H, indole-CH_3), 3.28 (d, J = 12.3 Hz, 2H, CH_2), 2.98 (t, J = 2.3 Hz, 1H, C≡CH), 2.77−2.70 (m 5H, CH_2 + N-CH_3), 1.76 (d, J = 13.9 Hz, 2H, CH_2), 1.61−1.51 (m, 2H, CH_2), 1.41−1.23 (m, 3H, CH + CH_2), 1.29−1.05 (m, 4H). Anal. Calcd for $C_{30}H_{39}N_3O{\cdot}2HCl$: C, 67.91; H, 7.79; Cl, 13.36; N, 7.92. Found: C, 67.54; H, 7.45; Cl, 13.25; N, 8.10;

***N*-{[5-(2-Bromoethoxy)-1-methyl-1*H*-indol-2-yl)methyl}-*N*-methylprop-2-yn-1-amine (25).** A mixture of 1-methyl-2-{[ethyl-(prop-2-yn-1-yl)amino]ethyl}-1*H*-indol-5-ol **14**[52] (0.215 g, 0.942 mmol), 1,2-dibromoethane (1.77 g, 9.42 mmol), and potassium carbonate (0.65 g, 4.71 mmol) in 2-butanone (8 mL) was reacted at 85 °C for 6 h. The mixture was evaporated in vacuo, and the residue was partitioned between dichloromethane (10 mL) and water (10 mL). The organic layer was dried (Na_2SO_4) and evaporated. The residue was purified by column chromatography, eluting with 4% methanol in dichloromethane, affording compound **25** (117.3 mg, 37%): R_f = 0.76 (CH_2Cl_2/AcOEt, 10:1); mp 75−77 °C; IR 3274, 29712937, 2877, 2800, 1619, 1579, 1488, 1473, 1400, 1267, 1205, 1198, 1159, 1118, 1025, 889, 842, 794, 776, 690 cm^{-1}; ^1H NMR (300 MHz, $CDCl_3$) δ 7.2 (d, J = 8.8 Hz, 1H, CH7-indole), 7.07 (d, J = 2.4 Hz, 1H, CH4-indole), 6.9 (dd, J = 8.8, 2.5 Hz, 1H, CH6-indole), 6.36 (s, 1H, CH3-indole), 4.33 (t, J = 6.4 Hz, 2H, -CH_2-O-), 3.75 (s, 3H, N-CH_3), 3.69 (s, 2H, N-CH_2), 3.66 (t, J = 6.4 Hz, 2H, -CH_2-Br), 3.32 (d, J = 2.4 Hz, 2H, N-CH_2-C≡), 2.36 (s, 3H, N-CH_3), 2.31 (t, J = 2.4 Hz, 1H, ≡CH); ^{13}C NMR (75 MHz, $CDCl_3$) δ 152.2 (C5-indole), 137.3 (C2-indole), 133.8 (C7a-indole), 127.4 (C3a-indole), 112.2 (CH6-indole), 109.7 (CH7-indole), 104.4 (CH4-indole), 102.1 (CH3-indole), 78.3 (-C≡), 73.5 (≡CH), 69.1 (CH_2-O), 51.7 (CH_2-N), 44.7 (-CH_2-C≡), 41.5 (N-CH_3), 29.9 (N-CH_3), 29.6 (CH_2-Br); MS (EI) *m/z*(%): 131 (48), 160 (66) $[M - ((Br(CH_2)_2)$-$NCH_3CH_2C{\equiv}CH)]^+$, 267 (100) $[M - NCH_3CH_2C{\equiv}CH)]^+$, 334 (25)$[M]^+$. Anal. Calcd for $C_{16}H_{19}BrN_2O$: C, 57.32; H, 5.71; Br, 23.83; N, 8.36. Found: C, 57.50; H, 5.70; Br, 23.24; N, 8.54.

***N*-{[5-(2-(4-Benzylpiperidin-1-yl)ethoxy)-1-methyl-1*H*-indol-2-yl]methyl}-*N*-methylprop-2-yn-1-amine (7).** 4-Benzylpiperidine (36 μL, 0.2 mmol) was added to a mixture of **25** (34 mg, 0.1 mmol) and potassium carbonate (42 mg, 0.3 mmol) in *N*,*N*-dimethylformamide (1 mL). The reactants were heated at 80 °C overnight under an atmosphere of argon. The reaction mixture was poured into water (5 mL) and extracted with dichloromethane (3 × 20 mL). The organic layers were combined, dried (Na_2SO_4), and concentrated. The residue was purified by column chromatography, eluting with 3.3% methanol in dichloromethane, affording compound **7** (33.5 mg, 77%): white solid; R_f = 0.49 (CH_2Cl_2/MeOH, 10:1); ^{1}H NMR (400 MHz, $CDCl_3$) δ 7.31−7.25 (m, 2H), 7.23−7.14 (m, 4H), 7.06 (d, *J* = 2.36 Hz, 1H, CH4-indole), 6.88 (dd, *J* = 8.83 and 2.43 Hz, 1H, CH6-indole), 6.35 (s, 1H, CH3-indole), 4.16 (t, *J* = 6.06 Hz, 2H, -CH_2-O), 3.74 (s, 3H, CH_3), 3.68 (s, 2H, N-CH_2), 3.32 (d, *J* = 2.35 Hz, 2H, CH_2), 3.034 (d, *J* = 11.7 Hz, CH_2), 2.83 (t, *J* = 6.03 Hz, CH_2), 2.56 (d, *J* = 7.016 Hz, CH_2), 2.35 (s, 3H, CH_3), 2.31 (t, *J* = 2.37 Hz, C≡CH), 2.086 (td, *J* = 11.77, 2.18 Hz, 1H, CH_2), 1.67 (d, *J* = 12.87 Hz, CH_2), 1.56 (m, CH), 1.38 (qd, *J* = 12.15, 3.79 Hz, CH_2); ^{13}C NMR (100 MHz, $CDCl_3$) δ 152.9 (C5-indole), 140.6 (C-Ph), 137.0 (C2-indole), 133.3 (C7a-indole), 129.0 (2 × CH-Ph), 128.0 (2 × CH-Ph), 127.4 (C3a-indole), 125.7 (CH-Ph), 111.0 (CH6-indole), 109.5 (CH7-indole), 103.4 (CH4-indole), 102.0 (CH3-indole), 78.3 (≡CH), 73.4 (-C≡), 66.6 (CH_2O), 57.6 (CH_2), 54.2 (2 × CH_2), 51.7 (indole-CH_2), 44.65 (CH_2), 43.1 (CH_2), 41.5 (N-CH_3), 37.67 (CH), 32.0 (2 × CH_2), 29.8 (CH_3); MS (EI) *m*/*z* (%) 188 (100), 202 (42), 429 (6)[M]$^+$. **7**·2HCl: white powder; mp 218−220 °C; IR (KBr) ν 3421, 3189, 2929, 2498, 1619, 1486, 1208, 1163 cm^{-1}; ^{1}H NMR (300 MHz, D_2O) δ 7.28 (d, *J* = 8.9 Hz, 1H, CH7-indole), 7.20−7.15 (m, 2H), 7.10−7.06 (m, 4H), 6.87 (dd, *J* = 9.0, 1.9 Hz, 1H, CH6-indole), 6.61 (s, 1H, CH3-indole), 4.49 (s, 2H, CH_2), 4.25−4.13 (m, 2H, -CH_2O), 3.87 (d, *J* = 1.8 Hz, 2H, CH_2), 3.60 (s, 3H, CH_3), 3.47 (d, *J* = 12.2 Hz, 2H, CH_2), 3.39−3.30 (m, 2H, CH_2), 2.98 (t, *J* = 1.9 Hz, 1H, C≡CH), 2.87−2.77 (m, 5H, CH_2 + N-CH_3), 2.43 (d, *J* = 6.6 Hz, 2H, CH_2), 1.75−1.71 (m, 3H, CH + CH_2), 1.41−1.28 (m, 2H, CH_2). Anal. Calcd for $C_{28}H_{37}Cl_2N_3O\cdot{}^2/_3(H_2O)$: C, 65.36; H, 7.51; N, 8.17. Found: C, 65.08; H, 7.74; N, 8.40.

***N*-{[5-(3-Bromopropoxy)-1-methyl-1*H*-indol-2-yl]methyl}-*N*-methylprop-2-yn-1-amine (26).** A mixture of 1-methyl-2-{[ethyl-(prop-2-yn-1-yl)amino]ethyl}-1*H*-indol-5-ol **14**[52] (21 mg, 0.092 mmol), 1,3-dibromopropane (186 mg, 0.92 mmol), and potassium carbonate (64 mg, 0.46 mmol) in 2-butanone (1 mL) was reacted at 85 °C for 6 h. The mixture was evaporated, and the residue was partitioned between dichloromethane (10 mL) and water (10 mL). The organic layer was dried (Na_2SO_4) and evaporated in vacuo to give compound **26** (25.4 mg, 80%): R_f = 0.62 (CH_2Cl_2/AcOEt, 10:1); mp 71−2 °C; IR (KBr) ν 3275, 1488, 1468, 1206, 1026 cm^{-1}; ^{1}H NMR (400 MHz, $CDCl_3$) δ 7.2 (d, *J* = 8.9 Hz, 1H, CH7-indole), 7.07 (d, *J* = 2.4 Hz, 1H, CH4-indole), 6.87 (dd, *J* = 8.8 and 2.4 Hz, 1H, CH6-indole), 6.35 (s, 1H, CH3-indole), 4.14 (t, *J* = 5.8 Hz, 2H, -CH_2-OH), 3.75 (s, 3H, N-CH_3), 3.69 (s, 2H, ind-CH_2-N), 3.65 (t, *J* = 6.5 Hz, 2H, -CH_2-Br), 3.32 (d, *J* = 2.4 Hz, 2H, CH_2-C≡), 2.36 (s, 3H, N-CH_3), 2.33 [t, *J* = 5.9 Hz, CH_2-(CH_2O)], 2.30 (t, *J* = 2.4 Hz, 1H, ≡CH); ^{13}C NMR (100 MHz, $CDCl_3$) δ 152.8 (C5-indole), 137.1 (C2-indole), 133.5 (C7a-indole), 127.2 (C3a-indole), 111.9 (CH6-indole), 109.6 (CH7-indole), 103.6 (CH4-indole), 102.1 (CH3-indole), 78.3 (-C≡), 73.4 (≡CH), 66.3 (CH_2-O), 51.7 (CH_2-N), 44.6 (CH_2-C≡), 41.5 (N-CH_3), 32.6 [CH_2-(CH_2O)], 30.3 (CH_2−Br), 29.8 (N-CH_3); MS (EI) *m*/*z* (%): 131 (60), 160 (100) [M − ((Br(CH_2)$_3$)-$CH_3NCH_2C{\equiv}CH$)]$^+$, 227 (7) [M − (Br(CH_2)$_3$)]$^+$, 281 (96) [$CH_3NCH_2C{\equiv}CH$)]$^+$, 348 (21)[M]$^+$. Anal. Calcd for $C_{17}H_{21}BrN_2O$: C, 58.46; H, 6.06; Br, 22.88; N, 8.02. Found: C, 58.49; H, 6.08; Br, 22.11; N, 8.23.

***N*-{[5-(3-(4-Benzylpiperidin-1-yl)propoxy)-1-methyl-1*H*-indol-2-yl]methyl}-*N*-methylprop-2-yn-1-amine (8).** 4-Benzylpiperidine (0.111 mL, 0.632 mmol, 2 equiv) was added to a mixture of **26** (111 mg, 0.316 mmol, 1 equiv) and potassium carbonate (131 mg, 0.648 mmol, 3 equiv) in *N*,*N*-dimethylformamide (4 mL). The reaction mixture was heated at 70 °C for 7 h under an atmosphere of argon. The reaction mixture was poured into water (5 mL) and extracted into dichloromethane (3 × 20 mL). The organic layers were combined, dried (Na_2SO_4), and concentrated. The residue was purified by column chromatography, eluting with 4% methanol in dichloromethane, affording compound **8** (89.2 mg, 64%) as white crystalline solid: R_f = 0.43 (CH_2Cl_2/MeOH, 10:1); mp 82−3 °C; IR (KBr) ν 3274, 2923, 1619, 1487, 1469, 1390, 1205, 1133, 1027 cm^{-1}; ^{1}H NMR (400 MHz, $CDCl_3$) δ 7.31−7.25 (m, 2H), 7.21−7.12 (m, 4H), 7.02 (d, *J* = 2.26 Hz, 1H, CH4-indole), 6.83 (dd, *J* = 8.83 and 2.43 Hz, 1H, CH6-indole), 6.32 (s, 1H, CH3-indole), 4.03 (t, *J* = 6.28 Hz, 2H, -CH_2O), 3.73 (s, 3H, CH_3), 3.67 (s, 2H, CH_2-N), 3.30 (d, *J* = 2.36 Hz, 2H, CH_2≡), 3.02 (d, *J* = 11.45 Hz, CH_2), 2.59 (t, *J* = 7.37 Hz, CH_2), 2.55 (d, *J* = 6.77 Hz, CH_2), 2.34 (s, 3H, CH_3), 2.29 (t, *J* = 2.33 Hz, C≡CH), 2.08−1.92 (m, 4H, 2 × CH_2), 1.66 (d, *J* = 12.7 Hz, CH_2), 1.55 (m, CH), 1.40 (qd, *J* = 12.19, 3.24 Hz, CH_2); ^{13}C NMR (100 MHz, $CDCl_3$) δ 153.1 (C5-indole), 140.5 (C-Ph), 137.0 (C2-indole), 133.3 (C7a-indole), 129.0 (2 × CH-Ph), 128.1 (2 × CH-Ph), 127.4 (C3a-indole), 125.7 (CH-Ph), 111.9 (CH6-indole), 109.5 (CH7-indole), 103.4 (CH4-indole), 102.0 (CH3-indole), 78.3 (≡CH), 73.4 (-C≡), 67.2 (CH_2-O), 55.7 (CH_2), 53.8 (2 × CH_2), 51.7 (CH_2), 44.7 (CH_2), 43.0 (CH_2), 41.5 (N-CH_3), 37.7 (CH), 31.7 (2 × CH_2), 29.8 (CH_3), 26.7 (CH_2); MS (ES) *m*/*z* (%) 188 (99), 444 (100) [M + H]$^+$, 445 (40) [M + 2H]$^+$, 466 (2)[M + Na]$^+$. Anal. Calcd for $C_{29}H_{37}N_3O$: C, 78.51; H, 8.41; N, 9.47. Found: C, 78.63; H, 8.59; N, 9.44. **8**·2HCl: white powder; mp 216−218 °C; IR (KBr) ν 3196, 2931, 2559, 2509, 1619, 1485, 1472, 1454, 1250, 1211 cm^{-1}; ^{1}H NMR (300 MHz, D_2O) δ 7.27 (d, *J* = 9.1 Hz, 1H, CH7-indole), 7.20−7.15 (m, 2H), 7.10−7.06 (m, 4H), 6.84 (dd, *J* = 9.0, 1.5 Hz, 1H, CH6-indole), 6.60 (s, 1H, CH3-indole), 4.48 (s, 2H, CH_2), 3.99 (t, *J* = 5.4 Hz, 2H, -CH_2O), 3.87 (s, 2H, CH_2), 3.59 (s, 3H, CH_3), 3.41 (d, *J* = 11.8 Hz, 2H, CH_2), 3.16−3.05 (m, 2H), 2.99−2.97 (m,1H, C≡CH), 2.81−267 (m, 5H, CH_2 + N-CH_3), 2.43 (d, *J* = 6.1 Hz, 2H, CH_2), 2.06−1.97 (m, 2H, CH_2), 1.74−1.70 (m, 3H, CH + CH_2), 1.34−1.22 (m, 2H, CH_2). Anal. Calcd for $C_{29}H_{37}N_3O\cdot2HCl\cdot{}^1/_2(H_2O)$: C, 66.27; H, 7.67; Cl, 13.49; N, 8.00. Found: C, 66.02; H, 7.62; Cl, 13.45; N, 8.25.

***N*-{[5-(3-(4-Benzylpiperazin-1-yl)propoxy)-1-methyl-1*H*-indol-2-yl]methyl}-*N*-methylprop-2-yn-1-amine (9).** 1-Benzylpiperazine (0.148 g, 0.845 mmol) was added to a mixture of **26** (0.147 g, 0.422 mmol) and potassium carbonate (0.116 g, 0.845 mmol) in *N*,*N*-dimethylformamide (10 mL). The reactants were heated at 70 °C overnight under an atmosphere of argon. The reaction mixture was poured into water (50 mL) and extracted into ethyl acetate (3 × 100 mL). The organic layers were combined, dried (Na_2SO_4), and concentrated in vacuo. The residue was purified by column chromatography, eluting with 2% MeOH in CH_2Cl_2, affording compound **9** (0.16 g, 85%) as a solid: R_f = 0.43 (CH_2Cl_2/MeOH, 10:1); mp 103−4 °C; IR (KBr) ν 3138, 2958, 2943, 2806, 2762, 1621, 1492, 1480, 1207, 1159 cm^{-1}; ^{1}H NMR (400 MHz, $CDCl_3$) δ 7.37−7.25 (m, 5H), 7.19 (d, *J* = 8.8 Hz, 1H, CH7-indole), 7.07 (d, *J* = 2.4 Hz, 1H, CH4-indole), 6.88 (dd, *J* = 8.8 and 2.4 Hz, 1H, CH6-indole), 6.35 (s, 1H, CH3-indole), 4.06 (t, *J* = 6.4 Hz, 2H, -CH_2O), 3.75 (s, 3H, N-CH_3), 3.69 (s, 2H, CH_2Ph), 3.54 (s, 2H, CH_2-N), 3.33 (d, *J* = 2.3 Hz, 2H, CH_2C≡), 2.53 (m, 8H, 4 × CH_2), 2.36 (s, 3H, N-CH_3), 2.32 (t, *J* = 2.3 Hz, 1H, C≡CH), 2.01 [m, 2H, CH_2(CH_2O)]; ^{13}C NMR (100 MHz, $CDCl_3$) δ 153.1 (C5-indole), 138.0 (C-Ph), 136.9 (C2-indole), 133.2 (C7a-indole), 129.1 (2 × CH-Ph), 128.1 (2 × CH-Ph), 127.4 (C3a-indole), 126.9 (CH-Ph), 111.9 (CH6-indole), 109.5 (CH7-indole), 103.2 (CH4-indole), 101.9 (CH3-indole), 78.3 (-C≡), 73.4 (≡CH), 67.1 (CH_2-O), 63.0 (CH_2-N), 55.33 (CH_2), 53.1 (CH_2), 53.0 (2 × CH_2), 51.7 (CH_2), 44.6 (CH_2), 41.5 (N-CH_3), 29.8 (N-CH_3), 26.9 [CH_2(CH_2O)]; MS (ES) *m*/*z* (%) 445 (100) [M + H]$^+$, 467 (2) [M + Na]$^+$. Anal. Calcd for $C_{28}H_{36}N_4O$: C, 75.64; H, 8.16; N, 12.60. Found: C, 75.39; H, 8.40; N, 12.52. **9**·3HCl: white powder; mp 227−230 °C; IR (KBr) ν 3195, 2953, 2561, 2516, 2442, 1620, 1485, 1472, 1442, 1211 cm^{-1}; ^{1}H NMR (300 MHz, D_2O) δ 7.36−7.31 (m, 5H), 7.27 (d, *J* = 9.1 Hz, 1H, CH7-indole), 7.05 (d, *J* = 2.4 Hz, 1H, CH4-indole), 6.84 (dd, *J* = 9.0, 2.5 Hz, 1H, CH6-indole), 6.61 (s, 1H, CH3-indole), 4.50 (s, 2H, CH_2), 4.21 (s, 2H, CH_2), 4.00 (t, *J* = 5.7 Hz, 2H, -CH_2O), 3.88 (d, *J* = 2.5 Hz, 2H, CH_2-C≡), 3.60 (s, 3H, CH_3), 3.50−3.35 (m, 4H), 3.33−3.22 (m, 2H), 2.98 (t, *J* = 2.5

Hz, 1H, C≡CH), 2.78 (s, 3H, N-CH_3), 2.14−1.98 (m, 2H, CH_2). Anal. Calcd for $C_{28}H_{39}Cl_3N_4O\cdot{}^1/_2(H_2O)$: C, 59.73; H, 7.16; N, 9.95. Found: C, 59.59; H, 7.49; N, 10.20.

Biological Evaluation. Inhibition Experiments of AChE and BuChE. To assess the inhibitory activity of the compounds toward AChE (EC 3.1.1.7) or BuChE (EC 3.1.1.8), we followed the spectrophotometric method of Ellman[78] using purified AChE from *Electrophorus electricus* (type V-S) or human recombinant (expressed in the HEK-293 cell line) or BuChE from equine or human serum (lyophilized powder) (Sigma-Aldrich, Madrid, Spain). The reaction took place in a final volume of 3 mL of a phosphate-buffered solution (0.1 M) at pH 8, containing 0.035 U/mL *Ee*AChE, 0.24 U/mL hrAChE, or 0.05 U/mL BuChE, and 0.35 mM 5,5′-dithiobis-2-nitrobenzoic acid (DTNB, Sigma-Aldrich, Madrid, Spain). Inhibition curves were made by preincubating this mixture with at least nine concentrations of each compound for 10 min. A sample with no compound was always present to determine the 100% of enzyme activity. After this preincubation period, acetylthiocholine iodide (0.35 mM) or butyrylthiocholine iodide (0.5 mM) (Sigma-Aldrich, Madrid, Spain) was added, allowing 15 min more of incubation, where the DTNB produces the yellow anion 5-thio-2-nitrobenzoic acid along with the enzymatic degradation of acetylthiocholine iodide or butyrylthiocholine iodide. Changes in absorbance were detected at 405 nm in a spectrophotometric plate reader (FluoStar OPTIMA, BMG Labtech). Compounds inhibiting AChE or BuChE activity would reduce the color generation; thus, IC_{50} values were calculated as the concentration of compound that produces 50% AChE activity inhibition. Data are expressed as the mean ± SEM of at least three different experiments in quadruplicate.

Kinetic Analysis of AChE Inhibition. To obtain estimates of the mechanism of action of compound **5**, reciprocal plots of $1/V$ versus $1/[S]$ were constructed at different concentrations of the substrate acetylthiocholine (0.1−1 mM) by using Ellman's method.[78] Experiments were performed in a transparent 48-well plate, each well containing 350 μL of the DTNB solution in PBS and 1 μL of buffer (control) or inhibitor solution to give the desired final concentration. Final volume (1 mL) was reached by adding phosphate buffer solution (pH 8). Reaction was initiated by adding 45 μL of AChE at 30 °C to give a final concentration of 0.18 U/mL. Progress curves were monitored at 412 nm over 1.33 min in a fluorescence plate reader Fluostar Optima (BMG-Technologies, Germany). Progress curves were characterized by a linear steady-state turnover of the substrate, and values of a linear regression were fitted according to Lineweaver−Burk replots using Origin software. The plots were assessed by a weighted least-squares analysis. Determination of Michaelis constant for the substrate ATCh was done at seven different concentrations (0.1−1 mM) to give K_M = 0.29 ± 0.01 mM and V_{max} = 2.82 ± 0.06 min^{-1}. Slopes of the reciprocal plots were then plotted against the concentration of **5** (0−10 μM) as previously described[80] to evaluate K_i data. Data analysis was performed with Origin Pro 7.5 software (Origin Lab Corp.).

Inhibition Experiments of MAO-A and MAO-B. A purification of mitochondria from rat liver homogenates was prepared as previously described[81] and used as source for MAO activities. Total protein was measured by the method of Bradford using bovine-serum albumin as standard. The inhibitory activity of the compounds toward MAO-A and MAO-B was determined following the method of Fowler and Tipton[82] using ^{14}C-labeled substrates (Perkinelmer, USA). MAO-B activity was determined toward 20 μM [^{14}C]phenylethylamine (PEA) (2.5 mCi/mmol) and MAO-A activity toward 100 μM [^{14}C]-(5-hydroxy-triptamine) (5-HT) (0.5 mCi/mmol). Inhibition curves were made by preincubating this mixture with at least nine concentrations of each compound for 30 min. A sample without compound was always present to determine the 100% of enzyme activity. The reaction was carried out at 37 °C in a final volume of 225 μL in 50 mM phosphate buffer (pH 7.2) and stopped by the addition of 100 μL of 2 M citric acid. Radiolabeled aldehyde product was extracted into toluene/ethyl acetate (1:1, v/v) containing 0.6% (w/v) 2, 5-diphenyloxazole (PPO) before liquid scintillation counting (Tri-Carb 2810TR). Data are the mean ± SEM of at least four different experiments in triplicate.

Reversibility Studies. To study the nature of the enzymatic inhibition exerted by **5**, we determined the activity of the enzyme in the presence and in the absence of the inhibitor by two different methods: after three consecutive washings with buffer and after different times of preincubation of the enzyme with the inhibitor. For the first method, enzyme samples were preincubated for 30 min at 37 °C with 6 nM compound **5** for MAO-A and 45 nM for MAO-B. Samples were then washed and centrifuged at 25000*g* for 10 min at 4 °C consecutively three times. Finally, total protein was measured and MAO-A and MAO-B activities were determined as above-described. For the second method, samples of enzyme and inhibitor **5** at the indicated concentration were preincubated for 0, 5, 15, and 30 min before measuring MAO-A and MAO-B activities as above-described.

Progress Curves of Substrate Consumption. To clarify the behavior of **5** toward MAO-A and MAO-B, the inhibitor was preincubated for long periods (0−420 min) with MAO-A (10 nM inhibitor concentration) and MAO-B (100 nM inhibitor concentration). The concentrations of **5** used in this assay were 2 times the corresponding IC_{50} value. After the corresponding periods, substrates were added and MAO activities were determined as above-described. Data are the mean ± SEM of three independent esperiments in triplicate.

Kinetic Analysis of MAO-B Inhibition. To obtain estimates of the mechanism of action of compound **5**, reciprocal plots of $1/V$ versus $1/[S]$ were constructed at different concentrations of the substrate β-phenylethylamine (1−200 μM) by using Fowler and Tipton's method.[82] The plots were assessed by a weighted least-squares analysis. Data analysis was performed with GraphPad Prism 3.0 software (GraphPad Software Inc.). Determination of Michaelis constants gave K_M = 6.7 ± 0.3 μM and V_{max} = 277.8 ± 6.1 pmol/min. Slopes of the reciprocal plots were then plotted against the concentration of **5** (0−10 μM) as previously described[79] to evaluate K_i data.

Inhibitory Capacity on $A\beta_{1-42}$ Self-Aggregation. The inhibition of $A\beta_{1-42}$ self-aggregation by compound **5** was studied by using the thioflavin T-based fluorometric assay previously described by Bartolini et al.[83] with little modifications. Briefly, $A\beta_{1-42}$ peptide (Bachem AG, Switzerland) was pretreatted with 1,1,1,3,3,3-hexafloro-2-propanol (HFIP, Sigma Chemicals) and redissolved in 10 mM phosphate buffer (PBS, pH 11.2 adjusted with NH_4OH). Final $A\beta_{1-42}$ stock solution concentration was 443 μM. To study the effect of **5** on fibril formation, experiments were performed by incubating the peptide (final Aβ concentration of 40 μM) with and without 10 μM compound **5** (Aβ/inhibitor = 4/1). Blanks containing only the inhibitor were also prepared. Propidium iodide (PI, Sigma-Aldrich) was used as reference compound in the experiments at the conditions described aboved and also at equimolar ratio Aβ/PI. Samples were diluted to a final volume of 200 μL with 10 mM PBS (pH 7.4), and 35 μM thioflavin T in 50 mM glycine−NaOH buffer (pH 8.5) was added. Experiments were performed on a Synergy HT microplate spectrofluorometer (Bio-Tek, U.S.). The fluorescence intensity was carried out (λ_{exc} = 485 nm; λ_{em} = 528 nm) every 10 min for 10 h, and values at plateau (400 min) were averaged after subtracting the background fluorescence of 35 μM thioflavin T solution. The fluorescence intensities were compared, and the percent inhibition due to the presence of the inhibitor was calculated by the following expression: $100 - [(IF_i/IF_0) \times 100]$, where IF_i and IF_0 are the fluorescence intensities obtained in the presence and absence of inhibitor, respectively.

Inhibition of hAChE-Induced $A\beta_{1-40}$ Aggregation. Aliquots of 231 μM $A\beta_{1-40}$ (Bachem AG, Switzerland) lyophilized from 1 mg/mL HFIP solution were redissolved in 10 mM phosphate buffer (PBS, pH 11.2 adjusted with NH_4OH). For co-incubation experiments, aliquots of human recombinant AChE (Sigma Chemicals) (0.4 μM final concentration, ratio Aβ/AChE = 10/1) in the presence of 100 μM compound **5** were added. Blanks containing Aβ, AChE, Aβ plus compound **5**, and AChE plus compound **5** were also prepared. To quantify the amyloid fibril formation, the thioflavin T fluorescence

method[82] was performed as above-described. The fluorescence intensities were compared, and the percent inhibition due to the presence of the inhibitor was calculated by the following expression: $100 - [(IF_i/IF_0) \times 100]$ where IF_i and IF_0 are the fluorescence intensities obtained in the presence and absence of inhibitor, respectively.

Molecular Modeling. Setup of the Systems. All protein models were derived from X-ray crystallographic structures taken from the Protein Data Bank (PDB). AChE models were built up from the AChE–donepezil complex 1EVE.[59] The enzyme was modeled in its physiological active form with neutral His440 and deprotonated Glu327, which together with Ser200 forms the catalytic triad. The standard ionization state at neutral pH was considered for the rest of the ionizable residues with the exception of Asp392 and Glu443, which were neutral, and His471, which was protonated, according to previous studies.[84] Three disulfide bridges were defined between Cys residues 66–93, 254–265, 402–521, and histidine residues 398 and 440 were set up to represent the δ tautomer.[85] MAO models were built up using X-ray structures 2Z5X[67] and 2C65[86] for isoforms A and B, respectively. Structural waters were defined as those common to five different high-resolution X-ray crystallographic structures (PDB entries 2Z5X, 2Z5Y, 2V5Z, 2C70, 2VZ2).

Docking. The binding mode of compound **5** was explored by means of docking calculations carried out with rDock, which is an extension of the program RiboDock, using an empirical scoring function calibrated on the basis of protein–ligand complexes.[64,65] Docking computations were performed with a 2-fold purpose: (1) to explore suitable starting orientations of the inhibitor in the binding site of AChE, MAO-A, and MAO-B and (2) to examine the docking of compound **5** for the three main orientations adopted by the indole ring of Trp279 in the peripheral binding site in *Torpedo californica* AChE.[61] At this point, it is worth noting that the reliability of rDock has been assessed by docking a set of known dual binding site IAChEs, taking advantage of the X-ray crystallographic structures of their complexes with AChE.[60] The docking of **5** in AChE was then explored using the three structural models of the target AChE differing in the orientations of Trp279 (PDB entries 1EVE, 1Q83, and 2CKM). Structural water molecules that mediate relevant interactions between the benzylpiperidine moiety and the enzyme were retained in the target models. Similarly, five water molecules found in the binding site of MAO-A and MAO-B were retained in docking calculations. The docking volume was defined as the space covered by catalytic, mid-gorge, and peripheral sites in AChE and by the substrate and entrance cavities in MAO. Suitable restraints were introduced to position the benzylpiperidine moiety of **5** in AChE. Each compound was subjected to 100 docking runs. Whereas the protein was kept rigid, rDock accounts for the conformational flexibility of the ligand around rotatable bonds during docking calculations. The output docking modes were analyzed by visual inspection in conjunction with the docking scores.

The X-ray structure of the recombinant human BuChE (PDB entry 2PM8)[87] was used to explore the binding mode of **5** in this enzyme. Some graphical manipulation was required, including addition of the hydrogen atoms according to the parm99SB force field and modeling of poorly resolved loop between residues Leu478 and Lys486, which was modeled using the X-ray structure of the BChE–tabun complex (PDB entry 3DJY).[88] Additionally, three disulfide bonds were defined between residues 94–120, 280–291, and 428–547. Residue Glu469 was modeled in the protonated state, and residue His466 was modeled as the Nδ-H tautomer. Docking calculations were performed using the same protocol mentioned above.

MM-PBSA Analysis. The ligand–protein poses were clusterized and reranked using the MM-PBSA approach in conjunction with the parmm99 force field of the AMBER (version 9) package.[89] The partial atomic charges of compound **5** were derived using the RESP protocol[90] by fitting to the molecular electrostatic potential calculated at the HF/6-31G* level with Gaussian 03.[91] Calculations were performed for 100 snapshots taken evenly during the last 5 ns of the simulations. The internal conformational energy was determined using the standard formalism and parameters implemented in AMBER. The electrostatic contribution was computed using a dielectric constant of 78.4 for the aqueous environment, while a dielectric constant of 1 was assigned to the interior of the protein. Even though the choice of the internal dielectric constant is a subject of debate, this value is usually adopted when calculations are performed for ensembles of snapshots taken from simulations, whereas higher values are generally used for calculations of static structures.[92,93] The electrostatic potentials were calculated using a grid spacing of 0.25 Å. Besides the standard atomic radii implemented in AMBER, calculations were also performed using a set of optimized radii developed for MM/PBSA computations with the AMBER force field.[66] The nonpolar contribution was calculated using a linear dependence with the solvent-accessible surface as implemented in AMBER. Finally, entropy changes upon complexation were assumed to cancel out in the comparison of the different poses.

Molecular Dynamics. The binding mode of compound **5** was explored by means of 20 ns molecular dynamics (MD) simulations performed for their complexes to AChE (using three different models; see above), MAO-A, and MAO-B. An additional MD simulation was run for the complex with donepezil and used to calibrate the results of the simulations performed for AChE complexes. In addition, MD simulations were also performed for the complexes corresponding to the covalent adduct formed between **5** and FAD in both MAO-A and MAO-B. To this end, suitable parameters were developed for the corresponding imine fragment formed in the chemical reaction (parameters available upon request to the authors).

The simulation protocol was based on the computational strategy used in our previous studies,[60] which is briefly summarized here. MD simulations were run using the PMEMD module of AMBER 9 and the parm99SB parameters for the protein.[94] The GAFF force field[95,96] was used to assign parameters to the inhibitor (and to the FAD cofactor in MAO simulations). The charge distribution of the inhibitor was further refined based on the electrostatic charges determined from a fit to the "HF/6-31G(d)" electrostatic potential obtained with Gaussian 03[91] using the RESP procedure. Na^+ cations were added to neutralize the negative charge of the system with the XLEAP module of AMBER 9. The system was immersed in an octahedral box of TIP3P[97] water molecules, preserving the crystallographic waters inside the binding cavity. The final systems contained the protein–ligand complex, Na^+ cations, and around 17 000 water molecules, leading to simulations systems that comprise around 53 000 atoms.

The geometry of the system was minimized in four steps. First, the position of hydrogen atoms was optimized using 3000 steps of steepest descent algorithm. Then water molecules were refined through 2000 steps of steepest descent followed by 3000 steps of conjugate gradient. Next, the ligand, water molecules, and counterions were optimized with 2000 steps of steepest descent and 4000 steps of conjugate gradient, and finally the whole system was optimized with 3000 steps of steepest descent and 7000 steps of conjugate gradient. Thermalization of the system was performed in five steps of 25 ps, increasing the temperature from 100 to 298 K. Concomitantly, the residues that define the binding site were restrained during thermalization using a variable restraining force. Thus, a force constant of 25 kcal mol^{-1} $Å^{-2}$ was used in the first stage of the thermalization and was subsequently decreased by increments of 5 kcal mol^{-1} $Å^{-2}$ in the next stages. Then a series of 20 ns trajectories were run for the two compounds using a time step of 1 fs. In MAO simulations, an additional restraint force was used for the backbone of residues 487–492, which define the transmembrane segment at the C-terminus of the protein. SHAKE was used for those bonds containing hydrogen atoms, in conjunction with periodic boundary conditions at constant pressure (1 atm) and temperature (298 K), particle mesh Ewald for the treatment of long-range electrostatic interactions, and a cutoff of 11 Å for nonbonded interactions.

■ ASSOCIATED CONTENT

Ⓢ Supporting Information

Representation of structural models derived from docking and MD simulations, as well as energetic analysis. This material is available free of charge via the Internet at http://pubs.acs.org.

AUTHOR INFORMATION

Corresponding Author

*For M.U.: phone, +34-93-5811439; fax, +34-93-5811573; e-mail, mercedes.unzeta@uab.es. For J.M.-C.: phone, +34-91-5622900; fax, +34-91-5644853; e-mail, iqoc21@iqog.csic.es.

Author Contributions

⊥These authors have contributed equally to this work.

ACKNOWLEDGMENTS

We thank the Ministerio de Ciencia e Innovación (Grants SAF2006-08764-C02-01, SAF2009-07271, and SAF2008-05595), Generalitat de Catalunya (2009-SGR00298), Comunidad de Madrid (Grant S/SAL-0275-2006), Instituto de Salud Carlos III [Retic RENEVAS (Grant RD06/0026/1002), Fundacion CIEN, Miguel Servet Program (Grant CP10/00531)], and COST Action D34/0003/05 (2005−2010) for financial support and the Centro de Supercomputació de Catalunya (CESCA) for computational facilities. A.S. and M.C. thank CSIC and Instituto de Salud Carlos III for postdoctoral I3P and "Sara Borrell" contracts, respectively. C.d.l.R. thanks MICINN for a Juan de la Cierva contract (2006−2008) and Instituto de Salud Carlos III for a Miguel Servet contract (2011−2016). J.J.-J. thanks Instituto de Salud Carlos III for PFIS fellowship FI10/00292. J.M.-C. thanks Prof. A. G. García (Departamento de Farmacología y Terapéutica, Facultad de Medicina, Universidad Autónoma de Madrid, Spain) for his interest and support. This work was realized in the framework of COST working group: D34/0003/05.

ABBREVIATIONS USED

AD, Alzheimer's disease; ACh, acetylcholine; AChE, acetylcholinesterase; Aβ, β-amyloid peptide; BuChE, butyrylcholinesterase; AChEI, acetylcholinesterase inhibitor; hAChE, human acetylcholinesterase; Ee, *Electrophorus electricus*; CAS, catalytic active site; PAS, peripheral anionic site; MAO, monoamine oxidase A/B; IMAO, monoamine oxidase inhibitor

REFERENCES

(1) Goedert, M.; Spillantini, M. G. A Century of Alzheimer's Disease. *Science* **2006**, *314*, 777−781.

(2) Terry, R. D.; Gonatas, N. K; Weiss, M. Ultrastructural Studies in Alzheimer's Presenile Dementia. *Ann. J. Pathol.* **1964**, *44*, 269−297.

(3) Grundke-Iqbal, I.; Iqbal, K.; Tung, Y. C.; Quinlan, M.; Wisniewski, H. M; Binder, L. I. Abnormal Phosphorylation of the Microtubule-Associated Protein τ (Tau) in Alzheimer Cystoskeletal Pathology. *Proc. Natl. Acad. Sci U.S.A.* **1986**, *93*, 4913−4917.

(4) Coyle, J. T; Puttfarcken, P. Oxidative Stress, Glutamate and Neurodegenerative Disorders. *Science* **1993**, *262*, 689−695.

(5) Gella, A.; Durany, N. Oxidative Stress in Alzheimer Disease. *Cell Adhes. Migr.* **2009**, *3*, 88−93.

(6) Perry, E. K.; Tomlinson, B. E.; Blesseed, G.; Bergmann, K.; Gibson, P. H.; Perry, R. H. Correlation of Cholinergic Abnormalities with Senile Plaques and Mental Test Scores in Senile Dementia. *Br. Med. J.* **1978**, *2*, 1457−1459.

(7) Talesa, V. N. Acetylcholinesterase in Alzheimer's Disease. *Mech. Ageing Dev.* **2001**, *122*, 1961−1969.

(8) García-Alloza, M.; Gil-Bea, F. J.; Díez-Ariza, M.; Chen, C. P.; Francis, P. T.; Lasheras, B.; Ramirez, M. J. Cholinergic−Serotonergic Imbalance Contributes to Cognitive and Behavioral Symptoms in Alzheimer's Disease. *Neurophsychologia* **2005**, *43*, 442−449.

(9) Terry, A. V.; Buccafusco, J. J.; Wilson, C. Cognitive Dysfunction in Neuropsychiatric Disorders: Selected Serotonin Receptor Subtypes as Therapeutic Targets. *Behav. Brain Res.* **2008**, *195*, 30−38.

(10) Dringenberg, H. C. Alzheimer's Disease: More Than a "Cholinergic Disorder": Evidence That Cholinergic−Monominergic Interactions Contribute to EEG Slowing and Dementia. *Behav. Brain Res.* **2000**, *115*, 235−249.

(11) Riederer, P.; Danielczyk, W.; Grünblatt, E. Monoamine Oxidase-B Inhibition in Alzheimer's Disease. *Neurotoxicology* **2004**, *25*, 271−277.

(12) Youdim, M. B.; Edmonson, D.; Tipton, K F. The Therapeutic Potential of Monoamine Oxidase Inhibitors. *Nat. Rev. Neurosci.* **2006**, *7*, 295−309.

(13) Youdim, M. B. H.; Finberg, J. P. M.; Tipton, K. F. Monoamine Oxidase. In *Handbook of Experimental Pharmacology*; Tredelenburg, U., Weiner, N., Eds.; Springer-Verlag: Berlin, 1988; Vol. *90*, pp 119−192.

(14) Johnston, J. P. Some Observations upon a New Inhibitor of Monoamine Oxidase in Brain Tissue. *Biochem. Pharmacol.* **1968**, *17*, 1285−1297.

(15) Grimsby, J.; Lan, N. C.; Neve, R.; Chen, K.; Shih, J. C. Tissue Distribution of Human Monoamine Oxidase A and B mRNA. *J. Neurochem.* **1990**, *55*, 1166−1169.

(16) Riederer, P.; Youdim, M. B. Monoamine Oxidase Activity and Monoamine Metabolism in the Brains of Parkinsonian Patients Treated with l-Deprenyl. *J. Neurochem.* **1986**, *46*, 1359−1365.

(17) Kristal, B. S.; Conway, A. D.; Brown, A. M.; Jain, J. C.; Ulluci, P. A.; Li, S. W.; Burke, J. W. Selective Dopaminergic Vulnerability: 3,4-Dihydroxyphenylacetaldehyde Targets Mitochondria. *Free Radical Biol. Med.* **2001**, *30*, 924−931.

(18) Pizzinat, N.; Copin, N.; Vindis, C.; Parini, A.; Cambon, C. Reactive Oxygen Species Production by Monoamineoxidases in Intact Cells. *Naunyn Schmiedeberg's Arch. Pharmacol.* **1999**, *359*, 428−431.

(19) Caraci, F.; Copani, A.; Nicoletti, F.; Drago, F. Depression and Alzheimer's Disease: Neurobiological Links and Common Pharmacological Targets. *Eur. J. Pharmacol.* **2010**, *626*, 64−71.

(20) Birks, J.; Harvey, R. Donepezil for Dementia Due to Alzheimer's Disease. *Cochrane Database Syst. Rev.* **2006**, No. 1, CD001190.

(21) Loy, C.; Schneider, L. Galantamine for Alzheimer's Disease. *Cochrane Database Syst. Rev.* **2004**, No. 4, CD001747.

(22) Birks, J.; Grimley, E. J.; Iakovidou, V. Rivastigmine for Alzheimer's Disease. *Cochrane Database Syst. Rev.* **2000**, No. 4, CD001191.

(23) Racchi, M.; Mazzucchelli, M.; Porrello, E.; Lanni, C.; Govoni, S. Acetylcholinesterase Inhibitors: Novel Activities of Old Molecules. *Pharmacol. Res.* **2004**, *50*, 441−451.

(24) Muñoz-Torrero, D. Acetylcholinesterase Inhibitors as Disease-Modifying Therapies for Alzheimer's Disease. *Curr. Med. Chem.* **2008**, *15*, 2433−2455.

(25) Castro, A.; Martínez, A. Targeting Beta-Amyloid Pathogenesis through Acetylcholinesterase Inhibitors. *Curr. Pharm. Des.* **2006**, *12*, 4377−4387.

(26) Cavalli, A.; Bolognesi, M. L.; Minarini, A.; Rosini, M.; Tumiatti, V.; Recanatini, M.; Melchiorre, C. Multi-Target-Directed Ligands To Combat Neurodegenerative Diseases. *J. Med. Chem.* **2008**, *51*, 347−372.

(27) Youdim, M. B.; Buccafusco, J. J. Multifunctional Drugs for Various CNS Targets in the Treatment of Neurodegenerative Disorders. *Trends Pharmacol. Sci.* **2005**, *26*, 27−35.

(28) Rodríguez-Franco, M. I.; Fernández-Bachiller, M. I.; Pérez, C.; Castro, A.; Martínez, A. Design and Synthesis of *N*-Benzylpiperidine-Purine Derivatives as New Dual Inhibitors of Acetyl- and Butyrylcholinesterase. *Bioorg. Med. Chem.* **2005**, *13*, 6795−6802.

(29) Rosini, M.; Antonello, A.; Cavalli, A.; Bolognesi, M. L.; Minarini, A.; Marucci, G.; Poggesi, E.; Leonardi, A.; Melchiorre, C. Prazosin-Related Compounds. Effect of Transforming the Piperazinylquinazoline Moiety into an Aminomethyltetrahydroacridine System on the Affinity for alpha1-Adrenoreceptors. *J. Med. Chem.* **2003**, *46*, 4895−4903.

(30) Elsinghorst, P. W.; Cieslik, J. S.; Mohr, K.; Tränkle, C.; Gütschow, M. The First Gallamine−Tacrine Hybrid: Design and Characterization at Cholinesterases and the M_2 Muscarinic Receptor. *J. Med. Chem.* **2007**, *50*, 5685−5695.

(31) Fang, L.; Appenroth, D.; Decker, M.; Kiehntopf, M.; Roegler, C.; Deufel, T.; Fleck, C.; Peng, S.; Zhang, Y.; Lehmann, J. Synthesis and Biological Evaluation of NO-Donor-Tacrine Hybrids as Hepatoprotective Anti-Alzheimer Drug Candidates. *J. Med. Chem.* **2008**, *51*, 713−716.
(32) Marco-Conelles, J.; León, R.; de los Ríos, C.; Guglietta, A.; Terencio, J.; López, M. G.; García, A. G.; Villarroya, M. Novel Multipotent Tacrine−Dihydropyridine Hybrids with Improved Acetylcholinesterase Inhibitory and Neuroprotective. Activities as Potential Drugs for the Treatment of Alzheimer's Disease. *J. Med. Chem.* **2006**, *49*, 7607−7610.
(33) Zheng, H.; Youdim, M. B. H.; Fridkin, M. Site-Activated Multifunctional Chelator with Acetylcholinesterase and Neuroprotective−Neurorestorative Moieties for Alzheimer's Therapy. *J. Med. Chem.* **2009**, *52*, 4095−4098.
(34) Sterling, J.; Herzig, Y.; Goren, T.; Finkelstein, N.; Lerner, D.; Goldenberg, W.; Mikcolczi, I.; Molnar, S.; Rantal, F.; Tamas, T.; Toth, G.; Zagyva, A.; Zekany, A.; Finberg, J.; Lavian, G.; Gross, A.; Friedman, R.; Razin, M.; Huang, W.; Krais, B.; Chorev, M.; Youdim, M. B.; Weinstock, M. Novel Dual Inhibitors of AChE and MAO Derived from Hydroxyl Aminoindan and Phenethylamine as Potential Treatment for Alzheimer's Disease. *J. Med. Chem.* **2002**, *54*, 5260−5279.
(35) Yogev-Falach, M.; Bar-Am, O.; Amit, T.; Weinreb, O.; Youdim, M. B. A Multifunctional, Neuroprotective Drug, Ladostigil (TV3326), Regulates Holo-APP Translation and Processing. *FASEB J.* **2006**, *20*, 2177−2179.
(36) Youdim, M. B.; Weinstock, M. Molecular Basis of Neuroprotective Activities of Rasagiline and the Anti-Alzheimer Drug TV3326, [(*N*-Propargyl-(3*R*)Aminoindan-5-yL)-ethyl methyl carbamate]. *Cell. Mol. Neurobiol.* **2002**, *21*, 555−573.
(37) Youdim, M. B.; Amit, T.; Bar-Am, O.; Weinreb, O.; Yogev-Falach, M. Implications of Co-Morbidity for Etiology and Treatment of Neurodegenerative Diseases with Multifunctional, Neuroprotective−Neurorescue Drugs; Ladostigil. *Neurotoxic. Res.* **2006**, *10*, 181−192.
(38) Bar-Am, O.; Amit, T.; Weinreb, O.; Youdim, M. B.; Mandel, S. Propargylamine-Containing Compounds as Modulators of Proteolitic Cleavage of Amyloid-Beta Protein Precursor: Involvement of MAPK and PKC Activation. *J. Alzheimer's Dis.* **2010**, *21*, 361−371.
(39) Elsinghorst, P. W.; Härtig, W.; Goldhammer, S.; Grosche, J.; Gütschow, M. A Gorge-Spanning, High Affinity, Cholinesterase Inhibitor to Explore Beta-Amyloid Plaques. *Org. Biomol. Chem.* **2009**, *7*, 3940−3946.
(40) Zheng, H.; Youdim, M. B.; Fridkin, M. Site-Activated Chelators Targeting Acetylcholinesterase and Monoamine Oxidase for Alzheimer's Therapy. *ACS Chem. Biol.* **2010**, *5*, 603−610.
(41) Palermo, M.; Bores, G.; Huger, F.; Kurys, B.; Merriman, M.; Olsen, G.; Ong, H.; Petko, W.; O'Malley, G. Combined AChE and Reversible MAO Inhibition as a Potential Therapeutic Approach for Senile Dementia of the Alzheimer Type. *Abstracts of Papers*, 205th National Meeting of the American Chemical Society, 1993; American Chemical Society: Washington DC, 1993.
(42) Fink, D. M.; Palermo, M. G.; Bores, G. M.; Huger, F.; Kurys, B.; Merriman, M.; Olsen, G.; Ong, H.; Petko, W.; O'Malley, G. Imino 1,2,3,4-Tetrahydrocyclopent[*b*]-indole Carbamates as Dual Inhibitors of Acetylcholinesterase and Monoamine Oxidase. *Bioorg. Med. Chem. Lett.* **1996**, *6*, 625−630.
(43) Bruhlmann, C.; Ooms, F.; Carrupt, P. A.; Testa, B.; Catto, M.; Leonetti, F.; Altomare, C.; Carotti, A. Coumarins Derivatives as Dual Inhibitors of Acetylcholinesterase and Monoamine Oxidase. *J. Med. Chem.* **2001**, *44*, 3195−3198.
(44) Cruces, M. A.; Elorriaga, C.; Fernandez-Alvarez, E.; Nieto, O. Acetylenic and Allenic Derivatives of 2-(5-Methoxyindolyl)methylamine Synthesis and Evaluation as Selective Inhibitors of Monoamine Oxidases A and B. *Eur. J. Med. Chem.* **1990**, *25*, 257−265.
(45) Morón, J. A.; Campillo, M.; Pérez, V.; Unzeta, M.; Pardo, L. Molecular Determinants of MAO Selectivity in a Series of Indolylmethylamine Derivatives: Biological Activities, 3D-QSAR/CoMFA Analysis, and Computational Simulation of Ligand Recognition. *J. Med. Chem.* **2000**, *43*, 1684−1691.
(46) Pérez, V.; Marco, J. L.; Fernández-Álvarez, E.; Unzeta, M. Relevance of Benzyloxy Group in 2-Indolyl Methylamines in the Selective MAO-B Inhibition. *Br. J. Pharmacol.* **1999**, *127*, 869−876.
(47) Inestrosa, N. C.; Alvarez, A.; Pérez, C. A.; Moreno, R. D.; Vicente, M.; Linker, C.; Casanueva, O. I.; Soto, C.; Garrido, J. Acetylcholinestearse Accelerates Assembly of Amyloid-Beta-Peptides into Alzheimer's Fibrils: Possible Role of the Peripheral Site of the Enzyme. *Neuron* **1996**, *16*, 881−891.
(48) De Ferrari, G. V.; Canales, M. A.; Shin, I.; Weiner, L. M.; Silman, I.; Inestrosa, N. C. A Structural Motif of Acetylcholinesterase That Promotes Amyloid Beta-Peptide Fibril Formation. *Biochemistry* **2001**, *40*, 10447−10457.
(49) Rees, T. M.; Berson, A.; Sklan, E. H.; Younkin, L.; Younkin, S.; Brimijoin, S.; Soreq, H. Memory Deficits Correlating with Acetylcholinesterase Splice Shift and Amyloid Burden in Doubly Transgenic Mice. *Curr. Alzheimer Res.* **2005**, *2*, 291−300.
(50) Dinamarca, M. C.; Sagal, J. P.; Quintanilla, R. A.; Godoy, J. A.; Arrázola, M. S.; Inestrosa, N. C. Amyloid-beta-Acetylcholinesterase Complexes Potentiate Neurodegenerative Changes Induced by the Abeta Peptide. Implications for the Pathogenesis of Alzheimer's Disease. *Mol. Neurodegener.* **2010**, *5*, 4.
(51) Cruces, M. A.; Elorriaga, C.; Fernández-Álvarez, E. The Kinetics of Monoamine Oxidase Inhibition by Three 2-Indolylmethylamine Derivatives. *Biochem. Pharmacol.* **1990**, *40*, 535−543.
(52) Contreras, J. M.; Parrot, I.; Sippl, W.; Rival, Y. M.; Wermuth, C. G. Design, Synthesis, and Structure−Activity Relationships of a Series of 3-[2-(1-Benzylpiperidin-4-yl)ethylamino]pyridazine Derivatives as Acetylcholinesterase Inhibitors. *J. Med. Chem.* **2001**, *44*, 2707−2718.
(53) Hallinan, E. A.; Hagen, T. J.; Husa, R. K.; Tsymbalov, S.; Rao, S. N.; van Hoeck, J. P.; Rafferty, M. F.; Stapelfeld, A.; Savage, M. A.; Reichman, M. N. Substituted Dibenzoxazepines as Analgesic PGE2 Antagonists. *J. Med. Chem.* **1993**, *36*, 3293−3299.
(54) Yamanaka, T.; Ohkubo, M.; Kuroda, S.; Nakamura, H.; Takahashi, F.; Aoki, T.; Mihara, K.; Seki, J.; Kato, M. Design, Synthesis, and Structure−Activity Relationships of Potent GPIIb/IIIa Antagonists: Discovery of FK419. *Bioorg. Med. Chem.* **2005**, *13*, 4343−4352.
(55) Frølund, B.; Kristiansen, U.; Brehm, L.; Hansen, A. B.; Krogsgaard-Larsen, P.; Falch, E. Partial GABAA Receptor Agonists. Synthesis and in Vitro Pharmacology of a Series of Nonannulated Analogs of 4,5,6,7-Tetrahydroisoxazolo[4,5-*c*]pyridin-3-ol. *J. Med. Chem.* **1995**, *38*, 3287−3296.
(56) Kitbunnadaj, R.; Zuiderveld, O. P.; De Esch, I. J. P.; Vollinga, R. C.; Bakker, R.; Lutz, M.; Spek, A. L.; Cavoy, E.; Deltent, M. F.; Menge, W. M. P. B.; Timmerman, H.; Leurs, R. Synthesis and Structure−Activity Relationships of Conformationally Constrained Histamine H_3 Receptor Agonists. *J. Med. Chem.* **2003**, *46*, 5445−5457.
(57) Mandelli, G. R.; Maiorana, S.; Terni, P.; Lamperti, G.; Colibretti, M. L.; Imbimbo, B. P. Synthesis of New Cardioselective M_2 Muscarinic Receptor Antagonists. *Chem. Pharm. Bull.* **2000**, *48*, 1611−1622.
(58) Greig, N. H.; Utsuki, T.; Ingram, D.; Wang, K. Y.; Pepeu, G.; Scali, C.; Yu, Q. S.; Mamczarz, J.; Holloway, H. W.; Giordano, T.; Chen, D.; Furukawa, K.; Sambamurti, K.; Brossi, A.; Lahiri, D. K. Selective Butyrylcholinesterase Inhibition Elevates Brain Acetylcholine, Augments Learning and Lowers Amyloid-β Peptide in Rodents. *Proc. Natl. Acad. Sci. U.S.A.* **2005**, *102*, 17213−17218.
(59) Kryger, G.; Silman, I.; Sussman, J. L. Structure of Acetylcholinesterase Complexed with E2020 (Aricept): Implications for the Design of New Anti-Alzheimer Drugs. *Structure* **1999**, *7*, 297−307.
(60) Camps, P.; Formosa, X.; Galdeano, C.; Muñoz-Torrero, D.; Ramírez, L.; Gómez, E.; Isambert, N.; Lavilla, R.; Badia, A.; Clos, M. V.; Bartolini, M.; Mancini, F.; Andrisano, V.; Arce, M. P.; Rodríguez-Franco, M. I.; Huertas, O.; Dafni, T.; Luque, F. J. Pyrano[3,2-*c*]quinoline-6-chlorotacrine Hybrids as a Novel Family of

Acetylcholinesterase- and Beta-Amyloid-Directed Anti-Alzheimer Compounds. *J. Med. Chem.* **2009**, *52*, 5365−5379.
(61) Galdeano, C.; Viayna, E.; Arroyo, P.; Bidon-Chanal, A.; Blas, J. R.; Muñoz-Torrero, D.; Luque, F. J. Structural Determinants of the Multifunctional Profile of Dual Binding Site Acetylcholinesterase Inhibitors as Anti-Alzheimer Agents. *Curr. Pharm. Des.* **2010**, *16*, 2818−2836.
(62) Rydberg, E. H.; Brumshtein, B.; Greenblatt, H. M.; Wong, D. M.; Shaya, D.; Williams, L. D.; Carlier, P. R.; Pang, Y.-P.; Silman, I.; Sussman, J. L. Complexes of Alkylene-Linked Tacrine Dimers with *Torpedo californica* Acetylcholinesterase: Binding of Bis(5)-tacrine Produces a Dramatic Rearrangement in the Active-Site Gorge. *J. Med. Chem.* **2006**, *49*, 5491−5500.
(63) Bourne, Y.; Kolb, H. C.; Radic, Z; Sharpless, K. B.; Taylor, P.; Marchot, P. Freeze-Frame Inhibitor Captures Acetylcholinesterase in a Unique Conformation. *Proc. Natl. Acad. Sci. U.S.A.* **2004**, *101*, 1449−1454.
(64) Morley, S. D.; Afshar, M. Validation of an Empirical RNA-Ligand Scoring Function for Fast Flexible Docking Using RiboDock. *J. Comput.-Aided Mol. Des.* **2004**, *18*, 189−208.
(65) Barril, X.; Hubbard, R. E.; Morley, S. D. Virtual Screening in Structure-Based Drug Discovery. *Mini-Rev. Med. Chem.* **2004**, *4*, 779−791.
(66) Swanson, J. M. J.; Adcock, S. A.; McCammon, J. A. Optimized Radii for Poisson−Boltzmann Calculations with the AMBER Force Field. *J. Chem. Theory Comput.* **2005**, *1*, 484−493.
(67) Son, S.-Y.; Ma, J.; Kondou, Y.; Yoshimura, M.; Yamashita, E.; Tsukihara, T. Structure of Human Monoamine Oxidase A at 2.2-Å Resolution: The Control of Opening the Entry for Substrates/Inhibitors. *Proc. Natl. Acad. Sci. U.S.A.* **2008**, *105*, 5739−5744.
(68) De Colibus, L.; Li, M.; Binda, C.; Lustig, A.; Edmondson, D. E.; Mattevi, A. Three-Dimensional Structure of Human Monoamino Oxidase A (MAO A): Relation to the Structures of Rat MAO A and Human MAO B. *Proc. Natl. Acad. Sci. U.S.A.* **2005**, *102*, 12684−12689.
(69) Binda, C.; Hubálek, F.; Li, M.; Herzig, Y.; Sterling, J.; Edmonson, D. E.; Mattevi, A. Crystal Structures of Monoamine Oxidase B in Complex with Four Inhibitors of the *N*-Propargylaminoindan Class. *J. Med. Chem.* **2004**, *47*, 1767−1774.
(70) Cavalli, A.; Bolognesi, M. L.; Capsoni, S.; Andrisano, V.; Bartolini, M.; Margotti, E.; Cattaneo, A.; Recanatini, M.; Melchiorre, C. A Small Molecule Targeting the Multifactorial Nature of Alzheimer's Disease. *Angew. Chem., Int. Ed.* **2007**, *46*, 3689−3692.
(71) Muñoz-Ruiz, P.; Rubio, L.; García-Palomero, E.; Dorronsoro, I.; del Monte-Millán, M.; Valenzuela, R.; Usán, P.; de Austria, C.; Bartolini, M.; Andrisano, V.; Bidon-Chanal, A.; Orozco, M.; Luque, F. J.; Medina, M.; Martínez, A. Design, Synthesis, and Biological Evaluation of Dual Binding Site Acetylcholinesterase Inhibitors: New Disease-Modifying Agents for Alzheimer's Disease. *J. Med. Chem.* **2005**, *48*, 7223−7233.
(72) Bolognesi, M. L.; Banzi, R.; Bartolini, M.; Cavalli, A.; Tarozzi, A.; Andrisano, V.; Minarini, A.; Rosini, M.; Tumiatti, V.; Bergamini, C.; Fato, R.; Lenaz, G.; Hrelia, P.; Cattaneo, A.; Recanatini, M.; Melchiorre, C. Novel Class of Quinone-Bearing Polyamines as Multi-Target-Directed Ligands To Combat Alzheimer's Disease. *J. Med. Chem.* **2007**, *50*, 4882−4897.
(73) Tumiatti, V.; Milelli, A.; Minarini, A.; Rosini, M.; Bolognesi, M. L.; Micco, M.; Andrisano, V.; Bartolini, M.; Mancini, F.; Recanatini, M.; Cavalli, A.; Melchiorre, C. Structure−Activity Relationships of Acetylcholinesterase Noncovalent Inhibitors Based on a Polyamine Backbone. 4. Further Investigation on the Inner Spacer. *J. Med. Chem.* **2008**, *51*, 7308−7312.
(74) Bolognesi, M. L.; Bartolini, M.; Rosini, M.; Andrisano, V.; Melchiorre, C. Structure−Activity Relationships of Memoquin: Influence of the Chain Chirality in the Multi-Target Mechanism of Action. *Bioorg. Med. Chem. Lett.* **2009**, *19*, 4312−4315.
(75) Zhou, Y.; Jiang, C.; Zhang, Y.; Liang, Z.; liu, W.; Wang, L.; Luo, C.; Zhong, T.; Sun, Y.; Zhao, L.; Xie, X.; Jiang, H.; Zhou, N.; Liu, D.; Liu, H. Structural Optimization and Biological Evaluation of Substituted Bisphenol A Derivatives as beta-Amyloid Peptide Aggregation Inhibitors. *J. Med. Chem.* **2010**, *53*, 5449−5466.
(76) Jacob-Roetne, R.; Jacobsen, H. Alzheimer's Disease: From Pathology to Therapeutic Approaches. *Angew. Chem., Int. Ed.* **2009**, *48*, 3030−3059.
(77) Perry, E. K.; Perry, R. H.; Blessed, G.; Tomlinson, B. E. Changes in Brain Cholinesterases in Senile Dementia of Alzheimer Type. *Neuropathol. Appl. Neurobiol.* **1978**, *4*, 273−277.
(78) Greig, N. H.; Utsuki, T.; Yu, Q.; Zhu, X.; Holloway, H. W.; Perry, T.; Lee, B.; Ingram, D. K.; Lahiri, K. A New Therapeutic Target in Alzheimer's Disease Treatment: Attention to Butyrylcholinesterase. *Curr. Med. Res. Opin.* **2001**, *17*, 159−165.
(79) Ellman, G. L.; Courtney, K. D.; Andres, V.; Featherstone, R. M. A New and Rapid Colorimetric Determination of Acetylcholinesterase Activity. *Biochem. Pharmacol.* **1961**, *7*, 88−95.
(80) Segel, I. H. *Enzyme Kinetics*; John Wiley: Toronto, Canada, 1975; p 838.
(81) Gomez, N.; Unzeta, M.; Tipton, K. F.; Anderson, M. C.; O'Carrol, A. M. Determination of Monoamino Oxidase Concentrations in Rat Liver by Inhibitor Binding. *Biochem. Pharmacol.* **1986**, *35*, 4467−4472.
(82) Fowler, C. J.; Tipton, K. F. Concentration Dependence of the Oxidation of Tyramine by the Two Forms of Rat Liver Mitochondrial Monoamine Oxidase. *Biochem. Pharmacol.* **1981**, *30*, 3329−3332.
(83) Bartolini, M.; Bertucci, C.; Cavrini, V.; Andrisano, V. Beta-Amyloid Aggregation Induced by Human Acetylcholinestrase: Inhibition Studies. *Biochem. Pharmacol.* **2003**, *65*, 407−416.
(84) Wlodek, S. T.; Antosiewicz, J.; McCammon, J. A.; Straatsma, T. P.; Gilson, M. K.; Briggs, J. M.; Humblet, C.; Sussman, J. L. Binding of Tacrine and 6-Chlorotacrine by Acetylcholinesterase. *Biopolymers* **1996**, *38*, 109−117.
(85) Dvir, H.; Wong, D. M.; Harel, M.; Barril, X.; Orozco, M.; Luque, F. J.; Muñoz-Torrero, D.; Camps, P.; Rosenberry, T. L.; Silman, I.; Sussman, J. L. 3D Structure of *Torpedo californica* Acetylcholinesterase Complexed with Huprine X at 2.1 Å Resolution: Kinetic and Molecular Dynamic Correlates. *Biochemistry* **2002**, *41*, 2970−2981.
(86) Binda, C.; Hubalek, F.; Li, M.; Herzig, Y.; Sterling, J.; Edmonson, D. E.; Mattevi, A. Binding of Rasagiline-Related Inhibitors to Human Monoamine Oxidases: A Kinetic and Crystallographic Analysis. *J. Med. Chem.* **2005**, *48*, 8148−8154.
(87) Ngamelue, M. N.; Homma, K.; Lockridge, O.; Asojo, O. A. Crystallization and X-ray Structure of Full-Length Recombinant Human Butytylcholinesterase. *Acta Crystallogr., Sect. F* **2007**, *63*, 723−727.
(88) Carletti, E.; Li, H.; Li, B.; Ekström, F.; Nicolet, Y.; Loiodice, M.; Gillon, E.; Froment, M. T.; Lockridge, O.; Schopfer, L. M.; Masson, P.; Nachon, F. Aging of Cholinesterases Phosphylated by Tabun Proceeds through O-Dealkylation. *J. Am. Chem. Soc.* **2008**, *130*, 16011−16020.
(89) Case, D. A.; Darden, T. A.; Cheatham, T. E., III; Simmerling, C. L.; Wang, J.; Duke, R. E.; Luo, R.; Merz, K. M.; Pearlman, D. A.; Crowley, M.; Walker, R. C.; Zhang, W.; Wang, B.; Hayik, S.; Roitberg, A.; Seabra, G.; Wong, K. F.; Paesani, F.; Wu, X.; Brozell, S.; Tsui, V.; Gohlke, H.; Yang, L.; Tan, C.; Mongan, J.; Hornak, V.; Cui, G.; Beroza, P.; Mathews, D. H.; Schafmeister, C.; Ross, W. S.; Kollman, P. A. *AMBER*, version 9; University of California: San Francisco, CA, 2006.
(90) Bayly, C. I.; Cieplak, P.; Cornell, W. D.; Kollman, P. A. *J. Phys. Chem.* **1993**, *97*, 10269−10280.
(91) Frisch, M. J.; Trucks, G. W.; Schlegel, H. B.; Scuseria, G. E.; Robb, M. A.; Cheeseman, J. R.; Montgomery, J. A., Jr.; Vreven,T.; Kudin, K. N.; Burant, J. C.; Millam, J. M.; Iyengar, S. S.; Tomasi, J.; Barone, V.; Mennucci, B.; Cossi, M.; Scalmani, G.;Rega, N.; Petersson, G. A.; Nakatsuji, H.; Hada, M.; Ehara, M.; Toyota, K.; Fukuda, R.; Hasegawa, J.; Ishida, M.; Nakajima, T.; Honda, Y.; Kitao, O.; Nakai, H.; Klene, M.; Li, X.; Knox, J. E.; Hratchian, H. P.; Cross, J. B.; Adamo, C.; Jaramillo, J.; Gomperts, R.; Stratmann, R. E.; Yazyev, O.; Austin, A. J.; Cammi, R.; Pomelli, C.; Ochterski, J. W.; Ayala, P. Y.; Morokuma, K.; Voth, G. A.; Salvador, P.; Dannenberg, J. J.; Zakrzewski, V. G.; Dapprich, S.; Daniels, A. D.; Strain, M. C.;

Farkas, O.; Malick, D. K.; Rabuck, A. D.; Raghavachari, K.; Foresman, J. B.; Ortiz, J. V.; Cui, Q.; Baboul, A. G.; Clifford, S.; Cioslowski, J.; Stefanov, B. B.; Liu, G.; Liashenko, A.; Piskorz, P.; Komaromi, I.; Martin, R. L.; Fox, D. J.; Keith, T.; Al-Laham, M. A.; Peng, C. Y.; Nanayakkara, A.; Challacombe, M.; Gill, P. M. W.; Johnson, B.; Chen, W.; Wong, M. W.; Gonzalez, C.; Pople, J. A. *Gaussian 03*, revision B.04, Gaussian, Inc.: Pittsburgh PA, 2003.

(92) Srinivasan, J.; Cheatham, T. E. III; Cieplak, P.; Kollman, P. A.; Case, D. A. Continuum Solvent Studies of the Stability of DNA, RNA and Phosphoramidate-DNA Helices. *J. Am. Chem. Soc.* **1998**, *120*, 9401−9409.

(93) Stoica, I.; Sadiq, S. K.; Coveney, P. V. Rapid and Accurate Prediction of Binding Free Energies for Saquinavir-Bound HIV-1 Proteases. *J. Am. Chem. Soc.* **2008**, *130*, 2639−2648.

(94) Homak, V.; Abel, R.; Okur, A.; Strockbine, B.; Roitberg, A.; Simmerling, C. Comparison of Multiple Amber Force Fields and Development of Improved Protein Backbone Parameters. *Proteins* **2006**, *65*, 712−725.

(95) Wang, J.; Wolf, R. M.; Caldwell, J. W.; Kollman, P. A.; Case, D. A. Development and Testing of a General AMBER Force Field. *J. Comput. Chem.* **2004**, *25*, 1157−1174.

(96) Wang, J.; Wang, W.; Kollman, P. A.; Case, D. A. Automatic Atom Type and Bond Type Perception in Molecular Mechanical Calculations. *J. Mol. Graphics Modell.* **2006**, *25*, 247−260.

(97) Jorgensen, W. L.; Chandrasekhar, J.; Madura, J. D.; Impey, R. W.; Klein, M. L. Comparison of Simple Potential Functions for Simulating Liquid Water. *J. Chem. Phys.* **1983**, *79*, 926−935.

Supporting Information

Synthesis, Biological Evaluation and Molecular Modeling of Donepezil and *N*-[(5-(Benzyloxy)-1-methyl-1*H*-indol-2-yl)methyl]-*N*-methylprop-2-yn-1-amine Hybrids, as New Multipotent Cholinesterase/Monoamine oxidase Inhibitors for the Treatment of Alzheimer's Disease

Irene Bolea,[±,#] Jordi Juárez-Jiménez,[&,#] Cristóbal de los Ríos,[‡] Mourad Chioua,[¶] Ramón Pouplana,[&] F. Javier Luque,[&] Mercedes Unzeta,[±,*] and José Marco-Contelles[¶,*] Abdelouahid Samadi[¶,]

Departament de Bioquímica i Biología Molecular, Facultat de Medicina. Institut de Neurociències. Universitat Autònoma de Barcelona, 08193 Bellaterra, Barcelona, Spain; Departament de Fisicoquímica, Facultat de Farmàcia, and Institut de Biomedicina (IBUB), Universitat de Barcelona, Av. Diagonal 643, E-08028, Barcelona, Spain; Laboratorio de Radicales Libres y Química Computacional (IOG, CSIC), Juan de la Cierva 3, E-28006, Madrid, Spain; Instituto Teófilo Hernando, Fundación de Investigación Biómedica, Hospital Universitario de la Princesa, C/ Diego de León, 62, E-28029, Madrid, Spain

[#] *Those authors have contributed equally to this work.*

Table of contents

Figure S1. Potential energy for AChE simulations 3
Figure S2. RMSD profiles for AChE simulations 4
Figure S3. Torsional profiles for Trp270 at the PAS 5
Figure S4. Binding mode of donepezil and **5** bound to AChE 6
Figure S5. View of the stacking of **5** with Tyr334 and Trp279 7
Figure S6. View of the Asp72/Glu198 residues at the CAS 8
Figure S7. View of the reverted binding mode of **5** in AChE 9
Figure S8. Docking poses of **5** in BuChE 11
Figure S9. Potential energy for the MAO simulations of the noncovalently bound inhibitor **5**. 12
Figure S10. RMSD profiles for MAO simulations 13
Figure S11. Views of the binding of **5** to MAO-A 14
Figure S12. Views of the binding of **5** to MAO-B 15
Figure S13. Distance from compound **5** to FAD in MAO-A and MAO-B. 16
Figure S14. Potential energy for the MAO simulations of the covalently adduct between **5** and FAD. 17
Table S1. MM-PBSA analysis for the binding of **5** to AChE 18
Table S2. Comparison of MM/PBSA free energies determined for the AChE-**5** complex. 19
Table S3. Comparison of MM/PBSA free energies determined for the MAO-**5** complex. 20

Figure S1. Time (ns) evolution of the potential energy (x 10^3; kcal/mol) for the MD simulations of (*top; left*) the AChE-donepezil complex, and the complexes of **5** bound to (*top; right*) AChE(1EVE), (*bottom; left*) AChE(2CKM) and (*bottom; right*) AChE(1Q83).

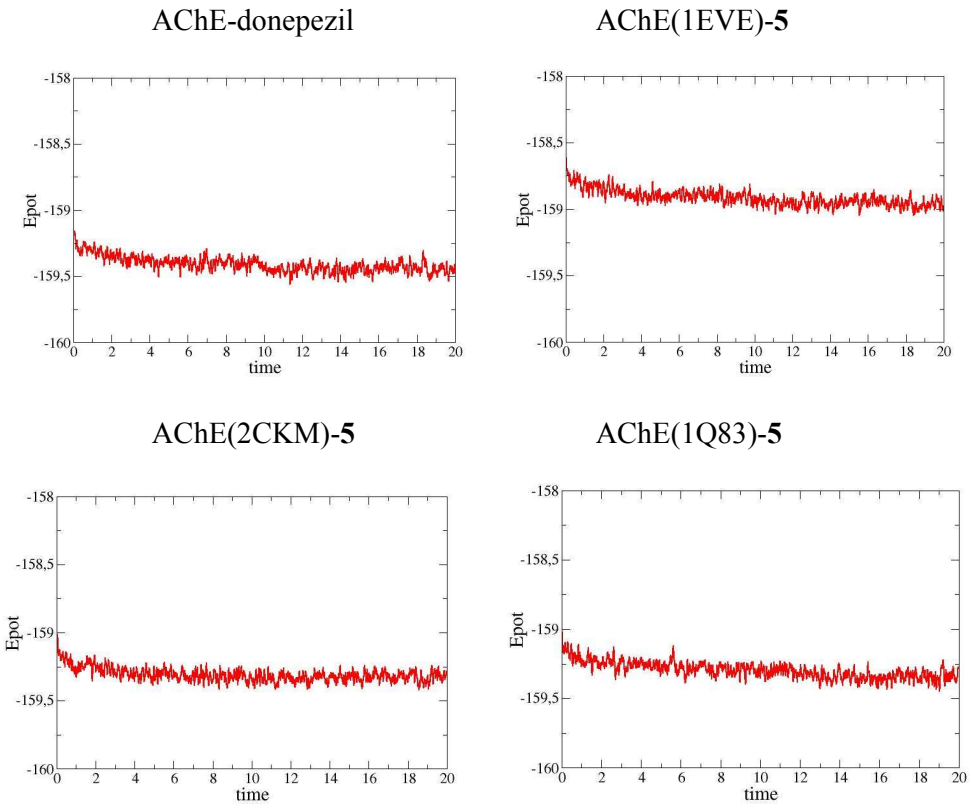

Figure S2. Time (ns) evolution of the positional root-mean square deviation (RMSD; Å) for the MD simulations of (*top; left*) the AChE-donepezil complex, and the complexes of **5** bound to (*top; right*) AChE(1EVE), (*bottom; left*) AChE(2CKM) and (*bottom; right*) AChE(1Q83). The RMSD was determined for the backbone atoms (black), and the heavy atoms of the residues that delineate the binding site (red) relative to the energy minimized structure of each AChE-**5** complex.

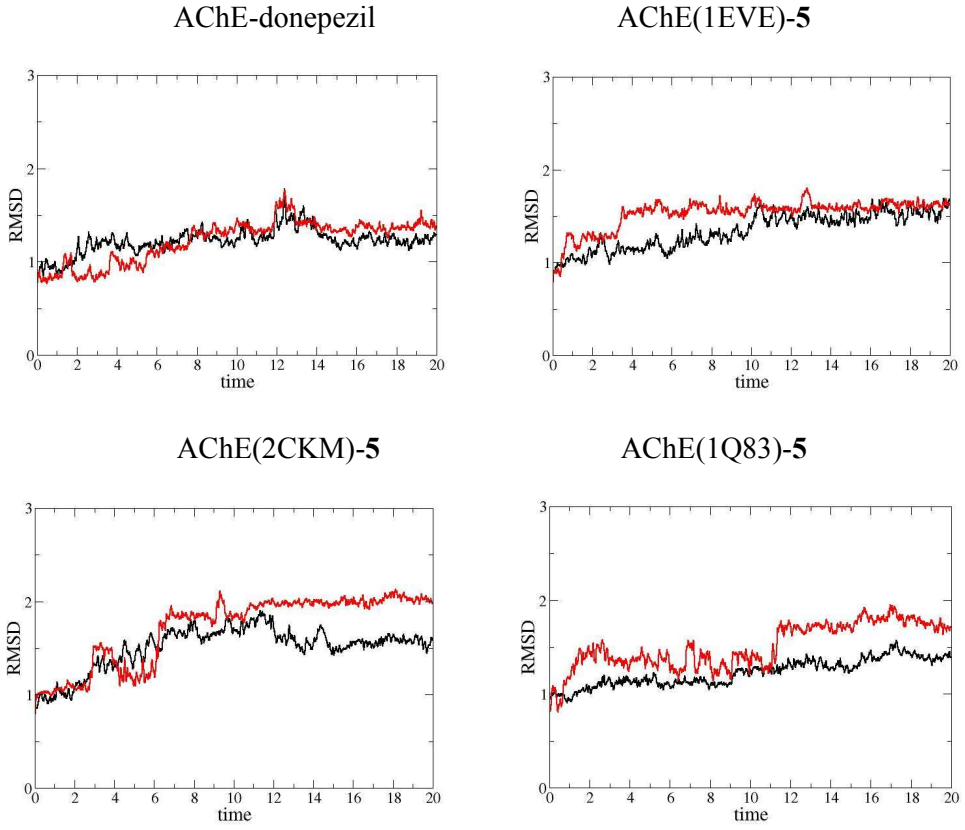

Figure S3. Time (ns) evolution of the torsional angles (degrees) that define the orientation of the side chain of Trp279 for the MD simulations of (*top; left*) AChE-donepezil complex, and the complexes of **5** bound to (*top; right*) AChE(1EVE), (*bottom; left*) AChE(2CKM) and (*bottom; right*) AChE(1Q83). Dihedral angles N–C_α–C_β–C_γ and C_α–C_β–C_γ–C_δ are shown in orange and blue, respectively.

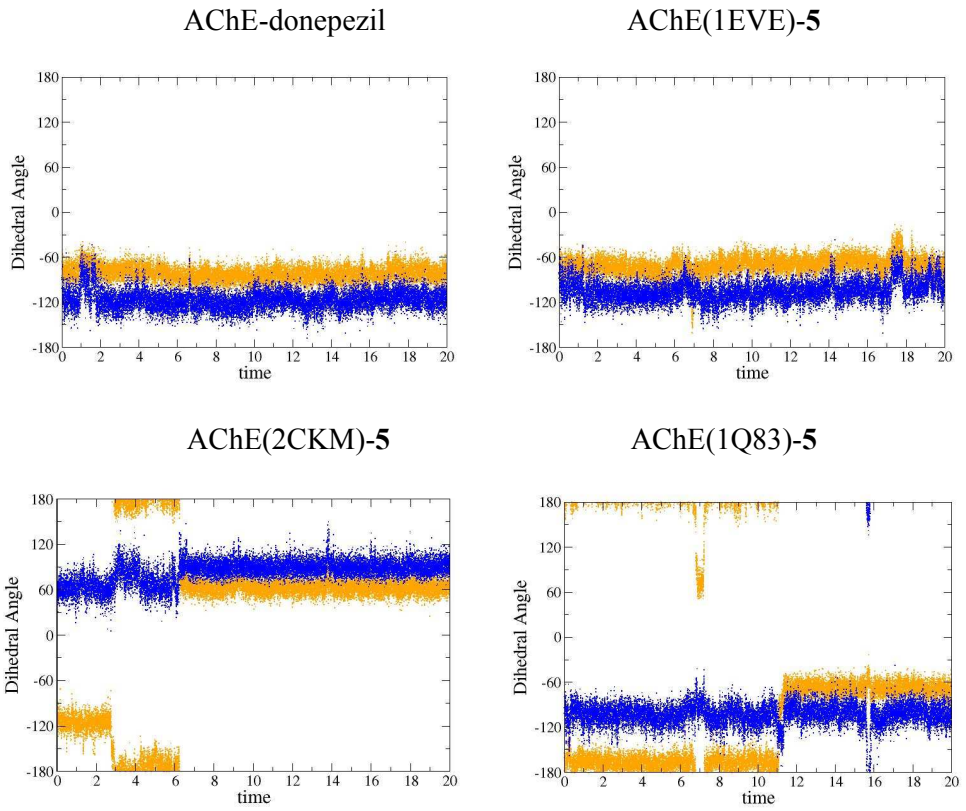

Figure S4. Representation of the binding mode of (*top*) donepezil and (*bottom*) **5** bound to AChE. The binding mode of donepezil is taken from the X-ray structure (PDB entry 1EVE). For the binding of **5** to AChE(1EVE), five snapshots taken every ns along the last 5 ns of the trajectory are superposed. Selected residues in the binding site are shown as yellow (X-ray) and green (AChE(1EVE)) sticks, whereas the ligand is shown as orange (donepezil) and blue (**5**) sticks.

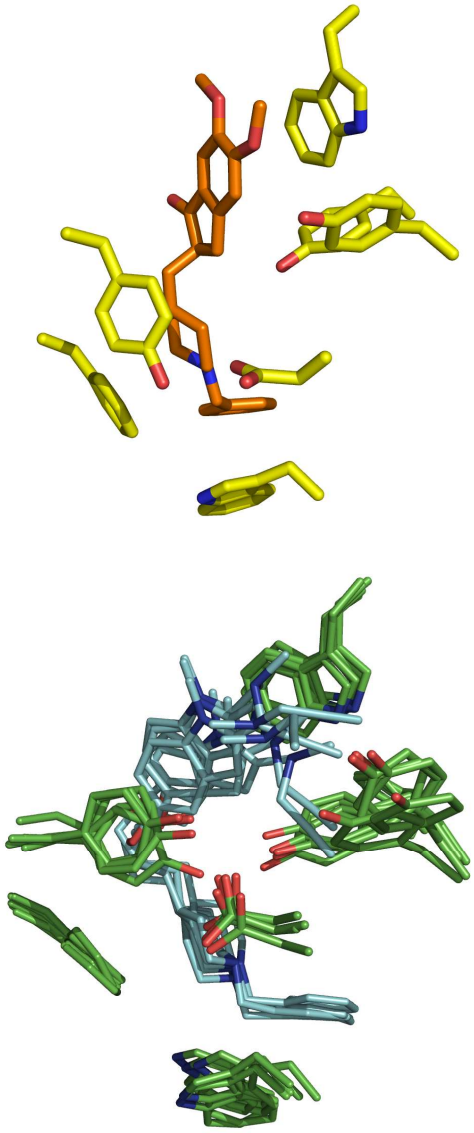

Figure S5. View of the stacking interaction formed by the indole ring of **5** with the aromatic rings of Tyr334 and Trp279. Shortening or lengthening of the tether should be accompanied by displacements of the indole ring along the gorge that would increase the stacking against Tyr334 or Trp279.

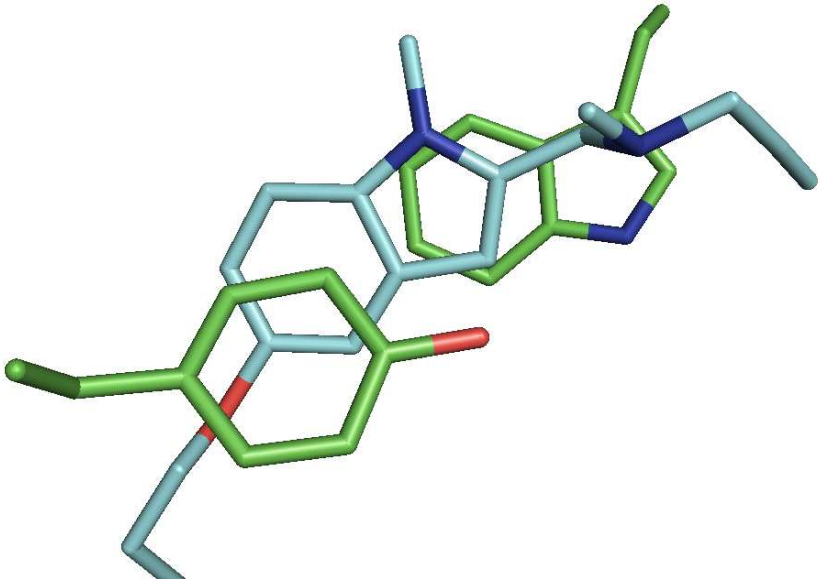

Figure S6. View of the spatial location of residues Asp70 and Glu198 in the CAS for (*top*) the X-ray structure of the complex between AChE (yellow) and donepezil (orange), and (*bottom*) the complex between AChE(1EVE) (green) and **5** (blue). Selected distances are given in angstroms.

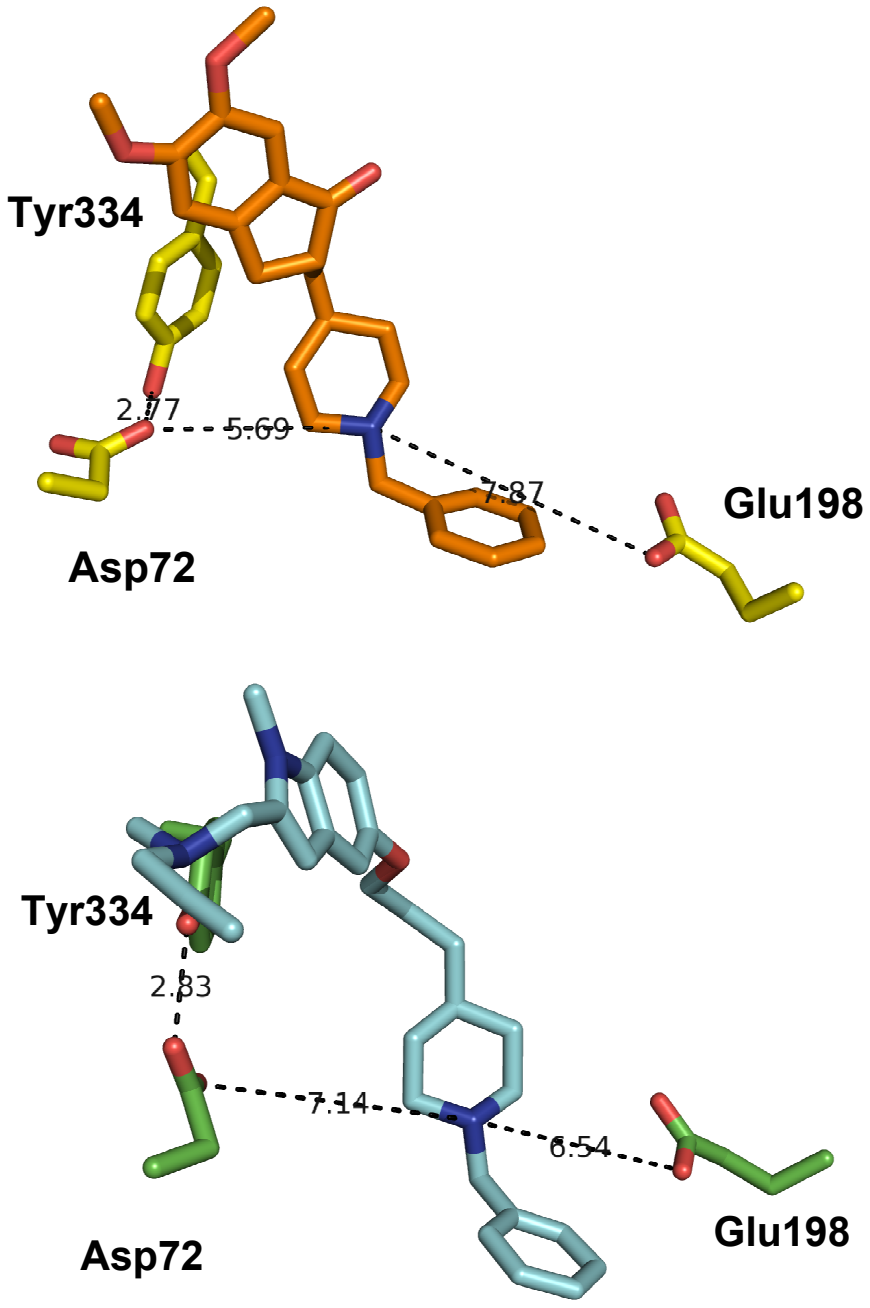

Figure S7. Representation of the inverted binding mode of **5** in the binding site of AChE for the AChE_1EVE model. Superposition of the snapshots taken every 2 ns along the last 10 ns of the trajectory for the complex with (top) AChE_1EVE, (middle) AChE_1Q83 and (bottom) AChE_2CKM. The ligand is shown in orange, and selected residues at the CAS (Trp84, Phe330) and PAS (Tyr70, Trp279) are shown in green.

ACHE_1EVE

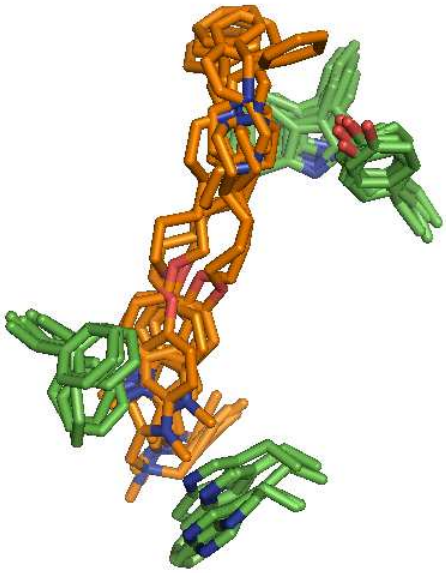

ACHE_1Q83

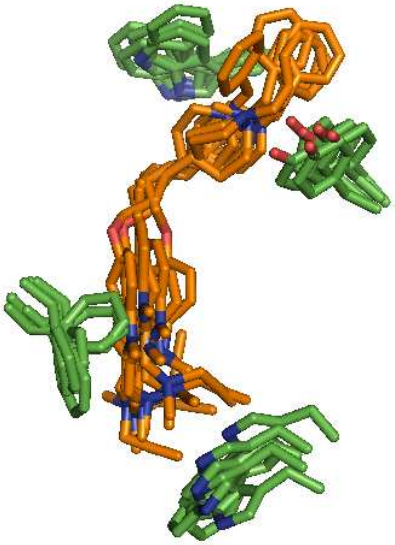

ACHE_2CKM

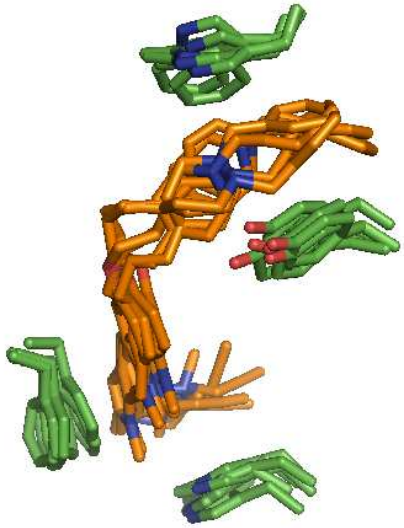

Figure S8. Representation of poses 1, 3, 5, 7 and 12 (covering a range of 5 kcal/mol in the score) obtained upon docking of compound **5** (blue) into the binding site of BuChE. Selected residues in the binding site of BuChE are also shown (green) together with the residue numbered in the enzyme (PDB entry 2PM8), and the corresponding residues in AChE.

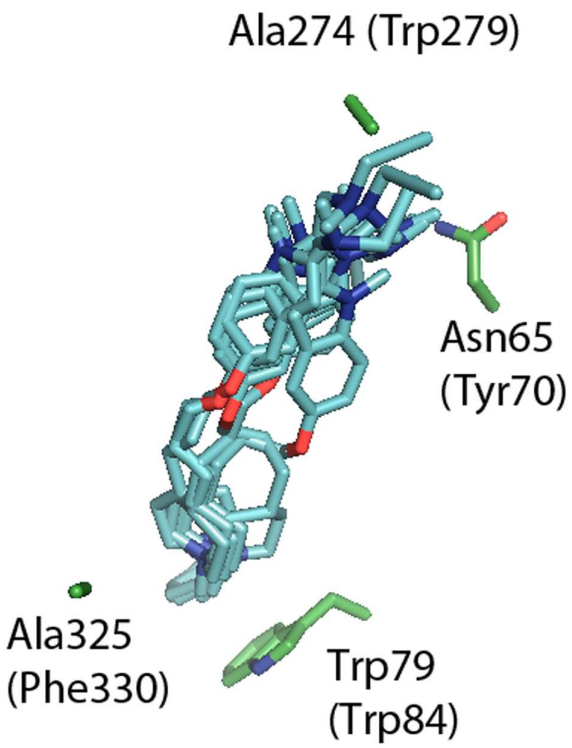

Figure S9. Time (ns) evolution of the potential energy (x 10^3; kcal/mol) for the MD simulations of **5** noncovalently bound to (*top*) MAO-A and (*bottom*) MAO-B.

MAO-A

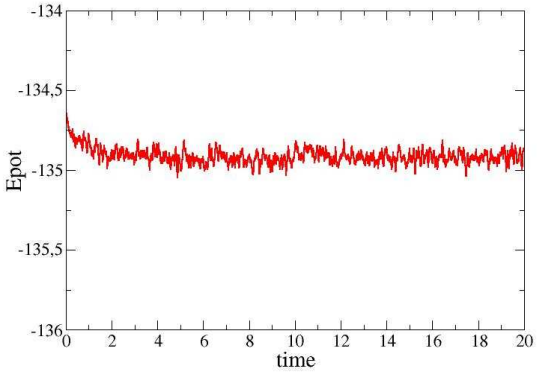

MAO-B

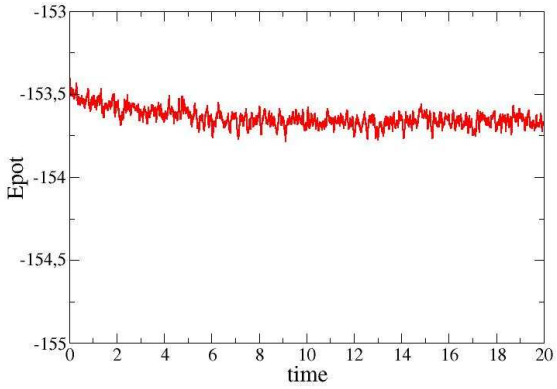

Figure S10. Time (ns) evolution of the positional root-mean square deviation (RMSD; Å) for the MD simulations of hybrid **5** bound to (*top*) MAO-A and (*bottom*) MAO-B. The RMSD was determined for the backbone atoms (black) and the heavy atoms of the residues that delineate the binding site (red).

MAO-A

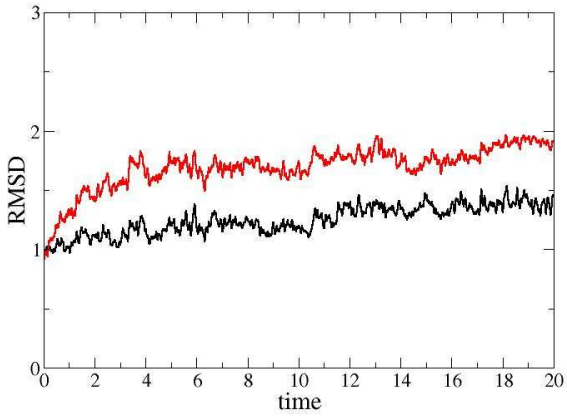

MAO-B

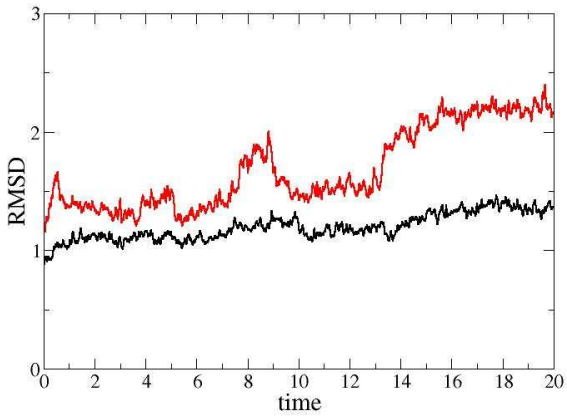

Figure S11. (*Top*) Superposition of the last snapshot obtained from the MD simulation run for the MAO-A complex of **5** with harmine (shown as magenta sticks) as found in the X-ray structure of its complex to human MAO-A (PDB entry 2Z5X). (*Bottom*) Superposition of the initial (yellow sticks) and final snapshots of the 20 ns MD simulation run for the MAO-A-**5** complex.

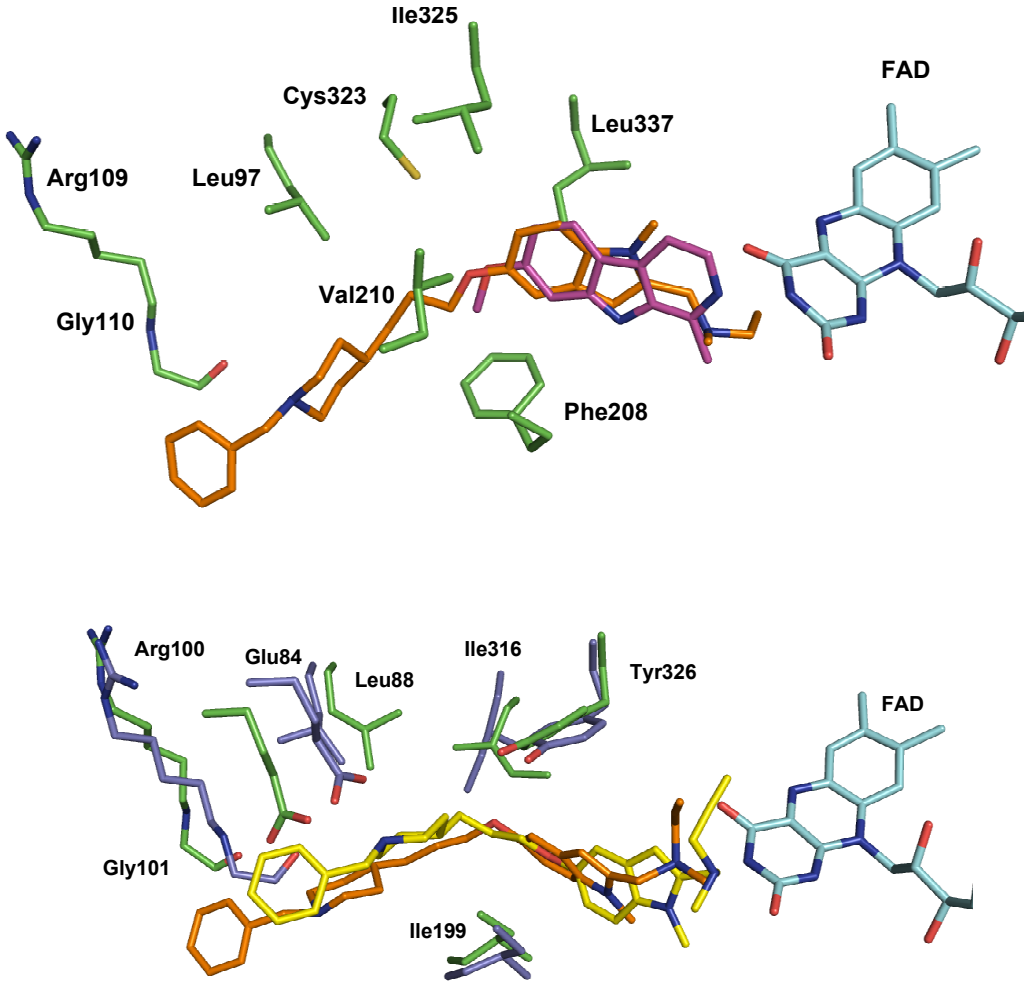

Figure S12. (*Top*) Superposition of the last snapshot obtained from the MD simulation run for the MAO-B complex of **5** with deprenyl (shown as magenta sticks) and rasagiline (shown as white sticks) as found in the X-ray structures of their complexes to human MAO-B (PDB entries 2BYB and 1S2Q, respectively). (*Bottom*) Superposition of the initial (yellow sticks) and final snapshots of the 20 ns-MD simulation run for the MAO-A-**5** complex.

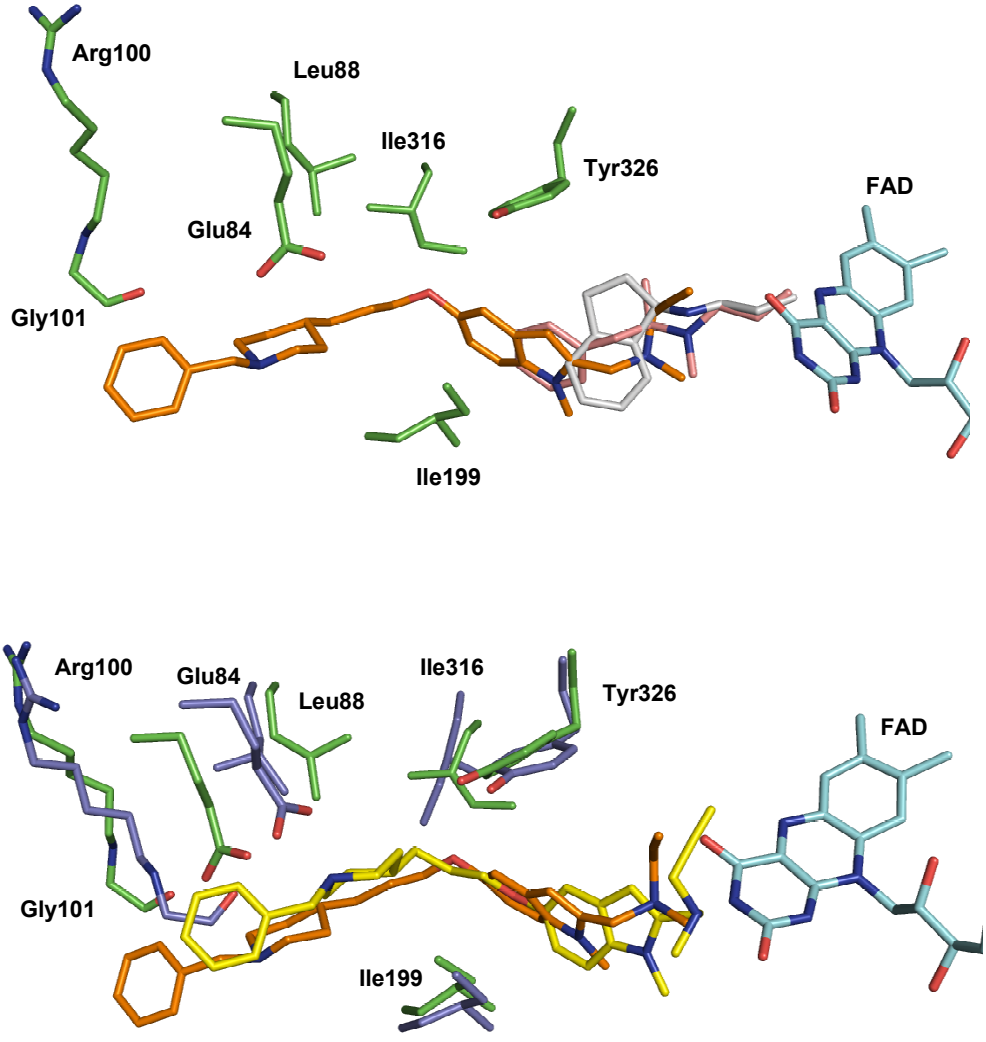

Figure S13. Time evolution (ns) of the distance (Å) from the carbon atom that bears the protonated amine in **5** to the nitrogen atom involved in chemical modification of FAD by deprenyl and rasagiline. Profiles for MAO-A and MAO-B are shown in blue and orange, respectively.

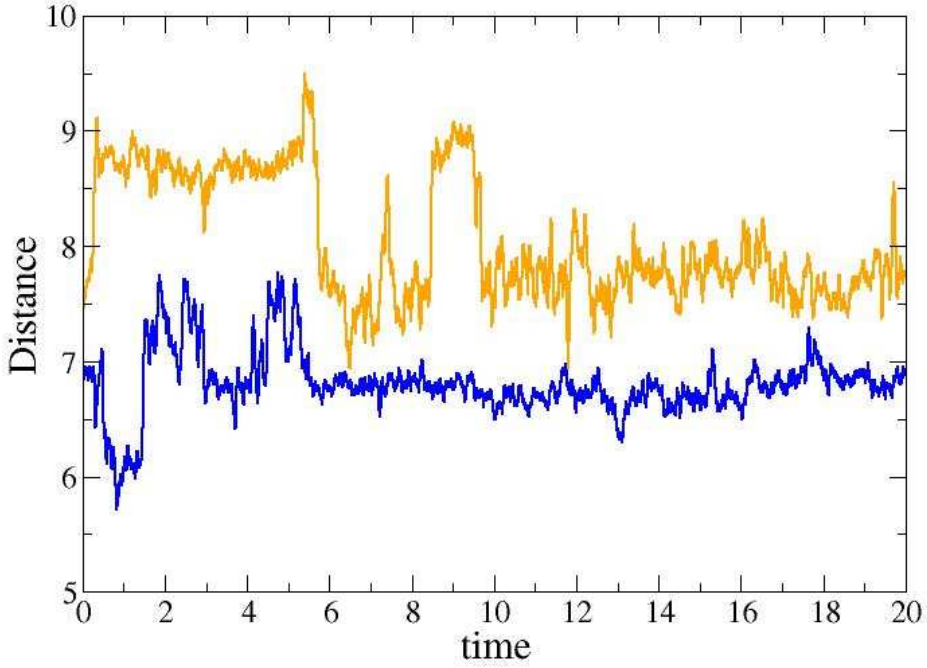

Figure S14. Time (ns) evolution of the potential energy (x 10^3; kcal/mol) for the MD simulations of **5** covalently bound to (*top*) MAO-A and (*bottom*) MAO-B.

MAO-A

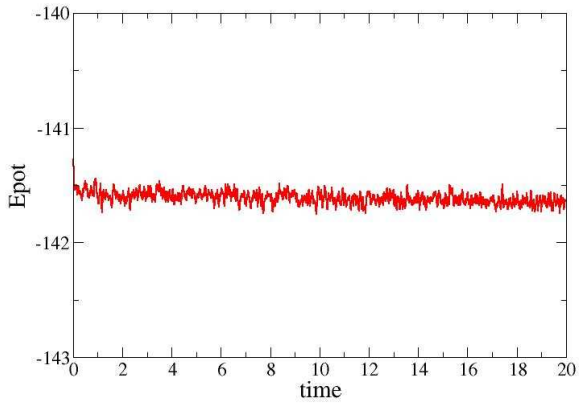

MAO-B

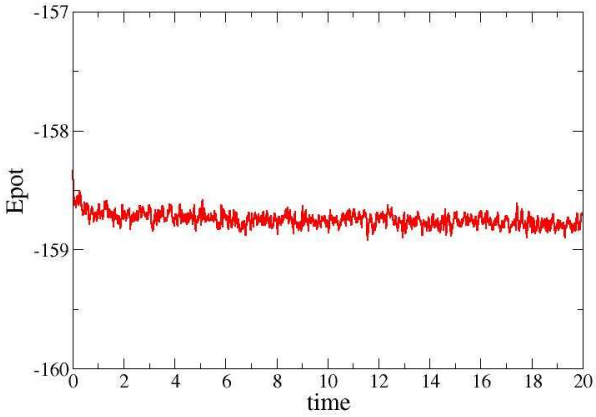

Table S1. MM–PBSA analysis of the binding affinity (kcal/mol) of compound **5** to AChE(1EVE) and AChE(2CKM). Calculations were performed for a set of 100 snapshots taken during the last 5 ns of the simulations (A) using standard atomic radii implemented in AMBER force field, and (B) the atomic radii optimized for MM/PBSA calculations with the AMBER force field.

A) Standard atomic radii.

Target	ΔG_{MM} (ele/vW)	ΔG_{ele}^{sol}	$\Delta G_{non-polar}^{sol}$	$\Delta G_{binding}$	$\Delta\Delta G_{binding}$
1EVE	-500.4 (-443.5/-56.9)	470.9	-7.3	-36.8	0.0
2CKM	-511.9 (-455.2/-53.2)	484.6	-7.3	-34.5	+2.3

B) Optimized atomic radii

Target	ΔG_{MM} (ele/vW)	ΔG_{ele}^{sol}	$\Delta G_{non-polar}^{sol}$	$\Delta G_{binding}$	$\Delta\Delta G_{binding}$
1EVE	-500.4 (-443.5/-56.9)	444.9	-7.3	-62.7	0.0
2CKM	-511.9 (-455.2/-53.2)	460.6	-7.3	-58.7	+4.0

Table S2. MM–PBSA analysis of the relative stability (kcal/mol) of the different complexes between **5** and AChE(1EVE) and AChE(2CKM). Normal and inverted denote the orientation with the benzylpiperidine moiety in the CAS or in the PAS, respectively. Calculations were performed for a set of 100 snapshots taken during the last 5 ns of the simulations using standard atomic radii implemented in AMBER force field.

Target	$\Delta\Delta G_{MM}$	$\Delta\Delta G_{ele}^{sol}$	$\Delta\Delta G_{non-polar}^{sol}$	$\Delta\Delta G_{binding}$
Normal orientation				
1EVE	0.0	0.0	0.0	0.0
2CKM	-29.3	149.2	-1.6	118.2
Inverted orientation				
1EVE	-69.6	175.2	-3.3	102.3
1Q83	-2.0	69.4	-1.4	65.9
2CKM	-9.0	124.1	-2.4	112.6

Since the initial state of the binding process of **5** to AChE is common for all the different complexes, the relative stability of the distinct binding modes can be directly taken from the comparison of the stabilities of the bound state (i.e., the AChE-**5** complex), which takes into account not only the interaction between ligand and protein, but also the contribution due to structural deformations.

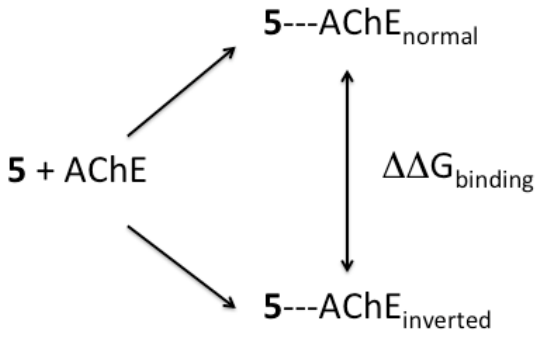

Table S3. MM–PBSA analysis of the binding affinity (kcal/mol) of compound **5** to MAO-A and MAO-B. Calculations were performed for a set of 100 snapshots taken during the last 5 ns of the simulations using standard atomic radii implemented in AMBER force field.

a) Simulation of compound **5** in the binding site prior to chemical reaction with FAD. Data determined for the whole ligand.

Target	ΔG_{MM} (ele/vW)	ΔG_{ele}^{sol}	$\Delta G_{non-polar}^{sol}$	$\Delta G_{binding}$
MAOA	-127.1 (-66.5/-60.6)	108.4	-7.1	-25.7
MAOB	-253.1 (-194.3/-58.8)	219.6	-7.1	-40.5

b) Simulation of compound **5** in the binding site prior to chemical reaction with FAD. Data determined for a truncated ligand where the propargyl unit has been replaced by a dummy atom.

Target	ΔG_{MM} (ele/vW)	ΔG_{ele}^{sol}	$\Delta G_{non-polar}^{sol}$	$\Delta G_{binding}$
MAOA	-104.6 (-51.9/-52.7)	89.0	-7.0	-22.6
MAOB	-225.5 (-172.6/-52.4)	193.2	-7.0	-38.8

c) Simulation of the adduct formed by compound **5** after chemical reaction with FAD. Data determined for a truncated ligand where the propargyl unit has been replaced by a dummy atom.

Note that due to the covalent linkage with FAD, there is a substantial charge redistribution in the ligand, which affects the magnitude of ΔG_{MM} and ΔG_{ele}^{sol} in MM/PBSA calculations compared to the noncovalently form of **5**. Therefore, caution is required for the comparison of the separate free energy components in the noncovalent and covalent forms of the inhibitor.

Target	ΔG_{MM} (ele/vW)	ΔG_{ele}^{sol}	$\Delta G_{non-polar}^{sol}$	$\Delta G_{binding}$
MAOA	-69.7 (-14.4/-55.3)	50.7	-7.0	-26.0
MAOB2	-167.0 (-105.3/-61.7)	129.6	-7.0	-44.4

4.2 Publicación:

Exploring the structural basis of the selective inhibition of monoamine oxidase A by dicarbonitrile aminoheterocycles: Role of Asn181 and Ile335 validated by spectroscopic and computational studies.

Biochimica et Biophysica Acta Proteins and Proteomics

(Biochimica et Biophysica Acta **2014**,1844, 389-397)

Jordi Juárez-Jiménez[‡], Eduarda Mendes[†], Carles Galdeano[‡], Carla Martins[†], Daniel B. Silva[†], José Marco-Contelles[&], Maria do Carmo Carreiras[†], F.Javier Luque[‡], Rona R. Ramsay[§*].

[‡]Departament de Fisicoquímica, Facultat de Farmàcia and institut de Biomedicina (IBUB), Universitat de Barcelona, Av. Prat de la Riba 171, 08921 Santa Coloma de Gramanet, Spain.

[†]iMed.UL – Research Institute For Medicines and Pharmaceutical Sciences, Faculty of Pharmacy, University of Lisbon, Av. Prof. Gama Pinto, 1649-003 Lisbon,Portugal.

[&] Laboratorio de Radicales Libres y Química Computacional (IQOG, CSIC), C\ Juan de la Cierva 3, E-28006, Madrid, Spain.

[§]School of Biology, Biomedical Science Research Complex, University of St Andrews, St Andrews KY16 9ST, UK

Biochimica et Biophysica Acta 1844 (2014) 389–397

Contents lists available at ScienceDirect

Biochimica et Biophysica Acta

journal homepage: www.elsevier.com/locate/bbapap

Exploring the structural basis of the selective inhibition of monoamine oxidase A by dicarbonitrile aminoheterocycles: Role of Asn181 and Ile335 validated by spectroscopic and computational studies

Jordi Juárez-Jiménez [a], Eduarda Mendes [b], Carles Galdeano [a], Carla Martins [b], Daniel B. Silva [b], José Marco-Contelles [c], Maria do Carmo Carreiras [b], F. Javier Luque [a], Rona R. Ramsay [d,*]

[a] Department of Physical Chemistry, Faculty of Pharmacy and Institute of Biomedicine (IBUB), University of Barcelona, Avda. Prat de la Riba 171, 08921 Santa Coloma de Gramenet, Spain
[b] iMed.UL — Research Institute for Medicines and Pharmaceutical Sciences, Faculty of Pharmacy, University of Lisbon, Avda. Prof. Gama Pinto, 1649-003 Lisbon, Portugal
[c] Laboratorio de Radicales Libres y Química Computacional, Instituto de Química Orgánica General, Consejo Superior de Investigaciones Científicas, c/. Juan de la Cierva 3, 28006 Madrid, Spain
[d] School of Biology, Biomedical Sciences Research Complex, University of St Andrews, St Andrews KY16 9ST, UK

ARTICLE INFO

Article history:
Received 7 October 2013
Received in revised form 7 November 2013
Accepted 9 November 2013
Available online 15 November 2013

Keywords:
Carbonitrile aminofuran
Monoamine oxidase
Selective binding
Docking
Molecular dynamics
Altered flavin spectrum

ABSTRACT

Since cyanide potentiates the inhibitory activity of several monoamine oxidase (MAO) inhibitors, a series of carbonitrile-containing aminoheterocycles was examined to explore the role of nitriles in determining the inhibitory activity against MAO. Dicarbonitrile aminofurans were found to be potent, selective inhibitors against MAO A. The origin of the MAO A selectivity was identified by combining spectroscopic and computational methods. Spectroscopic changes induced in MAO A by mono- and dicarbonitrile inhibitors were different, providing experimental evidence for distinct binding modes to the enzyme. Similar differences were also found between the binding of dicarbonitrile compounds to MAO A and to MAO B. Stabilization of the flavin anionic semiquinone by monocarbonitrile compounds, but destabilization by dicarbonitriles, provided further support to the distinct binding modes of these compounds and their interaction with the flavin ring. Molecular modeling studies supported the role played by the nitrile and amino groups in anchoring the inhibitor to the binding cavity. In particular, the results highlight the role of Asn181 and Ile335 in assisting the interaction of the nitrile-containing aminofuran ring. The network of interactions afforded by the specific attachment of these functional groups provides useful guidelines for the design of selective, reversible MAO A inhibitors.

© 2013 Elsevier B.V. All rights reserved.

1. Introduction

Monoamine oxidase (MAO) catalyzes the oxidative deamination of biogenic amines. Two isoforms of MAO (A and B) coded by distinct gene loci are found in mammalian tissues. Although the first MAO inhibitors were used for the treatment of depression [1], MAO inhibition is also valuable for the treatment of several neurodegenerative disorders. While non-specific and MAO A inhibitors are effective antidepressants, MAO B blockers have been emphasized in the treatment of Parkinson's and Alzheimer's diseases [2–4].

The two isoforms exhibit different substrate specificities, as noted in the fact that serotonin is primarily metabolized by MAO A, whereas 2-phenylethylamine is a better substrate of MAO B. Furthermore, the activity of the two isoforms can be distinguished by their sensitivity to selective inhibitors: MAO A is inhibited by low concentrations of clorgyline, while MAO B is blocked by low concentrations of selegiline (*l*-deprenyl). Non-specific irreversible inhibitors have been associated with unfavorable adverse effects, such as the well known "cheese effect" due to the inhibition of tyramine oxidation by intestinal MAO A. As a result, efforts have been invested in the development of selective inhibitors, such as the anti-Parkinson MAO B drug rasagiline, which bears an *N*-propargyl group that also confers neuroprotective properties [6–10]. The development of selective reversible MAO A inhibitors has also been pursued to minimize side effects resulting from inhibition of intestinal MAO A; reversibility allows dietary tyramine to displace them from the peripheral enzyme [11–14]. To avoid side effects on blood pressure, reversible inhibitors are now considered a safer goal for future development [5].

Knowledge of the structural similarities and differences between the binding sites of the two MAO isoforms is useful for the design of selective ligands. This is facilitated by the availability of high-resolution X-ray structures [15–19], which revealed the existence of a very high similarity between the residues that shape the substrate cavity of human MAO A and B. A relevant difference between the two isoforms is the replacement of the pair Phe208/Ile335 in MAO A by Ile199/Tyr326 in MAO B, since it alters the shape of the substrate cavity, leading to the distinction between "substrate" and "entrance" sites in MAO B. Moreover, these residues have been implicated in the affinity and selective recognition of substrates and inhibitors, as noted for the binding of

Abbreviations: MAO, monoamine oxidase; FAD, flavin adenine dinucleotide; QM/MM, quantum mechanics/molecular mechanics

* Corresponding author. Tel.: +44 1334 463411; fax: +44 1334 462595.
E-mail address: rrr@st-andrews.ac.uk (R.R. Ramsay).

1570-9639/$ – see front matter © 2013 Elsevier B.V. All rights reserved.
http://dx.doi.org/10.1016/j.bbapap.2013.11.003

the antiepileptic drug zonisamide to MAO B [20]. The replacements of Ile180/Asn181 and Val210 in MAO A by Leu171/Cys172 and Thr201 in MAO B are additional distinctive features between the substrate cavities of the two isoforms.

This study examines the effect of nitrile groups on the inhibitory activity against MAO A and B in light of the implications of these differences for the design of selective reversible inhibitors. Even though cyanide is known to be a poor reversible inhibitor of the oxidation of benzylamine by MAO [21], previous studies have indicated that the inhibitory activity of several compounds against MAO is potentiated by cyanide [22–24]. Thus, an earlier study from Davison on the inhibition of mitochondrial MAO by the irreversible inhibitor iproniazid revealed that although at low concentrations this compound alone had little effect on enzyme activity, the inhibitory activity was significantly enhanced in the presence of cyanide ions [22]. A similar potentiating effect was also reported for phenelzine and pheniprazine [23]. Remarkably, Tipton and collaborators demonstrated that, in the case of pheniprazine, cyanide potentiates the inhibition by increasing the apparent binding affinity to MAO, without causing significant changes in the rate of the reaction that yields the irreversibly inhibited species [24]. This finding suggests that the potentiating effect of cyanide can be ascribed to an activation mechanism whereby cyanide assists the binding of the inhibitor to the enzyme.

In this context, this work reports the pharmacological behavior of a series of carbonitrile-containing aminoheterocycles as inhibitors of MAO. The inhibitory capacity against MAO A and B was determined through experimental assays for the enzyme in solution and bound to the membrane. The selective binding of the most potent dicarbonitrile compounds to MAO A was then explored by measuring the differential spectroscopic changes triggered upon ligand binding in conjunction with molecular modeling studies. The results allow us to identify the molecular determinants that modulate the selective inhibition of MAO A by this compound, providing guidelines that may be valuable for the design of novel selective inhibitors.

2. Materials and methods

2.1. Carbonitrile compounds

To investigate the potential role of cyanide in assisting the binding of MAO inhibitors, a series of mono- and dicarbonitrile-containing aminoheterocycles (**1**–**7**; see Table 1) were synthesized following the procedure described in previous studies [25–27]. In order to complete the analysis of structure–activity relationships, two novel compounds, **5d** and **8**, were synthesized and characterized (see Supplementary information). The melting point was determined on a Koffler apparatus and was uncorrected. The assignment of chemical shifts was based on standard NMR experiments (^{1}H, ^{13}C-DEPT, ^{1}H, ^{1}H-COSY, gHSQC, gHMBC). Mass spectra were recorded on a GC/MS spectrometer with an API-ES ionization source. Elemental analyses were performed on a LECO CHNS-932 apparatus. TLC was performed on silica F254 and detection by UV light at 254 nm or by charring with either ninhydrin and anisaldehyde, or phosphomolybdic-H_2SO_4 dyeing reagents. Column chromatography was performed on silica gel 60 (230 mesh).

2.2. Pharmacological assays

Kynuramine, benzylamine, Ampliflu Red™ (10-acetyl-3,7-dihydroxyphenoxazine), and membrane-bound human MAO A and MAO B were purchased from Sigma-Aldrich, UK. For the purified enzymes, MAO A and MAO B (human liver forms) were purified after expression in yeast [28–30].

Each inhibitor was dissolved in DMSO (in glass vials). Dilutions were prepared in DMSO so that a constant volume of 10 μl was added to each 1 ml assay. The control assay contained the same amount of DMSO (1% v/v final concentration). Human MAO A (usually around 30 nM) in 50 mM potassium phosphate, pH 7.4, containing 0.05% Triton X100 was assayed spectrophotometrically following the formation of product at 314 nm at 30 °C with kynuramine as the substrate. For the inhibition studies, MAO A activity was determined using 0.36 mM kynuramine ($2 \times K_M$) and MAO B with 0.6 mM benzylamine ($2 \times K_M$). The activity of membrane-bound MAO A and MAO B (1 nM) with the same substrates was assayed by coupling the generation of H_2O_2 to horse-radish peroxidase to generate the fluorescent compound, resorufin [31,32].

Table 1
IC_{50} and K_i values (μM) for inhibition of human MAO A by compounds **1**–**8**. IC_{50} values were determined using a substrate concentration twice the K_M value for purified MAO A. K_i values for selected compounds were determined for purified MAO A in the spectrophotometric assay by varying both substrate (kynuramine) and inhibitor, where all the compounds showed a competitive inhibition.

Compound		X, Y, Z	MAO A	
			IC_{50} (μM)	K_i (μM)
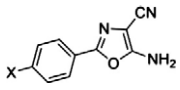	**1a**	X═Cl	19	3.0
	1b	X═CH_3	10	
	1c	X═H	35	
	1d	X═NO_2	22	
	1e	X═OCH_3	39	
	1f	X═F	89	26
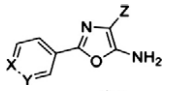	**2a**	X═N, Y═CH, Z═CN	40% at 500 μM	
	2b	X═CH, Y═N, Z═CN	130	
	2c	X═N, Y═CH, Z═CO_2H	None	
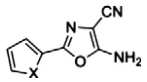	**3a**	X═O	475	
	3b	X═S	67	
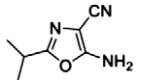	**4**		50% at 1 mM	
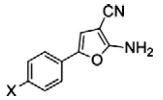	**5a**	X═Cl	6.6	2
	5b	X═CH_3	15	3.4
	5c	X═H	23	
	5d	X═OCH_3	11	7.5
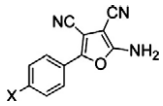	**6a**	X═Cl	0.77	0.10
	6b	X═CH_3	0.55	0.08
	6c	X═OCH_3	0.10	0.02
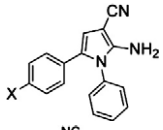	**7a**	X═Cl	None	
	7b	X═CH_3	10% at 30 μM	
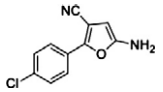	**8**		1.2	0.17

2.3. Determination of IC_{50} and K_i

Enzyme was added last to buffer containing substrate ($2 \times K_M$) and fixed concentrations of inhibitors. The IC_{50} values for the MAO inhibition were calculated by plotting the remaining activity of the enzyme (determined at multiple concentrations of the compounds) against the log concentration of compound. The inhibition constants (K_i) were determined using a substrate range of 0.1–0.9 mM kynuramine at six different inhibitor concentrations over a 10-fold range. The program GraphPad Prism v4 (GraphPad Software Inc.) was used to analyze the data by non-linear regression for the dose–response curves and global analysis for the K_i determination.

2.4. Spectral measurements

Spectra were recorded using a Shimadzu UV2101 spectrophotometer following the protocol described in previous studies [33]. Briefly, absorbance spectra were obtained for the enzyme (9–20 μM, 300 μl in a low-volume quartz cuvette) in 50 mM potassium phosphate buffer

(pH 7.4, 25 °C) containing 0.05% Brij. Since inhibitor-induced spectral changes are known to be fast [34,35], spectra were recorded as soon as the absorbance had stabilized. Aliquots of dithionite were subsequently added to the anaerobic enzyme–inhibitor mixture to reduce the flavin. Spectra were recorded 10 min after the additions to allow redox equilibration.

2.5. Docking

The binding mode of one of the most potent compounds was explored by combining docking calculations and molecular dynamics (MD) simulations. The protein models for MAO A were derived from the X-ray crystallographic structure of the complex with harmine (PDB ID: 2Z5X) [36]. The structure was refined by removal of the co-crystallized inhibitor, shortening of the transmembrane domain to residue Lys503, and addition of missing hydrogen atoms using the parm99SB [37] force field. A thioether bond was created between residue Cys406 and the FAD cofactor. Finally, structural waters common to five different high-resolution X-ray crystallographic structures of MAO (PDB IDs: 2Z5X, 2Z5Y, 2V5Z, 2C70, 2VZ2) were retained.

Docking was performed with the rDock program (derived from RiboDock), which uses an empirical scoring function calibrated on the basis of protein–ligand complexes [38,39]. Calculations were carried out following the procedure adopted in recent studies [40]. Briefly, a cavity of 12 Å of radius centered on the FAD N5 atom was defined as the docking volume. While rDock accounts for the conformational flexibility of the ligand around rotatable bonds and the reorientation of water molecules, conformational adjustments of the side chains of residues were accounted for indirectly by rescaling the van der Waals volume of the side chains (by a factor of 0.9). Each compound was subjected to 100 docking runs, and the poses were sorted according to its docking score. The top 25 best scored poses were further analyzed by visual inspection.

2.6. Molecular dynamics simulations

The structural integrity of the binding mode was further explored by means of 30 ns MD simulations performed for the complexes with the oxidized and reduced forms of MAO A. Simulations were run using the PMEMD module of the Amber software package [41]. The parm99SB parameters were used for the protein and the gaff force field [42] was used to assign parameters to the ligand. The torsion between phenyl and furan rings was parameterized by fitting to the quantum mechanical energies derived at the MP2/6-31G(d) level, and the charge distribution of the inhibitor was refined using RESP charges [43] fitted to the B3LYP/6-31G(d) electrostatic potential obtained with Gaussian03 [44]. Sodium cations were added to neutralize the system, which was immersed in an octahedral box of around 13,000 TIP3P water molecules [45].

The simulation system was equilibrated using a multistep protocol. First, the system was energy minimized in a sequential way: i) water molecules and counterions (5000 steps of steepest descent algorithm followed by 10,000 steps of conjugate gradient), ii) hydrogen atoms (500 steps of steepest descent and 4500 steps of conjugate gradient), iii) hydrogen atoms, water molecules and counterions (15,000 steps of conjugate gradient.), and iv) the whole system was optimized (15,000 steps of conjugate gradient). Thermalization was performed in the NVT ensemble during five 25 ps steps, using a time step of 1 fs and increasing the temperature from 50 to 298 K. Concomitantly, the inhibitor and the residues that define the binding site were restrained during thermalization using a variable restraint force. A force constant of 25 kcal mol^{-1} $Å^{-2}$ was used in the first stage of thermalization, and was subsequently decreased by increments of 5 kcal mol^{-1} $Å^{-2}$ in the next stages. Prior to the production runs, a short MD simulation of 1 ns in the NPT ensemble was conducted in order to allow the system to achieve a stable density value at 1 atm. Then, a 30 ns production trajectory was run using SHAKE to all those bonds involving hydrogen atoms, allowing for a timestep of 2 fs, in conjunction with periodic boundary conditions at constant volume and temperature (298 K; Langevin thermostat with a collision frequency of 3 ps^{-1}), particle mesh Ewald for long-range electrostatic interactions, and a cutoff of 10 Å for nonbonded interactions. Through the complete simulation a restraint force of 20 kcal mol^{-1} $Å^{-2}$ was applied to the backbone of the residues 498–503, which define the transmembrane segment at the C-terminus of MAO A.

Comparison of the binding free energy of distinct poses for the inhibitor was performed using the SIETRAJ module, which is based in the Solvated Interaction Energy (SIE) approach [46,47]. SIE relies on the MM/PBSA technique and uses parameters that have been fitted to reproduce the binding free energies of a data set of 99 protein–ligand complexes. The binding affinity was estimated by averaging the results obtained for 100 snapshots taken evenly during the last 5 ns of the trajectories.

2.7. Quantum mechanical/molecular mechanical calculations

Time-dependent DFT calculations were performed to estimate the electronic spectra properties of the inhibitor–MAO complex following the procedure reported by Götze et al. [48]. To this end, geometries of the isoxazoline ring, a water molecule and compound **6a** were independently optimized at the CAM-B3LYP/6-31G(d) level. Later, a subset of 100 snapshots taken evenly along the last 5 ns of the trajectories were used for quantum mechanical/molecular mechanical (QM/MM) computations. For each snapshot the QM cluster included the isoxazoline ring, the inhibitor and all the water molecules at a distance up to 8 Å of the FAD N5 atom. Then, the optimized geometries of the isoxazoline ring, water and compound **6a** were separately superimposed to the corresponding moieties in the QM cluster. All the surrounding residues around 12 Å of the isoxazoline ring and not included in the QM part were treated classically. CAM-B3LYP, a Coulomb-attenuated version of the B3LYP functional [49], with a 6-31G(d) basis was used for time-dependent calculations. Test calculations showed that this method reduced the occurrence of non-relevant dark states, while keeping the quality of the B3LYP functional. The calculated energies and oscillator strengths for the first excited states were calculated and averaged over the 100 snapshots.

3. Results

3.1. Carbonitrile-containing compounds as potential MAO inhibitors

To investigate the potential role of cyanide in assisting the binding of MAO inhibitors, a series of mono- and dicarbonitrile-containing aminoheterocycles, including oxazole, furan, thiophene and pyrrole derivatives, has been studied (see Table 1). The series includes compounds containing a single nitrile unit *ortho* to the amino group in 5-amino-2-alkyl(aryl)oxazole-4-carbonitriles (**1**–**4**). The influence of the heteroaromatic ring and of the attachment of an additional nitrile was explored by testing 2-amino-5-phenylfuran-3-carbonitriles (**5**), 2-amino-5-phenylfuran-3,4-dicarbonitriles (**6**), 2-amino-1,5-diphenyl-1H-pyrrole-3-carbonitriles (**7**) and 5-amino-2-phenylfuran-3-carbonitrile (**8**).

The choice of these compounds was motivated by several reasons. First, among pentatomic systems, previous studies have pointed out that the inhibitory activity does not appear to be affected by the heteroatom in the heterocyclic ring [50–52], suggesting that they may be used as bioisosteric moieties [53,54]. In addition, the phenylfuran derivatives are structurally similar to brofaromine (4-(7-bromo-5-methoxy-2-benzofuranyl)-piperidine), which is a reversible inhibitor of MAO A. Finally, while the presence of an aryl unit is expected to facilitate the binding to the hydrophobic cavity present in MAO, the substitution pattern is expected to modulate the potency of reversible MAO inhibitors [55,56]. In particular, the nucleophilic character of the cyano nitrogen atom assisted by the hydrogen-bond donor ability of the neighboring

amino group might synergistically modulate the formation of specific interactions with both the flavin ring and residues in the substrate cavity.

3.2. MAO inhibitory activity of carbonitrile-containing compounds

In the initial screening against the purified MAO A and B, the type **1** compounds were found to act as moderate inhibitors of purified human MAO A (Table 1), but only weak inhibition of MAO B (data not shown) was detected up to the limits of solubility of each compound. The substitution of the C2 phenyl ring with polar heterocycles (pyridine, furan and thiophene; types **2** and **3**) or an isopropyl group (type **4**) led to a notable decrease in the inhibitory activity. In contrast, replacement of the oxazole ring in **1** by furan in the 5-amino-2-phenylfuran-4-carbonitrile series (**5**) enhanced the inhibitory activity, leading to a K_i of 2 μM for the chloro derivative (**5a**).

The introduction of an additional nitrile group at C4 in type **6** compounds was successful in leading the enzyme inhibition to submicromolar levels, leading to a 20-fold reduction in the K_i for the chloro derivative (**6a**) compared to the monocarbonitrile compound (**5a**). The most potent compound is **6c** (X═OCH_3), with a K_i of 20 nM, though the electronic properties of the substituent seem to play a moderate effect because the K_i is 4- and 5-fold lower compared with **6b** (X═CH_3) and **6a** (X═Cl), respectively. In fact, QM calculations showed no relevant differences in the charge distribution of the furan ring for these compounds (see Fig. S1 in Supporting information). This suggests that the aminofuran moiety of compounds **6a**–**c** may form similar interactions at the binding site, and that the larger inhibitory potency of **6c** likely stems from a better steric complementarity of the methoxybenzene moiety to the binding cavity. In contrast, the attachment of a phenyl unit to the pyrrole ring in **7** nearly abolishes the inhibitory activity. Finally, comparison of compounds **5a**, **6a** and **8** clearly shows that the addition of the second nitrile unit in type **6** compounds is the crucial factor for the enhancement in inhibitory potency, because the K_i of **8** (0.17 μM) nearly matches the value determined for **6a** (K_i of 0.10 μM).

Species origin and membrane attachment are known to influence the binding of some ligands to MAO [57–60]. Therefore, key compounds of types **5**, **6** and **8** were re-tested with membrane-bound human MAO A and B (Table 2). The compounds inhibit the two isoforms of human MAO. However, the most striking observation is the selective inhibition of MAO A by the 2-amino-5-phenylfuran-3,4-dicarbonitrile series (**6**). Thus, whereas type **5** monocarbonitrile derivatives exhibit similar inhibitory activities on MAO A and MAO B, the compound **8** monocarbonitrile exhibits a moderate selectivity toward MAO A inhibition, and the dicarbonitrile compounds (**6**) were between 11- and 77-fold more potent against MAO A compared to MAO B (see Fig. 1 and Table 2). The IC_{50} values determined for the membrane-bound MAO A are similar or slightly lower than the data measured for the enzyme in solution (see Tables 1 and 2). The ratio of the IC_{50} values of compounds **6a** and **6c** is decreased from 7.7 for the solubilized MAO A to 2.9 for the membrane-bound form, suggesting that partitioning to the membrane has a modest effect on the inhibitory potency.

Overall, these findings show that the 2-amino-5-phenylfuran-3,4-dicarbonitriles (**6**) behave as selective inhibitors of MAO A, and that the nitrile group attached to C4 is crucial in conferring the selectivity against MAO A.

Table 2
Inhibition of membrane-bound human MAO A and B. MAO activity was measured using the coupled assay with kynuramine as substrate (0.3 mM kynuramine for MAO A and 0.08 mM for MAO B). The IC50 values are mean ± s.d. from at least 3 experiments.

Compound	X	IC_{50} (μM)	
		MAO A	MAO B
5a	Cl	1.3 ± 0.2	3.5 ± 1.9
5b	CH_3	4.0 ± 0.8	3.1 ± 0.4
5d	OCH_3	4.1 ± 0.7	6.1 ± 0.8
6a	Cl	0.29 ± 0.03	3.2 ± 0.3
6b	CH_3	0.11 ± 0.01	8 ± 1
6c	OCH_3	0.10 ± 0.02	2.3 ± 0.2
8		5.6 ± 0.8	>10

3.3. Mechanism of inhibition

The 2-amino-5-phenylfuran-3-carbonitriles (**5**) and 2-amino-5-phenylfuran-3,4-dicarbonitriles (**6**) were used to investigate the mechanism of inhibition of MAO A. All compounds studied were reversible inhibitors as demonstrated by recovery of activity after either dilution or size exclusion filtration before addition of substrate. Kinetic data (initial rates) were fitted to the competitive inhibitor version of the Michaelis–Menten equation by non-linear regression in PRISM (Fig. S2 in Supporting information), giving the competitive K_i values shown in Table 1. Other modes of inhibition did not fit the data.

3.4. Potential as substrates for MAO A and MAO B

Compound **5a** acted as a very poor substrate for MAO A, reducing the flavin cofactor by 47% when incubated with MAO A anaerobically overnight (15 h). The oxidation product from **5a** was characterized by a strong absorbance peak at 360 nm (extinction coefficient 15,200 M^{-1} cm^{-1}) but has not yet been characterized. This establishes that **5a** can adopt a catalytically competent pose close to the N5-C4a atoms of the flavin cofactor. This proximity is also supported by the steady-state kinetic assays performed with kynuramine as the substrate, since at concentrations of **5a** above 1 μM there was apparently incomplete inhibition (Fig. 1). Furthermore, in the absence of kynuramine, hydrogen peroxide was generated in the presence of **5a** alone at concentrations above 1 μM. Using the sensitive coupled assay, a K_M of 1.6 ± 0.5 μM was obtained, and the k_{cat} was 0.005 ± 0.004 s^{-1} (i.e., about 0.16% of the k_{cat} value determined for kynuramine). It should be noted that the raw data were only just above the noise in the coupled assay and the resulting uncertainty is reflected in the standard errors.

Compound **6a** incubated alone with MAO A did not produce detectable hydrogen peroxide. No flavin reduction was observed during overnight anaerobic incubation of **6a** with MAO A. Nevertheless, a slow leak of oxygen in that single experiment could not be excluded because a new absorbance peak at 300 nm formed at the rate of 0.003 absorbance units per hour at the expense of the 360 nm absorbance of **6a**, thus suggesting some extremely slow conversion of **6a** in this incubation.

With regard to MAO B, both **5a** and **6a** acted as very poor substrates as they reduced the flavin cofactor by 26% and 39% respectively over 15 h under anaerobic conditions. However, in the Ampliflu Red coupled assay, the resorufin fluorescence detecting hydrogen peroxide generation was not significantly different from the control wells without any substrate or inhibitor present. In inhibition assays performed using either benzylamine or phenylethylamine as substrate, full inhibition of the hydrogen peroxide generation was observed. Thus, any oxidation of these compounds by MAO B in steady state assays is negligible.

Summing up, these findings indicate that **5a** and **6a** can reach the substrate cavity with the amine close to the flavin, but they are only very poor substrates, and thus exert enzyme inhibition through a reversible competitive inhibition mechanism.

3.5. Interaction with the FAD prosthetic group of MAO A

Changes in the spectral properties of prosthetic groups in proteins are informative about alterations in their environment. This is the case of flavin in MAO A, since several studies have reported changes in the visible absorption spectrum when a ligand occupies the active site [33,35,61]. We have therefore examined the influence exerted by the

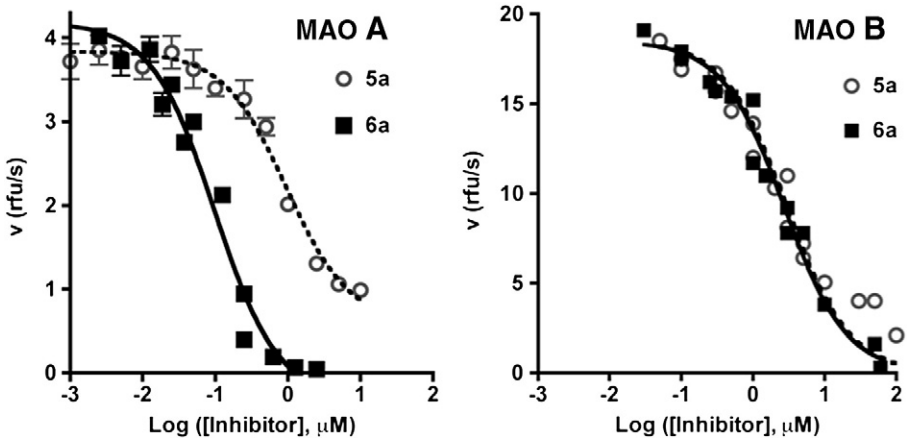

Fig. 1. Inhibition of membrane-bound MAO A and B. MAO activity was measured by detection of hydrogen peroxide in the coupled assay using 0.3 mM kynuramine as the substrate for MAO A (left) and 0.6 mM benzylamine for MAO B (right). These concentrations represent approximately 2 × K_M for each enzyme. The points are mean ± se (n = 3) but the error bars are smaller than the symbols in the MAO B graph (right).

binding of carbonitrile compounds on the spectral properties of the flavin.

Fig. 2 shows that compound **5a** induced a clear decrease in the intensity of the MAO A spectrum in the 400–500 nm region and a shift in the peak absorbance from 455 nm to 453 nm. In contrast, compound **6a** induced an increase in the absorbance around 500 nm and a red shift in the absorbance maximum from 456 to 459 nm. Each of three inhibitors with a single carbonitrile group (**5a**–**c**) induced a three-band pattern of decreased absorbance in the spectrum of MAO A, but all 3,4-dicarbonitrile compounds (**6a**–**c**) promoted a distinct increase at 502 nm (as shown for **5a** and **6a** in Fig. 2). The different trends of these spectral changes suggest the involvement of distinct interaction patterns in the MAO A substrate cavity for mono- and dicarbonitrile compounds.

The interaction of a ligand with the active site of MAO A also alters the redox properties of the flavin co-factor [33,35,61]. Fig. 3 shows that type **5** compounds enhance the yield of semiquinone (seen as the 412 nm absorbance peak) observed during chemical reduction compared to the enzyme titrated with dithionite in the absence of inhibitors. In contrast, type **6** compounds prevent the formation of the semiquinone species and no 412 nm peak is observed. This finding also suggests the occurrence of differences in the interaction of these compounds with the flavin unit.

A further confirmation of the occurrence of distinct binding modes for monocarbonitriles comes from the spectral changes recorded for **8**. The binding of this compound decreased the absorbance of MAO A at 500 nm in the same way as monocarbonitrile (**5a**) rather than increasing it (like **6a**). However, unlike **5a**, no semiquinone was observed during reduction of the MAO A-**8** complex with dithionite (data not shown). Thus, both carbonitrile groups are necessary for the specific effects on the flavin cofactor triggered upon binding of **6a** to MAO A.

The change in the absorbance spectrum of MAO B triggered upon binding of compound **6a** is shown in Fig. 4 which, for the sake of comparison, also shows the spectral change found in MAO A. Fig. 4 shows that binding of **6a** leads to a decrease in absorbance, centered at 495 nm, which differs from the increase at 500 nm found upon binding to MAO A, but similar to the reduction observed for the binding of **5a** to MAO A (see Fig. 2). Keeping in mind that the IC_{50} values for **5a** and **6a** against MAO B are the same (see Table 2), these findings allow us to hypothesize that if a specific interaction mediates the binding of **6a** to MAO A and stabilizes a close contact with the flavin cofactor, then it should be absent in the MAO B complex.

3.6. Molecular modeling: binding to the oxidized MAO A

Docking studies were performed to explore the binding mode of compound **6a** to the oxidized form of MAO A. The analysis of the set of 25 best ranked poses showed two distinct binding modes. In one case the inhibitor is oriented so that the amino group is pointing toward Asn181, and the nitrile unit at position C3 lies below the plane of the flavin ring (see Fig. 5A; hereafter termed *down* pose). In the other case, the

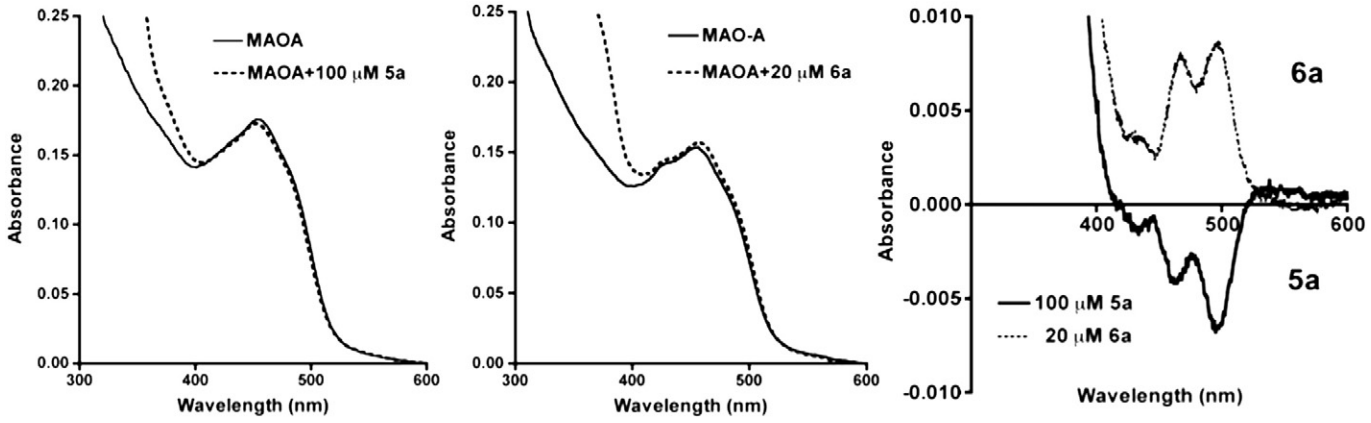

Fig. 2. Spectral changes in MAO A. (Left) 13.4 μM MAO A alone (solid line) and with 100 μM **5a** (dotted line); (middle) 12 μM MAO A alone (solid line) and with 20 μM **6a** (dotted line); (right) on an expanded scale, the difference spectra for the MAO A-inhibitor complexes minus MAO A alone.

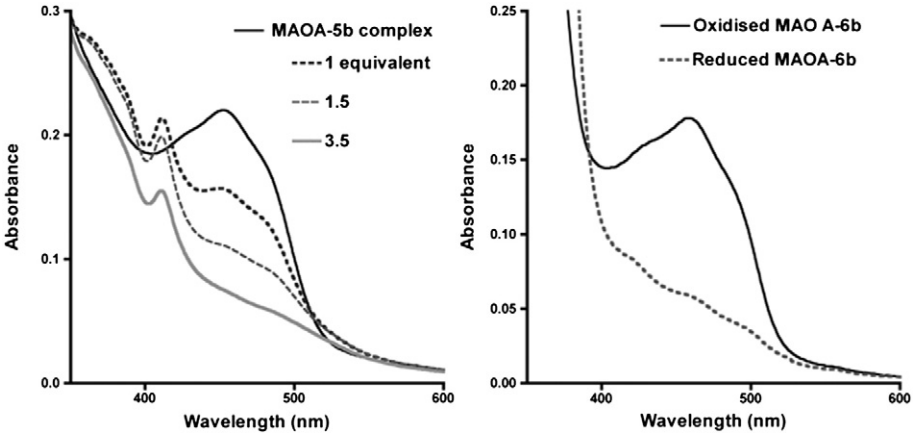

Fig. 3. Reduction of MAO A-inhibitor complexes with dithionite. (Left) Anaerobic MAO A (18.2 μM) complexed with 50 μM **5b** (about 15 × K_i, limited by the solubility of the compound in buffer) formed semiquinone during chemical reduction. (Right) In contrast, the complex of MAO A (15 μM) with 30 μM (375 × K_i) **6b** was reduced immediately to the fully reduced form by addition of one equivalent of dithionite.

inhibitor is flipped by ~180° along the molecular axis (see Fig. 5B; denoted *up* pose in the following), so that the amino group is pointing toward the flavin N5 atom. The suitability of the two binding modes was then examined by means of MD simulations (30 ns).

The trajectory run for the *down* pose revealed a stable binding mode. In particular, the structural integrity of the residues that shape the binding cavity is reflected in a root-mean square deviation (RMSD) lower than 1.5 Å (see Fig. S3 in Supporting information). The stability of the binding mode is also confirmed by the close superimposition of the poses of the ligand, which is tightly bound at the substrate cavity (see Fig. 5A). The amino group participates in two chains of water-mediated interactions. Thus, a water molecule acts as a bridge linking the amino group with the side chain amido unit of Asn181 and with the carbonyl group of Ile207. In the other chain, the amino group is linked to the carbonyl group of Gly443. Furthermore, the nitrile on C3 is slightly displaced from the flavin unit (average distance of N(nitrile)-N5(flavin) close to 3.6 Å) and interacts with a water molecule, which is hydrogen-bonded to the flavin N5 atom and to the amino group of Lys305. Note that similar water-bridged interactions have been observed in the X-ray structures for the sulfonamide group of zonisamide (PDB ID: 3PO7) and for one of the carbonyl groups of isatin (PDB ID: 2BK5) in MAO B [20,62]. On the other hand, the nitrile group on C4 anchors in a lipophilic pocket defined by Tyr69, Ile335, Leu337, Met350 and Phe352. Finally, the chlorine atom attached to the phenyl group interacts with Leu97.

In contrast, the trajectory run for the *up* pose showed a fast structural rearrangement of the inhibitor at the beginning of the simulation (see Fig. S4 in Supporting information). Moreover, the inhibitor exhibited larger fluctuations in the binding site, as expected from the lower number of specific interactions formed by the ligand, which suggests a poor fit to the binding cavity (see Fig. 5B). Moreover, it is located more distant from the FAD cofactor (average distance of N(amino)…N5(flavin) of 6.2 Å; see Fig. 5B), so that the shell of water molecules that surround the flavin ring is not disrupted.

The energetic stability of the two binding modes was examined using the Solvent Interaction Energy (SIE) technique. Note that the comparison of the binding affinities predicted for *down* and *up* poses of compound **6a** will also benefit from the cancelation of certain contributions to the binding free energy. The binding affinities were estimated for 100 snapshots evenly taken along the last 5 ns of the trajectories, which should suffice to obtain stable estimates of the predicted binding affinity [63]. The results point out that the *down* pose is the preferred binding mode for **6a** by nearly 1 kcal/mol, as the average binding affinities estimated for the *down* and *up* poses amount to −7.2 and −6.3 kcal/mol, respectively.

Further support to the *down* binding mode was provided by time-dependent QM/MM calculations carried out to determine the change in the oscillator strength of the first allowed excited state, a property that is directly related to the integral of the absorption band [64]. Compared to the average value of the oscillator strength obtained for the

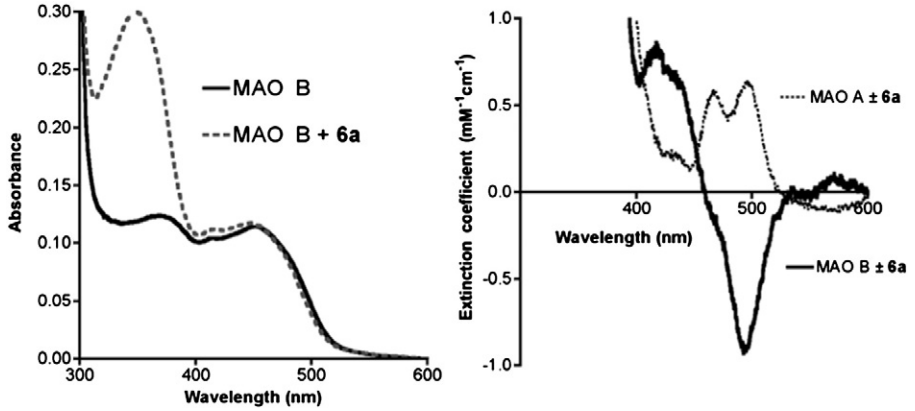

Fig. 4. Comparison of the spectral changes for **6a** binding in MAO A and MAO B. (Left) MAO B (9.4 μM) alone (solid line) or with 10 μM **6a**. (Right) Difference spectra for the MAO–**6a** complex minus MAO alone: MAO A (dotted line, data from Fig. 2) or MAO B (solid line).

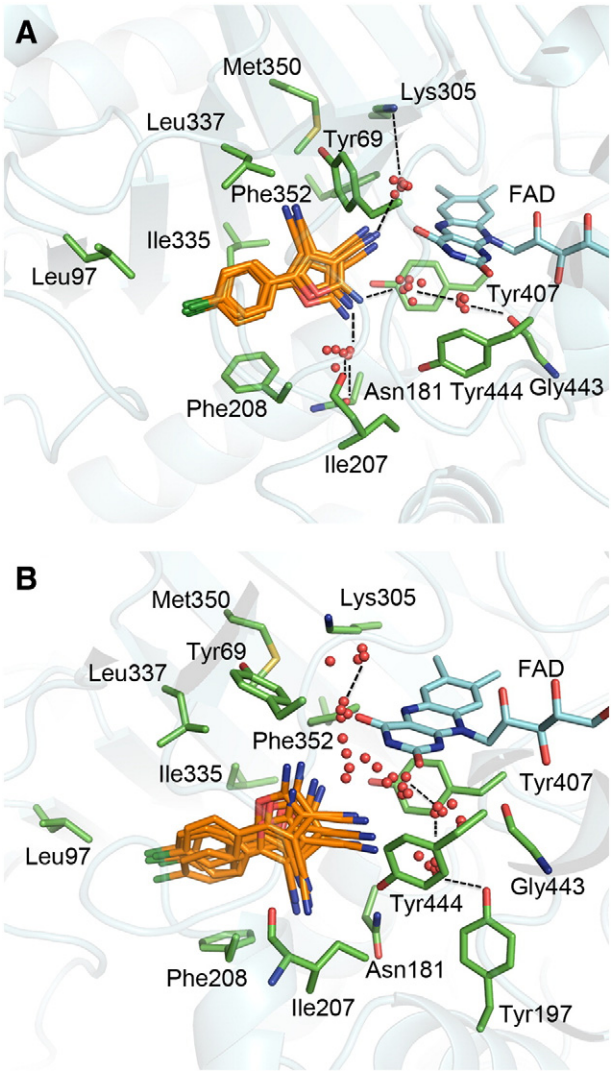

Fig. 5. Representation of the two binding modes (A: *down*; B: *up*) found in MD simulations for **6a** (shown as orange sticks) bound to the oxidized form of MAO A (selected residues shown as green sticks, the flavin cofactor as blue sticks and the backbone as light blue ribbon). Water molecules involved in hydrogen bonding are shown as red spheres. The plot shows the position of ligand and water molecules collected at 20, 22, 24, 26, 28 and 30 ns.

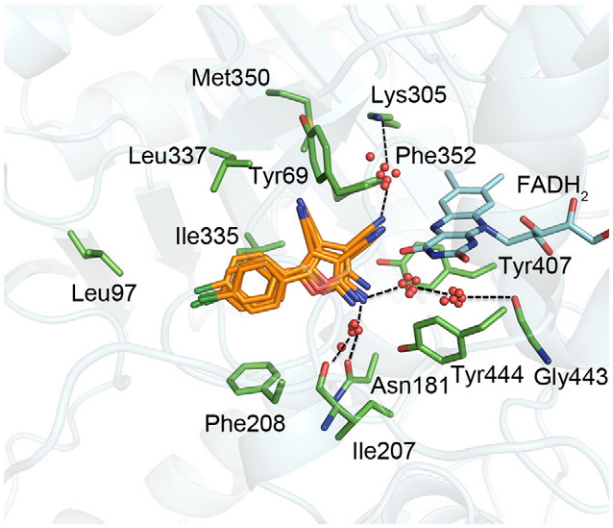

Fig. 6. Representation of the binding mode found in the MD simulation for **6a** (carbon atoms shown as orange sticks) bound to reduced MAO A (selected residues shown as green sticks, the flavin cofactor as blue sticks and the backbone as light blue ribbon). Water molecules involved in hydrogen bonding are shown as red spheres. The plot shows the position of ligand and water molecules collected at 20, 22, 24, 26, 28 and 30 ns.

unliganded enzyme (0.266 ± 0.004), the results obtained for the inhibitor in the *down* orientation indicate an increase in the oscillator strength of 0.008, which is in agreement with the increased absorbance observed experimentally for **6a** (see Fig. 2). In contrast, the same calculations for the *up* orientation showed no significant change (the oscillator strength was altered by less than 0.001), which is in agreement with the displacement of the inhibitor from the flavin cofactor found in MD simulations.

3.7. Molecular modeling: binding to the reduced MAO A

Docking studies were also performed to explore the binding mode of compound **6a** to the reduced form of MAO A. In this case, a single orientation was found for the inhibitor in the 25 best-scored poses taken from 100 independent docking runs (Fig. 6). This binding mode mimics the essential features of the *down* pose found for the oxidized enzyme (compare Figs. 5A and 6).

The structural integrity of the docked pose was explored by means of a 30 ns MD simulation of the complex between reduced MAO A and **6a**. The simulation yielded a stable trajectory, as noted in the stability of the positional RMSD for the residues in the binding site (around 1.7 Å; Fig. S5 in Supporting information). After 11 ns, the inhibitor was slightly shifted and adopted an orientation which remained stable along the rest of the trajectory. The amino group forms water-assisted hydrogen bonds with Asn181 and the flavin O4 atoms, and the nitrile group on C4 fills the lipophilic pocket defined by Tyr69, Ile335, Leu337, Met350 and Phe352. On the other hand, the nitrile unit at C3 forms a water-mediated hydrogen bond with Lys305. It is worth noting that this nitrile group is also hydrogen bonded to the flavin NH unit (average distance of 3.0 ± 0.2 Å). This binding mode can thus justify the experimental finding that **6a** favors full reduction of the flavin (see above) through the hydrogen bond formed by the nitrile group on C3.

4. Discussion

The pharmacological data determined for the carbonitrile-furan derivatives confirmed the suitability of the phenylfuran scaffold for the design of reversible MAO inhibitors. The properties of the aryl substituents play only a moderate effect on the inhibitory potency, and their influence is clearly less relevant than the presence of the nitrile units bound to the aminofuran moiety. Thus, whereas the IC50 values determined for the membrane-bound human MAO A for **6a–c** vary from 0.10 to 0.29 μM, monocarbonitriles are less potent by a factor varying from 4.5 (**5a**) to 41 (**5c**). More importantly, the presence of the nitrile groups is crucial for modulating the selectivity of the compounds. Thus, whereas dicarbonitriles are 11–73-fold more potent inhibitors of MAO A, type **5** compounds were nearly equally effective against the two MAO isoforms.

These findings suggest that the dicarbonitrile aminofuran moiety is crucial for the MAO A selectivity of type **6** compounds. Indeed, molecular modeling studies point out that both the amino and the nitrile unit on C4 provide anchoring points that keep the inhibitor tightly bound in the substrate cavity: i) the nitrile group fills a pocket defined by residues Tyr69, Leu337, Met350 and Phe352, and ii) the amino group participates in a network of water-mediated hydrogen bonds. This binding mode allows us to rationalize the lower inhibitory potency of the monocarbonitrile type **5** compounds (with K_i values between 2 and 7.5 μM compared to values of 0.02–0.10 μM for type **6** compounds; see Table 1), as the absence of the nitrile group on C4 eliminates one

of the anchoring points, thus weakening the interaction with residues at the substrate cavity. Likewise, it also justifies the similar potency of compounds **8** (K_i = 0.17 μM) and **6a** (K_i = 0.10 μM), as the structure of the former should preserve the formation of the same pattern of interactions found for dicarbonitrile compounds.

The binding mode of compound **6a** also provides a basis to rationalize the larger inhibitory potency toward MAO A compared to MAO B. Thus, the replacement of Asn181 in MAO A by Cys172 in MAO B would alter the network of water-mediated hydrogen bonds formed by the furan amino group. On the other hand, the replacement of Ile335 in MAO A by Tyr326 in MAO B should introduce severe clashes with the chlorophenyl ring and with the nitrile group at C4, which necessarily must alter the binding mode. To confirm the effect of these mutations on the binding mode of compound **6a**, a 30 ns MD simulation was run for the complex between **6a** and MAO B. The results revealed a dramatic alteration in the binding mode, because the inhibitor penetrates deeper in the substrate cavity, so that the aminofuran ring fills the cage defined by Tyr407 and Tyr444 below the flavin ring (see Fig. S6 in Supporting information). In fact, the binding mode mimics the orientation found for mofegiline upon binding to human MAO B [65] (see Fig. S7 in Supporting information).

Finally, the binding mode proposed for **6a** places the nitrile on C3 in the proximity of the flavin N5 atom, which disrupts the shell of hydrating water molecules around the flavin cofactor. This feature appears to be responsible for the distinct spectral changes observed for dicarbonitriles. First, the increase in absorbance at around 500 nm found for **6a** is in agreement with the enhanced oscillator strength predicted by time-dependent QM/MM calculations. Second, the nitrile group on C3 is capable of forming a hydrogen bond with the NH unit of the reduced flavin, thus explaining the experimental finding that **6a** favors full reduction of MAO A. Finally, since the charge distribution of the furan ring is not significantly altered by the electronic influence of the aryl substituents, these trends should be common to type **6** compounds, as found experimentally (see above).

To the best of our knowledge, only one previous study has examined the potential role of nitrile groups in the inhibition of MAO. In such study, the authors examined the inhibition of MAO B by a series of C4-subtituted phthalonitriles and a series of homologs lacking the nitrile units [66]. It was found that the nitrile unit was a requirement for high binding affinity to both MAO A and MAO B. However, phthalonitriles were found to be selective reversible inhibitors toward MAO B, in contrast to the selective MAO A inhibition found for dicarbonitrile aminofuran compounds here. The different MAO selectivity is even more surprising when one realizes that the *ortho* arrangement of the nitrile groups is a common structural feature exhibited by both phthalonitriles and dicarbonitrile aminofuran compounds (Fig. S8 in Supporting information). Though the replacement of the benzene ring in phthalonitriles by the furan moiety in type **6** compounds may modulate the fitting to the substrate cavity of the two MAO isoforms, we suggest that the specific pattern of interactions conferred by the nitrile at C4 and the amino group of the dicarbonitrile derivatives is responsible for the selective inhibition of MAO A.

Summing up, this study highlights the synergistic effect played by nitrile and amino groups in assisting the preferential binding of type **6** compounds to MAO A and to interpret their pharmacological and spectral properties, including the experimentally observed differences in binding to the oxidized and reduced forms of the enzyme during turnover [67,68]. In particular, the MAO A selective inhibition is assisted by the interactions formed with Asn181, while its replacement by Cys172 (in conjunction with the steric clash due to the mutation of Ile335 by Tyr326) contributes to the weakened potency against MAO B. Thus, the ability to consider the substitution of Asn181 in MAO A by Cys172 in MAO B and the corresponding alteration of the network of interactions formed with nitrile and amino groups offers promise for the rational design of selective MAO inhibitors.

Acknowledgements

C. Curutchet is acknowledged for insightful comments on the QM/MM calculations. This work was supported by the Spanish Ministerio de Innovación y Ciencia (SAF2011-27642), the Xarxa de Recerca en Química Teòrica I Computacional (XRQTC), Institució Catalana de Recerca i Estudis Avançats (ICREA) and the Generalitat de Catalunya (2009-SGR00249). J.J-J. thanks the Instituto de Salud Carlos III for PFIS fellowship FI10/00292. CM thanks FCT, Ministério da Ciência, Tecnologia e Ensino Superior of Portugal for her PhD grant SFRH/BD/17577/2004. DBS thanks FCT, Ministério da Ciência, Tecnologia e Ensino Superior of Portugal, for his grant from project PTDC/SAU-NEU/64151/2006. RRR thanks the Biochemical Society for a Guildford Bench Methodology Fund award. MEM and RRR thank COST Action D34 for funding short-term scientific missions. The collaboration was facilitated by COST Action D34, and is continued under COST Action CM1103 "Structure-based drug design for diagnosis and treatment of neurological diseases: dissecting and modulating complex function in the monoaminergic systems of the brain". Computational facilities provided by the Centre de Serveis Acadèmics i Científics de Catalunya (CESCA) are acknowledged.

Appendix A. Supplementary data

Supplementary data to this article can be found online at http://dx.doi.org/10.1016/j.bbapap.2013.11.003. The Supporting Information file includes details of the chemical synthesis and characterisation of the compounds and eight supplementary data figures as mentioned in the text, including an overlay of the binding modes found in MD simulations for **6a** bound to MAO A and MAO B.

References

[1] H.-P. Volz, C.H. Gleiter, Monoamine oxidase inhibitors — a perspective on their use in the elderly, Drugs Aging 13 (1998) 341–355.
[2] L.W. Elmer, J.M. Bertoni, The increasing role of monoamine oxidase type B in Parkinson's disease, Expert. Opin. Pharmacother. 9 (2009) 2759–2772.
[3] M.B.H. Youdim, D. Edmondson, K.F. Tipton, The therapeutic potential of monoamine oxidase inhibitors, Nat. Rev. Neurosci. 7 (2006) 295–309.
[4] P. Riederer, W. Danielczyk, E. Grünblatt, Monoamine oxidase-B inhibition in Alzheimer's disease, Neurotoxicology 25 (2004) 271–277.
[5] J. Wouters, F. Moreau, G. Evrard, J.-J. Koenig, S. Jegham, P. George, F. Durant, A reversible monoamine oxidase A inhibitor, beflotaxone: structural approach of its mechanism of action, Bioorg. Med. Chem. 7 (1999) 1683–1693.
[6] P.H. Yu, Pharmacological and clinical implications of MAO-B inhibitors, Gen. Pharmacol. 25 (1994) 1527–1539.
[7] W. Maruyama, Y. Akao, M.C. Carrillo, K. Kitani, M.B.H. Youdim, M. Naoi, Neuroprotection by propargylamines in Parkinson's disease. Suppression of apoptosis and induction of prosurvival genes, Neurotoxicol. Teratol. 24 (2002) 675–682.
[8] O. Bar-Am, O. Weinreb, T. Amit, M.B.H. Youdim, Regulation of Bcl-2 family proteins, neurotrophic factors, and APP processing in the neurorescue activity of propargylamine, FASEB J. 19 (2005) 1899–1901.
[9] H. Yi, W. Maruyama, Y. Akao, T. Takahashi, K. Iwasa, M.B.H. Youdim, M. Naoi, N-propargylamine protects SH-SY5Y cells from apoptosis induced by an endogenous neurotoxin, *N*-methyl(R)salsolinol, through stabilization of mitochondrial membrane and induction of anti-apoptotic Bcl-2, J. Neural Transm. 113 (2006) 21–32.
[10] M.B.H. Youdim, Y.S. Bakhle, Monoamine oxidase: isoforms and inhibitors in Parkinson's disease and depressive illness, Br. J. Pharmacol. 147 (2006) S287–S296.
[11] O. Curet, G. Damoiseau, N. Aubin, N. Sontag, V. Roxel, F.X. Jarreau, Befloxatone, a new reversible and selective monoamine oxidase-A inhibiotr. I. Biochemical profile, J. Pharmacol. Exp. Ther. 277 (1996) 253–264.
[12] U. Bonnet, Moclobemide: therapeutic use and clinical studies, CNS Drug Rev. 9 (2003) 97–140.
[13] S. Valente, S. Tomassi, G. Tempera, S. Saccoccio, E. Agostinelli, A. Mai, Novel reversible monoamine oxidase a inhibitors: highly potent and selective 3-(1H-pyrrol-3-yl)-2-oxazolidinones, J. Med. Chem. 54 (2011) 8228–8232.
[14] O.M. Aldelhafez, K.M. Amin, H.I. Ali, M.M. Abdalla, R.Z. Batran, Synthesis of new 7-oxocoumarin derivatives as potent and selective monoamine oxidase A inhibitors, J. Med. Chem. 55 (2012) 10424–10436.
[15] C. Binda, P. Newton-Vinson, F. Hubálek, D.E. Edmonson, A. Mattevi, Structure of human monoamine oxidase B, a drug target for the treatment of neurological disorders, Nat. Struct. Biol. 9 (2002) 22–26.
[16] C. Binda, M. Li, F. Hubálek, N. Restelli, D.E. Edmonson, A. Mattevi, Insights into the mode of inhibition of human mitochondrial monoamine oxidase B from high-resolution crystal structures, Proc. Natl. Acad. Sci. U. S. A. 100 (2003) 9750–9755.

[17] C. Binda, F. Hubálek, M. Li, Y. Herzig, J. Sterling, D.E. Edmonson, A. Mattevi, Crystal structures of monoamine oxidase B in complex with four inhibitors of the N-propargylamino-indan class, J. Med. Chem. 47 (2004) 1767–1774.
[18] L. de Colibus, M. Li, C. Binda, A. Lustig, D.E. Edmonson, A. Mattevi, Three-dimensional structure of human monoamine oxidase A (MAO A): relation to the structures of rat MAO A and human MAO B, Proc. Natl. Acad. Sci. U. S. A. 102 (2005) 12684–12689.
[19] S.Y. Son, J. Ma, Y. Kondou, M. Yoshimura, E. Yamashita, T. Tsukihara, Structure of human monoamine oxidase A at 2.2-Å resolution: the control of opening the entry for substrates/inhibitors, Proc. Natl. Acad. Sci. U. S. A. 105 (2008) 5739–5744.
[20] C. Binda, M. Aldeco, A. Mattevi, D.E. Edmonson, Interactions of monoamine oxidases with the antiepileptic drug zonisamide: specificity of inhibition and structure of the human monoamine oxidase B complex, J. Med. Chem. 54 (2011) 909–912.
[21] M.D. Houslay, K.D. Tipton, The reaction pathway of rat liver monoamine oxidase, Biochem. J. 135 (1973) 173–186.
[22] A.N. Davison, The mechanism of the irreversible inhibition of rat-liver monomine oxidase by iproniazid, Biochem. J. 67 (1957) 316–322.
[23] Z.B. Ramadan, P. Dostert, K.F. Tipton, Some peculiar aspects of monoamine oxidase inhibition, Neurobiology 7 (1999) 159–174.
[24] Z.B. Ramadan, M.L. Wrang, K.F. Tipton, Species differences in the selective inhibition of monoamine oxidase (1-methyl-2-phenylethyl)hydrazine and its potentiation by cyanide, Neurochem. Res. 32 (2007) 1783–1790.
[25] J.L. Marco, C. de los Ríos, A.G. García, M. Villarroya, M.C. Carreiras, C. Martins, A. Eleuterio, A. Morreale, M. Orozco, F.J. Luque, Synthesis, biological evaluation and molecular modelling of diversely functionalized heterocyclic derivatives as inhibitors of acetylcholinesterase/butyrylcholinesterase and modulators of Ca^{2+} channels and nicotinic receptors, Bioorg. Med. Chem. 12 (2004) 2199–2218.
[26] M.C. Carreiras, A. Eleutério, C. Dias, M.A. Brito, D. Brites, J. Marco-Contelles, E. Gómez-Sánchez, Synthesis and Friedländer reactions of 5-amino-4-cyano-1,3-oxazoles, Heterocycles 71 (2007) 2249–2262.
[27] C. Martins, A. Eleutério, M.C. Carreiras, A. Samadi, E. Soriano, R. Léon, J. Marco-Contelles, A reinvestigation of the acid-promoted heterocyclization of 2-(2-oxo-2-arylethyl) malononitriles in the presence of amines, Mol. Divers. 13 (2009) 459–468.
[28] W. Weyler, J.I. Salach, Purification and properties of mitochondrial monoamine-oxidase type-A from human placenta, J. Biol. Chem. 260 (1985) 3199–3207.
[29] A.K. Tan, W. Weyler, J.I. Salach, T.P. Singer, Differences in substrate specificities of monoamine oxidase A from liver and placenta, Biochem. Biophys. Res. Commun. 181 (1991) 1084–1088.
[30] A.P.B. Vintem, N.T. Price, R.B. Silverman, R.R. Ramsay, Mutation of surface cysteine 374 to alanine in monoamine oxidase A alters substrate turnover and inactivation by cyclopropylamines, Bioorg. Med. Chem. 13 (2005) 3487–3495.
[31] M. Zhou, Z. Diwu, N. Panchuk-Voloshina, R.P. Haugland, A stable nonfluorescent derivative of resorufin for the fluorometric determination of trace hydrogen peroxide: applications in detecting the activity of phagocyte NADPH oxidase and other oxidases, Anal. Biochem. 253 (1997) 162–168.
[32] G.R. McDonald, A. Olivieri, R.R. Ramsay, A. Holt, On the formation and nature of the imidazoline I2 binding site on human monoamine oxidase-B, Pharmacol. Res. 62 (2010) 475–488.
[33] T.Z.E. Jones, P. Fleming, C.J. Eyermann, M.B. Gravestock, R.R. Ramsay, Orientation of oxazolidinones in the active site of monoamine oxidase, Biochem. Pharmacol. 70 (2005) 407–416.
[34] R.R. Ramsay, D.B. Hunter, Inhibitors alter the spectrum and redox properties of monoamine oxidase A, Biochim. Biophys. Acta, Proteins Proteomics 1601 (2002) 178–184.
[35] R.M.G. Hynson, S.M. Kelly, N.C. Price, R.R. Ramsay, Conformational changes in monoamine oxidase A in response to ligand binding or reduction, Biochim. Biophys. Acta 1672 (2004) 60–66.
[36] S.Y. Son, J. Ma, Y. Kondou, M. Yohimura, E. Yamashita, T. Tsukihara, Structure of human monomamine oxidase A at 2.2-Å resolution: the control of opening the entry for substrates/inhibitors, Proc. Natl. Acad. Sci. U. S. A. 105 (2008) 5739–5744.
[37] V. Hornak, R. Abel, A. Okur, B. Strockbine, A. Roitberg, C. Simmerling, Comparison of multiple amber force fields and development of improved protein backbone parameters, Proteins 65 (2006) 712–725.
[38] S.D. Morley, M. Afshar, Validation of an empirical RNA–ligand scoring function for fast flexible docking using RiboDock, J. Comput. Aided Mol. Des. 18 (2004) 189–208.
[39] X. Barril, R.E. Hubbard, S.D. Morley, Virtual screening in structure-based drug discovery, Mini-Rev. Med. Chem. 4 (2004) 779–791.
[40] I. Bolea, J. Juárez-Jiménez, C. De los Rios, M. Chioua, R. Pouplana, F.J. Luque, M. Unzeta, J. Marco-Contelles, A.S. Samadi, Synthesis, biological evaluation and molecular modelling of donepezil and N-([5-(benzyloxy)-q-methyl-1H-indol-2-yl)methyl]-N-methylprop-2-yn-1-amine hybrids, as new multipotent cholinesterase/monoamine oxidase inhibitors for the treatment of Alzheimer's disease, J. Med. Chem. 54 (2011) 8251–8270.
[41] D.A. Case, T.A. Darden, T.E. Cheatham III, C.L. Simmerling, J. Wang, R.E. Duke, R. Luo, K.M. Merz, D.A. Pearlman, M. Crowley, R.C. Walker, W. Zhang, B. Wang, S. Hayik, A. Roitberg, G. Seabra, K.F. Wong, F. Paesani, X. Wu, S. Brozell, V. Tsui, H. Gohlke, L. Yang, C. Tan, J. Mongan, V. Hornak, G. Cui, P. Beroza, D.H. Mathews, C. Schafmeister, W.S. Ross, P.A. Kollman, Amber, Version 9, University of California, San Francisco, CA, 2006.
[42] J. Wang, R.M. Wolf, J.W. Caldwell, P.A. Kollman, D.A. Case, Development and testing of a general amber force field, J. Comput. Chem. 25 (2004) 1157–1174.
[43] C.I. Bayly, P. Cieplak, W.D. Cornell, P.A. Kollman, A well-behaved electrostatic potential based method using charge restraints for deriving atomic charges, J. Phys. Chem. 97 (1993) 10269–10280.
[44] M.J. Frisch, G.W. Trucks, H.B. Schlegel, G.E. Scuseria, M.A. Robb, J.R. Cheeseman Jr., J.A. Montgomery, T. Vreven, K.N. Kudin, J.C. Burant, J.M. Millam, S.S. Iyengar, J. Tomasi, V. Barone, B. Mennucci, M. Cossi, G. Scalmani, N. Rega, G.A. Petersson, H. Nakatsuji, M. Hada, M. Ehara, K. Toyota, R. Fukuda, J. Hasegawa, M. Ishida, T. Nakajima, Y. Honda, O. Kitao, H. Nakai, M. Klene, X. Li, J.E. Knox, H.P. Hratchian, J.B. Cross, C. Adamo, J. Jaramillo, R. Gomperts, R.E. Stratmann, O. Yazyev, A.J. Austin, R. Cammi, C. Pomelli, J.W. Ochterski, P.Y. Ayala, K. Morokuma, G.A. Voth, P. Salvador, J.J. Dannenberg, V.G. Zakrzewski, S. Dapprich, A.D. Daniels, M.C. Strain, O. Farkas, D.K. Malick, A.D. Rabuck, K. Raghavachari, J.B. Foresman, J.V. Ortiz, Q. Cui, A.G. Baboul, S. Clifford, J. Cioslowski, B.B. Stefanov, G. Liu, A. Liashenko, P. Piskorz, I. Komaromi, R.L. Martin, D.J. Fox, T. Keith, M.A. Al-Laham, C.Y. Peng, A. Nanayakkara, M. Challacombe, P.M.W. Gill, B. Johnson, W. Chen, M.W. Wong, C. Gonzalez, J.A. Pople, Gaussian 03, Revision B.01, Gaussian, Inc., Pittsburgh PA, 2003.
[45] W.L. Jorgensen, J. Chandrasekhar, J.D. Madura, R. Impey, M.L. Klein, Comparison of simple potential functions for simulating liquid water, J. Chem. Phys. 79 (1983) 926–935.
[46] M. Naim, S. Bhat, K.N. Rankin, S. Dennis, S.F. Chowdhury, I. Siddiqi, P. Drabik, T. Sulea, C.I. Bayly, A. Jakalian, E.O. Purisima, Solvated interaction energy (SIE) for scoring protein–ligand binding affinities.1. Exploring the parameter space, J. Chem. Inf. Model. 47 (2007) 122–133.
[47] Q. Cui, T. Sulea, J.D. Schrag, C. Munger, M.-N. Hung, M. Naim, M. Cygler, E.O. Purisima, Molecular dynamics-solvated interaction energy studies of protein–protein interactions: the MP1–p14 scaffolding complex, J. Mol. Biol. 379 (2008) 787–802.
[48] J.P. Götze, C. Greco, R. Mitrić, V. Bonačić-Koutecký, P. Saalfrank, BLUF hydrogen network dynamics and UV/Vis spectra: a combined molecular dynamics and quantum chemical study, J. Comput. Chem. 33 (2012) 2233–2242.
[49] T. Yanai, D.P. Tew, N.C. Handy, A new hybrid exchange-correlation functional using the Coulomb-attenuating method (CAM-B3LYP), Chem. Phys. Lett. 393 (2004) 51–57.
[50] J. Wouters, Structural aspects of monoamine oxidase and its reversible inhibition, Curr. Med. Chem. 5 (1998) 137–162.
[51] F. Gentili, N. Pizzinat, C. Ordener, S. Marchal-Victorion, A. Maurel, R. Hofmann, P. Renard, P. Delagrange, M. Pigini, A. Parini, M. Gianella, 3-[5-(4,5-Dihydro-1*H*-imidazol-2-yl)-furan-2-yl]phenylamine (amifuraline), a promising reversible and selective peripheral MAO-A inhibitor, J. Med. Chem. 49 (2006) 5578–5586.
[52] P. Dostert, M.S. Benedetti, K.F. Tipton, Interactions of monoamino oxidase with substrates and inhibitors, Med. Chem. Res. 9 (1989) 45–89.
[53] B. Quirico, R. Jakob-Rotne, R. Kettler, S. Röver, M. Scalone, Design and synthesis of novel and potent monoamine oxidase inhibitors, Chimia 49 (1995) 381–385.
[54] R. Silvestri, G. La Regina, G. De Martino, M. Artico, O. Befani, M. Palumbo, E. Agostinelli, P. Turini, Simple, potent, and selective pyrrole inhibitors of monoamine oxidase types A and B, J. Med. Chem. 46 (2003) 917–920.
[55] C. Altomare, S. Cellamare, L. Summo, M. Catto, A. Carotti, U. Thull, P.-A. Carrupt, B. Testa, H. Stoeckli-Evans, Inhibition of monoamino oxidase-B by condensed pyridazines and pyrimidines: effects of lipophilicity and structure–activity relationships, J. Med. Chem. 41 (1998) 3812–3820.
[56] L. Pisani, G. Muncipinto, T.F. Miscioscia, O. Nicolotti, F. Leonetti, M. Catto, C. Caccia, P. Salvati, R. Soto-Otero, E. Mendez-Alvarez, Celine Passeleu, A. Carotti, Discovery of a novel class of potent coumarin monoamine oxidase B inhibitors: development and biopharmacological profiling of 7-[(3-chlorobenzyl)oxy]-4-[(methylamino)methyl]-2H-chromen-2-one methanesulfonate (NW-1772) as a highly potent, selective, reversible, and orally active monoamine oxidase B inhibitor, J. Med. Chem. 52 (2009) 6685–6706.
[57] J. Wang, D.E. Edmondson, Do monomeric vs dimeric forms of MAO-A make a difference? A direct comparison of the catalytic properties of rat and human MAO-A's, J. Neural Transm. 114 (2007) 721–724.
[58] D.E. Edmonson, C. Binda, J. Wang, A.K. Upadhyay, A. Mattevi, Molecular and mechanistic properties of the membrane-bound mitochondrial monoamine oxidases, Biochemistry 48 (2009) 4220–4230.
[59] A.K. Upadhyay, J. Wang, D.E. Edmonson, Comparison of the structural properties of the active site cavities of human and rat monoamine oxidase A and B in their soluble and membrane-bound forms, Biochemistry 47 (2008) 526–536.
[60] R. Apostolov, Y. Yonezawa, D.M. Standley, G. Kikugawa, Y. Takano, H. Nakamura, Membrane attachment facilitates ligand access to the active site in monoamine oxidase A, Biochemistry 48 (2009) 5864–5873.
[61] R.M.G. Hynson, J. Wouters, R.R. Ramsay, Monoamine oxidase A inhibitory potency and flavin perturbation are influenced by different aspects of pirlindole inhibitor structure, Biochem. Pharmacol. 65 (2003) 1867–1874.
[62] C. Binda, M. Li, F. Hubalek, N. Restelli, D.E. Edmondson, Insights into the mode of inhibition of human mitochondrial monoamine oxidase B from high-resolution crystal structures, J. Med. Chem. 100 (2003) 9750–9755.
[63] M.A. Lill, J.J. Thompson, Solvent Interaction Energy calculations on molecular dynamics trajectories: increasing the efficiency using systematic frame selection, J. Chem. Inf. Model. 51 (2011) 2680–2689.
[64] B. Valeur, Molecular Fluorescence: Principles and Applications, Wiley-VCH, 2001. 20–33.
[65] E.M. Milczek, D. Bonivento, C. Binda, A. Mattevi, I.A. McDonald, D.E. Edmonson, Structural and mechanistic studies of mofegiline inhibition of recombinant human monoamine oxidase B, J. Med. Chem. 51 (2008) 8019–8026.
[66] C.I. Manly-King, J.J. Bergh, J.P. Petzer, Monoamine oxidase inhibition by C4-substituted phthalonitriles, Bioorg. Chem. 40 (2012) 114–124.
[67] A.K. Tan, R.R. Ramsay, Substrate-specific enhancement of the oxidative half-reaction of monoamine-oxidase, Biochemistry 32 (1993) 2137–2143.
[68] R.R. Ramsay, A. Olivieri, A. Holt, An improved approach to steady-state analysis of monoamine oxidases, J. Neural Transm. 118 (2011) 1003–1019.

Supporting Information

Exploring the structural basis of the selective inhibition of Monoamino oxidase A by carbonitrile aminoheterocycles: Role of Asn181 and Ile335 validated by spectroscopic and computational studies

Jordi Juárez-Jiménez[a], Eduarda Mendes[b], Carles Galdeano[a], Carla Martins[b], Daniel B. Silva[b], José Marco-Contelles[c], Maria do Carmo Carreiras[b], F. Javier Luque[a] and Rona R. Ramsay[d,*]

[a] *Department of Physical Chemistry, Faculty of Pharmacy and Institute of Biomedicine (IBUB), University of Barcelona, Avda. Prat de la Riba 171, 08921 Santa Coloma de Gramenet, Spain*

[b] *iMed.UL - Research Institute for Medicines and Pharmaceutical Sciences, Faculty of Pharmacy, University of Lisbon, Avda. Prof. Gama Pinto, 1649-003 Lisbon, Portugal*

[c] *Laboratorio de Radicales Libres y Química Computacional, Instituto de Química Orgánica General, Consejo Superior de Investigaciones Científicas, c/. Juan de la Cierva 3, 28006 Madrid, Spain*

[d] *School of Biology, Biomedical Sciences Research Complex, University of St Andrews, St Andrews, KY16 9ST, UK*

Chemistry

The synthesis of mono- and dicarbonitrile aminoheterocycles followed the procedure described in previous studies [1-3]. The series includes compounds containing a single nitrile unit in *ortho* to the amino group in 5-amino-2-alkyl(aryl)oxazole-4-carbonitriles (**1**-**4**; Scheme 1).

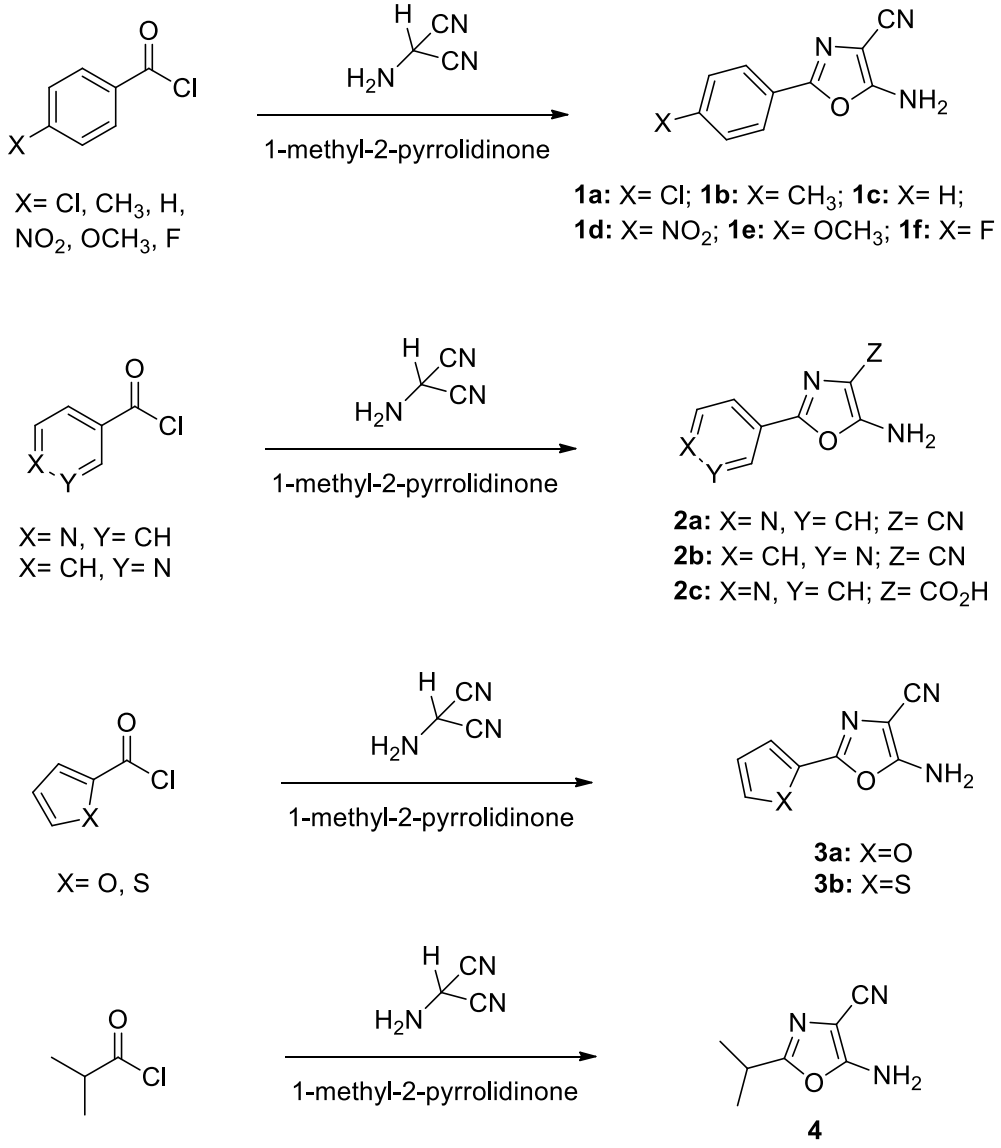

Scheme 1. Synthesis of 5-amino-2-alkyl(aryl)oxazole-4-carbonitriles (**1-4**) [1, 2].

The influence of the heteroaromatic ring and of the attachment of an additional nitrile was explored by synthesizing 2-amino-5-phenylfuran-3-carbonitriles (**5**), 2-amino-5-phenylfuran-3,4-dicarbonitriles (**6**) and 2-amino-1,5-diphenyl-1*H*-pyrrole-3-carbonitriles (**7**) (Scheme 2).

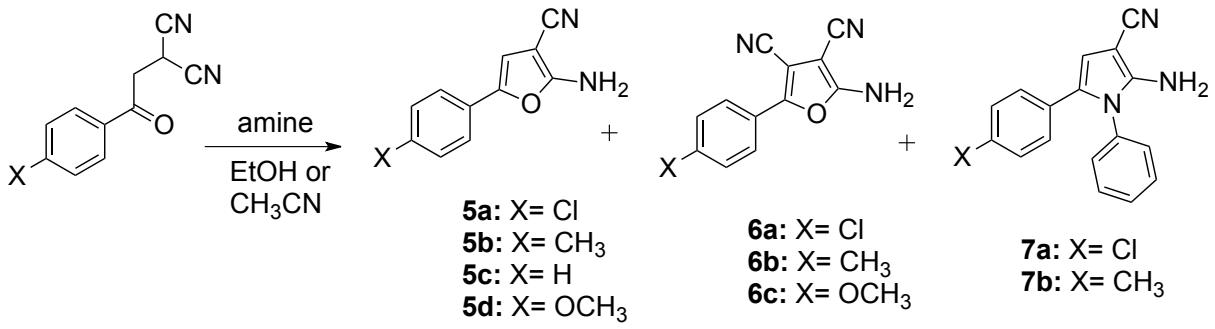

Scheme 2. Syntheses of the 2-amino-5-phenylfuran-3-carbonitriles (**5**), 2-amino-5-phenylfuran-3,4-dicarbonitriles (**6**), and 2-amino-1,5-diphenyl-1*H*-pyrrole-3-carbonitriles (**7**) [3].

Compound **5d** was synthesized following the protocol described in previous studies [4, 5]. To gain further insight into the role of the nitrile group attached to positions 3 and 4 in mediating the inhibitory activity of type **6** compounds, which were the most potent in the series (see below), carbonitrile **8** was also synthesized to facilitate comparison with the structurally related compounds **5a** and **6a** (Scheme 3).

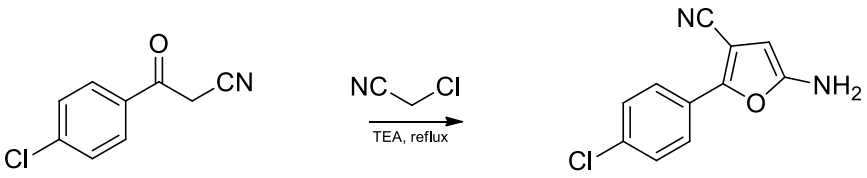

8

Scheme 3. Synthetic route adopted to derive the 5-amino-2-phenylfuran-3-carbonitrile (**8**).

Attempts were made to synthesize a derivative that replaces the 4-chlorophenyl present in **8** with 4-methoxyphenyl in order to explore the effect of electron delocalization on the inhibitory activity, but they were unsuccessful. Keeping in mind the low yield (~ 11%) found in the synthesis of **8**, it seems that changing the electron-withdrawing character of chlorine by the electro-donating methoxy prevented the synthesis of the desired compound.

Chemical synthesis of compounds 5d and 8

*2-amino-5-(4-methoxyphenyl)-furan-3-carbonitrile (**5d**)*

To a suspension of 2-[2-(4-methoxy-phenyl)-2-oxo-ethyl]-malonitrile (259.4 mg, 1.21 mmols), prepared as described in [6], in glacial acetic acid (2.5 mL) was added conc. hydrogen chloride (0.3 mL). The mixture was stirred at room temperature for 2 h., and then poured into water. The resultant precipitation was filtrated, washed with water and ethanol, and dried under reduced pressure to afford **5d** (41 %, 105 mg). Mp. 216-218 ºC; IR (ATR) ν3409 (NH), 3321, 2204 (CN), 1642, 1593, 1578, 1507, 1452, 1441, 1298, 1242, 1178, 1068, 1025, 826, 797, 698, 574; ^{1}H-RMN (400 MHz, $CDCl_3$) δ 7.42 (d, J = 8.8 Hz, 2H, H-2, H-6), 6.90 (d, J = 8.4 Hz, 2H, H-3, H-5), 6.38 (s, 1H, H-4

furan), 4.74 (br s, 2H, NH_2), 3.83 (s, 3H, -OMe). ^{13}C NMR (101 MHz, $(CD_3)_2SO$): 163.7 (C4-Ph), 158.1 (C-2 furan), 142.0 (C-5 furan), 123.7 (C-2, C-6 Ph), 122.3 (C-1 Ph), 116.2 (CN), 114.4 (C-3, C-5 Ph), 104.5 (C4-furan), 65.9 (C-3 furan), 55.2 (- OMe); HRMS (ESI): Calcd. for $C_{12}H_{10}N_2O_2$: 214.0815; found: 214.0815.

*5-amino-2-(4-chlorophenyl)furan-3-carbonitrile (**8**)*

To a suspension of 4-chlorobenzoylacetonitrile (1.065 g; 5.75 mmol) in triethylamine (15 mL) was added dropwise chloroacetonitrile (0.42 mL, 6.57 mmol) over an ice bath. The mixture was refluxed for 64 h. After the end of reaction, cold water was poured down over the mixture and the suspension was extracted with dichloromethane (5x50 mL). The organic phase was dried with Na_2SO_4 and the solvent was evaporated to dryness. The solid residue was fractionated by column chromatography using hexane-ethyl acetate 15% as eluent, affording a dark orange solid (11 %; 143 mg); Mp. Dec.143-146º C;IR (KBr) ν3436 (NH), 3345, 2922, 2228 (CN), 1888, 1639, 1576, 1553, 1487, 1412, 1394, 1283, 1167, 1096, 1010, 1001, 821, 768, 728, 706, 666, 502, 481 cm^{-1}; ^1H NMR (400 MHz, $CDCl_3$) δ 7.79 (d, J = 8.8 Hz, 2H, H-2, H-6 Ph), 7.40 (d, J = 8.8 Hz, 2H, H-3, H-5 Ph), 5.50 (s, 1H, H-4 furan), 4.02 (s, 2H; NH_2); ^{13}C NMR (101 MHz, $CDCl_3$) δ 154.2 (C-5 furan), 150.4 (C-2 furan), 134.5 (C-4 Ph), 129.2 (C-3, C-5 Ph), 126.8 (C-1 Ph), 125.4 (C-2, C-6 Ph), 115.3 (CN), 93.3 (C-3 furan), 88.0 (C-4 furan); MS (EI+) *m/z*: 220 [(^{37}Cl)M^+, 33], 218 [(^{35}Cl)M^+, 100), 183 (M-Cl^+, 15), 174 (14), 163 (7), 139 (36), 128 (13), 111 [M-$C_5H_3N_2O^+$, 30], 105 (11), 101 (5), 85 (7), 75 (26), 63 (7), 52 (14); MS (ESI) *m/z:* 243 [(^{37}Cl)M+Na]$^+$, 241 [(^{35}Cl) M+Na]$^+$; 221 [(^{37}Cl)M+H]$^+$, 219 [(^{35}Cl)M+H]$^+$; HRMS(ESI): Calcd for $C_{11}H_7N_2OCl$: 218.0247; found: 218.0257.

[1] J.L. Marco, C. de los Ríos, A.G. García, M. Villarroya, M.C. Carreiras, C. Martins, A. Eleuterio, A. Morreale, M Orozco, F.J. Luque, Synthesis, biological evaluation and molecular modelling of diversely functionalized heterocyclic derivatives as inhibitors of acetylcholinesterase/butyrylcholinesterase and modulators of Ca2+ channels and nicotinic receptors, Bioorg. Med. Chem. 12 (2004) 2199–2218.

[2] M.C. Carreiras, A. Eleutério, C. Dias, M.A. Brito, D. Brites, J. Marco-Contelles, E. Gómez-Sánchez, Synthesis and Friedländer reactions of 5-amino-4-cyano-1,3-oxazoles, Heterocycles 71 (2007) 2249–2262.

[3] C. Martins, A. Eleutério, M.C. Carreiras, A. Samadi, E. Soriano, R. Léon, J. Marco- Contelles, A reinvestigation of the acid-promoted heterocyclization of 2-(2-oxo-2- arylethyl)malononitriles in the presence of amines, Mol. Divers. 13 (2009) 459–468.

[4] Y. Maeda, M. Nakano, H. Sato, Y. Miyazaki, S. L. Schweiker, J. L. Smith, A. T. Truesdale, 4-Acylamino-6-arylfuro[2,3-d]pyrimidines: potent and selective glycogen synthase kinase-3 inhibitors, Bioorg. Med. Chem. Lett. 14 (2004) 3907-3911.

[5] Y. Miyazaki, S. Matsunaga, J. Tang, Y. Maeda, M. Nakano, R. J. Philippe, M. Shibahara, W. Liu, H. Sato, L. Wang, R. T. Nolte, novel 4-amino-furo[2,3-d]pyrimidines as Tie-2 and VEGFR2 dual inhibitors, Bioorg. Med. Chem. Lett. 15 (2005) 2203-2207.

[6] M. Nakano, Y. Maeda, (2005) WO 2005/061516 A1.

Figure S1. Charge distribution (determined at the HF/6-31G(d) level) of compounds **6a** and **6c.**

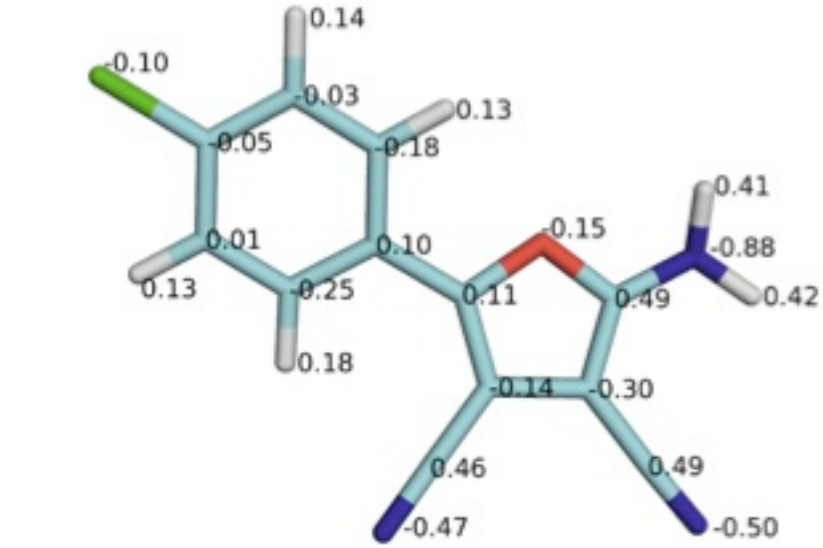

6a

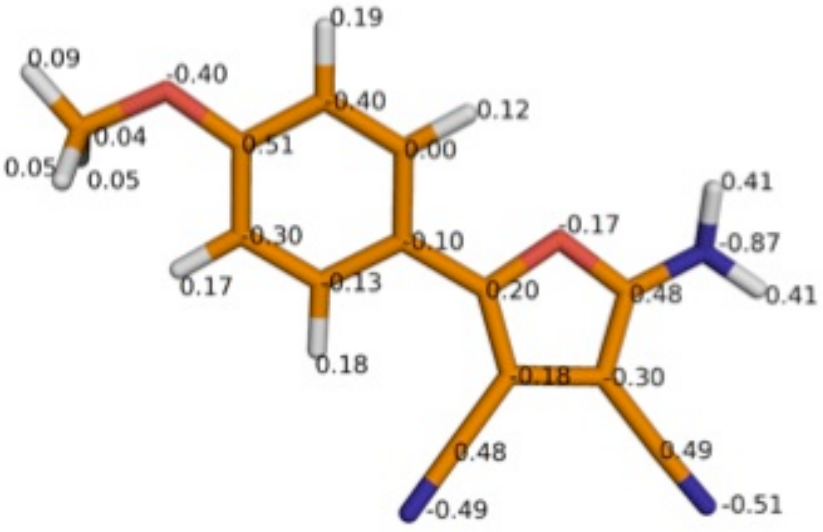

6c

Figure S2. Lineweaver-Burk plot illustration of the competitive inhibition of MAO A by **6c.** The enzyme was added last to the cuvette to ensure initial rate data and analysed using non-linear regression with the Michaelis-Menten equation. K_i values were the mean of 3 experiments. The linearised plot of a single experiment is shown here to illustrated the competitive pattern of inhibition.

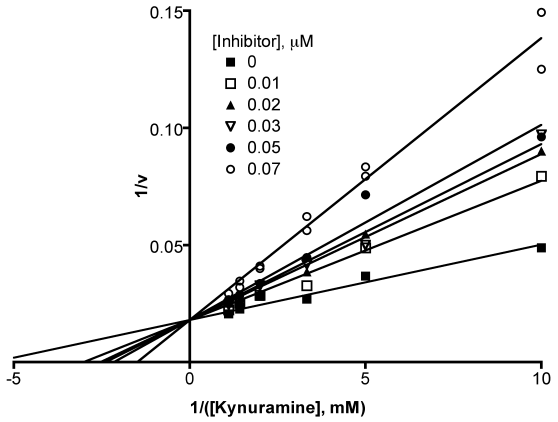

Figure S3. Time evolution of the potential energy (x 10^3 kcal/mol) and root-mean square deviation (Å; backbone in black, residues in binding site in red, and ligand in green) for the complex between compound **6a** in the *down* orientation and the oxidized enzyme.

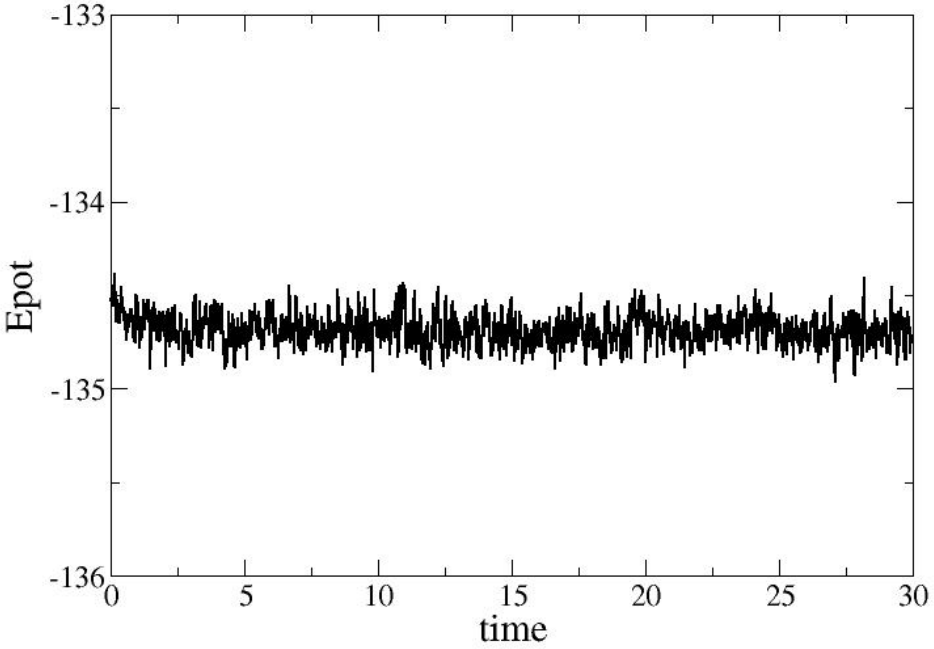

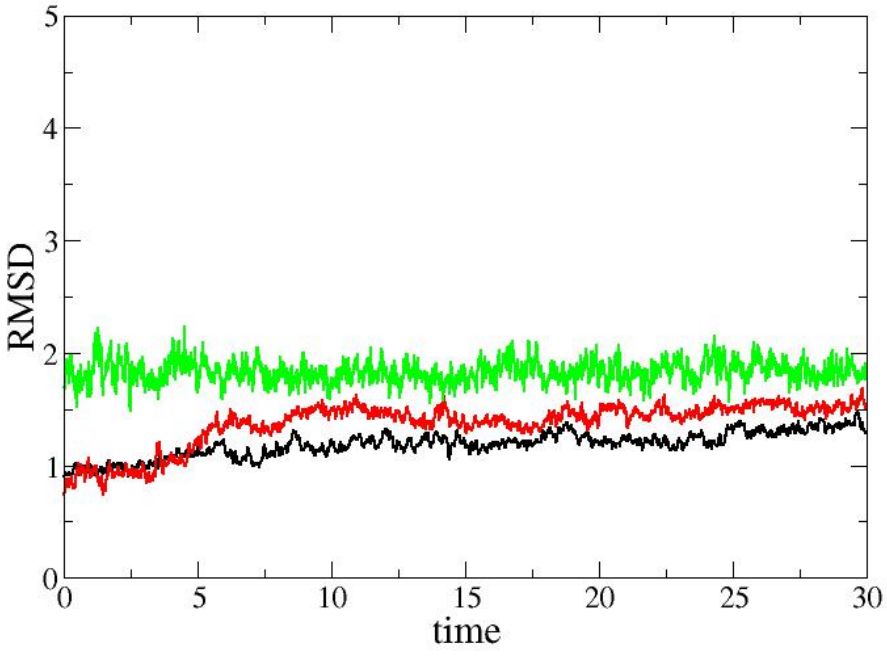

Figure S4. Time evolution of the potential energy (x 10^3 kcal/mol) and root-mean square deviation (Å; backbone in black, residues in binding site in red, and ligand in green) for the complex between compound **6a** in the *up* orientation and the oxidized enzyme.

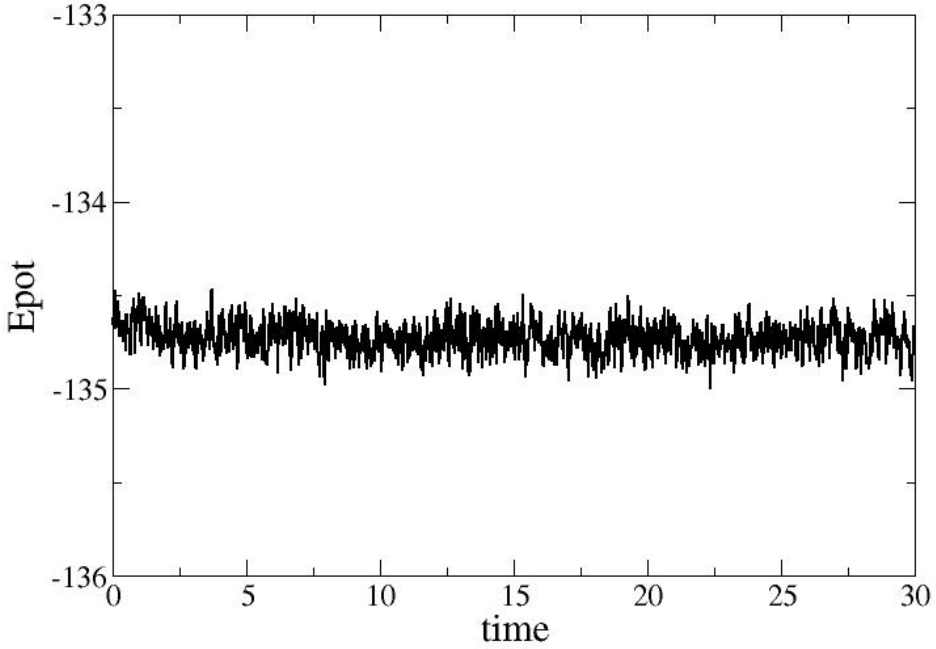

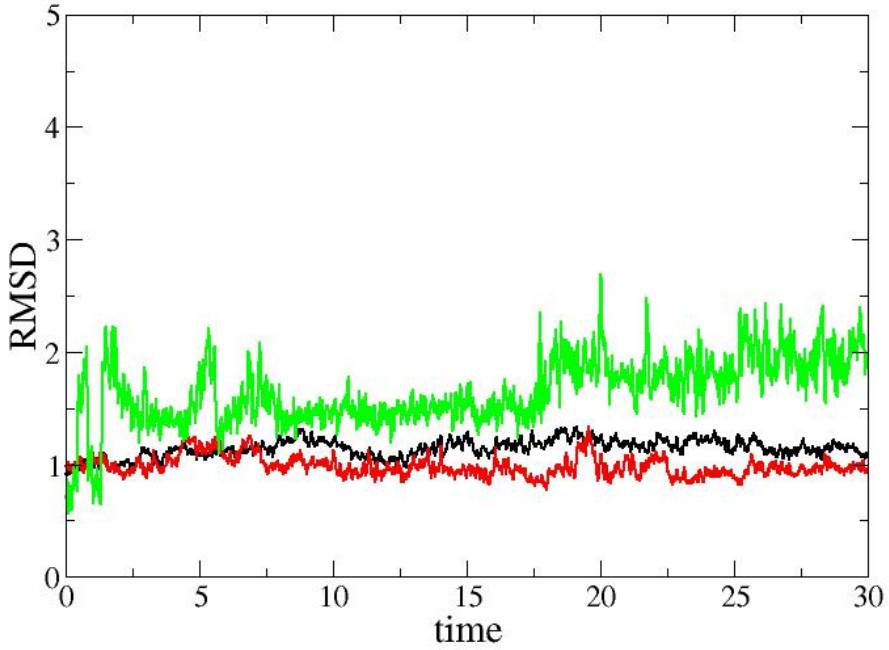

Figure S5. Time evolution of the potential energy (x 10^3 kcal/mol) and root-mean square deviation (Å; backbone in black, residues in binding site in red, and ligand in green) for the complex between compound **6a** and the reduced enzyme.

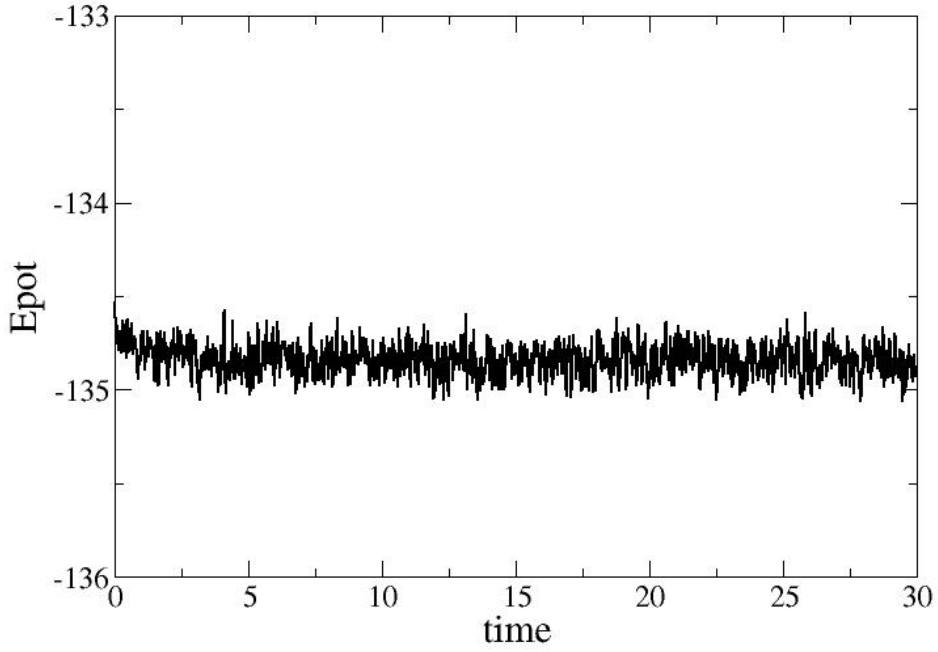

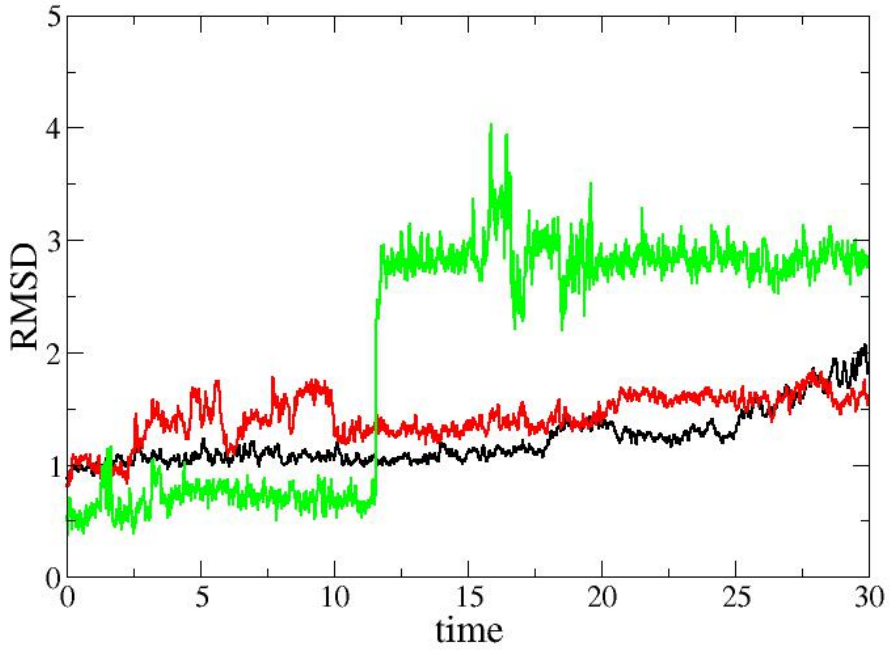

Figure S6. Representation of the binding modes found in MD simulations for **6a** bound to MAO A and MAO B. The inhibitor is shown as orange and yellow sticks in MAO A and MAO B, respectively. Common residues to the two binding cavities are shown as blue sticks, whereas the mutated residues are shown as green and magenta sticks for MAO A and MAO B, respectively. The flavin cofactor is shown as blue sticks and the backbone as light blue ribbon. For the sake of clarity, only mutated residues are labelled.

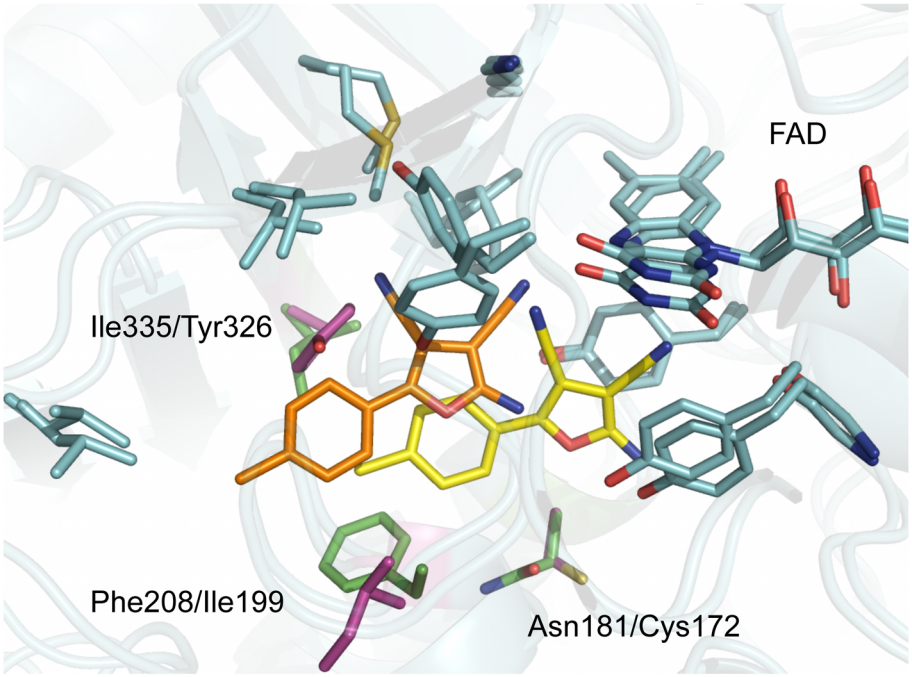

Figure S7. Superposition of the binding mode found in MD simulations for **6a** (yellow sticks) bound to MAO B and the adduct formed by mofegiline (magenta sticks) in MAO B as found in the X-ray crystallographic structure (PBD entry 2VZ2). The flavin cofactor is shown as blue (MD simulation) and magenta (X-ray structure) sticks.

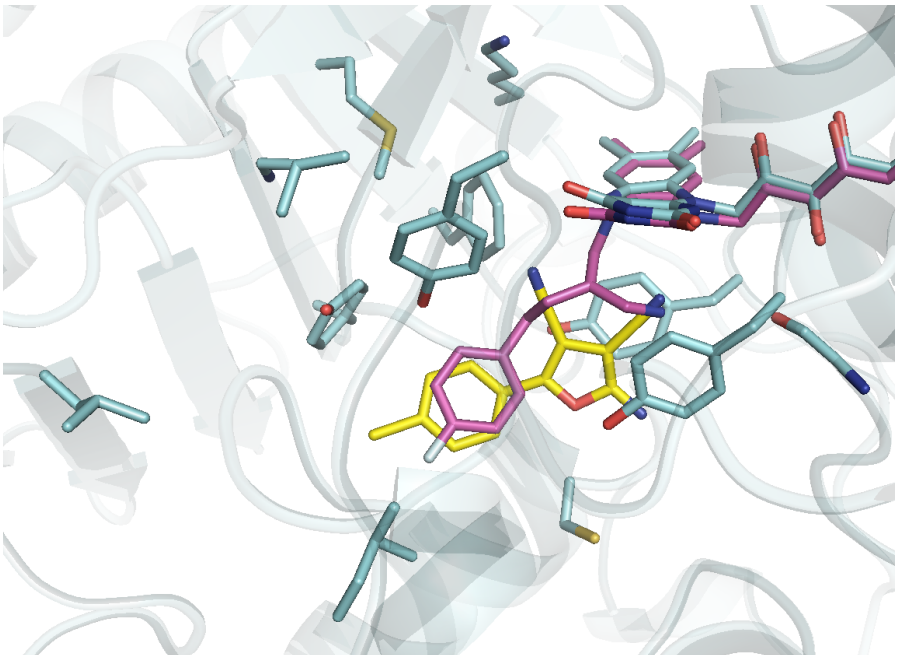

Figure S8. Schematic representation of C4-substituted phthalonitriles (green; ref. 66) and dicarbonitriles aminofurans (blue; this work).

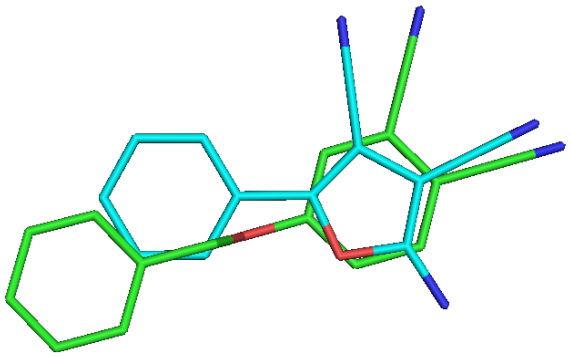

4.3 Publicación:

Synthesis and Multitarget Biological Profiling of a Novel Family of Rhein Derivatives As Disease-Modifying Anti-Alzheimer Agents.

Journal of Medicinal Chemistry

(*J. Med. Chem.* **2011,** 57, 2549-2567**)**

Elisabet Viayna[†§], Irene Sola[†§], Manuela Bartolini[&], Angela De Simone[=], Cheril Tapia-Rojas[±], Felipe G. Serrano[±], Raimon Sabaté[‡×], Jordi Juárez-Jiménez[‡§], Belén Pérez[∞], F. Javier Luque[‡§], Vincenza Andrisano[=], M. Victòria Clos[∞], Nibaldo C. Inestrosa[±] and Diego Muñoz-Torrero[†§].

[†]Laboratori de Química Farmacéutica (Unitat Associada al CSIC), Facultat de Farmàcia, Universitat de Barcelona, Av. Joan XXIII 27-31, E-08028, Barcelona Spain.

[‡]Departament de Fisicoquímica, Facultat de Farmàcia), Universitat de Barcelona, E-08028, Barcelona, Spain.

[§]Institut de Biomedicina (IBUB), Universitat de Barcelona, E-08028, Barcelona, Spain.

[&]Departament of Pharmacy and Biotechnology, Alma Mater Studiorum University of Bologna, via Belmeloro 6, I-40126 Bologna, Italy.

[=]Department for Life Quality Studies, University of Bologna, Corso d'Augusto 237, I-47921, Rimini, Italy.

[±]Centro de Envejecimiento y Regeneración (CARE) Departamento de Biología Celular y Molecular, Facultad de Ciencias Biológicas, Pontificia Universidad Católica de Chile, Alameda 340, 8331150 Santiago, Chile.

[×]Institut de Nanociència i Nanotecnologia (IN^2UB), Universitat de Barcelona, E-08028, Barcelona, Spain.

[∞]Departament de Farmacologia, de Terapéutica i de Toxicologia, Institut de Neurociències, Universitat Autònoma de Barcelona, E-08193 Bellaterra, Barcelona, Spain.

Journal of Medicinal Chemistry

Article

pubs.acs.org/jmc

Synthesis and Multitarget Biological Profiling of a Novel Family of Rhein Derivatives As Disease-Modifying Anti-Alzheimer Agents

Elisabet Viayna,[†,‡,◆] Irene Sola,[†,‡] Manuela Bartolini,[§] Angela De Simone,[∥] Cheril Tapia-Rojas,[⊥] Felipe G. Serrano,[⊥] Raimon Sabaté,[#,∇] Jordi Juárez-Jiménez,[‡,#] Belén Pérez,[○] F. Javier Luque,[‡,#] Vincenza Andrisano,[∥] M. Victòria Clos,[○] Nibaldo C. Inestrosa,[⊥] and Diego Muñoz-Torrero*[,†,‡]

[†]Laboratori de Química Farmacèutica (Unitat Associada al CSIC), Facultat de Farmàcia, Universitat de Barcelona, Av. Joan XXIII 27-31, E-08028 Barcelona, Spain

[‡]Institut de Biomedicina (IBUB), Universitat de Barcelona, E-08028 Barcelona, Spain

[§]Department of Pharmacy and Biotechnology, Alma Mater Studiorum University of Bologna, Via Belmeloro 6, I-40126 Bologna, Italy

[∥]Department for Life Quality Studies, University of Bologna, Corso d'Augusto 237, I-47921 Rimini, Italy

[⊥]Centro de Envejecimiento y Regeneración (CARE), Departamento de Biología Celular y Molecular, Facultad de Ciencias Biológicas, Pontificia Universidad Católica de Chile, Alameda 340, 8331150 Santiago, Chile

[#]Departament de Fisicoquímica, Facultat de Farmàcia, Universitat de Barcelona, E-08028 Barcelona, Spain

[∇]Institut de Nanociència i Nanotecnologia (IN^{2}UB), Universitat de Barcelona, E-08028 Barcelona, Spain

[○]Departament de Farmacologia, de Terapèutica i de Toxicologia, Institut de Neurociències, Universitat Autònoma de Barcelona, E-08193 Bellaterra, Barcelona, Spain

Supporting Information

ABSTRACT: We have synthesized a family of rhein–huprine hybrids to hit several key targets for Alzheimer's disease. Biological screening performed in vitro and in *Escherichia coli* cells has shown that these hybrids exhibit potent inhibitory activities against human acetylcholinesterase, butyrylcholinesterase, and BACE-1, dual Aβ42 and tau antiaggregating activity, and brain permeability. Ex vivo studies with the leads (+)- and (−)-**7e** in brain slices of C57bl6 mice have revealed that they efficiently protect against the Aβ-induced synaptic dysfunction, preventing the loss of synaptic proteins and/or have a positive effect on the induction of long-term potentiation. In vivo studies in APP-PS1 transgenic mice treated ip for 4 weeks with (+)- and (−)-**7e** have shown a central soluble Aβ lowering effect, accompanied by an increase in the levels of mature amyloid precursor protein (APP). Thus, (+)- and (−)-**7e** emerge as very promising disease-modifying anti-Alzheimer drug candidates.

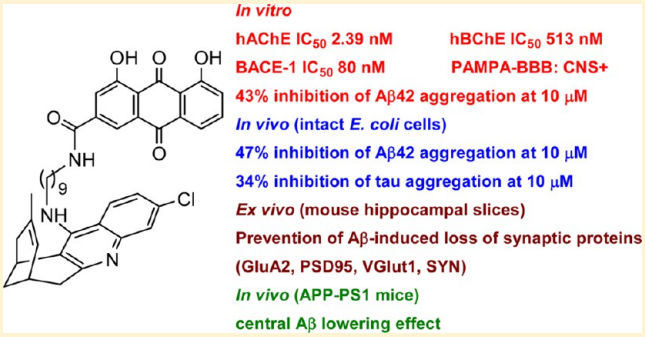

INTRODUCTION

Alzheimer's disease (AD), the most common type of dementia, is associated with ever increasing unacceptable personal and economic costs owing to its high prevalence, mortality and, worryingly, to the elusiveness of efficacious drugs.[1]

There has been a general consensus that β-amyloid peptide (Aβ) is the main culprit of a straightforward cascade process that begins with its increased formation by processing of the amyloid precursor protein (APP) by β-secretase (BACE-1) and γ-secretase and aggregation into oligomers and fibrils. This follows with a series of downstream events including synaptic dysfunction, tau protein hyperphosphorylation and aggregation, neuroinflammation and oxidative stress, and eventually leads to neuronal death and neurotransmitter deficits.[2,3] Because these deficits account for the cognitive and functional decline, which are the main diagnostic criteria for AD, the first and so far the sole marketed anti-Alzheimer drugs, namely the acetylcholinesterase (AChE) inhibitors tacrine, donepezil, rivastigmine, and galantamine and the NMDA receptor antagonist memantine, were developed to hit those neurotransmitter deficits, particularly cholinergic and glutamatergic, but are regarded as merely symptomatic.

In the past years, there has been an intense research activity for developing drugs able to tackle the underlying mechanism of AD by hitting Aβ formation or aggregation or, to a minor extent, other downstream targets.[4] However, despite the acute need and the hopes raised for the discovery of effective disease-modifying anti-Alzheimer drugs, a number of clinically advanced Aβ-directed drug candidates have recently failed to show efficacy over placebo or they have been discontinued because of their toxicity. The efficacy issues of these drug candidates have been ascribed, at least partly, to the fact that AD pathology might not

Received: November 26, 2013
Published: February 25, 2014

 © 2014 American Chemical Society

result from a straightforward process but from a robust network of interconnected events, whereby Aβ aggregation is not *the* cause but just *one* of the causes, together with tau hyperphosphorylation and aggregation, synaptic dysfunction, or neuroinflammation.[5] This novel conception of AD would allow explaining why modulation of a single target might be ineffective, whereas simultaneous modulation of several targets of the network, including Aβ, holds promise for deriving the eagerly awaited effective disease-modifying anti-Alzheimer drugs.[6−10]

In the past years, many research groups have pursued the development of multitarget anti-Alzheimer drugs as an advantageous approach over multitarget multidrug strategies (drug cocktails and fixed-dose combinations).[11−15] Multitarget compounds have been usually designed to hit at least Aβ formation and aggregation and AChE activity,[16] especially prompted by the finding that AChE can bind Aβ, thereby promoting its aggregation and increasing its neurotoxicity.[17−19] The recognition site of Aβ within AChE is the so-called peripheral anionic site (PAS), and it is located at the entrance of a 20 Å deep narrow gorge that leads to the catalytic anionic site (CAS).[20] The design of inhibitors able to simultaneously reach both sites of AChE, i.e., dual binding site AChE inhibitors (AChEIs), emerged some years ago as a promising source of multitarget anti-Alzheimer compounds, inasmuch as they should be endowed at least with potent anticholinesterase and Aβ antiaggregating effects.[21−29] Moreover, the multitarget profile of these compounds can be enlarged by introducing pharmacophoric moieties that are also suitable for separate interactions with additional targets of interest other than AChE and Aβ. Two major challenges in the design and therapeutic potential of multitarget anti-Alzheimer agents are the choice of the targets to be hit and the potency of the compounds at the different targets. Indeed, it must be recognized that the timing of the different events in the progression of AD can be overlooked when selecting the biological targets to be hit. However, this issue will remain very difficult to be addressed until a precise description of the sequence of events that give rise to the neuropathogenesis of AD becomes available. On the other hand, a multitarget action will be only effective when balanced activities are achieved at the different targets, which is also not an easy task.

Recently, the hydroxyanthraquinone derivatives emodin, **1**, and PHF016, **2** (Chart 1), have been shown to inhibit tau aggregation in vitro with IC_{50} values in the low micromolar range.[30,31] The structurally related compound rhein, **3** (Chart 1), is a natural product found in the traditional Chinese herbal medicine rhubarb, which is well tolerated in humans.[32] In the form of a doubly acetylated prodrug, diacerein, it is used for the treatment of arthritis. Even though rhein has been reported to be essentially inactive as inhibitor of AChE[33,34] and of Aβ aggregation,[35] its aromatic rings seem appropriate for establishing π-stacking interactions with the characteristic aromatic residue at the PAS of AChE, namely Trp286 (human AChE (hAChE) numbering). Moreover, its hydroxyanthraquinone scaffold might confer tau antiaggregating properties to its derivatives. Thus, we inferred that combination in a hybrid of the hydroxyanthraquinone system of rhein with a moiety with high affinity for the CAS of AChE might result in a multitarget compound of interest for the treatment of AD, which should be endowed at least with AChE, Aβ aggregation, and tau aggregation inhibitory activities.

Chart 1. Structures of Tau Aggregation Inhibitors 1 and 2, Rhein and Huprine Y

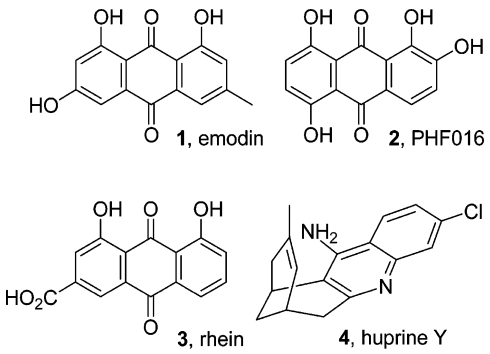

Herein, we describe the synthesis, biological profiling, and investigation of the mechanism of action of a novel family of multitarget hybrid compounds, which are composed of a unit of rhein attached, through different linkers, to a unit of huprine Y, **4** (Chart 1), a high affinity AChE's CAS inhibitor, developed in our group some years ago.[36−39] The biological profiling includes (i) the in vitro evaluation of the inhibitory activities against hAChE, human butyrylcholinesterase (hBChE), hAChE-induced, and self-induced Aβ aggregation and human BACE-1 (hBACE-1), (ii) the evaluation of the Aβ and tau antiaggregating activities in intact *Escherichia coli* cells overexpressing these peptides, (iii) the evaluation of the protective effects on synaptic integrity from Aβ-induced alterations by measuring the induction of long-term potentiation and levels of synaptic proteins in hippocampal slices of 2-month-old C57bl6 mice, (iv) the in vivo evaluation of the central Aβ lowering effect in APP-PS1 mice, and (v) the assessment of their brain permeability using an artificial membrane model. Furthermore, kinetic and molecular modeling studies have been performed to shed light on the binding mode of these compounds with two of their main targets, namely AChE and BACE-1.

RESULTS AND DISCUSSION

Chemistry. The linkage between the huprine and rhein moieties was envisioned at one end through an N−C bond from the exocyclic amino group of huprine Y, as in a recently reported family of huprine-based dual binding site AChEI hybrids[40] and at the other end through an amide bond from the carboxylic acid of rhein. Such linkages have proven to be chemically stable at physiological pH up to 4 days at 37 °C in a structurally related family of hybrid compounds.[41] Chains from 5 to 11 methylene groups were considered for the linkers (in hybrids **7a−g**, Scheme 1) to afford suitable distances between huprine and rhein moieties to achieve a dual site binding to AChE and to explore the effect of the length of the linker in a target with a large binding site such as BACE-1. The incorporation of an aromatic ring within the linker, i.e., a 1,4-phenylene-bis(methylene) linker (in hybrid **7h**, Scheme 1), was also envisaged to explore potential additional interactions with the targets, i.e., interactions with midgorge residues of AChE or disruption of protein−protein interactions in the case of Aβ and tau aggregation.

Rhein−huprine hybrids **7a−h** were synthesized through a three- or four-step sequence from readily available racemic or enantiopure huprine Y, (±)-, (−)-, or (+)-**4**,[36−38] and commercial rhein, **3** (Scheme 1). Alkylation of racemic huprine Y with commercial or described ω-bromoalkanenitriles[42−44] in the presence of KOH in DMSO afforded nitriles (±)-**5a−g** in moderate yields (25−87%). Nitrile (±)-**5h** was prepared in 72% overall yield by condensation of racemic huprine with 4-cyanobenzaldehyde followed by $NaBH_3CN$ reduction of the resulting imine. $LiAlH_4$ reduction of nitriles (±)-**5a−h** gave in excellent yields amines (±)-**6a−h**, which were reacted with the

dx.doi.org/10.1021/jm401824w | J. Med. Chem. 2014, 57, 2549−2567

Scheme 1. Synthesis of the Rhein−Huprine Hybrids 7a−h

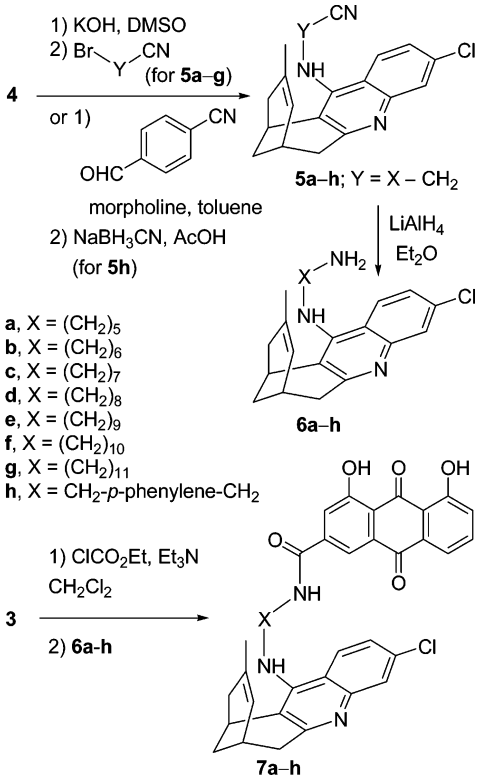

mixed anhydride formed from rhein and ethyl chloroformate to afford in 9−27% yield the rhein−huprine hybrids (±)-7**a**−**h**.

In the light of the biological results obtained for the racemic hybrids 7**a**−**h**, we decided to synthesize the two enantiomers of the most interesting racemic hybrid, namely 7**e**. Thus, enantiopure (−)- and (+)-7**e** were prepared from (−)- and (+)-**4** (>99% ee) using the same methodology.

The novel rhein−huprine hybrids were fully characterized in the form of hydrochloride salts through their spectroscopic data (IR, ^{1}H, and ^{13}C NMR), HRMS and elemental analysis. Hydrochloride salts were also used for the activity profile assessment.

In Vitro Biological Profiling of Racemic Rhein−Huprine Hybrids. *Inhibition of Human Cholinesterases and Molecular Modeling Study of hAChE Inhibition.* Apart from AChE, BChE is another target of interest in the search for anti-Alzheimer drugs, inasmuch as this enzyme exerts a compensatory effect in response to a greatly decreased AChE activity in central nervous system (CNS) when AD progresses.[45] Accordingly, the inhibitory activity of the novel rhein−huprine hybrids and of the reference compounds rhein and huprine Y against human recombinant AChE (hAChE) and human serum BChE (hBChE) was evaluated by the method of Ellman et al.[46]

All the racemic hybrids, (±)-7**a**−**h**, turned out to be potent inhibitors of hAChE, with IC_{50} values in the low nanomolar range (Table 1), even though both the length of the linker and the presence of an aromatic ring in the linker seemed to have only a moderate effect on the hAChE inhibitory activity. Indeed, the inhibitory potency gradually decreased from the shortest pentamethylene-linked hybrid (±)-7**a** to the longest undecamethylene homologue, (±)-7**g** (16-fold less potent), whereas introduction of an aromatic ring within the linker seemed to be detrimental for hAChE inhibitory activity, hybrid (±)-7**h** being 12-fold less potent than hybrid (±)-7**b** with a similar tether length. Hybrid (±)-7**a**, the most potent hAChEI of the series (IC_{50} 1.07 nM), was equipotent to the parent racemic huprine Y [(±)-**4**]. In agreement with the reported data,[33,34] the parent rhein, **3**, was found essentially inactive against hAChE.

The binding mode of the rhein−huprine hybrids to AChE was explored for compound 7**h**, taking advantage of the reduced flexibility imposed by the aromatic ring. Docking studies showed that (−)-7**h** binds much more favorably than (+)-7**h**, as expected from the fact that the eutomer of huprines for AChE inhibition is the levorotatory (7*S*,11*S*)-enantiomer, (−)-**4**. The results show that (−)-7**h** may fit the hAChE gorge (Figure 1), placing (i) the huprine moiety in an orientation that perfectly matches the arrangement of (−)-huprine X, the 9-ethyl-analogue of (−)-huprine Y, in the CAS (PDB entry 1E66, Supporting Information Figure S1), and (ii) the hydroxyanthraquinone system of rhein stacked between

Table 1. Inhibitory Activities of the Hydrochlorides of Rhein−Huprine Hybrids and Reference Compounds toward AChE, BChE, BACE-1, and AChE-Induced and Self-Induced Aβ Aggregation and BBB Predicted Permeabilities[a]

compd	hAChE IC_{50} (nM)[b]	hBChE IC_{50} (nM)[b]	hBACE-1 IC_{50} (nM)[b]	hAChE-induced Aβ40 aggregation (% inhib.)[c]	self-induced Aβ42 aggregation (% inhib.)[d]	P_e (10^{-6} cm s^{-1})[e] (prediction)
(±)-7**a**	1.07 ± 0.05	950 ± 30	na[f]	45.0 ± 7.5	38.7 ± 5.0	20.0 ± 1.0 (CNS+)
(±)-7**b**	1.52 ± 0.08	1070 ± 40	na[f]	50.5 ± 8.7	40.8 ± 5.7	nd[g]
(±)-7**c**	3.18 ± 0.16	1460 ± 160	na[f]	52.5 ± 2.9	40.6 ± 1.9	27.5 ± 0.7 (CNS+)
(±)-7**d**	4.36 ± 0.22	350 ± 20	980 ± 170	44.7 ± 8.4	33.1 ± 5.4	22.4 ± 1.3 (CNS+)
(±)-7**e**	3.60 ± 0.21	620 ± 20	120 ± 90	48.7 ± 8.4	38.0 ± 4.6	21.5 ± 0.7 (CNS+)
(+)-7**e**	2930 ± 285	265 ± 21	80 ± 10	36.9 ± 3.4	38.4 ± 5.5	nd[g]
(−)-7**e**	2.39 ± 0.17	513 ± 58	80 ± 10	38.1 ± 0.7	43.2 ± 4.7	nd[g]
(±)-7**f**	7.61 ± 0.45	1100 ± 40	1190 ± 180	29.2 ± 2.4	40.9 ± 4.4	18.1 ± 0.7 (CNS+)
(±)-7**g**	17.4 ± 2.2	645 ± 67	1200 ± 150	38.2 ± 2.6	35.3 ± 4.0	16.4 ± 1.0 (CNS+)
(±)-7**h**	18.2 ± 2.2	510 ± 20	2020 ± 440	35.2 ± 1.8	32.4 ± 3.6	16.3 ± 2.5 (CNS+)
3	>10000	17000 ± 4220	na[h]	nd[g]	nd[g]	2.7 ± 0.1 (CNS±)
(±)-**4**	1.07 ± 0.05	181 ± 15	nd[g]	17.1 ± 4.5	nd[g]	23.8 ± 2.7 (CNS+)
(+)-**4**	321 ± 16	170 ± 17	>5000[i]	9.1 ± 3.6	13.2 ± 1.9	25.4 ± 2.9 (CNS+)
(−)-**4**	0.74 ± 0.06	222 ± 17	>5000[j]	24.7 ± 1.3	11.5 ± 5.2	23.6 ± 1.1 (CNS+)

[a]Values are expressed as mean ± standard error of the mean (SEM) of at least three experiments (n = 3), each performed in duplicate. [b]IC_{50} inhibitory concentration (nM) of human recombinant AChE, human serum BChE, or human recombinant BACE-1. [c]% inhibition with inhibitor at 100 μM, Aβ40 at 230 μM, and hAChE at 2.3 μM. [d]% inhibition with inhibitor at 10 μM and Aβ42 at 50 μM ([Aβ]/[I] = 5/1). [e]Permeability values from the PAMPA-BBB assay. [f]Not active at 1 μM. [g]Not determined. [h]Not active. [i]13.6 ± 2.3% inhibition at 5 μM. [j]14.0 ± 0.1% inhibition at 5 μM.

dx.doi.org/10.1021/jm401824w | J. Med. Chem. 2014, 57, 2549−2567

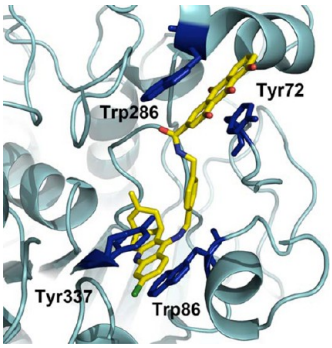

Figure 1. Binding mode of compound (−)-**7h** (shown as yellow sticks) in the AChE gorge.

the aromatic rings of Trp286 and Tyr72 in the PAS, mimicking the arrangement of the tacrine unit of bis(7)-tacrine (PDB entry 2CKM, Supporting Information Figure S2).[47] Even though these findings support the ability of the hybrids to interact simultaneously at both CAS and PAS, the inhibitory potencies in Table 1 suggest that the rhein unit has a weak contribution to the binding, presumably due to the lack of a positive charge that would reinforce the stacking interaction, as compared with the inhibitory potency of bis(7)-tacrine (IC_{50} hAChE 0.81 nM)[48] and huprine−tacrine hybrids (IC_{50} hAChE up to 0.31 nM)[40] and to the lack of specific interactions formed by the polar groups of the hydroxyanthraquinone moiety at the PAS, thereby preventing a net gain in potency compared to huprine Y, (±)-**4**.

All the rhein−huprine hybrids turned out to be selective for hAChE over hBChE inhibition, with selectivities in the range 28−888. However, these hybrids still exhibited a moderately potent hBChE inhibitory activity, with IC_{50} values in the submicromolar to low micromolar range (Table 1). The most potent hBChE inhibitor of the series, (±)-**7d** (IC_{50} = 350 nM), was slightly less potent than the parent huprine (2-fold) but 50-fold more potent than the parent rhein, **3**.

Inhibition of AChE-Induced Aβ Aggregation. The occupancy of the AChE's PAS by the rhein−huprine hybrids, predicted by docking simulations (see above), should result in a hindrance of the interaction of Aβ with AChE and, hence, in a blockade of the Aβ proaggregating action of the enzyme. The inhibitory activity of these hybrids and the parent rhein and huprine Y against the AChE-induced aggregation of Aβ40 was assessed using a thioflavin T-based fluorescent method.[49] Rhein−huprine hybrids exhibited a significant inhibitory activity against the AChE-induced Aβ40 aggregation, exhibiting percentages of inhibition ranging from 29 to 52% at a 100 μM concentration, which are clearly superior to that found for the AChE's CAS inhibitor huprine Y, **4** (Table 1). These activities are similar to those reported for other families of dual binding site AChEIs,[40,50−55] even though more potent inhibitors of the AChE-induced Aβ40 aggregation have been described.[56,57] In agreement with the hypothesis that both inhibitory activities are related to some extent to the ability of interacting with the AChE's PAS, the inhibitory activities of the rhein−huprine hybrids against the AChE-induced Aβ40 aggregation roughly match the SAR trends for hAChE inhibition, i.e., the shorter homologues are the most potent and the presence of a benzene ring in the linker is slightly detrimental for the activity.

Inhibition of Self-Induced Aβ Aggregation. The inhibitory activity of the rhein−huprine hybrids against the spontaneous aggregation of Aβ42 was determined in vitro using a thioflavin T-based fluorometric assay.[58] These compounds exhibit a significant Aβ42 antiaggregating activity, displaying percentages of inhibition in the narrow range 32−41% when tested at a concentration equal to 1/5 of that of Aβ42 ([I] = 10 μM, [Aβ42] = 50 μM), these being clearly more potent than the parent huprine Y (Table 1). Of note, rhein could not be evaluated because of solubility problems under the assay conditions.

Inhibition of Human BACE-1 and Molecular Modeling Study. BACE-1 catalyzes the first and rate-limiting step of the biosynthesis of Aβ from APP, thereby constituting a prime target in the search for disease-modifying anti-Alzheimer drugs.[59,60] Strikingly, a number of dual binding site AChEIs have been found to be potent or moderately potent inhibitors of BACE-1, even if they were not purported to display this activity.[61] In most cases, these compounds inhibit BACE-1 with low micromolar IC_{50} values, as it happens with the prototypic dual binding site AChEI bis(7)-tacrine (IC_{50} 7.5 μM)[62] or with huprine−tacrine heterodimers (IC_{50} 4.9−7.3 μM).[40] However, another dual binding site AChEI with more potent BACE-1 inhibitory activity, i.e., memoquin (IC_{50} 108 nM),[56] has also been reported.

In the light of these results, the novel racemic rhein−huprine hybrids were tested in vitro against human recombinant BACE-1 using a FRET assay.[63] Results clearly showed the importance of the linker chain length. The pentamethylene- to heptamethylene-linked hybrids (±)-**7a**−**c** were inactive for BACE-1 inhibition at a concentration of 1 μM, whereas the longer homologues (±)-**7d**, (±)-**7f**, and (±)-**7g**, as well as (±)-**7h**, containing an aromatic ring in the linker, exhibited a moderately potent BACE-1 inhibitory activity, with IC_{50} values around 1−2 μM (Table 1). Far beyond our expectations, the BACE-1 inhibitory activity in this series peaked for the nonamethylene-linked hybrid (±)-**7e**, with a remarkable IC_{50} value of 120 nM. Thus, (±)-**7e** was roughly equipotent to memoquin,[56] about 50-fold more potent than bis(7)-tacrine[62] and other huprine-based hybrids.[40] Very interestingly, the BACE-1 inhibitory activity of (±)-**7e** seems to be slightly higher than that of the Lilly's BACE-1 inhibitor LY2811376, a very promising anti-Alzheimer drug candidate whose phase I clinical trials were recently discontinued due to toxicity issues unrelated to BACE-1 inhibition,[59] even though a head-to-head test in the same assay conditions would be required to confirm that point. Thus, the combination of huprine Y and rhein in a new hybrid molecule with a proper linker chain led to a significant enlargement of the activity profile, namely the strong inhibitory activity on BACE-1 that is not present in any of the parent compounds.

The preceding findings made it worthwhile to determine the binding mode of the hybrids to BACE-1. In a first step, this was accomplished by examining the druggable pockets present in the enzyme in order to determine their ability to accommodate the huprine and hydroxyanthraquinone moieties (see Experimental Section). Among the seven druggable pockets shared by the four X-ray structures explored with the MDpocket program (PDB entries 1M4H, 1SGZ, 2OHL, and 3CIB), only two of them, namely BS1, which encompasses the catalytic site, and BS2, which includes subsites P5−P7 (Figure S3, Supporting Information), were found to be suitable for binding of the huprine and hydroxyanthraquinone moieties present in hybrids. Furthermore, the distance between the centroids of the most populated clusters of huprine and hydroxyanthraquinone in these pockets was comprised between 7 and 11 Å, thus satisfying the geometrical criteria required for the tether in the rhein−huprine hybrids. Accordingly, docking of (+)-**7h** and (−)-**7h** was performed by exploring the volume defined by both BS1 and BS2 sites. Even though this compound is not the most potent within the series, it was chosen due to the limited number of rotatable

bonds, which thus makes it easier to perform a more exhaustive exploration of the binding mode and examine the potential interaction at the two pockets identified separately for huprine and hydroxyanthraquinone moieties. Calculations led to a clear binding mode, in which the huprine moiety is accommodated at the BS1 pocket, and the hydroxyanthraquinone moiety fills the BS2 site. The structural integrity of this binding mode was supported by the analysis of four independent 50 ns molecular dynamics simulations run for both (+)-**7h** and (−)-**7h** bound to the enzyme (Figure 2). The huprine moiety remains tightly

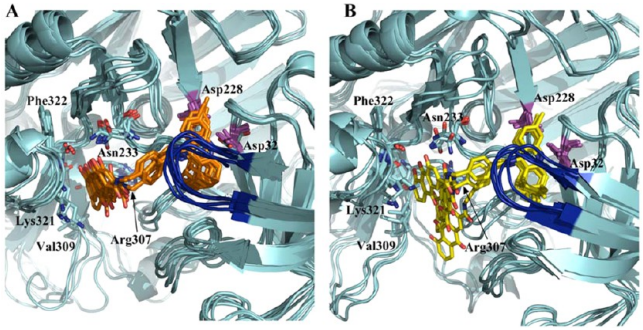

Figure 2. Superposition of the last snapshots sampled in four independent MD simulations of hybrid compounds (A) (+)-**7h** (shown as orange sticks) and (B) (−)-**7h** (shown as yellow sticks) bound to BACE-1 (shown as cyan cartoon). Selected residues that mediate the binding of the hybrids are shown as sticks, and the "flap" loop is shown in blue.

bound to BS1 in all cases, as expected from the electrostatic stabilization between the protonated aminoquinoline system and the catalytic dyad (Asp32 and Asp228), whereas the bicyclic system of the huprine moiety fills the hydrophobic pocket formed by residues Leu30, Phe108, Ile110, and Ile118 from subsites P2 and P3. On the other hand, the hydroxyanthraquinone moiety in (+)-**7h** exhibits a common binding mode, which involves the electrostatic interaction with Lys321, hydrogen bonds with the backbone of Phe322 and the side chain of Asn233, and hydrophobic contacts with Val309. For (−)-**7h**, the results show that, besides the preceding binding mode, the hydroxyanthraquinone moiety can adopt an alternative arrangement, which mainly involves the direct electrostatic interaction with Arg307. On the basis of these findings, it is reasonable to expect that the larger flexibility afforded by the linker in **7e** will facilitate a proper accommodation to both BS1 and BS2 in BACE-1, thus explaining the increase in BACE-1 inhibitory activity compared to **7h**. Overall, this analysis suggests that BS2 may be exploited to find novel moieties, leading to enhanced binding affinity and hence to hybrid compounds with more potent inhibitory activity against BACE-1.

In Vitro Biological Profiling of Enantiopure Rhein−Huprine Hybrids (+)- and (−)-7e. After the in vitro biological profiling of the racemic rhein−huprine hybrids, (±)-**7e** emerged as the most interesting member of the series, mainly by virtue of its outstanding BACE-1 inhibitory potency, but also because it was one of the most potent compounds of the series for hAChE, hBChE, AChE-induced, and self-induced Aβ aggregation. To further optimize the lead of the series, the two enantiomers of **7e** were synthesized separately (see above) and subjected to in vitro biological profiling with the aim of unveiling potential enantioselective interactions with the different targets.

In agreement with the stereoselective interaction of the parent huprine Y, the levorotatory rhein−huprine hybrid (−)-**7e** was a far more potent hAChE inhibitor than its enantiomer (+)-**7e**, with an enantioselectivity (1200-fold) somewhat more pronounced than that found for the parent huprine Y (430-fold) (Table 1), in agreement with the docking calculations (Figure 1). To further confirm the inhibition mechanism, a kinetic study of the interaction of (−)-**7e** with hAChE was also carried out. The mode of inhibition of (−)-**7e** was determined with the aid of Lineweaver−Burk double reciprocal plot. The interception of the lines in the Lineweaver−Burk plot above the *x*-axis (Figure 3)

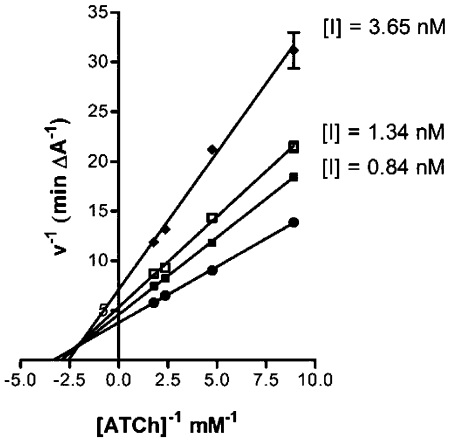

Figure 3. Kinetic study on the mechanism of AChE inhibition by (−)-**7e**. Overlaid Lineweaver−Burk reciprocal plots of AChE initial velocity at increasing substrate concentration (ATCh, 0.56−0.11 mM) in the absence and in the presence (0.84−3.65 nM) of (−)-**7e** are shown. Lines were derived from a weighted least-squares analysis of the data points.

demonstrated that (−)-**7e** acts as a mixed-type inhibitor of hAChE.

The inhibitor dissociation constants K_i and K'_i, which denote the dissociation constant for the enzyme−inhibitor and enzyme−substrate−inhibitor complexes, respectively (see Experimental Section), were estimated and resulted to be 2.65 and 3.41 nM, respectively.

Contrary to the inhibition of hAChE by the enantiomers of huprines, for hBChE inhibition the eutomer is the dextrorotatory (7*R*,11*R*)-enantiomer, (+)-**4**. Thus, not unexpectedly, for hBChE inhibition, the rhein−huprine hybrid (+)-**7e** was 2-fold more potent than (−)-**7e**, the enantioselectivity being quite similar to that found for huprine Y (1.3-fold) (Table 1).

In contrast to hAChE and hBChE inhibition and in agreement with the idea that the enantioselective inhibition of the cholinesterase catalytic activity is related to the interaction with CAS, no enantioselectivity was found in the inhibition by (+)- and (−)-**7e** of the AChE-induced aggregation of Aβ40 (37−38% inhibition at 100 μM). Similarly, no differences were highlighted for the inhibition of the self-induced aggregation of Aβ42 (38−43% inhibition at 10 μM) and hBACE-1 activity (IC_{50} 80 nM in both enantiomers) by (+)- and (−)-**7e**.

In Vitro Blood−Brain Barrier Permeation Assay. CNS drugs must be able to efficiently cross the blood−brain barrier (BBB). However, cell permeability and brain penetration constitute a major hurdle in the development of some classes of anti-Alzheimer drugs, particularly in BACE-1 inhibitors and in Aβ and tau aggregation inhibitors.[4,31,60,64] Moreover, compounds designed by combination of two pharmacophoric moieties, such as the novel rhein−huprine hybrids, usually have molecular weights

dx.doi.org/10.1021/jm401824w | J. Med. Chem. 2014, 57, 2549−2567

over 500, which might challenge their ability to cross cell membranes.[65,66] However, different families of anti-Alzheimer hybrid compounds with molecular weights over 500 have shown good oral availability and/or brain permeability in ex vivo and in vivo studies in mice.[12,40,67,68] Even though the potential of a CNS drug to enter into the brain also depends on a low P-glycoprotein efflux liability,[69,70] a good brain permeability is a necessary requirement. In this work, the brain permeability of the novel rhein−huprine hybrids has been predicted through the widely known parallel artificial membrane permeation assay (PAMPA-BBB).[71] The in vitro permeability (P_e) of racemic rhein−huprine hybrids through a lipid extract of porcine brain was determined using phosphate-buffered saline (PBS)/EtOH 70:30. Assay validation was carried out by comparing the experimental and literature permeability values of 14 commercial drugs (Table S1, Supporting Information), which gave a good linear correlation: P_e (exp) = 1.4525 P_e (lit) − 0.4926 (R^2 = 0.9199). Using this equation and the limits established by Di et al. for BBB permeation,[71] the following ranges of permeability were established: P_e (10^{-6} cm s^{-1}) > 5.3 for compounds with high BBB permeation (CNS+), P_e (10^{-6} cm s^{-1}) < 2.4 for compounds with low BBB permeation (CNS−), and 5.3 > P_e (10^{-6} cm s^{-1}) > 2.4 for compounds with uncertain BBB permeation (CNS±). All the tested rhein−huprine hybrids were predicted to be able to cross the BBB, their measured P_e values being far above the threshold for high BBB permeation (Table 1), as it is also the case for the parent huprine Y, (±)-**4**, but not for rhein, **3**, for which an uncertain BBB permeability was predicted. Indeed, rhein is therapeutically used against arthritis in the form of the more lipophilic and cell permeable doubly acetylated prodrug diacerein.

Inhibition of Aβ42 and Tau Aggregation in Intact *Escherichia coli* Cells. The aggregation of two amyloidogenic proteins, namely Aβ and tau, plays a pivotal role in the pathological network of AD. Protein aggregation also occurs during the production of heterologous proteins in bacteria, leading to the formation of insoluble inclusion bodies (IBs). Because IBs contain highly ordered amyloid-like structures and their formation seems to share mechanistic features with amyloid self-assembly, they have been recently proposed as a model to study amyloid aggregation.[72,73] We have recently developed a methodology that allows a fast, simple, and inexpensive evaluation of the antiaggregating activity of putative inhibitors, which is based on the in vivo staining with thioflavin S of IBs in intact *E. coli* cells that overexpress a given amyloidogenic protein in the presence and absence of the inhibitors and monitoring of the corresponding changes in the fluorescence of thioflavin S.[74] The applicability of this method to the screening of both Aβ42 and tau aggregation inhibitors has been recently demonstrated.[74] It is worth noting that the Aβ42 antiaggregating activities determined through this method for a number of known active and inactive inhibitors were very similar to those previously reported in in vitro assays using synthetic peptides, thereby validating this methodology.[74] A potential limitation of this method lies in the fact that only compounds that are membrane permeable can be detected, whereas potential hits that are active as aggregation inhibitors but unable to cross biological membranes would remain undetected. In light of the results obtained in the PAMPA-BBB assays, this should not be an issue for the novel rhein−huprine hybrids, which were tested for their ability to inhibit both Aβ42 and tau aggregation in intact *E. coli* cells (Table 2).

All the rhein−huprine hybrids exhibited a moderately potent Aβ42 antiaggregating activity in *E. coli* cells, with percentages of inhibition in the range 41−68% at 10 μM and, hence, with IC_{50} values below 10 μM in most cases (Table 2). Some clear SAR trends became apparent, namely a higher Aβ42 antiaggregating activity for the hybrids with the shortest oligomethylene linkers and for the dextrorotatory over the levorotatory enantiomer of **7e**. The presence of an aromatic ring within the linker seemed not to be detrimental for Aβ42 antiaggregating activity, hybrid (±)-**7h** displaying a notable 58% inhibition at 10 μM, albeit slightly lower than that of the oligomethylene-linked hybrid of similar tether length, (±)-**7b**. Interestingly, the Aβ42 antiaggregating activities measured for the rhein−huprine hybrids in intact *E. coli* cells were of similar magnitude to those determined in the in vitro assay, albeit somewhat higher in most cases. Regarding the parent compounds, huprine Y was found to be essentially inactive in *E. coli* as it was in the in vitro assay, whereas rhein, which could not be evaluated in vitro for solubility problems under the assay conditions, was found to exhibit an interesting 50% inhibition at 10 μM in *E. coli* cells.

Table 2. Inhibitory Activities of the Hydrochlorides of Rhein−Huprine Hybrids and Reference Compounds Toward Aβ42 and Tau Aggregation in Intact *E. coli* Cells[a]

compd	Aβ42 aggregation (% inhibition)[b]	tau aggregation (% inhibition)[b]
(±)-**7a**	68.0 ± 0.8	43.7 ± 1.1
(±)-**7b**	68.4 ± 8.9	30.9 ± 3.1
(±)-**7c**	63.2 ± 9.8	52.0 ± 1.1
(±)-**7d**	50.2 ± 5.6	29.2 ± 1.3
(±)-**7e**	47.9 ± 14.5	29.6 ± 8.5
(+)-**7e**	58.6 ± 7.1	24.9 ± 0.4
(−)-**7e**	47.2 ± 5.1	34.3 ± 0.1
(±)-**7f**	43.3 ± 4.1	57.1 ± 1.9
(±)-**7g**	40.7 ± 2.2	46.3 ± 0.7
(±)-**7h**	57.9 ± 0.0	23.1 ± 5.1
3	49.9 ± 6.4	40.8 ± 0.7
(±)-**4**	na[c]	na[c]

[a]Values are expressed as mean ± standard error of the mean (SEM) of four independent experiments (n = 4). [b]% inhibition with inhibitor at 10 μM. [c]Not active.

In agreement with our design strategy, the parent hydroxyanthraquinone derivative rhein was found to be active as inhibitor of tau aggregation in intact *E. coli* cells (41% inhibition at 10 μM), and this was also the case for the novel rhein−huprine hybrids (23−57% inhibition at 10 μM) but not for the parent huprine Y, which was inactive, as expected (Table 2). For the inhibitory activity on tau aggregation, the presence of an aromatic ring within the linker seemed to be detrimental and the levorotatory enantiomer of **7e** was more potent than (+)-**7e**. However, a clear SAR trend regarding the length of the linker could not be derived.

The dual Aβ42 and tau antiaggregating action of the novel rhein−huprine hybrids seems very promising for anti-Alzheimer drug candidates. These results are also important in the context of the treatment of amyloidoses in general, insofar as they support the increasingly accepted notion that all diseases that involve the pathological aggregation of a particular protein might share common mechanisms and common therapeutic interventions.[75,76] Indeed, other examples of compounds able to inhibit the aggregation of several amyloidogenic proteins have been reported.[40,75,77]

Protection Against the Synaptic Failure Induced by Aβ Oligomers in Hippocampal Slices of C57bl6Mice. In light of the outstanding multitarget pharmacological profile found in vitro and in *E. coli* cells for the enantiopure rhein−huprine hybrids (+)- and (−)-**7e**, involving the modulation of crucial

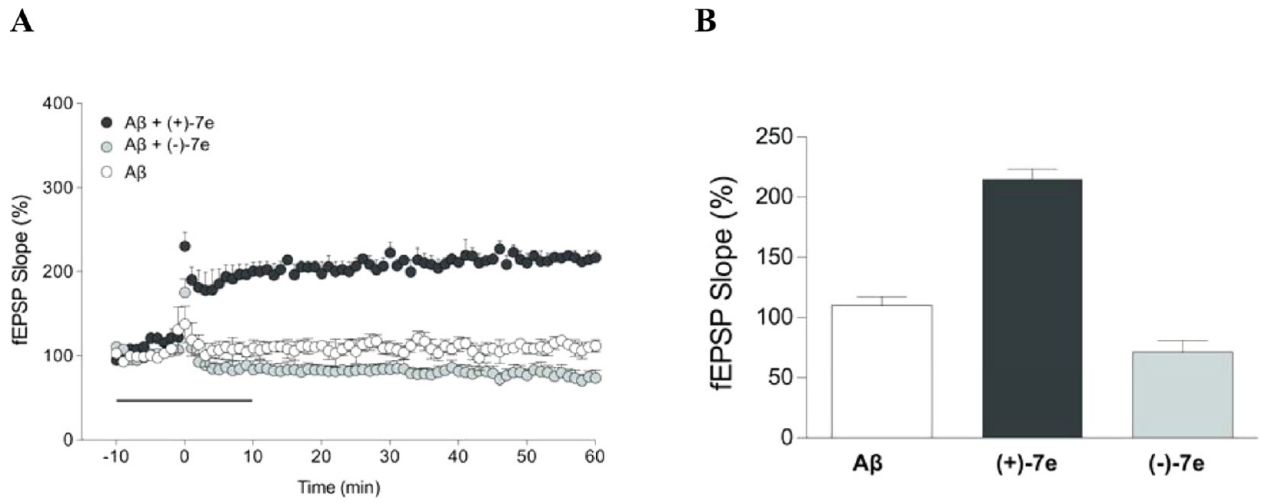

Figure 4. Electrophysiological assays in hippocampal slices of 2-month-old C57bl6 mice incubated with Aβ oligomers (1 μM) and (+)- or (−)-**7e** (10 μM). (A) Electrophysiological registers. (B) Quantification of field excitatory postsynaptic potentials (fEPSP).

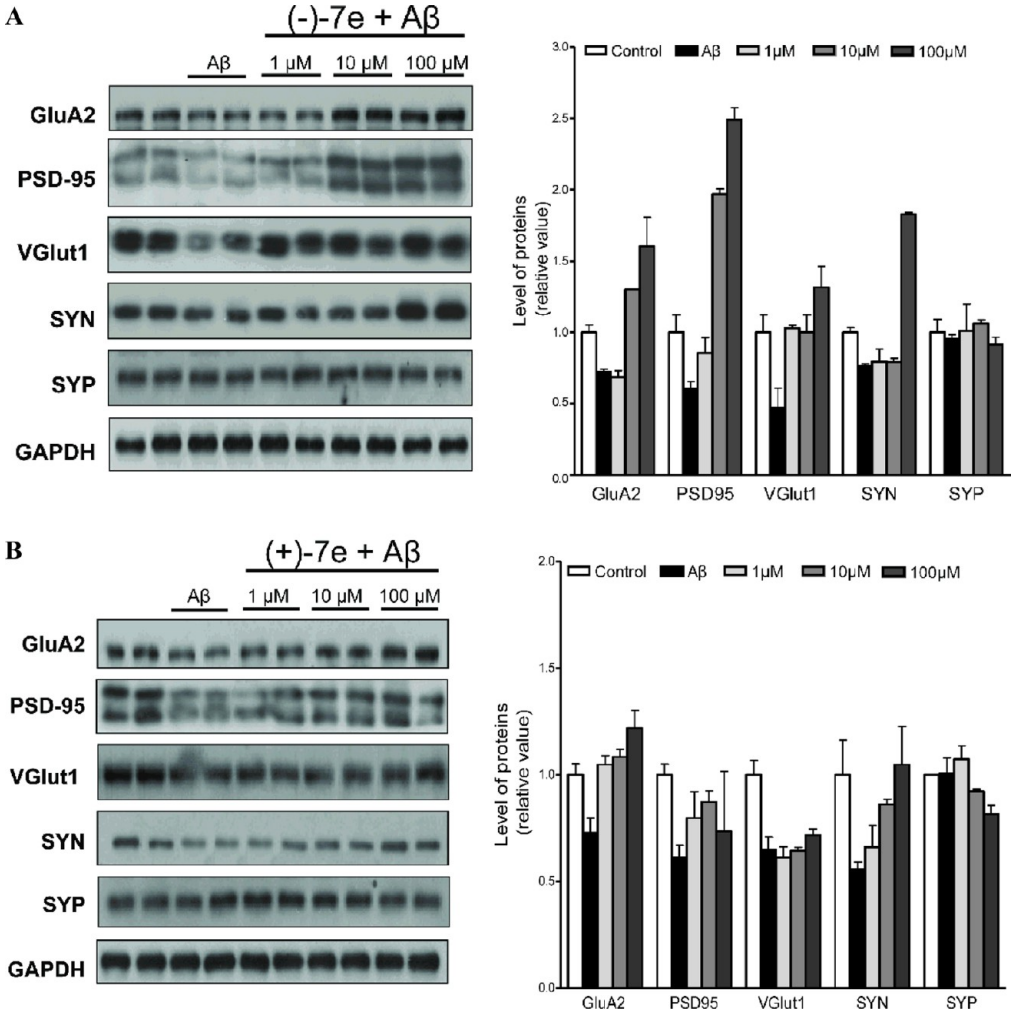

Figure 5. Synaptic protein levels of hippocampal slices of 2-month-old C57bl6 mice incubated with Aβ oligomers and (−)-**7e** (A) or (+)-**7e** (B).

targets of the pathological network of AD, these compounds were selected as leads for further pharmacological characterization.

Even though all aggregated forms of Aβ are likely pathological,[78] it has been reported that Aβ oligomers (Aβ-o) cause an impairment of synaptic functions observed in AD patients and mouse models of AD.[79] Because the target of Aβ-o is located at the postsynaptic region,[80,81] processes associated to synaptic plasticity as long-term potentiation (LTP) are critically altered, leading to diminished synaptic strength and efficacy. These dysfunctions are correlated with reduction in the levels of

dx.doi.org/10.1021/jm401824w | J. Med. Chem. 2014, 57, 2549−2567

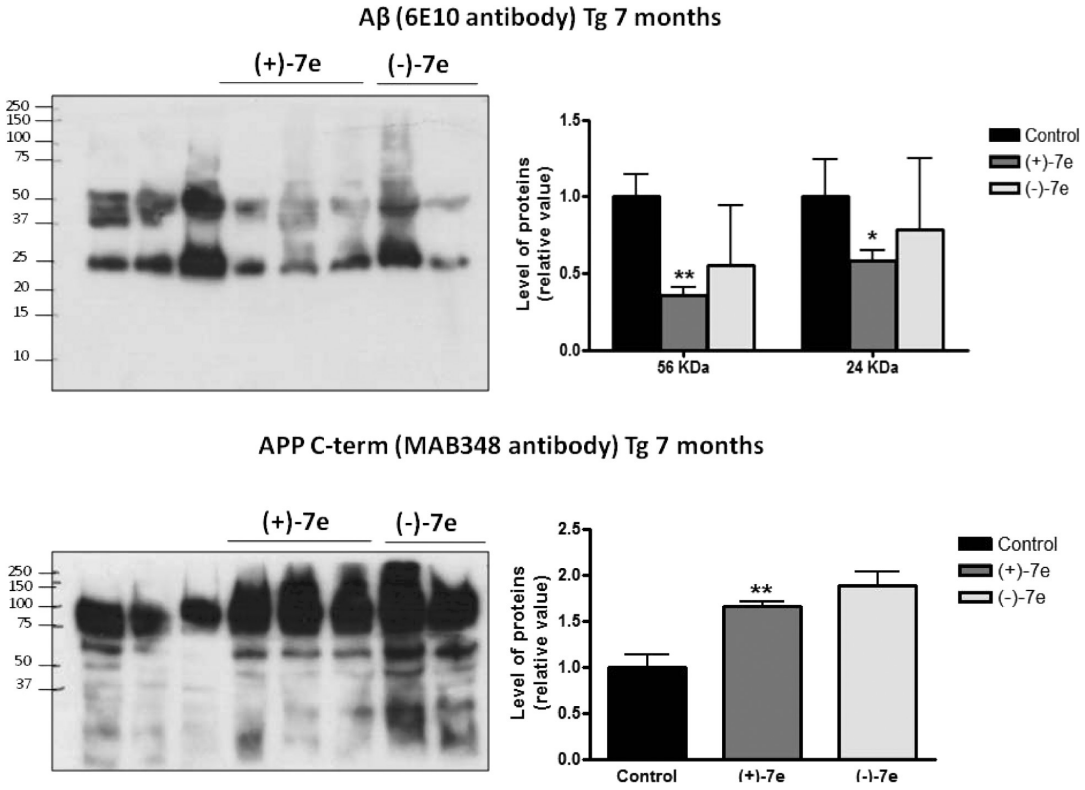

Figure 6. Soluble Aβ and APP protein levels of hippocampal samples from 7-month-old APP-PS1 mice treated with (−)-**7e** or (+)-**7e** for 4 weeks. Lanes 1−3 show hippocampus lysates from control mice (n = 3), lanes 4−6 show hippocampus lysates from (+)-**7e** treated mice (n = 3), and lanes 7−8 show hippocampus lysates from (−)-**7e** treated mice (n = 2), each lane being an independent animal.

synaptic proteins that participate in events associated with learning and memory such as glutamatergic receptors and scaffold proteins.[82] To further assess the disease-modifying effects of the rhein−huprine hybrids (+)- and (−)-**7e**, their potential protective effect on synaptic integrity was assessed in hippocampal slices of 2-month-old C57bl6 male mice incubated with Aβ42 oligomers.

Electrophysiological Assays. First, electrophysiological registers of the hippocampal slices were used to evaluate synaptic transmission through the LTP. Hippocampal slices were incubated with Aβ42 oligomers (1 μM) 10 min prior and 10 min after LTP induction. No induction of LTP was observed in hippocampal slices incubated either with Aβ42 oligomers alone or with Aβ42 oligomers and (−)-**7e** (10 μM) (Figure 4A, white circles and light-gray circles, respectively). On the contrary, treatment with (+)-**7e** (10 μM) led to a 200% LTP induction (Figure 4A, dark-gray circles), similarly to the effect found in the control slices treated only with artificial cerebrospinal fluid (ACSF). In Figure 4B, the quantification at min 60 of the field excitatory postsynaptic potentials (fEPSP) are shown. Treatment with (+)-**7e** led to a 200% magnitude response when compared to slices treated either with Aβ42 oligomers alone or with Aβ42 oligomers and (−)-**7e**. These results indicate that (+)-**7e** protects against the synaptic failure induced by acute treatments with Aβ42 oligomers within the context of LTP induction.

Synaptic Protein Levels. Changes in the synaptic protein levels of hippocampal slices of 2-month-old C57bl6 mice treated with Aβ42 oligomers and different concentrations of (+)- and (−)-**7e** (1−100 μM) for 1 h were studied by densitometric analysis of Western blots gels. Treatment of the hippocampal slices with Aβ42 oligomers (Figure 5, black bars) produced a decrease in the levels of the postsynaptic proteins GluA2 (a subunit of the AMPA receptor) and PSD95 (postsynaptic density protein 95, a scaffold protein within the postsynaptic density) and of the presynaptic proteins synapsin (SYN) and the vesicular glutamate transporter 1 (VGlut1) in comparison with control slices (Figure 5, white bars), whereas the levels of the presynaptic protein synaptophysin (SYP) remained unchanged. In hippocampal slices cotreated with (−)-**7e** (Figure 5A), a neuroprotective effect was observed. Evident increases in the levels of GluA2 and PSD95 were observed at 10 and 100 μM and in the levels of VGlut1 for every used concentration of (−)-**7e**, whereas increases in the levels of SYN and SYP were found only at the highest assayed concentration or were not observed. Co-treatment with (+)-**7e** produced increases, albeit more modest, in the levels of GluA2, PSD95, and SYN with every used concentration, whereas it had no effect on the levels of VGlut1 and SYP. Thus, both (+)- and (−)-**7e** exert a protective effect on synaptic proteins related with the stability of the synapses and the synaptic plasticity in the hippocampus.

Prevention of the Aβ-o-induced loss of synaptic proteins by treatment of hippocampal slices of 2-month-old C57bl6 mice with (+)-**7e** is in agreement with the results found in the electrophysiological assays and with the antiamyloid activities found in the in vitro and in *E. coli* assays, namely its potent BACE-1 and Aβ aggregation inhibitory activities. Thus, the protective effects of (+)-**7e** and also (−)-**7e** on synaptic integrity might be ascribed to a reduction of the amount of Aβ aggregated species or to a reduction of Aβ production through the inhibition of APP processing, although participation of alternative or additional mechanisms can not be ruled out. For example, it has been reported that the increased levels of neurotransmitter acetylcholine due to AChE inhibition may promote changes in synaptic plasticity improving LTP.[83,84] Indeed, (−)-**7e**, the

dx.doi.org/10.1021/jm401824w | J. Med. Chem. 2014, 57, 2549−2567

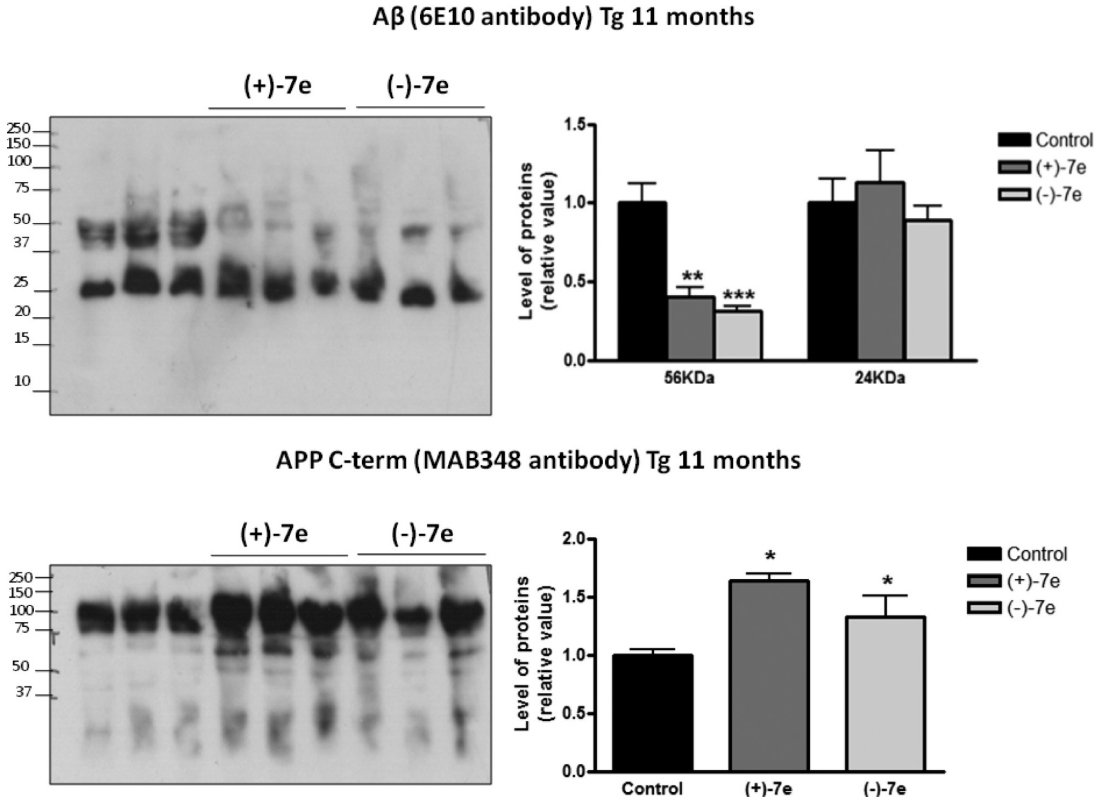

Figure 7. Soluble Aβ and APP protein levels of hippocampal samples from 11-month-old APP-PS1 mice treated with (−)-**7e** or (+)-**7e** for 4 weeks. Lanes 1−3 show hippocampus lysates from control mice (n = 3), lanes 4−6 show hippocampus lysates from (+)-**7e** treated mice (n = 3), and lanes 7−9 show hippocampus lysates from (−)-**7e** treated mice (n = 3), each lane being an independent animal.

eutomer for hAChE inhibition, seems to be more potent regarding the preservation of synaptic proteins even though it does not improve LTP. Different mechanisms are likely involved in the neuroprotective effect shown by (+)- and (−)-**7e**.

In Vivo Aβ Lowering Effect. Among the different interesting biological activities found in vitro, in *E. coli*, and ex vivo for the enantiopure rhein−huprine hybrids (+)-**7e** and (−)-**7e**, likely the most notable effect is the potent inhibition of BACE-1 (IC_{50} 80 nM). To gain further insight into the relevance of this activity, we have determined the in vivo effects of (+)-**7e** and (−)-**7e** on the level of total soluble Aβ oligomers, thought to be involved in synapse destruction and memory impairment in AD.[85] To this end, we used a well-established animal model of AD, namely the double transgenic mice APP-PS1 (see Experimental Section). This aggressive model of AD has been characterized both in the generation of senile plaques in the brain and in their behavioral changes,[86] describing the age at which these animals exhibit early senile plaques and cognitive impairment from 7 months of age, which occur mainly in the cortex and hippocampus.[86] Six- and 10-month-old APP-PS1 mice were treated with 2 mg/kg of (+)-**7e** or (−)-**7e** intraperitoneally three times per week for 4 weeks to evaluate the effects of these compounds on the production and aggregation of Aβ species in two different stages of the AD model, initial and severe, respectively. The soluble protein fraction from hippocampus homogenates of control and treated APP-PS1 mice was separated in tris-tricine gels, each lane being a different mouse, and specific mouse anti-β peptide 6E10 antibody was used, followed by immunoblot analysis.

Young (7-month-old after the treatment, n = 3 control, n = 3 (+)-**7e** treated, and n = 2 (−)-**7e** treated APP-PS1 mice) and aged (11-month-old after the treatment, n = 3 control, n = 3 (+)-**7e** treated, and n = 3 (−)-**7e** treated APP-PS1 mice) APP-PS1 mice exhibit several forms of Aβ peptides, including hexamers (ca. 24 kDa) and higher levels of Aβ dodecamers (ca. 56 kDa). Interestingly, young and aged APP-PS1 mice treated with (+)-**7e** showed a significant decrease in the levels of dodecamers, whereas only in young mice a reduction in the levels of hexamers was observed (Figures 6 and 7). In addition, young APP-PS1 mice treated with (−)-**7e** showed a tendency toward decreased levels of both oligomeric species, whereas aged APP-PS1 mice treated with (−)-**7e** showed a diminution in the levels of dodecamers without altering the levels of hexamers (Figures 6 and 7). The results observed in 11-month-old mice might be due to the high load of Aβ present in aging APP-PS1 mice. However, the reduction in the levels of dodecamers, considered to be synaptotoxic, is very important, because it might be indicative of a reversion in the neurodegenerative process observed in the animal. More studies are necessary to corroborate this possibility. Together, these results suggest that rhein−huprine hybrids (+)-**7e** and (−)-**7e** either could favor the formation of senile plaques and the decrease of the soluble Aβ forms or prevent the APP processing and the subsequent aggregation through inhibition of BACE-1. To corroborate the last hypothesis, the levels of APP protein were analyzed in the same gel described before where each lane represents an independent animal. The results showed that in young and aged APP-PS1 mice treated with (+)-**7e** and (−)-**7e**, the levels of mature APP (ca. 100 KDa) are increased (Figures 6 and 7), indicating that these rhein−huprine hybrids are able to prevent APP processing, Aβ production, and aggregation.

CONCLUSIONS

We have synthesized a series of racemic and enantiopure hybrid compounds that combine a unit of the hydroxyanthraquinone

dx.doi.org/10.1021/jm401824w | J. Med. Chem. 2014, 57, 2549−2567

drug rhein and a unit of the potent AChE's CAS inhibitor huprine Y, connected through penta- to undecamethylene or 1,4-phenylene-bis(methylene) linkers. These hybrids were purportedly designed to exhibit a multitarget profile of interest for the efficient management of AD, which included the inhibitory actions expected for dual binding site inhibitors of AChE against the catalytic and the Aβ-proaggregating activities of this enzyme and the tau antiaggregating effect known for some hydroxyanthraquinone compounds similar to rhein. In agreement with the design rationale, the novel rhein–huprine hybrids are endowed with very potent hAChE inhibitory activity and moderately potent inhibitory activities against hAChE-induced and self-induced aggregation of Aβ and against hBChE. Far beyond our expectations, some rhein–huprine hybrids additionally display a very potent BACE-1 inhibitory activity. Of note, these hybrids have been predicted to be able to cross the BBB using an artificial membrane model, likely having the ability to exert the same actions in vivo. Both cell permeability and the Aβ antiaggregating activity found in vitro for the rhein–huprine hybrids, as well as their expected tau antiaggregating activity, have been confirmed by some assays based on the direct thioflavin S staining of IBs in intact *E. coli* cells that were genetically altered to overexpress Aβ42 and tau protein. On the basis of the biological profiling in vitro and in *E. coli*, (+)- and (−)-**7e** have been selected as lead rhein–huprine hybrids and their protective effects against the synaptic failure induced by Aβ oligomers in hippocampal slices of 2-month-old C57bl6 mice have been assessed. These studies have shown that both hybrids prevent the loss of synaptic proteins. Additionally, the beneficial effects of (+)-**7e** on synaptic integrity were apparent in the context of LTP induction. Finally, in vivo experiments with transgenic APP-PS1 mice have shown that (+)- and (−)-**7e** are able to lower the levels of hippocampal total soluble Aβ and increase the levels of APP both in initial and advanced stages of this AD model, thus suggesting a reduction of APP processing, as expected from their potent BACE-1 inhibitory activity. Overall, the novel rhein–huprine hybrids (+)- and (−)-**7e** emerge as very promising multitarget anti-Alzheimer drug candidates with potential to positively modify the underlying mechanisms of this disease.

EXPERIMENTAL SECTION

Chemistry. Melting points were determined in open capillary tubes with a MFB 595010 M Gallenkamp melting point apparatus. 400 MHz ^{1}H/100.6 MHz ^{13}C NMR spectra, and 500 MHz 1H/125.7 MHz ^{13}C NMR spectra were recorded on Varian Mercury 400 and Varian Inova 500 spectrometers, respectively. The chemical shifts are reported in ppm (δ scale) relative to internal tetramethylsilane, and coupling constants are reported in hertz (Hz). Assignments given for the NMR spectra of the new compounds were carried out on the basis of DEPT, COSY ^{1}H/^{1}H (standard procedures), and COSY ^{1}H/^{13}C (gHSQC or gHMBC sequences) experiments. The *syn* (*anti*) notation of the protons at position 13 of the huprine moiety of the hybrids means that the corresponding proton at position 13 is on the same (different) side of the quinoline moiety with respect to the cyclohexene ring. IR spectra were run on a Perkin-Elmer Spectrum RX I spectrophotometer. Absorption values are expressed as wavenumbers (cm^{-1}); only significant absorption bands are given. Optical rotations were measured on a Perkin-Elmer model 241 polarimeter. The specific rotation has not been corrected for the presence of solvent of crystallization. Column chromatography was performed on silica gel 60 AC.C (40–60 mesh, SDS, ref 2000027). Thin-layer chromatography was performed with aluminum-backed sheets with silica gel 60 F_{254} (Merck, ref 1.05554), and spots were visualized with UV light and 1% aqueous $KMnO_4$. NMR spectra of all of the new compounds were performed at the Centres Científics i Tecnològics of the University of Barcelona (CCiTUB), while elemental analyses and high resolution mass spectra were carried out at the Mycroanalysis Service of the IIQAB (CSIC, Barcelona, Spain) with a Carlo Erba 1106 analyzer and at the CCiTUB with a LC/MSD TOF Agilent Technologies spectrometer, respectively. The synthetic procedures for the preparation of the intermediate nitriles **5a–h** and amines **6a–h** are exemplified through the synthesis of **5a** and **6a**. The synthesis of the rest of nitriles and amines is included in the Supporting Information. The analytical samples of all of the rhein–huprine hybrids which were subjected to pharmacological evaluation possess a purity ≥95% as evidenced by their elemental analyses.

*(±)-5-[(3-Chloro-6,7,10,11-tetrahydro-9-methyl-7,11-methanocycloocta[b]quinolin-12-yl)amino]pentanenitrile [(±)-**5a**].* A suspension of (±)-huprine Y, (±)-**4** (300 mg, 1.06 mmol), and finely powdered KOH (85% purity, 139 mg, 2.11 mmol), and 4 Å molecular sieves in anhyd DMSO (6 mL) was stirred, heating every 10 min approximately with a heat gun for 1 h and at rt one additional hour, and then treated with 5-bromovaleronitrile (0.15 mL, 208 mg, 1.28 mmol). The reaction mixture was stirred at rt overnight, diluted with 5N NaOH (25 mL), and extracted with EtOAc (3 × 40 mL). The combined organic extracts were washed with H_2O (3 × 50 mL), dried over anhyd Na_2SO_4, and evaporated under reduced pressure to give a yellow oil (469 mg), which was purified by column chromatography (40–60 μm silica gel, CH_2Cl_2/MeOH/50% aq NH_4OH mixtures, gradient elution). On elution with CH_2Cl_2/50% aq NH_4OH 100:0.2, the *N*,*N*-dialkylated derivative (±)-**8a** (78 mg, 16% yield) was isolated as a yellow oil. On elution with CH_2Cl_2/MeOH/50% aq NH_4OH 99:1:0.2, nitrile (±)-**5a** (273 mg, 70% yield) was isolated as a beige solid; $R_{f[(\pm)\text{-}5a]}$ 0.50, $R_{f[(\pm)\text{-}8a]}$ 0.77 (CH_2Cl_2/MeOH/50% aq NH_4OH 9:1:0.05).

A solution of (±)-**5a** (52 mg, 0.14 mmol) in CH_2Cl_2 (4.5 mL) was filtered through a 0.2 μm PTFE filter, treated with methanolic HCl (1.40 N, 0.30 mL), and evaporated under reduced pressure. The resulting solid was washed with pentane (3 × 2 mL) to give, after drying at 65 °C/2 Torr for 48 h, (±)-**5a**·HCl (58 mg) as a yellow solid: mp 181–183 °C (CH_2Cl_2/MeOH 94:6). IR (KBr) ν 3500–2500 (max at 3364, 3254, 3049, 3014, 2926, 2885, 2651, N-H, N^+-H, and C-H st), 2243 (CN st), 1635, 1629, 1602, 1582, 1570, 1562 (ar-C-C and ar-C-N st) cm^{-1}. ^{1}H NMR (400 MHz, CD_3OD) δ 1.59 (s, 3H, 9′-CH_3), 1.79 (tt, $J \approx J' \approx 7.2$ Hz, 2H, 3-H_2), 1.93 (d, $J = 17.6$ Hz, 1H, 10′-H_{endo}), superimposed in part 1.92–1.98 (m, 1H, 13′-H_{syn}), 2.01 (tt, $J \approx J' \approx 7.2$ Hz, 2H, 4-H_2), 2.09 (dm, $J = 12.8$ Hz, 1H, 13′-H_{anti}), 2.56 (t, $J = 7.2$ Hz, 2H, 2-H_2), superimposed in part 2.53–2.60 (m, 1H, 10′-H_{exo}), 2.77 (m, 1H, 7′-H), 2.88 (ddd, $J = 18.0$ Hz, $J' = J'' = 1.6$ Hz, 1H, 6′-H_{endo}), 3.22 (dd, $J = 18.0$ Hz, $J' = 5.2$ Hz, 1H, 6′-H_{exo}), 3.47 (m, 1H, 11′-H), 4.03 (t, $J = 7.6$ Hz, 2H, 5-H_2), 4.85 (s, NH and $^+$NH), 5.59 (br d, $J = 4.4$ Hz, 1H, 8′-H), 7.57 (dd, $J = 9.2$ Hz, $J' = 2.0$ Hz, 1H, 2′-H), 7.78 (d, $J \approx 2.0$ Hz, 1H, 4′-H), 8.40 (d, $J \approx 9.2$ Hz, 1H, 1′-H). ^{13}C NMR (100.6 MHz, CD_3OD) δ 17.1 (CH_2, C2), 23.4 (CH_3, 9′-CH_3), 23.9 (CH_2, C3), 27.3 (CH, C11′), 27.9 (CH, C7′), 29.3 (CH_2, C13′), 30.3 (CH_2, C4), 36.1 (CH_2), 36.2 (CH_2) (C6′, C10′), 48.8 (CH_2, C5), 115.8 (C, C12a′), 117.9 (C, C11a′), 119.2 (CH, C4′), 120.9 (C, CN), 125.1 (CH, C8′), 126.8 (CH, C2′), 129.4 (CH, C1′), 134.6 (C, C9′), 140.3 (C, C3′), 141.0 (C, C4a′), 151.5 (C, C5a′), 157.0 (C, C12′). HRMS (ESI) calcd for ($C_{22}H_{24}{}^{35}ClN_3 + H^+$), 366.1732; found, 366.1729.

A solution of (±)-**8a** (78 mg, 0.17 mmol) in CH_2Cl_2 (4.5 mL) was filtered through a 0.2 μm PTFE filter, treated with methanolic HCl (0.65N, 0.64 mL), and evaporated under reduced pressure. The resulting solid was washed with pentane (3 × 2 mL) to give, after drying at 65 °C/2 Torr for 48 h, (±)-**8a**·HCl (80 mg) as a yellow solid; mp 196–198 °C (CH_2Cl_2/MeOH 88:12). IR (KBr) ν 3500–2450 (max at 3430, 3044, 2919, 2875, 2464, N^+-H and C-H st), 2243 (CN st), 1632, 1604, 1574 (ar-C-C and ar-C-N st) cm^{-1}. ^{1}H NMR (400 MHz, CD_3OD) δ 1.59 (s, 3H, 9′-CH_3), 1.65 (tt, $J \approx J' \approx 7.2$ Hz, 4H, 3-H_2), 1.72–1.98 (complex signal, 4H, 4-H_2), 2.00 (br d, $J = 17.6$ Hz, 1H, 10′-H_{endo}), superimposed in part 2.06 (dm, $J \approx 12.8$ Hz, 1H, 13′-H_{syn}), 2.12 (dm, $J = 12.8$ Hz, 1H, 13′-H_{anti}), 2.48 (t, $J = 7.2$ Hz, 4H, 2-H_2), 2.69 (dd, $J = 17.6$ Hz, $J' = 5.6$ Hz, 1H, 10′-H_{exo}), 2.82 (m, 1H, 7′-H), 3.17 (ddd, $J = 18.0$ Hz, $J' \approx J'' \approx 1.8$ Hz, 1H, 6′-H_{endo}), 3.39 (dd, $J = 18.0$ Hz, $J' = 5.6$ Hz, 1H, 6′-H_{exo}), superimposed in part 3.73 (m, 1H, 11′-H), 3.73 (ddd, $J = 13.6$ Hz, $J' = 9.6$ Hz, $J'' = 5.6$ Hz, 2H) and 3.80 (ddd, $J = 13.6$ Hz, $J' = 9.2$ Hz, $J'' = 6.0$ Hz, 2H) (5-H_2), 4.84 (s, $^+$NH), 5.68 (br d, $J = 4.4$ Hz, 1H,

dx.doi.org/10.1021/jm401824w | J. Med. Chem. 2014, 57, 2549–2567

8′-H), 7.72 (dd, J = 9.2 Hz, J' = 2.4 Hz, 1H, 2′-H), 7.99 (d, J = 2.4 Hz, 1H, 4′-H), 8.26 (d, J = 9.2 Hz, 1H, 1′-H). ^{13}C NMR (100.6 MHz, CD_3OD) δ 17.1 (CH_2, C2), 23.3 (CH_3, 9′-CH_3), 23.9 (CH_2, C3), 27.6 (CH, C7′), 28.6 (CH_2, C13′), 28.9 (CH_2, C4), 29.7 (CH, C11′), 37.7 (CH_2, C6′), 38.7 (CH_2, C10′), 55.1 (CH_2, C5), 120.0 (CH, C4′), 120.9 (C, CN), 125.5 (C, C12a′), 125.7 (CH, C8′), 192.2 (CH, C2′), 130.1 (CH, C1′), 132.5 (C, C11a′), 134.3 (C, C9′), 140.36 (C), 140.43 (C) (C3′, C4a′), 157.6 (C, C5a′), 163.9 (C, C12′). HRMS (ESI) calcd for ($C_{27}H_{31}{}^{35}ClN_4$ + H^+), 447.2310; found, 447.2309.

*(±)-N-(3-Chloro-6,7,10,11-tetrahydro-9-methyl-7,11-methanocycloocta[b]quinolin-12-yl)pentane-1,5-diamine [(±)-**6a**].* To a suspension of $LiAlH_4$ (0.17 g, 4.47 mmol) in anhyd Et_2O (63 mL), nitrile (±)-**5a** (0.76 g, 2.08 mmol) was added, and the reaction mixture was stirred at rt overnight. The resulting mixture was treated with wet Et_2O (200 mL) and evaporated under reduced pressure. The solid was suspended in CH_2Cl_2, filtered through Celite, and evaporated under reduced pressure to give amine (±)-**6a** (750 mg, 98% yield) as a yellow oil; R_f 0.03 (CH_2Cl_2/MeOH/50% aq NH_4OH 9:1:0.05).

A solution of (±)-**6a** (50 mg, 0.14 mmol) in CH_2Cl_2 (3.5 mL) was filtered through a 0.2 μm PTFE filter, treated with methanolic HCl (1.4N, 0.87 mL), and evaporated under reduced pressure. The resulting solid was washed with pentane (3 × 2 mL) to give, after drying at 65 °C/2 Torr for 48 h, (±)-**6a**·2HCl (54 mg) as a yellow solid; mp 193−194 °C (CH_2Cl_2/MeOH 80:20). IR (KBr) ν 3500−2500 (max at 3396, 3253, 2925, 2856, N-H, N^+-H and C-H st), 1628, 1583, 1570, 1558 (ar-C-C and ar-C-N st) cm^{-1}. ^{1}H NMR (400 MHz, CD_3OD) δ 1.55 (tt, $J \approx J' \approx$ 7.6 Hz, 2H, 3-H_2), 1.59 (s, 3H, 9′-CH_3), 1.76 (m, 2H, 4-H_2), 1.90−2.02 (complex signal, 4H, 10′-H_{endo}, 13′-H_{syn}, 2-H_2), 2.09 (dm, J = 12.8 Hz, 1H, 13′-H_{anti}), 2.57 (ddm, J = 17.6 Hz, J' = 6.0 Hz, 1H, 10′-H_{exo}), 2.78 (m, 1H, 7′-H), 2.87 (br d, J = 18.0 Hz, 1H, 6′-H_{endo}), 2.97 (t, J = 7.6 Hz, 2H, 5-H_2), 3.21 (dd, J = 18.0 Hz, J' = 5.6 Hz, 1H, 6′-H_{exo}), 3.49 (m, 1H, 11′-H), 4.01 (t, $J \approx$ 7.6 Hz, 2H, 1-H_2), 4.85 (s, NH and $^+$NH), 5.59 (br d, J = 4.4 Hz, 1H, 8′-H), 7.57 (dd, J = 9.2 Hz, J' = 2.0 Hz, 1H, 2′-H), 7.78 (d, J = 2.0 Hz, 1H, 4′-H), 8.41 (d, J = 9.2 Hz, 1H, 1′-H). ^{13}C NMR (100.6 MHz, CD_3OD) δ 23.5 (CH_3, 9′-CH_3), 24.7 (CH_2, C3), 27.3 (CH, C11′), 27.9 (CH, C7′), 28.2 (CH_2, C4), 29.3 (CH_2, C13′), 30.8 (CH_2, C2), 36.0 (CH_2), 36.2 (CH_2) (C6′, C10′), 40.5 (CH_2, C5), 49.4 (CH_2, C1), 115.7 (C, C12a′), 117.8 (C, C11a′), 119.2 (CH, C4′), 125.1 (CH, C8′), 126.8 (CH, C2′), 129.4 (CH, C1′), 134.6 (C, C9′), 140.3 (C, C3′), 141.0 (C, C4a′), 151.4 (C, C5a′), 156.9 (C, C12′). HRMS (ESI) calcd for ($C_{22}H_{28}{}^{35}ClN_3$ + H^+), 370.2045; found, 370.2041.

*(±)-N-{5-[(3-Chloro-6,7,10,11-tetrahydro-9-methyl-7,11-methanocycloocta[b]quinolin-12-yl)amino]pentyl}-9,10-dihydro-4,5-dihydroxy-9,10-dioxoanthracene-2-carboxamide [(±)-**7a**].* A suspension of rhein, **3** (477 mg, 1.68 mmol), in anhyd CH_2Cl_2 (6 mL) was cooled to 0 °C with an ice bath and treated dropwise with freshly distilled Et_3N (0.47 mL, 341 mg, 3.38 mmol) and $ClCO_2Et$ (0.16 mL, 182 mg, 1.68 mmol). The resulting solution was stirred at 0 °C for 30 min and treated with a solution of amine (±)-**6a** (621 mg, 1.68 mmol) in anhyd CH_2Cl_2 (6 mL). The reaction mixture was stirred at rt for 3 days, diluted with 10% aq Na_2CO_3 (50 mL), the phases were separated, and the aqueous phase was extracted with CH_2Cl_2 (3 × 35 mL). The combined organic extracts were dried over anhyd Na_2SO_4 and evaporated under reduced pressure to give a red solid (770 mg), which was purified by column chromatography (40−60 μm silica gel, CH_2Cl_2/MeOH/50% aq NH_4OH mixtures, gradient elution). On elution with CH_2Cl_2/MeOH/50% aq NH_4OH 99:1:0.2, hybrid (±)-**7a** (140 mg, 13% yield) was isolated as a red solid; R_f 0.45 (CH_2Cl_2/MeOH/50% aq NH_4OH 9:1:0.05).

A solution of hybrid (±)-**7a** (79 mg, 0.12 mmol) in CH_2Cl_2 (4 mL) was filtered through a 0.2 μm PTFE filter, treated with methanolic HCl (1.4N, 0.26 mL) and evaporated under reduced pressure. The resulting solid was washed with pentane (3 × 2 mL) to give, after drying at 65 °C/2 Torr for 48 h, (±)-**7a**·HCl (80 mg) as a yellow solid; mp 213-215 °C (CH_2Cl_2/MeOH 94:6). IR (KBr) ν 3500−2500 (max at 3224, 3047, 3005, 2923, 2852, O-H, N-H, N^+-H, and C-H st), 1669, 1628, 1582, 1565 (C═O, ar-C-C and ar-C-N st) cm^{-1}. ^{1}H NMR (500 MHz, CD_3OD) δ 1.54−1.64 (complex signal, 2H, 3′-H_2), superimposed in part 1.59 (s, 3H, 9″-CH_3), 1.77 (tt, $J \approx J' \approx$ 7.0 Hz, 2H, 2′-H_2), superimposed in part 1.90−2.00 (complex signal, 3H, 4′-H_2, 13″-H_{syn}), 1.94 (d, $J \approx$ 17.0 Hz, 1H, 10″-H_{endo}), 2.08 (br d, J = 12.5 Hz, 1H, 13″-H_{anti}), 2.56 (br dd, J = 17.0 Hz, J' = 4.0 Hz, 1H, 10″-H_{exo}), 2.77 (m, 1H, 7″-H), 2.84 (d, J = 17.5 Hz, 1H, 6″-H_{endo}), 3.18 (dd, J = 17.5 Hz, J' = 5.5 Hz, 1H, 6″-H_{exo}), 3.42−3.52 (complex signal, 3H, 1′-H_2, 11″-H), 4.00 (dt, J=J' = 7.5 Hz, 2H, 5′-H_2), 4.87 (s, NH, $^+$NH and OH), 5.58 (br d, J = 4.5 Hz, 1H, 8″-H), 7.35 (dd, J = 7.5 Hz, J' = 2.0 Hz, 1H, 6-H), 7.47 (br d, J = 8.5 Hz, 1H, 2″-H), 7.62 (br s, 2H, 3-H, 4″-H), 7.76 (d, J = 7.5 Hz, 1H, 8-H), 7.78 (dd, J = J' = 7.5 Hz, 1H, 7-H), 8.04 (s, 1H, 1-H), 8.34 (d, J = 8.5 Hz, 1H, 1″-H). ^{13}C NMR (125.7 MHz, CD_3OD) δ 23.5 (CH_3, 9″-CH_3), 25.1 (CH_2, C3′), 27.3 (CH, C11″), 27.9 (CH, C7″), 29.3 (CH_2, C13″), 29.9 (CH_2, C2′), 31.0 (CH_2, C4′), 36.1 (CH_2, C6″), 36.2 (CH_2, C10″), 40.7 (CH_2, C1′), 49.5 (CH_2, C5′), 115.7 (C, C12a″), 117.0 (C, C10a), 117.6 (C, C11a″), 118.6 (C, C4a), 118.8 (CH, C1), 119.1 (CH, C4″), 120.9 (CH, C8), 123.7 (CH, C3), 125.1 (CH, C8″), 125.8 (CH, C6), 126.7 (CH, C2″), 129.3 (CH, C1″), 134.6 (C, C9″), 134.8 (C, C8a), 135.2 (C, C9a), 138.8 (CH, C7), 140.2 (C, C3″), 140.9 (C, C4a″), 143.4 (C, C2), 151.4 (C, C5a″), 156.7 (C, C12″), 163.4 (C, C4), 163.7 (C, C5), 167.3 (C, CONH), 182.2 (C, C9), 193.7 (C, C10). HRMS (ESI) calcd for ($C_{37}H_{34}{}^{35}ClN_3O_5$ + H^+), 636.2260; found, 636.2255. Anal. ($C_{37}H_{34}ClN_3O_5$·HCl·1.5H_2O) C, H, N, Cl.

*(±)-N-{6-[(3-Chloro-6,7,10,11-tetrahydro-9-methyl-7,11-methanocycloocta[b]quinolin-12-yl)amino]hexyl}-9,10-dihydro-4,5-dihydroxy-9,10-dioxoanthracene-2-carboxamide [(±)-**7b**].* It was prepared as described for (±)-**7a**. From rhein, **3** (1.19 g, 4.18 mmol), and amine (±)-**6b** (1.60 g, 4.18 mmol), a red solid (2.00 g) was obtained and purified by column chromatography (40−60 μm silica gel, hexane/EtOAc/MeOH/Et_3N mixtures, gradient elution). On elution with hexane/EtOAc/MeOH/Et_3N 10:90:0:0.2 to 0:80:20:0.2, hybrid (±)-**7b** (647 mg, 24% yield) was isolated as a red solid; R_f 0.54 (CH_2Cl_2/MeOH/50% aq NH_4OH 9:1:0.05).

*(±)-**7b**·HCl.* Melting point 203−205 °C (CH_2Cl_2/MeOH 89:11). IR (KBr) ν 3500−2500 (max at 3228, 3042, 2927, 2859, 2722, O-H, N-H, N^+-H and C-H st), 1627, 1586, 1570 (C═O, ar-C-C and ar-C-N st) cm^{-1}. ^{1}H NMR (500 MHz, CD_3OD) δ 1.49−1.56 (complex signal, 4H, 3′-H_2, 4′-H_2), 1.59 (s, 3H, 9″-CH_3), 1.70 (tt, $J \approx J' \approx$ 6.7 Hz, 2H, 2′-H_2), superimposed in part 1.87−1.94 (complex signal, 3H, 5′-H_2, 13″-H_{syn}), superimposed in part 1.94 (br d, J = 17.5 Hz, 1H, 10″-H_{endo}), 2.07 (dm, J = 12.0 Hz, 1H, 13″-H_{anti}), 2.54 (br dd, $J \approx$ 17.5 Hz, $J' \approx$ 3.5 Hz, 1H, 10″-H_{exo}), 2.77 (m, 1H, 7″-H), 2.82 (br d, J = 18.0 Hz, 1H, 6″-H_{endo}), 3.17 (dd, J = 18.0 Hz, J' = 5.0 Hz, 1H, 6″-H_{exo}), 3.39−3.49 (complex signal, 3H, 1′-H_2, 11″-H), 3.96 (dt, J =J' = 6.7 Hz, 2H, 6′-H_2), 4.84 (s, NH, $^+$NH and OH), 5.58 (br d, J = 5.0 Hz, 1H, 8″-H), 7.35 (dd, J = 7.5 Hz, J' = 1.5 Hz, 1H, 6-H), 7.46 (d, $J \approx$ 9.0 Hz, 1H, 2″-H), 7.60 (s, 1H, 4″-H), 7.64 (s, 1H, 3-H), superimposed in part 7.75 (d, J = 8.0 Hz, 1H, 8-H), superimposed in part 7.77 (dd, $J \approx J' \approx$ 8.0 Hz, 1H, 7-H), 8.07 (s, 1H, 1-H), 8.32 (d, $J \approx$ 9.0 Hz, 1H, 1″-H). ^{13}C NMR (125.7 MHz, CD_3OD) δ 23.4 (CH_3, 9″-CH_3), 27.2 (CH, C11″), 27.3 (2CH_2, C3′, C4′), 27.9 (CH, C7″), 29.3 (CH_2, C13″), 30.0 (CH_2, C2′), 31.1 (CH_2, C5′), 36.1 (2CH_2, C6″, C10″), 40.7 (CH_2, C1′), 49.5 (CH_2, C6′), 115.7 (C, C12a″), 117.0 (C, C10a), 117.7 (C, C11a″), 118.6 (C, C4a), 118.8 (CH, C1), 119.1 (CH, C4″), 120.9 (CH, C8), 123.7 (CH, C3), 125.1 (CH, C8″), 125.8 (CH, C6), 126.6 (CH, C2″), 129.4 (CH, C1″), 134.6 (C, C9″), 134.8 (C, C8a), 135.3 (C, C9a), 138.8 (CH, C7), 140.2 (C, C3″), 141.0 (C, C4a″), 143.6 (C, C2), 151.3 (C, C5a″), 156.8 (C, C12″), 163.4 (C, C4), 163.8 (C, C5), 167.3 (C, CONH), 182.2 (C, C9), 193.8 (C, C10). HRMS (ESI) calcd for ($C_{38}H_{36}{}^{35}ClN_3O_5$ + H^+), 650.2416; found, 650.2414. Anal. ($C_{38}H_{36}ClN_3O_5$·HCl·1.25H_2O) C, H, N, Cl.

*(±)-N-{7-[(3-Chloro-6,7,10,11-tetrahydro-9-methyl-7,11-methanocycloocta[b]quinolin-12-yl)amino]heptyl}-9,10-dihydro-4,5-dihydroxy-9,10-dioxoanthracene-2-carboxamide [(±)-**7c**].* It was prepared as described for (±)-**7a**. From rhein, **3** (1.43 g, 5.04 mmol), and amine (±)-**6c** (2.00 g, 5.04 mmol), a red solid (2.20 g) was obtained and purified by column chromatography (40−60 μm silica gel, hexane/EtOAc/MeOH/Et_3N mixtures, gradient elution). On elution with hexane/EtOAc/MeOH/Et_3N 40:60:0:0.2 to 0:80:20:0.2, hybrid (±)-**7c** (864 mg, 26% yield) was isolated as a red solid; R_f 0.48 (CH_2Cl_2/MeOH/50% aq NH_4OH 9:1:0.05).

*(±)-**7c**·HCl.* Melting point 202−203 °C (EtOAc/CH_2Cl_2/MeOH 75:19:6). IR (KBr) ν 3500−2500 (max at 3048, 2926, 2855, 2742, O-H, N-H, N^+-H and C-H st), 1654, 1628, 1593, 1583, 1569, 1546 (C═O,

dx.doi.org/10.1021/jm401824w | J. Med. Chem. 2014, 57, 2549−2567

ar-C-C and ar-C-N st) cm^{-1}. ^1H NMR (500 MHz, CD_3OD) δ 1.49 (complex signal, 6H, 3′-H_2, 4′-H_2, 5′-H_2), 1.58 (s, 3H, 9″-CH_3), 1.69 (tt, $J \approx J' \approx 6.5$ Hz, 2H, 2′-H_2), superimposed in part 1.87−1.94 (complex signal, 3H, 6′-H_2, 13″-H_{syn}), superimposed in part 1.94 (br d, $J \approx 18.0$ Hz, 1H, 10″-H_{endo}), 2.07 (dm, $J = 12.0$ Hz, 1H, 13-H_{anti}), 2.53 (br dd, $J = 18.0$ Hz, $J' = 5.0$ Hz, 1H, 10-H_{exo}), 2.75 (m, 1H, 7″-H), 2.79 (br d, $J \approx 18.0$ Hz, 1H, 6″-H_{endo}), 3.14 (dd, $J \approx 18.0$ Hz, $J' = 5.5$ Hz, 1H, 6″-H_{exo}), 3.37−3.48 (complex signal, 3H, 1′-H_2, 11″-H), 3.92 (dt, $J = 7.5$ Hz, $J' = 4.0$ Hz, 2H, 7′-H_2), 4.84 (s, NH, $^+$NH and OH), 5.58 (br d, $J = 5.0$ Hz, 1H, 8″-H), 7.36 (dd, $J = 8.5$ Hz, $J' = 1.0$ Hz, 1H, 6-H), 7.44 (dd, $J \approx 9.0$ Hz, $J' = 2.0$ Hz, 1H, 2″-H), 7.59 (d, $J = 2.0$ Hz, 1H, 4″-H), 7.66 (d, $J \approx 2.0$ Hz, 1H, 3-H), 7.73 (dd, $J = 7.5$ Hz, $J' \approx 1.0$ Hz, 1H, 8-H), 7.78 (dd, $J \approx J' \approx 7.5$ Hz, 1H, 7-H), 8.09 (d, $J = 2.0$ Hz, 1H, 1-H), 8.26 (d, $J = 9.0$ Hz, 1H, 1″-H). ^{13}C NMR (125.7 MHz, CD_3OD) δ 23.4 (CH_3, 9″-CH_3), 27.3 (CH, C11″), 27.6 (CH_2), 27.7 (CH_2) (C4′, C5′), 27.9 (CH, C7″), 29.3 (CH_2, C13″), 29.7 (CH_2), 29.9 (CH_2) (C2′, C3′), 31.1 (CH_2, C6′), 36.0 (CH_2), 36.1 (CH_2) (C6″, C10″), 41.0 (CH_2, C1′), 49.7 (CH_2, C7′), 115.6 (C, C12a″), 117.1 (C, C10a), 117.6 (C, C11a″), 118.6 (C, C4a), 118.7 (CH, C1), 119.2 (CH, C4″), 120.9 (CH, C8), 123.7 (CH, C3), 125.1 (CH, C8″), 125.8 (CH, C6), 126.6 (CH, C2″), 129.3 (CH, C1″), 134.6 (C, C9″), 134.8 (C, C8a), 135.3 (C, C9a), 138.8 (CH, C7), 140.2 (C, C3″), 141.0 (C, C4a″), 143.7 (C, C2), 151.3 (C, C5a″), 156.6 (C, C12″), 163.5 (C, C4), 163.8 (C, C5), 167.4 (C, CONH), 182.2 (C, C9), 193.6 (C, C10). HRMS (ESI) calcd for ($C_{39}H_{38}{}^{35}ClN_3O_5 + H^+$), 664.2573; found, 664.2569. Anal. ($C_{39}H_{38}ClN_3O_5$·HCl·0.5H_2O) C, H, N, Cl.

*(±)-N-{8-[(3-Chloro-6,7,10,11-tetrahydro-9-methyl-7,11-methanocycloocta[b]quinolin-12-yl)amino]octyl}-9,10-dihydro-4,5-dihydroxy-9,10-dioxoanthracene-2-carboxamide [(±)-**7d**].* It was prepared as described for (±)-**7a**. From rhein, **3** (213 mg, 0.75 mmol), and amine (±)-**6d** (307 mg, 0.75 mmol), a red solid (740 mg) was obtained and purified by column chromatography (40−60 μm silica gel, CH_2Cl_2/MeOH/50% aq NH_4OH mixtures, gradient elution). On elution with CH_2Cl_2/MeOH/50% aq NH_4OH 98:2:0.2 to 80:20:0.2, hybrid (±)-**7d** (80 mg, 16% yield) was isolated as a red solid; R_f 0.30 (CH_2Cl_2/MeOH/50% aq NH_4OH 9:1:0.05).

*(±)-**7d**·HCl.* Melting point 180−182 °C (EtOAc/CH_2Cl_2/MeOH 66:17:17). IR (KBr) ν 3500−2500 (max at 3222, 3047, 3007, 2924, 2852, 2640, O-H, N-H, N^+-H, and C-H st), 1766, 1674, 1628, 1607, 1582, 1566, 1522 (C═O, ar-C-C and ar-C-N st) cm^{-1}. ^1H NMR (500 MHz, CD_3OD) δ 1.44 (complex signal, 8H, 3′-H_2, 4′-H_2, 5′-H_2, 6′H_2), 1.59 (s, 3H, 9″-CH_3), 1.67 (tt, $J \approx J' \approx 7.0$ Hz, 2H, 2′-H_2), superimposed in part 1.86 (tt, $J \approx J' \approx 7.0$ Hz, 2H, 7′-H_2), superimposed 1.85−1.94 (m, 1H, 13″-H_{syn}), superimposed in part 1.93 (br d, $J \approx 18.0$ Hz, 1H, 10″-H_{endo}), 2.06 (dm, $J = 12.0$ Hz, 1H, 13″-H_{anti}), 2.53 (br dd, $J \approx 18.0$ Hz, $J' = 4.5$ Hz, 1H, 10″-H_{exo}), 2.75 (m, 1H, 7″-H), 2.82 (br d, $J = 18.0$ Hz, 1H, 6″-H_{endo}), 3.13 (dd, $J = 18.0$ Hz, $J' = 5.0$ Hz, 1H, 6″-H_{exo}), 3.39−3.47 (complex signal, 3H, 1′-H_2, 11″-H), 3.87 (dt, $J \approx J' \approx 6.0$ Hz, 2H, 8′-H_2), 4.86 (s, NH, $^+$NH and OH), 5.58 (br d, $J = 5.0$ Hz, 1H, 8″-H), 7.26 (d, $J = 8.5$ Hz, 1H, 6-H), 7.35 (d, $J \approx 9.0$ Hz, 1H, 2″-H), 7.54 (s, 1H, 4″-H), 7.58 (s, 1H, 3-H), superimposed in part 7.57−7.61 (m, 1H, 8-H), 7.69 (dd, $J \approx J' \approx 8.0$ Hz, 1H, 7-H), 7.97 (s, 1H, 1-H), 8.19 (d, $J = 9.0$ Hz, 1H, 1″-H). ^{13}C NMR (125.7 MHz, CD_3OD) δ 23.5 (CH_3, 9″-CH_3), 27.2 (CH, C11″), 27.5 (CH_2), 27.6 (CH_2), (C5′, C6′), 27.8 (CH, C7″), 29.3 (CH_2, C13″), 29.86 (CH_2), 29.92 (CH_2), 30.0 (CH_2) (C2′, C3′, C4′), 31.1 (CH_2, C7′), 36.0 (2CH_2, C6″, C10″), 41.0 (CH_2, C1′), 49.7 (CH_2, C8′), 115.4 (C, C12a″), 116.7 (C, C10a), 117.5 (C, C11a″), 118.3 (C, C4a), 118.8 (CH, C1), 119.0 (CH, C4″), 120.8 (CH, C8), 123.7 (CH, C3), 125.1 (CH, C8″), 125.8 (CH, C6), 126.6 (CH, C2″), 129.2 (CH, C1″), 134.4 (C, C9″), 134.6 (C, C8a), 134.9 (C, C9a), 138.8 (CH, C7), 140.1 (C, C3″), 140.8 (C, C4a″), 143.6 (C, C2), 151.1 (C, C5a″), 156.5 (C, C12″), 163.3 (C, C4), 163.5 (C, C5), 167.1 (C, CONH), 181.8 (C, C9), 193.4 (C, C10). HRMS (ESI) calcd for ($C_{40}H_{40}{}^{35}ClN_3O_5 + H^+$), 678.2729; found, 678.2734. Anal. ($C_{40}H_{40}ClN_3O_5$·HCl·H_2O) C, H, N, Cl.

*(±)-N-{9-[(3-Chloro-6,7,10,11-tetrahydro-9-methyl-7,11-methanocycloocta[b]quinolin-12-yl)amino]nonyl}-9,10-dihydro-4,5-dihydroxy-9,10-dioxoanthracene-2-carboxamide [(±)-**7e**].* It was prepared as described for (±)-**7a**. From rhein, **3** (213 mg, 0.75 mmol), and amine (±)-**6e** (321 mg, 0.75 mmol), a red solid (550 mg) was obtained and purified by column chromatography (40−60 μm silica gel, hexane/EtOAc/MeOH/Et_3N mixtures, gradient elution). On elution with hexane/EtOAc/MeOH/Et_3N 20:80:0:0.2 to 0:80:20:0.2, hybrid (±)-**7e** (118 mg, 23% yield) was isolated as a red solid; R_f 0.33 (CH_2Cl_2/MeOH/50% aq NH_4OH 9:1:0.05).

*(±)-**7e**·HCl.* Melting point 192−193 °C (EtOAc/CH_2Cl_2/MeOH 70:15:15). IR (KBr) ν 3500−2500 (max at 3401, 2925, 2853, O-H, N-H, N^+-H, and C-H st), 1628, 1584, 1566, 1524 (C═O, ar-C-C and ar-C-N st) cm^{-1}. ^1H NMR (500 MHz, CD_3OD) δ 1.41 (complex signal, 10H, 3′-H_2, 4′-H_2, 5′-H_2, 6′H_2, 7′-H_2), 1.59 (s, 3H, 9″-CH_3), superimposed in part 1.64 (m, 2H, 2′-H_2), superimposed in part 1.66 (tt, $J \approx J' \approx 6.0$ Hz, 2H, 8′-H_2), superimposed 1.84−1.94 (m, 1H, 13″-H_{syn}), superimposed in part 1.92 (br d, $J = 17.0$ Hz, 1H, 10″-H_{endo}), 2.06 (dm, $J \approx 10.5$ Hz, 1H, 13″-H_{anti}), 2.53 (dm, $J \approx 17.0$ Hz, 1H, 10″-H_{exo}), 2.76 (m, 1H, 7″-H), superimposed in part 2.79 (br d, $J \approx 18.0$ Hz, 1H, 6″-H_{endo}), 3.14 (dd, $J = 18.0$ Hz, $J' = 3.5$ Hz, 1H, 6″-H_{exo}), 3.38−3.42 (complex signal, 3H, 1′-H_2, 11″-H), 3.86−3.96 (m, 2H, 9′-H_2), 4.85 (s, NH, $^+$NH and OH), 5.58 (br d, $J = 4.0$ Hz, 1H, 8″-H), 7.31 (d, $J = 8.5$ Hz, 1H, 6-H), 7.38 (d, $J = 8.5$ Hz, 1H, 2″-H), 7.57 (s, 1H, 4″-H), 7.63 (s, 1H, 3-H), superimposed in part 7.64 (d, $J = 7.0$ Hz, 1H, 8-H), 7.72 (dd, $J \approx J' \approx 8.0$ Hz, 1H, 7-H), 8.04 (s, 1H, 1-H), 8.20 (d, $J = 8.5$ Hz, 1H, 1″-H), 8.82 (br s, 1H, CONH). ^{13}C NMR (125.7 MHz, CD_3OD) δ 23.5 (CH_3, 9″-CH_3), 27.2 (CH, C11″), 27.5 (CH_2), 27.6 (CH_2) (C6′, C7′), 27.8 (CH, C7″), 29.3 (CH_2, C13″), 29.7 (2CH_2), 30.0 (CH_2), 30.1 (CH_2) (C2′, C3′, C4′, C5′), 31.2 (CH_2, C8′), 36.0 (2CH_2, C6″, C10″), 41.0 (CH_2, C1′), 49.6 (CH_2, C9′), 115.4 (C, C12a″), 116.8 (C, C10a), 117.5 (C, C11a″), 118.4 (C, C4a), 118.8 (CH, C1), 119.1 (CH, C4″), 120.8 (CH, C8), 123.7 (CH, C3), 125.1 (CH, C8″), 125.8 (CH, C6), 126.6 (CH, C2″), 129.2 (CH, C1″), 134.6 (2C, C8a, C9″), 135.1 (C, C9a), 138.7 (CH, C7), 140.2 (C, C3″), 140.8 (C, C4a″), 143.7 (C, C2), 151.0 (C, C5a″), 156.6 (C, C12″), 163.4 (C, C4), 163.6 (C, C5), 167.3 (C, CONH), 182.0 (C, C9), 193.5 (C, C10). HRMS (ESI) calcd for ($C_{41}H_{42}{}^{35}ClN_3O_5 + H^+$), 692.2886; found, 692.2873. Anal. ($C_{41}H_{42}ClN_3O_5$·1.3HCl·1.25H_2O) C, H, N, Cl.

*(−)-N-{9-[(3-Chloro-6,7,10,11-tetrahydro-9-methyl-7,11-methanocycloocta[b]quinolin-12-yl)amino]nonyl}-9,10-dihydro-4,5-dihydroxy-9,10-dioxoanthracene-2-carboxamide [(−)-**7e**].* It was prepared as described for (±)-**7a**. From rhein, **3** (422 mg, 1.49 mmol), and amine (−)-**6e** (632 mg, 1.49 mmol), a red solid (1.10 g) was obtained and purified by column chromatography (40−60 μm silica gel, CH_2Cl_2/MeOH/50% aq NH_4OH mixtures, gradient elution). On elution with CH_2Cl_2/MeOH/50% aq NH_4OH 99:1:0.2, hybrid (−)-**7e** (101 mg, 10% yield) was isolated as a red solid; R_f 0.33 (CH_2Cl_2/MeOH/50% aq NH_4OH 9:1:0.05).

*(−)-**7e**·HCl.* Melting point 168−170 °C (CH_2Cl_2/MeOH 83:17); $[\alpha]^{20}_D = -154$ ($c = 0.10$, MeOH). IR (KBr) ν 3500−2500 (max at 3226, 3048, 3002, 2925, 2853, 2743, O-H, N-H, N^+-H and C-H st), 1766, 1705, 1675, 1629, 1604, 1582, 1566, 1524, 1509 (C═O, ar-C-C and ar-C-N st) cm^{-1}. The ^1H NMR and ^{13}C NMR spectra were identical to those of (±)-**7e**. HRMS (ESI) calcd for ($C_{41}H_{42}{}^{35}ClN_3O_5 + H^+$), 692.2886; found, 692.2891. Anal. ($C_{41}H_{42}ClN_3O_5$·HCl·H_2O) C, H, N, Cl.

*(+)-N-{9-[(3-Chloro-6,7,10,11-tetrahydro-9-methyl-7,11-methanocycloocta[b]quinolin-12-yl)amino]nonyl}-9,10-dihydro-4,5-dihydroxy-9,10-dioxoanthracene-2-carboxamide [(+)-**7e**].* It was prepared as described for (±)-**7a**. From rhein, **3** (477 mg, 1.68 mmol), and amine (+)-**6e** (715 mg, 1.68 mmol), a red solid (1.50 g) was obtained and purified by column chromatography (40−60 μm silica gel, CH_2Cl_2/MeOH/50% aq NH_4OH mixtures, gradient elution). On elution with CH_2Cl_2/MeOH/50% aq NH_4OH 99:1:0.2, hybrid (+)-**7e** (191 mg, 16% yield) was isolated as a red solid; R_f 0.33 (CH_2Cl_2/MeOH/50% aq NH_4OH 9:1:0.05).

*(+)-**7e**·HCl.* Melting point 164−165 °C (CH_2Cl_2/MeOH 88:12); $[\alpha]^{20}_D = +154$ ($c = 0.10$, MeOH). IR (KBr) ν 3500−2500 (max at 3226, 3049, 2926, 2852, O-H, N-H, N^+-H, and C-H st), 1763, 1739, 1723, 1710, 1656, 1629, 1583, 1566, 1555, 1537, 1511, 1501 (C═O, ar-C-C and ar-C-N st) cm^{-1}. The ^1H NMR and ^{13}C NMR spectra were identical to those of (±)-**7e**. HRMS (ESI) calcd for ($C_{41}H_{42}{}^{35}ClN_3O_5 + H^+$), 692.2886; found, 692.2877. Anal. ($C_{41}H_{42}ClN_3O_5$·1.25HCl·0.75H_2O) C, H, N, Cl.

*(±)-N-{10-[(3-Chloro-6,7,10,11-tetrahydro-9-methyl-7,11-methanocycloocta[b]quinolin-12-yl)amino]decyl}-9,10-dihydro-4,5-dihydroxy-9,10-dioxoanthracene-2-carboxamide [(±)-**7f**].* It was prepared as described for (±)-**7a**. From rhein, **3** (344 mg, 1.21 mmol),

dx.doi.org/10.1021/jm401824w | J. Med. Chem. 2014, 57, 2549−2567

and amine (±)-**6f** (530 mg, 1.21 mmol), a red solid (900 mg) was obtained and purified by column chromatography (40−60 μm silica gel, CH_2Cl_2/MeOH/50% aq NH_4OH mixtures, gradient elution). On elution with CH_2Cl_2/MeOH/50% aq NH_4OH 99:1:0.2, hybrid (±)-**7f** (115 mg, 13% yield) was isolated as a red solid; R_f 0.53 (CH_2Cl_2/MeOH/50% aq NH_4OH 9:1:0.05).

*(±)-**7f**·HCl.* Melting point 171−173 °C (EtOAc/CH_2Cl_2/MeOH 72:14:14). IR (KBr) ν 3500−2500 (max at 3229, 3049, 3002, 2925, 2852, O-H, N-H, N^+-H, and C-H st), 1767, 1739, 1715, 1675, 1629, 1604, 1583, 1567, 1524 (C═O, ar-C-C and ar-C-N st) cm^{-1}. ^1H NMR (500 MHz, CD_3OD) δ 1.34−1.44 (complex signal, 12H, 3′-H_2, 4′-H_2, 5′-H_2, 6′H_2, 7′-H_2, 8′-H_2), 1.58 (s, 3H, 9″-CH_3), 1.66 (tt, $J \approx J' \approx 7.0$ Hz, 2H, 2′-H_2), 1.83 (tt, $J \approx J' \approx 7.0$ Hz, 2H, 9′-H_2), superimposed 1.90−1.93 (m, 1H, 13″-H_{syn}), superimposed in part 1.92 (br d, J = 17.0 Hz, 1H, 10″-H_{endo}), 2.06 (dm, $J \approx$ 12.0 Hz, 1H, 13″-H_{anti}), 2.52 (br dd, $J \approx$ 17.0 Hz, $J' \approx$ 4.3 Hz, 1H, 10″-H_{exo}), 2.75 (m, 1H, 7″-H), 2.82 (br d, J = 18.0 Hz, 1H, 6″-H_{endo}), 3.15 (dd, $J \approx$ 18.0 Hz, J' = 5.3 Hz, 1H, 6″-H_{exo}), 3.38−3.45 (complex signal, 3H, 1′-H_2, 11″-H), 3.87 (dt, $J \approx J' \approx$ 6.5 Hz, 2H, 10′-H_2), 4.85 (s, NH, $^+$NH and OH), 5.57 (br d, J = 5.5 Hz, 1H, 8″-H), 7.27 (dd, J = 8.5 Hz, J' = 1.0 Hz, 1H, 6-H), 7.39 (dd, J = 9.5 Hz, J' = 1.5 Hz, 1H, 2″-H), superimposed in part 7.59 (s, 1H, 4″-H), 7.60 (d, J = 1.5 Hz, 1H, 3-H), 7.63 (dd, J = 7.5 Hz, J' = 1.0 Hz, 1H, 8-H), 7.70 (dd, $J \approx J' \approx$ 8.0 Hz, 1H, 7-H), 8.01 (d, J = 1.5 Hz, 1H, 1-H), 8.21 (d, J = 9.5 Hz, 1H, 1″-H). ^{13}C NMR (125.7 MHz, CD_3OD) δ 23.5 (CH_3, 9″-CH_3), 27.2 (CH, C11″), 27.7 (2CH_2), 27.8 (CH + CH_2) (C6′, C7′, C8′, C7″), 29.3 (CH_2, C13″), 30.03 (CH_2), 30.05 (CH_2), 30.22 (CH_2), 30.25 (CH_2) (C2′, C3′, C4′, C5′), 31.2 (CH_2, C9′), 36.0 (2CH_2, C6″, C10″), 41.1 (CH_2, C1′), 49.6 (CH_2, C10′), 115.5 (C, C12a″), 116.8 (C, C10a), 117.5 (C, C11a″), 118.4 (C, C4a), 118.9 (CH, C1), 119.1 (CH, C4″), 120.9 (CH, C8), 123.7 (CH, C3), 125.1 (CH, C8″), 125.8 (CH, C6), 126.7 (CH, C2″), 129.3 (CH, C1″), 134.6 (2C, C8a, C9″), 135.0 (C, C9a), 138.7 (CH, C7), 140.2 (C, C3″), 140.8 (C, C4a″), 143.7 (C, C2), 151.0 (C, C5a″), 156.6 (C, C12″), 163.3 (C, C4), 163.6 (C, C5), 167.2 (C, CONH), 181.9 (C, C9), 193.5 (C, C10). HRMS (ESI) calcd for ($C_{42}H_{44}{}^{35}ClN_3O_5$ + H^+), 706.3042; found, 706.3038. Anal. ($C_{42}H_{44}ClN_3O_5$·HCl·0.5H_2O) C, H, N, Cl.

*(±)-N-{11-[(3-Chloro-6,7,10,11-tetrahydro-9-methyl-7,11-methanocycloocta[b]quinolin-12-yl)amino]undecyl}-9,10-dihydro-4,5-dihydroxy-9,10-dioxoanthracene-2-carboxamide [(±)-**7g**].* It was prepared as described for (±)-**7a**. From rhein, **3** (491 mg, 1.73 mmol), and amine (±)-**6g** (785 mg, 1.73 mmol), a red solid (1.60 g) was obtained and purified by column chromatography (40−60 μm silica gel, CH_2Cl_2/MeOH/50% aq NH_4OH mixtures, gradient elution). On elution with CH_2Cl_2/MeOH/50% aq NH_4OH 99:1:0.2, hybrid (±)-**7g** (338 mg, 27% yield) was isolated as a red solid; R_f 0.50 (CH_2Cl_2/MeOH/50% aq NH_4OH 9:1:0.05).

*(±)-**7g**·HCl.* Melting point 171−172 °C (EtOAc/CH_2Cl_2/MeOH 60:20:20). IR (KBr) ν 3500−2500 (max at 3226, 3048, 3007, 2924, 2852, 2645, O-H, N-H, N^+-H and C-H st), 1765, 1675, 1628, 1607, 1583, 1567, 1522 (C═O, ar-C-C and ar-C-N st) cm^{-1}. ^1H NMR (500 MHz, CD_3OD) δ 1.33−1.43 (complex signal, 14H, 3′-H_2, 4′-H_2, 5′-H_2, 6′H_2, 7′-H_2, 8′-H_2, 9′-H_2), 1.58 (s, 3H, 9″-CH_3), 1.66 (tt, $J \approx J' \approx$ 7.0 Hz, 2H, 2′-H_2), 1.82 (tt, $J \approx J' \approx$ 17.0 Hz, 2H, 10′-H_2), superimposed 1.89−1.93 (m, 1H, 13″-H_{syn}), superimposed in part 1.91 (br d, J = 17.0 Hz, 1H, 10″-H_{endo}), 2.05 (dm, $J \approx$ 10.5 Hz, Hz, 1H, 13″-H_{anti}), 2.52 (br dd, $J \approx$ 17.0 Hz, $J' \approx$ 4.5 Hz, 1H, 10″-H_{exo}), 2.75 (m, 1H, 7″-H), 2.82 (br d, J = 18.0 Hz, 1H, 6″-H_{endo}), 3.14 (dd, $J \approx$ 18.0 Hz, J' = 5.5 Hz, 1H, 6″-H_{exo}), superimposed in part 3.37 (m, 1H, 11″-H), superimposed in part 3.40 (tt, $J \approx J' \approx$ 7.0 Hz, 2H, 1′-H_2), 3.86 (dt, $J \approx J' \approx$ 7.0 Hz, 2H, 11′-H_2), 4.85 (s, NH, $^+$NH and OH), 5.57 (br d, J = 5.5 Hz, 1H, 8″-H), 7.23 (dd, J = 8.5 Hz, J' = 1.0 Hz, 1H, 6-H), 7.37 (dd, J = 9.0 Hz, $J' \approx$ 1.5 Hz, 1H, 2″-H), superimposed in part 7.57 (d, J = 1.5 Hz, 1H, 4″-H), superimposed in part 7.58 (d, J = 2.0 Hz, 1H, 3-H), superimposed in part 7.58 (dd, J = 8.0 Hz, J' = 1.0 Hz, 1H, 8-H), 7.67 (dd, $J \approx J' \approx$ 8.0 Hz, 1H, 7-H), 7.97 (d, J = 1.5 Hz, 1H, 1-H), 8.20 (d, J = 9.0 Hz, 1H, 1″-H). ^{13}C NMR (125.7 MHz, CD_3OD) δ 23.5 (CH_3, 9″-CH_3), 27.2 (CH, C11″), 27.7 (CH_2), 27.82 (CH, C7″), 27.83 (2CH_2) (C7′, C8′, C9′), 29.3 (CH_2, C13″), 30.1 (2CH_2), 30.2 (CH_2), 30.36 (CH_2), 30.40 (CH_2) (C2′, C3′, C4′, C5′, C6′), 31.2 (CH_2, C10′), 36.0 (2CH_2, C6″, C10″), 41.2 (CH_2, C1′), 49.6 (CH_2, C11′), 115.4 (C, C12a″), 116.7 (C, C10a), 117.5 (C, C11a″), 118.3 (C, C4a), 118.9 (CH, C1), 119.1 (CH, C4″), 120.8 (CH, C8), 123.7 (CH, C3), 125.1 (CH, C8‴), 125.8 (CH, C6), 126.6 (CH, C2″), 129.3 (CH, C1″), 134.5 (C, C9″), 134.6 (C, C8a), 134.9 (C, C9a), 138.7 (CH, C7), 140.2 (C, C3″), 140.8 (C, C4a″), 143.7 (C, C2), 151.0 (C, C5a″), 156.6 (C, C12″), 163.3 (C, C4), 163.5 (C, C5), 167.1 (C, CONH), 181.8 (C, C9), 193.4 (C, C10). HRMS (ESI) calcd for ($C_{43}H_{46}{}^{35}ClN_3O_5$ + H^+), 720.3199; found, 720.3195. Anal. ($C_{43}H_{46}ClN_3O_5$·HCl·0.5H_2O) C, H, N, Cl.

*(±)-N-{4-{[(3-Chloro-6,7,10,11-tetrahydro-9-methyl-7,11-methanocycloocta[b]quinolin-12-yl)amino]methyl}benzyl}-9,10-dihydro-4,5-dihydroxy-9,10-dioxoanthracene-2-carboxamide [(±)-**7h**].* It was prepared as described for (±)-**7a**. From rhein, **3** (548 mg, 1.93 mmol), and amine (±)-**6h** (780 mg, 1.93 mmol), a red solid (1.07 g) was obtained and purified by column chromatography (40−60 μm silica gel, hexane/EtOAc/Et_3N mixtures, gradient elution). On elution with hexane/EtOAc/Et_3N 40:60:0.2, hybrid (±)-**7h** (113 mg, 9% yield) was isolated as a red solid; R_f 0.57 (CH_2Cl_2/MeOH/50% aq NH_4OH 9:1:0.05).

*(±)-**7h**·HCl.* Melting point 129−130 °C (EtOAc/CH_2Cl_2/MeOH 66:17:17). IR (KBr) ν 3500−2500 (max at 3245, 3055, 2925, 2852, 2790, O-H, N-H, N^+-H, and C-H st), 1705, 1673, 1629, 1607, 1583, 1560, 1516 (C═O, ar-C-C, and ar-C-N st) cm^{-1}. ^1H NMR (400 MHz, CD_3OD) δ 1.59 (s, 3H, 9″-CH_3), superimposed 1.92−1.98 (m, 1H, 13″-H_{syn}), 1.97 (br d, J = 16.8 Hz, 1H, 10″-H_{endo}), 2.08 (dm, J = 12.4 Hz, 1H, 13″-H_{anti}), 2.53 (br dd, $J \approx$ 16.8 Hz, $J' \approx$ 5.0 Hz, 1H, 10″-H_{exo}), 2.78 (m, 1H, 7″-H), 2.86 (br d, J = 18.0 Hz, 1H, 6″-H_{endo}), 3.20 (dd, $J \approx$ 18.0 Hz, J' = 5.6 Hz, 1H, 6″-H_{exo}), 3.47 (m, 1H, 11″-H), 4.60 (s, 2H, CH_2NH), 4.85 (s, NH, $^+$NH and OH), 5.18 (s, 2H, CH_2NHCO), 5.59 (m, 1H, 8″-H), 7.28 (dd, J = 9.2 Hz, J' = 2.0 Hz, 1H, 2″-H), 7.34 (dd, J = 8.0 Hz, J' = 2.0 Hz, 1H, 6-H), 7.41 (d, J = 8.4 Hz, 2H) and 7.47 (d, J = 8.4 Hz, 2H) [2′(6′)-H_2, 3′(5′)-H_2], 7.67 (d, J = 2.0 Hz, 1H) and 7.69 (d, J = 2.0 Hz, 1H) (3-H, 4″-H), 7.76 (dd, $J \approx J' \approx$ 7.2 Hz, 1H, 7-H), 7.79 (dd, J = 7.2 Hz, J' = 2.0 Hz, 1H, 8-H), 8.15 (d, $J \approx$ 2.0 Hz, 1H, 1-H), 8.21 (d, J = 9.2 Hz, 1H, 1″-H). ^{13}C NMR (125.7 MHz, CD_3OD) δ 23.5 (CH_3, 9″-CH_3), 27.5 (CH, C11″), 27.8 (CH, C7″), 29.3 (CH_2, C13″), 36.0 (CH_2, C6″), 36.2 (CH_2, C10″), 44.3 (CH_2, CH_2NH), 51.9 (CH_2, CH_2NHCO), 115.4 (C, C12a″), 116.9 (C, C10a), 118.2 (C, C11a″), 118.5 (C, C4a), 118.8 (CH, C1), 119.0 (CH, C4″), 120.9 (CH, C8), 123.7 (CH, C3), 125.0 (CH, C8″), 125.8 (CH, C6), 126.6 (CH, C2″), 128.1 (CH), 129.8 (CH) [C2′(6′), C3′(5′)], 129.3 (CH, C1″), 134.6 (C, C9″), 134.7 (C, C8a), 135.0 (C, C9a), 137.8 (C) and 139.2 (C) (C1′, C4′), 138.8 (CH, C7), 140.2 (C, C3″), 140.7 (C, C4a″), 143.1 (C, C2), 151.6 (C, C5a″), 157.1 (C, C12″), 163.3 (C, C4), 163.6 (C, C5), 167.1 (C, CONH), 182.0 (C, C9), 193.5 (C, C10). HRMS (ESI) calcd for ($C_{40}H_{32}{}^{35}ClN_3O_5$ + H^+), 670.2103; found, 670.2104. Anal. ($C_{40}H_{32}ClN_3O_5$·1.1HCl·1.4H_2O) C, H, N, Cl.

In Vitro Biological Studies. *AChE and BChE Inhibition Assay.* Human recombinant AChE (Sigma, Milan, Italy) inhibitory activity was evaluated spectrophotometrically by the method of Ellman et al.[46] Initial rate assays were performed at 37 °C with a Jasco V-530 double beam spectrophotometer. Stock solutions of the tested compounds (1 mM) were prepared in MeOH and diluted in MeOH. The assay solution consisted of a 0.1 M potassium phosphate buffer, pH 8.0, with the addition of 340 μM 5,5′-dithiobis(2-nitrobenzoic acid) (DTNB, used to produce the yellow anion of 5-thio-2-nitrobenzoic acid), 0.02 unit/mL hAChE, and 550 μM substrate (acetylthiocholine iodide). Assay solutions with and without inhibitor were preincubated at 37 °C for 20 min, followed by the addition of substrate. Blank solutions containing all components except hAChE were prepared in parallel to account for the nonenzymatic hydrolysis of the substrate. Five increasing concentrations of the inhibitor were used, able to give an inhibition of the enzymatic activity in the range of 20−80%. The results were plotted by placing the percentage of inhibition in function of the decimal log of the final inhibitor concentration. Linear regression and IC_{50} values were calculated using Microcal Origin 3.5 software (Microcal Software, Inc.).

Human serum BChE inhibitory activities were also evaluated spectrophotometrically by the method of Ellman et al.[46] The reactions took place in a final volume of 300 μL of 0.1 M phosphate-buffered solution pH 8.0, containing hBChE (0.02 u/mL) and 333 μM DTNB solution. Inhibition curves were performed in duplicates using at least 10 increasing concentrations of inhibitor and preincubated for 20 min at

37 °C. One duplicate sample without inhibitor was always present to yield 100% of BChE activity. Then substrate butyrylthiocholine iodide (300 μM, Sigma-Aldrich) was added and the reaction was developed for 5 min at 37 °C. The color production was measured at 414 nm using a labsystems Multiskan spectrophotometer. Data from concentration–inhibition experiments of the inhibitors were calculated by nonlinear regression analysis, using the GraphPad Prism program package (GraphPad Software; San Diego, USA), which gave estimates of the IC_{50} values. Results are expressed as mean ± SEM of at least four experiments performed in duplicate.

Kinetic Analysis of AChE Inhibition. To assess the mechanism of action of hybrid (−)-7**e**, reciprocal plots of 1/velocity versus 1/[Substrate] were constructed at relatively low concentration of substrate (0.562–0.112 mM) by using Ellman's method[46] and human recombinant AChE (Sigma, Milan, Italy). Three concentrations of inhibitor were selected for this study: 0.84, 1.34, 3.65 nM. The plots were assessed by a weighted least-squares analysis that assumed the variance of the velocity (v) to be a constant percentage of v for the entire data set. Data analysis was performed with GraphPad Prism 4.03 software (GraphPad Software Inc.).

Calculation of the inhibitor constant (K_i) value was carried out by replotting slopes of lines from the Lineweaver–Burk plot versus the inhibitor concentration and K_i was determined as the intersect on the negative x-axis. K_i' (dissociation constant for the enzyme–substrate–inhibitor complex) value was determined by plotting the apparent $1/v_{max}$ versus inhibitor concentration.[87]

AChE-Induced Aβ40 Aggregation Inhibition Assay.[49] Thioflavin T (Basic Yellow 1), human recombinant AChE lyophilized powder, and 1,1,1,3,3,3-hexafluoro-2-propanol (HFIP) were purchased from Sigma Chemicals. Buffers and other chemicals were of analytical grade. Absolute DMSO over molecular sieves was from Fluka. Water was deionized and doubly distilled. Aβ40, supplied as trifluoroacetate salt, was purchased from Bachem AG (Germany). Aβ40 (2 mg mL^{-1}) was dissolved in HFIP, lyophilized, and then resolubilized in DMSO to get a 2.3 mM Aβ40 solution. One mM solutions of tested inhibitors were prepared by dissolution in MeOH.

Aliquots of 2 μL of Aβ40 peptide were incubated for 24 h at room temperature in 0.215 M sodium phosphate buffer (pH 8.0) at a final concentration of 230 μM. For coincubation experiments, aliquots (16 μL) of hAChE (final concentration 2.30 μM, Aβ/AChE molar ratio 100:1) and AChE in the presence of 2 μL of the tested inhibitor (final inhibitor concentration 100 μM) in 0.215 M sodium phosphate buffer pH 8.0 solution were added. Blanks containing Aβ40 alone, human recombinant AChE alone, and Aβ40 plus tested inhibitors in 0.215 M sodium phosphate buffer (pH 8.0) were prepared. The final volume of each vial was 20 μL. Each assay was run in duplicate. To quantify amyloid fibril formation, the thioflavin T fluorescence method was then applied.[88] The fluorescence intensities due to β-sheet conformation were monitored for 300 s at λ_{em} = 490 nm (λ_{exc} = 446 nm). The percent inhibition of the AChE-induced aggregation due to the presence of the tested compound was calculated by the following expression: $100 - (IF_i/IF_o \times 100)$ where IF_i and IF_o are the fluorescence intensities obtained for Aβ plus AChE in the presence and in the absence of inhibitor, respectively, minus the fluorescence intensities due to the respective blanks.

Aβ42 Self-Aggregation Inhibition Assay. As reported in a previously published protocol,[58] HFIP pretreated Aβ42 samples (Bachem AG, Switzerland) were first solubilized with a CH_3CN/0.3 mM Na_2CO_3/250 mM NaOH (48.4:48.4:3.2) mixture to obtain a 500 μM solution. Experiments were performed by incubating the peptide in 10 mM phosphate buffer (pH = 8.0) containing 10 mM NaCl, at 30 °C for 24 h (final Aβ concentration 50 μM) with and without inhibitor (10 μM, Aβ/inhibitor = 5/1). Blanks containing the tested inhibitors were also prepared and tested. To quantify amyloid fibrils formation, the thioflavin T fluorescence method was used.[88] After incubation, samples were diluted to a final volume of 2.0 mL with 50 mM glycine–NaOH buffer (pH 8.5) containing 1.5 μM thioflavin T. A 300 s time scan of fluorescence intensity was carried out (λ_{exc} = 446 nm; λ_{em} = 490 nm, FP-6200 fluorometer, Jasco Europe), and values at plateau were averaged after subtracting the background fluorescence of 1.5 μM thioflavin T solution. The fluorescence intensities were compared and the percent inhibition due to the presence of the inhibitor was calculated by the following formula: $100 - (IF_i/IF_o \times 100)$ where IF_i and IF_o are the fluorescence intensities obtained for Aβ42 in the presence and in the absence of inhibitor, respectively.

BACE-1 Inhibition Assay. β-Secretase (BACE-1, Sigma) inhibition studies were performed by employing a peptide mimicking APP sequence as substrate (methoxycoumarin-Ser-Glu-Val-Asn-Leu-Asp-Ala-Glu-Phe-Lys-dinitrophenyl, M-2420, Bachem, Germany). The following procedure was employed: 5 μL of test compounds (or DMSO, if preparing a control well) were preincubated with 175 μL of enzyme (in 20 mM sodium acetate pH 4.5 containing CHAPS 0.1% w/v) for 1 h at room temperature. The substrate (3 μM, final concentration) was then added and left to react for 15 min. The fluorescence signal was read at λ_{em} = 405 nm (λ_{exc} = 320 nm). The DMSO concentration in the final mixture was maintained below 5% (v/v) to guarantee no significant loss of enzyme activity. The fluorescence intensities with and without inhibitor were compared, and the percent inhibition due to the presence of test compounds was calculated. The background signal was measured in control wells containing all the reagents, except BACE-1, and subtracted. The % inhibition due to the presence of increasing test compound concentration was calculated by the following expression: $100 - (IF_i/IF_o \times 100)$ where IF_i and IF_o are the fluorescence intensities obtained for BACE-1 in the presence and in the absence of inhibitor, respectively. Inhibition curves were obtained by plotting the % inhibition versus the logarithm of inhibitor concentration in the assay sample, when possible. The linear regression parameters were determined and the IC_{50} extrapolated (GraphPad Prism 4.0, GraphPad Software Inc.). To demonstrate inhibition of BACE-1 activity a peptidomimetic inhibitor (β-secretase inhibitor IV, Calbiochem) was serially diluted into the reactions' wells (IC_{50} = 13.0 ± 0.1 nM).

BBB Permeation Assay. The brain penetration of the synthesized hybrids was assessed using the parallel artificial membrane permeation assay for blood–brain barrier described by Di et al.[71] The in vitro permeability (P_e) of 14 commercial drugs through lipid extract of porcine brain membrane together with that of the test compounds was determined. Commercial drugs and synthesized hybrids were tested using a mixture of PBS/EtOH 70:30. Assay validation was made by comparing the experimental permeability of the different compounds with the literature values of the commercial drugs, which showed a good correlation: P_e (exp) = 1.4525 P_e (lit) − 0.4926 (R^2 = 0.9199). From this equation and taking into account the limits established by Di et al. for BBB permeation, we established the following ranges of permeability: compounds of high BBB permeation (CNS+), P_e (10^{-6} cm s^{-1}) > 5.3; compounds of low BBB permeation (CNS−), P_e (10^{-6} cm s^{-1}) < 2.4, and compounds of uncertain BBB permeation (CNS±), 5.3 > P_e (10^{-6} cm s^{-1}) > 2.4.

Aβ42 Aggregation Inhibition Assay in Intact Escherichia coli Cells Overexpressing Aβ42 and Tau. Cloning and overexpression of Aβ42 peptide: *Escherichia coli* competent cells BL21 (DE3) were transformed with the pET28a vector (Novagen, Inc., Madison, WI, USA) carrying the DNA sequence of Aβ42. Because of the addition of the initiation codon ATG in front of both genes, the overexpressed peptide contains an additional methionine residue at its N terminus. For overnight culture preparation, 10 mL of lysogeny broth (LB) medium containing 50 μg·mL^{-1} of kanamycin were inoculated with a colony of BL21 (DE3) bearing the plasmid to be expressed at 37 °C. After overnight growth, the OD600 was usually 2–2.5. For expression of Aβ42 peptide, 20 μL of overnight culture were transferred into Eppendorf tubes of 1.5 mL containing 980 μL of LB medium with 50 μg·mL^{-1} of kanamycin, 1 mM of isopropyl 1-thio-β-D-galactopyranoside (IPTG) and 10 μM of each hybrid 7 or reference compound to be tested in DMSO. The samples were grown for 24 h at 37 °C and 1400 rpm using a Thermomixer (Eppendorf, Hamburg, Germany). In the negative control (without drug), the same amount of DMSO was added in the sample.

Cloning and overexpression of tau protein: *E. coli* BL21 (DE3) competent cells were transformed with pTARA containing the RNA-polymerase gen of T7 phage (T7RP) under the control of the promoter pBAD. *E. coli* BL21 (DE3) with pTARA competent cells were transformed with pRKT42 vector encoding four repeats of tau protein in two inserts. For overnight culture preparation, 10 mL of M9 medium containing 0.5% of glucose, 50 μg·mL^{-1} of ampicillin, and 12.5 μg·mL^{-1}

of chloramphenicol were inoculated with a colony of BL21 (DE3) bearing the plasmids to be expressed at 37 °C. After overnight growth, the OD600 was usually 2−2.5. For expression of tau protein, 20 μL of overnight culture were transferred into Eppendorf tubes of 1.5 mL containing 980 μL of M9 medium containing 0.25% of arabinose, 0.5% of glucose, 50 $\mu g \cdot mL^{-1}$ of ampicillin, and 12.5 $\mu g \cdot mL^{-1}$ of chloramphenicol and 10 μM of each hybrid **7** or reference compound to be tested in DMSO. The samples were grown for 24 h at 37 °C and 1400 rpm using a Thermomixer (Eppendorf, Hamburg, Germany). In the negative control (without drug), the same amount of DMSO was added in the sample.

Thioflavin-S (Th-S) steady-state fluorescence: Th-S (T1892) and other chemical reagents were purchased from Sigma (St. Louis, MO). Th-S stock solution (250 mM) was prepared in double-distilled water purified through a Milli-Q system (Millipore, USA). Fluorescent spectral scans of Th-S were analyzed using an Aminco Bowman series 2 luminescence spectrophotometer (Aminco-Bowman AB2, SLM Aminco, Rochester, NY, USA). For the fluorescence assay, 25 μM of Th-S (20 μL of Th-S in 180 μL of sample) were added to samples and spectra were recorded after 15 min equilibration at 37 °C. Excitation and emission slit widths of 5 nm were used. Finally, the fluorescence emission at 520 nm, when exciting at 440 nm, was recorded. To normalize the Th-S fluorescence as a function of the bacterial concentration, OD600 was obtained using a Shimadzu UV-2401 PC UV−vis spectrophotometer (Shimadzu, Japan). Note that the fluorescence normalization has been carried out considering as 100% the Th-S fluorescence of the bacterial cells expressing the peptide or protein in the absence of drug and 0% the Th-S fluorescence of the bacterial cells nonexpressing the peptide or protein.

Ex Vivo Studies in C57bl6 Mice. *Electrophysiological Assays in Hippocampal Slices Incubated with Aβ Oligomers.* Hippocampal slices were prepared according to standard procedures previously described.[89,90] Briefly, transverse slices (350 μm) from the dorsal hippocampus were cut under cold artificial cerebrospinal fluid (ACSF, in mM, 124 NaCl, 2.6 $NaHCO_3$, 10 D-glucose, 2.69 KCl, 1.25 KH_2PO_4 2.5 $CaCl_2$, 1.3 $MgSO_4$, and 2.60 $NaHPO_4$) using a Vibratome (Leica VT 1000s, Germany) and incubated in ACSF for 1 h at room temperature. In all experiments, 10 μM picrotoxin (PTX) was added to suppress inhibitory GABAA transmission. Slices were transferred to an experimental chamber (2 mL), superfused (3 mL/min, at 20−22 °C) with gassed ACSF, and visualized by trans-illumination with a binocular microscope (MSZ-10, Nikon, Melville, NY). To evoke field excitatory postsynaptic potentials (fEPSPs), we stimulated with bipolar concentric electrodes (platinum/iridium, 125 μm OD diameter, FHC Inc., Bowdoin, ME) generated by a stimulator (Axon 700b, Molecular Devices, Sunnyvale, CA) and connected to an isolation unit (Isoflex, AMPI, Jerusalem, Israel). The stimulation was in the stratum radiatum within 100−200 μm from the recording site. The paired pulse facilitation index was calculated by ((R2 − R1)/R1), where R1 and R2 were the peak amplitudes of the first and second fEPSP, respectively. To generate LTP, we used theta burst stimulation (TBS) consisting of 5 trains of stimulus with an intertrain interval of 20 s. Each train consisted of 10 bursts at 5 Hz and each burst having four pulses at 100 Hz. To generate LTD we used low frequency stimulation (LFS) consisting in 900 paired pulses at 1 Hz. Recordings were filtered at 2.0−3.0 kHz, sampled at 4.0 kHz using an A/D converter, and stored with pClamp 10 (Molecular Devices). Evoked postsynaptic responses were analyzed off-line, using an analysis software (pClampfit, Molecular Devices), which allowed visual detection of events, computing only those events that exceeded an arbitrary threshold.

Determination of Synaptic Protein Levels in Hippocampal Slices Incubated with Aβ Oligomers. Immunoblotting: The hippocampus of C57bl6 mice were dissected on ice and immediately frozen at −150 °C or processed. Briefly, hippocampal tissue was homogenized in RIPA buffer (50 mM Tris-Cl, pH 7.5, 150 mM NaCl, 1% NP-40, 0.5% sodium deoxycholate, and 1% SDS) supplemented with a protease inhibitor cocktail (Sigma-Aldrich P8340) and phosphatase inhibitors (50 mM NaF, 1 mM Na_3VO_4, and 30 μM $Na_4P_2O_7$) using a Potter homogenizator and then passed sequentially through different caliber syringes. Protein samples were centrifuged at 14000 rpm at 4 °C twice for 10 min. Protein concentration was determined using the BCA protein assay kit (Pierce Biotechnology, Rockford, IL). Then 20 and 40 μg of hippocampal samples were resolved by 10% SDS-PAGE, transferred to a PVDF membrane. The reactions were followed by incubation with primary antibodies, secondary antibodies antimouse, antigoat, or antirabbit IgG peroxidase conjugated (Pierce) and developed using an ECL kit (Western Lightning Plus ECL, PerkinElmer).

In Vivo Studies in APP-PS1 Mice. *Animals and Treatment.* APPswe/PSEN1ΔE9 (APP-PS1) mice, which express the Swedish mutation of APP (K595N/M596L) and PS1 with the deletion of exon 9 were obtained from The Jackson Laboratory (Bar Harbor, ME; mice stock no. 004462). All animals were housed in temperature- and light-controlled rooms, with food and water ad libitum during the treatment. Six and 10 month-old mice were treated and handled according to the National Institutes of Health guidelines (NIH, Baltimore, MD). Treatments were performed by intraperitoneal (ip) injection of 2.0 mg/kg enantiopure rhein−huprine hybrids (+)-**7e** or (−)-**7e** with saline solution as vehicle, three times per week during 4 weeks. Transgenic control animals were injected only with the vehicle.

Immunoblotting. The hippocampus from control or treated APP-PS1 mice were dissected on ice and immediately frozen at −150 °C or processed as detailed previously.[90,91] Briefly, hippocampus were homogenized in RIPA buffer (50 mM Tris-Cl, pH 7.5, 150 mM NaCl, 1% NP-40, 0.5% sodium deoxycholate, and 1% SDS) supplemented with a protease inhibitor cocktail (Sigma-Aldrich P8340) and phosphatase inhibitors (50 mM NaF, 1 mM Na_3VO_4, and 30 μM $Na_4P_2O_7$) using a Potter homogenizator and then passed sequentially through different caliber syringes. Protein samples were centrifuged at 14000 rpm at 4 °C twice for 20 min. Protein concentration was determined using the BCA protein assay kit (Pierce Biotechnology, Rockford, IL).

Aβ detection. For the detection of soluble Aβ peptides, samples from hippocampus were centrifugated to 20000*g* for 1 h, and the protein concentration from supernatant was determined using the BCA protein assay kit (Pierce Biotechnology, Rockford, IL). Then 80 μg of proteins were resolved in 17.5% SDS polyacrylamide Tris-tricine gels, followed by immunoblotting on PVDF membranes using mouse anti-Aβ protein 6E10 (Covance). To analyze the levels of APP the antibody MAB348 (Millipore) was utilized. Band intensities were visualized by ECL kit (Western Lightning Plus ECL, PerkinElmer), scanned, and densitometrically quantified using ImageJ software.[85,92]

Docking in AChE. AChE models were built up from the human recombinant AChE structure 3LII.[93] The structure was refined by addition of missing hydrogen atoms, removal of nonstandard residues, and generation of disulfide bonds Cys69−Cys96, Cys257−Cys272, and Cys405−Cys524. Because the fragment between residues Gly264 and Pro258 is not observed in the X-ray structure, it was modeled from the equivalent fragment of *Torpedo californica* AChE (*Tc*AChE). Finally, the enzyme was modeled in its physiological active form with neutral His447 and neutral Glu334, which together with Ser203 forms the catalytic triad. We considered the standard ionization state at physiological pH for the rest of ionizable residues with exception of Glu450, which was modeled in its neutral state.

The binding mode of (−)-**7h** and (+)-**7h** to AChE was explored by means of docking calculations performed with rDock, whose reliability in predicting binding mode for dual site inhibitors of AChE has been largely demonstrated in previous studies.[94] The orientation of Tyr337 residue was modified to mimic the conformation of the equivalent residue Phe330 in the complex between *Tc*AChE and (−)-huprine X (PDB 1E66).[39] To explore the binding at the PAS, three different AChE models differing in the orientation of Trp286 were built. The side chain of Trp286 was oriented following the three orientations found in X-ray structures deposited in the Protein Data Bank, which can be characterized by dihedral angles χ_1 ($N-C_\alpha-C_\beta-C_\gamma$) and χ_2 ($C_\alpha-C_\beta-C_\gamma-C_{\delta 2}$) close to (i) −60° and −80°, (ii) −120° and +50°, and (iii) −160° and −120°. PDB structures 1N5R (AChE−propidium complex), 2CKM (AChE−bis(7)-tacrine complex), and 1Q83 (AChE−*syn*-TZ2PA6 complex), respectively, are representative cases of these orientations and were used to generate the corresponding models. The docking volume was defined as the space covered by the catalytic, midgorge, and peripheral sites, and each compound was subjected to 100 docking runs and solutions clustered according to the RMSD among its heavy atoms using a threshold of 2.0 Å, selecting the best ranked pose to be

representative of the cluster. The resulting binding modes were analyzed by visual inspection in conjunction with the docking scores.

Docking and Molecular Dynamics in BACE-1. To explore the binding mode of rhein−huprine hybrids, druggable pockets were identified using the MDpocket program.[95] Calculations were performed for X-ray structures 1M4H, 1SGZ, 2OHL, and 3CIB chosen to account for structural variability in the flexible "flap" loop located over the catalytic site and of certain regions (loops 9−12 and 263−268) and side chains in the peptide binding groove. The structures were refined by addition of missing hydrogen atoms, removal of nonstandard residues, and generation of disulfide bonds Cys155−Cys359, Cys217−Cys382, and Cys269−Cys319. Only druggable pockets that shared α-spheres in at least three different structures were retained and ranked according to druggability criteria.[96]

GLIDE[97] was used to explore the preferred binding sites of the huprine and hydroxyanthraquinone moieties (obtained by replacing the methylene chain by a methyl group) to the druggable sites and to explore the binding mode of compound **7h**. The docking cavity was defined as a 13824 Å^3 cube whose center was located among residues Gly13, Leu30, Tyr71, Ile110, Trp115, and Gly230. Three different protonation states were considered for the catalytic diad (Asp32, Asp228), including the doubly deprotonated form and the two single deprotonated forms. Default settings were used, and the best poses were clustered according to the RMSD between its heavy atoms, with a threshold of 2.0 Å, and subsequently evaluated using the Glide-XP scoring function.

The binding modes proposed for (−)-**7h** and (+)-**7h** were assessed by means of molecular dynamics (MD) using GPU-accelerated PMEMD[98] module from the AMBER12 software package.[99] The Parm99SB[100] force field was used for the protein, and the gaff force field[101] was used to assign parameters to both ligands. Na^+ cations added to neutralize the system were treated according with Joung and Cheatham parameters.[102] The ligands charge distribution were determined from a fit to the HF/6-31G(d) electrostatic potential obtained with Gaussian09[103] using the RESP[104] protocol as implemented in the Antechamber module of AmberTools12 software package.

Each system comprised around 46000 atoms, including the protein−ligand complex and eight Na^+ cations solvated on a truncated octahedral box of 13000 TIP3P water molecules.[105] The geometry of the system was minimized in four steps. First, water molecules were refined though 4500 steepest descent algorithm followed by 10500 steps of conjugate gradient. Then, protein and ligand hydrogen atoms positions were optimized using 500 steps of steepest descent and 4500 of conjugate gradient. Next, the ligand, water molecules, and counterions were further optimized with 2000 steps of steepest descent and 6000 of conjugate gradient and, at the last step, the whole system was optimized with 2500 steps of steepest descent and 4500 of conjugate gradient. At this point, five different replicas for each ligand were generated by randomly assigning different sets of velocities to the initial coordinates, all fitting a Maxwell distribution for a temperature of 50K. For each one of the replicas, thermalization was performed in the canonical ensemble during five 25 ps steps, using a time step of 1 fs and increasing the temperature from 50 to 298 K. Concomitantly, the inhibitor and the residues in the binding site were restrained during thermalization using a variable restraint force that was decreased sequentially from 5 to 0 kcal mol^{-1} Å^{-2} using increments of 1 kcal mol^{-1} Å^{-2} within the different thermalization stages. Prior to the production runs, a short 1 ns simulation in the isothermal−isobaric ensemble was performed in other to reach a stable density value of 1003 kg m^{-3}. Production runs consisted of 50 ns trajectories (accounting for a global simulation time of 200 ns per ligand) using SHAKE for bonds involving hydrogen atoms, allowing for a time step of 2 fs, in conjunction with periodic boundary conditions at constant volume and temperature (298 K; Langevin thermostat with a collision frequency of 3 ps^{-1}), particle mesh Ewald for long-range electrostatic interactions, and a cutoff of 10 Å for nonbonded interactions.

■ ASSOCIATED CONTENT

Supporting Information

Synthetic procedures and chemical characterization of intermediate nitriles **5a−h** and amines **6a−h**, additional figures of the molecular modeling studies on AChE and BACE-1, additional data of PAMPA-BBB studies. This material is available free of charge via the Internet at http://pubs.acs.org.

■ AUTHOR INFORMATION

Corresponding Author

*Phone: +34-934024533. Fax: +34-934035941. E-mail: dmunoztorrero@ub.edu.

Present Address

◆For E.V.: Drug Discovery Unit, College of Life Sciences, University of Dundee, Dundee DD1 5EH, UK.

Notes

The authors declare no competing financial interest.

■ ACKNOWLEDGMENTS

This work was supported by Ministerio de Ciencia e Innovación (MICINN) (CTQ2011-22433, SAF2009-10553, SAF2011-27642, start-up grant of the Ramón y Cajal program for R.S.), Generalitat de Catalunya (GC) (2009SGR1396, 2009SGR249), University of Bologna, Italian Ministry of Education (MIUR, FFO—Fondo Finanziamento Ordinario) and Uni-Rimini SpA, and CONICYT-PFB (12/2007). Fellowships from GC to E.V. and I.S., from FIS to J.J.-J., from CONICYT to C.T.R., a contract from the Ramón y Cajal program of MICINN to R.S., and the ICREA support to F.J.L. are gratefully acknowledged. The Center for Scientific and Academic Services of Catalonia (CESCA) is acknowledged for providing access to computational facilities.

■ ABBREVIATIONS USED

Aβ, β-amyloid peptide; Aβ-o, Aβ oligomers; AChE, acetylcholinesterase; AChEI, AChE inhibitor; ACSF, artificial cerebrospinal fluid; AD, Alzheimer's disease; APP, amyloid precursor protein; BBB, blood−brain barrier; BACE-1, β-site APP cleaving enzyme 1; BChE, butyrylcholinesterase; CAS, catalytic anionic site; CNS, central nervous system; DTNB, 5,5′-dithiobis(2-nitrobenzoic acid); fEPSP, field excitatory postsynaptic potentials; hAChE, human acetylcholinesterase; hBChE, human butyrylcholinesterase; HFIP, 1,1,1,3,3,3-hexafluoro-2-propanol; IBs, inclusion bodies; LTP, long-term potentiation; PAS, peripheral anionic site; PBS, phosphate-buffered saline; SYN, synapsin; SYP, synaptophysin; *Tc*AChE, *Torpedo californica* acetylcholinesterase

■ REFERENCES

(1) Batsch, N. L.; Mittelman, M. S. *World Alzheimer Report 2012. Overcoming the Stigma of Dementia*; Alzheimer's Disease International: London, 2012; http://www.alz.co.uk.

(2) Hardy, J.; Selkoe, D. J. The amyloid hypothesis of Alzheimer's disease: progress and problems on the road to therapeutics. *Science* **2002**, *297*, 353−356.

(3) Kung, H. F. The β-amyloid hypothesis in Alzheimer's disease: seeing is believing. *ACS Med. Chem. Lett.* **2012**, *3*, 265−267.

(4) Citron, M. Alzheimer's disease: strategies for disease modification. *Nature Rev. Drug Discovery* **2010**, *9*, 387−398.

(5) Pimplikar, S. W. Reassessing the amyloid cascade hypothesis of Alzheimer's disease. *Int. J. Biochem. Cell Biol.* **2009**, *41*, 1261−1268.

(6) Cavalli, A.; Bolognesi, M. L.; Minarini, A.; Rosini, M.; Tumiatti, V.; Recanatini, M.; Melchiorre, C. Multi-target-directed ligands to combat neurodegenerative diseases. *J. Med. Chem.* **2008**, *51*, 347−372.

(7) Bajda, M.; Guzior, N.; Ignasik, M.; Malawska, B. Multi-target-directed ligands in Alzheimer's disease treatment. *Curr. Med. Chem.* **2011**, *18*, 4949−4975.

(8) Geldenhuys, W. J.; Van der Schyf, C. J. Rationally designed multi-targeted agents against neurodegenerative diseases. *Curr. Med. Chem.* **2013**, *20*, 1662−1672.
(9) Chen, X.; Decker, M. Multi-target compounds acting in the central nervous system designed from natural products. *Curr. Med. Chem.* **2013**, *20*, 1673−1685.
(10) Russo, P.; Frustaci, A.; Del Bufalo, A.; Fini, M.; Cesario, A. Multitarget drugs of plants origin acting on Alzheimer's disease. *Curr. Med. Chem.* **2013**, *20*, 1686−1693.
(11) For recent examples, see refs 11−15. Butini, S.; Brindisi, M.; Brogi, S.; Maramai, S.; Guarino, E.; Panico, A.; Saxena, A.; Chauhan, V.; Colombo, R.; Verga, L.; De Lorenzi, E.; Bartolini, M.; Andrisano, V.; Novellino, E.; Campiani, G.; Gemma, S. Multifunctional cholinesterase and amyloid beta fibrillization modulators. Synthesis and biological investigation. *ACS Med. Chem. Lett.* **2013**, *4*, 1178−1182.
(12) Capurro, V.; Busquet, P.; Lopes, J. P.; Bertorelli, R.; Tarozzo, G.; Bolognesi, M. L.; Piomelli, D.; Reggiani, A.; Cavalli, A. Pharmacological characterization of memoquin, a multi-target compound for the treatment of Alzheimer's disease. *PLoS One* **2013**, *8*, e56870.
(13) Kochi, A.; Eckroat, T. J.; Green, K. D.; Mayhoub, A. S.; Lim, M. H.; Garneau-Tsodikova, S. A novel hybrid of 6-chlorotacrine and metal−amyloid-β modulator for inhibition of acetylcholinesterase and metal-induced amyloid-β aggregation. *Chem. Sci.* **2013**, *4*, 4137−4145.
(14) Xie, S.-S.; Wang, X.-B.; Li, J.-Y.; Yang, L.; Kong, L.-Y. Design, synthesis and evaluation of novel tacrine−coumarin hybrids as multifunctional cholinesterase inhibitors against Alzheimer's disease. *Eur. J. Med. Chem.* **2013**, *64*, 540−553.
(15) Prinz, M.; Parlar, S.; Bayraktar, G.; Alptüzün, V.; Erciyas, E.; Fallarero, A.; Karlsson, D.; Vuorela, P.; Burek, M.; Förster, C.; Turunc, E.; Armagan, G.; Yalcin, A.; Schiller, C.; Leuner, K.; Krug, M.; Sotriffer, C. A.; Holzgrabe, U. 1,4-Substituted 4-(1*H*)-pyridylene-hydrazone-type inhibitors of AChE, BChE, and amyloid-β aggregation crossing the blood−brain barrier. *Eur. J. Pharm. Sci.* **2013**, *49*, 603−613.
(16) Viayna, E.; Sabate, R.; Muñoz-Torrero, D. Dual inhibitors of β-amyloid aggregation and acetylcholinesterase as multi-target anti-Alzheimer drug candidates. *Curr. Top. Med. Chem.* **2013**, *13*, 1820−1842.
(17) Inestrosa, N. C.; Alvarez, A.; Pérez, C. A.; Moreno, R. D.; Vicente, M.; Linker, C.; Casanueva, O. I.; Soto, C.; Garrido, J. Acetylcholinesterase accelerates assembly of amyloid-β-peptides into Alzheimer's fibrils: possible role of the peripheral site of the enzyme. *Neuron* **1996**, *16*, 881−891.
(18) Alvarez, A.; Alarcón, R.; Opazo, C.; Campos, E. O.; Muñoz, F. J.; Calderón, F. H.; Dajas, F.; Gentry, M. K.; Doctor, B. P.; De Mello, F. G.; Inestrosa, N. C. Stable complexes involving acetylcholinesterase and amyloid-β-peptide change the biochemical properties of the enzyme and increase the neurotoxicity of Alzheimer's fibrils. *J. Neurosci.* **1998**, *18*, 3213−3223.
(19) De Ferrari, G. V.; Canales, M. A.; Shin, I.; Weiner, L. M.; Silman, I.; Inestrosa, N. C. A structural motif of acetylcholinesterase that promotes amyloid beta-peptide fibril formation. *Biochemistry* **2001**, *40*, 10447−10457.
(20) Sussman, J. L.; Harel, M.; Frolow, F.; Oefner, C.; Goldman, A.; Toker, L.; Silman, I. Atomic structure of acetylcholinesterase from *Torpedo californica*: a prototypic acetylcholine-binding protein. *Science* **1991**, *253*, 872−879.
(21) Du, D.-M.; Carlier, P. R. Development of bivalent acetylcholinesterase inhibitors as potential therapeutic drugs for Alzheimer's disease. *Curr. Pharm. Des.* **2004**, *10*, 3141−3156.
(22) Recanatini, M.; Valenti, P. Acetylcholinesterase inhibitors as a starting point towards improved Alzheimer's disease therapeutics. *Curr. Pharm. Des.* **2004**, *10*, 3157−3166.
(23) Castro, A.; Martinez, A. Targeting beta-amyloid pathogenesis through acetylcholinesterase inhibitors. *Curr. Pharm. Des.* **2006**, *12*, 4377−4387.
(24) Li, W. M.; Kan, K. K. W.; Carlier, P. R.; Pang, Y. P.; Han, Y. F. East meets West in the search for Alzheimer's therapeutics—novel dimeric inhibitors from tacrine and huperzine A. *Curr. Alzheimer Res.* **2007**, *4*, 386−396.
(25) Holzgrabe, U.; Kapková, P.; Alptüzün, V.; Scheiber, J.; Kugelmann, E. Targeting acetylcholinesterase to treat neurodegeneration. *Expert Opin. Ther. Targets* **2007**, *11*, 161−179.
(26) Musial, A.; Bajda, M.; Malawska, B. Recent developments in cholinesterases inhibitors for Alzheimer's disease treatment. *Curr. Med. Chem.* **2007**, *14*, 2654−2679.
(27) Haviv, H.; Wong, D. M.; Silman, I.; Sussman, J. L. Bivalent ligands derived from huperzine A as acetylcholinesterase inhibitors. *Curr. Top. Med. Chem.* **2007**, *7*, 375−387.
(28) Muñoz-Torrero, D. Acetylcholinesterase inhibitors as disease-modifying therapies for Alzheimer's disease. *Curr. Med. Chem.* **2008**, *15*, 2433−2455.
(29) Rampa, A.; Belluti, F.; Gobbi, S.; Bisi, A. Hybrid-based multi-target ligands for the treatment of Alzheimer's disease. *Curr. Top. Med. Chem.* **2011**, *11*, 2716−2730.
(30) Pickhardt, M.; Gazova, Z.; von Bergen, M.; Khlistunova, I.; Wang, Y.; Hascher, A.; Mandelkow, E.-M.; Biernat, J.; Mandelkow, E. Anthraquinones inhibit tau aggregation and dissolve Alzheimer's paired helical filaments in vitro and in cells. *J. Biol. Chem.* **2005**, *280*, 3628−3635.
(31) Bulic, B.; Pickhardt, M.; Schmidt, B.; Mandelkow, E.-M.; Waldmann, H.; Mandelkow, E. Development of tau aggregation inhibitors for Alzheimer's disease. *Angew. Chem., Int. Ed.* **2009**, *48*, 1740−1752.
(32) Yang, X.; Sun, G.; Yang, C.; Wang, B. Novel rhein analogues as potential anticancer agents. *ChemMedChem* **2011**, *6*, 2294−2301.
(33) Shi, D.-H.; Huang, W.; Li, C.; Wang, L.-T.; Wang, S.-F. Synthesis, biological evaluation and molecular modeling of aloe−emodin derivatives as new acetylcholinesterase inhibitors. *Bioorg. Med. Chem.* **2013**, *21*, 1064−1073.
(34) Orhan, I.; Tosun, F.; Şener, B. Coumarin, anthroquinone and stilbene derivatives with anticholinesterase activity. *Z. Naturforsch.* **2008**, *63c*, 366−370.
(35) Guo, J.-P.; Yu, S.; McGeer, P. L. Simple in vitro assay to identify amyloid-β aggregation blockers for Alzheimer's disease therapy. *J. Alzheimer's Dis.* **2010**, *19*, 1359−1370.
(36) Camps, P.; Contreras, J.; Font-Bardia, M.; Morral, J.; Muñoz-Torrero, D.; Solans, X. Enantioselective synthesis of tacrine−huperzine A hybrids. Preparative chiral MPLC separation of their racemic mixtures and absolute configuration assignments by X-ray diffraction analysis. *Tetrahedron: Asymmetry* **1998**, *9*, 835−849.
(37) Camps, P.; El Achab, R.; Morral, J.; Muñoz-Torrero, D.; Badia, A.; Baños, J. E.; Vivas, N. M.; Barril, X.; Orozco, M.; Luque, F. J. New tacrine−huperzine A hybrids (huprines): highly potent tight-binding acetylcholinesterase inhibitors of interest for the treatment of Alzheimer's disease. *J. Med. Chem.* **2000**, *43*, 4657−4666.
(38) Camps, P.; Cusack, B.; Mallender, W. D.; El Achab, R.; Morral, J.; Muñoz-Torrero, D.; Rosenberry, T. L. Huprine X is a novel high-affinity inhibitor of acetylcholinesterase that is of interest for the treatment of Alzheimer's disease. *Mol. Pharmacol.* **2000**, *57*, 409−417.
(39) Dvir, H.; Wong, D. M.; Harel, M.; Barril, X.; Orozco, M.; Luque, F. J.; Muñoz-Torrero, D.; Camps, P.; Rosenberry, T. L.; Silman, I.; Sussman, J. L. 3D Structure of *Torpedo californica* acetylcholinesterase complexed with huprine X at 2.1 Å resolution: Kinetic and molecular dynamics correlates. *Biochemistry* **2002**, *41*, 2970−2981.
(40) Galdeano, C.; Viayna, E.; Sola, I.; Formosa, X.; Camps, P.; Badia, A.; Clos, M. V.; Relat, J.; Ratia, M.; Bartolini, M.; Mancini, F.; Andrisano, V.; Salmona, M.; Minguillón, C.; González-Muñoz, G. C.; Rodríguez-Franco, M. I.; Bidon-Chanal, A.; Luque, F. J.; Muñoz-Torrero, D. Huprine−tacrine heterodimers as anti-amyloidogenic compounds of potential interest against Alzheimer's and prion diseases. *J. Med. Chem.* **2012**, *55*, 661−669.
(41) Camps, P.; Formosa, X.; Galdeano, C.; Muñoz-Torrero, D.; Ramírez, L.; Gómez, E.; Isambert, N.; Lavilla, R.; Badia, A.; Clos, M. V.; Bartolini, M.; Mancini, F.; Andrisano, V.; Arce, M. P.; Rodríguez-Franco, M. I.; Huertas, O.; Dafni, T.; Luque, F. J. Pyrano[3,2-*c*]quinoline-6-chlorotacrine hybrids as a novel family of acetylcholinesterase- and β-amyloid-directed anti-Alzheimer compounds. *J. Med. Chem.* **2009**, *52*, 5365−5379.

(42) Best, M.; Gifford, A. N.; Kim, S. W.; Babst, B.; Piel, M.; Rösch, F.; Fowler, J. S. Rapid radiosynthesis of [^{11}C] and [^{14}C]azelaic, suberic, and sebacic acids for in vivo mechanistic studies of systemic acquired resistance in plants. *J. Labelled Compd. Radiopharm.* **2012**, *55*, 39−43.
(43) Taber, D. F.; Kong, S. Alkylation of acetonitrile. *J. Org. Chem.* **1997**, *62*, 8575−8576.
(44) Lethesh, K. C.; Van Hecke, K.; Van Meervelt, L.; Nockemann, P.; Kirchner, B.; Zahn, S.; Parac-Vogt, T. N.; Dehaen, W.; Binnemans, K. Nitrile-functionalized pyridinium, pyrrolidinium, and piperidinium ionic liquids. *J. Phys. Chem. B* **2011**, *115*, 8424−8438.
(45) Lane, R. M.; Potkin, S. G.; Enz, A. Targeting acetylcholinesterase and butyrylcholinesterase in dementia. *Int. J. Neuropsychopharmacol.* **2006**, *9*, 101−124.
(46) Ellman, G. L.; Courtney, K. D.; Andres, V., Jr.; Featherstone, R. M. A new and rapid colorimetric determination of acetylcholinesterase activity. *Biochem. Pharmacol.* **1961**, *7*, 88−95.
(47) Rydberg, E. H.; Brumshtein, B.; Greenblatt, H. M.; Wong, D. M.; Shaya, D.; Williams, L. D.; Carlier, P. R.; Pang, Y.-P.; Silman, I.; Sussman, J. L. Complexes of alkylene-linked tacrine dimers with *Torpedo californica* acetylcholinesterase: binding of bis(5)-tacrine produces a dramatic rearrangement in the active site gorge. *J. Med. Chem.* **2006**, *49*, 5491−5500.
(48) Bolognesi, M. L.; Cavalli, A.; Valgimigli, L.; Bartolini, M.; Rosini, M.; Andrisano, V.; Recanatini, M.; Melchiorre, C. Multi-target-directed drug design strategy: from a dual binding site acetylcholinesterase inhibitor to a trifunctional compound against Alzheimer's disease. *J. Med. Chem.* **2007**, *50*, 6446−6449.
(49) Bartolini, M.; Bertucci, C.; Cavrini, V.; Andrisano, V. β-Amyloid aggregation induced by human acetylcholinesterase: inhibition studies. *Biochem. Pharmacol.* **2003**, *65*, 407−416.
(50) Rouleau, J.; Iorga, B. I.; Guillou, C. New potent human acetylcholinesterase inhibitors in the tetracyclic triperpene series with inhibitory potency on amyloid β aggregation. *Eur. J. Med. Chem.* **2011**, *46*, 2193−2205.
(51) Mohamed, T.; Yeung, J. C. K.; Rao, P. P. N. Development of 2-substituted-*N*-(naphth-1-ylmethyl) and *N*-benzhydrylpyrimidin-4-amines as dual cholinesterase and Aβ-aggregation inhibitors: synthesis and biological evaluation. *Bioorg. Med. Chem. Lett.* **2011**, *21*, 5881−5887.
(52) Bolognesi, M. L.; Bartolini, M.; Mancini, F.; Chiriano, G.; Ceccarini, L.; Rosini, M.; Milelli, A.; Tumiatti, V.; Andrisano, V.; Melchiorre, C. Bis(7)-tacrine derivatives as multitarget-directed ligands: focus on anticholinesterase and antiamyloid activities. *ChemMedChem* **2010**, *5*, 1215−1220.
(53) Minarini, A.; Milelli, A.; Tumiatti, V.; Rosini, M.; Simoni, E.; Bolognesi, M. L.; Andrisano, V.; Bartolini, M.; Motori, E.; Angeloni, C.; Hrelia, S. Cystamine−tacrine dimer: a new multi-target-directed ligand as potential therapeutic agent for Alzheimer's disease treatment. *Neuropharmacology* **2012**, *62*, 997−1003.
(54) Rizzo, S.; Bisi, A.; Bartolini, M.; Mancini, F.; Belluti, F.; Gobbi, S.; Andrisano, V.; Rampa, A. Multi-target strategy to address Alzheimer's disease: design, synthesis and biological evaluation of new tacrine-based dimers. *Eur. J. Med. Chem.* **2011**, *46*, 4336−4343.
(55) Belluti, F.; Bartolini, M.; Bottegoni, G.; Bisi, A.; Cavalli, A.; Andrisano, V.; Rampa, A. Benzophenone-based derivatives: a novel series of potent and selective dual inhibitors of acetylcholinesterase and acetylcholinesterase-induced beta-amyloid aggregation. *Eur. J. Med. Chem.* **2011**, *46*, 1682−1693.
(56) Cavalli, A.; Bolognesi, M. L.; Capsoni, S.; Andrisano, V.; Bartolini, M.; Margotti, E.; Cattaneo, A.; Recanatini, M.; Melchiorre, C. A small molecule targeting the multifactorial nature of Alzheimer's disease. *Angew. Chem., Int. Ed.* **2007**, *46*, 3689−3692.
(57) Muñoz-Ruiz, P.; Rubio, L.; García-Palomero, E.; Dorronsoro, I.; del Monte-Millán, M.; Valenzuela, R.; Usán, P.; de Austria, C.; Bartolini, M.; Andrisano, V.; Bidon-Chanal, A.; Orozco, M.; Luque, F. J.; Medina, M.; Martínez, A. Design, synthesis, and biological evaluation of dual binding site acetylcholinesterase inhibitors: new disease-modifying agents for Alzheimer's disease. *J. Med. Chem.* **2005**, *48*, 7223−7233.
(58) Bartolini, M.; Bertucci, C.; Bolognesi, M. L.; Cavalli, A.; Melchiorre, C.; Andrisano, V. Insight into the kinetic of amyloid beta (1−42) peptide self-aggregation: elucidation of inhibitors' mechanism of action. *ChemBioChem* **2007**, *8*, 2152−2161.
(59) May, P. C.; Dean, R. A.; Lowe, S. L.; Martenyi, F.; Sheehan, S. M.; Boggs, L. N.; Monk, S. A.; Mathes, B. M.; Mergott, D. J.; Watson, B. M.; Stout, S. L.; Timm, D. E.; Smith LaBell, E.; Gonzales, C. R.; Nakano, M.; Jhee, S. S.; Yen, M.; Ereshefsky, L.; Lindstrom, T. D.; Calligaro, D. O.; Cocke, P. J.; Hall, D. G.; Friedrich, S.; Citron, M.; Audia, J. E. Robust central reduction of amyloid-β in humans with an orally available, non-peptidic β-secretase inhibitor. *J. Neurosci.* **2011**, *31*, 16507−16516.
(60) Butini, S.; Brogi, S.; Novellino, E.; Campiani, G.; Ghosh, A. K.; Brindisi, M.; Gemma, S. The structural evolution of β-secretase inhibitors: a focus on the development of small-molecule inhibitors. *Curr. Top. Med. Chem.* **2013**, *13*, 1787−1807.
(61) Galdeano, C.; Viayna, E.; Arroyo, P.; Bidon-Chanal, A.; Blas, J. R.; Muñoz-Torrero, D.; Luque, F. J. Structural determinants of the multifunctional profile of dual binding site acetylcholinesterase inhibitors as anti-Alzheimer agents. *Curr. Pharm. Des.* **2010**, *16*, 2818−2836.
(62) Fu, H.; Li, W.; Luo, J.; Lee, N. T. K.; Li, M.; Tsim, K. W. K.; Pang, Y.; Youdim, M. B. H.; Han, Y. Promising anti-Alzheimer's dimer bis(7)-tacrine reduces β-amyloid generation by directly inhibiting BACE-1 activity. *Biochem. Biophys. Res. Commun.* **2008**, *366*, 631−636.
(63) Hanessian, S.; Yun, H.; Hou, Y.; Yang, G.; Bayrakdarian, M.; Therrien, E.; Moitessier, N.; Roggo, S.; Veenstra, S.; Tintelnot-Blomley, M.; Rondeau, J.-M.; Ostermeier, C.; Strauss, A.; Ramage, P.; Paganetti, P.; Neumann, U.; Betschart, C. Structure-based design, synthesis, and memapsin 2 (BACE) inhibitory activity of carbocyclic and heterocyclic peptidomimetics. *J. Med. Chem.* **2005**, *48*, 5175−5190.
(64) Ballatore, C.; Brunden, K. R.; Piscitelli, F.; James, M. J.; Crowe, A.; Yao, Y.; Hyde, E.; Trojanowski, J. Q.; Lee, V. M.-Y.; Smith, A. B., III Discovery of brain-penetrant, orally bioavailable aminothienopyridazine inhibitors of Tau aggregation. *J. Med. Chem.* **2010**, *53*, 3739−3747.
(65) Lipinski, C. A.; Lombardo, F.; Dominy, B. W.; Feeney, P. J. Experimental and computational approaches to estimate solubility and permeability in drug discovery and development settings. *Adv. Drug Delivery Rev.* **1997**, *23*, 3−25.
(66) Morphy, R.; Rankovic, Z. Designing multiple ligands—medicinal chemistry strategies and challenges. *Curr. Pharm. Des.* **2009**, *15*, 587−600.
(67) García-Palomero, E.; Muñoz, P.; Usan, P.; Garcia, P.; De Austria, C.; Valenzuela, R.; Rubio, L.; Medina, M.; Martínez, A. Potent β-amyloid modulators. *Neurodegener. Dis.* **2008**, *5*, 153−156.
(68) Spuch, C.; Antequera, D.; Fernandez-Bachiller, M. I.; Rodríguez-Franco, M. I.; Carro, E. A new tacrine−melatonin hybrid reduces amyloid burden and behavioral deficits in a mouse model of Alzheimer's disease. *Neurotoxicol. Res.* **2010**, *17*, 421−431.
(69) Efremov, I. V.; Vajdos, F. F.; Borzilleri, K. A.; Capetta, S.; Chen, H.; Dorff, P. H.; Dutra, J. K.; Goldstein, S. W.; Mansour, M.; McColl, A.; Noell, S.; Oborski, C. E.; O'Connell, T. N.; O'Sullivan, T. J.; Pandit, J.; Wang, H.; Wei, B.; Withka, J. M. Discovery and optimization of a novel spiropyrrolidine inhibitor of β-secretase (BACE1) through fragment-based drug design. *J. Med. Chem.* **2012**, *55*, 9069−9088.
(70) Lu, K.; Jiang, Y.; Chen, B.; Eldemenky, E. M.; Ma, G.; Packiarajan, M.; Chandrasena, G.; White, A. D.; Jones, K. A.; Li, B.; Hong, S.-P. Strategies to lower the Pgp efflux liability in a series of potent indole azetidine MCHR1 antagonists. *Bioorg. Med. Chem. Lett.* **2011**, *21*, 5310−5314.
(71) Di, L.; Kerns, E. H.; Fan, K.; McConnell, O. J.; Carter, G. T. High throughput artificial membrane permeability assay for blood−brain barrier. *Eur. J. Med. Chem.* **2003**, *38*, 223−232.
(72) Ami, D.; Natalello, A.; Lotti, M.; Doglia, S. M. Why and how protein aggregation has to be studied in vivo. *Microb. Cell Fact.* **2013**, *12*, 17.
(73) Villar-Piqué, A.; Ventura, S. Modeling amyloids in bacteria. *Microb. Cell Fact.* **2012**, *11*, 166.
(74) Pouplana, S.; Espargaró, A.; Galdeano, C.; Viayna, E.; Sola, I.; Ventura, S.; Muñoz-Torrero, D.; Sabate, R. Thioflavin-S staining of bacterial inclusion bodies for the fast, simple, and inexpensive screening

of amyloid aggregation inhibitors. *Curr. Med. Chem.* **2014**, *21*, 1152−1159.
(75) Porat, Y.; Abramowitz, A.; Gazit, E. Inhibition of amyloid fibril formation by polyphenols: structural similarity and aromatic interactions as a common inhibition mechanism. *Chem. Biol. Drug Des.* **2006**, *67*, 27−37.
(76) Zhang, H.-Y. Same causes, same cures. *Biochem. Biophys. Res. Commun.* **2006**, *351*, 578−581.
(77) Narlawar, R.; Pickhardt, M.; Leuchtenberger, S.; Baumann, K.; Krause, S.; Dyrks, T.; Weggen, S.; Mandelkow, E.; Schmidt, B. Curcumin-derived pyrazoles and isoxazoles: Swiss army knives or blunt tools for Alzheimer's disease? *ChemMedChem* **2008**, *3*, 165−172.
(78) LaFerla, F. M. Pathways linking Aβ and tau pathologies. *Biochem. Soc. Trans.* **2010**, *38*, 993−995.
(79) Shankar, G. M.; Walsh, D. M. Alzheimer's disease: synaptic dysfunction and Aβ. *Mol Neurodegener.* **2009**, *4*, 48.
(80) Lacor, P. N.; Buniel, M. C.; Chang, L.; Fernandez, S. J.; Gong, Y.; Viola, K. L.; Lambert, M. P.; Velasco, P. T.; Bigio, E. H.; Finch, C. E.; Krafft, G. A.; Klein, W. L. Synaptic targeting by Alzheimer's-related amyloid beta oligomers. *J. Neurosci.* **2004**, *24*, 10191−10200.
(81) Walsh, D. M.; Klyubin, I.; Fadeeva, J. V.; Cullen, W. K.; Anwyl, R.; Wolfe, M. S.; Rowan, M. J.; Selkoe, D. J. Naturally secreted oligomers of amyloid β protein potently inhibit hippocampal long-term potentiation in vivo. *Nature* **2002**, *416*, 535−539.
(82) Serrano-Pozo, A.; Frosch, M. P.; Masliah, E.; Hyman, B. T. Neuropathological alterations in Alzheimer disease. *Cold Spring Harbor Perspect. Med.* **2011**, *1*, a006189.
(83) Alkondon, M.; Albuquerque, E. X.; Pereira, E. F. R. Acetylcholinesterase inhibition reveals endogenous nicotinic modulation of glutamate inputs to CA1 stratum radiatum interneurons in hippocampal slices. *Neurotoxicology* **2013**, *36*, 72−81.
(84) Ye, L.; Qi, J. S.; Qiao, J. T. Long-term potentiation in hippocampus of rats is enhanced by endogenous acetylcholine in a way that is independent of *N*-methyl-D-aspartate receptors. *Neurosci. Lett.* **2001**, *300*, 145−148.
(85) Ardiles, A. O.; Tapia-Rojas, C. C.; Mandal, M.; Alexandre, F.; Kirkwood, A.; Inestrosa, N. C.; Palacios, A. G. Postsynaptic dysfunction is associated with spatial and object recognition memory loss in a natural model of Alzheimer's disease. *Proc. Natl. Acad. Sci. U. S. A.* **2012**, *109*, 13835−13840.
(86) Garcia-Alloza, M.; Robbins, E. M.; Zhang-Nunes, S. X.; Purcell, S. M.; Betensky, R. A.; Raju, S.; Prada, C.; Greenberg, S. M.; Bacskai, B. J.; Frosch, M. P. Characterization of amyloid deposition in the APPswe/PS1dE9 mouse model of Alzheimer disease. *Neurobiol. Dis.* **2006**, *24*, 516−524.
(87) Silverman, R. B. *The Organic Chemistry of Enzyme-Catalyzed Reactions*; Academic Press: San Diego, 2000.
(88) Naiki, H.; Higuchi, K.; Nakakuki, K.; Takeda, T. Kinetic analysis of amyloid fibril polymerization in vitro. *Lab. Invest.* **1991**, *65*, 104−110.
(89) Varela-Nallar, L.; Alfaro, I. E.; Serrano, F. G.; Parodi, J.; Inestrosa, N. C. Wingless-type family member 5a (Wnt-5a) stimulates synaptic differentiation and function of glutamatergic synapses. *Proc. Natl. Acad. Sci. U. S. A.* **2010**, *107*, 21164−21169.
(90) Inestrosa, N. C.; Carvajal, F. J.; Zolezzi, J. M.; Tapia-Rojas, C.; Serrano, F.; Karmelic, D.; Toledo, E. M.; Toro, A.; Toro, J.; Santos, M. J. Peroxisome proliferator reduce spatial memory impairment, synaptic failure, and neurodegeneration in brains of a double transgenic mice model of Alzheimer's disease. *J. Alzheimer's Dis.* **2013**, *33*, 941−959.
(91) Carvajal, F. J.; Zolezzi, J. M.; Tapia-Rojas, C.; Godoy, J. A.; Inestrosa, N. C. Tetrahydrohyperforin decreases cholinergic markers associated with amyloid-β plaques, 4-hydroxynonenal formation, and caspase-3 activation in AβPP/PS1 mice. *J. Alzheimer's Dis.* **2013**, *36*, 99−118.
(92) Dinamarca, M. C.; Sagal, J. P.; Quintanilla, R. A.; Godoy, J. A.; Arrázola, M. S.; Inestrosa, N. C. Amyloid-β-acetylcholinesterase complexes potentiate neurodegenerative changes induced by the Aβ peptide. Implications for the pathogenesis of Alzheimer's disease. *Mol. Neurodegener.* **2010**, *5*, 4.
(93) Dvir, H.; Silman, I.; Harel, M.; Rosenberry, T. L.; Sussman, J. L. Acetylcholinesterase: from 3D structure to function. *Chem.−Biol. Interact.* **2010**, *187*, 10−22.
(94) Morley, S. D.; Afshar, M. Validation of an empirical RNA−ligand scoring function for fast flexible docking using RiboDock. *J. Comput.-Aided Mol. Des.* **2004**, *18*, 189−208.
(95) Schmidtke, P.; Bidon-Chanal, A.; Luque, F. J.; Barril, X. MDpocket: open source cavity detection and characterization on molecular dynamics trajectories. *Bioinformatics* **2011**, *27*, 3276−3285.
(96) Schmidtke, P.; Barril, X. Understanding and predicting druggability. A high-throughput method for detection of drug binding sites. *J. Med. Chem.* **2010**, *53*, 5858−5867.
(97) Friesner, R. A.; Murphy, R. B.; Repasky, M. P.; Frye, L. L.; Greenwood, J. R.; Halgren, T. A.; Sanschagrin, P. C.; Mainz, D. T. Extra precision Glide: docking and scoring incorporating a model of hydrophobic enclosure for protein−ligand complexes. *J. Med. Chem.* **2006**, *49*, 6177−6196.
(98) Salomon-Ferrer, R.; Goetz, A. W.; Poole, D.; Le Grand, S.; Walker, R. C. Routine microsecond molecular dynamics simulations with AMBER on GPUs. 2. Explicit solvent Particle Mesh Ewald. *J. Chem. Theory Comput.* **2013**, *9*, 3878−3888.
(99) Case, D. A.; Darden, T. A.; Cheatham, T. E., III; Simmerling, C. L.; Wang, J.; Duke, R. E.; Luo, R.; Walker, R. C.; Zhang, W.; Merz, K. M.; Roberts, B.; Hayik, S.; Roitberg, A.; Seabra, G.; Swails, J.; Goetz, A. W.; Kolossváry, I.; Wong, K. F.; Paesani, F.; Vanicek, J.; Wolf, R. M.; Liu, J.; Wu, X.; Brozell, S. R.; Steinbrecher, T.; Gohlke, H.; Cai, Q.; Ye, X.; Wang, J.; Hsieh, M.-J.; Cui, G.; Roe, D. R.; Mathews, D. H.; Seetin, M. G.; Salomon-Ferrer, R.; Sagui, C.; Babin, V.; Luchko, T.; Gusarov, S.; Kovalenko, A.; Kollman, P. A. *AMBER 12*; University of California: San Francisco, 2012.
(100) Hornak, V.; Abel, R.; Okur, A.; Strockbine, B.; Roitberg, A.; Simmerling, C. Comparison of multiple Amber force fields and development of improved protein backbone parameters. *Proteins* **2006**, *65*, 712−725.
(101) Wang, J. M.; Wolf, R. M.; Caldwell, J. W.; Kollman, P. A.; Case, D. A. Development and testing of a general amber force field. *J. Comput. Chem.* **2005**, *26*, 1157−1174.
(102) Joung, I. S.; Cheatham, T. E. Molecular dynamics simulations of the dynamic and energetic properties of alkali and halide ions using water-model-specific ion parameters. *J. Phys. Chem. B* **2009**, *113*, 13279−13290.
(103) Frisch, M. J.; Trucks, G. W.; Schlegel, H. B.; Scuseria, G. E.; Robb, M. A.; Cheeseman, J. R.; Scalmani, G.; Barone, V.; Mennucci, B.; Petersson, G. A.; Nakatsuji, H.; Caricato, M.; Li, X.; Hratchian, H. P.; Izmaylov, A. F.; Bloino, J.; Zheng, G.; Sonnenberg, J. L.; Hada, M.; Ehara, M.; Toyota, K.; Fukuda, R.; Hasegawa, J.; Ishida, M.; Nakajima, T.; Honda, Y.; Kitao, O.; Nakai, H.; Vreven, T.; Montgomery, J. A., Jr.; Peralta, J. E.; Ogliaro, F.; Bearpark, M.; Heyd, J. J.; Brothers, E.; Kudin, K. N.; Staroverov, V. N.; Kobayashi, R.; Normand, J.; Raghavachari, K.; Rendell, A.; Burant, J. C.; Iyengar, S. S.; Tomasi, J.; Cossi, M.; Rega, N.; Millam, J. M.; Klene, M.; Knox, J. E.; Cross, J. B.; Bakken, V.; Adamo, C.; Jaramillo, J.; Gomperts, R.; Stratmann, R. E.; Yazyev, O.; Austin, A. J.; Cammi, R.; Pomelli, C.; Ochterski, J. W.; Martin, R. L.; Morokuma, K.; Zakrzewski, V. G.; Voth, G. A.; Salvador, P.; Dannenberg, J. J.; Dapprich, S.; Daniels, A. D.; Farkas, Ö.; Foresman, J. B.; Ortiz, J. V.; Cioslowski, J.; Fox, D. J. *Gaussian 09*, revision C.01; Gaussian, Inc.: Wallingford CT, 2009.
(104) Bayly, C. I.; Cieplak, P.; Cornell, W.; Kollman, P. A. A well-behaved electrostatic potential based method using charge restraints for deriving atomic charges: the RESP model. *J. Phys. Chem.* **1993**, *97*, 10269−10280.
(105) Jorgensen, W. L.; Chandrasekhar, J.; Madura, J. D.; Impey, R. W.; Klein, M. L. Comparison of simple potential functions for simulating liquid water. *J. Chem. Phys.* **1983**, *79*, 926−935.

SUPPORTING INFORMATION

Synthesis and multi-target biological profiling of a novel family of rhein derivatives as disease-modifying anti-Alzheimer agents

Elisabet Viayna,[†,‡,Δ] Irene Sola,[†,‡] Manuela Bartolini,[§] Angela De Simone,[¶] Cheril Tapia-Rojas,[#] Felipe G. Serrano,[#] Raimon Sabaté,[⊥,//] Jordi Juárez-Jiménez,[‡,⊥] Belén Pérez,[◊] F. Javier Luque,[‡,⊥] Vincenza Andrisano,[¶] M. Victòria Clos,[◊] Nibaldo C. Inestrosa,[#] and Diego Muñoz-Torrero[,†,‡]*

[†] Laboratori de Química Farmacèutica (Unitat Associada al CSIC), Facultat de Farmàcia, Universitat de Barcelona, Av. Joan XXIII 27-31, E-08028, Barcelona, Spain

[‡] Institut de Biomedicina (IBUB), Universitat de Barcelona, Barcelona, Spain

[§] Department of Pharmacy and Biotechnology, Alma Mater Studiorum University of Bologna, Via Belmeloro 6, I-40126, Bologna, Italy

[¶] Department for Life Quality Studies, University of Bologna, Corso d'Augusto 237, I-47921-Rimini, Italy

[#] Centro de Envejecimiento y Regeneración (CARE), Departamento de Biología Celular y Molecular, Facultad de Ciencias Biológicas, Pontificia Universidad Católica de Chile, Alameda 340, 8331150-Santiago, Chile

[⊥] Departament de Fisicoquímica, Facultat de Farmàcia, Universitat de Barcelona, Barcelona, Spain

[||] Institut de Nanociència i Nanotecnologia (IN^{2}UB), Universitat de Barcelona, Barcelona, Spain

[◊] Departament de Farmacologia, de Terapèutica i de Toxicologia, Institut de Neurociències, Universitat Autònoma de Barcelona, E-08193, Bellaterra, Barcelona, Spain

[Δ] Present address of E.V.: Drug Discovery Unit, College of Life Sciences, University of Dundee, Dundee, DD1 5EH, UK

TABLE OF CONTENTS

Synthetic procedures for intermediates **5a**–**h** and **6a**–**h** S3

Figure S1. Superposition of (–)-**7h** and huprine X in AChE S23

Figure S2. Superposition of (–)-**7h** and *bis*(7)-tacrine in AChE S24

Figure S3. Representation of BS1 and BS2 sites in BACE-1 S25

Table S1. PAMPA-BBB assay results of commercial drugs for assay validation S26

References S27

Appendix (elemental analysis data) S28

Synthetic Procedures for Intermediates 5a–h and 6a–h

(±)-5-[(3-Chloro-6,7,10,11-tetrahydro-9-methyl-7,11-methanocycloocta[*b*]quinolin-12-yl)amino]pentanenitrile [(±)-5a]. A suspension of (±)-huprine Y, (±)-**4** (300 mg, 1.06 mmol) and finely powdered KOH (85% purity, 139 mg, 2.11 mmol), and 4 Å molecular sieves in anhyd DMSO (6 mL) was stirred, heating every 10 min approximately with a heat gun for 1 h and at rt one additional hour, and then treated with 5-bromovaleronitrile (0.15 mL, 208 mg, 1.28 mmol). The reaction mixture was stirred at rt overnight, diluted with 5N NaOH (25 mL) and extracted with EtOAc (3×40 mL). The combined organic extracts were washed with H_2O (3×50 mL), dried over anhyd Na_2SO_4, and evaporated under reduced pressure to give a yellow oil (469 mg), which was purified by column chromatography (40–60 μm silica gel, CH_2Cl_2/MeOH/50% aq. NH_4OH mixtures, gradient elution). On elution with CH_2Cl_2/50% aq. NH_4OH 100:0.2, the *N*,*N*-dialkylated derivative (±)-**8a** (78 mg, 16% yield) was isolated as a yellow oil. On elution with CH_2Cl_2/MeOH/50% aq. NH_4OH 99:1:0.2, nitrile (±)-**5a** (273 mg, 70% yield) was isolated as a beige solid; $R_{f[(\pm)\text{-}\mathbf{5a}]}$ 0.50; $R_{f[(\pm)\text{-}\mathbf{8a}]}$ 0.77 (CH_2Cl_2/MeOH/50% aq. NH_4OH 9:1:0.05).

A solution of (±)-**5a** (52 mg, 0.14 mmol) in CH_2Cl_2 (4.5 mL) was filtered through a 0.2 μm PTFE filter, treated with methanolic HCl (1.40N, 0.30 mL) and evaporated under reduced pressure. The resulting solid was washed with pentane (3×2 mL) to give, after drying at 65 ºC/2 Torr for 48 h, (±)-**5a**·HCl (58 mg) as a yellow solid: mp 181−183 °C (CH_2Cl_2/MeOH 94:6); IR (KBr) ν 3500–2500 (max at 3364, 3254, 3049, 3014, 2926, 2885, 2651, N-H, N^+-H and C-H st), 2243 (CN st), 1635, 1629, 1602, 1582, 1570, 1562 (ar-C-C and ar-C-N st) cm^{-1}; ^1H NMR (400 MHz, CD_3OD) δ 1.59 (s, 3H, 9'-CH_3), 1.79 (tt, $J \approx J' \approx 7.2$ Hz, 2H, 3-H_2), 1.93 (d, J=17.6 Hz, 1H, 10'-H_{endo}), superimposed in part 1.92–1.98 (m, 1H, 13'-H_{syn}), 2.01 (tt, $J \approx J' \approx 7.2$ Hz, 2H, 4-H_2), 2.09

(dm, *J*=12.8 Hz, 1H, 13'-H_{anti}), 2.56 (t, *J*=7.2 Hz, 2H, 2-H_2), superimposed in part 2.53–2.60 (m, 1H, 10'-H_{exo}), 2.77 (m, 1H, 7'-H), 2.88 (ddd, *J*=18.0 Hz, *J'*=*J''*=1.6 Hz, 1H, 6'-H_{endo}), 3.22 (dd, *J*=18.0 Hz, *J'*=5.2 Hz, 1H, 6'-H_{exo}), 3.47 (m, 1H, 11'-H), 4.03 (t, *J*= 7.6 Hz, 2H, 5-H_2), 4.85 (s, NH and $^+$NH), 5.59 (br d, *J*=4.4 Hz, 1H, 8'-H), 7.57 (dd, *J*=9.2 Hz, *J'*=2.0 Hz, 1H, 2'-H), 7.78 (d, *J*≈2.0 Hz, 1H, 4'-H), 8.40 (d, *J*≈9.2 Hz, 1H, 1'-H); ^{13}C NMR (100.6 MHz, CD_3OD) δ 17.1 (CH_2, C2), 23.4 (CH_3, 9'-CH_3), 23.9 (CH_2, C3), 27.3 (CH, C11'), 27.9 (CH, C7'), 29.3 (CH_2, C13'), 30.3 (CH_2, C4), 36.1 (CH_2), 36.2 (CH_2) (C6', C10'), 48.8 (CH_2, C5), 115.8 (C, C12a'), 117.9 (C, C11a'), 119.2 (CH, C4'), 120.9 (C, CN), 125.1 (CH, C8'), 126.8 (CH, C2'), 129.4 (CH, C1'), 134.6 (C, C9'), 140.3 (C, C3'), 141.0 (C, C4a'), 151.5 (C, C5a'), 157.0 (C, C12'). HRMS (ESI) calcd for ($C_{22}H_{24}{}^{35}ClN_3$ + H^+): 366.1732, found 366.1729.

A solution of (±)-**8a** (78 mg, 0.17 mmol) in CH_2Cl_2 (4.5 mL) was filtered through a 0.2 μm PTFE filter, treated with methanolic HCl (0.65N, 0.64 mL) and evaporated under reduced pressure. The resulting solid was washed with pentane (3×2 mL) to give, after drying at 65 ºC/2 Torr for 48 h, (±)-**8a**·HCl (80 mg) as a yellow solid: mp 196–198 ºC (CH_2Cl_2/MeOH 88:12); IR (KBr) *ν* 3500–2450 (max at 3430, 3044, 2919, 2875, 2464, N^+-H and C-H st), 2243 (CN st), 1632, 1604, 1574 (ar-C-C and ar-C-N st) cm^{-1}; ^{1}H NMR (400 MHz, CD_3OD) δ 1.59 (s, 3H, 9'-CH_3), 1.65 (tt, *J*≈*J'*≈7.2 Hz, 4H, 3-H_2), 1.72–1.98 (complex signal, 4H, 4-H_2), 2.00 (br d, *J*=17.6 Hz, 1H, 10'-H_{endo}), superimposed in part 2.06 (dm, *J*≈12.8 Hz, 1H, 13'-H_{syn}), 2.12 (dm, *J*=12.8 Hz, 1H, 13'-H_{anti}), 2.48 (t, *J*=7.2 Hz, 4H, 2-H_2), 2.69 (dd, *J*=17.6 Hz, *J'*=5.6 Hz, 1H, 10'-H_{exo}), 2.82 (m, 1H, 7'-H), 3.17 (ddd, *J*=18.0 Hz, *J'*≈*J''*≈1.8 Hz, 1H, 6'-H_{endo}), 3.39 (dd, *J*=18.0 Hz, *J'*=5.6 Hz, 1H, 6'-H_{exo}), superimposed in part 3.73 (m, 1H, 11'-H), 3.73 (ddd, *J*=13.6 Hz, *J'*=9.6 Hz, *J''*=5.6 Hz, 2H) and 3.80 (ddd, *J*=13.6 Hz, *J'*=9.2 Hz, *J''*=6.0 Hz, 2H) (5-H_2), 4.84 (s, $^+$NH), 5.68 (br d, *J*=4.4 Hz, 1H, 8'-H), 7.72 (dd, *J*=9.2 Hz, *J'*=2.4 Hz,

1H, 2'-H), 7.99 (d, *J*=2.4 Hz, 1H, 4'-H), 8.26 (d, *J*=9.2 Hz, 1H, 1'-H); ^{13}C NMR (100.6 MHz, CD_3OD) δ 17.1 (CH_2, C2), 23.3 (CH_3, 9'-CH_3), 23.9 (CH_2, C3), 27.6 (CH, C7'), 28.6 (CH_2, C13'), 28.9 (CH_2, C4), 29.7 (CH, C11'), 37.7 (CH_2, C6'), 38.7 (CH_2, C10'), 55.1 (CH_2, C5), 120.0 (CH, C4'), 120.9 (C, CN), 125.5 (C, C12a'), 125.7 (CH, C8'), 192.2 (CH, C2'), 130.1 (CH, C1'), 132.5 (C, C11a'), 134.3 (C, C9'), 140.36 (C), 140.43 (C) (C3', C4a'), 157.6 (C, C5a'), 163.9 (C, C12'); HRMS (ESI) calcd for ($C_{27}H_{31}{}^{35}ClN_4$ + H^+) 447.2310, found 447.2309.

(±)-6-[(3-Chloro-6,7,10,11-tetrahydro-9-methyl-7,11-methanocycloocta[*b*]quinolin-12-yl)amino]hexanenitrile [(±)-5b]. It was prepared as described for (±)-**5a**. From (±)-huprine Y, (±)-**4** (1.50 g, 5.28 mmol) and 6-bromohexanenitrile (0.77 mL, 1.02 g, 5.80 mmol), a yellow oil (2.88 g) was obtained and purified by column chromatography (40–60 μm silica gel, CH_2Cl_2/50% aq. NH_4OH 100:0.2), to afford (±)-**5b** (1.26 g, 63% yield) as a yellow solid; R_f 0.77 (CH_2Cl_2/MeOH/50% aq. NH_4OH 9:1:0.05).

(±)-5b·HCl: mp 143–145 °C (CH_2Cl_2/MeOH 92:8); IR (KBr) *v* 3500–2500 (max at 3398, 3245, 3048, 2924, 2853, 2734, N-H, N^+-H and C-H st), 2242 (CN st), 1724, 1618, 1572 (ar-C-C and ar-C-N st) cm^{-1}; ^{1}H NMR (400 MHz, CD_3OD) δ 1.59 (s, 3H, 9'-CH_3), superimposed in part 1.54–1.62 (m, 2H, 4-H_2), 1.71 (m, 2H, 3-H_2), superimposed in part 1.91 (tt, *J*≈*J'*≈7.6 Hz, 2H, 5-H_2), superimposed 1.90–1.95 (m, 1H, 10'-H_{endo}), superimposed in part 1.92–1.98 (dm, *J*≈12.8 Hz, 1H, 13'-H_{syn}), 2.09 (dm, *J*≈12.8 Hz, 1H, 13'-H_{anti}), 2.48 (t, *J*≈7.2 Hz, 2H, 2-H_2), 2.56 (dm, *J*≈17.2 Hz, 1H, 10'-H_{exo}), 2.77 (m, 1H, 7'-H), 2.87 (ddd, *J*=17.6 Hz, *J'*=*J''*=1.6 Hz, 1H, 6'-H_{endo}), 3.21 (dd, *J*=17.6 Hz, *J'*≈5.6 Hz, 1H, 6'-H_{exo}), 3.46 (m, 1H, 11'-H), 4.01 (t, *J*≈7.6 Hz, 2H, 6-H_2), 4.85 (s, NH and $^+$NH), 5.59 (br d, *J*=4.4 Hz, 1H, 8'-H), 7.57 (dd, *J*=9.2 Hz, *J'*=2.0 Hz, 1H, 2'-H), 7.77 (d, *J*=2.0 Hz, 1H, 4'-H), 8.40 (d, *J*≈9.2 Hz, 1H, 1'-H); ^{13}C NMR (100.6 MHz,

CD_3OD) δ 17.2 (CH_2, C2), 23.4 (CH_3, 9'-CH_3), 26.0 (CH_2, C3), 26.8 (CH_2, C4), 27.3 (CH, C11'), 27.9 (CH, C7'), 29.3 (CH_2, C13'), 30.5 (CH_2, C5), 36.0 (CH_2), 36.2 (CH_2) (C6', C10'), 49.4 (CH_2, C6), 115.7 (C, C12a'), 117.8 (C, C11a'), 119.2 (CH, C4'), 121.0 (C, CN), 125.1 (CH, C8'), 126.8 (CH, C2'), 129.4 (CH, C1'), 134.6 (C, C9'), 140.3 (C, C3'), 141.0 (C, C4a'), 151.4 (C, C5a'), 157.0 (C, C12'); HRMS (ESI) calcd for ($C_{23}H_{26}{}^{35}ClN_3 + H^+$) 380.1888, found 380.1889.

(±)-7-[(3-Chloro-6,7,10,11-tetrahydro-9-methyl-7,11-methanocycloocta[*b*]quinolin-12-yl)amino]heptanenitrile [(±)-5c]. It was prepared as described for (±)-**5a**. From (±)-huprine Y, (±)-**4** (2.00 g, 7.04 mmol) and 7-bromoheptanenitrile (1.21 mL, 1.53 g, 8.05 mmol), a yellow oil (3.50 g) was obtained and purified by column chromatography (40–60 μm silica gel, CH_2Cl_2/50% aq. NH_4OH 100:0.2), to afford (±)-**5c** (2.40 g, 87% yield) as a yellow solid; R_f 0.66 (CH_2Cl_2/MeOH/50% aq. NH_4OH 9:1:0.05).

(±)-5c·HCl: mp 125–126 °C (CH_2Cl_2/MeOH 94:6); IR (KBr) ν 3500–2500 (max at 3219, 3049, 2927, 2852, 2733, 2651, N-H, N^+-H and C-H st), 2242 (CN st), 1620, 1571 (ar-C-C and ar-C-N st) cm^{-1}; ^1H NMR (400 MHz, CD_3OD) δ 1.44–1.56 (complex signal, 4H, 4-H_2 and 5-H_2), 1.59 (s, 3H, 9'-CH_3), 1.62–1.70 (m, 2H, 3-H_2), 1.91 (tt, J=J'=7.2 Hz, 2H, 6-H_2), superimposed 1.86–1.98 (complex signal, 2H, 10'-H_{endo}, 13'-H_{syn}), 2.09 (dm, J=13.2 Hz, 1H, 13'-H_{anti}), 2.46 (t, J=7.2 Hz, 2H, 2-H_2), 2.56 (dm, J=17.6 Hz, 10'-H_{exo}), 2.77 (m, 1H, 7'-H), 2.87 (dm, J≈18.0 Hz, 1H, 6'-H_{endo}), 3.21 (dd, J=18.0 Hz, J'=5.6 Hz, 1H, 6'-H_{exo}), 3.46 (m, 1H, 11'-H), 3.99 (t, J≈7.2 Hz, 2H, 7-H_2), 4.85 (s, NH and $^+$NH), 5.59 (br d, J=4.4 Hz, 1H, 8'-H), 7.56 (dd, J=9.6 Hz, J'=2.0 Hz, 2'-H), 7.77 (d, J=2.0 Hz, 1H, 4'-H), 8.40 (d, J=9.6 Hz, 1H, 1'-H); ^{13}C NMR (100.6 MHz, CD_3OD) δ 17.2 (CH_2, C2), 23.4 (CH_3, 9'-CH_3), 26.3 (CH_2, C3), 27.0 (CH_2, C5), 27.3 (CH, C11'), 27.9 (CH, C7'), 29.3 (2CH_2, C4 and C13'), 31.0 (CH_2, C6), 36.0

(CH_2), 36.1 (CH_2), (C6', C10'), 49.6 (CH_2, C7), 115.7 (C, C12a'), 117.7 (C, C11a'), 119.2 (CH, C4'), 121.1 (C, CN), 125.1 (CH, C8'), 126.7 (CH, C2'), 129.5 (CH, C1'), 134.6 (C, C9'), 140.2 (C, C3'), 141.0 (C, C4a'), 151.3 (C, C5a'), 156.9 (C, C12'). HRMS (ESI) calcd for ($C_{24}H_{28}{}^{35}ClN_3 + H^+$) 394.2045, found 394.2049.

(±)-8-[(3-Chloro-6,7,10,11-tetrahydro-9-methyl-7,11-methanocycloocta[*b*]quinolin-12-yl)amino]octanenitrile [(±)-5d]. It was prepared as described for (±)-**5a**. From (±)-huprine Y·HCl, (±)-**4**·HCl (1.86 g, 5.81 mmol) and 8-bromooctanenitrile (1.39 g, 6.81 mmol), a yellow oil (2.30 g) was obtained and purified by column chromatography (40–60 μm silica gel, CH_2Cl_2/50% aq. NH_4OH 100:0.2), to afford (±)-**5d** (1.00 g, 42% yield) as a yellow solid; R_f 0.65 (CH_2Cl_2/MeOH/50% aq. NH_4OH 9:1:0.05).

(±)-5d·HCl: mp 130–131 °C (CH_2Cl_2/MeOH 81:19); IR (KBr) ν 3500–2500 (max at 3397, 3244, 3108, 3048, 3007, 2925, 2852, N-H, N^+-H and C-H st), 2242 (CN st), 1701, 1624, 1562 (ar-C-C and ar-C-N st) cm^{-1}; ^1H NMR (400 MHz, CD_3OD) δ 1.40–1.52 (complex signal, 6H, 4-H_2, 5-H_2 and 6-H_2), 1.58 (s, 3H, 9'-CH_3), 1.64 (tt, $J \approx J' \approx 7.6$ Hz, 2H, 3-H_2), superimposed in part 1.88 (tt, $J \approx J' \approx 7.2$ Hz, 2H, 7-H_2), superimposed in part 1.94 (br d, J=17.2 Hz, 1H, 10'-H_{endo}), superimposed 1.90–1.98 (m, 1H, 13'-H_{syn}), 2.08 (dm, J=12.4 Hz, 1H, 13'-H_{anti}), 2.44 (t, $J \approx 7.2$ Hz, 2H, 2-H_2), 2.56 (br dd, J=17.6 Hz, J'=4.4 Hz, 1H, 10'-H_{exo}), 2.77 (m, 1H, 7'-H), 2.89 (br d, J=18.0 Hz, 1H, 6'-H_{endo}), 3.21 (dd, J=18.0 Hz, J'=5.6 Hz, 1H, 6'-H_{exo}), 3.47 (m, 1H, 11'-H), 3.99 (t, J=7.2 Hz, 2H, 8-H_2), 4.85 (s, NH and $^+$NH), 5.58 (br d, J=5.2 Hz, 1H, 8'-H), 7.54 (dd, J=9.6 Hz, J'=1.6 Hz, 1H, 2'-H), 7.79 (d, J=1.6 Hz, 1H, 4'-H), 8.40 (d, J=9.6 Hz, 1H, 1'-H); ^{13}C NMR (100.6 MHz, CD_3OD) δ 17.3 (CH_2, C2), 23.5 (CH_3, 9'-CH_3), 26.3 (CH_2, C3), 27.2 (CH, C11'), 27.5 (CH_2, C6), 27.8 (CH, C7'), 29.3 (CH_2, C13'), 29.4 (CH_2), 29.6 (CH_2) (C4, C5), 31.1 (CH_2, C7), 36.0 (CH_2), 36.1 (CH_2) (C6', C10'), 49.6 (CH_2, C8), 115.6 (C,

C12a'), 117.6 (C, C11a'), 119.1 (CH, C4'), 121.2 (C, CN), 125.1 (CH, C8'), 126.6 (CH, C2'), 129.5 (CH, C1'), 134.5 (C, C9'), 140.1 (C, C3'), 140.9 (C, C4a'), 151.2 (C, C5a'), 156.9 (C, C12'); HRMS (ESI) calcd for ($C_{25}H_{30}{}^{35}ClN_3$ + H^+) 408.2201, found 408.2203.

(±)-9-[(3-Chloro-6,7,10,11-tetrahydro-9-methyl-7,11-methanocycloocta[*b*]quinolin-12-yl)amino]nonanenitrile [(±)-5e]. It was prepared as described for (±)-**5a**. From (±)-huprine Y·HCl, (±)-**4**·HCl (1.89 g, 5.91 mmol) and 9-bromononanenitrile (1.56 g, 7.16 mmol), a yellow oil (2.86 g) was obtained and purified by column chromatography (40–60 μm silica gel, CH_2Cl_2/50% aq. NH_4OH 100:0.2), to afford (±)-**5e** (1.65 g, 66% yield) as a yellow solid; R_f 0.56 (CH_2Cl_2/MeOH/50% aq. NH_4OH 9:1:0.05).

(±)-5e·HCl: mp 121–123 °C (CH_2Cl_2/MeOH 81:19); IR (KBr) ν 3500–2500 (max at 3228, 3108, 3048, 3001, 2926, 2854, 2745, N-H, N^+-H and C-H st), 2242 (CN st), 1718, 1630, 1582, 1569, 1501 (ar-C-C and ar-C-N st) cm^{-1}; ^1H NMR (400 MHz, CD_3OD) δ 1.32–1.50 (complex signal, 8H, 4-H_2, 5-H_2, 6-H_2 and 7-H_2), 1.59 (s, 3H, 9'-CH_3), superimposed in part 1.62 (tt, $J \approx J' \approx 7.2$ Hz, 2H, 3-H_2), superimposed in part 1.87 (tt, $J \approx J' \approx 7.2$ Hz, 2H, 8-H_2), superimposed in part 1.93 (br d, J=18.0 Hz, 1H, 10'-H_{endo}), superimposed 1.90–1.96 (m, 1H, 13'-H_{syn}), 2.08 (dm, J=12.4 Hz, 1H, 13'-H_{anti}), 2.43 (t, J=7.2 Hz, 2H, 2-H_2), 2.56 (dm, J=17.6 Hz, J'=4.8 Hz, 1H, 10'-H_{exo}), 2.77 (m, 1H, 7'-H), 2.88 (br d, J=17.6 Hz, 1H, 6'-H_{endo}), 3.21 (dd, $J \approx 17.6$ Hz, $J' \approx 5.6$ Hz, 1H, 6'-H_{exo}), 3.46 (m, 1H, 11'-H), 3.99 (t, J=7.2 Hz, 2H, 9-H_2), 4.85 (s, NH and $^+$NH), 5.59 (d, J=4.4 Hz, 1H, 8'-H), 7.55 (dd, J=9.6 Hz, J'=2.4 Hz, 1H, 2'-H), 7.78 (d, J=2.4 Hz, 1H, 4'-H), 8.40 (d, J=9.6 Hz, 1H, 1'-H); ^{13}C NMR (100.6 MHz, CD_3OD) δ 17.3 (CH_2, C2), 23.5 (CH_3, 9'-CH_3), 26.4 (CH_2, C3), 27.3 (CH, C11'), 27.7 (CH_2, C7), 27.8 (CH, C7'), 29.3 (CH_2, C13'), 29.6 (CH_2), 29.7 (CH_2), 30.0 (CH_2) (C4, C5, C6), 31.2 (CH_2, C8), 36.0

(CH_2), 36.1 (CH_2) (C6', C10'), 49.6 (CH_2, C9), 115.6 (C, C12a'), 117.6 (C, C11a'), 119.1 (CH, C4'), 121.2 (C, CN), 125.1 (CH, C8'), 126.6 (CH, C2'), 129.5 (CH, C1'), 134.5 (C, C9'), 140.2 (C, C3'), 141.0 (C, C4a'), 151.2 (C, C5a'), 156.9 (C, C12'); HRMS (ESI) calcd for ($C_{26}H_{32}{}^{35}ClN_3 + H^+$) 422.2358, found 422.2363.

(–)-9-[(3-Chloro-6,7,10,11-tetrahydro-9-methyl-7,11-methanocycloocta[*b*]quinolin-12-yl)amino]nonanenitrile [(–)-5e]. It was prepared as described for (±)-**5a**. From (–)-huprine Y, (–)-**4** (>99% ee, 1.50 g, 5.28 mmol) and 9-bromononanenitrile (1.39 g, 6.40 mmol), a yellow oil (2.20 g) was obtained and purified by column chromatography (40–60 μm silica gel, CH_2Cl_2/50% aq. NH_4OH 100:0.2), to afford (–)-**5e** (750 mg, 34% yield) as a yellow solid; R_f 0.56 (CH_2Cl_2/MeOH/50% aq. NH_4OH 9:1:0.05).

(–)-5e·HCl: $[\alpha]^{20}_D$ = –212 (*c*=0.10, MeOH); mp 106–107 °C (CH_2Cl_2/MeOH 89:11); IR (KBr) *v* 3500–2500 (max at 3341, 3136, 3064, 2928, 2858, 2671, N-H, N^+-H and C-H st), 2245 (CN st), 1605, 1573, 1525 (ar-C-C and ar-C-N st) cm^{-1}; the ^1H NMR and ^{13}C NMR spectra were identical to those of (±)-**5e**; HRMS (ESI) calcd for ($C_{26}H_{32}{}^{35}ClN_3 + H^+$) 422.2358, found 422.2362.

(+)-9-[(3-Chloro-6,7,10,11-tetrahydro-9-methyl-7,11-methanocycloocta[*b*]quinolin-12-yl)amino]nonanenitrile [(+)-5e]. It was prepared as described for (±)-**5a**. From (+)-huprine Y, (+)-**4** (>99% ee, 1.50 g, 5.28 mmol) and 9-bromononanenitrile (1.39 g, 6.40 mmol), a yellow oil (2.20 g) was obtained and purified by column chromatography (40–60 μm silica gel, CH_2Cl_2/50% aq. NH_4OH 100:0.2), to afford (+)-**5e** (929 mg, 42% yield) as a yellow solid; R_f 0.56 (CH_2Cl_2/MeOH/50% aq. NH_4OH 9:1:0.05).

(+)-5e·HCl: $[\alpha]^{20}_D$ = +213 (*c*=0.10, MeOH); mp 109–111 °C (CH_2Cl_2/MeOH 93:7); IR (KBr) *v* 3500–2500 (max at 3379, 3228, 3111, 3038, 3007, 2926, 2854, N-H, N^+-H

and C-H st), 2242 (CN st), 1627, 1620, 1576, 1558, 1542, 1522, 1511 (ar-C-C and ar-C-N st) cm^{-1}; the ^{1}H NMR and ^{13}C NMR spectra were identical to those of (±)-**5e**; HRMS (ESI) calcd for ($C_{26}H_{32}{}^{35}ClN_3 + H^+$) 422.2358, found 422.2356.

(±)-10-[(3-Chloro-6,7,10,11-tetrahydro-9-methyl-7,11-methanocycloocta[*b*]quinolin-12-yl)amino]decanenitrile [(±)-5f]. It was prepared as described for (±)-**5a**. From (±)-huprine Y, (±)-**4** (2.00 g, 7.04 mmol) and 10-bromodecanenitrile (87% purity, 2.15 g, 8.06 mmol), a yellow oil (2.84 g) was obtained and purified by column chromatography (40–60 μm silica gel, CH_2Cl_2/MeOH/50% aq. NH_4OH mixtures, gradient elution). On elution with CH_2Cl_2/50% aq. NH_4OH 100:0.2, (±)-**5f** (756 mg, 25% yield) was isolated as a yellow solid. On elution with CH_2Cl_2/MeOH/50% aq. NH_4OH 98:2:0.2, starting (±)-**4** (382 mg) was recovered; $R_{f[(\pm)\text{-}\mathbf{5f}]}$ 0.66 (CH_2Cl_2/MeOH/50% aq. NH_4OH 9:1:0.05).

(±)-5f·HCl: mp 129–130 °C (CH_2Cl_2/MeOH 89:11); IR (KBr) *v* 3500–2500 (max at 3229, 3105, 3047, 3007, 2926, 2853, 2740, 2640, N-H, N^+-H and C-H st), 2242 (CN st), 1630, 1582, 1549, 1511 (ar-C-C and ar-C-N st) cm^{-1}; ^{1}H NMR (400 MHz, CD_3OD) δ 1.35–1.45 (complex signal, 10H, 4-H_2, 5-H_2, 6-H_2, 7-H_2 and 8-H_2), 1.59 (s, 3H, 9'-CH_3), superimposed in part 1.61 (tt, $J \approx J' \approx 7.2$ Hz, 2H, 3-H_2), superimposed in part 1.87 (tt, $J \approx J' \approx 7.2$ Hz, 2H, 9-H_2), superimposed 1.85–1.96 (complex signal, 1H, 13'-H_{syn}), superimposed in part 1.94 (d, $J \approx 16.8$ Hz, 1H, 10'-H_{endo}), 2.09 (dm, $J = 12.8$ Hz, 1H, 13'-H_{anti}), 2.43 (t, $J \approx 7.0$ Hz, 2H, 2-H_2), 2.55 (dd, $J = 17.6$ Hz, $J' = 4.4$ Hz, 1H, 10'-H_{exo}), 2.77 (m, 1H, 7'-H), 2.88 (br d, $J = 17.6$ Hz, 1H, 6'-H_{endo}), 3.21 (dd, $J = 17.6$ Hz, $J' = 5.6$ Hz, 1H, 6'-H_{exo}), 3.46 (m, 1H, 11'-H), 3.98 (t, $J \approx 6.8$ Hz, 2H, 10-H_2), 4.85 (s, NH and $^+$NH), 5.59 (d, $J = 4.8$ Hz, 1H, 8'-H), 7.55 (dd, $J = 9.6$ Hz, $J' = 2.0$ Hz, 1H, 2'-H), 7.77 (d, $J = 2.0$ Hz, 1H, 4'-H), 8.40 (d, $J = 9.6$ Hz, 1H, 1'-H); ^{13}C NMR (100.6 MHz, CD_3OD) δ 17.3 (CH_2, C2), 23.5 (CH_3, 9'-CH_3), 26.4 (CH_2, C3), 27.3 (CH, C11'), 27.7 (CH_2, C8), 27.8 (CH,

C7'), 29.3 (CH_2, C13'), 29.6 (CH_2), 29.7 (CH_2), 30.1 (CH_2), 30.3 (CH_2) (C4, C5, C6, C7), 31.2 (CH_2, C9), 36.0 (CH_2), 36.1 (CH_2) (C6', C10'), 49.7 (CH_2, C10), 115.6 (C, C12a'), 117.6 (C, C11a'), 119.1 (CH, C4'), 121.2 (C, CN), 125.1 (CH, C8'), 126.6 (CH, C2'), 129.5 (CH, C1'), 134.5 (C, C9'), 140.2 (C, C3'), 141.0 (C, C4a'), 151.2 (C, C5a'), 156.9 (C, C12'); HRMS (ESI) calcd for ($C_{27}H_{34}{}^{35}ClN_3$ + H^+) 436.2514, found 436.2508.

(±)-11-[(3-Chloro-6,7,10,11-tetrahydro-9-methyl-7,11-methanocycloocta[*b*]quinolin-12-yl)amino]undecanenitrile [(±)-5g]. It was prepared as described for (±)-**5a**. From (±)-huprine Y, (±)-**4** (1.70 g, 5.99 mmol) and 11-bromoundecanenitrile (80% purity, 2.11 g, 6.86 mmol), a yellow oil (2.20 g) was obtained and purified by column chromatography (40–60 μm silica gel, CH_2Cl_2/50% aq. NH_4OH 100:0.2), to afford (±)-**5g** (1.09 g, 40% yield) as a yellow solid; R_f 0.62 (CH_2Cl_2/MeOH/50% aq. NH_4OH 9:1:0.05).

(±)-5g·HCl: mp 131–133 °C (CH_2Cl_2/MeOH 93:7); IR (KBr) ν 3500–2500 (max at 3395, 3231, 3111, 3048, 3012, 2925, 2853, 2742, 2645, N-H, N^+-H and C-H st), 2242 (CN st), 1628, 1582, 1559, 1542, 1521, 1507 (ar-C-C and ar-C-N st) cm^{-1}; ^1H NMR (400 MHz, CD_3OD) δ 1.27–1.44 (complex signal, 12H, 4-H_2, 5-H_2, 6-H_2, 7-H_2, 8-H_2 and 9-H_2), 1.59 (s, 3H, 9'-CH_3), superimposed in part 1.62 (tt, $J \approx J' \approx 7.2$ Hz, 2H, 3-H_2), superimposed in part 1.87 (tt, $J \approx J' \approx 7.2$ Hz, 2H, 10-H_2), superimposed 1.86–1.96 (complex signal, 1H, 13'-H_{syn}), superimposed in part 1.94 (d, $J \approx 17.2$ Hz, 1H, 10'-H_{endo}), 2.08 (dm, J=12.4 Hz, 1H, 13'-H_{anti}), 2.43 (t, $J \approx 7.0$ Hz, 2H, 2-H_2), 2.56 (dd, J=17.6 Hz, J'=4.4 Hz, 1H, 10'-H_{exo}), 2.77 (m, 1H, 7'-H), 2.88 (d, J=18.0 Hz, 1H, 6'-H_{endo}), 3.21 (dd, $J \approx 18.0$ Hz, J'=5.6 Hz, 1H, 6'-H_{exo}), 3.46 (m, 1H, 11'-H), 3.99 (t, $J \approx 6.6$ Hz, 2H, 11-H_2), 4.85 (s, NH and $^+$NH), 5.59 (br d, J=4.8 Hz, 1H, 8'-H), 7.54 (dd, J=9.6 Hz, J'=2.0 Hz, 1H, 2'-H), 7.79 (d, J=2.0 Hz, 1H, 4'-H), 8.40 (d, J=9.6 Hz, 1H, 1'-H); ^{13}C NMR

(100.6 MHz, CD_3OD) δ 17.3 (CH_2, C2), 23.5 (CH_3, 9'-CH_3), 26.4 (CH_2, C3), 27.3 (CH, C11'), 27.76 (CH_2, C9), 27.83 (CH, C7'), 29.3 (CH_2, C13'), 29.7 (CH_2), 29.8 (CH_2), 30.2 (CH_2), 30.3 (CH_2), 30.4 (CH_2) (C4, C5, C6, C7, C8), 31.2 (CH_2, C10), 36.0 (CH_2), 36.1 (CH_2) (C6', C10'), 49.6 (CH_2, C11), 115.6 (C, C12a'), 117.6 (C, C11a'), 119.1 (CH, C4'), 121.2 (C, CN), 125.1 (CH, C8'), 126.6 (CH, C2'), 129.5 (CH, C1'), 134.5 (C, C9'), 140.2 (C, C3'), 141.0 (C, C4a'), 151.2 (C, C5a'), 156.9 (C, C12'); HRMS (ESI) calcd for ($C_{28}H_{36}{}^{35}ClN_3 + H^+$) 450.2671, found 450.2664.

(±)-4-{[(3-Chloro-6,7,10,11-tetrahydro-9-methyl-7,11-methanocycloocta[*b*]quinolin-12-yl)amino]methyl}benzonitrile [(±)-5h].

1) Preparation of the imine (±)-4-{[(3-chloro-6,7,10,11-tetrahydro-9-methyl-7,11-methanocycloocta[*b*]quinolin-12-yl)imino]methyl}benzonitrile, (±)-9. A suspension of (±)-huprine Y, (±)-**4** (2.00 g, 7.04 mmol) and 4 Å molecular sieves in anhyd toluene (19 mL) was treated with freshly distilled morpholine (0.67 mL, 675 mg, 7.75 mmol) and *p*-cyanobenzaldehyde (1.80 g, 13.7 mmol). The reaction mixture was stirred under reflux for 48 h, concentrated under reduced pressure. The resulting solid residue was purified through column chromatography (40–60 μm silica gel, CH_2Cl_2), to afford (±)-**9** (2.20 g, 79% yield) as a yellow solid; R_f 0.17 (CH_2Cl_2).

A solution of (±)-**9** (100 mg, 0.25 mmol) in CH_2Cl_2 (6.6 mL) was filtered through a 0.2 μm PTFE filter and evaporated under reduced pressure. The resulting solid was washed with pentane (3×2 mL) to give, after drying at 65 ºC/2 Torr for 48 h, the analytical sample of (±)-**9** (94 mg) as a yellow solid: mp 208–210 °C (CH_2Cl_2); IR (KBr) ν 2225 (CN st), 1721, 1639, 1600, 1570, 1553, 1500, 1479, 1455 (ar-C-C and ar-C-N st) cm^{-1}; ^1H NMR (400 MHz, $CDCl_3$) δ 1.52 (s, 3H, 9'-CH_3), 1.85 (br d, J=17.2 Hz, 1H, 10'-H_{endo}), 1.95–1.97 (complex signal, 2H, 13'-H_{syn} and 13'-H_{anti}), 2.35 (dd, J=17.2 Hz, J'=4.6 Hz, 1H, 10'-H_{exo}), 2.78 (m, 1H, 7'-H), 3.12 (br d, J=18.0 Hz, 1H, 6'-

H_{endo}), 3.21 (dd, J≈18.0 Hz, J'=5.2 Hz, 1H, 6'-H_{exo}), 3.35 (m, 1H, 11'-H), 5.56 (br d, J=5.2 Hz, 1H, 8'-H), 7.31, (dd, J=9.2 Hz, J'=2.0 Hz, 1H, 2'-H), 7.47 (d, J=9.2 Hz, 1H, 1'-H), 7.86 [dt, J=8.0 Hz, J'=1.6 Hz, 2H, 2(6)-H], 8.00 (d, J=2.0 Hz, 2H, 4'-H), 8.12 [d, J≈8.0 Hz, 2H, 3(5)-H], 8.42 (s, 1H, C*H*N); ^{13}C NMR (100.6 MHz, $CDCl_3$) δ 23.4 (CH_3, 9'-CH_3), 28.1 (CH, C11'), 28.3 (CH, C7'), 28.6 (CH_2, C13'), 37.1 (CH_2, C10'), 40.0 (CH_2, C6'), 115.8 (C, C1), 117.8 (C, C12a'), 118.1 (C, CN), 122.9 (C, C11a'), 123.9 (CH, C1'), 125.3 (CH, C8'), 126.4 (CH, C2'), 127.3 (CH, C4'), 129.4 [CH, C3(5)], 132.3 (C, C9'), 132.8 [CH, C2(6)], 134.9 (C, C3'), 138.5 (C, C4), 147.2 (C, C4a'), 153.4 (C, C12'), 159.8 (C, C5a'), 162.1 (CH, CHN); HRMS (ESI) calcd for ($C_{25}H_{20}{}^{35}ClN_3 + H^+$) 398.1419, found 398.1426.

2) Reduction of imine (±)-9. A solution of (±)-**9** (2.30 g, 5.79 mmol) in glacial AcOH (40 mL) was treated with $NaBH_3CN$ (764 mg, 12.2 mmol) portionwise for 1 h. The reaction mixture was stirred at rt for 3 h, cooled to 0 ºC with an ice bath, treated with 10N NaOH until pH 14, and extracted with EtOAc (2×200 mL). The combined organic extracts were dried over anhyd Na_2SO_4 and concentrated under reduced pressure, to give (±)-**5h** (2.10 g, 91% yield) as a yellow solid; R_f 0.75 (CH_2Cl_2/MeOH/50% aq. NH_4OH 9:1:0.05).

A solution of (±)-**5h** (60 mg, 0.15 mmol) in CH_2Cl_2 (5 mL) was filtered through a 0.2 μm PTFE filter, treated with methanolic HCl (0.53N, 0.85 mL), and evaporated under reduced pressure. The resulting solid was washed with pentane (3×2 mL), to give, after drying at 65 ºC/2 Torr for 48 h, (±)-**5h**·HCl (62 mg) as a yellow solid: mp 217–218 °C (CH_2Cl_2/MeOH 85:15); IR (KBr) ν 3500–2500 (max at 3229, 3101, 3050, 2999, 2901, 2722, N-H, N^+-H and C-H st), 2226 (CN st), 1718, 1631, 1582, 1555, 1507 (ar-C-C and ar-C-N st) cm^{-1}; ^{1}H NMR (400 MHz, CD_3OD) δ 1.61 (s, 3H, 9'-CH_3), 1.98 (br d, J=17.6 Hz, 1H, 10-H_{endo}), superimposed 2.00 (m, 1H, 13'-H_{syn}), 2.10 (dm, J=12.4 Hz,

1H, 13'-H_{anti}), 2.57 (dd, *J*=18.0 Hz, *J'*=4.8 Hz, 1H, 10'-H_{exo}), 2.80 (m, 1H, 7'-H), 2.94 (br d, *J*=18.0 Hz, 1H, 6'-H_{endo}), 3.26 (dd, *J*=18.0 Hz, *J'*=5.4 Hz, 1H, 6'-H_{exo}), 3.53 (m, 1H, 11'-H), 4.85 (s, NH and $^{+}$NH), 5.28 (s, 2H, CH_2N), 5.61 (br d, *J*=4.8 Hz, 1H, 8'-H), 7.39, (dd, *J*=9.2 Hz, *J'*=2.0 Hz, 1H, 2'-H), 7.63 [d, *J*=8.8 Hz, 2H, 3(5)-H], 7.79 [complex signal, 3H, 4'-H, 2(6)-H], 8.10 (d, *J*=9.2 Hz, 1H, 1'-H); ^{13}C NMR (100.6 MHz, CD_3OD) δ 23.4 (CH_3, 9'-CH_3), 27.6 (CH, C11'), 27.8 (CH, C7'), 29.2 (CH_2, C13'), 36.2 (CH_2), 36.4 (CH_2) (C6', C10'), 112.8 (C, C1), 115.7 (C, CN), 118.7 (C, C12a'), 119.4 (CH + C, C4', C11a'), 125.1 (CH, C8'), 127.0 (CH, C2'), 128.7 [CH, C3(5)], 128.9 (CH, C1'), 134.0 [CH, C2(6)], 134.6 (C, C9'), 140.4 (C, C3'), 140.8 (C, C4a'), 144.6 (C, C4), 152.2 (C, C5a'), 157.4 (C, C12'); HRMS (ESI) calcd for ($C_{25}H_{22}{}^{35}ClN_3 + H^+$) 400.1575, found 400.1582.

(±)-*N*-(3-Chloro-6,7,10,11-tetrahydro-9-methyl-7,11-methanocycloocta[*b*]quinolin-12-yl)pentane-1,5-diamine [(±)-6a]. To a suspension of $LiAlH_4$ (0.17 g, 4.47 mmol) in anhyd Et_2O (63 mL), nitrile (±)-**5a** (0.76 g, 2.08 mmol) was added, and the reaction mixture was stirred at rt overnight. The resulting mixture was treated with wet Et_2O (200 mL) and evaporated under reduced pressure. The solid was suspended in CH_2Cl_2, filtered through Celite® and evaporated under reduced pressure, to give amine (±)-**6a** (750 mg, 98% yield) as a yellow oil; R_f 0.03 (CH_2Cl_2/MeOH/50% aq. NH_4OH 9:1:0.05).

A solution of (±)-**6a** (50 mg, 0.14 mmol) in CH_2Cl_2 (3.5 mL) was filtered through a 0.2 μm PTFE filter, treated with methanolic HCl (1.4N, 0.87 mL), and evaporated under reduced pressure. The resulting solid was washed with pentane (3×2 mL) to give, after drying at 65 ºC/2 Torr for 48 h, (±)-**6a**·2HCl (54 mg) as a yellow solid: mp 193–194 ºC (CH_2Cl_2/MeOH 80:20); IR (KBr) *v* 3500–2500 (max at 3396, 3253, 2925, 2856, N-H, N^+-H and C-H st), 1628, 1583, 1570, 1558 (ar-C-C and ar-C-N st) cm^{-1}; ^{1}H NMR (400

MHz, CD_3OD) δ 1.55 (tt, $J \approx J' \approx 7.6$ Hz, 2H, 3-H_2), 1.59 (s, 3H, 9'-CH_3), 1.76 (m, 2H, 4-H_2), 1.90–2.02 (complex signal, 4H, 10'-H_{endo}, 13'-H_{syn}, 2-H_2), 2.09 (dm, J=12.8 Hz, 1H, 13'-H_{anti}), 2.57 (ddm, J=17.6 Hz, J'=6.0 Hz, 1H, 10'-H_{exo}), 2.78 (m, 1H, 7'-H), 2.87 (br d, J=18.0 Hz, 1H, 6'-H_{endo}), 2.97 (t, J=7.6 Hz, 2H, 5-H_2), 3.21 (dd, J=18.0 Hz, J'=5.6 Hz, 1H, 6'-H_{exo}), 3.49 (m, 1H, 11'-H), 4.01 (t, $J \approx 7.6$ Hz, 2H, 1-H_2), 4.85 (s, NH and $^+$NH), 5.59 (br d, J=4.4 Hz, 1H, 8'-H), 7.57 (dd, J=9.2 Hz, J'=2.0 Hz, 1H, 2'-H), 7.78 (d, J=2.0 Hz, 1H, 4'-H), 8.41 (d, J=9.2 Hz, 1H, 1'-H); ^{13}C NMR (100.6 MHz, CD_3OD) δ 23.5 (CH_3, 9'-CH_3), 24.7 (CH_2, C3), 27.3 (CH, C11'), 27.9 (CH, C7'), 28.2 (CH_2, C4), 29.3 (CH_2, C13'), 30.8 (CH_2, C2), 36.0 (CH_2), 36.2 (CH_2) (C6', C10'), 40.5 (CH_2, C5), 49.4 (CH_2, C1), 115.7 (C, C12a'), 117.8 (C, C11a'), 119.2 (CH, C4'), 125.1 (CH, C8'), 126.8 (CH, C2'), 129.4 (CH, C1'), 134.6 (C, C9'), 140.3 (C, C3'), 141.0 (C, C4a'), 151.4 (C, C5a'), 156.9 (C, C12'); HRMS (ESI) calcd for ($C_{22}H_{28}{}^{35}ClN_3 + H^+$) 370.2045, found 370.2041.

(±)-*N*-(3-Chloro-6,7,10,11-tetrahydro-9-methyl-7,11-methanocycloocta[*b*]quinolin-12-yl)hexane-1,6-diamine [(±)-6b]. It was prepared as described for (±)-**6a**. From nitrile (±)-**5b** (1.26 g, 3.32 mmol), amine (±)-**6b** (1.23 g, 97% yield) was obtained as a yellow oil; R_f 0.02 (CH_2Cl_2/MeOH/50% aq. NH_4OH 9:1:0.05).

(±)-6b·2HCl: mp 180–181 ºC (CH_2Cl_2/MeOH 79:21); IR (KBr) ν 3500–2500 (max at 3403, 3240, 2926, 2852, N-H, N^+-H and C-H st), 1728, 1624, 1578 (ar-C-C and ar-C-N st) cm^{-1}; ^{1}H NMR (400 MHz, CD_3OD) δ 1.46–1.51 (complex signal, 4H, 3-H_2, 4-H_2), 1.59 (s, 3H, 9'-CH_3), 1.70 (tt, $J \approx J' \approx 7.4$ Hz, 2H, 5-H_2), 1.85–1.97 (complex signal, 4H, 2-H_2, 10'-H_{endo}, 13'-H_{syn}), 2.09 (dm, $J \approx 12.6$ Hz, 1H, 13'-H_{anti}), 2.56 (dd, J=17.6 Hz, J'=4.8 Hz, 1H, 10'-H_{exo}), 2.78 (m, 1H, 7'-H), 2.87 (dm, $J \approx 18.0$ Hz, 1H, 6'-H_{endo}), 2.94 (t, J=7.6 Hz, 2H, 6-H_2), 3.21 (dd, J=18.0 Hz, J'=5.6 Hz, 1H, 6'-H_{exo}), 3.47 (m, 1H, 11'-

H), 4.00 (t, *J*=7.6 Hz, 2H, 1-H_2), 4.85 (s, NH and $^{+}$NH), 5.59 (br d, *J*=4.4 Hz, 1H, 8'-H), 7.57 (dd, *J*=9.2 Hz, *J'*=2.4 Hz, 1H, 2'-H), 7.77 (d, *J*=2.4 Hz, 1H, 4'-H), 8.41 (d, *J*≈9.2 Hz, 1H, 1'-H); ^{13}C NMR (100.6 MHz, CD_3OD) δ 23.5 (CH_3, 9'-CH_3), 27.1 (CH_2, C3), 27.3 (CH, C11'), 27.4 (CH_2, C4), 27.9 (CH, C7'), 28.5 (CH_2, C5), 29.3 (CH_2, C13'), 31.1 (CH_2, C2), 36.08 (CH_2), 36.15 (CH_2) (C6', C10'), 40.6 (CH_2, C6), 49.5 (CH_2, C1), 115.7 (C, C12a'), 117.7 (C, C11a'), 119.2 (CH, C4'), 125.1 (CH, C8'), 126.7 (CH, C2'), 129.5 (CH, C1'), 134.6 (C, C9'), 140.2 (C, C3'), 141.0 (C, C4a'), 151.3 (C, C5a'), 156.9 (C, C12'); HRMS (ESI) calcd for ($C_{23}H_{30}{}^{35}ClN_3 + H^+$) 384.2201; found 384.2197.

(±)-*N*-(3-Chloro-6,7,10,11-tetrahydro-9-methyl-7,11-methanocycloocta[*b*]quinolin-12-yl)heptane-1,7diamine [(±)-6c]. It was prepared as described for (±)-**6a**. From nitrile (±)-**5c** (2.20 g, 5.60 mmol), amine (±)-**6c** (1.98 g, 89% yield) was obtained as a yellow oil; R_f 0.07 (CH_2Cl_2/MeOH/50% aq. NH_4OH 9:1:0.05).

(±)-6c·2HCl: mp 181–183 ºC (CH_2Cl_2/MeOH 75:25); IR (KBr) *v* 3500–2500 (max at 3233, 2927, 2877, 2849, 2782, N-H, N^+-H and C-H st), 1628, 1582, 1566, 1550, 1524, 1508, 1492, 1476 (ar-C-C and ar-C-N st) cm^{-1}; ^{1}H NMR (400 MHz, CD_3OD) δ 1.41–1.52 (complex signal, 6H, 3-H_2, 4-H_2, 5-H_2), 1.59 (s, 3H, 9'-CH_3), 1.68 (tt, *J*≈*J'*≈7.2 Hz, 2H, 6-H_2), 1.84–1.95 (complex signal, 4H, 10'-H_{endo}, 13'-H_{syn}, 2-H_2), 2.09 (dm, *J*=13.2 Hz, 1H, 13'-H_{anti}), 2.56 (dd, *J*=17.6 Hz, *J'*=4.8 Hz, 1H, 10'-H_{exo}), 2.77 (m, 1H, 7'-H), 2.87 (ddd, *J*=18.0 Hz, *J'*≈*J''*≈1.6 Hz, 1H, 6'-H_{endo}), superimposed in part 2.93 (t, *J*=7.6 Hz, 2H, 7-H_2), 3.21 (dd, *J*=18.0 Hz, *J'*=5.6 Hz, 1H, 6'-H_{exo}), 3.47 (m, 1H, 11'-H), 3.99 (t, *J*≈7.6 Hz, 2H, 1-H_2), 4.85 (s, NH and $^{+}$NH), 5.59 (br d, *J*=4.4 Hz, 1H, 8'-H), 7.56 (dd, *J*=9.6 Hz, *J'*=2.0 Hz, 1H, 2'-H), 7.78 (d, *J*=2.0 Hz, 1H, 4'-H), 8.41 (d, *J*=9.6 Hz, 1H, 1'-H); ^{13}C NMR (100.6 MHz, CD_3OD) δ 23.5 (CH_3, 9'-CH_3), 27.3 (CH,

C11'), 27.4 (CH_2, C5), 27.7 (CH_2, C4), 27.8 (CH, C7'), 28.5 (CH_2, C3), 29.3 (CH_2, C13'), 29.8 (CH_2, C2), 31.2 (CH_2, C6), 36.0 (CH_2), 36.1 (CH_2) (C6', C10'), 40.7 (CH_2, C7), 49.6 (CH_2, C1), 115.6 (C, C12a'), 117.6 (C, C11a'), 119.1 (CH, C4'), 125.1 (CH, C8'), 126.7 (CH, C2'), 129.5 (CH, C1'), 134.6 (C, C9'), 140.2 (C, C3'), 141.0 (C, C4a'), 151.3 (C, C5a'), 156.9 (C, C12'); HRMS (ESI) calcd for ($C_{24}H_{32}{}^{35}ClN_3 + H^+$) 398.2358, found 398.2357.

(±)-*N*-(3-Chloro-6,7,10,11-tetrahydro-9-methyl-7,11-methanocycloocta[*b*]quinolin-12-yl)octane-1,8-diamine [(±)-6d]. It was prepared as described for (±)-**6a**. From nitrile (±)-**5d** (1.09 g, 2.68 mmol), amine (±)-**6d** (1.14 g, quantitative) was obtained as a yellow oil; R_f 0.07 (CH_2Cl_2/MeOH/50% aq. NH_4OH 9:1:0.05).

(±)-6d·2HCl: mp 209–211 °C (CH_2Cl_2/MeOH 77:23); IR (KBr) *v* 3500–2500 (max at 3395, 3245, 2927, 2854, 2780, N-H, N^+-H and C-H st), 1628, 1583, 1524, 1508, 1501 (ar-C-C and ar-C-N st) cm^{-1}; ^1H NMR (400 MHz, CD_3OD) δ 1.40–1.48 (complex signal, 8H, 3-H_2, 4-H_2, 5-H_2, 6-H_2), 1.59 (s, 3H, 9'-CH_3), 1.66 (tt, $J \approx J' \approx 7.2$ Hz, 2H, 7-H_2), superimposed 1.84–1.95 (m, 1H, 13'-H_{syn}), superimposed in part 1.84–1.93 (tt, $J \approx J' \approx 7.2$ Hz, 2H, 2-H_2), superimposed in part 1.93 (br d, J=17.6 Hz, 1H, 10'-H_{endo}), 2.10 (dm, $J \approx 10.4$ Hz, 1H, 13'-H_{anti}), 2.56 (dd, J=17.6 Hz, J'=4.8 Hz, 1H, 10'-H_{exo}), 2.77 (m, 1H, 7'-H), superimposed in part 2.87 (ddd, $J \approx 17.6$ Hz, $J' \approx J'' \approx 1.6$ Hz, 1H, 6'-H_{endo}), 2.92 (tt, $J \approx J' \approx 7.6$ Hz, 2H, 8-H_2), 3.21 (dd, J=17.6 Hz, J'=5.6 Hz, 1H, 6'-H_{exo}), 3.46 (m, 1H, 11'-H), 3.99 (tt, $J \approx J' \approx 7.6$ Hz, 2H, 1-H_2), 4.85 (s, NH and $^+$NH), 5.59 (br d, J=4.8 Hz, 1H, 8'-H), 7.56 (dd, J=9.6 Hz, J'=2.0 Hz, 1H, 2'-H), 7.78 (d, J=2.0 Hz, 1H, 4'-H), 8.40 (d, $J \approx 9.6$ Hz, 1H, 1'-H); ^{13}C NMR (100.6 MHz, CD_3OD) δ 23.5 (CH_3, 9'-CH_3), 27.3 (CH, C11'), 27.4 (CH_2, C3), 27.8 (CH_2, C4), 27.9 (CH, C7'), 28.5 (CH_2, C5), 29.2 (CH_2, C13'), 30.1 ($2CH_2$, C6, C7), 31.3 (CH_2, C2), 36.0 (CH_2), 36.1 (CH_2) (C6', C10'),

40.7 (CH_2, C8), 49.7 (CH_2, C1), 115.6 (C, C12a'), 117.6 (C, C11a'), 119.1 (CH, C4'), 125.1 (CH, C8'), 126.7 (CH, C2'), 129.5 (CH, C1'), 134.5 (C, C9'), 140.2 (C, C3'), 141.0 (C, C4a'), 151.2 (C, C5a'), 156.9 (C, C12'); HRMS (ESI) calcd for ($C_{25}H_{34}{}^{35}ClN_3$ + H^+) 412.2514, found 412.2509.

(±)-*N*-(3-Chloro-6,7,10,11-tetrahydro-9-methyl-7,11-methanocycloocta[*b*]quinolin-12-yl)nonane-1,9-diamine [(±)-6e]. It was prepared as described for (±)-**6a**. From nitrile (±)-**5e** (1.60 g, 3.80 mmol), amine (±)-**6e** (1.39 g, 86% yield) was obtained as a yellow oil; R_f 0.10 (CH_2Cl_2/MeOH/50% aq. NH_4OH 9:1:0.05).

(±)-6e·2HCl: mp 169–171 °C (CH_2Cl_2/MeOH 81:19); IR (KBr) *v* 3500–2500 (max at 3397, 3245, 2925, 2853, 2795, N-H, N^+-H and C-H st), 1629, 1582, 1508 (ar-C-C and ar-C-N st) cm^{-1}; ^1H NMR (400 MHz, CD_3OD) δ 1.34–1.48 (complex signal, 10H, 3-H_2, 4-H_2, 5-H_2, 6-H_2, 7-H_2), 1.59 (s, 3H, 9'-CH_3), 1.66 (tt, $J \approx J' \approx 6.8$ Hz, 2H, 8-H_2), superimposed in part 1.87 (tt, $J \approx J' \approx 7.6$ Hz, 2H, 2-H_2), superimposed 1.83–1.96 (m, 1H, 13'-H_{syn}), superimposed in part 1.93 (br d, $J \approx 18.0$ Hz, 1H, 10'-H_{endo}), 2.09 (dm, J=14.8 Hz, 1H, 13'-H_{anti}), 2.56 (dd, J=18.0 Hz, J'=4.8 Hz, 1H, 10'-H_{exo}), 2.77 (m, 1H, 7'-H), superimposed in part 2.87 (ddd, J=17.6 Hz, $J' \approx J'' \approx 1.6$ Hz, 1H, 6'-H_{endo}), 2.91 (br t, J=7.2 Hz, 2H, 9-H_2), 3.21 (dd, J=17.6 Hz, J'=5.6 Hz, 1H, 6'-H_{exo}), 3.46 (m, 1H, 11'-H), 3.98 (tt, $J \approx J' \approx 7.2$ Hz, 2H, 1-H_2), 4.85 (s, NH and $^+$NH), 5.59 (br d, J=4.8 Hz, 1H, 8'-H), 7.56 (dd, J=9.6 Hz, J'=2.0 Hz, 1H, 2'-H), 7.78 (d, J=2.0 Hz, 1H, 4'-H), 8.40 (d, J=9.6 Hz, 1H, 1'-H); ^{13}C NMR (100.6 MHz, CD_3OD) δ 23.5 (CH_3, 9'-CH_3), 27.3 (CH, C11'), 27.5 (CH_2, C3), 27.8 (CH + CH_2, C7', C4), 28.6 (CH_2, C5), 29.3 (CH_2, C13'), 30.1 (CH_2), 30.2 (CH_2), 30.4 (CH_2) (C6, C7, C8), 31.3 (CH_2, C2), 36.0 (CH_2), 36.1 (CH_2) (C6', C10'), 40.8 (CH_2, C9), 49.7 (CH_2, C1), 115.6 (C, C12a'), 117.6 (C, C11a'), 119.1 (CH, C4'), 125.1 (CH, C8'), 126.6 (CH, C2'), 129.5 (CH, C1'), 134.5 (C, C9'), 140.2

(C, C3'), 141.0 (C, C4a'), 151.2 (C, C5a'), 156.9 (C, C12'); HRMS (ESI) calcd for ($C_{26}H_{36}{}^{35}ClN_3 + H^+$) 426.2671, found 426.2664.

(–)-*N*-(3-Chloro-6,7,10,11-tetrahydro-9-methyl-7,11-methanocycloocta[*b*]quinolin-12-yl)nonane-1,9-diamine [(–)-6e]. It was prepared as described for (±)-**6a**. From nitrile (–)-**5e** (664 mg, 1.58 mmol), amine (–)-**6e** (652 mg, 97% yield) was obtained as a yellow oil; R_f 0.10 (CH_2Cl_2/MeOH/50% aq. NH_4OH 9:1:0.05).

(–)-6e·2HCl: $[\alpha]^{20}_D$=–170 (*c*=0.10, MeOH); mp 126–128 °C (CH_2Cl_2/MeOH 81:19); IR (KBr) *v* 3500–2500 (max at 3251, 2923, 2853, N-H, N^+-H and C-H st), 1629, 1582, 1512, 1501 (ar-C-C and ar-C-N st) cm^{-1}; the ^1H NMR and ^{13}C NMR spectra were identical to those of (±)-**6e**; HRMS (ESI) calcd for ($C_{26}H_{36}{}^{35}ClN_3 + H^+$) 426.2671, found 426.2656.

(+)-*N*-(3-Chloro-6,7,10,11-tetrahydro-9-methyl-7,11-methanocycloocta[*b*]quinolin-12-yl)nonane-1,9-diamine [(+)-6e]. It was prepared as described for (±)-**6a**. From nitrile (+)-**5e** (499 mg, 1.18 mmol), amine (+)-**6e** (429 mg, 86% yield) was obtained as a yellow oil; R_f 0.10 (CH_2Cl_2/MeOH/50% aq. NH_4OH 9:1:0.05).

(+)-6e·2HCl: $[\alpha]^{20}_D$=+186 (*c*=0.10, MeOH); mp 127–128 °C (CH_2Cl_2/MeOH 65:35); IR (KBr) *v* 3500–2500 (max at 3250, 2922, 2853, N-H, N^+-H and C-H st), 1629, 1582, 1512 (ar-C-C and ar-C-N st) cm^{-1}; the ^1H NMR and ^{13}C NMR spectra were identical to those of (±)-**6e**; HRMS (ESI) calcd for ($C_{26}H_{36}{}^{35}ClN_3 + H^+$) 426.2671, found 426.2668.

(±)-*N*-(3-Chloro-6,7,10,11-tetrahydro-9-methyl-7,11-methanocycloocta[*b*]quinolin-12-yl)decane-1,10-diamine [(±)-6f]. It was prepared as described for (±)-**6a**. From nitrile (±)-**5f** (645 mg, 1.48 mmol), amine (±)-**6f** (581 mg,

90% yield) was obtained as a yellow oil; R_f 0.06 (CH_2Cl_2/MeOH/50% aq. NH_4OH 9:1:0.05).

(±)-6f·2HCl: mp 179–180 °C (CH_2Cl_2/MeOH 82:18); IR (KBr) *v* 3500–2500 (max at 3382, 3235, 2997, 2926, 2853, 2790, N-H, N^+-H and C-H st), 1630, 1582, 1512 (ar-C-C and ar-C-N st) cm^{-1}; ^1H NMR (400 MHz, CD_3OD) δ 1.30–1.46 (complex signal, 12H, 3-H_2, 4-H_2, 5-H_2, 6-H_2, 7-H_2, 8-H_2), 1.58 (s, 3H, 9'-CH_3), 1.66 (tt, $J \approx J' \approx 7.2$ Hz, 2H, 9-H_2), superimposed in part 1.87 (tt, $J \approx J' \approx 7.6$ Hz, 2H, 2-H_2), superimposed 1.83–1.96 (m, 1H, 13'-H_{syn}), superimposed in part 1.94 (br d, $J \approx 17.6$ Hz, 1H, 10'-H_{endo}), 2.08 (dm, $J \approx 12.4$ Hz, 1H, 13'-H_{anti}), 2.56 (dd, $J = 17.6$ Hz, $J' = 4.4$ Hz, 1H, 10'-H_{exo}), 2.77 (m, 1H, 7'-H), superimposed in part 2.88 (d, $J = 18.0$ Hz, 6'-H_{endo}), superimposed in part 2.91 (tt, $J \approx J' \approx 7.8$ Hz, 2H, 10-H_2), 3.21 (dd, $J = 18.0$ Hz, $J' = 5.6$ Hz, 1H, 6'-H_{exo}), 3.47 (m, 1H, 11'-H), 3.99 (tt, $J \approx J' \approx 7.2$ Hz, 2H, 1-H_2), 4.85 (s, NH and $^+$NH), 5.59 (br d, $J = 4.8$ Hz, 1H, 8'-H), 7.55 (dd, $J = 9.6$ Hz, $J' \approx 2.0$ Hz, 1H, 2'-H), 7.80 (d, $J = 2.0$ Hz, 1H, 4'-H), 8.40 (d, $J = 9.6$ Hz, 1H, 1'-H); ^{13}C NMR (100.6 MHz, CD_3OD) δ 23.5 (CH_3, 9'-CH_3), 27.3 (CH, C11'), 27.5 (CH_2, C3), 27.8 (CH + CH_2, C7', C4), 28.6 (CH_2, C5), 29.3 (CH_2, C13'), 30.2 (CH_2), 30.3 (CH_2), 30.4 (CH_2), 30.5 (CH_2) (C6, C7, C8, C9), 31.3 (CH_2, C2), 36.0 (CH_2), 36.1 (CH_2) (C6', C10'), 40.8 (CH_2, C10), 49.7 (CH_2, C1), 115.6 (C, C12a'), 117.6 (C, C11a'), 119.1 (CH, C4'), 125.1 (CH, C8'), 126.6 (CH, C2'), 129.5 (CH, C1'), 134.5 (C, C9'), 140.2 (C, C3'), 141.0 (C, C4a'), 151.2 (C, C5a'), 156.9 (C, C12'); HRMS (ESI) calcd for ($C_{27}H_{38}{}^{35}ClN_3 + H^+$) 440.2827, found 440.2820.

(±)-*N*-(3-Chloro-6,7,10,11-tetrahydro-9-methyl-7,11-methanocycloocta[*b*]quinolin-12-yl)undecane-1,11-diamine [(±)-6g]. It was prepared as described for (±)-**6a**. From nitrile (±)-**5g** (1.05 g, 2.33 mmol), amine (±)-**6g** (849 mg, 81% yield) was obtained as a yellow oil; R_f 0.05 (CH_2Cl_2/MeOH/50% aq. NH_4OH 9:1:0.05).

(±)-6g·2HCl: mp 164–165 °C (CH_2Cl_2/MeOH 79:21); IR (KBr) *v* 3500–2500 (max at 3385, 3232, 3043, 2924, 2852, 2790, 2651, N-H, N^+-H and C-H st), 1630, 1582, 1512 (ar-C-C and ar-C-N st) cm^{-1}; ^1H NMR (400 MHz, CD_3OD) δ 1.26–1.44 (complex signal, 14H, 3-H_2, 4-H_2, 5-H_2, 6-H_2, 7-H_2, 8-H_2, 9-H_2), 1.58 (s, 3H, 9'-CH_3), 1.67 (tt, *J*≈*J'*≈6.8 Hz, 2H, 10-H_2), superimposed in part 1.87 (tt, *J*≈*J'*≈7.2 Hz, 2H, 2-H_2), superimposed 1.81–1.93 (m, 1H, 13'-H_{syn}), superimposed in part 1.94 (br d, *J*=17.2 Hz, 1H, 10'-H_{endo}), 2.08 (dm, *J* = 12.4 Hz, 1H, 13'-H_{anti}), 2.56 (dd, *J*=17.2 Hz, *J'*=4.4 Hz, 1H, 10'-H_{exo}), 2.77 (m, 1H, 7'-H), superimposed in part 2.91 (d, *J*=17.6, Hz, 6'-H_{endo}), superimposed in part 2.93 (tt, *J*≈*J'*≈7.6 Hz, 2H, 11-H_2), 3.21 (dd, *J*=17.6 Hz, *J'*=5.6 Hz, 1H, 6'-H_{exo}), 3.49 (m, 1H, 11'-H), 3.99 (tt, *J*≈*J'*≈7.2 Hz, 2H, 1-H_2), 4.85 (s, NH and $^+$NH), 5.58 (br d, *J*=5.2 Hz, 1H, 8'-H), 7.53 (dd, *J*≈9.6 Hz, *J'*=2.0 Hz, 1H, 2'-H), 7.82 (d, *J*=2.0 Hz, 1H, 4'-H), 8.40 (d, *J*=9.6 Hz, 1H, 1'-H); ^{13}C NMR (100.6 MHz, CD_3OD) δ 23.5 (CH_3, 9'-CH_3), 27.3 (CH, C11'), 27.5 (CH_2, C3), 27.8 (CH + CH_2, C7', C4), 28.5 (CH_2, C5), 29.3 (CH_2, C13'), 30.2 (CH_2), 30.3 (CH_2), 30.47 (CH_2), 30.51 (CH_2), 30.6 (CH_2) (C6, C7, C8, C9, C10), 31.2 (CH_2, C2), 36.0 (CH_2), 36.1 (CH_2) (C6', C10'), 40.8 (CH_2, C11), 49.6 (CH_2, C1), 115.6 (C, C12a'), 117.6 (C, C11a'), 119.1 (CH, C4'), 125.1 (CH, C8'), 126.6 (CH, C2'), 129.5 (CH, C1'), 134.5 (C, C9'), 140.1 (C, C3'), 140.9 (C, C4a'), 151.2 (C, C5a'), 156.9 (C, C12'); HRMS (ESI) calcd for ($C_{28}H_{40}{}^{35}ClN_3$ + H^+) 454.2984; found 454.2969.

(±)-4-{[(3-Chloro-6,7,10,11-tetrahydro-9-methyl-7,11-methanocycloocta[*b*]quinolin-12-yl)amino]methyl}benzylamine [(±)-6h]. It was prepared as described for (±)-**6a**. From nitrile (±)-**5h** (370 mg, 0.93 mmol), amine (±)-**6h** (352 mg, 94% yield) was obtained as a yellow oil; R_f 0.11 (CH_2Cl_2/MeOH/50% aq. NH_4OH 9:1:0.05).

(±)-6h·2HCl: mp 151–152 °C (CH_2Cl_2/MeOH 75:25); IR (KBr) *v* 3500–2500 (max at 3390, 3245, 3043, 3002, 2899, 2795, 2609, N-H, N^+-H and C-H st), 1715, 1700, 1631, 1583, 1517 (ar-C-C and ar-C-N st) cm^{-1}; ^1H NMR (400 MHz, CD_3OD) δ 1.61 (s, 3H, 9'-CH_3), superimposed in part 2.00 (br d, *J*=18.4 Hz, 1H, 10'-H_{endo}), superimposed 1.96–2.00 (m, 1H, 13'-H_{syn}), 2.10 (dm, *J*=12.4 Hz, 1H, 13'-H_{anti}), 2.57 (dd, *J*≈18.4 Hz, *J'*≈4.8 Hz, 1H, 10'-H_{exo}), 2.80 (m, 1H, 7'-H), 2.82 (dm, *J*=18.0 Hz, 1H, 6'-H_{endo}), 3.25 (dd, *J*=18.0 Hz, *J'*=5.8 Hz, 1H, 6'-H_{exo}), 3.54 (m, 1H, 11'-H), 4.14 (s, 2H, CH_2NH_2), 4.85 (s, NH and $^+$NH), 5.25 (s, 2H, CH_2NH), 5.61 (br d, *J*=4.8 Hz, 1H, 8'-H), 7.34 (dd, *J*=9.2 Hz, *J'*=2.4 Hz, 1H, 2'-H), 7.50–7.57 [complex signal, 4H, 2(6)-H_2 and 3(5)-H_2), 7.78 (d, *J*=2.4 Hz, 1H, 4'-H), 8.21 (d, *J*=9.2 Hz, 1H, 1'-H); ^{13}C NMR (100.6 MHz, CD_3OD) δ 23.5 (CH_3, 9'-CH_3), 27.6 (CH, C11'), 27.9 (CH, C7'), 29.3 (CH_2, C13'), 36.1 (CH_2), 36.3 (CH_2) (C6', C10'), 43.9 (CH_2, CH_2NH), 51.7 (CH_2, CH_2NH_2), 115.6 (C, C12a'), 118.4 (C, C11a'), 119.3 (CH, C4'), 125.1 (CH, C8'), 126.7 (CH, C2'), 128.5 [CH, C2(6)], 129.3 (CH, C1'), 130.9 [CH, C3(5)], 134.2 (C), 134.6 (C), 140.0 (C) (C1, C4, C9'), 140.3 (C, C3'), 140.9 (C, C4a'), 151.9 (C, C5a'), 157.3 (C, C12'); HRMS (ESI) calcd for ($C_{25}H_{26}{}^{35}ClN_3 + H^+$) 403.1575, found 403.1578.

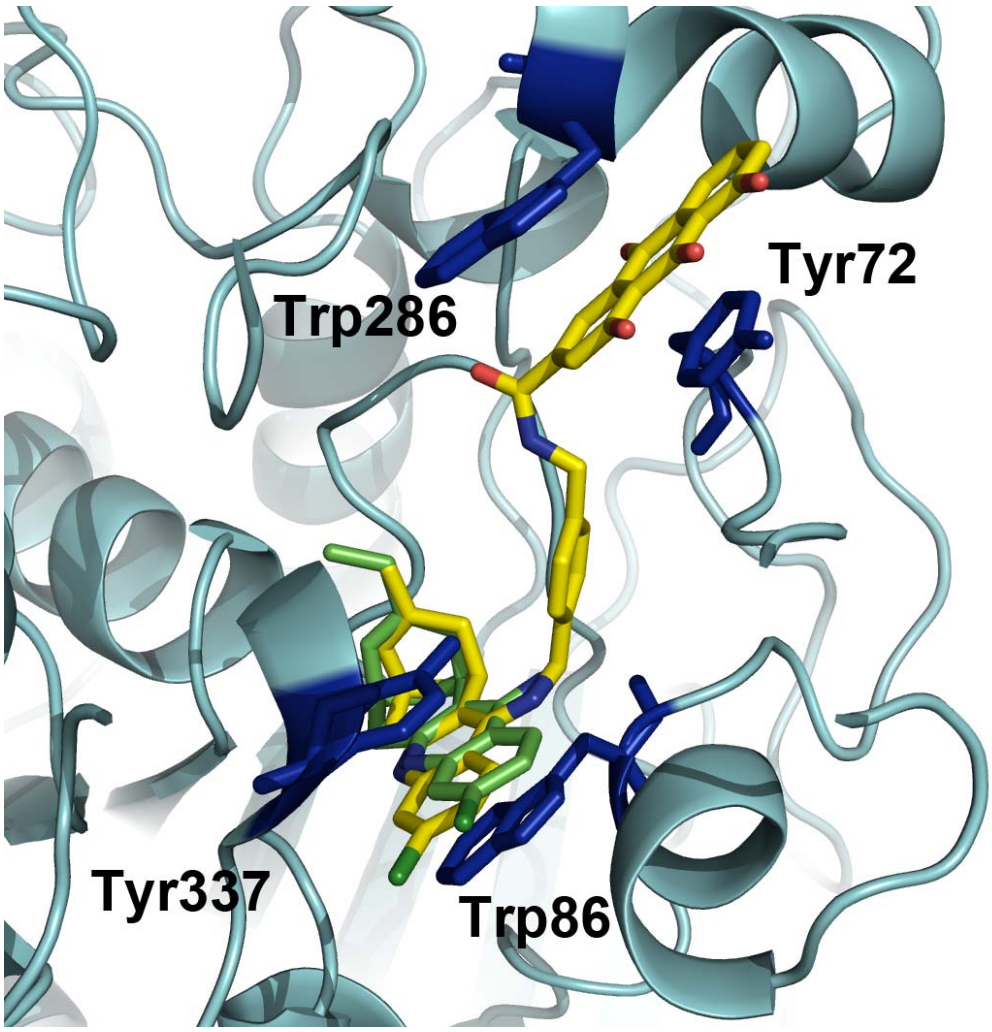

Figure S1. Superposition of hybrid (–)-**7h** (bound to human AChE; shown as yellow sticks) and huprine X (bound to *Torpedo californica* AChE; shown as green sticks).

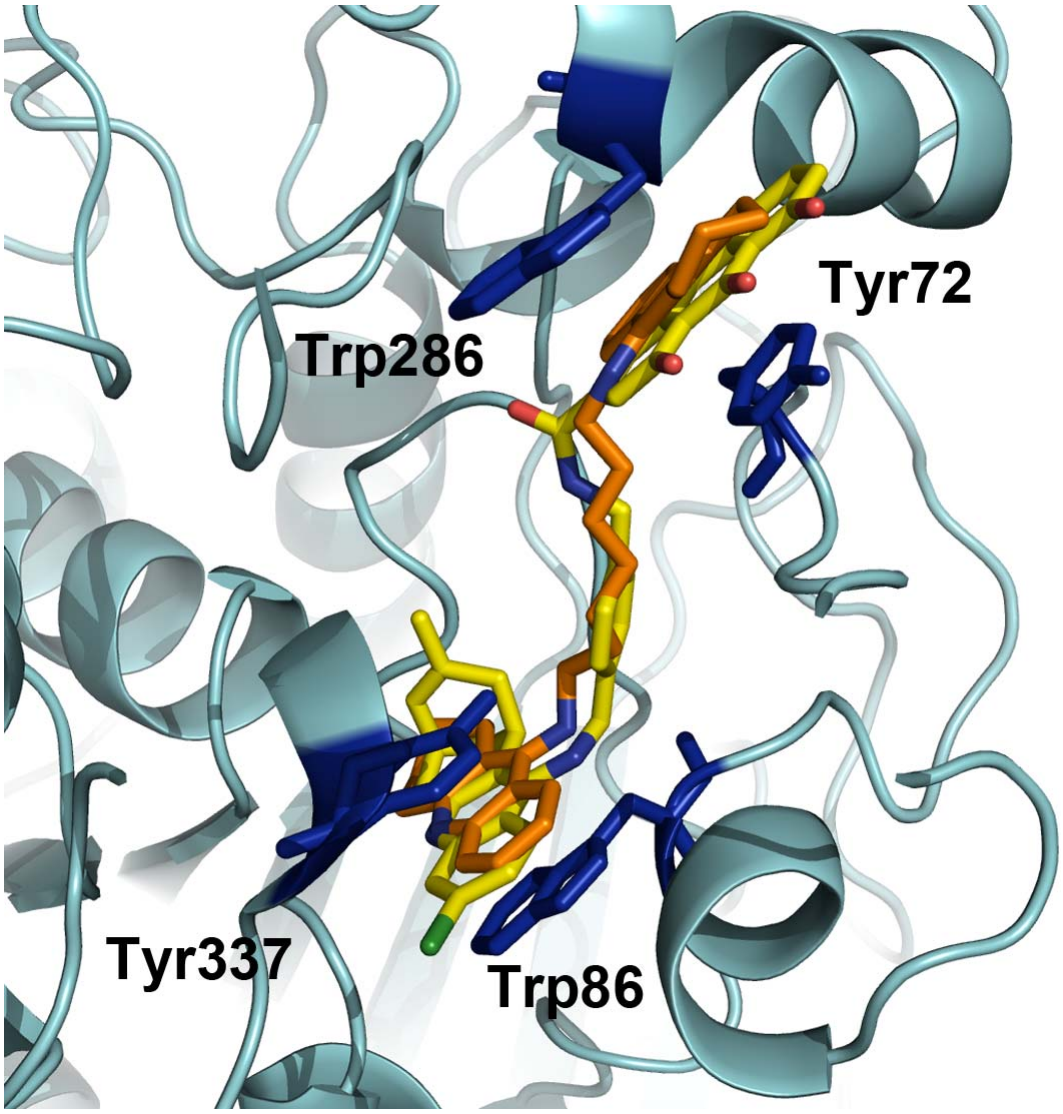

Figure S2. Superposition of hybrid (–)-**7h** (bound to human AChE; shown as yellow sticks) and *bis*(7)-tacrine (bound to *Torpedo californica* AChE; shown as orange sticks).

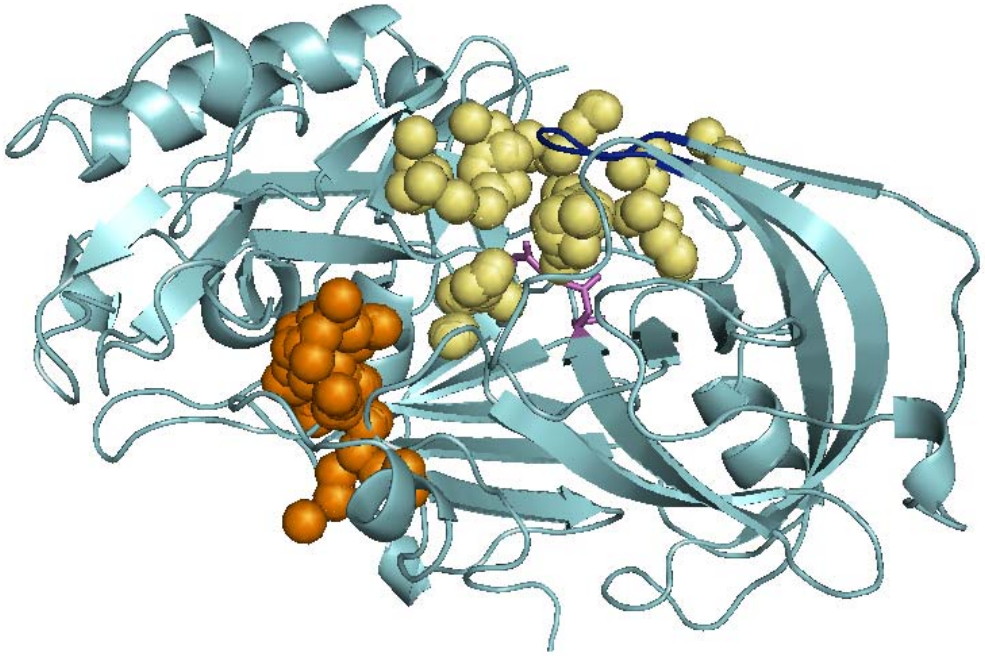

Figure S3. Representation of the two druggable sites in BACE-1 (shown as cyan cartoon) obtained from the analysis of MDpocket suitable to accommodate the huprine and hydroxyanthraquinone moieties present in the hybrids. The first binding site (BS1; yellow spheres) encompasses the catalytic site, including Asp32 and Asp228 (shown as magenta sticks) and is shaped by the β-hairpin loop commonly known as the "flap" (shown in blue). The second binding site (BS2; orange spheres) encompasses the exosites P5–P7 reported by Turner et al.[1]

BBB Permeation Assay.

Table S1. Literature and Experimental Permeability (*Pe* 10^{-6} cm s^{-1}) Values in the PAMPA-BBB Assay of 14 Commercial Drugs Used for Assay Validation.

Compound	**Bibliography value**[a]	**Experimental value (n=3) ± S.D.**
Verapamil	16	23.4 ± 3.21
Testosterone	17	22.6 ± 2.10
Costicosterone	5.1	8.02 ± 0.90
Clonidine	5.3	7.7 ± 0.5
Ofloxacin	0.8	0.08 ± 0.01
Lomefloxacin	1.1	0.70 ± 0.08
Progesterone	9.3	16.8 ± 0.03
Promazine	8.8	13.8 ± 0.4
Imipramine	13	12.3 ± 0.1
Hydrocortisone	1.9	1.52 ± 0.21
Piroxicam	2.5	1.92 ± 0.29
Desipramine	12	17.8 ± 0.1
Cimetidine	0.0	0.7 ± 0.03
Norfloxacin	0.1	0.9 ± 0.02

[a] From ref. 2.

References

1. Turner, R. T., III; Hong, L.; Koelsch, G.; Ghosh, A. K.; Tang, J. Structural locations and functional roles of new subsites S5, S6, and S7 in memapsin 2 (β-secretase). *Biochemistry* **2005**, *44*, 105–112.

2. Di, L.; Kerns, E. H.; Fan, K.; McConnell, O. J.; Carter, G. T. High throughput artificial membrane permeability assay for blood-brain barrier. *Eur. J. Med. Chem.* **2003**, *38*, 223–232.

Appendix (elemental analysis data)

Compound	**Molecular Formula**	**Calculated**				**Found**			
		C	H	N	Cl	C	H	N	Cl
(±)-**7a**·HCl·1.5H_2O	$C_{37}H_{34}ClN_3O_5$·HCl·1.5H_2O	63.52	5.47	6.01	10.13	63.39	5.72	5.64	10.91
(±)-**7b**·HCl·1.25H_2O	$C_{38}H_{36}ClN_3O_5$·HCl·1.25H_2O	64.36	5.61	5.93	10.00	64.52	5.55	5.83	10.50
(±)-**7c**·HCl·0.5H_2O	$C_{39}H_{38}ClN_3O_5$·HCl·0.5H_2O	66.01	5.68	5.92	9.99	66.26	5.64	5.90	9.63
(±)-**7d**·HCl·H_2O	$C_{40}H_{40}ClN_3O_5$·HCl·H_2O	65.57	5.92	5.73	9.68	65.52	5.86	5.83	9.35
(±)-**7e**·1.3HCl·1.25H_2O	$C_{41}H_{42}ClN_3O_5$·1.3HCl·1.25H_2O	64.61	6.06	5.51	10.70	64.51	6.00	6.10	10.97
(–)-**7e**·HCl·H_2O	$C_{41}H_{42}ClN_3O_5$·HCl·H_2O	65.95	6.07	5.63	9.50	65.50	6.07	5.20	9.91
(+)-**7e**·1.25HCl·0.75H_2O	$C_{41}H_{42}ClN_3O_5$·1.25HCl·0.75H_2O	65.54	6.00	5.59	10.62	65.79	6.28	5.80	10.89
(±)-**7f**·HCl·0.5H_2O	$C_{42}H_{44}ClN_3O_5$·HCl·0.5H_2O	67.11	6.17	5.59	9.43	66.76	6.26	5.27	9.91
(±)-**7g**·HCl·0.5H_2O	$C_{43}H_{46}ClN_3O_5$·HCl·0.5H_2O	67.44	6.32	5.49	9.26	67.52	6.46	5.30	9.51
(±)-**7h**·1.1HCl·1.4H_2O	$C_{40}H_{32}ClN_3O_5$·1.1HCl·1.4H_2O	65.32	4.92	5.71	10.12	65.32	5.06	6.09	10.15

4.4 Inhibidores Multipotentes ChE-MAO: Híbridos donepezilo-PFN9601

La primera aproximación para obtener una familia de compuestos multipotentes de utilidad terapéutica en la EA partió de la amplia experiencia del grupo en el diseño de inhibidores de AChE[69,91–93], y en concreto, de híbridos basados en donepezilo[94–96]. En colaboración con el grupo de la Prof. Mercedes Unzeta de la Universidad Autónoma de Barcelona se llevó a cabo el diseño de una familia de híbridos que combinaban características estructurales de donepezilo y de PFN9601[97], un inhibidor irreversible selectivo de MAO B, unidos mediante una cadena oligometilénica. La nueva familia de híbridos combinaría los efectos de mejora cognitiva de los inhibidores de AChE con el retraso en la neurodegeneración asociada a los iMAO B. Además, debido a su longitud y a la presencia de dos grupos cargados positivamente a pH fisiológico, los compuestos podrían actuar como inhibidores de sitio de unión dual en AChE, lo que permitiría reducir la agregación Aß inducida por este enzima[34].

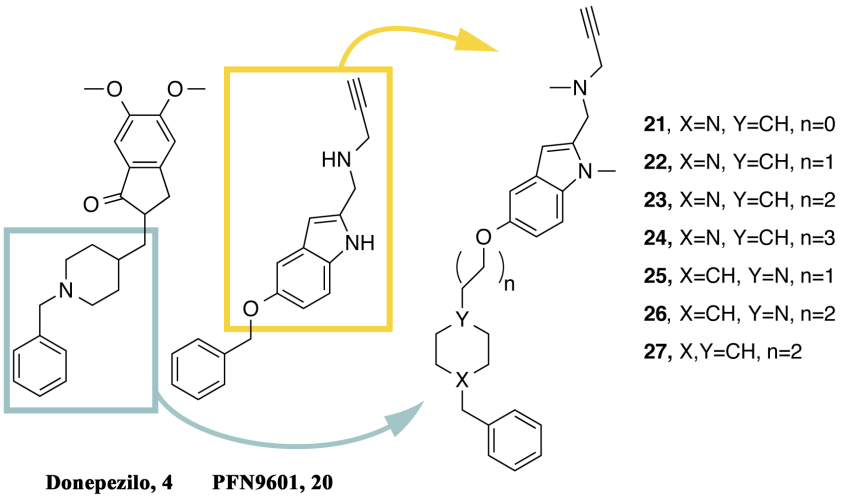

Figura 4.1. Estrategia de hibridación conjuntiva planteada para la obtención de híbridos donepezilo-PFN9601. El motivo benzylpiperidina debería alojarse en el CAS de AChE, mientras que grupo indoil-propargyl-amino reúne las características para interaccionar con el PAS de AChE y actuar como inhibidor irreversible de MAO.

En base a la evaluación farmacológica llevada a cabo como parte del proyecto de tesis de la Dra. Irene Bolea en la Facultad de Medicina de la Universidad Autónoma de Barcelona, se propuso el compuesto **23** como cabeza de serie para su ulterior desarrollo.

	IC_{50} (μM)			IC_{50} (nM)		
	AChE	**BuChE**	**Selectividad AChE /BuChE**	**MAO A**	**MAO B**	**Selectividad B/A**
4, donepezilo	0.007	7.4	1100	850000	15000	-
20, PFN9601	>100	>100	-	100	63	0.63
21	0.31	1.1	3.5	82	750	9.1
22	0.42	2.1	5.0	6.7	130	19
23	0.35	0.46	1.3	5.2	43	8.3
24	0.26	0.99	3.8	10	2700	260
25	>100	0.80	-	140	1400	10
26	18.1	2.2	0.12	65	11000	170
27	>100	7.6	-	31	1600	54

Tabla 4.1. Principales actividades farmacológicas de los híbridos donepezilo-PFN9601. Las principales singularidades de la relaciones estructura actividad se relacionan con la longitud de la cadena oligometilénica.

A pesar de su moderada actividad frente a AChE y BuChE, el perfil farmacológico de **23** resultaba atractivo por su potente actividad inhibidora de ambas isoformas de MAO (mayor que la del compuesto original PFN9601), así como por su capacidad de inhibir tanto la autoagregación de ßA como la agregación inducida por AChE de forma similar a donepezilo (22% de inhibición a una concentración de 100μM).

Dentro del prometedor perfil farmacológico de **23**, las relaciones estructura-actividad presentaban algunas características llamativas. En primer lugar, la inhibición

de AChE no se veía afectada cuando la longitud de la cadena oligometilénica variaba de 1 a 4 carbonos, pero esta misma modificación tenía un efecto significativo en la actividad frente a ambas isoformas de MAO. En segundo lugar, la posición del nitrógeno en el anillo de piperidina tenía un marcado efecto en la inhibición de todos los enzimas. Por último, **23** provocaba una rápida inhibición de MAO A, pero la inhibición de MAO B era más lenta y requería de un tiempo de incubación más prolongado para originar una inhibición irreversible. Con objeto de proporcionar una base estructural a las cuestiones anteriores, se llevaron a cabo una serie de estudios de modelización en los que se combinaron *docking,* dinámica molecular y métodos de estimación de la energía de unión.

4.4.1 Inhibición de AChE

La estructura de **23** reunía las características necesarias para actuar como inhibidor dual de AChE, y por este motivo era necesario considerar la plasticidad del sitio de unión periférico. Las diferentes conformaciones del PAS quedan determinadas principalmente por la orientación del residuo Trp286 (Trp279 en *Tc*AChE) , dado que este residuo es capaz de adoptar al menos tres orientaciones diferentes en función del compuesto que ocupa la garganta catalítica (Tabla 4.2). Para representar dicha variabilidad estructural, se emplearon tres modelos de proteína en los que se conservó la orientación de los residuos del CAS correspondiente al complejo donepezilo-*Tc*AChE y se varió la orientación del residuo Trp286 en el PAS.

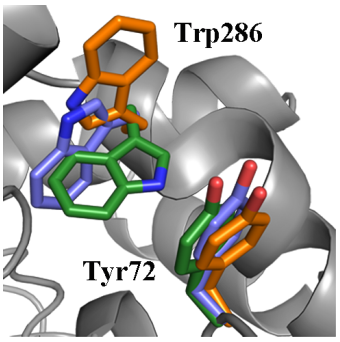

Código PDB	Ligando	χ_1: N-C_α-C_β-C_γ	χ_2: C_α-C_β-C_γ-$C_{\delta 2}$
1EVE[98]	Donepezilo	308	276
1Q83[99]	*syn*-TZ2PA6	198	196
2CKM[100]	*bis*(7)-tacrina	239	44

Tabla 4.2 Conformaciones descritas mediante cristalografía de rayos X para el residuo Trp286. Adaptada de Camps *et. al.*[71]

Tras seleccionar 3 modos de unión posibles (1 por cada modelo de proteína) mediante cálculos de docking, las simulaciones de dinámica molecular demostraron la estabilidad del modo de unión AChE (1EVE), en el cual el compuesto **23** reproducía los rasgos estructurales hallados para donepezilo en su complejo con *Tc*AChE. (Figura 4.2).

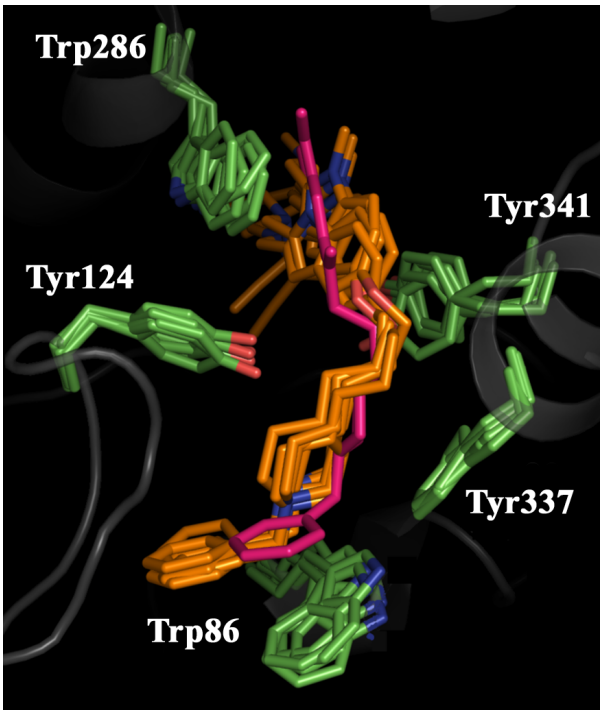

Figura 4.2. Modo de unión de 23 en AChE. Los rasgos estructurales del sitio de unión y la orientación del compuesto son similares a los descritos para donepezilo. Se sobreponen la posición del ligando (átomos de C en naranja) y de los residuos del sitio de unión (átomos de C en verde) durante los últimos 5 ns de dinámica molecular. La posición de donepezilo se representa en rosa.

En ambos casos el motivo benzilpiperidina ocuparía el sitio de unión catalítico, estableciendo una interacción de tipo π-*stacking* (asistida por la presencia de una carga positiva) con el residuo Trp86 (Trp84 en *Tc*AChE), aunque esta interacción parecía menos estable en el caso de **23**, ya que la movilidad del compuesto era mayor. El cambio de orientación del residuo Tyr341 (Tyr334 en *Tc*AChE) facilitaría el acomodamiento del anillo de indol de **23** entre este residuo y el residuo Trp286 en el PAS. Una molécula de agua se situaría entre el nitrógeno protonado del motivo piperidina y el hidroxilo de los residuos Tyr124 y Ser125 (Tyr121 y Ser122 en *Tc*AChE), mediando una interacción de puente de hidrógeno.

Las relaciones estructura-actividad quedarían explicadas por el modelo AChE(1EVE), ya que en compuestos con una cadena oligometilénica más corta, asumiendo que el motivo benzilpiperidina ocupa el centro catalítico, podrían acomodarse fácilmente en la garganta catalítica y el anillo de indol podría acomodarse de forma similar, manteniendo la interacción por π-*stacking* con los residuos Trp286 y Tyr341. Por el contrario, la falta de afinidad observada al invertir el motivo piperidina estaría motivada por la pérdida de la interacción mediada por agua con los residuos Tyr124 y Ser125) y por un debilitamiento de la interacción con el residuo Trp86.

4.4.2 Inhibición de MAO

El punto de mayor interés en la unión a MAO concierne al diferente comportamiento cinético de **23** en ambas isoformas. En primer lugar, mediante cálculos de *docking* molecular se obtuvieron modelos iniciales de unión a ambas isoformas en los que los que el motivo indolilpropargilamino quedaba acomodado en la cavidad catalítica, cerca del anillo de isoxazolina del cofactor. Los modelos obtenidos se validaron empleando simulaciones de dinámica molecular, que en ambos casos

originaron trayectorias estables, con valores promedio de rmsd del esqueleto peptídico inferiores a 1.4 Å y de los residuos de la cavidad catalítica inferior a 2.0 Å. La relación de la actividad con la longitud de la cadena oligometilénica puede explicarse por el hecho de que es precisamente esta sección de la molécula la que ocupa la región de *bottleneck*, situada entre el sitio de entrada y la cavidad catalítica y definida por los residuos Phe208 e Ile325 en MAO A, y por Tyr326 e Ile199 en MAO B. Los derivados con cadenas oligometilénicas más cortas (de 0 y 1 metilenos) carecerían de la flexibilidad necesaria para acomodarse a través de este cuello de botella, mientras que en el caso del compuesto **17**, con una cadena de 3 metilenos, sería demasiado largo para quedar alojado en el sitio de unión lo que explicaría su menor actividad inhibitoria (Figura 4.3).

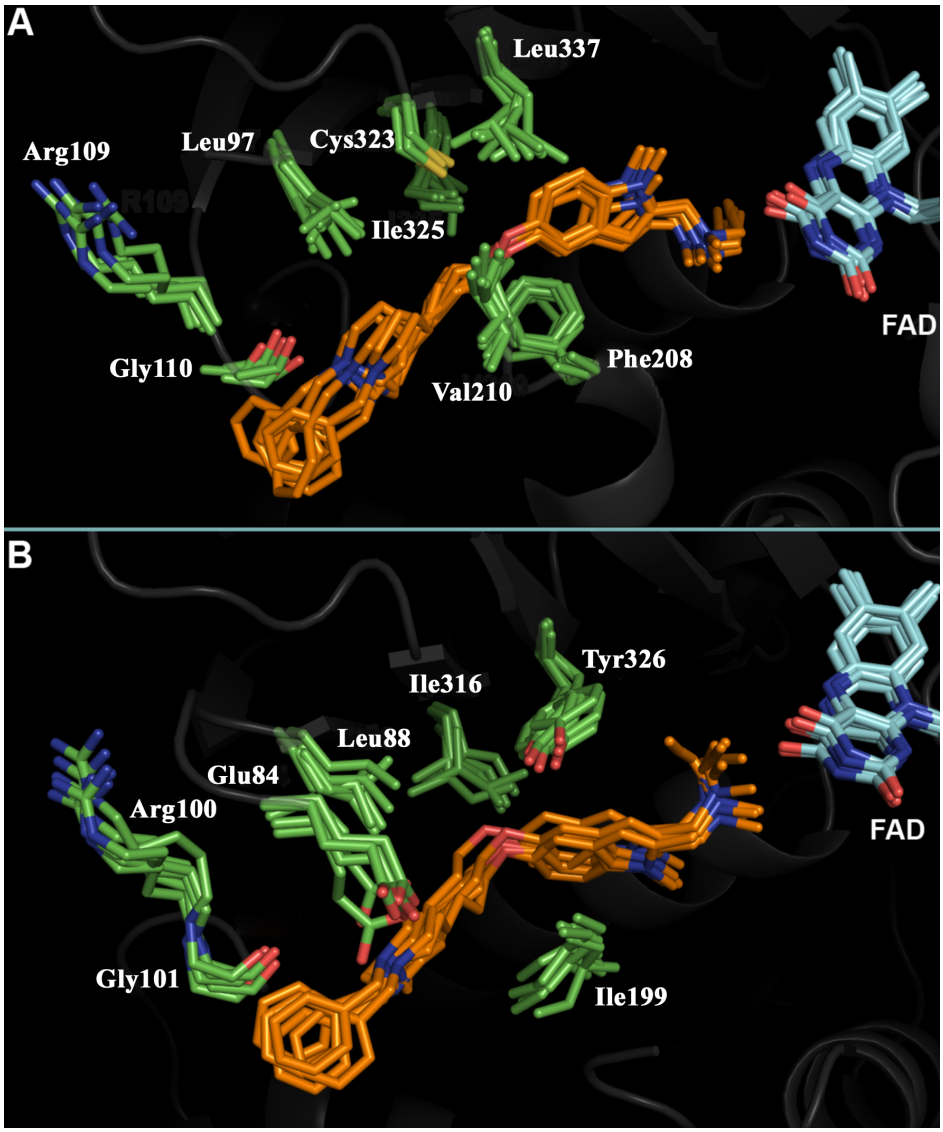

Figura 4.3. Modo de unión de 23 en MAO A (A) y MAO B (B). La posición del compuesto en ambos casos es similar aunque la orientación es diferente. Se sobreponen la posición del ligando (átomos de C en naranja) y de los residuos del sitio de unión (átomos de C en verde) durante los últimos 5 ns de dinámica molecular.

La estabilidad estructural de los modelos de unión en ambas isoformas (traducida a su vez en predicciones de energía libre de unión similares) no permitía explicar las diferencias en la cinética de inhibición de ambos compuestos. Sin embargo, cabe destacar que a pesar de compartir la mayor parte de los rasgos estructurales, los modelos divergían en la posición del grupo propargilamina. Así, al comparar la distancia entre el átomo de nitrógeno del FAD que queda modificado en la inhibición

covalente y el átomo de carbono unido al nitrógeno protonado del grupo propargilamina de **23**, podía observarse que en MAO A esta distancia era, en promedio durante los últimos 5 ns de trayectoria de MD, de 6.8 Å, mientras que en MAO B era de 7.7 Å. El análisis de las estructuras cristalográficas de complejos de MAO modificados covalentemente con derivados tipo propargilamina, reveló que en estos complejos el carbono que soporta el nitrógeno protonado ocupa una posición cercana a la observada en el modelo **23**-MAO A (Figura 4.4), lo que podría explicar la mayor velocidad de inhibición.

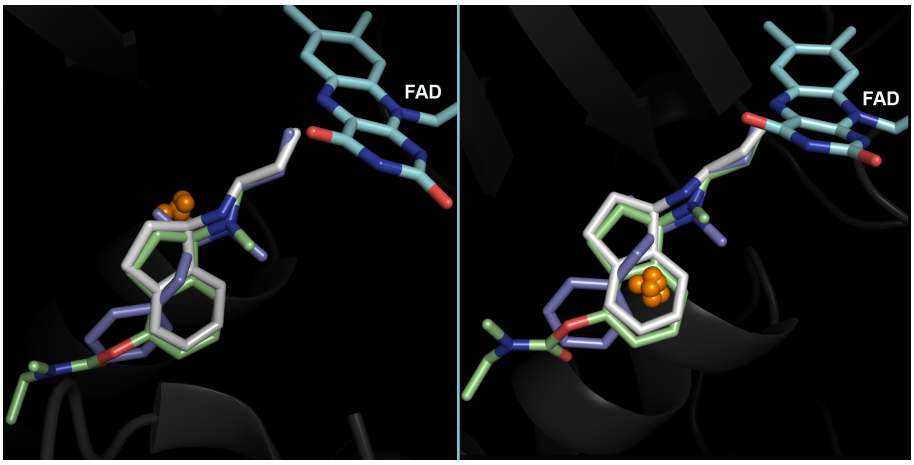

Figura 4.4. Superposición de las estructuras cristalográficas de los complejos de MAO B con selegilina (átomos de C en lila), rasagilina (átomos de C en blanco) y uno de sus derivados (átomos C en verde). Las esferas marcan la posición del carbono de **23** unido al nitrógeno cargado a lo largo de los últimos 5 ns de dinámica molecular en MAO A (izquierda) y MAO B (derecha).

Para probar la hipótesis anterior, se emplearon dos aproximaciones. En primer lugar, mediante restricciones en cálculos de simulaciones de dinámica molecular se forzó que **23** ocupara la posición que debería tener tras reaccionar con el FAD, y se empleo la técnica de MM/PBSA para evaluar la estabilidad energética de las posiciones intermedias. En el caso del modelo **23**-MAO A se observó que la energía de interacción era 7 kcal/mol más favorable en la posición reactiva que en la inicial, mientras que en el caso de MAO B se observó la tendencia opuesta, siendo la posición final menos estable

en 6 kcal/mol. Estos cambios indicarían que la adopción de una conformación reactiva está más impedida en MAO B, en concordancia con los resultados experimentales. En segundo lugar, la confirmación de los resultados anteriores se llevo a cabo realizando simulaciones de dinámica molecular del complejo post-reactivo entre **23** y el FAD. Ambos modelos dieron lugar a trayectorias estables, pero en el caso del modelo **23**-MAO B se observó que acomodar el complejo post-reactivo requería una mayor deformación de los residuos del sitio de unión, reflejada en un incremento mayor del rmsd con respecto a MAO A (Figura 4.5).

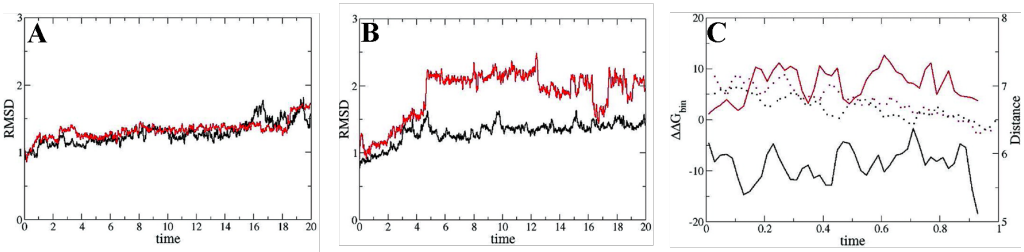

Figura 4.5. Gráficos de evolución frente al tiempo de simulación de A) rmsd del complejo post-reactivo **23**-MAO A **B)** rmsd del complejo post-reactivo **23**-MAO B. En negro se representa el rmsd del esqueleto peptídico y rojo el rmsd de los resiudos que delimitan el sitio de unión. **C)** Distancia de **23** al FAD (puntos) y energía libre de unión relativa con respecto a la posición inicial (línea) en MAO A (negro) y MAO B (rojo).

En conjunto, los resultados de modelado permitieron racionalizar las inconsistencias detectadas en las relaciones estructura-actividad de los inhibidores AChe-MAO y permitieron definir las modificaciones que podrían contribuir a mejorar el perfil farmacológico, principalmente en cuanto a la selectividad MAO A – MAO B y reducir los riesgos de desencadenar las crisis hipertensivas asociadas al síndrome del queso. Una primera aproximación consistiría en extender la cadena oligometilénica y sustituir el fragmento correspondiente a PFN9601 un motivo estructural más pequeño que permitiera una mejor adaptación de los híbridos al sitio de unión de MAO B y no

modificara sustancialmente la capacidad de inhibición sobre AChE. Alternativamente, el empleo de motivos estructurales diferentes en el fragmento iMAO podría emplearse para obtener inhibidores reversibles de perfil farmacológico más seguro y que mantuvieran la actividad antidepresiva de los híbridos, ausentes en derivados selectivos MAO B.

4.5 Exploración de la selectividad de inhibidores en MAO: Dicarbonitrilo aminoheterociclos

Modular la actividad inhibitoria frente a ambas isoformas de MAO era uno de los aspectos en los que existía mayor margen de mejora del perfil farmacológico de los inhibidores multipotentes ChE-MAO. Debido a los efectos adversos asociados al uso de inhibidores irreversibles MAO A, un inhibidor ChE-MAO irreversible debería ser selectivo MAO B. Alternativamente, un perfil de inhibidor reversible permitiría la obtención de fármacos con acción antidepresiva, neuroprotectora y con menor probabilidad de causar efectos adversos, ya que en el intestino podrían ser desplazados por las aminas bioactivas ingeridas con la dieta[101–104]. Debido a la elevada identidad de secuencia (73%) entre las isoformas A y B de MAO, la selectividad de sustrato está determinada por sutiles diferencias en la estructura y el diseño racional de compuestos selectivos requiere conocer los factores moleculares que la determinan.

En este contexto, en el grupo se inició una colaboración con el grupo de la Dra. Rona Ramsay de la Universidad de St. Andrews en Escocia, con el objetivo de identificar residuos aminoacídicos que pudieran jugar un rol en la selectividad de los inhibidores. Como modelo se escogió una serie de aminoheterociclos relacionados estructuralmente con brofaromina (Tabla 4.3), un inhibidor MAO A reversible, que presentaban una estructura tipo biarilo y cuya actividad estaba fuertemente influenciada

por el patrón de sustituciones. La presencia de sustituyentes tipo carbonitrilo pretendía reproducir el efecto potenciador de la inhibición de MAO previamente descrito para el ion cianuro[105,106].

Compuesto		X, Y, Z	MAO A	
			IC_{50}	K_i
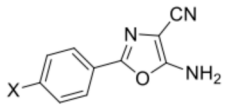	**28a**	X= Cl	19	3.0
	28b	X= CH_3	10	-
	28c	X= H	35	-
	28d	X= NO_2	22	-
	28e	X= OCH_3	39	-
	28f	X= F	89	26
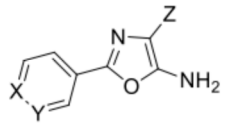	**29a**	X= N, Y= CH, Z= CN	40% at 500 µM	-
	29b	X=CH, Y= N, Z= CN	130	-
	29c	X= N, Y= CH, Z= CO_2H	none	-
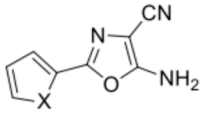	**30a**	X= O	475	-
	30b	X= S	67	-
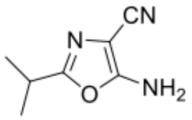	**31**	-	50% at 1 mM	-
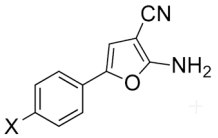	**32a**	X= Cl	6.6	2
	32b	X= CH_3	15	3.4
	32c	X= H	23	-
	32d	X= OCH_3	11	7.5
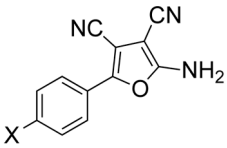	**33a**	X= Cl	0.77	0.10
	33b	X= CH_3	0.55	0.08
	33c	X= OCH_3	0.10	0.02
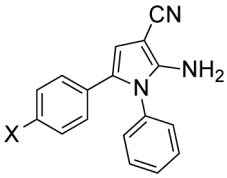	**34a**	X= Cl	none	-
	34b	X= CH_3	10% at 30 µM	-
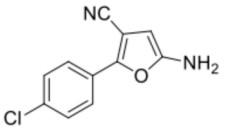	**35**	-	1.2	0.17

Tabla 4.3. Principales actividades farmacológicas de los dicarbonitrilo aminoheterociclos. El patrón de substituciones es clave en la actividad de los compuestos

Sólo en el caso de los compuestos tipo **33** la serie alcanzaba valores de actividad submicromolar, siendo destacable el hecho de que la inclusión del segundo sustituyente carbonitrilo originaba una disminución en la constante de inhibición (*Ki*) de entre 20 (X=Cl) a 350 veces (X=OCH3) con respecto a los derivados con un sólo sustituyente carbonitrilo. Por otra parte, la actividad inhibitoria de MAO B de ambos tipos de compuestos era muy similar (**32a** 3.5 μM / **33a** 3.2 μM). El dato más llamativo, sin embargo, lo aportaron los estudios espectroscópicos realizados por la Dra. Ramsay, que demostró que las propiedades espectroscópicas del FAD eran alteradas de forma diferente por la unión de compuestos de la familia **33** o de la familia **32**. Así, la unión de los primeros originaba efectos batocrómicos (desplazamiento del máximo de absorbancia de 456 a 459 nm) e hipercrómicos (aumento de la intensidad de absorción a 500 nm). Contrariamente, la incubación de MAO A junto a compuestos de tipo **32** ocasionaban un efecto hipocrómico en la región de 400 a 500 nm y un desplazamiento hipsocrómico (máximo de absorbancia desplazado de 455 a 453 nm). Por último la unión de **33a** a la isoforma B producía un efecto hipocrómico a 495 nm similar al observado para el complejo **32a**-MAO A. Paralelamente a los cambios espectroscópicos, la Dra. Ramsay también describió como ambas familias alteraban de forma diferente las propiedades redox del FAD, hecho reflejado en la aparición de una banda espectroscópica correspondiente a la presencia de la especie semiquinona ($FADH^{\bullet}$) durante la titulación del complejo **32a**-MAO A con ditionito sódico. Por el contrario, la titulación del complejo **33a**-MAO A no reveló la aparición de la especie semiquinona (Figura 4.6).

Los cambios de las propiedades espectroscópicas y redox del cofactor reflejan las alteraciones en su entorno provocadas por la unión del ligando[107–109], por lo que los diferentes efectos promovidos por la unión de compuestos tipo **32** y tipo **33** sugería que

la red de interacciones establecida por ambos tipos de compuesto en MAO A era diferente y, por tanto, implicaban modos de unión diferentes.

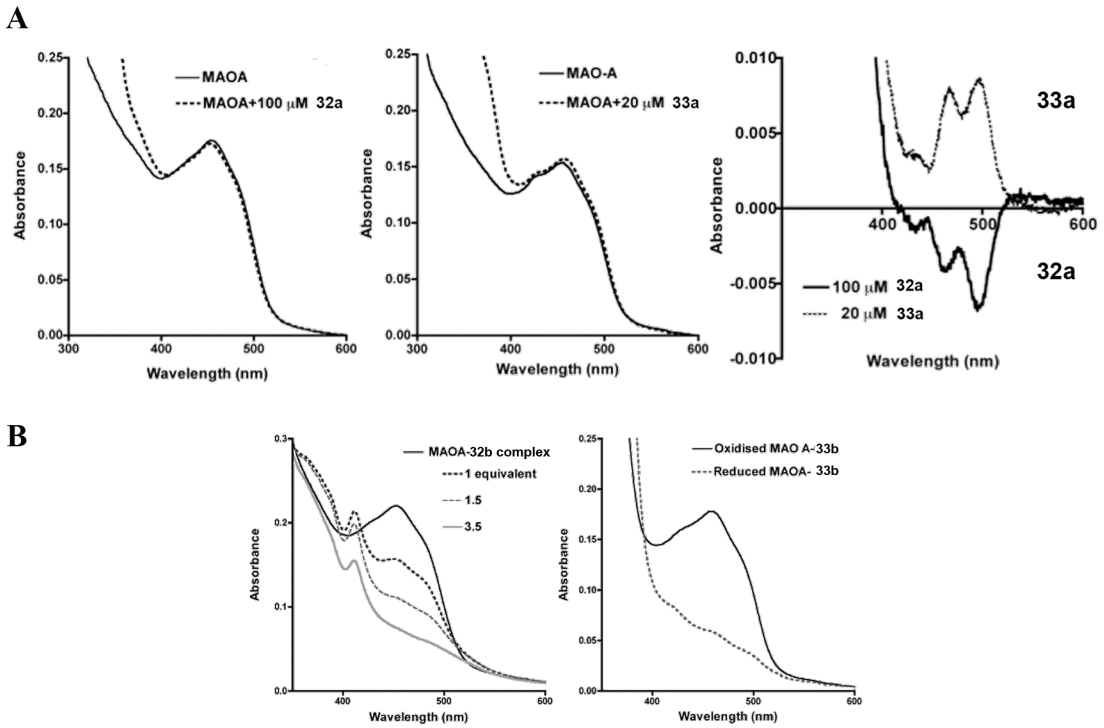

Figura 4.6. Evidencias espectroscópicas de redes de interacciones diferentes para 32a y 33a en MAO A. A) Espectros de substracción para los complejos **32a**-MAO A y **33a**-MAO A **B)** Titulación con ditionito sódico de los complejos **32a**-MAO A y **33a**-MAO A.

4.5.1 Modelización de la unión de **33a** a MAO A oxidada

Mediante la utilización de estudios de *docking* molecular se obtuvieron dos posibles modos de unión del compuesto **33a** a la forma oxidada de MAO A. En el primero de ellos (modo *NH_2-down*) la orientación del compuesto encaraba el sustituyente amino y el residuo Asn181, mientras que el grupo nitrilo en posición C3 se localizaba por debajo del anillo de isoxazolina del FAD. En el segundo modo de unión (modo *NH_2-up*), la orientación del compuesto era opuesta, reflejando un giro de aproximadamente 180 grados respecto al modo *NH_2-down*: el sustituyente amino quedaba orientado hacia el nitrógeno N5 del grupo prostético.

La combinación de simulaciones de dinámica molecular con la estimación de energía libre de unión obtenida con la técnica de *Solvent Interaction Energy* (SIE) permitió establecer la mayor estabilidad estructural y energética del modo *NH_2-down*. En este modo de unión, la amina participaría en dos interacciones de puente de hidrógeno mediadas por agua con los residuos Asn181 y los carbonilos del esqueleto peptídico de los residuos Ile207 y Gly443. El grupo nitrilo en C3 interaccionaría con una molécula de agua, que a su vez se encontraría unida por puentes de hidrógeno al grupo amino del residuo Lys305 y al átomo de nitrógeno N5 del FAD, en una interacción similar a la observada para un grupo sulfonamida en el complejo entre zonisamida y MAO B (PDB ID: 3PO7[110]). El grupo nitrilo en C4 ocuparía la cavidad hidrofóbica definida por los residuos Tyr69, Ile335, Leu337, Met350 y Phe352. El átomo de cloro unido al benceno interaccionaría con el residuo Leu97. Estas interacciones anclarían firmemente **33a** en la cavidad catalítica y explicarían la mínima distorsión ocasionada a los residuos que delimitan el sitio de unión (RMSD < 1.5 Å) y la energía de unión más favorable ($\Delta\Delta G_{bin}$ ~ -1 kcal/mol).

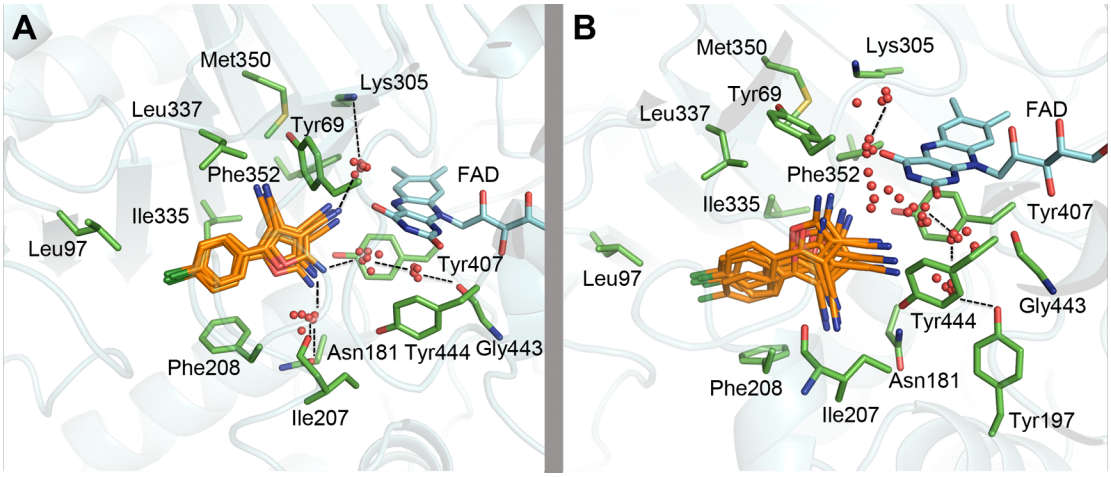

Figura 4.7 Representación de los modos de *NH2-down* (A) y *NH2-up* (B) para 33a en la forma oxidada de MAO A. Cada uno de ellos presenta una red interacciones característica. Se representan la posición del ligando (átomos de C en naranja) y de las moléculas de agua relevantes (esferas rojas) a 20, 22, 24,26,28 y 30 ns.

4.5.2 Modelización de la unión de **33a** a MAO A reducida

En contraste con los resultados obtenidos en la forma oxidada, los resultados de *docking* en la forma reducida de MAO A proporcionaron un sólo modo de unión entre las soluciones mejor puntuadas. Este modo de unión compartiría los principales rasgos estructurales del modo *NH_2-down* en la forma oxidada. El refinado mediante dinámica molecular dio lugar a un modo de unión con una red de interacciones muy similar al hallado para la forma oxidada, pero en la que se establecía una interacción por puente de hidrógeno entre el nitrilo en C3 y el N5 del FAD, que en su forma reducida ($FADH_2$) se comportaría como donador de puente de hidrógeno. Esta interacción estabilizaría la forma totalmente reducida del cofactor y permitiría explicar la desaparición del pico correspondiente a la especie semiquinona en los estudios espectroscópicos.

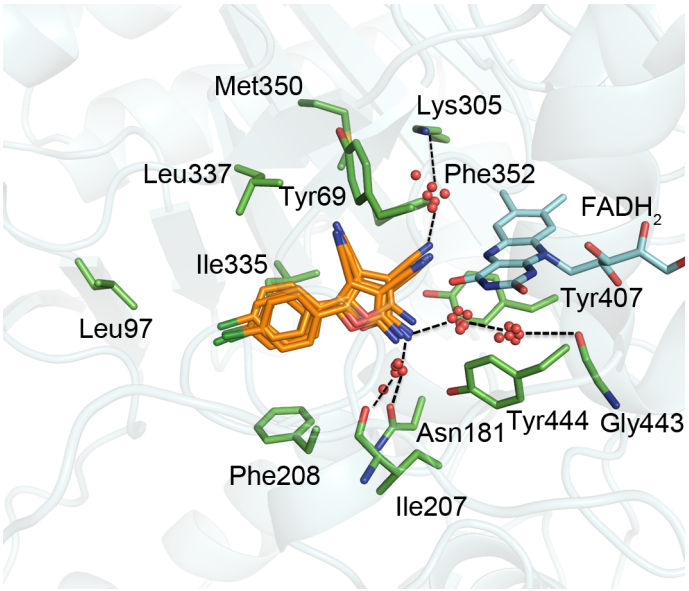

Figura 4.8 Representación del modo de unión de 33a a la forma reducida de MAO A. El modo de unión presenta similitudes con el modo de unión *NH2-down* hallado en el caso de la forma oxidada. Se representan la posición del ligando (átomos de C en naranja) y de las moléculas de agua relevantes (esferas rojas) a 20, 22, 24,26,28 y 30 ns.

De esta forma, los resultados de modelado molecular permitieron identificar como los sustituyentes amino y nitrilo en C4 modulaban la actividad y selectividad de

los compuestos. En primer lugar, el grupo amino sería el nodo central de una red de puentes de hidrógeno mediados por agua y, en segundo lugar, el nitrilo proporcionaría un punto de anclaje adicional al ocupar la cavidad hidrofóbica formada por los residuos Tyr69, Leu337, Met350 y Phe352. Este punto de anclaje explicaría la menor actividad de los compuestos tipo **32** (K_i en el rango μM bajo) y la similar actividad de los compuestos **33a** (K_i = 0.10 μM) y **28** (K_i = 0.17 μM).

Mediante los modos de unión obtenidos para **33a** también fue posible explicar la selectividad MAO A de los compuestos. En primer lugar el cambio Ile335>Tyr326 que ocurre en la región entre la entrada y la cavidad catalítica conlleva una modificación del sitio de unión del anillo de clorofenilo y del nitrilo en C4, originando alteraciones en el modo de unión. En segundo lugar, la red de interacciones propuesta quedaría alterada por el cambio Asn181>Cys172 que ocurre en el sitio de unión de la isoforma B. Esta última alteración es especialmente importante, ya que abre la puerta al diseño racional de nuevos inhibidores selectivos de MAO en base al diferente patrón de interacciones establecidas con estos dos residuos. Así, compuestos capaces de establecer una red de interacciones similar a los aminoheterociclos dicarbonitrilados deberían presentar selectividad MAO A. En el otro extremo, sustituyentes capaces de interaccionar de forma estable con el grupo tiol del residuo Cys172 debería conducir al desarrollo de inhibidores de MAO B altamente selectivos.

4.6 Híbridos huprina-rheína: Hacia un fármaco con capacidad modificadora de la progresión de la enfermedad de Alzheimer

Paralelamente al desarrollo de los híbridos iChE-iMAO, en el grupo de investigación se planteó la modelización de una familia de compuestos híbridos huprina

–rheína sintetizados como parte de la tesis de la Dra. Elisabet Viayna en el grupo del Dr. Diego Muñoz-Torrero de la Universidad de Barcelona. Dichos compuestos habían sido diseñados en base a la inhibición de AChE por parte de huprina Y, así como a la actividad inhibidora de la agregación de τ que se asocia a derivados de hidroxiantraquinona como emodina o PHF016[111,112], bajo la premisa de que la unión de ambos compuestos mediante una cadena hidrofóbica permitiría obtener inhibidores de AChE de sitio de unión dual (el motivo hidroxiantraquinona reúne las características moleculares necesarias para interaccionar mediante π-*stacking* con el Trp286 del PAS). Dichos compuestos, en base a las actividades descritas para emodina y PHF016, también debería reducir la agregación de τ, originando compuestos con potencial de retrasar la progresión de las dos características histopatológicas principales de la EA.

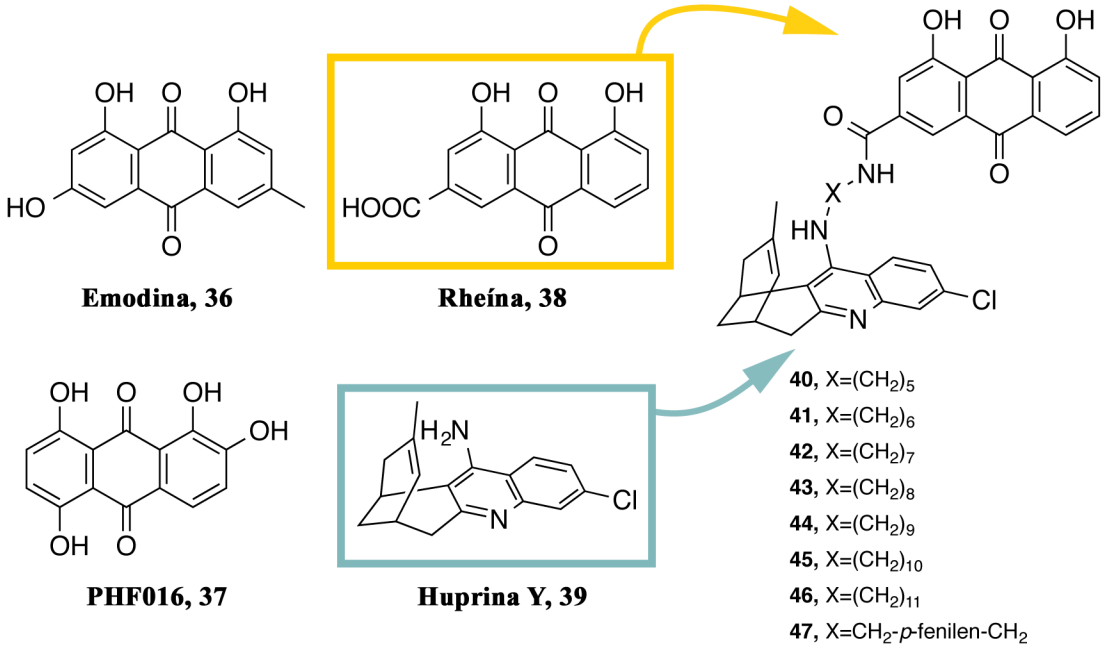

Figura 4.9. Estrategia de hibridación conjuntiva planteada para la obtención de híbridos huprina-rheína. La unidad de huprina se incorporó para ser alojada en el CAS de AChE, mientras que el motivo antraquinónico de rheína se incorporó para actuar sobre la agregación de la proteína τ.

El perfil farmacológico de algunos de estos híbridos resultó más amplio de lo esperado, ya que, además de inhibidores en rango nM de AChE e inhibidores

moderados de la agregación de Aβ y τ, sorprendentemente los compuestos con cadenas de 8, 10 y 11 metilenos, así como el derivado con un anillo aromático en la cadena, resultaron inhibidores moderados de BACE-1, una actividad ausente en los compuestos originales. Especial mención requiere el compuesto con la cadena de nueve metilenos **45**, que en forma racémica resultó ser un inhibidor comparable a memoquina[74] y al candidato LY2811376 (descartado en ensayos clínicos de fase I por toxicidad ajena a la inhibición BACE-1)[113].

	hAChE IC_{50} (nM)[b]	hBChE IC_{50} (nM)[b]	hBACE-1 IC_{50} (nM)[b]	Agregación de ßA inducida por AChE (% inhib.)[c]	P_e (10^{-6} cm s^{-1})[e] (Predicción)
(±)-**40**	1.07 ± 0.05	950 ± 30	na[f]	45.0 ± 7.5	20.0 ± 1.0 (SNC+)
(±)-**41**	1.52 ± 0.08	1070 ± 40	na[f]	50.5 ± 8.7	nd[g]
(±)-**42**	3.18 ± 0.16	1460 ± 160	na[f]	52.5 ± 2.9	27.5 ± 0.7 (SNC+)
(±)-**43**	4.36 ± 0.22	350 ± 20	980 ± 170	44.7 ± 8.4	22.4 ± 1.3 (SNC+)
(±)-**44**	3.60 ± 0.21	620 ± 20	120 ± 90	48.7 ± 8.4	21.5 ± 0.7 (SNC+)
(+)-**45**	2930 ± 285	265 ± 21	80 ± 10	36.9 ± 3.4	nd[g]
(−)-**45**	2.39 ± 0.17	513 ± 58	80 ± 10	38.1 ± 0.7	nd[g]
(±)-**45**	7.61 ± 0.45	1100 ± 40	1190 ± 180	29.2 ± 2.4	18.1 ± 0.7 (SNC+)
(±)-**46**	17.4 ± 2.2	645 ± 67	1200 ± 150	38.2 ± 2.6	16.4 ± 1.0 (SNC+)
(±)-**47**	18.2 ± 2.2	510 ± 20	2020 ± 440	35.2 ± 1.8	16.3 ± 2.5 (SNC+)
38	>10000	17000 ± 4220	na[h]	nd[g]	2.7 ± 0.1 (SNC+/–)
(±)-**39**	1.07 ± 0.05	181 ± 15	nd[g]	17.1 ± 4.5	23.8 ± 2.7 (SNC+)
(+)-**39**	321 ± 16	170 ± 17	>5000[i]	9.1 ± 3.6	25.4 ± 2.9 (SNC+)
(−)-**39**	0.74 ± 0.06	222 ± 17	>5000[j]	24.7 ± 1.3	23.6 ± 1.1 (SNC+)

Tabla 4.4. Principales actividades farmacológicas de los híbridos huprina-rheína. De forma inesperada, algunos compuestos resultaron ser potentes inhibidores de BACE-1.

4.6.1 Inhibición de AChE

Para determinar el modo de unión de los híbridos huprina Y-rheína a AChE, se utilizó el compuesto con menor flexibilidad de la serie **47**. Mediante un protocolo de *docking* similar al descrito en el caso de los compuestos iChE-iMAO, se propuso un modo de unión en el que el motivo huprina ocuparía el CAS, de forma similar al complejo entre (−)-huprina X y AChE (PDB id: 1E66), mientras que el motivo rheína

formaría una doble interacción por π-*stacking*, quedando empaquetado entre los residuos Trp286 y Tyr72 del PAS, análogamente a lo que ocurre con una de las unidades de tacrina en el complejo entre AChE y bis(7)-tacrina (PDB ID: 2CKM), aunque en el caso de los híbridos huprina-rheína no existiría una carga positiva capaz de reforzar esta interacción (Figura 4.10). Esta menor intensidad del empaquetamiento, unido a la ausencia de interacciones específicas entre los grupos polares de la unidad de rheína y los residuos del PAS explicaría por que, comparados con huprina Y, todos los compuestos de la serie resultaron aproximadamente equipotentes.

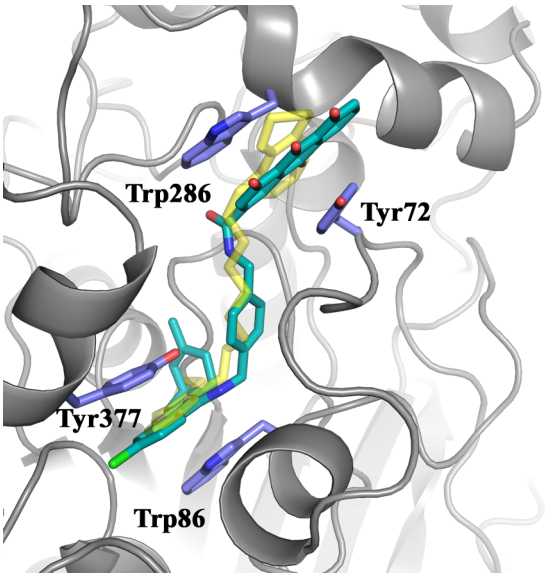

Figura 4.10. **Modo de unión de 47 en AChE**. Los rasgos estructurales del sitio de unión (lila) y la orientación del compuesto (azul) son similares a los descritos para bis(7)-tacrina (amarillo). Se muestra el modo de unión obtenido mediante cálculos de *docking*.

4.6.2 Inhibición de BACE-1

El modo de unión de los híbridos huprina–rheína a BACE-1 se estudió en tres etapas. En primer lugar se empleo el programa MDpocket[114] para localizar cavidades capaces de alojar moléculas tipo fármaco en un set de 4 estructuras obtenidas por cristalografía de Rayos X (PDB IDs: 1M4H[115], 1SGZ[116], 2OHL[117] y 3CIB[118]). A continuación, en aquellas cavidades comunes a las 4 estructuras, se realizaron cálculos

de *docking* de las unidades huprina y rheína, lo que permitió identificar 2 sitios de unión que reunían las características fisicoquímicas necesarias para albergarlas. El primero de ellos (SU1) correspondía al sitio catalítico donde se localiza la díada Asp32-Asp228 responsable de la actividad de la enzima. El segundo sitio de unión (SU2) se localizaba en la hendidura que acomoda el sustrato natural, a 9 Å de SU1. Finalmente, la tercera etapa consistió en explorar posibles modos de unión de los enantiómeros (+)**47** y (−)**47** a SU1 y SU2. La elección de **47** como compuesto modelo se debió a que, a pesar de ser el compuesto menos potente, su mayor rigidez estructural facilitaba una exploración exhaustiva de los posibles modos de unión.

Combinando *docking* y simulaciones de dinámica molecular se identificó un modo de unión en el que la unidad de huprina Y ocuparía el sitio catalítico, mientras que el motivo hidroxiantraquinona ocuparía la cavidad SU2 (Figura 4.11). Concretamente, el motivo aminoquinolina de la unidad de huprina, protonado a pH fisiológico, establecería una interacción de puente salino con la díada catalítica, y el biciclo ocuparía la cavidad lipófila definida por los residuos Leu30, Phe108, Ile110 e Ile118. El motivo hidroxiantraquinona quedaría estabilizado por interacciones electrostáticas con la cadena lateral del residuo Lys321 y por puentes de hidrógeno con el carbonilo del esqueleto peptídico del residuo Phe332 y con la cadena lateral del residuo Asn223. Además, en el caso del enantiómero (−)**47**, se encontró un modo de unión alternativo de rheína a SU2 caracterizado por la interacción electrostática con el residuo Arg307. En ambos casos, la mayor flexibilidad de la cadena nonametilénica de **45** con respecto a la cadena de **47** permitiría un mejor acomodo a ambos sitios de unión, explicando la mayor actividad del primero.

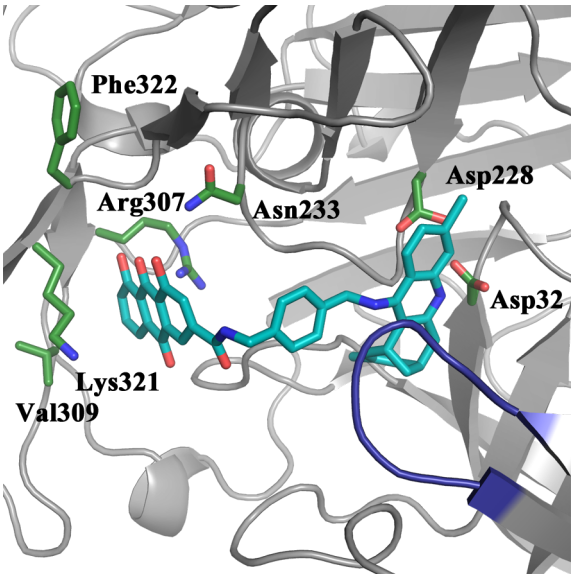

Figura 4.11. **Modo de unión de 47 en BACE-1**. El motivo huprina interacciona con el residuo Asp32, mientras que la unidad de rheína queda acomodado en el sitio de unión SU2.

Recapitulando, el modelado molecular permitió describir como los híbridos huprina Y–rheína se unían a AChE, dando explicación a la ausencia de mejora de los híbridos con respecto al compuesto original y, principalmente, permitió obtener un modo de unión a BACE-1 en el que se identificaba una cavidad que, en nuestro conocimiento, no ha sido previamente explotada en el diseño basado en estructura de inhibidores de BACE-1, abriendo la puerta al diseño racional de nuevos inhibidores mas potentes.

Capítulo

5 Summary

The selective interaction of two chemical entities is a phenomenon relevant to almost any biological process. Starting from earlier works by Fisher and his "lock-and-key" mechanism at the late XIXth century, to the latest reformulations of the "conformational selection" or "induced fit" mechanisms, more than a century of studies has attempted to unravel the key determinants that underlie molecular recognition[2–5]. In the framework of drug design, it is especially interesting to determine how physicochemical properties such as size, shape, hydrophobicity and polarity interplay to maximize the electrostatic, steric and hydrophobic complementarity of a small ligand with the binding site of a receptor.

The extraordinary expansion of the Molecular Modeling field in the last years has facilitated the design of more and more complex computational experiments, reaching a stage where quasi-quantitative predictions of the physicochemical properties are feasible for very complex biomolecular systems. In this context, this Doctoral Thesis presents the results obtained in the development of new computational techniques aimed to the study of drug-like molecules and in the application of already established techniques to the rational design of new multitarget directed ligands.

The objectives pursued during this Doctoral Thesis are focused on two major research lines. The first aim deals with the extension and validation of the Multilevel strategy (MLS)[22] developed earlier in the research group for the exploration of conformational preferences of small ligands in condensed phase. The second one follows a multidisciplinary effort to rationally design new multitarget directed ligands[61–64] of potential therapeutic utility in Alzheimer's Disease (AD). In particular, the objectives proposed were:

A) Extension of the Multilevel strategy.

A.1) To explore the suitability of sampling methods based in classical force fields and to examine their reliability with those obtained with semiempirical methods.

A.2) To apply the Multilevel strategy to charged ligands with the aim to calibrate the limits in the applicability of the method.

B) Development of multitarget directed ligands against Alzheimer's Disease.

B.1) To design hybrid ChEi – MAOi compounds and to elucidate the molecular determinants that influence their pharmacological profile.

B.2) To explore the interaction pattern of selective MAO A inhibitors in order to identify residues involved in isoform selectivity, which might then be utilized as guidelines to optimize the pharmacological profile of ChEi - MAOi compounds.

B.3) To model huprine-rhein hybrids and to disclose the binding mode to AChE and BACE-1.

5.1 Extension of the Multilevel strategy

The Multilevel strategy relies in the *Predominant States Approximation*[23] developed by Gilson and co workers and pursues the quantitative prediction of the conformational preferences of small bioactive molecules, which is still a major unsolved challenge in drug design.

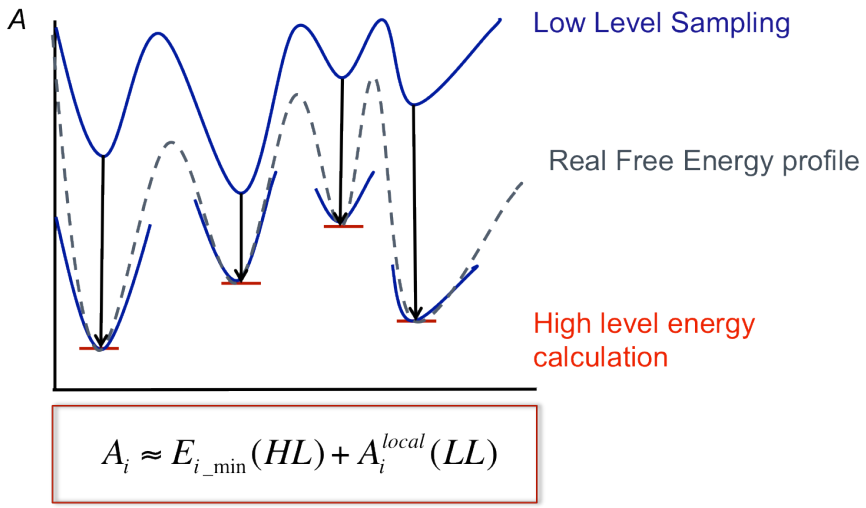

Figure 5.1. Schematic representation of the Multilevel approach. Minima located during the low level sampling (semiempirical or classical methods) are re-scaled according to the energy determined at the high level (*ab initio* methods).

In the original implementation, a Metropolis-Montecarlo[25] simulation (performed with the semiempirical RM1 hamiltonian[27]) was used to explore the conformational landscape of molecules and to locate energy wells. Subsequently, the relative stability of those wells was recalibrated using *ab initio* techniques (post-HF or DFT). Although the initial studies supported the viability of the methodology, its applicability was mainly limited by the computational burden associated to the semiempirical sampling, even though this choice avoided an *ad hoc* parametrization of the molecules. On the other hand, the performance of the technique when dealing with charged species remained to be explored.

In this work the suitability of the MLS was tested using two distinct molecular systems. We first developed a new implementation that allowed the use of classical forcefields for the conformational exploration of a small set of arylethylamines. The obtained results were in agreement with the available experimental values and no significative differences were found with respect to the results obtained with the prior implementation of the method (Figure 5.2).

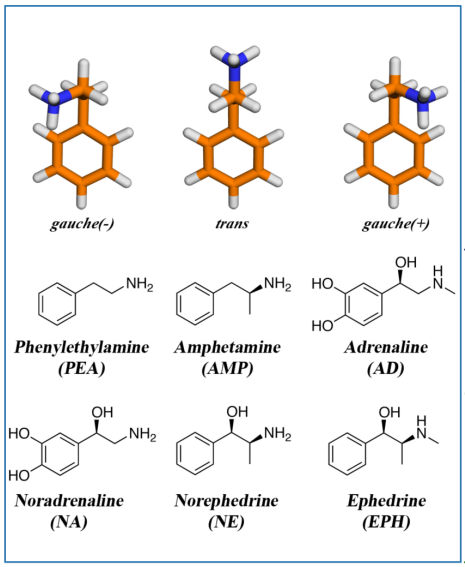

	MC (IEF-MST/RM1)			MD (gaff)			Experimental		
	g (-)	*trans*	*g(+)*	*g (-)*	*trans*	*g(+)*	*g (-)*	*trans*	*g(+)*
PEA	2	90	2	22	56	22	22	56	22
AMP	0	87	4	5	39	53	5	50	45
AD	5	80	12	15	69	13	6	77	17
NA	1	71	24	27	62	11	10	76	14
EPH	53	40	2	13	61	22	10	90	
NE	81	4	2	17	53	30	21	79	

	MC (IEF-MST/RM1)			MD (gaff)			Experimental		
	g (-)	*trans*	*g(+)*	*g (-)*	*trans*	*g(+)*	*g (-)*	*trans*	*g(+)*
PEA	20	54	26	33	33	34	22	56	22
AMP	2	75	23	6	55	38	5	50	45
AD	3	96	1	3	95	2	6	77	17
NA	3	91	6	12	80	7	10	76	14
EPH	1	92	7	1	92	7	10	90	
NE	2	64	34	2	76	22	21	79	

Figure 5.2. Conformational preferences of the arylehtylamines set in aqueous solution. Results are shown as relative percentual populations predicted for the classical rotamers *gauche(+)-trans-gauche(−)*. Comparison of results obtained with the low level sampling performed using the RM1 semiempirical and the gaff classical forcefield[75] (upper table). The multilevel refinement is able to correct the discrepancies between low level methods (lower table).

In the second system we established the conformational preferences of the aminoglucoside antibiotic streptomycin. With three aliphatic rings and three ionizable groups at physiological pH, this molecule poses a scientific challenge and represents an excellent example of the complexity of bioactive compounds. Using the MLS we identified two major conformational families. The first conformation (ML1, accounting for 85% of the population) was attributed to a structure similar to the one previously identified using NMR studies[79]. A second conformation (ML2, with 15% abundance) was characterized by a highly tensioned arrangement that allowed for a better solvation of the polar groups. Such arrangement was not described in the NMR-derived conformational preferences of the free streptomycin in solution. This discrepancy should be attributed to the difficulty of accurately reproduce the subtle balance between internal energy of conformers and the hydration contribution.

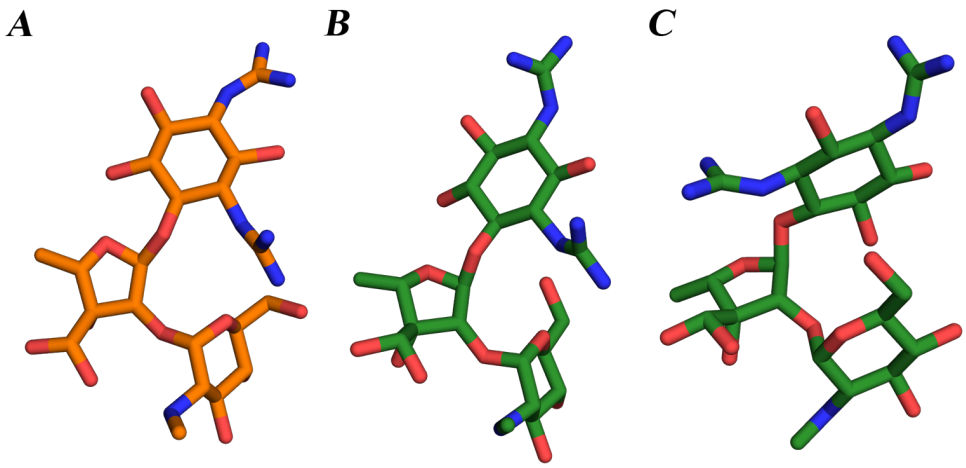

Figure 5.3. Comparison of the representative conformation of streptomycin in aqueous solution. Major conformation found with NMR (A) and the Multilevel strategy (B) are highly similar. The minor conformation found with the Multilevel strategy (C) is characterized by a larger solvent exposure of the polar groups

Altogether, the results established the validity of the new implementation of the Multilevel strategy that combines classical force fields with high-level *ab initio* methods. Nevertheless, future studies will be performed to introduce specific refinements, such as a more accurate description of solvent effects in high-level calculations.

5.2 Development of multitarget directed ligands against Alzheimer's Disease

In the framework of the multidisciplinary collaboration maintained with other medicinal chemistry research groups, this doctoral thesis included the modeling of two different families of multipotent ligands directed towards validated targets in AD.

5.2.1 Multipotent ChEi-MAOi: Donepezil-PFN9601 hybrids

The first family of compounds was developed by molecular hybridization combining donepezil, a known AChE inhibitor, and PFN9601, a selective MAO B

inhibitor, in collaboration with Prof. Mercedes Unzeta (Universitat Autònoma de Barcelona). Modeling studies were performed to gain insight into the molecular determinants that explain the structure-activity relationship (SAR) for the hybrid compounds. First, the AChE inhibition was not significantly affected upon extension of the methylene chain (from 1 to 4 carbons), but the length of the tether had a dramatic effect in the affinity towards both MAO isoforms. Second, the position of the nitrogen atom in the piperidine ring was relevant to the inhibition of all enzymes. Last, but not least, incubation of MAO A with compound **23** leads to a fast irreversible inhibition, but longer incubation times were required to achieve similar results in the case of the isoform B.

Combining docking and molecular dynamics techniques, it was established that **23** mimicked the binding mode of the parent compound donepezil in AChE. In the case of MAO, subtle differences arose between isoforms A and B. Thus, although in both cases the propargylamino moiety was found to occupy the catalytic cavity of the protein, accounting for its irreversible character, in MAO B the orientation of the ligand was slightly different and placed the propargylamino moiety 1.1 Å further from the FAD cofactor that in the case of MAO A. The greater distance found in MAO B will preclude the propargylamino to be readily available to react with the FAD and will probably explain the increased incubation time required to observe the irreversible inhibition of the enzyme.

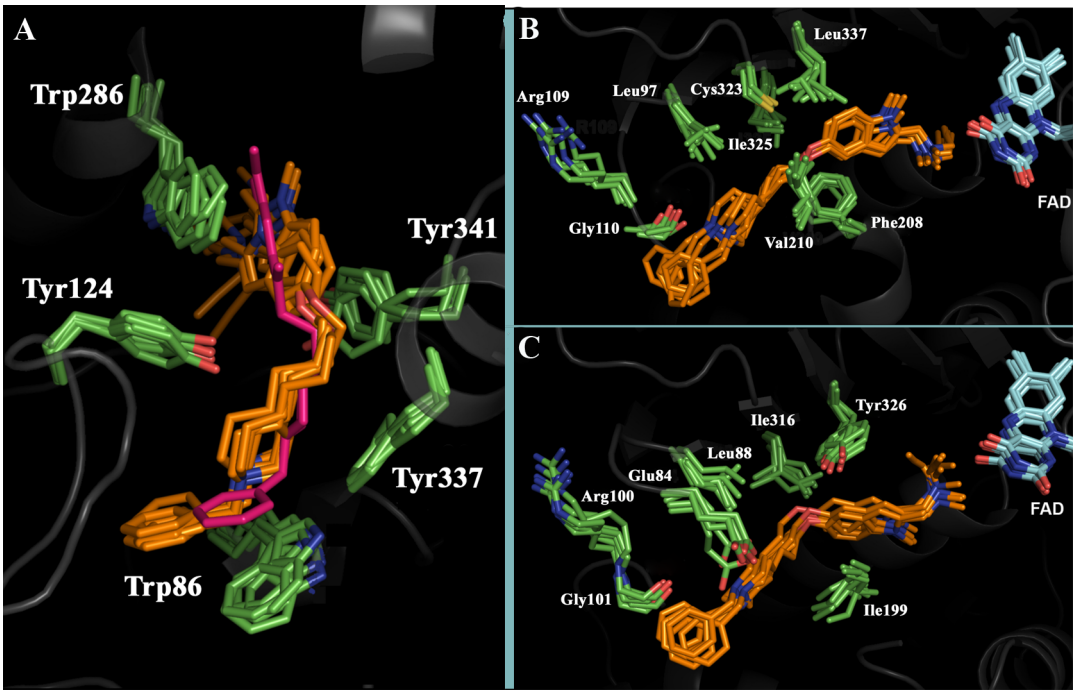

Figure 5.4. Binding modes proposed for compound 23 to its main targets. A) AChE **B)** MAO A and **C)** MAO B. Superposition over the last 5 ns of Molecular Dynamics simulations.

5.2.2 Exploring the selective inhibition of MAO: Dicarbonitrile aminoheterocycles

Despite the promising pharmacological profile of the lead compound, the inhibitory balance between MAO isoforms was the major concern because the combination of MAO A selectivity and irreversible inhibition behavior has been strongly associated with the so-called cheese effect[57]. For this reason, in collaboration with Prof. Rona Ramsay (University of St. Andrews), we explored the binding of a series of dicarbonitrile-containing aminoheterocycles to identify residues that influence inhibitor selectivity.

Combining docking, molecular dynamics simulations and hybrid QM/MM calculations with experimental spectral measurements, we explored the molecular patterns that dictated isoform selectivity, but also how the oxidation state of the FAD cofactor may influence the binding of these compounds. The results suggested that

mono- and dicarbonitrile compounds adopt a distinct binding mode, which explained the differential spectral changes occurred upon compound binding. Additionally, they allowed us to firmly establishing the role of the substitution pattern of the molecules with regard to selectivity and, lastly, identified how the change Asn181 in MAO A to Cys172 in isoform B was crucial to explain the MAO A selectivity of the dicarbonitrile-aminoheterocycle scaffold.

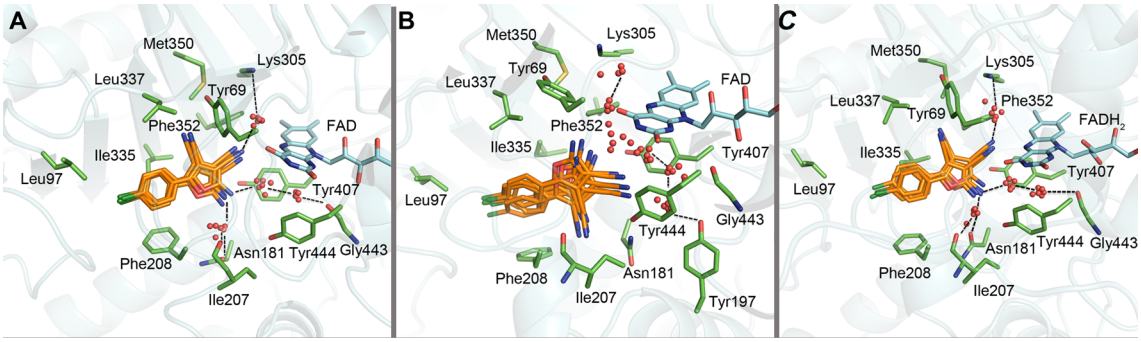

Figure 5.5. Binding modes proposed for dicarbonitrile aminoheterocycle to the oxidized (A and B) and reduced (C) form of MAO A. Superposition over the last 10 ns of Molecular Dynamics simulations.

5.2.3 Huprine-rhein hybrids: Toward a disease modifying agent for Alzheimer's Disease

The second family of multipotent compounds modeled was a series of huprine-rhein hybrids of promising pharmacological profile. Surprisingly, in addition to the intended AChE inhibition and anti-aggregation activity, some of the compounds showed an unexpected mild-to-potent BACE-1 inhibition that implied a potential role as disease modifying agents.

In this context, docking and molecular dynamics simulations were complemented with the use of the MDpocket[114] software to search for druggable cavities. The binding mode of the hybrids to AChE resembled the one described for the

bis-7-tacrine[67] (PDB id: 2CKM[100]). In the case of BACE-1, the putative binding mode accommodated the huprine moiety close to the catalytic dyad, Asp32-Asp228, while the rhein unit was bound to an accessory pocket interacting with residues Arg307 and Lys321 (Figure 5.6). It is worth noticing that this cavity is located at the catalytic groove, but beyond the usually considered accessory pockets and, to the best of our knowledge, has not been previously exploited for rational drug design purposes.

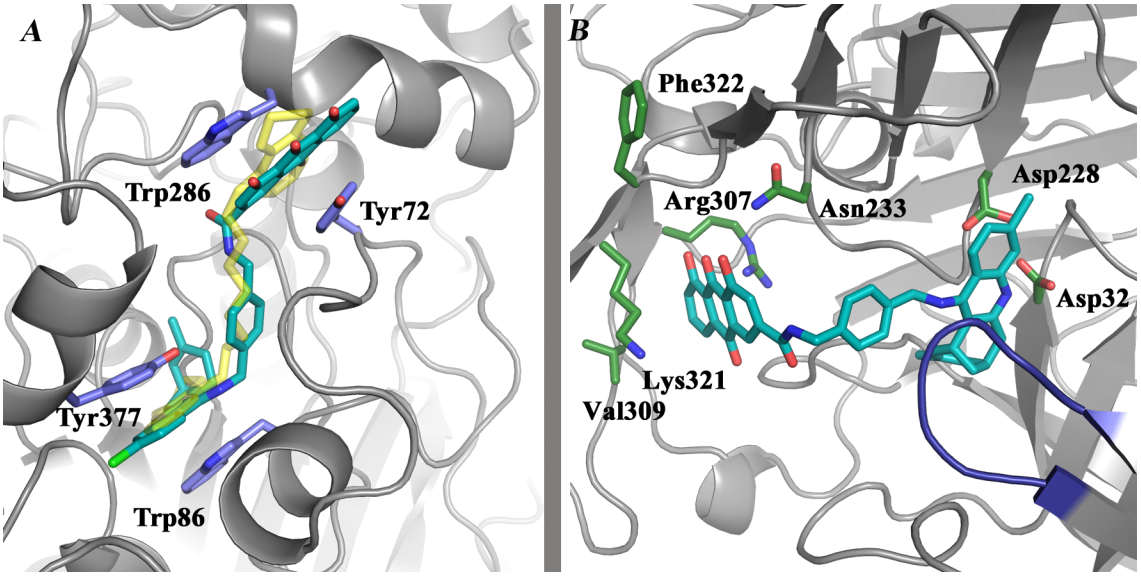

Figure 5.6. Binding modes proposed for the huprine-rhein hybrids. A) To AChE, as established from docking calculations **B)** To BACE-1. Putative binding mode obtained by combining Mdpocket, docking and Molecular Dynamics simulations.

Capítulo

6 Conclusions

6.1 Extension of the Multilevel strategy

- The new implementation of the Multilevel strategy has been successfully assessed, providing evidences that the results do not depend on the Low Level sampling technique, since the High Level re-calibration of the minima corrects the initial differences found between classical and RM1 samplings.
- The Multilevel strategy predicts the *trans/gauche* conformational preferences of the series of charged arylethylamines with an uncertainty less than 0.4 kcal/mol.
- The major conformation of streptomycin, a very challenging test due to the presence of three charged groups, is correctly identified, even though the results also suggest that further refinements might be advisable to improve the quantitative predictive power of the method.

6.2 Development of multitarget directed ligands against Alzheimer's Disease

6.2.1 Multipotent ChEi-MAOi: Donepezil-PFN9601 hybrids

- Compound **23** mimics the binding mode of donepezil in the catalytic gorge of AChE. Differences in the tether should have minor impact regarding the accommodation of the indolylpropargylamine unit at the PAS.
- In MAO A and B, the indolylpropargylamine moiety fills the catalytic site close to the FAD accounting for the irreversible inhibition. The accommodation of the linker at the bottleneck region explains the dependence of the inhibitory activity on the length of the tether.

- The different positioning of the indolylpropargylamine moiety explains the kinetic differences in inhibiting MAO A and B.

6.2.2 Exploring the selective inhibition of MAO: Dicarbonitrile aminoheterocycles

- The different spectral changes triggered in MAO A upon binding of mono- or dicarbonitrile compounds likely reflect the different orientation of these compounds at the substrate site.
- The amino and nitrile (at C4 position) susbtituents are essential for the inhibitory activity of dicarbonitrile compounds due to the key interactions formed at the substrate cavity.
- The change of Asn181 in MAO A to Cys172 in MAO B is a major contributor to the MAO A selectivity exhibited by dicarbonitrile compounds and can be further exploited in the design of selective MAO inhibitors.

6.2.3 Huprine-rhein hybrids: Toward a disease modifying agent for Alzheimer's Disease

- The huprine–rhein hybrids bind to AChE in a binding mode that resembles *bis*-7-tacrine bound to AChE. While the interaction at the CAS retains the recognition trends described for (−)-huprine Y, the absence of a positive charge at the rhein unit weakens the interaction at the PAS, which likely accounts for the lower inhibitory activity with respect to the parent compound.
- The proposed binding mode in BACE-1 places the huprine moiety close to the catalytic dyad, stabilized by an electrostatic interaction with residue Asp32. In

turn, the rhein moiety is accommodated in an accessory pocket identified using computational tools and, to the best of our knowledge, previously unexploited for rational drug design purposes.

Capítulo

7 Bibliografía

(1) Berg, J. M.; Tymoczko, J. L.; Stryer, L. Biochemistry. 5th Edition. In *Biochemistry textbook*; **2006**; p. 1120.

(2) Fisher, E. Einfluss Der Configuration Auf Die Wirkung Der Enzyme. *Ber. Dtsch. Chem. Ges.* **1894**, *27*, 2985–2993.

(3) Koshland, D. E. Application of a Theory of Enzyme Specificity to Protein Synthesis. *Proc. Natl. Acad. Sci. U. S. A.* **1958**, *44*, 98–104.

(4) Závodszky, P.; Hajdú, I. Evolution of the Concept of Conformational Dynamics of Enzyme Functions over Half of a Century: A Personal View. *Biopolymers* **2013**, *99*, 263–269.

(5) Kar, G.; Keskin, O.; Gursoy, A.; Nussinov, R. Allostery and Population Shift in Drug Discovery. *Current Opinion in Pharmacology*, **2010**, *10*, 715–722.

(6) Gibbs, A. C. Elements and Modulation of Functional Dynamics. *J. Med. Chem.* **2014**, *57*, 7819–7837.

(7) Changeux, J.-P.; Edelstein, S. Conformational Selection or Induced Fit? 50 Years of Debate Resolved. *F1000 Biol. Rep.* **2011**, *3*, 19.

(8) Boehr, D. D.; Nussinov, R.; Wright, P. E. The Role of Dynamic Conformational Ensembles in Biomolecular Recognition. *Nat. Chem. Biol.* **2009**, *5*, 789–796.

(9) Fenwick, R. B.; Esteban-Martín, S.; Salvatella, X. Understanding Biomolecular Motion, Recognition, and Allostery by Use of Conformational Ensembles. *Eur. Biophys. J.* **2011**, *40*, 1339–1355.

(10) Vogt, A. D.; Di Cera, E. Conformational Selection or Induced Fit? A Critical Appraisal of the Kinetic Mechanism. *Biochemistry* **2012**, *51*, 5894–5902.

(11) Tummino, P. J.; Copeland, R. A. Residence Time of Receptor-Ligand Complexes and Its Effect on Biological Function. *Biochemistry* **2008**, *47*, 5481–5492.

(12) Vogt, A. D.; Di Cera, E. Conformational Selection Is a Dominant Mechanism of Ligand Binding. *Biochemistry* **2013**, *52*, 5723–5729.

(13) Anthis, N. J.; Doucleff, M.; Marius Clore, G. M. Transient, Sparsely Populated Compact States of Apo and Calcium-Loaded Calmodulin Probed by Paramagnetic Relaxation Enhancement: Interplay of Conformational Selection and Induced Fit. *J. Am. Chem. Soc.* **2011**, *133*, 18966–18974.

(14) Ferenczy, G. G.; Keserü, G. M. Thermodynamics of Ligand Binding. In *Physico-Chemical and Computational Approaches to Drug Discovery*; Luque, F. J.; Barril, X., Eds.; The Royal Society of Chemistry: Cambridge, **2012**; pp. 23–79.

(15) Bissantz, C.; Kuhn, B.; Stahl, M. A Medicinal Chemist's Guide to Molecular Interactions. *J. Med. Chem.*, **2010**, *53*, 5061–5084.

(16) Hunter, C. A. Quantifying Intermolecular Interactions: Guidelines for the Molecular Recognition Toolbox. *Angew Chem Int Ed Engl*, **2004**, *43*, 5310–5324.

(17) Spyrakis, F.; BidonChanal, A.; Barril, X.; Luque, F. J. Protein Flexibility and Ligand Recognition: Challenges for Molecular Modeling. *Curr. Top. Med. Chem.* **2011**, *11*, 192–210.

(18) Carlson, H. A. Protein Flexibility Is an Important Component of Structure-Based Drug Discovery. *Curr Pharm Des* **2002**, *8*, 1571–1578.

(19) Cavasotto, C. N.; Singh, N. Docking and High Throughput Docking: Successes and the Challenge of Protein Flexibility. *Current Computer - Aided Drug Design*, **2008**, *4*, 221–234.

(20) Dirac, P. A. M. Quantum Mechanics of Many-Electron Systems. *Proc. R. Soc. A* **1929**, *123*, 714–733.

(21) Muñoz-Muriedas, J. Estudio Teórico de Interacciones Moleculares: Aplicación Al Diseño de Fármacos, Universitat de Barcelona, **2008**, pp. 3–10.

(22) Forti, F.; Cavasotto, C. N.; Orozco, M.; Barril, X.; Luque, F. J. A Multilevel Strategy for the Exploration of the Conformational Flexibility of Small Molecules. *J. Chem. Theory Comput.* **2012**, *8*, 1808–1819.

(23) Head, M.; Given, J.; Gilson, M. "Mining Minima": Direct Computation of Conformational Free Energy. *J. Phys. Chem. A.* **1997**, *5639*, 1609–1618.

(24) Chen, W.; Chang, C.-E.; Gilson, M. K. Calculation of Cyclodextrin Binding Affinities: Energy, Entropy, and Implications for Drug Design. *Biophys. J.* **2004**, *87*, 3035–3049.

(25) Metropolis, N. The Beginning of the Monte Carlo Method. *Los Alamos Sci.* **1987**, *15*, 125–130.

(26) Metropolis, N.; Ulam, S. The Monte Carlo Method. *J Am Stat Assoc* **1949**, *44*, 335–341.

(27) Rocha, G. B.; Freire, R. O.; Simas, A. M.; Stewart, J. J. P. RM1: A Reparameterization of AM1 for H, C, N, O, P, S, F, Cl, Br, and I. *J. Comput. Chem.* **2006**, *27*, 1101–1111.

(28) Forti, F.; Barril, X.; Luque, F. J.; Orozco, M. Extension of the MST Continuum Solvation Model to the RM1 Semiempirical Hamiltonian. *J. Comput. Chem.* **2008**, *29*, 578–587.

(29) Riley, K. E.; Op't Holt, B. T.; Merz, K. M. Critical Assessment of the Performance of Density Functional Methods for Several Atomic and Molecular Properties. *J. Chem. Theory Comput.* **2007**, *3*, 407–433.

(30) Goedert, M.; Spillantini, M. G. A Century of Alzheimer's Disease. *Science* **2006**, *314*, 777–781.

(31) Lleó, A.; Greenberg, S. M.; Growdon, J. H. Current Pharmacotherapy for Alzheimer's Disease. *Annu. Rev. Med.* **2006**, *57*, 513–533.

(32) Camps, P.; Muñoz-Torrero, D. Cholinergic Drugs in Pharmacotherapy of Alzheimer's Disease. *Mini Rev. Med. Chem.* **2002**, *2*, 11–25.

(33) Szegletes, T.; Mallender, W. D.; Thomas, P. J.; Rosenberry, T. L. Substrate Binding to the Peripheral Site of Acetylcholinesterase Initiates Enzymatic Catalysis. Substrate Inhibition Arises as a Secondary Effect. *Biochemistry* **1999**, *38*, 122–133.

(34) Inestrosa, N. C.; Alvarez, A.; Pérez, C. A.; Moreno, R. D.; Vicente, M.; Linker, C.; Casanueva, O. I.; Soto, C.; Garrido, J. Acetylcholinesterase Accelerates

Assembly of Amyloid-B-Peptides into Alzheimer's Fibrils: Possible Role of the Peripheral Site of the Enzyme. *Neuron* **1996**, *16*, 881–891.

(35) Rogawski, M. A. Low Affinity Channel Blocking (Uncompetitive) NMDA Receptor Antagonists as Therapeutic Agents – toward an Understanding of Their Favorable Tolerability Review Article. *Amino Acids* **2000**, 133–149.

(36) Danysz, W.; Parsons, C. G.; Mobius, H.; Stoffler, A. Neuroprotective and Symptomatological Action of Memantine Relevant for Alzheimer ' S Disease - A Unified Glutamatergic Hypothesis on the Mechanism of Action. *Neurotox. Res.* **2000**, *2*, 85–97.

(37) Francis, P. T.; Parsons, C. G.; Jones, R. W. Rationale for Combining Glutamatergic and Cholinergic Approaches in the Symptomatic Treatment of Alzheimer's Disease. *Expert Rev. Neurother.* **2012**, *12*, 1351–1365.

(38) Hardy, J.; Allsop, D. Amyloid Deposition as the Central Event in the Aetiology of Alzheimer's Disease. *Trends Pharmacol Sci*, **1991**, *12*, 383–388.

(39) Hardy, J. Has the Amyloid Cascade Hypothesis for Alzheimer's Disease Been Proved? *Curr. Alzheimer Res.* **2006**, *3*, 71–73.

(40) Coughlan, C. M.; Breen, K. C. Factors Influencing the Processing and Function of the Amyloid Beta Precursor Protein — a Potential Therapeutic Target in Alzheimer's Disease? *Pharmacol. Ther.* **2000**, *86*, 111–144.

(41) Findeis, M. a. The Role of Amyloid Beta Peptide 42 in Alzheimer's Disease. *Pharmacol. Ther.* **2007**, *116*, 266–286.

(42) Citron, M. Alzheimer's Disease: Strategies for Disease Modification. *Nat. Rev. Drug Discov.* **2010**, *9*, 387–398.

(43) Fleisher, A. S.; Raman, R.; Siemers, E. R.; Becerra, L.; Clark, C. M.; Dean, R. A.; Farlow, M. R.; Galvin, J. E.; Peskind, E. R.; Quinn, J. F.; et al. *Phase 2 Safety Trial Targeting Amyloid Beta Production with a Gamma-Secretase Inhibitor in Alzheimer Disease.*; **2008**; Vol. 65, pp. 1031–1038.

(44) Bard, F.; Cannon, C.; Barbour, R.; Burke, R. L.; Games, D.; Grajeda, H.; Guido, T.; Hu, K.; Huang, J.; Johnson-Wood, K.; et al. Peripherally Administered Antibodies against Amyloid Beta-Peptide Enter the Central Nervous System and Reduce Pathology in a Mouse Model of Alzheimer Disease. *Nat. Med.* **2000**, *6*, 916–919.

(45) Salloway, S.; Sperling, R.; Gilman, S.; Fox, N. C.; Blennow, K.; Raskind, M.; Sabbagh, M.; Honig, L. S.; Doody, R.; Van Dyck, C. H.; et al. A Phase 2 Multiple Ascending Dose Trial of Bapineuzumab in Mild to Moderate Alzheimer Disease. *Neurology* **2009**, *73*, 2061–2070.

(46) Citron, M. Beta-Secretase Inhibition for the Treatment of Alzheimer's Disease--Promise and Challenge. *Trends Pharmacol. Sci.* **2004**, *25*, 92–97.

(47) De Strooper, B.; Annaert, W.; Cupers, P.; Saftig, P.; Craessaerts, K.; Mumm, J. S.; Schroeter, E. H.; Schrijvers, V.; Wolfe, M. S.; Ray, W. J.; et al. A Presenilin-1-Dependent Gamma-Secretase-like Protease Mediates Release of Notch Intracellular Domain. *Nature* **1999**, *398*, 518–522.

(48) Savonenko, A. V; Melnikova, T.; Laird, F. M.; Stewart, K.-A.; Price, D. L.; Wong, P. C. Alteration of BACE1-Dependent NRG1/ErbB4 Signaling and

Schizophrenia-like Phenotypes in BACE1-Null Mice. *Proc. Natl. Acad. Sci. U. S. A.* **2008**, *105*, 5585–5590.

(49) Fleck, D.; N. Garratt, A.; Haass, C.; Willem, M. BACE1 Dependent Neuregulin Processing: Review. *Curr Alzheimer Res*, **2012**, *9*, 178–183.

(50) Sankaranarayanan, S.; Holahan, M. A.; Colussi, D.; Crouthamel, M.-C.; Devanarayan, V.; Ellis, J.; Espeseth, A.; Gates, A. T.; Graham, S. L.; Gregro, A. R.; et al. First Demonstration of Cerebrospinal Fluid and Plasma A Beta Lowering with Oral Administration of a Beta-Site Amyloid Precursor Protein-Cleaving Enzyme 1 Inhibitor in Nonhuman Primates. *J. Pharmacol. Exp. Ther.* **2009**, *328*, 131–140.

(51) Kacker, P.; Bottegoni, G.; Cavalli, a. Computational Methods in the Discovery and Design of BACE-1 Inhibitors. *Curr. Med. Chem.* **2012**, *19*, 6095–6111.

(52) Goedert, M.; Klug, A. Tau Protein, the Paired Helical Filament of Alzheimer's Disease. *J Alzheimers Dis*, **2006**, 9(3Supl), 195-207.

(53) Dringenberg, H. C. Alzheimer's Disease: More than a "Cholinergic Disorder" - Evidence That Cholinergic-Monoaminergic Interactions Contribute to EEG Slowing and Dementia. *Behavioural Brain Research*, **2000**, *115*, 235–249.

(54) Garcia-Alloza, M.; Gil-Bea, F. J.; Diez-Ariza, M.; Chen, C. P. L. H.; Francis, P. T.; Lasheras, B.; Ramirez, M. J. Cholinergic-Serotonergic Imbalance Contributes to Cognitive and Behavioral Symptoms in Alzheimer's Disease. *Neuropsychologia* **2005**, *43*, 442–449.

(55) Binda, C.; Newton-Vinson, P.; Hubálek, F.; Edmondson, D. E.; Mattevi, A. Structure of Human Monoamine Oxidase B, a Drug Target for the Treatment of Neurological Disorders. *Nat. Struct. Biol.* **2002**, *9*, 22–26.

(56) Grimsby, J.; Lan, N. C.; Neve, R.; Chen, K.; Shih, J. C. Tissue Distribution of Human Monoamine Oxidase A and B mRNA. *J Neurochem* **1990**, *55*, 1166–1169.

(57) Youdim, M. B. H.; Weinstock, M. Therapeutic Applications of Selective and Non-Selective Inhibitors of Monoamine Oxidase A and B That Do Not Cause Significant Tyramine Potentiation. *Neurotoxicology*, **2004**, *25*, 243–250.

(58) Caraci, F.; Copani, A.; Nicoletti, F.; Drago, F. Depression and Alzheimer's Disease: Neurobiological Links and Common Pharmacological Targets. *Eur J Pharmacol*, **2010**, *626*, 64–71.

(59) Christen, Y. Oxidative Stress and Alzheimer Disease. *Am J Clin Nutr* **2000**, *71*, 621S–629S.

(60) Riederer, P.; Danielczyk, W.; Grünblatt, E. Monoamine Oxidase-B Inhibition in Alzheimer's Disease. *Neurotoxicology*, **2004**, *25*, 271–277.

(61) Morphy, R.; Kay, C.; Rankovic, Z. From Magic Bullets to Designed Multiple Ligands. *Drug Discov Today*, **2004**, *9*, 641–651.

(62) Morphy, R.; Rankovic, Z. Designed Multiple Ligands. An Emerging Drug Discovery Paradigm. *J. Med. Chem.*, **2005**, *48*, 6523–6543.

(63) Morphy, R.; Rankovic, Z. Fragments, Network Biology and Designing Multiple Ligands. *Drug Discov Today*, **2007**, *12*, 156–160.

(64) Cavalli, A.; Bolognesi, M. L.; Mìnarini, A.; Rosini, M.; Tumiatti, V.; Recanatini, M.; Melchiorre, C. Multi-Target-Directed Ligands to Combat Neurodegenerative Diseases. *J. Med. Chem.*, **2008**, *51*, 347–372.

(65) Lipinski, C. A.; Lombardo, F.; Dominy, B. W.; Feeney, P. J. Experimental and Computational Approaches to Estimate Solubility and Permeability in Drug Discovery and Development Settings. *Adv Drug Deliv Rev*, **2012**, *64*, 4–17.

(66) Ogura, H.; Kosasa, T.; Kuriya, Y.; Yamanishi, Y. Donepezil, a Centrally Acting Acetylcholinesterase Inhibitor, Alleviates Learning Deficits in Hypocholinergic Models in Rats. *Methods Find. Exp. Clin. Pharmacol.* **2000**, *22*, 89–95.

(67) Pang, Y. P.; Quiram, P.; Jelacic, T.; Hong, F.; Brimijoin, S. Highly Potent, Selective, and Low Cost Bis-Tetrahydroaminacrine Inhibitors of Acetylcholinesterase. Steps toward Novel Drugs for Treating Alzheimer's Disease. *J. Biol. Chem.* **1996**, *271*, 23646–23649.

(68) Piazzi, L.; Rampa, A.; Bisi, A.; Gobbi, S.; Belluti, F.; Cavalli, A.; Bartolini, M.; Andrisano, V.; Valenti, P.; Recanatini, M. 3-(4-{[benzyl(methyl)amino]methyl}-Phenyl)-6,7-Dimethoxy-2H-2-Chromenone (AP2238) Inhibits Both Acetylcholinesterase and Acetylcholinesterase-Induced β-Amyloid Aggregation: A Dual Function Lead for Alzheimer's Disease Therapy. *J. Med. Chem.* **2003**, *46*, 2279–2282.

(69) Muñoz-Ruiz, P.; Rubio, L.; García-Palomero, E.; Dorronsoro, I.; Del Monte-Millán, M.; Valenzuela, R.; Usán, P.; De Austria, C.; Bartolini, M.; Andrisano, V.; et al. Design, Synthesis, and Biological Evaluation of Dual Binding Site Acetylcholinesterase Inhibitors: New Disease-Modifying Agents for Alzheimer's Disease. *J. Med. Chem.* **2005**, *48*, 7223–7233.

(70) Galdeano, C.; Viayna, E.; Sola, I.; Formosa, X.; Camps, P.; Badia, A.; Clos, M. V.; Relat, J.; Ratia, M.; Bartolini, M.; et al. Huprine-Tacrine Heterodimers as Anti-Amyloidogenic Compounds of Potential Interest against Alzheimer's and Prion Diseases. *J. Med. Chem.* **2012**, *55*, 661–669.

(71) Camps, P.; Formosa, X.; Galdeano, C.; Muñoz-Torrero, D.; Ramírez, L.; Gómez, E.; Isambert, N.; Lavilla, R.; Badia, A.; Clos, M. V.; et al. Pyrano[3,2-C]quinoline-6-Chlorotacrine Hybrids as a Novel Family of Acetylcholinesterase- and Beta-Amyloid-Directed Anti-Alzheimer Compounds. *J. Med. Chem.* **2009**, *52*, 5365–5379.

(72) Sterling, J.; Herzig, Y.; Goren, T.; Finkelstein, N.; Lerner, D.; Goldenberg, W.; Miskolczi, I.; Molnar, S.; Rantal, F.; Tamas, T.; et al. Novel Dual Inhibitors of AChE and MAO Derived from Hydroxy Aminoindan and Phenethylamine as Potential Treatment for Alzheimer's Disease. *J. Med. Chem.* **2002**, *45*, 5260–5279.

(73) Goelman, G.; Ilinca, R.; Zohar, I.; Weinstock, M. Functional Connectivity in Prenatally Stressed Rats with and without Maternal Treatment with Ladostigil, a Brain-Selective Monoamine Oxidase Inhibitor. *Eur. J. Neurosci.* **2014**, n/a–n/a.

(74) Cavalli, A.; Bolognesi, M. L.; Capsoni, S.; Andrisano, V.; Bartolini, M.; Margotti, E.; Cattaneo, A.; Recanatini, M.; Melchiorre, C. A Small Molecule Targeting the Multifactorial Nature of Alzheimer's Disease. *Angew. Chemie - Int. Ed.* **2007**, *46*, 3689–3692.

(75) Wang, J.; Wolf, R. M.; Caldwell, J. W.; Kollman, P. A.; Case, D. A. Development and Testing of a General Amber Force Field. *J. Comput. Chem.* **2004**, *25*, 1157–1174.

(76) Hornak, V.; Abel, R.; Okur, A.; Strockbine, B.; Roitberg, A.; Simmerling, C. Comparison of Multiple Amber Force Fields and Development of Improved Protein Backbone Parameters. *Proteins.* **2006**, *65*, 712–725.

(77) Lindorff-Larsen, K.; Piana, S.; Palmo, K.; Maragakis, P.; Klepeis, J. L.; Dror, R. O.; Shaw, D. E. Improved Side-Chain Torsion Potentials for the Amber ff99SB Protein Force Field. *Proteins,* **2010**, *78*, 1950–1958.

(78) Corzana, F.; Cuesta, I.; Bastida, A.; Hidalgo, A.; Latorre, M.; González, C.; García-Junceda, E.; Jiménez-Barbero, J.; Asensio, J. L. Molecular Recognition of Aminoglycoside Antibiotics by Bacterial Defence Proteins: NMR Study of the Structural and Conformational Features of Streptomycin Inactivation by Bacillus Subtilis Aminoglycoside-6-Adenyl Transferase. *Chem. - A Eur. J.* **2005**, *11*, 5102–5113.

(79) Blundell, C. D.; Packer, M. J.; Almond, A. Quantification of Free Ligand Conformational Preferences by NMR and Their Relationship to the Bioactive Conformation. *Bioorganic Med. Chem.* **2013**, *21*, 4976–4987.

(80) Neville, G. A.; Deslauriers, R.; Blackburn, B.; Smith, I. C. P. Conformational Studies of Amphetamine and Medicinally Important Derivatives by Nuclear Magnetic Resonance Spectroscopy. *J. Med. Chem.* **1971**, *14*, 717–721.

(81) Bright, S.; Platano, J.; Jacobus, J. Amphetamine. Specific Labeling and Solution Conformation. *J. Org. Chem.* **1973**, *38*, 2554–2555.

(82) Berg, R. W.; Shim, I.; White, P. C.; Abdali, S. Raman Optical Activity and Raman Spectra of Amphetamine Species — Quantum Chemical Model Calculations and Experiments. *Am. J. Anal. Chem.* **2012**, *2012*, 410–421.

(83) Godfrey, P. D.; Hatherley, L. D.; Brown, R. D.; April, R. The Shapes of Neurotransmitters by Millimeter-Wave Spectroscopy : 2-Phenylethylamine. *J. Am. Chem. Soc.* **1995**, *117*, 8204–8210.

(84) Godfrey, P. D.; McGlone, S. J.; Brown, R. D. The Shapes of Neurotransmitters by Millimetrewave Spectroscopy: Amphetamine. *J. Mol. Struct.* **2001**, *599*, 139–152.

(85) Ison, R. R.; Partington, P.; Roberts, G. C. K. The Conformation of Catecholamines and Related Compounds in Solution. *Mol. Pharmacol.* **1973**, *9*, 756–765.

(86) Melandri, S.; Ragno, S.; Maris, A. Shape of Biomolecules by Free Jet Microwave Spectroscopy: 2-Amino-1-Phenylethanol and 2-Methylamino-1-Phenylethanol. *J. Phys. Chem. A* **2009**, *113*, 7769–7773.

(87) Graham, R. J.; Kroemer, R. T.; Mons, M.; Robertson, E. G.; Snoek, L. C.; Simons, J. P. Infrared Ion Dip Spectroscopy of a Noradrenaline Analogue: Hydrogen Bonding in 2-Amino-1-Phenylethanol and Its Singly Hydrated Complex. *J. Phys. Chem.* **1999**, *103*, 9706–9711.

(88) Snoek, L. C.; Van Mourik, T.; Simons, J. P. Neurotransmitters in the Gas Phase: A Computational and Spectroscopic Study of Noradrenaline. *Mol. Phys.* **2003**, *101*, 1239–1248.

(89) Çarçabal, P.; Snoek *, L. C.; Van Mourik, T. A Computational and Spectroscopic Study of the Gas-Phase Conformers of Adrenaline. *Mol. Phys.* **2005**, *103*, 1633–1639.

(90) Mourik, T. Van. The Shape of Neurotransmitters in the Gas Phase: A Theoretical Study of Adrenaline, Pseudoadrenaline, and Hydrated Adrenaline. *Phys. Chem. Chem. Phys.* **2004**.

(91) Dvir, H.; Wong, D. M.; Harel, M.; Barril, X.; Orozco, M.; Luque, F. J.; Muñoz-Torrero, D.; Camps, P.; Rosenberry, T. L.; Silman, I.; et al. 3D Structure of Torpedo Californica Acetylcholinesterase Complexed with Huprine X at 2.1 Å Resolution: Kinetic and Molecular Dynamic Correlates. *Biochemistry* **2002**, *41*, 2970–2981.

(92) Barril, X.; Orozco, M.; Luque, F. J. Predicting Relative Binding Free Energies of Tacrine-Huperzine A Hybrids as Inhibitors of Acetylcholinesterase. *J. Med. Chem.* **1999**, *42*, 5110–5119.

(93) Camps, P.; El Achab, R.; Morral, J.; Munoz-Torrero, D.; Badia, A.; Eladi Banos, J.; Vivas, N. M.; Barril, X.; Orozco, M.; Javier Luque, F. New Tacrine-Huperzine A Hybrids (huprines): Highly Potent Tight-Binding Acetylcholinesterase Inhibitors of Interest for the Treatment of Alzheimer's Disease. *J. Med. Chem.* **2000**, *43*, 4657–4666.

(94) Camps, P.; Formosa, X.; Galdeano, C.; Gómez, T.; Muñoz-Torrero, D.; Scarpellini, M.; Viayna, E.; Badia, A.; Clos, M. V.; Camins, A.; et al. Novel Donepezil-Based Inhibitors of Acetyl- and Butyrylcholinesterase and Acetylcholinesterase-Induced B-Amyloid Aggregation. *J. Med. Chem.* **2008**, *51*, 3588–3598.

(95) Alonso, D.; Dorronsoro, I.; Rubio, L.; Muñoz, P.; García-Palomero, E.; Del Monte, M.; Bidon-Chanal, A.; Orozco, M.; Luque, F. J.; Castro, A.; et al. Donepezil-Tacrine Hybrid Related Derivatives as New Dual Binding Site Inhibitors of AChE. *Bioorganic Med. Chem.* **2005**, *13*, 6588–6597.

(96) Viayna, E.; Gómez, T.; Galdeano, C.; Ramírez, L.; Ratia, M.; Badia, A.; Clos, M. V.; Verdaguer, E.; Junyent, F.; Camins, A.; et al. Novel Huprine Derivatives with Inhibitory Activity toward B-Amyloid Aggregation and Formation as Disease-Modifying Anti-Alzheimer Drug Candidates. *ChemMedChem* **2010**, *5*, 1855–1870.

(97) Pérez, V.; Marco, J. L.; Fernández-Alvarez, E.; Unzeta, M. Relevance of Benzyloxy Group in 2-Indolyl Methylamines in the Selective MAO-B Inhibition. *Br. J. Pharmacol.* **1999**, *127*, 869–876.

(98) Kryger, G.; Silman, I.; Sussman, J. L. Structure of Acetylcholinesterase Complexed with E2020 (Aricept): Implications for the Design of New Anti-Alzheimer Drugs. *Structure* **1999**, *7*, 297–307.

(99) Bourne, Y.; Kolb, H. C.; Radić, Z.; Sharpless, K. B.; Taylor, P.; Marchot, P. Freeze-Frame Inhibitor Captures Acetylcholinesterase in a Unique Conformation. *Proc. Natl. Acad. Sci. U. S. A.* **2004**, *101*, 1449–1454.

(100) Rydberg, E. H.; Brumshtein, B.; Greenblatt, H. M.; Wong, D. M.; Shaya, D.; Williams, L. D.; Carlier, P. R.; Pang, Y. P.; Silman, I.; Sussman, J. L. Complexes of Alkylene-Linked Tacrine Dimers with Torpedo Californica Acetylcholinesterase: Binding of bis(5)-Tacrine Produces a Dramatic Rearrangement in the Active-Site Gorge. *J. Med. Chem.* **2006**, *49*, 5491–5500.

(101) Caille, D.; Bergis, O. E.; Fankhauser, C.; Gardes, A.; Adam, R.; Charieras, T.; Grosset, A.; Rovei, V.; Jarreau, F. X. Befloxatone, a New Reversible and Selective Monoamine Oxidase-A Inhibitor. II. Pharmacological Profile. *J. Pharmacol. Exp. Ther.* **1996**, *277*, 265–277.

(102) Bonnet, U. Moclobemide: Therapeutic Use and Clinical Studies. *CNS Drug Rev.* **2003**, *9*, 97–140.

(103) Valente, S.; Tomassi, S.; Tempera, G.; Saccoccio, S.; Agostinelli, E.; Mai, A. Novel Reversible Monoamine Oxidase A Inhibitors: Highly Potent and Selective 3-(1H-Pyrrol-3-Yl)-2-Oxazolidinones. *J. Med. Chem.* **2011**, *54*, 8228–8232.

(104) Abdelhafez, O. M.; Amin, K. M.; Ali, H. I.; Abdalla, M. M.; Batran, R. Z. Synthesis of New 7-Oxycoumarin Derivatives as Potent and Selective Monoamine Oxidase A Inhibitors. *J. Med. Chem.* **2012**, *55*, 10424–10436.

(105) Ramadan, Z. B.; Dostert, P.; Tipton, K. F. Some Peculiar Aspects of Monoamine Oxidase Inhibition. *Neurobiology (Bp).* **1999**, *7*, 159–174.

(106) Ramadan, Z. Ben; Wrang, M. L.; Tipton, K. F. Species Differences in the Selective Inhibition of Monoamine Oxidase (1-Methyl-2-Phenylethyl)hydrazine and Its Potentiation by Cyanide. *Neurochem. Res.* **2007**, *32*, 1783–1790.

(107) Ramsay, R. R.; Hunter, D. J. B. Inhibitors Alter the Spectrum and Redox Properties of Monoamine Oxidase A. *Biochim. Biophys. Acta - Proteins Proteomics* **2002**, *1601*, 178–184.

(108) Jones, T. Z. E.; Fleming, P.; Eyermann, C. J.; Gravestock, M. B.; Ramsay, R. R. Orientation of Oxazolidinones in the Active Site of Monoamine Oxidase. *Biochem. Pharmacol.* **2005**, *70*, 407–416.

(109) Hynson, R. M. G.; Wouters, J.; Ramsay, R. R. Monoamine Oxidase A Inhibitory Potency and Flavin Perturbation Are Influenced by Different Aspects of Pirlindole Inhibitor Structure. *Biochem. Pharmacol.* **2003**, *65*, 1867–1874.

(110) Binda, C.; Aldeco, M.; Mattevi, A.; Edmondson, D. E. Interactions of Monoamine Oxidases with the Antiepileptic Drug Zonisamide: Specificity of Inhibition and Structure of the Human Monoamine Oxidase B Complex. *J. Med. Chem.* **2011**, *54*, 909–912.

(111) Pickhardt, M.; Gazova, Z.; Von Bergen, M.; Khlistunova, I.; Wang, Y.; Hascher, A.; Mandelkow, E. M.; Biernat, J.; Mandelkow, E. Anthraquinones Inhibit Tau Aggregation and Dissolve Alzheimer's Paired Helical Filaments in Vitro and in Cells. *J. Biol. Chem.* **2005**, *280*, 3628–3635.

(112) Bulic, B.; Pickhardt, M.; Schmidt, B.; Mandelkow, E. M.; Waldmann, H.; Mandelkow, E. Development of Tau Aggregation Inhibitors for Alzheimer's Disease. *Angew Chem Int Ed Engl*, **2009**, *48*, 1740–1752.

(113) May, P. C.; Dean, R. A.; Lowe, S. L.; Martenyi, F.; Sheehan, S. M.; Boggs, L. N.; Monk, S. A.; Mathes, B. M.; Mergott, D. J.; Watson, B. M.; et al. Robust

Central Reduction of Amyloid-Beta in Humans with an Orally Available, Non-Peptidic Beta-Secretase Inhibitor. *J. Neurosci.* **2011**, *31*, 16507–16516.

(114) Schmidtke, P.; Bidon-Chanal, A.; Luque, F. J.; Barril, X. MDpocket: Open-Source Cavity Detection and Characterization on Molecular Dynamics Trajectories. *Bioinformatics* **2011**, *27*, 3276–3285.

(115) Hong, L.; Turner, R. T.; Koelsch, G.; Shin, D.; Ghosh, A. K.; Tang, J. Crystal Structure of Memapsin 2 (β-Secretase) in Complex with an Inhibitor OM00-3. *Biochemistry* **2002**, *41*, 10963–10967.

(116) Hong, L.; Tang, J. Flap Position of Free Memapsin 2 (β-Secretase), a Model for Flap Opening in Aspartic Protease Catalysis. *Biochemistry* **2004**, *43*, 4689–4695.

(117) Murray, C. W.; Callaghan, O.; Chessari, G.; Cleasby, A.; Congreve, M.; Frederickson, M.; Hartshorn, M. J.; McMenamin, R.; Patel, S.; Wallis, N. Application of Fragment Screening by X-Ray Crystallography to Beta-Secretase. *J. Med. Chem.* **2007**, *50*, 1116.

(118) Cumming, J. N.; Le, T. X.; Babu, S.; Carroll, C.; Chen, X.; Favreau, L.; Gaspari, P.; Guo, T.; Hobbs, D. W.; Huang, Y.; et al. Rational Design of Novel, Potent Piperazinone and Imidazolidinone BACE1 Inhibitors. *Bioorganic Med. Chem. Lett.* **2008**, *18*, 3236–3241.

Anexo

I Otras publicaciones

1. M.D. Duque, C. Ma, E. Torres, J. Wang, L. Naessens, J. Juárez-Jiménez, P. Camps , F.J. Luque, W.F. DeGrado, R.A. Lamb, L.H. Pinto, S. Vazquez.
Exploring the size limit of templates for inhibitors of the M2 ion channel of influenza A virus.
Journal of Medicinal Chemistry, **2011**, 54(8) 2646.
DOI: 10.1021/jm101334y

2. S. Llabres, J. Juárez-Jiménez, F. Forti, R. Pouplana, F.J. Luque .
Recognition of ligands by macromolecular targets in Physico-Chemical and Computational Approaches to Drug Discovery, Royal Society of Chemistry (**2012**)

3. O. Di Pietro, E. Viayna, E. Vicente-García, M. Bartolini, R. Ramón, J. Juárez-Jiménez, M.V. Clos, B. Pérez, V. Andrisano, F.J. Luque, R. Lavilla, D. Muñoz-Torrero.
1,2,3,4-Tetrahydrobenzo[h][1,6]naphthyridines as a new family of potent peripheral-to-midgorge-site inhibitors of acetylcholinesterase: Synthesis, pharmacological evaluation and mechanistic studies.
European Journal of Medicinal Chemistry, **2014**, 73(12), 141.
DOI:10.1016/j.ejmech.2013.12.008

4. M. Rey-Carrizo, M. Barniol-Xicota, C Ma, M Frigolé-Vivas, E. Torres, L. Naessens, S. Llabrés, J. Juárez-Jiménez, F.J. Luque, W. DeGrado, R. Lamb, L. Pinto, S. Vázquez.
Easily Accessible Polycyclic Amines as Inhibitors of the Amantadine-Resistant V27A and L26F Mutants of the M2 Channel of Influenza A Virus
Journal of Medicinal Chemistry, **2014,** 57, 5738**.**
DOI: 10.1021/jm5005804

5. O. Di Pietro, F.J. Pérez-Areales, A. Espargaró, M.V. Clos, B. Pérez, J. Juárez-Jiménez, R. Lavilla, R. Sabaté, F.J. Luque, D. Muñoz-Torrero.
Tetrahydrobenzo[h][1,6]naphthyridine-6-chlorotacrine hybrids as a new family of anti-Alzheimer agents targeting beta-amyloid, tau, and cholinesterase pathologies
European Journal of Medicinal Chemistry, **2014,** 84, 107
DOI: 10.1016/j.ejmech.2014.07.021

6. P. Delcanale, B. Rodríguez-Amigo, G. Rotger, J. Juárez-Jiménez, S. Abbruzzeti, A. Summer, M. Agut, F.J. Luque, S. Nonell, C. Viappiani.

The complex of hypericin with β- lactoglobulin has antimicrobial activity with perspective applications in dairy industry

Journal of Dairy Science, **en prensa.**

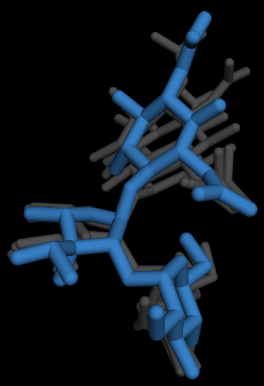

Departament de Fisicoquímica
Facultat de Farmàcia

Universitat de Barcelona